

Earth Pressure Balance (EPB) Shield Tunneling in Bangkok: Ground Response and Prediction of Surface Settlements Using Artificial Neural Networks

by

Suchatvee Suwansawat

Bachelor of Engineering in Civil Engineering (1994)
King Mongkut's Institute of Technology Ladkrabang, Bangkok, Thailand

Master of Science in Civil and Environmental Engineering (1997)
The University of Wisconsin-Madison, Madison, USA

Submitted to the Department of Civil and Environmental Engineering
in Partial Fulfillment of the Requirements for the degree of

Doctor of Science in Civil and Environmental Engineering

at the

Massachusetts Institute of Technology
June 2002

© 2002 Massachusetts Institute of Technology
All rights reserved.

Signature of Author.....



Department of Civil and Environmental Engineering
May 27, 2002

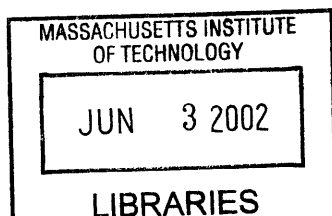
Certified by.....

Prof. Herbert H. Einstein
Professor of Civil and Environmental Engineering
Thesis Supervisor

Accepted by.....



Prof. Oral Buyukozturk
Chairman, Departmental Committee on Graduate Studies



BARKER

Earth Pressure Balance (EPB) Shield Tunneling in Bangkok: Ground Response and Prediction of Surface Settlements Using Artificial Neural Networks

by

Suchatvee Suwansawat

Submitted to the Department of Civil and Environmental Engineering
on May 27, 2002, in Partial Fulfillment of the Requirements for the degree of
Doctor of Science in Civil and Environmental Engineering

ABSTRACT

Although Earth Pressure Balance (EPB) shields have been used for several decades, very little information exists about the actual mechanisms of shield-ground interaction. The ground response mechanism induced by EPB tunneling is difficult to understand, because this requires not only reliable ground deformation measurements in the field but also operational records of the shield. Numerous empirical and analytical relations between characteristics of traditional shields and surface and subsurface deformations exist; also 2-D and 3-D numerical analyses have been applied to such tunneling problems. However, very few approaches have been developed for EPB tunneling.

This research makes use of the fact that in the Bangkok MRTA project, data on ground deformation and shield operation were collected. The tunnel sizes are practically identical and the subsurface conditions over long distances are comparable, which allow one to establish relationships between ground characteristics and EPB-operation on the one hand, and surface and subsurface deformations on the other hand. A computerized database, which records much of the information on a ring-by-ring (1.2 meter interval) basis, was developed for this purpose. After using the information to identify which ground- and EPB-characteristic have the greatest influence on ground movements, an approach based on Artificial Neural Networks (ANN) was used to develop predictive relations.

Since the method has the ability to map input to output patterns, ANN enable one to map all influencing parameters to surface settlements. Combining the extensive computerized database and the knowledge of what influences the surface settlements, ANN can become a useful predictive method. This research attempts to evaluate the potential as well as the limitations of ANN for predicting surface settlements caused by EPB shield tunneling and to develop optimal neural network models for this purpose. Specifically, this involves settlement predictions over the tunnel axes of single and twin tunnels; together with other interpretations, it is also possible to predict settlement troughs. Other shield effects such as lateral deformation and liner deformation of the first tunnel caused by the second tunnel are also evaluated.

Thesis supervisor:

Prof. Herbert H. Einstein, Professor of Civil and Environmental Engineering

Dedicated to my beloved country
THAILAND

ACKNOWLEDGEMENTS

My journey at MIT has been a unique experience. There have been so many things I have learned and so many people I have gotten to know. And this alone has made my life here memorable. Firstly, it has been my true honor to work with Prof. Herbert H. Einstein. He is great both as a teacher and supervisor. Prof. Einstein has always believed in my potential and has always supported my initiative. Without his vision, effort and encouragement, this thesis could never have reached completion. I also owe a heart felt thanks to Dr. John T. Germaine, Prof. Charles C. Ladd, and Prof. Andrew J. Whittle, who served as my thesis committee. Their expertise significantly shaped this thesis.

I am indebted to the Royal Thai Government for providing financial support for my excellent education at MIT. I am grateful to MRTA for supporting me for the one year I worked on the tunnel project. In this regard, I am deeply indebted to Mr. Chukiat Photayanuvat, who has supported my research since the beginning. He has contributed significantly to this work. I wish to thank Dr. Doug Maconochie who provided me with some excellent engineering practices. I am also grateful to Mr. Pairoj Podpong, who supported my work at CSC1. I wish to express my appreciation to Mr. Shinnavat Chanchaya and Mr. Vasin Kiattikomol, who helped me in creating the tunnel database. I also thank all my colleagues from the various parties in the project, for their support during that year.

I would like to thank my officemates, Jean Louis Locsin and Karim Karam. They made my office a great work environment. My special appreciation is extended to my colleagues: Maria Nikolinakou, N. Kartal Toker, and other Geotech people. Their friendship means a great deal to me. My gratitude also goes to Yo-Ming Hsieh, my friend who always helped me in solving several computer problems. I would like to thank my Thai friends here at MIT and Boston, who have made my life here very enjoyable, in particular, Sakda Chaiworawitkul and Attasit Korchaiyapruk who have always provided me great emotional and technical support. Special thanks go to all the people who came to support me at my doctoral defense and helped make it a memorable and successful event.

I wish to thank Carol L. Frederick at Baker Library for encouraging me every time I needed it. I sincerely appreciate the kind advice of Cynthia Stewart and Sydney Miller as well as the help of Alice Kalemkarian and Carolyn Jundzilo-Comer during my study here.

My special appreciation goes to Rushani Wirasinghe, my sweetest friend who always stood beside me. Her love, strength, and wisdom have inspired me to be the best I can be through many difficult times. Finally, I owe my deepest gratitude to my parents, Teerasak and Vallee Suwansawat; their love is the greatest power in the world and has driven me to succeed in every goal I have dreamed of.

Suchatvee (Vince) Suwansawat
May 2002

TABLE OF CONTENTS

List of Figures..... 15

List of Tables.....33

CHAPTER 1

Introduction.....35

1.1 Background.....35

1.2 Problem Identification.....38

1.3 Research Objectives.....39

1.4 Outline of Thesis.....40

References.....41

CHAPTER 2

Earth Pressure Balance (EPB) Shield Tunneling Method.....43

2.1 Historical Development of Shield Tunneling.....43

2.2 Different Types of Shields.....49

2.3 Earth Pressure Balance Shield.....55

2.3.1 Introduction.....55

2.3.2 Excavation.....57

2.3.3 Tunnel Lining.....62

2.3.4 Segment Erection.....62

2.3.5 Tail Void Grouting.....71

2.3.6 Guidance System.....75

References.....79

CHAPTER 3

Review of Ground Response Induced by Shield Tunneling and Methods of Prediction.....81

3.1 Introduction.....81

3.2 Methods of Predicting Ground Deformation.....86

3.2.1 Stochastic and Empirical Methods.....89

3.2.1.1 Litwinniszyn (1956).....89

3.2.1.2 Peck (1969).....93

3.2.1.3 O'Reilly and New (1982).....95

3.2.1.4 Attewell and Woodman (1982).....103

3.2.2 Analytical Solutions.....106

3.2.2.1 Verruijt and Booker (1996).....106

3.2.2.2 Loganathan and Poulos (1998, 1999).....109

3.2.2.3 Pinto (1999).....120

3.2.3 Finite Element and Numerical Methods.....123

3.2.4 Laboratory Experiments.....131

3.2.4.1 Atkinson and Potts (1977).....131

3.2.4.2 Kimura and Mair (1981).....136

3.2.4.3 Nomoto et al. (1999).....	142
3.3 Summary.....	146
References.....	149

CHAPTER 4

Case Histories of Shield Tunneling.....	153
4.1 Introduction.....	153
4.2 Washington Metropolitan Area Transit Authority Project (WMATA).....	154
4.3 Taipei Rapid Transit Systems (TRTS).....	163
4.4 San Francisco Clean Water Project.....	168
4.5 Fukuoka City Subway Project.....	176
4.6 Milan Subway Project.....	180
4.7 Summary.....	186
References.....	189

CHAPTER 5

The Chaleom Ratchamongkhon Line, Bangkok MRTA Project.....	191
5.1 Project Background.....	191
5.2 Geological Background.....	194
5.2.1 Introduction.....	194
5.2.2 Geographical Setting.....	194
5.2.3 Bedrock Geology.....	197
5.2.4 Drift Deposits.....	197
5.2.5 Hydrology.....	199
5.2.6 Consolidation Settlement.....	203
5.3 Subsurface Conditions.....	205
5.3.1 Made Ground (Fill)	205
5.3.2 Bangkok Soft Clay.....	206
5.3.3 First Stiff Clay.....	207
5.3.4 Bangkok Aquifer.....	208
5.4 Tunneling of the MRTA Project.....	210
5.4.1 Earth Pressure Balance (EPB) Shield.....	210
5.4.2 Tunneling Methodology.....	216
5.5 Tunnel Drive Details.....	223
5.5.1 Tunneling Section A.....	223
5.5.2 Tunneling Section B.....	231
5.5.3 Tunneling Section C.....	237
5.5.4 Tunneling Section D.....	247
References.....	254

CHAPTER 6

Computerized Database Management.....	255
6.1 Introduction.....	255
6.2 Instrumentation Database.....	256
6.3 Operational Parameter Database.....	264

CHAPTER 7

Analysis of Observed Ground Response to EPB Tunneling on the MRTA Project

	269	
7.1	Introduction.....	269
7.2	Surface Settlements.....	271
7.2.1	Longitudinal Surface Settlements.....	273
7.2.1.1	Settlements in Section A.....	273
7.2.1.2	Settlements in Section B.....	285
7.2.1.3	Settlements in Section C.....	290
7.2.1.4	Settlements in Section D.....	294
7.2.2	Transverse Surface Settlements.....	303
7.3	Lateral Ground Deformations.....	330
7.4	Summary.....	344
	References.....	346

CHAPTER 8

Effect of the Second Tunnel on the First Tunnel

	347	
8.1	Introduction.....	347
8.2	Settlements above Twin Tunnels excavated Side-by-Side.....	348
8.3	Comparison with Predictive Methods.....	371
8.3.1	Symmetric Curve over the Twin Tunnels.....	371
8.3.2	Superposition Curve.....	377
8.3.3	Interaction between Twin Tunnels.....	385
8.4	Settlements above Stacked Tunnels.....	398
8.5	Summary.....	404
	References.....	405

CHAPTER 9

Analyses of Parameters Influencing Surface Settlements

	407	
9.1	Introduction.....	407
9.2	Face Pressure.....	408
9.3	Penetration Rate.....	416
9.4	Pitching Angle.....	419
9.5	Grouting Quality.....	420
9.6	Distance from Launching Station.....	425
9.7	Tunnel Depth.....	427
9.8	Geological Conditions.....	429
9.9	Summary.....	430
	References.....	431

CHAPTER 10

Artificial Neural Networks

	433	
10.1	Introduction.....	433
10.1.1	Biological Neurons.....	434
10.1.2	Artificial Neuron Networks (ANN).....	437

10.2	Type of Neural Networks.....	438
10.2.1	Feedforward Networks.....	438
10.2.2	Recurrent Networks.....	443
10.3	Neural Network Modeling.....	446
10.4	Learning Processes Using Back-Propagation Algorithm.....	452
10.5	Number of Hidden Neurons in Neural Networks.....	463
10.6	Number of Samples in Training Set.....	465
10.7	Overfitting.....	468
	References.....	470

CHAPTER 11

	Pilot Experiment and Network Validation.....	471
11.1	Introduction.....	471
11.2	Factors Affecting Surface Settlements.....	472
11.3	Development of the Neural Network Model.....	475
11.3.1	Sample and Subsample Selection.....	477
11.3.2	Neural Network Design.....	483
11.4	Model Validation.....	486
11.4.1	Training and Testing Results.....	494
11.4.2	Effect of Training Epoch.....	496
11.4.3	Effect of Hidden Layers and Hidden Nodes.....	499
11.5	Summary.....	502
	References.....	503

CHAPTER 12

	Applications of Artificial Neural Networks (ANN) on the MRTA Project.....	505
12.1	Introduction.....	505
12.2	Prediction of Maximum Surface Settlements induced by a Single Tunnel.....	506
12.2.1	Scenario 1: Trained with samples recorded from Section A for predicting settlements in other tunnel sections.....	506
12.2.1.1	Settlement Prediction in Section B.....	508
12.2.1.2	Settlement Prediction in Section C.....	512
12.2.1.3	Settlement Prediction in Section D.....	513
12.2.2	Scenario 2: Trained and tested with samples recorded from the same tunnel section.....	520
12.2.2.1	Settlement Prediction in Section B.....	520
12.2.2.2	Settlement Prediction in Section C.....	520
12.2.2.3	Settlement Prediction in Section D.....	521
12.2.3	Scenario 3: Trained and tested with samples recorded from Sections A and B (North Section).....	523
12.2.4	Scenario 4: Trained and tested with samples recorded from Sections A, B, and C.....	524
12.2.5	Scenario 5: Trained and tested with samples recorded from all Sections.....	526

12.2.6	Scenario 6: Trained and tested with samples recorded from all Sections (adding shield model node).....	526
12.2.7	Scenario 7: Reduction of input parameter nodes.....	529
12.2.7.1	Neural network model without the penetration rate input node	529
12.2.7.2	Neural network model without the grouting quality input nodes	533
12.2.7.3	Neural network model without the face pressure input node	536
12.2.8	Scenario 8: Settlement Prediction by Training Data Recorded at the Beginning of the Tunnel Drive.....	540
12.2.9	Scenario 9: Predicting surface settlements in Zone 2.....	553
12.2.10	Scenario 10: Predicting surface settlements in Zone 1.....	553
12.2.11	Result Summary of Scenarios 1 to 10.....	557
12.3	Prediction of Surface Settlements induced by EPB Tunneling in Clay.....	560
12.4	Prediction of Surface Settlements induced by Twin Tunnels.....	575

CHAPTER 13

	Summary, Conclusions, and Recommendations.....	589
13.1	Summary.....	589
13.2	Conclusions.....	592
13.3	Recommendations.....	595
	VITA.....	597

LIST OF FIGURES

Figure 1.1 MRTA Chaloeem Ratchamongkhon Line.....	36
Figure 2.1 Marc Brunel’s “screw” shield (1818).....	45
Figure 2.2 Marc Brunel’s “compartment” shield (1818).....	45
Figure 2.3 Marc Brunel’s shield for the tunnel underneath the Thames (1825-1843)...	46
Figure 2.4 Different measures of face supporting (after Maidl et al., 1996).....	50
Figure 2.5 Partial face shield (Herrenknecht).....	51
Figure 2.6 Open-faced shield used in Trans-Bay tube project (1969).....	52
Figure 2.7 Compressed air shield used in the express subway tunnel in Paris (1964)...	52
Figure 2.8 Slurry shield used for the construction of Mexico City sewer tunnel (1969)	53
Figure 2.9 EPB shield used in the Singapore MRT project.....	53
Figure 2.10 Mix shield used in the Fourth Elb Tunnel project, Germany.....	54
Figure 2.11 Blind shield manufactured by Mitsubishi.....	54
Figure 2.12 Earth Pressure Balance shield introduced by Sato Kogyo (1963).....	56
Figure 2.13 Belt conveyor transporting excavated soil from the screw conveyor (Bangkok-MRTA).....	58
Figure 2.14 Muck pumping pipe connecting directly to screw conveyor (Bangkok- MRTA)	59
Figure 2.15 Locomotive transporting excavated soil out of tunnel (Bangkok-MRTA)	59
Figure 2.16 Tunnel monitoring work flowchart.....	60
Figure 2.17 Shield operators monitoring all operational parameters during excavation	61
Figure 2.18 Hydraulic jacks behind the EPB shield.....	64
Figure 2.19 Hydraulic jacks push against installed lining during shield advancing.....	64
Figure 2.20 The Bangkok MRTA Project, reinforced concrete segmental lining.....	65
Figure 2.21 Segmental lining storage (Bangkok-MRTA, Thiam Ruam Mit Station)...	65
Figure 2.22 Schematic diagram showing a tail void between tunnel lining and the shield	66
Figure 2.23 Expanded segmental lining.....	67
Figure 2.24 Erector arm erecting a segment with the designated location.....	68
Figure 2.25 Connection of segments with curve bolt.....	68
Figure 2.26 Curve bolt.....	69
Figure 2.27 Worker securing a curve bolt between segments.....	69
Figure 2.28 Worker checking the position of the installed lining ring.....	70
Figure 2.29 Segment transferred to the erector via the tunnel invert.....	70
Figure 2.30 Tailskin seal (wire brush seal)	73
Figure 2.31 Grout injected through grout holes in the segmental lining.....	73
Figure 2.32 Grout as a mixing material between Material A and Material B.....	74
Figure 2.33 Components of the guidance system.....	76
Figure 2.34 Laser theodolite installed at lining ring behind the EPB shield.....	77
Figure 2.35 Laser target fixed behind the EPB shield.....	77
Figure 2.36 Shield driving monitoring system.....	78

Figure 2.37	Guidance information system in the control room.....	78
Figure 3.1	The collapse of the tunnel underneath the Thames River in 1828 (Maidl et al. 1996)	82
Figure 3.2	Ground loss at the shield face.....	83
Figure 3.3	Ground loss due to over-cutting.....	83
Figure 3.4	Ground loss due to pitching.....	84
Figure 3.5	Ground loss due to ground disturbance.....	84
Figure 3.6	Ground loss due to tail void closing.....	84
Figure 3.7	Typical ground deformation induced by shield tunneling.....	87
Figure 3.8	Surface heave ahead of the shield due to a positive volume balance.....	87
Figure 3.9	The settlement process modeled stochastically (after Attewell, 1978).....	90
Figure 3.10	Definitions of width $2a$ and closure thickness t	90
Figure 3.11	Normal probability curve used to described transverse settlement trough..	94
Figure 3.12	Relation between settlement trough width parameter and tunnel depth for different ground condition (details including data from actual projects are provided in Peck, 1969)	94
Figure 3.13	Soil deformation around model tunnel in clay (after Kimura and Mair, 1981)	97
Figure 3.14	Variation in trough width parameter of tunnels in clays.....	98
Figure 3.15	Soil deformations around tunnel in sand (after Potts, 1976).....	101
Figure 3.16	Soil deformations around tunnel in sand (after Cording et al., 1976).....	101
Figure 3.17	Generation of transverse settlement profile in sand (after Cording and Hansmire, 1975)	102
Figure 3.18	Longitudinal surface settlement caused by shield tunneling.....	103
Figure 3.19	Tunnel coordination system for longitudinal surface settlement (after Attewell and Woodman, 1982)	104
Figure 3.20	Longitudinal surface settlement shape proposed by Attewell and Woodman (1982)	106
Figure 3.21	Virtual image technique (after Sagasetta, 1987)	107
Figure 3.22	Ground loss and ovalization after Verruijt and Booker (1996)	109
Figure 3.23	Oval-shaped ground deformation around tunnel section.....	110
Figure 3.24	Simulation of ground loss (gap parameter), after Lee et al. (1992).....	111
Figure 3.25	Definition of GAP, after Lo et al. (1984) and Lee et al. (1992).....	112
Figure 3.26	Pressures acting on tunnel during excavation.....	114
Figure 3.27	Ground deformation patterns and ground loss boundary conditions (after Loganathan and Poulos, 1998)	116
Figure 3.28	Ground movement towards tunnel.....	117
Figure 3.29	Oval-shape ground deformation pattern around tunnel section proposed by Loganathan and Poulos (1998)	117
Figure 3.30	Deformation input parameters, u_ϵ and u_δ	121
Figure 3.31	Definition of parameters using in ground deformation determination (after Pinto, 1999)	123
Figure 3.32	Advance of the shield simulated by “excavation elements” (after Akagi and Komiya, 1996)	125

Figure 3.33 Measured data compared with 3D finite element analysis (after Akagi and Komiya, 1996)	126
Figure 3.34 Excavation sequencing and tunnel bench dimensions as incorporated into numerical models (Eberhardt, 2001)	127
Figure 3.35 Stress path plots of the principal stress magnitudes and orientations at fixed points in the tunnel roof and wall (after Eberhardt,2001)	128
Figure 3.36 Accumulation of deformations with tunnel face advancement for fixed points in the tunnel roof and wall (after Eberhardt, 2001)	130
Figure 3.37 Model tunnel tests – boundary conditions and dimensions (after Atkinson and Potts, 1977)	132
Figure 3.38 Comparison width of settlement trough (i/R) versus dimensionless depth of tunnel ($z/2R$) between Peck (1969)'s field data (dashed lines) and model testing results	135
Figure 3.39 Tunnel heading in soft ground (after Kimura and Mair, 1981).....	136
Figure 3.40 Dimension of 3D test series (after Kimura and Mair, 1981).....	137
Figure 3.41 View of a typical 2D model tunnel after failure (after Kimura and Mair, 1981)	138
Figure 3.42 Schematic diagram of the failure above the tunnel model.....	138
Figure 3.43 Model tunnel heading (3D Test) after failure for lined heading ($L/D = 0$) and $H/D = 1.5$ (after Kimura and Mair, 1981)	139
Figure 3.44 Schematic diagram of failure mechanism (see 3D ground movement at the face of the tunnel)	139
Figure 3.45 Model tunnel heading (3D Test) after failure for unlined heading ($L/D = 2.0$) and $H/D = 1.5$ (after Kimura and Mair, 1981)	141
Figure 3.46 Schematic diagram of failure mechanism (see 2D ground movement above the tunnel)	141
Figure 3.47 Miniature shield tunneling machine for centrifuge test scaled in mm. (after Nomoto et al., 1999)	143
Figure 3.48 The miniature shield and tail void formation process (after Nomoto et al., 1999)	143
Figure 3.49 Surface settlement profile from the shield test with void thickness, $v = 2$ mm (after Nomoto et al., 1999)	145
Figure 3.50 Earth pressure measurement results (after Nomoto et al., 1999).....	146
Figure 4.1 Plan view of tunneling project (after Clough and Leca, 1993)	154
Figure 4.2 Soil profile on F4 project (after Clough and Leca, 1993)	155
Figure 4.3 Hitachi machine used on F3a and F4 projects (after Leca, 1989).....	158
Figure 4.4 Lovat machine used on F3c project (after Leca, 1989).....	158
Figure 4.5 Surface settlement vs. shield position at SSI-4.....	159
Figure 4.6 Surface settlement vs. shield position at SSI-7.....	159
Figure 4.7 Surface settlement vs. shield position at SSI-8.....	160
Figure 4.8 Surface settlement vs. shield position at SSI-3.....	160
Figure 4.9 Settlements at different zones measured at SSI-4.....	161
Figure 4.10 Settlements at different zones measured at SSI-7.....	161
Figure 4.11 Settlements at different zones measured at SSI-8.....	162
Figure 4.12 Settlements at different zones measured at SSI-3.....	162

Figure 4.13	Initial network of Taipei Rapid Transit System.....	165
Figure 4.14	Typical soil profile and the location of an extensometer installed above tunnel centerline in the Taipei subway project (after Moh et. al, 1996)	166
Figure 4.15	The Herrenknecht EPB shield with 6.09 m diameter used in the TRTS project.....	166
Figure 4.16	Ground collapse during launching of the shield.....	167
Figure 4.17	Ground deformation above tunnel in Taipei (after Moh et al, 1996).....	167
Figure 4.18	The location of the San Francisco Clean Water Project (N-2 project).....	169
Figure 4.19	Subsurface condition of the N-2 project.....	170
Figure 4.20	Section of the Mitsubishi Earth Pressure Balance Shield used in N-2 project	171
Figure 4.21	Lateral displacement in the front of advancing shield (after Clough et al. 1983)	174
Figure 4.22	Surface settlement measured from N-2 tunnel project.....	175
Figure 4.23	Surface settlement versus average earth pressure recorded at N-2 project (after Finno and Clough, 1985)	175
Figure 4.24	Tunnel alignment and soil profile of the Fukuoka subway (after Matsushita et al., 1995)	176
Figure 4.25	Observed ground settlement and operation record (after Matsushita et al., 1995)	177
Figure 4.26	Slurry pressure versus settlement (after Matsushita et al., 1995).....	178
Figure 4.27	Pitching angle causing the ground deformation.....	179
Figure 4.28	Temporary lifting causing the ground heave.....	179
Figure 4.29	Milan Subway Project.....	181
Figure 4.30	Operational factors and the surface settlement measured at the Passante Ferroviario of the Milan project (after Chiorboli and Marcheselli, 1996)	182
Figure 4.31	Face pressure ratio versus surface settlement.....	184
Figure 4.32	Penetration rate versus surface settlement.....	185
Figure 4.33	Tunnel depth versus surface settlement.....	185
Figure 4.34	Distance from launching station versus surface settlement.....	186
Figure 5.1	MRTA Chaloem Ratchamongkhon Line.....	193
Figure 5.2	Soil profile of the North Tunnel section.....	195
Figure 5.3	Soil profile of the South Tunnel Section.....	195
Figure 5.4	Geological map of Thailand (Scale 1:10,000,000)	196
Figure 5.5	System of Aquifers under the Chao Phraya Plain.....	199
Figure 5.6	Typical pore water pressure profile in Bangkok.....	201
Figure 5.7	Piezometric Levels (meter from the ground surface) in the Phra Pradaeng Aquifer in 1979.....	202
Figure 5.8	Piezometric Levels (meter from the ground surface) in the Phra Pradaeng Aquifer in 1990.....	202
Figure 5.9	Total ground surface subsidence in centimeters between 1933 and 1987 (after Prinya et al., 1989)	204
Figure 5.10	Kawasaki EPB Shield (the model used in Sections A, B, C).....	212
Figure 5.11	Herrenknecht Earth Pressure Balance Shield used in Section D.....	212

Figure 5.12 Specification of the Earth Pressure Balance Shield used in the MRTA project (manufactured by Kawasaki)	213
Figure 5.13 Tunneling procedures of the North and the South sections.....	218
Figure 5.14 Tunnel drive sequence of Section A (North Section).....	219
Figure 5.15 Tunnel drive sequence of Section B (North Section).....	219
Figure 5.16 Tunnel drive sequence of Section C (South Section).....	220
Figure 5.17 Tunnel drive sequence of Section D (South Section).....	220
Figure 5.18 Diaphragm wall prepared for shield cutting through in Ratchada station (North Tunnel Section)	221
Figure 5.19 EPB shield cutting through the diaphragm wall.....	221
Figure 5.20 Breakthrough at Lumpini station (South Tunnel Section)	222
Figure 5.21 Breakout at Sirikit station (South Tunnel Section)	222
Figure 5.22 Map of Tunneling Section A showing the initial drive from Thiam Ruam Mit station.....	225
Figure 5.23 Schematic diagram of the initial drive of Section A showing station box, launching shaft and supporting system located in the ground surface.....	226
Figure 5.24 Shield cutting through piles of an underpinned canal bridge.....	227
Figure 5.25 Jet grouting zone providing stability during the inspection of the shield's cutting face.....	227
Figure 5.26 Workers installing grouting pipe used for soil improvement or grouting zone	228
Figure 5.27 Intervention shaft during construction.....	229
Figure 5.28 Thiam Ruam Mit station and typical tunnel alignment.....	230
Figure 5.29 Map of Tunneling Section B showing the initial drive from Ratchada station	233
Figure 5.30 Ratchada station and the tunnel alignment in Section B.....	234
Figure 5.31 Tunnel Section B from Lat Phrao station to Pahonyothin station.....	235
Figure 5.32 Location of Section B from Lat Phrao station to Phahonyothin station...	236
Figure 5.33 Rama IX area and typical tunnel alignment.....	239
Figure 5.34 Alignment of Tunnel Section C showing the initial drive from Phetchaburi station to Sukhumvit station and Khlong Saen Saep Bridge.....	240
Figure 5.35 Phetchaburi station and tunnel alignment.....	241
Figure 5.36 Breakthrough of the northbound shield at the Phetchaburi station diaphragm wall (Section C)	242
Figure 5.37 Worker fixing the bearing seals inside the earth chamber of the northbound shield (Section C)	242
Figure 5.38 Tunnel alignment along Asoke road (between Phetchaburi and Sukhumvit stations)	243
Figure 5.39 Location and tunnel section of the tunnel drive under Asoke road (between Phetchaburi and Sukhumvit stations)	244
Figure 5.40 Sukhumvit station and tunnel alignment.....	245
Figure 5.41 Schematic diagram showing the shield tail trapped at the diaphragm wall	246
Figure 5.42 Backup equipment installed behind the SB shield inside Sirikit station...	249
Figure 5.43 Tunnel alignment from Sirikit station to Bon Kai station.....	249
Figure 5.44 Bon Kai station and tunnel alignment.....	250

Figure 5.45 Lumphini station and tunnel alignment.....	251
Figure 5.46 Ground loss as the SB shield encountering a sand layer under Rama IV road	252
Figure 5.47 Ground loss occurring as the SB shield approaching Silom station.....	252
Figure 5.48 Tunnel alignment at Sam Yan station.....	253
Figure 6.1 Structure of the computerized database system for EPB tunneling in the MRTA project.....	257
Figure 6.2 Structure of main instrumentation database and its links.....	258
Figure 6.3 Surface settlement maker database and its links.....	259
Figure 6.4 Surface settlement marker array database and its links.....	260
Figure 6.5 Extensometer database and its links.....	261
Figure 6.6 Inclinator database and its links.....	262
Figure 6.7 Piezometer database and its links.....	263
Figure 6.8 An example of face pressure records.....	265
Figure 6.9 An example of penetration rate records.....	265
Figure 6.10 An example of pitching angle records.....	266
Figure 6.11 An example of thrust force records.....	266
Figure 6.12 An example of cutter torque records.....	267
Figure 6.13 An example of grouting pressure records.....	267
Figure 6.14 An example of grout filling records.....	268
Figure 6.15 An example of time-position records.....	268
Figure 7.1 Schematic diagram of typical instrumentation locations in the MRTA project	270
Figure 7.2 MRTA Chaloem Ratchamongkhon Line.....	272
Figure 7.3 Subsurface conditions of tunneling section (southbound) between Thiam Ruam Mit and Pracharat Bumphen (Section A)	274
Figure 7.4 Maximum surface settlements, face pressures, and penetration rates recorded between Thiam Ruam Mit and Pracharat Bumphen stations (Section A)	275
Figure 7.5 “Tunnel Eye” prepared before launching the shield (Thiam Ruam Mit station)	276
Figure 7.6 Reaction truss installed to support the initial drive (Thiam Ruam Mit station)	277
Figure 7.7 The shield launching through the diaphragm wall (Thiam Ruam Mit station)	277
Figure 7.8 Temporary lining rings (Thiam Ruam Mit station)	278
Figure 7.9 Schematic diagram of the initial shield drive.....	278
Figure 7.10 Back-up equipment train (Sirikit station)	279
Figure 7.11 Longitudinal surface settlements measured in the initial drive zone (Ring No. 49-southbound)	279
Figure 7.12 Failure mechanism at a tunnel face during a centrifuge test done by Kimura and Mair (1981)	280
Figure 7.13 Schematic diagram of ground deformation at the shield face.....	280
Figure 7.14 Longitudinal surface settlement profile measured at location “b” (Ring No. 101-southbound)	283

Figure 7.15 Longitudinal surface settlement profile measured at location “c” (Ring No. 164-southbound)	283
Figure 7.16 Longitudinal surface settlement profile measured at location “d” (Ring No. 208-southbound)	284
Figure 7.17 Schematic diagram of a typical longitudinal surface settlement profile...	285
Figure 7.18 Subsurface conditions of tunneling section (southbound) between Ratchada and Lat Phrao stations (Section B)	286
Figure 7.19 Maximum surface settlements, face pressures, and penetration rates recorded between Ratchada and Lat Phrao stations (Section B)	288
Figure 7.20 Muck pumping pipe used in Section B.....	289
Figure 7.21 Longitudinal surface settlement profile measured over southbound ring No. 86-southbound in Section B.....	289
Figure 7.22 Subsurface conditions of tunneling section (northbound) between Rama IX and Phetchaburi stations (Section C)	290
Figure 7.23 Maximum surface settlements, face pressures, and penetration rates recorded between Rama IX to Phetchaburi stations (Section C)	291
Figure 7.24 Longitudinal surface settlement profile measures at location “e” (Ring No. 303-northbound)	293
Figure 7.25 Longitudinal surface settlement profile measures at location “f” (Ring No. 366-northbound)	293
Figure 7.26 Subsurface conditions of tunneling section (southbound) between Sirikit and Bon Kai stations (Section D)	294
Figure 7.27 Instrumentation layout of the tunneling section from Sirikit to Bon Kai stations.....	296
Figure 7.28 Maximum surface settlements and operational parameters recorded from southbound tunnel of Sirikit - Bon Kai tunneling section.....	297
Figure 7.29 Subsurface settlements measured on RE-T5-001 (SB no.61)	300
Figure 7.30 Subsurface settlements measured on RE-T5-003 (SB no. 91)	300
Figure 7.31 Grout hole at the segmental lining (MRTA project)	301
Figure 7.32 Tail void grouting performed behind the shield after segmental linings are completely installed (MRTA project)	301
Figure 7.33 Effect of tail void grouting on ground settlement.....	302
Figure 7.34 Surface settlement trough measured on 23-AR-001 (southbound tunnel-Ring no.613) and the instrumentation layout.....	306
Figure 7.35 Surface settlement trough measured on 23-G3-007-019 (southbound tunnel-Ring no.52) and the instrumentation layout.....	307
Figure 7.36 Surface settlement trough measured on 26-AR-001 (southbound tunnel-Ring no.86) and the instrumentation layout.....	308
Figure 7.37 Surface settlement trough measured on 26-AR-002 (southbound tunnel-Ring no.36) and the instrumentation layout.....	309
Figure 7.38 Surface settlement trough measured on CS-9A (northbound tunnel-Ring no.16) and the instrumentation layout.....	310
Figure 7.39 Surface settlement trough measured on CS-8B (northbound tunnel-Ring no.571) and the instrumentation layout.....	311
Figure 7.40 Surface settlement trough measured on CS-8C (northbound tunnel-Ring no.451) and the instrumentation layout.....	312

Figure 7.41 Surface settlement trough measured on CS-8D (northbound tunnel-Ring no.345) and the instrumentation layout.....	313
Figure 7.42 Surface settlement trough measured on CS-8E (northbound tunnel-Ring no.230) and the instrumentation layout.....	314
Figure 7.43 Surface settlement trough measured on CS-8G (northbound tunnel-Ring no.48) and the instrumentation layout.....	315
Figure 7.44 Surface settlement trough measured on CS-7C (northbound tunnel-Ring no.466) and the instrumentation layout.....	316
Figure 7.45 Surface settlement trough measured on CS-7D (northbound tunnel-Ring no.284) and the instrumentation layout.....	317
Figure 7.46 Surface settlement trough measured on SS-5T-21a-o (southbound tunnel-Ring no.429) and the instrumentation layout.....	318
Figure 7.47 Surface settlement trough measured on SS-5T-22e-o (southbound tunnel-Ring no.365) and the instrumentation layout.....	319
Figure 7.48 Surface settlement trough measured on SS-5T-27A-N (southbound tunnel-Ring no.243) and the instrumentation layout.....	320
Figure 7.49 Surface settlement trough measured on SSS-5T-31A-D (southbound tunnel-Ring no.212) and the instrumentation layout.....	321
Figure 7.50 Surface settlement trough measured on SSS-5T-37A-E (southbound tunnel-Ring no.125) and the instrumentation layout.....	322
Figure 7.51 Surface settlement trough measured on SSS-5T-47A-F (southbound tunnel-Ring no.61) and the instrumentation layout.....	323
Figure 7.52 Surface settlement trough measured on SSS-5T-52A-E (southbound tunnel-Ring no.102) and the instrumentation layout.....	324
Figure 7.53 Surface settlement trough measured on SS-5T-52e-s (southbound tunnel-Ring no.102) and the instrumentation layout.....	325
Figure 7.54 Surface settlement trough measured on CS-4B (southbound tunnel-Ring no.369) and the instrumentation layout.....	326
Figure 7.55 Surface settlement trough measured on CS-4C (southbound tunnel-Ring no.584) and the instrumentation layout.....	327
Figure 7.56 Observed settlement trough parameters from the MRTA project in Peck's (1969) empirical chart.....	328
Figure 7.57 Observed settlement trough parameters from the MRTA project compared with the parameter recommended by O'Reilly and New (1982)	329
Figure 7.58 Observed settlement trough parameters from the MRTA project (only tunneling in clays) together with case history data collected by Mair and Taylor (1997)	329
Figure 7.59 Lateral deformation measured on 23-IE-002 after shield passing (SB) in Section A (Thiam Ruam Mit – Pracharat Bumphen) and the instrumentation layout..	333
Figure 7.60 Lateral deformation measured on 23-IE-008 after shield passing (NB) in Section A (Thaim Ruam Mit – Pracharat Bumphen stations) and the instrumentation layout.....	334
Figure 7.61 Lateral deformation measured on 28-IE-005 after shield passing (SB) in Section B (Lat Phrao – Phahoyothin stations) and the instrumentation layout.....	335
Figure 7.62 Lateral deformation measured on IN-T7-01 after shield passing (NB) in Section C (Phetchaburi – Sukhumvit stations) and the instrumentation layout.....	336

Figure 7.63 Lateral deformation measured on IN-T7-03 after shield passing (SB) in Section C (Phetchaburi –Sukhumvit stations) and the instrumentation layout.....	337
Figure 7.64 Lateral deformation measured on IN-T7-05 after shield passing (SB) in Section C (Phetchaburi –Sukhumvit stations) and the instrumentation layout.....	338
Figure 7.65 Lateral deformation measured on inclinometer IN-T7-04 during excavation of the northbound tunnel in Section C (Phetchaburi –Sukhumvit stations)	339
Figure 7.66 Schematic diagram of the shield position relative to the inclinometer location in Figure 7.65.....	340
Figure 7.67 Maximum lateral deformations relative to the shield position.....	341
Figure 7.68 Soil deformation around model tunnel in clay (after Kimura and Mair, 1981) and the effect on the inclinometer.....	342
Figure 7.69 Schematic diagram of the effect of tail void grouting on the ground response	343
Figure 7.70 Relationship between the grouting pressure and lateral deformations.....	344
Figure 8.1 Plan and Cross section at London Heathrow Central Terminal Area.....	350
Figure 8.2 Surface settlements observed during construction in the Piccadilly Line Inner tunnel (after Cooper et al., 2002)	351
Figure 8.3 Definitions of surface settlement trough.....	354
Figure 8.4 Surface settlement troughs measured in 23-AR-001 and operational parameters recorded from NB and SB shields as they pass the measurement section.....	355
Figure 8.5 Layout of the settlement array 23-AR-001.....	356
Figure 8.6 Surface settlement troughs measured in 26-AR-001 and operational parameters recorded from NB and SB shields as they pass the measurement section	357
Figure 8.7 Layout of the settlement array 26-AR-001.....	358
Figure 8.8 Surface settlement troughs measured in CS-8B and operational parameters recorded from NB and SB shields as they pass the measurement section.....	359
Figure 8.9 Layout of the settlement array CS-8B.....	360
Figure 8.10 Surface settlement troughs measured in CS-8D and operational parameters recorded from NB and SB shields as they pass the measurement section.....	361
Figure 8.11 Layout of the settlement array CS-8D.....	362
Figure 8.12 Surface settlement troughs measured from SS-5T-52e-s and operational parameters recorded from NB and SB shields as they pass the measurement section	363
Figure 8.13 Layout of the settlement array SS-5T-52e-s.....	364
Figure 8.14 Surface settlement troughs measured from SS-5T-22e-o and operational parameters recorded from NB and SB shields as they pass the measurement section	365
Figure 8.15 Layout of the settlement array SS-5T-22e-o.....	366
Figure 8.16 Surface settlement troughs measured from 23-G3-007-019 and operational parameters recorded from NB and SB shields as they pass the measurement section	367
Figure 8.17 Layout of the settlement array 23-G3-007-019.....	368

Figure 8.18 Surface settlement troughs measured from CS-8G and operational parameters recorded from NB and SB shields as they pass the measurement section	369
Figure 8.19 Layout of the settlement array CS-8G.....	370
Figure 8.20 Surface settlements measured in 23-AR-001 and settlement troughs described by Gaussian curves.....	373
Figure 8.21 Surface settlements measured in 26-AR-001 and settlement troughs described by Gaussian curves.....	373
Figure 8.22 Surface settlements measured in CS-8B and settlement troughs described by Gaussian curves.....	374
Figure 8.23 Surface settlements measured in CS-8D and settlement troughs described by Gaussian curves.....	374
Figure 8.24 Surface settlements measured in SS-5T-52e-s and settlement troughs described by Gaussian curves.....	375
Figure 8.25 Surface settlements measured in SS-5T-22e-o and settlement troughs described by Gaussian curves.....	375
Figure 8.26 Surface settlements measured in 23-G3-007-019 and settlement troughs described by Gaussian curves.....	376
Figure 8.27 Additional settlement developing after the first shield passing.....	380
Figure 8.28 Surface settlements measured in 23-AR-001, settlement troughs described by Gaussian curves and superposition curve.....	380
Figure 8.29 Surface settlements measured in 26-AR-001, settlement troughs described by Gaussian curves and superposition curve.....	381
Figure 8.30 Surface settlements measured in CS-8B, settlement troughs described by Gaussian curves and superposition curve.....	381
Figure 8.31 Surface settlements measured in CS-8D, settlement troughs described by Gaussian curves and superposition curve.....	382
Figure 8.32 Surface settlements measured in SS-5T-52e-s, settlement troughs described by Gaussian curves and superposition curve.....	382
Figure 8.33 Surface settlements measured in SS-5T-22e-o, settlement troughs described by Gaussian curves and superposition curve.....	383
Figure 8.34 Surface settlements measured in 23-G3-007-019, settlement troughs described by Gaussian curves and superposition curve.....	383
Figure 8.35 Settlement trough parameters obtained from additional (normalized) settlement curves over the second tunnel compared with the parameter recommended by O'Reilly and New (1982)	384
Figure 8.36 Schematic diagram of the twin tunnels and installed locations of convergence bolts in Tunneling Section D (Sirikit – Bon Kai)	387
Figure 8.37 Measurement points (convergence bolts) on SB tunnel lining Ring 449 and the lining response affected by the passing of the northbound shield.....	388
Figure 8.38 Deflection of SB tunnel Ring 449 during the passing of NB shield and operational parameters recorded in NB shield corresponding to the NB Ring 424.....	389
Figure 8.39 Measurement points (convergence bolts) on SB tunnel lining Ring 471 and the lining response affected by the passing of the northbound shield.....	390
Figure 8.40 Deflection of SB tunnel Ring 471 during the passing of NB shield and operational parameters recorded in NB shield corresponding to the NB Ring 446.....	391

Figure 8.41 Measurement points (convergence bolts) on SB tunnel lining Ring 483 and the lining response affected by the passing of the northbound shield.....	392
Figure 8.42 Deflection of SB tunnel Ring 483 during the passing of NB shield and operational parameters recorded in NB shield corresponding to the NB Ring 458.....	393
Figure 8.43 Measurement points (convergence bolts) on SB tunnel lining Ring 491 and the lining response affected by the passing of the northbound shield.....	394
Figure 8.44 Deflection of SB tunnel Ring 491 during the passing of NB shield and operational parameters recorded in NB shield corresponding to the NB Ring 466.....	395
Figure 8.45 Measurement points of (convergence bolts) on SB tunnel lining Ring 499 and the lining response affected by the passing of the northbound shield.....	396
Figure 8.46 Deflection of SB tunnel Ring 499 during the passing of NB shield and operational parameters recorded in NB shield corresponding to the NB Ring 474.....	397
Figure 8.47 Surface settlement troughs measured in CS-4C and the instrumentation layout	399
Figure 8.48 Surface settlements measured in CS-4C, settlement troughs described by Gaussian curves.....	402
Figure 8.49 operational parameters recorded from NB and SB shields as they pass the measurement section over lining Ring no. 584.....	403
Figure 9.1 Face pressure versus the maximum surface settlement after shield passing	409
Figure 9.2 Face pressure ratio versus the maximum surface settlement after shield passing.....	409
Figure 9.3 Face Pressure classified by geological conditions versus the maximum surface settlement after shield passing.....	410
Figure 9.4 Average face pressure and average penetration rate.....	412
Figure 9.5 Schematic diagram of a typical longitudinal surface settlement profile....	412
Figure 9.6 Face pressure versus surface settlement measured at the end of Zone 1...	413
Figure 9.7 Face pressure ratio versus surface settlement measured at the end of Zone 1	413
Figure 9.8 Face pressure vs. surface settlement developing in Zone 2.....	414
Figure 9.9 Face pressure ratio vs. surface settlement developing in Zone 2.....	414
Figure 9.10 Face pressure vs. surface settlement developing in Zone 3.....	415
Figure 9.11 Face pressure ratio vs. surface settlement developing in Zone 3.....	415
Figure 9.12 Penetration rate versus surface settlement.....	417
Figure 9.13 Penetration rate versus surface settlement measured at the end of Zone 1	418
Figure 9.14 Penetration rate versus surface settlement developing within Zone 2.....	418
Figure 9.15 Ground movement caused by pitching angle.....	419
Figure 9.16 Pitching angle versus the maximum surface settlement.....	420
Figure 9.17 Schematic diagram showing a tail void between tunnel lining and the shield	422
Figure 9.18 Grouting pressure and grout filling.....	422
Figure 9.19 Grouting pressure versus the maximum surface settlement after shield passing.....	423

Figure 9.20 Grout filling (%) versus the maximum surface settlement after shield passing	423
Figure 9.21 Grouting pressure versus surface settlement developing in Zone 3	424
Figure 9.22 Grout filling (%) versus surface settlement developing in Zone 3	424
Figure 9.23 Geometry parameter: distance from launching station	426
Figure 9.24 Distance from launching station versus the maximum surface settlement after shield passing	426
Figure 9.25 Tunnel depth versus the maximum surface settlement after shield passing	427
Figure 9.26 Geological conditions versus the maximum surface settlement after shield passing	428
Figure 9.27 Distance from tunnel invert to water table versus the maximum surface settlement after shield passing	428
Figure 10.1 Biological neural networks	435
Figure 10.2 A single inter-neuron in the retina of a rabbit	436
Figure 10.3 Synaptic connection and neurotransmitter	436
Figure 10.4 General details of a neuron	438
Figure 10.5 A feedforward network (multi-layer perceptron)	440
Figure 10.6 Learning vector quantization network	441
Figure 10.7 A basic CMAC module	442
Figure 10.8 Detail of a GMDH network	443
Figure 10.9 A Hopfield network	444
Figure 10.10 An Elman network	445
Figure 10.11 A Jordan network	445
Figure 10.12 Schematic diagram of neurons and transmission processes	447
Figure 10.13 Threshold or step function	448
Figure 10.14 Linear Function	449
Figure 10.15 Sigmoid function	450
Figure 10.16 Tangent sigmoid function	450
Figure 10.17 Sigmoid function with different slope parameters, w	451
Figure 10.18 Directions of two basic signal flows in a multi-layer perceptron: forward propagation of function signals and back-propagation of error signals	453
Figure 10.19 Signal-flow schematic diagram showing the detail of output neuron j	454
Figure 10.20 Gradient descent in weight space	458
Figure 10.21 Signal-flow schematic diagram showing the detail of output neuron k connected to hidden neuron j	460
Figure 10.22 Signal flow of a part of the adjoint system pertaining to back-propagation of error signal	462
Figure 10.23 An example of data processing for the neural network modeling	464
Figure 10.24 Example of training and testing domain	466
Figure 10.25 Effect of normalizing input of training data	467
Figure 11.1 Main factors causing the surface settlement	473

Figure 11.2 Geological parameters: geology at crown, geology at invert, and ground water table.....	474
Figure 11.3 Diagram of the ANN modeling development for settlement prediction...	476
Figure 11.4 Locations of the tunneling drive used as experimental training data.....	478
Figure 11.5 Location of the tunnel in Zone 23 (Thiam Ruam Mit - Pracharat Bumphen)	479
Figure 11.6 Location of the tunnel in Zone 24 (Pracharat Bumphen – Sutthisan).....	479
Figure 11.7 Location of the tunnel in Zone 25 (Sutthisan - Ratchada)	480
Figure 11.8 Measured operational parameters used for ANN inputs.....	481
Figure 11.9 Structure of two-layer neural network model for predicting the surface settlement.....	485
Figure 11.10 Performances of ANN with 1 hidden layer at 1,000 epochs: (a) Model 1 (10 hidden nodes), (b) Model 2 (15 hidden nodes), and (c) Model 3 (20 hidden nodes)...	488
Figure 11.11 Performances of ANN with 1 hidden layer at 2,000 epochs: (a) Model 4 (10 hidden nodes), (b) Model 5 (15 hidden nodes), and (c) Model 6 (20 hidden nodes)...	489
Figure 11.12 Performances of ANN with 1 hidden layer at 3,000 epochs: (a) Model 7 (10 hidden nodes), (b) Model 8 (15 hidden nodes), and (c) Model 9 (20 hidden nodes)...	490
Figure 11.13 Performances of ANN with 2 hidden layers at 1,000 epochs: (a) Model 10 (10 hidden nodes), (b) Model 11 (15 hidden nodes), and (c) Model 12 (20 hidden nodes)	491
Figure 11.14 Performances of ANN with 2 hidden layers at 2,000 epochs: (a) Model 13 (10 hidden nodes), (b) Model 14 (15 hidden nodes), and (c) Model 15 (20 hidden nodes)	492
Figure 11.15 Performances of ANN with 2 hidden layers at 3,000 epochs: (a) Model 16 (10 hidden nodes), (b) Model 17 (15 hidden nodes), and (c) Model 18 (20 hidden nodes)	493
Figure 11.16 Comparison of errors in training data and validation data.....	496
Figure 11.17 Number of training epochs versus RMSE as results from training samples	499
Figure 11.18 Number of training epochs versus RMSE as results from validation samples	499
Figure 11.19 Number of hidden nodes versus RMSE as results from training samples	500
Figure 11.20 RMSE as the number of hidden nodes changes from 5 to 20.....	501
Figure 11.21 Number of hidden nodes versus RMSE as results from validation samples	502
Figure 12.1 Training and testing results from Section A given by the optimal neural network model.....	508
Figure 12.2 Locations of tunnel sections in the MRTA project.....	510
Figure 12.3 Geological profile of North Tunnel Section representing Sections A and B	511
Figure 12.4 Results of using the neural network for predicting settlements in Section B	512
Figure 12.5 Ranges of penetration rate recorded in the MRTA project.....	515

Figure 12.6 Ranges of face pressure recorded in the MRTA project.....	515
Figure 12.7 Example of training sample and testing sample domains needed for neural network application (see also Section 10.6)	516
Figure 12.8 Example of training sample and testing sample domains actually applied in Scenario 1.1.....	516
Figure 12.9 Geological profile of South Tunnel Section representing Sections C and D	517
Figure 12.10 Results of using the network for predicting settlements in Section C...	518
Figure 12.11 Results of using the network for predicting settlements in Section D...	518
Figure 12.12 Ranges of tunnel depth in the MRTA project.....	519
Figure 12.13 Ranges of grouting pressure recorded in the MRTA project.....	519
Figure 12.14 Performances of neural networks on trained and tested data in Section B	522
Figure 12.15 Performance of neural networks on trained and tested data in Section C	522
Figure 12.16 Performance of neural networks on trained and tested data in Section D	523
Figure 12.17 Training and testing results from neural networks trained with data from Sections A and B (Scenario 3)	525
Figure 12.18 Training and testing results from neural networks trained with data from Sections A, B, and C (Scenario 4)	525
Figure 12.19 Training and testing results from neural networks trained with all data from all sections (Scenario 5)	527
Figure 12.20 Training and testing results from neural networks (adding machine model input node) trained with all data from all sections (Scenario 6)	527
Figure 12.21 Structure of the modified neural network model for predicting surface settlements in the entire MRTA project.....	528
Figure 12.22 Results from neural networks without penetration rate input node trained and tested with data from Section A.....	530
Figure 12.23 Results from neural networks without penetration rate input node trained and tested with data from Sections A and B.....	531
Figure 12.24 Results from neural networks without penetration rate input node trained and tested with data from Sections A, B, and C.....	531
Figure 12.25 Summary of training RMSE of neural network models with and without the penetration rate input node.....	532
Figure 12.26 Summary of testing RMSE of neural network models with and without the penetration rate input node.....	532
Figure 12.27 Results from neural networks without grouting quality input nodes trained and tested with data from Section A.....	534
Figure 12.28 Results from neural networks without grouting quality input nodes trained and tested with data from Sections A and B.....	534
Figure 12.29 Results from neural networks without grouting quality input nodes trained and tested with data from Sections A, B, and C.....	535
Figure 12.30 Summary of training RMSE of neural network models with and without the grouting quality input nodes.....	535

Figure 12.31 Summary of testing RMSE of neural network models with and without the grouting quality input nodes..... 536

Figure 12.32 Results from neural networks without the face pressure input node trained and tested with data from Section A.....537

Figure 12.33 Results from neural networks without the face pressure input node trained and tested with data from Sections A and B.....538

Figure 12.34 Results from neural networks without the face pressure input node trained and tested with data from Sections A, B, and C..... 538

Figure 12.35 Summary of training RMSE of neural network models with and without the face pressure input node..... 539

Figure 12.36 Summary of testing RMSE of neural network models with and without the face pressure input node..... 539

Figure 12.37 Results of using the model trained with the first 50% of data to predict surface settlements in the remaining 50% of Section A..... 544

Figure 12.38 Results of using the model trained with the first 50% of data to predict surface settlements in the remaining 50% of Section B..... 544

Figure 12.39 Results of using the model trained with the first 50% of data to predict surface settlements in the remaining 50% of Section C..... 545

Figure 12.40 Results of using the model trained with the first 50% of data to predict surface settlements in the remaining 50% of Section D..... 545

Figure 12.41 Results of using the model trained with the first 40% of data to predict surface settlements in the remaining 60% of Section A..... 546

Figure 12.42 Results of using the model trained with the first 40% of data to predict surface settlements in the remaining 60% of Section B..... 546

Figure 12.43 Results of using the model trained with the first 40% of data to predict surface settlements in the remaining 60% of Section C..... 547

Figure 12.44 Results of using the model trained with the first 40% of data to predict surface settlements in the remaining 60% of Section D..... 547

Figure 12.45 Results of using the model trained with the first 30% of data to predict surface settlements in the remaining 70% of Section A..... 548

Figure 12.46 Results of using the model trained with the first 30% of data to predict surface settlements in the remaining 70% of Section B..... 548

Figure 12.47 Results of using the model trained with the first 30% of data to predict surface settlements in the remaining 70% of Section C..... 549

Figure 12.48 Results of using the model trained with the first 30% of data to predict surface settlements in the remaining 70% of Section D..... 549

Figure 12.49 Results of using the model trained with the first 20% of data to predict surface settlements in the remaining 80% of Section A..... 550

Figure 12.50 Results of using the model trained with the first 20% of data to predict surface settlements in the remaining 80% of Section B..... 550

Figure 12.51 Results of using the model trained with the first 20% of data to predict surface settlements in the remaining 80% of Section C..... 551

Figure 12.52 Results of using the model trained with the first 20% of data to predict surface settlements in the remaining 80% of Section D..... 551

Figure 12.53 Comparison of samples used for network training..... 552

Figure 12.54 Comparison of errors in training samples..... 552

Figure 12.55 Comparison of errors in prediction.....	552
Figure 12.56 Schematic diagram of a typical longitudinal surface settlement profile	555
Figure 12.57 Performances of neural networks used for predicting surface settlements in Zone 2.....	555
Figure 12.58 Performances of neural networks used for predicting surface settlements in Zone 1.....	556
Figure 12.59 Summary of training and testing RMSE.....	558
Figure 12.60 Stability numbers (N) used as inputs for the network.....	562
Figure 12.61 Stability number (N) versus surface settlements.....	563
Figure 12.62 Overload factor (N') versus surface settlements.....	563
Figure 12.63 Structure of neural network model for predicting surface settlements induced by tunneling in clay.....	564
Figure 12.64 Summary of training and testing RMSE of neural network models used in the prediction of surface settlements induced by tunneling in clay.....	566
Figure 12.65 Performance of ANN with 1 hidden layer and 15 hidden nodes trained for 1,000 epochs for predicting settlements induced by tunneling in clays.....	567
Figure 12.66 Performance of ANN with 1 hidden layer and 20 hidden nodes trained for 1,000 epochs for predicting settlements induced by tunneling in clays.....	567
Figure 12.67 Performance of ANN with 1 hidden layer and 15 hidden nodes trained for 2,000 epochs for predicting settlements induced by tunneling in clays.....	568
Figure 12.68 Performance of ANN with 1 hidden layer and 20 hidden nodes trained for 2,000 epochs for predicting settlements induced by tunneling in clays.....	568
Figure 12.69 Performance of ANN with 1 hidden layer and 15 hidden nodes trained for 3,000 epochs for predicting settlements induced by tunneling in clays.....	569
Figure 12.70 Performance of ANN with 1 hidden layer and 20 hidden nodes trained for 3,000 epochs for predicting settlements induced by tunneling in clays.....	569
Figure 12.71 Performance of ANN with 1 hidden layer and 15 hidden nodes trained for 4,000 epochs for predicting settlements induced by tunneling in clays.....	570
Figure 12.72 Performance of ANN with 1 hidden layer and 20 hidden nodes trained for 4,000 epochs for predicting settlements induced by tunneling in clays.....	570
Figure 12.73 Performance of ANN with 2 hidden layers and 15 hidden nodes each trained for 1,000 epochs for predicting settlements induced by tunneling in clays.....	571
Figure 12.74 Performance of ANN with 2 hidden layers and 20 hidden nodes each trained for 1,000 epochs for predicting settlements induced by tunneling in clays.....	571
Figure 12.75 Performance of ANN with 2 hidden layers and 15 hidden nodes each trained for 2,000 epochs for predicting settlements induced by tunneling in clays.....	572
Figure 12.76 Performance of ANN with 2 hidden layers and 20 hidden nodes each trained for 2,000 epochs for predicting settlements induced by tunneling in clays.....	572
Figure 12.77 Performance of ANN with 2 hidden layers and 15 hidden nodes each trained for 3,000 epochs for predicting settlements induced by tunneling in clays.....	573
Figure 12.78 Performance of ANN with 2 hidden layers and 20 hidden nodes each trained for 3,000 epochs for predicting settlements induced by tunneling in clays.....	573
Figure 12.79 Performance of ANN with 2 hidden layers and 15 hidden nodes each trained for 4,000 epochs for predicting settlements induced by tunneling in clays.....	574

Figure 12.80 Performance of ANN with 2 hidden layers and 20 hidden nodes each trained for 4,000 epochs for predicting settlements induced by tunneling in clays..... 574

Figure 12.81 Surface settlements caused by twin-tunnels.....575

Figure 12.82 Structure of neural network model for predicting surface settlements over the second tunnel..... 580

Figure 12.83 Summary of training and testing RMSE of neural network models used in the prediction of surface settlements over the second tunnel..... 581

Figure 12.84 Performance of ANN (twin-tunnel model) with 1 hidden layer and 20 hidden nodes trained for 1,000 epochs..... 582

Figure 12.85 Performance of ANN (twin-tunnel model) with 1 hidden layer and 20 hidden nodes trained for 2,000 epochs..... 582

Figure 12.86 Performance of ANN (twin-tunnel model) with 1 hidden layer and 20 hidden nodes trained for 3,000 epochs..... 583

Figure 12.87 Performance of ANN (twin-tunnel model) with 1 hidden layer and 20 hidden nodes trained for 4,000 epochs..... 583

Figure 12.88 Performance of ANN (twin-tunnel model) with 2 hidden layers and 20 hidden nodes each trained for 3,000 epochs..... 584

Figure 12.89 Performance of ANN (twin-tunnel model) with 2 hidden layers and 20 hidden nodes each trained for 4,000 epochs..... 584

Figure 12.90 Performance of ANN (twin-tunnel model) with 2 hidden layers and 20 hidden nodes each trained for 5,000 epochs..... 585

Figure 12.91 Performance of ANN (twin-tunnel model) with 2 hidden layers and 20 hidden nodes each trained for 6,000 epochs..... 585

Figure 12.92 Performance of ANN (twin-tunnel model) with 2 hidden layers and 20 hidden nodes each trained for 7,000 epochs..... 586

Figure 12.93 Performance of ANN (twin-tunnel model) with 2 hidden layers and 20 hidden nodes each trained for 8,000 epochs..... 586

Figure 12.94 Predicted surface settlements using the combination of ANN and the normalization technique compared to measured surface settlements caused by twin tunnels in Section A..... 587

Figure 12.95 Predicted surface settlements using the combination of ANN and the normalization technique compared to measured surface settlements caused by twin tunnels in Section B..... 587

Figure 12.96 Predicted surface settlements using the combination of ANN and the normalization technique compared to measured surface settlements caused by twin tunnels in Section C..... 588

Figure 12.97 Predicted surface settlements using the combination of ANN and the normalization technique compared to measured surface settlements caused by twin tunnels in Section D..... 588

LIST OF TABLES

Table 2-1	Classification of shield tunneling machine.....	49
Table 2-2	Typical advantages of the EPB shield over other shields.....	56
Table 3-1	Summarized settlement trough data for a range of soils (after O'Reilly and New;1982)	96
Table 3-2	Tunnel database reported by Mair and Taylor (1997).....	100
Table 4-1	Average engineering properties of soils on F3 and F4 projects.....	155
Table 4-2	Comparison between face pressure and lateral displacement.....	173
Table 5-1	Typical soil profile beneath Bangkok.....	198
Table 5-2	Subsidence Rates beneath Bangkok in 1981 and 1996.....	203
Table 5-3	Typical design parameters of Made Ground.....	206
Table 5-4	Typical design parameters for the Bangkok Soft Clay.....	207
Table 5-5	Typical design parameters for the First Stiff Clay.....	208
Table 5-6	Typical design parameters for the Dense Sand.....	209
Table 5-7	Typical design parameters for the Second Hard Clay.....	210
Table 5-8	Comparison of EPB shields used in the MRTA project.....	214
Table 5-9	Drive sequence of the EPB shields.....	215
Table 7-1	Grouting pressures and maximum outward lateral deformations measured in the MRTA project.....	343
Table 10-1	Terminology between biological neural networks and artificial neural networks.....	437
Table 11-1	Summary of factors affecting the surface settlement.....	473
Table 11-2	Input parameters used for the NN model.....	480
Table 11-3	Samples used for training and validation testing.....	482
Table 11-4	Neural network models used in the pilot experiment.....	486
Table 11-5	Performance of the neural network models.....	487
Table 12-1	Summary of the scenarios used for settlement predictions.....	507
Table 12-2	Summary of testing results in Scenario 1.....	514
Table 12-3	Summary of training and testing results from Scenario 2.....	521
Table 12-4	Input parameters used for predicting surface settlements at the end of Zone 1	554
Table 12-5	Summary of prediction accuracies when using the neural network model in Scenarios 1-6.....	557
Table 12-6	Input parameters used for the NN model for clay.....	562
Table 12-7	Neural network models used in the prediction of surface settlements induced by tunneling in clay and their training and testing results.....	565
Table 12-8	Input parameters used for the ANN model using for predicting surface settlements over the second tunnel.....	579
Table 12-9	Neural network models used in the prediction of surface settlements induced by the twin tunnels and their training and testing results.....	581

CHAPTER 1

Introduction

1.1 Background

Although Earth Pressure Balance (EPB) shields have been used for several decades, very little reliable information exists about the actual mechanisms governing shield-ground interaction. The ground response mechanism induced by EPB tunneling is difficult to understand because this requires not only reliable ground deformation measurements in the field, but also operational records of the EPB shield. Until now, very few studies on EPB tunneling are available. Since there has been a significant increase in using this tunneling technique, especially in urban environments throughout the world, it is very important for engineers to gain a better understanding of how EPB tunneling variables affect ground deformations in order to minimize detrimental effects on the surrounding environment.

This research specifically deals with the Bangkok Subway Project. The project is the first phase of an integrated transportation plan for Bangkok, to be implemented in conjunction with other schemes, by the Metropolitan Rapid Transit Authority (MRTA). The project of 20-kilometers of twin tunnels is subdivided into two main tunnel sections namely, the North Tunnel Section and the South Tunnel Section, which in turn are divided into Sections A, B and C, D, respectively (Figure 1.1). The tunnel alignment covers heavily congested areas of the city. Each of the twin tunnels is 6.3 meters in outer diameter and 5.7 meters in inner diameter. Each section uses two shields, one each for excavating the

northbound and southbound tunnels. Hence, eight EPB shields were used in total for the entire project.

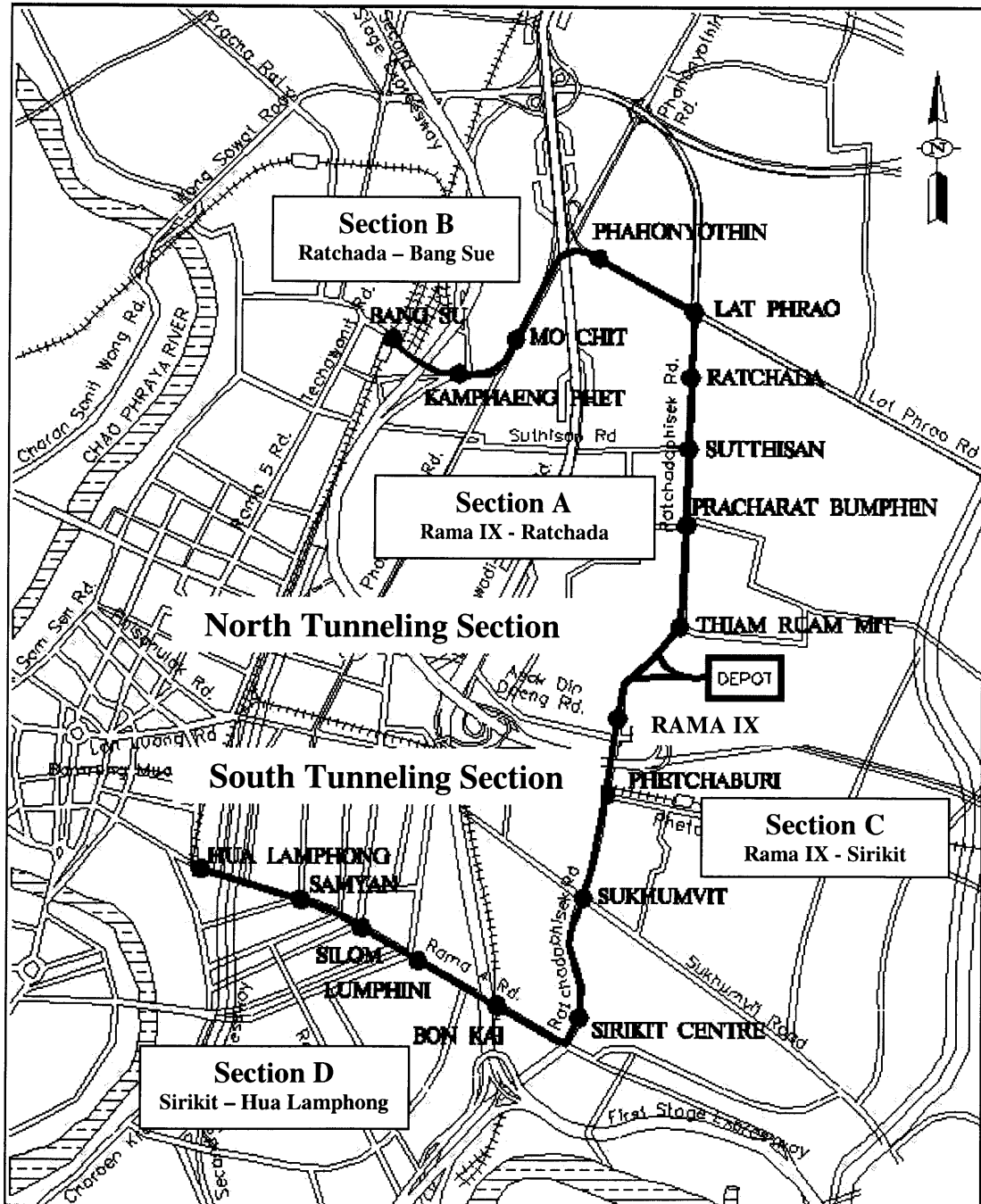


Figure 1.1 MRTA Chaloem Ratchamongkhon Line

Bangkok is a city of approximately 10 million people lying in the Chao Praya delta plain. Its topography is low and flat, being approximately 0.5 to 1 meter above sea level. Subsurface conditions along the MRTA project can also be subdivided into the North Tunnel Section and the South Tunnel Section. In the North Tunnel Section, the soil profile is very uniform with soft clay underlain by stiff clay along the tunnel alignment. In this section, the twin tunnels are excavated mostly within the stiff clay layer (i.e., about 15-25 m below ground surface). For the South Tunnel Section, most of the tunnel alignment is also located within a stiff clay layer. However, in some parts of the route, the tunnels are stacked so that the lower tunnel is excavated in a sand layer. Geological profiles of the project are shown in Section 5.2.

In Section A of the North Tunnel Section (Figure 1.1), two machines operated by Nishimatsu were driven northward from Thiam Ruam Mit station to Ratchada station. Obayashi operated two other machines for excavating the twin tunnels for Section B from Ratchada station to Bang Sue station. For the South Tunnel Section, two machines operated by Kumagai Gumi were launched from Rama IX station and driven southward to Sirikit station in Section C. The last section is Section D from Sirikit station to Hua Lumphong station excavated by Bilfinger & Berger. The six EPB machines used in Sections A, B, and C were similar models manufactured by Kawasaki and the other two used in Section D were Herrenknecht machines. All of the shields had very similar specifications. The details of each shield are provided in Chapter 5.

During the initial year of this research, the author observed the tunneling operations and collected all relevant data while the eight EPB shields were excavating the tunnels. This work developed the first comprehensive EPB tunneling database. The database contains monitoring results that include all shield operational records and field instrumentation readings. The database not only allows one to study the behavior of ground movements occurring during excavation, but also becomes a useful source for developing predictive models of the ground settlement.

1.2 Problem Identification

Peck (1969) addressed the issues associated with soft ground tunneling, and proposed an empirical relation based on field observations of several tunneling projects around the world. The empirical relation has become a classical framework widely used for predicting tunneling-induced ground movement. However, at the time of Peck's work, tunneling was mainly accomplished using either hand mining methods or open-faced shield methods, including several under compressed air. As a result, ground movements caused by the tunneling methods used at that time depended more on geological conditions than on the tunneling operational parameters. Empirical methods relating geological conditions to surface settlements were developed on this basis (Peck, 1969 and O'Reilly and New, 1982).

Since 1969, many innovations have been introduced to improve tunneling in soft ground. At present, the Earth Pressure Balance (EPB) Shield Tunneling Method, which was first developed in Japan (Stack 1982), has become one of the most popular methods for soft ground tunneling. With this tunneling technique, ground movement can be, in theory, controlled by balancing the pressure inside the earth pressure chamber relative to the outside ground pressure during excavation. To achieve the minimum settlement, there are many operational parameters involved such as face pressure, penetration rate, pitching angle, and grouting quality. All of this makes the shield-ground interaction complex.

Numerous empirical and analytical relations exist between shield tunnel characteristics and surface and subsurface deformation; also 2-D and 3-D numerical analyses have been applied to tunneling problems. Similar but substantially fewer approaches have been developed for EPB tunneling. This research makes use of the fact that in the Bangkok MRTA project, the tunnel sizes are practically identical and the subsurface conditions over long distances are comparable, thus allowing the establishment of relationships between ground characteristics and EPB-operation on the one hand, and surface and subsurface deformations on the other hand. A computerized database, which records much of the information on a ring-by-ring (1.2 meter interval) basis, was developed for

this purpose. After using the information to identify which ground- and EPB-characteristics have the greatest influence on ground movements, an approach based on Artificial Neural Networks (ANN) will be used to develop predictive relations.

1.3 Research Objectives

The goal of this study is to first develop a better fundamental understanding of the Earth Pressure Balance (EPB) Shield Tunneling method and ground responses. Since complex ground-shield interaction exists for this tunneling method, extensive field instrumentation data and continuous observation of operational parameters are essential. Using the extensive computerized database developed for this purpose, this research attempts to study the ground-shield behavior in detail, and to investigate the effect of influencing parameters on surface settlements. Hence, the collected data in the database forms the basis of the research in this project, which has the following objectives:

1. To investigate and analyze the behavior of ground response related to EPB tunneling based on other earlier case histories and the observed data from the MRTA project.
2. To investigate ground responses including surface settlements in the longitudinal and transverse directions, and lateral deformation affected by EPB tunneling.
3. To determine factors including geological conditions, tunnel geometry, and EPB operational parameters that may influence the ground movement.
4. To evaluate relationships between the influencing factors and surface settlements.
5. To investigate twin-tunnel issues including settlement troughs and effects of the second tunnel on the first tunnel
6. To examine whether available predictive methods can be used for predicting surface settlements induced by EPB tunneling

Artificial Neural Networks (ANN) are introduced to provide a better prediction of surface settlements caused by EPB tunneling. Since the method has the ability to map input to output patterns, ANN may enable one to map all influencing parameters to surface settlements. Combined with the extensive computerized database that provides all parameters needed for the network inputs and outputs and the knowledge of what influences the surface settlement, ANN can become a useful predictive method.

This research attempts to evaluate the potential as well as the limitations of ANN for predicting surface settlements caused by EPB shield tunneling and to develop optimal neural network models for this purpose. To achieve the objectives, many cases using data from the MRTA project will be used to assess the applicability of the ANN models.

1.4 Outline of Thesis

Chapter 2 provides an overview of the history of shield tunneling, basic terminology and developments of shield design including a variety of methods to provide support to the tunnel face in soft ground. Earth Pressure Balance (EPB) shield tunneling procedures are discussed. In Chapter 3, previous methods of predicting ground deformation are reviewed to determine if they are valid for EPB tunneling. Advantages and disadvantages of these methods are also discussed. In Chapter 4, several earlier case histories of shield tunneling around the world are summarized to investigate ground response induced by shield tunneling and to determine factors that might affect the behavior of the ground during excavation. Chapter 5 provides general descriptions of the Bangkok Subway (MRTA) project, including geological conditions, tunnel alignment, and methods of excavation. Details of tunneling drives are discussed in order to provide insight into the project.

In Chapter 6, the computerized database system using all information collected from the MRTA project is described. The chapter also explores the structure of the database system. In Chapter 7, ground movements associated with a single tunnel excavated by EPB shields in the MRTA project are evaluated, while in Chapter 8, effects of the second

tunnel on ground response and the first tunnel's lining are studied. In Chapter 9, the effect of influencing parameters on surface settlements is investigated.

The fundamentals of Artificial Neural Networks (ANN) are introduced in Chapter 10. Various types of ANN are discussed including feedforward networks which are used in this study. The learning process using a back-propagation algorithm is also explained in the chapter. The ability of artificial neural networks (ANN) for predicting surface settlements caused by EPB shield tunneling is investigated in Chapter 11, in which ANN models with various numbers of hidden layers and various numbers of hidden nodes are trained for various numbers of training epochs to obtain an optimal neural network model. In Chapter 12, the artificial neural networks (ANN) are used for predicting surface settlements induced by EPB tunneling. Finally, Chapter 13 contains conclusions from this research and recommendations for future works.

References

O'Reilly, M. P. and New, B. M. (1982). "Settlement above Tunnels in the United Kingdom – Their Magnitude and Prediction". *Tunneling* 88, London, pp. 231-241.

Peck, R. B. (1969). "Deep Excavations and Tunneling in Soft Ground". *Proc. 7th Int. Conf. on Soil Mechanics and Foundation Engineering*, Mexico City, State of the Art Volume, pp. 225-290.

Stack, B. (1982). *Handbook of Mining and Tunneling Machinery*, John Wiley & Sons, New York.

CHAPTER 2

Earth Pressure Balance (EPB) Shield Tunneling Method

2.1 Historical Development of Shield Tunneling

As its name implies, a “shield” simply provides within a tunnel a working area, which is protected against the collapse either of the walls or roof of that section of the tunnel, which has been recently excavated, and in which no tunnel lining or other means of support has yet been erected. Obviously, when the tunnel is being driven through stable ground no shield is necessary. However, as its importance as a tunneling tool extends beyond that of merely supporting the ground, it is not uncommon for one to use a simple shield when driving a tunnel in good ground. For instance, the shield provides shelter for segment erectors, muck disposal units, grouting equipment, etc. It also provides a bridge between the erected lining and the face so that work on extension of the lining and excavation of the face may be carried out simultaneously.

The history of shield tunneling started with soft ground shields developed by Marc Isambard Brunel in England. Brunel first introduced two types of circular shields patented in 1818. The shields consist of different cells. In each of these cells, one worker can work independently and fully secured. The first type is the “screw shield” in which

the whole shield skin was pushed forward by means of hydraulic jacks (Figure 2.1). The shield can be considered as the predecessor of the modern Earth Pressure Balance shield. In the second type, Brunel divided his shield into small compartments, which can be forced forward by jacks while workmen in each separate cell inside the shield remove the ground ahead of the shield. The individual cell could each be advanced independently (Figure 2.2). After the completion of each excavation cycle, thrust jacks positioned at the rear of the shield react against the newly erected tunnel lining or against a thrust ring and move the shield forward, together with all its face and trailing ancillary equipment.

The tunnel project underneath the Thames in London finally enabled Brunel to realize his ideas above. The Brunel's shield was made of cast iron as shown in Figure 2.3. It had a rectangular shape and consisted of twelve contiguous frames each about 1 m wide divided into three sections namely, an upper, middle, and lower sections. Each frame stood upon two swinging legs attached by ball joints to two massive flat shoes (base-plates). Each chamber had one worker so that there were altogether 36 workers. The shield functioned according to the following pattern: first, timber plates were pushed ahead into the soil with the help of spindles (see Figure 2.3). The timber plate was removed and soil was excavated only 6 inches each time. Then the plate was installed back and supported by spindles. The brick liner was built right behind the shield and served as abutment for the whole frame. This whole procedure was an excavation cycle of the shield. It was with great difficulties that work on the tunnel under the Thames started in 1825, and it was only in 1843 that the tunnel was completed after more than five serious cases of flooding. In 1869, James Henry Greathead excavated a tunnel underneath the Thames using a circular shield. For the first time, cast iron lining segments were employed. Greathead's circular shield became the model for most of the open-faced shields developed later. In 1876, John D. Brunton and George Burton built the first mechanized shield. The shield had a hemispherical rotating cutter head consisting of several plates. As late as 1959, Elmer C. Garden introduced a fluid supported tunnel face for a sewer tunnel with a diameter of 3.35 m in Germany. In 1967, the first slurry shield with a cutting wheel and hydraulic mucking was used in Japan. The development of Earth Pressure Balance shield started in 1966, also in Japan. Details of

shield development mentioned above can be found in Stack (1982) and Maidel et al. (1996).

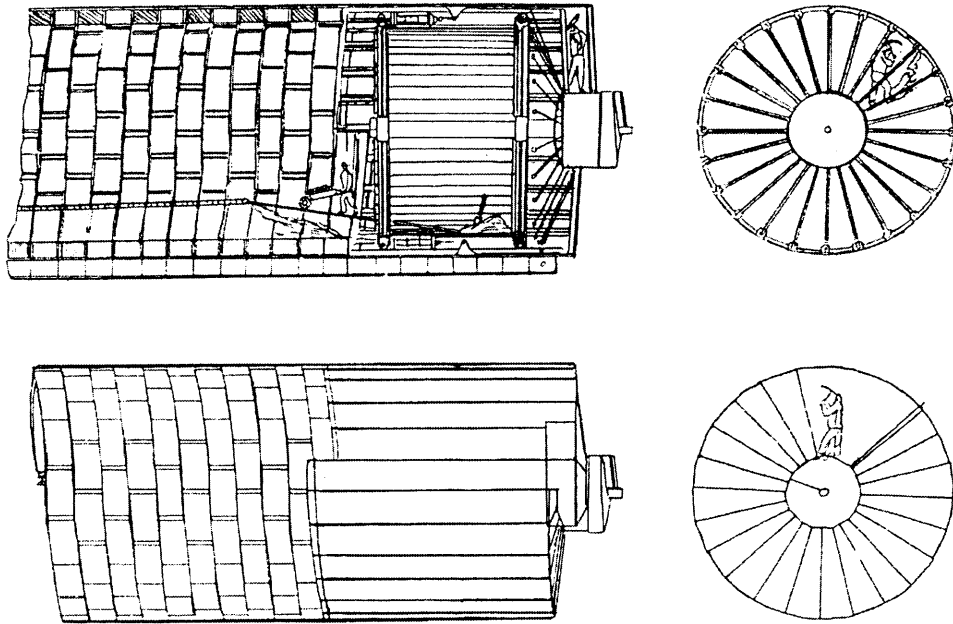


Figure 2.1 Marc Brunel's "screw" shield (1818)

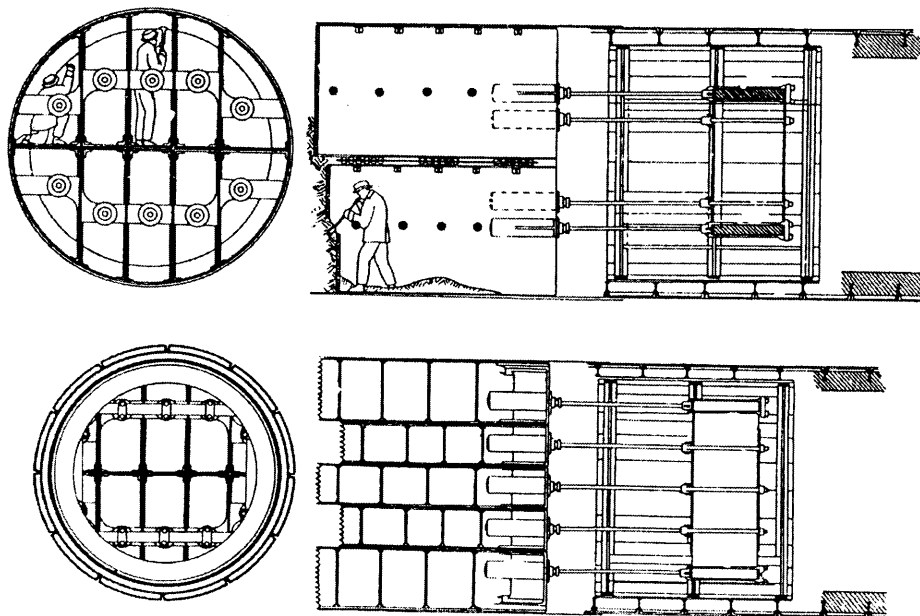


Figure 2.2 Marc Brunel's "compartment" shield (1818)

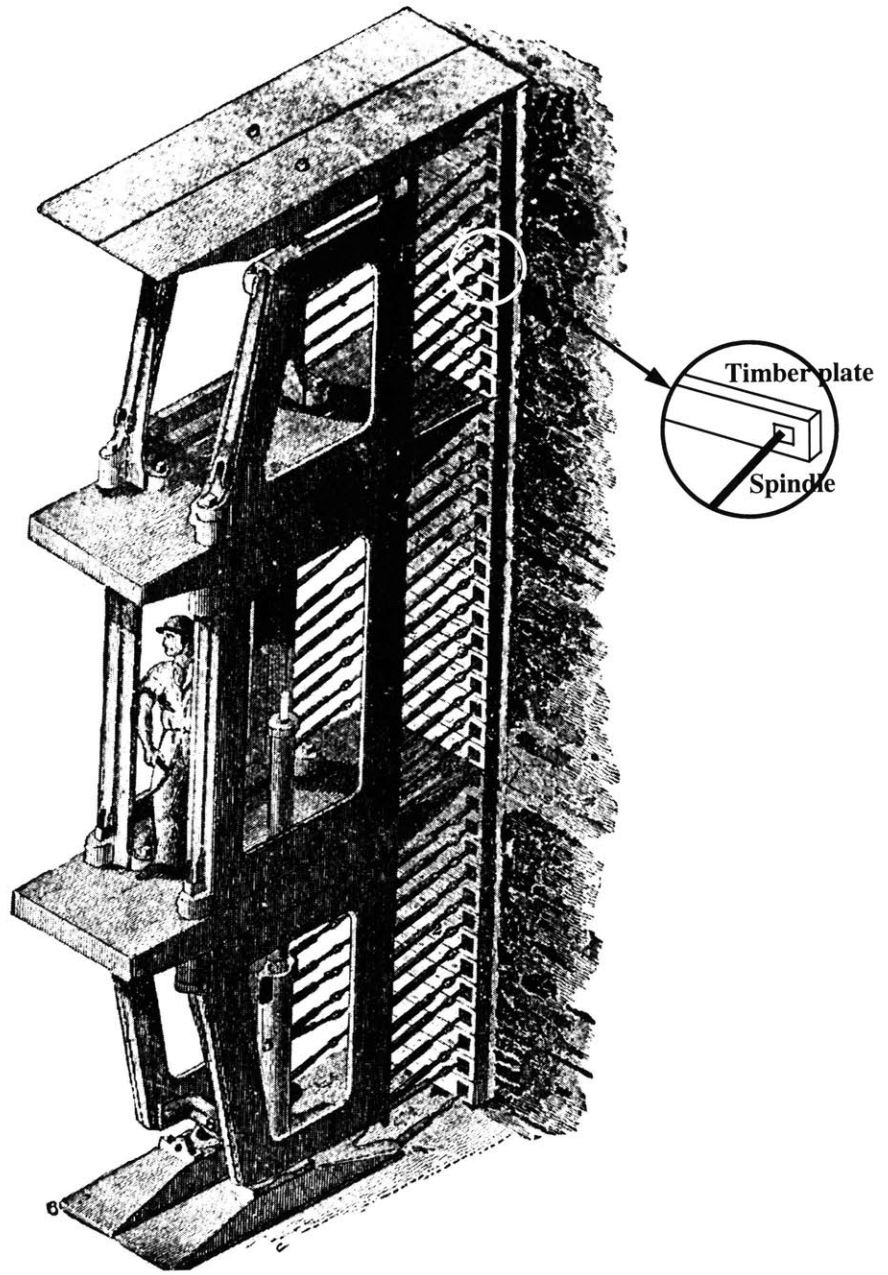


Figure 2.3 Marc Brunel's shield for the tunnel underneath the Thames (1825-1843)

2.2 Different Types of Shields

The general principle of a shield is based on a cylindrical steel assembly pushed forward in the axis of the tunnel while excavating the soil at the same time. The shield secures the excavated void until the preliminary or final tunnel lining is installed. The shield has to withstand the pressure of the surrounding ground and prevent the migration of ground water. While the void over the shield is held by the shield body itself, additional measures to secure the tunnel face are required depending on the ground and water condition. In Figure 2.4, five different measures for stabilizing the tunnel face are illustrated. These methods constitute a great advantage of the shield tunneling method. Contrary to other tunneling methods, the soil can be stabilized during the excavation.

Besides the specific mean of supporting the tunnel face, the specific method of soil excavation is also an important factor in shield machines. Manual excavation, hand shield, constitutes the simplest technique and is only used in special cases such as for short distance to be driven under specific geological conditions. However, more typical is the use of the machines where one distinguishes between mechanized partial-face and full-face excavation. Partial-face shield (i.e. classified as a “partially open shield” in Table 2-1) is shown in Figure 2.5. Equipment such as excavators and special cutter heads are used. They are guided and controlled either by the operating personnel or automatically. Depending on the geology encountered, full-face excavation (i.e. classified as a “closed-face shield” in Table 2-1) can be carried out by means of spoke wheels, rim wheels, or closed cutter heads as shown in Figure 2.7 through Figure 2.10.

Open-faced shields are shields without a system for pressure application at the tunnel face as shown in Figure 2.6. Typically, the open-faced shield can be used in ground conditions with no ground water or where the ground water was lowered beforehand. In cases where support of the tunnel face to counteract earth pressure is required, this can be achieved mechanically (Figure 2.4b). If the shields are operated below the water level, to prevent the ingress of ground water, compressed air can be applied. Compressed air shields (Figure 2.4c and Figure 2.7) can be hand shields as well as mechanical partial- or

full-face machines. A secure air supply is required as interruptions would lead to water entering the shield and the tunnel and the chambers under compressed air need to be airtight. For this purpose, a pressure bulkhead in the tunnel and an associated air lock separate the compressed air in the tunnel from the atmosphere.

The tunnel face can be supported by pressurized slurry in slurry shields (Figure 2.4d and Figure 2.8). The support medium of the face in slurry shields is a frictionless fluid. It consists of water and an additive that can form an impervious layer at the fluid-soil interface. This layer transfers the pressure of the support fluid to the tunnel face. Bentonite is generally used as the slurry additive. In EPB shields (Figure 2.9), the soil material itself supports the face as shown in Figure 2.4e. The pressure inside the earth chamber has to be maintained equal to the soil pressure acting on the shield face.

Due to special geological and hydro-geological conditions, it is sometimes not possible to excavate the entire tunnel route with a single machine design. For such reasons, the mix shield (Figure 2.10) was developed which can cope with changing geological formations. Slurry shields, EPB shields, and mix shields are all classified as closed-face shields (Table 2-1). The last type of shield is the blind or extrusion shield as shown in Figure 2.11. The shield is normally used in cases where very homogeneous ground with a low shear strength and very plastic behavior is encountered since the soil can be squeezed into the interior of the tunnel through several openings in the front.

In recent years, most soft ground tunneling projects have adopted the Earth Pressure Balance shield and slurry shield techniques. The EPB shield is usually considered particularly suitable for cohesive or silty ground that does not contain cobble or boulder obstructions and in which the water head at the face is not high. In other words, the more homogeneous and consistent the soil, the more successful the technique is. Although the EPB shield is capable of working in sandy conditions, this might be problematic. On the other hand, the slurry shield method is quite well suited for tunneling in non-cohesive ground.

Table 2-1 Classification of shield tunneling machine

	Face	Machine Type	Stabilization of Cutting Face	Excavating Method
Shield	Fully Open	Manual	Hood + Earth Retaining Jack	Hand
		Semi-Mechanical	Hood + Earth Retaining Jack	Back Hoe, etc.
		Mechanical	Cutter Disk or Spoke	Revolving Cutter
	Partially Open	Partial Face Extraction	Hood	Excavation shovel, bucket tooth
		Blind	Steel Bulkhead with slit	Extrusion
	Closed	Earth Pressure Balance (EPB)	Dug Soil + Cutter Disk or Spoke + (additive)	Revolving Cutter
		Slurry	Slurry + Cutter Disk or Spoke	Revolving Cutter
		Mixed	Slurry + EPB	Revolving Cutter

For the removal of the excavated material special transport systems are necessary to transfer the material through the shield to the surface. The most appropriate system has to be chosen depending upon the type of ground to be expected, the resulting excavation and face support method. These decisions have a direct impact on the mode of transport of the excavated material as will be discussed later.

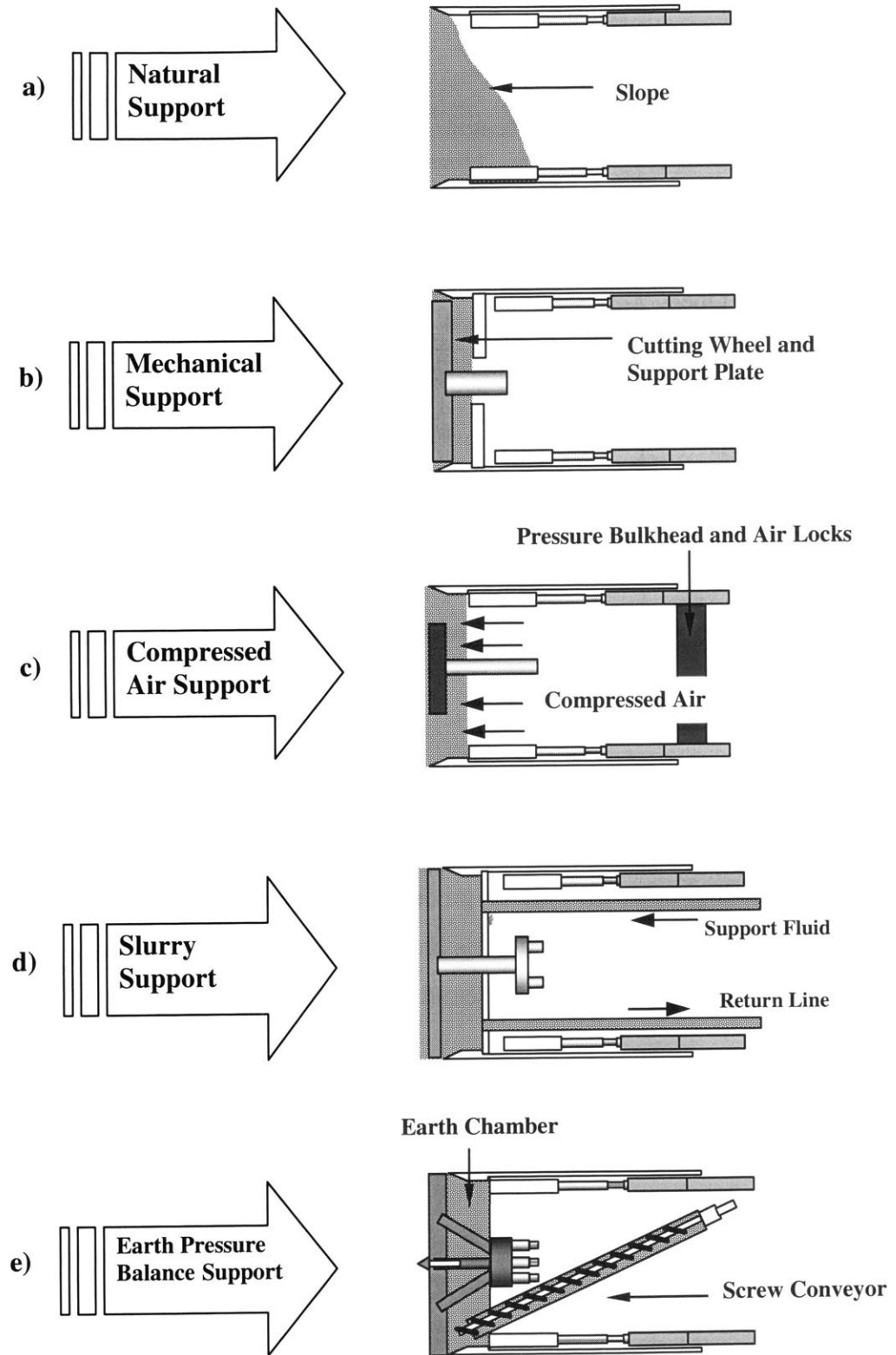
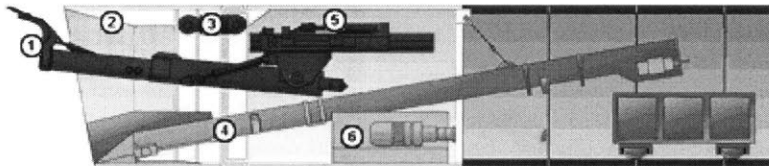
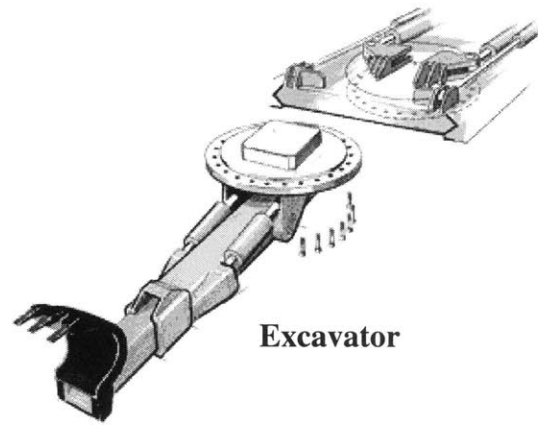
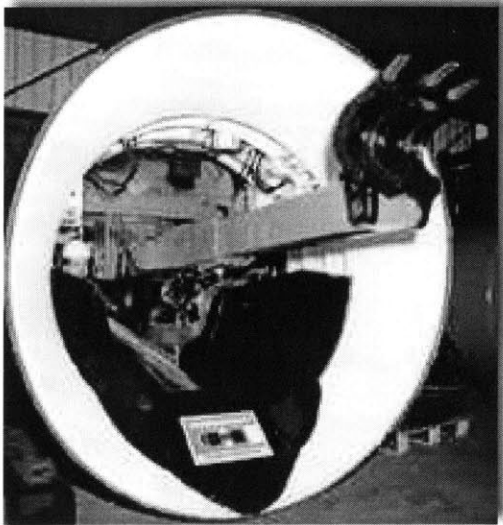


Figure 2.4 Different measures of face supporting (after Maidl et al., 1996)



1. Excavator
2. Shield
3. Steering cylinder
4. Conveyor belt
5. Machine pipe
6. Hydraulic power pack

Figure 2.5 Partial face shield (Herrenknecht)

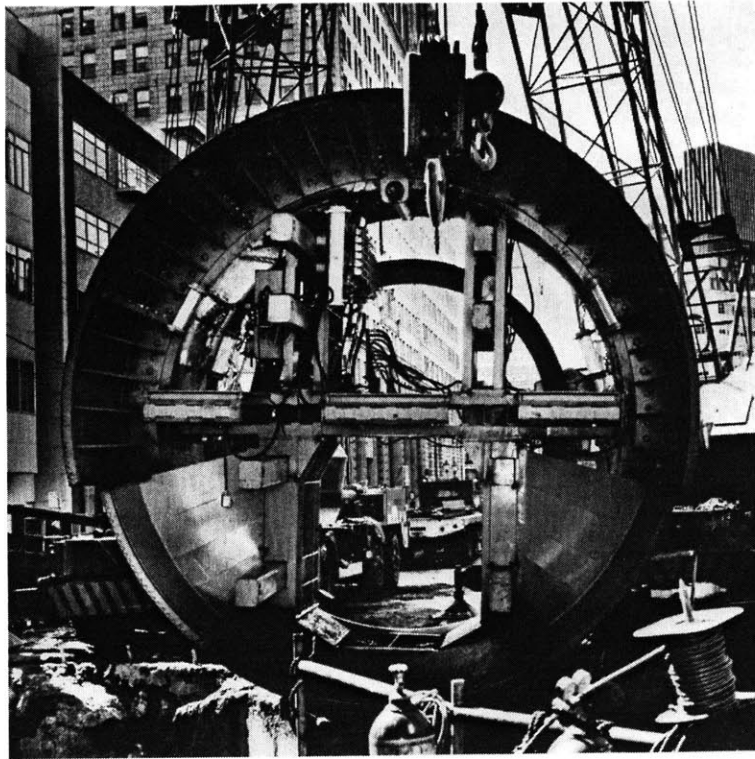


Figure 2.6 Open-faced shield used in Trans-Bay tube project (1969)

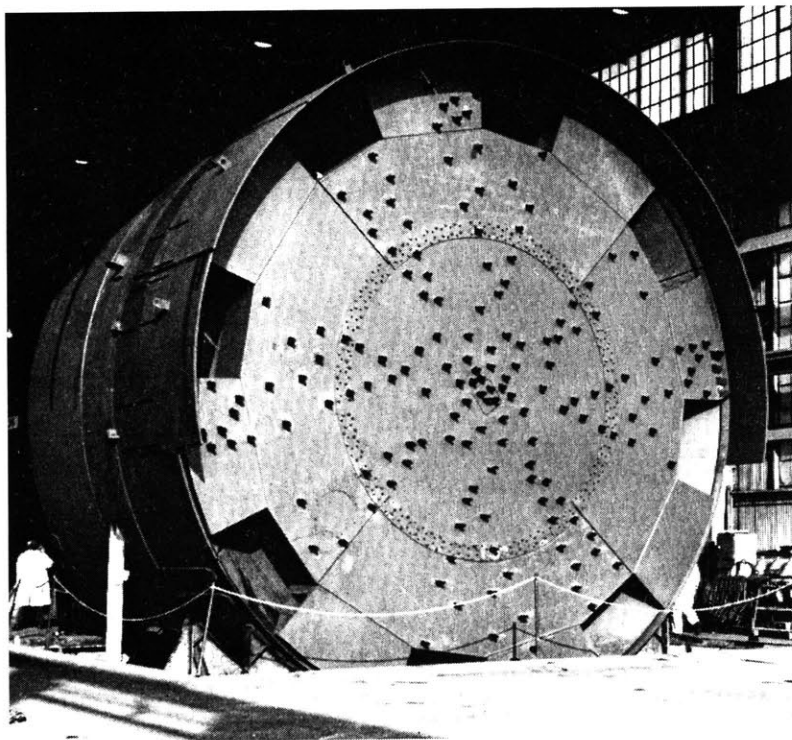


Figure 2.7 Compressed air shield used in the express subway tunnel in Paris (1964)

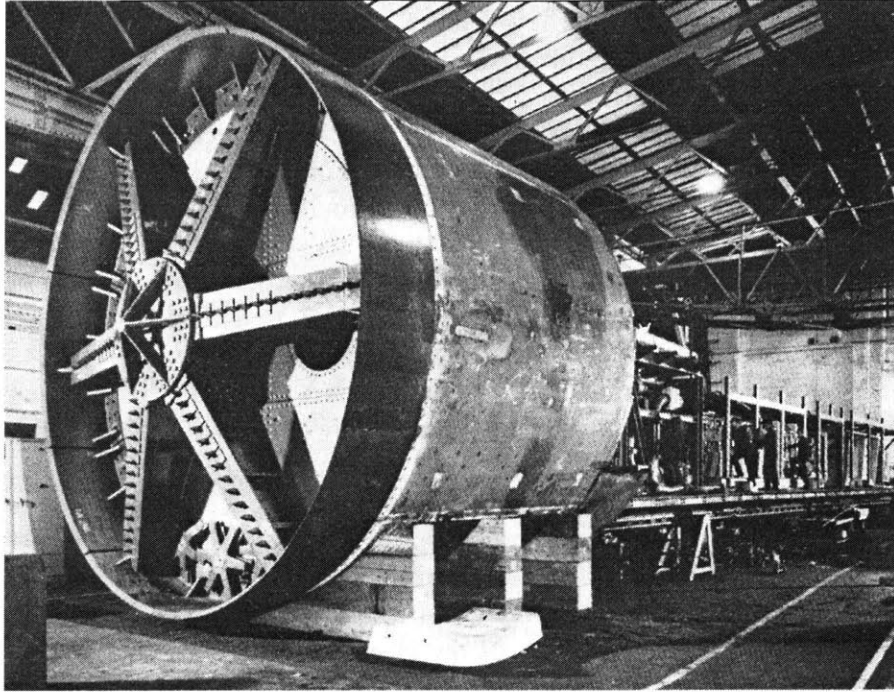


Figure 2.8 Slurry shield used for the construction of Mexico City sewer tunnel (1969)

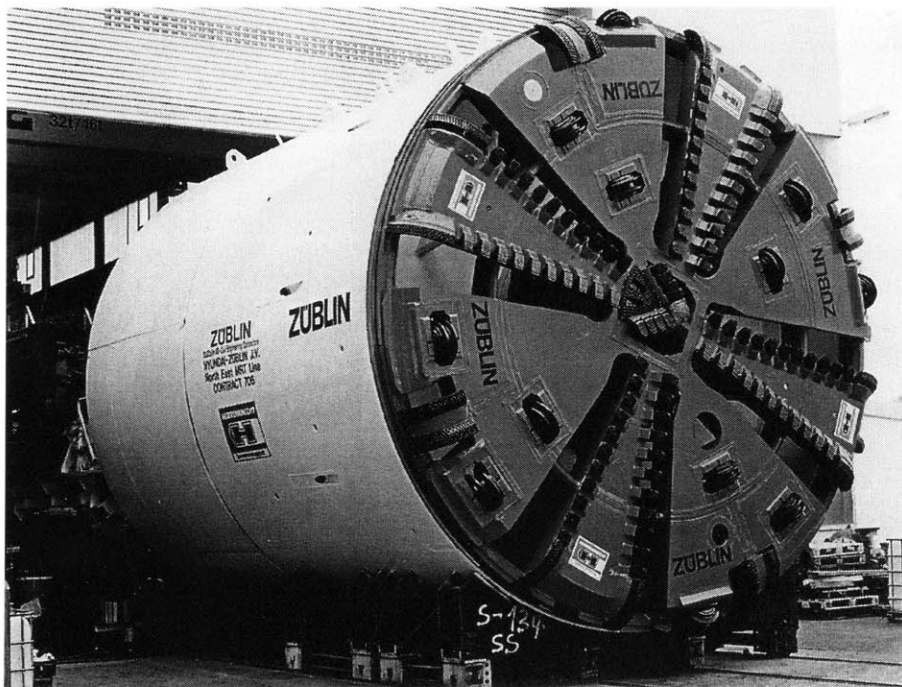


Figure 2.9 EPB shield used in the Singapore MRT project

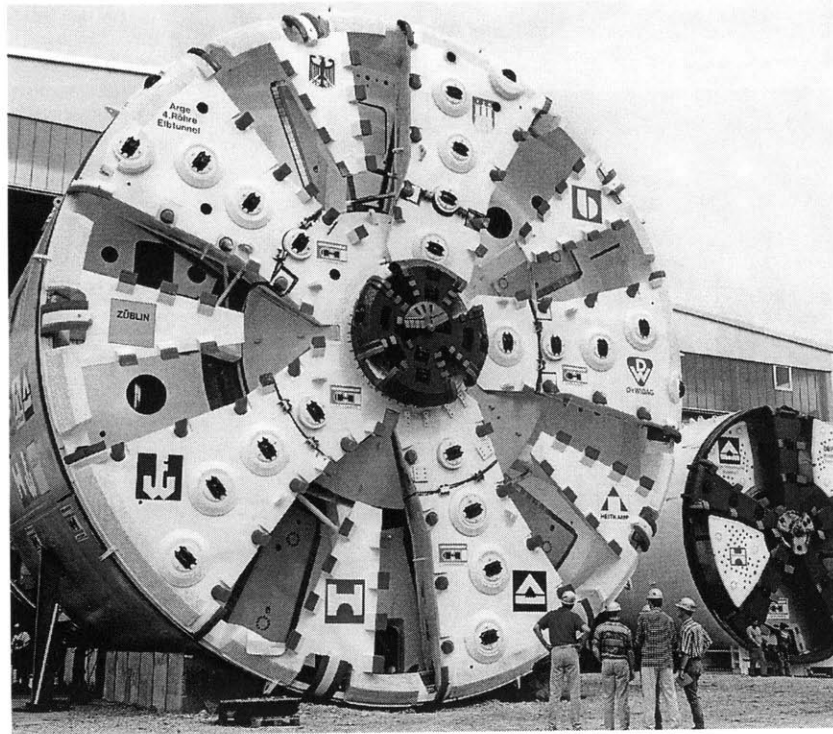


Figure 2.10 Mix shield used in the Fourth Elb Tunnel project, Germany

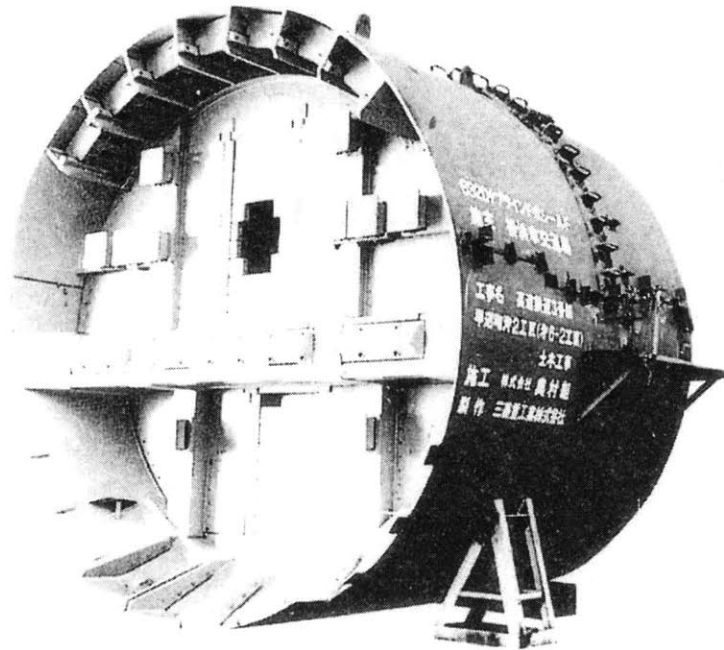


Figure 2.11 Blind shield manufactured by Mitsubishi

2.3 Earth Pressure Balance Shield

2.3.1 Introduction

The original concept of the EPB shield was pioneered by the Sato Kogyo Company Limited, a Japanese construction firm, who tried to find a method of tunneling through soft ground. Although, numerous tunneling projects with compressed air and slurry shields had already been successfully accomplished in Japan, there were disadvantages and limitations associated with these methods, which the Sato Kogyo Company sought to eliminate. At the time, slurry shields were widely used in soft ground tunneling. However, it was found to have high capital and operating cost because a slurry shield requires a separation plant on the surface. In particular, Sato Kogyo Company intended to find a machine, which would excavate efficiently yet comply with the environmental regulations and laws in force in many of the cities of Japan (Stack 1982). These included air and water pollution control laws, industrial water, waste disposal and public cleaning laws, and prevention of oxygen deficiency and prevention of compressed air hazard ordinances, etc. Developmental work on the earth pressure balance shield was therefore begun by the Sato Kogyo Company in 1963 and, after considerable research both in the laboratory and in the field, a unit was finally built by the Ishikawajima Harima Heavy Industries Company Ltd in 1966. In 1974, the first EPB shield with an outside diameter of 3.72 m was used for the tunnel excavation of 1,900 m collector drive in Tokyo. Figure 2.12 shows the schematic diagram of the EPB shield first introduced by Sata Kogyo.

In the following years, earth pressure balance shields were produced by an increasing number of manufacturers under different names such as earth pressure balance shield, pressure holding shield, slime shield, soil pressure shield, confined soil shield, mud pressurized shield or muddy soil shield. All of these terms principally apply to the same method, known as the earth pressure balance system. The Earth Pressure Balance shield has advantages over other types of shields as shown in Table 2-2.

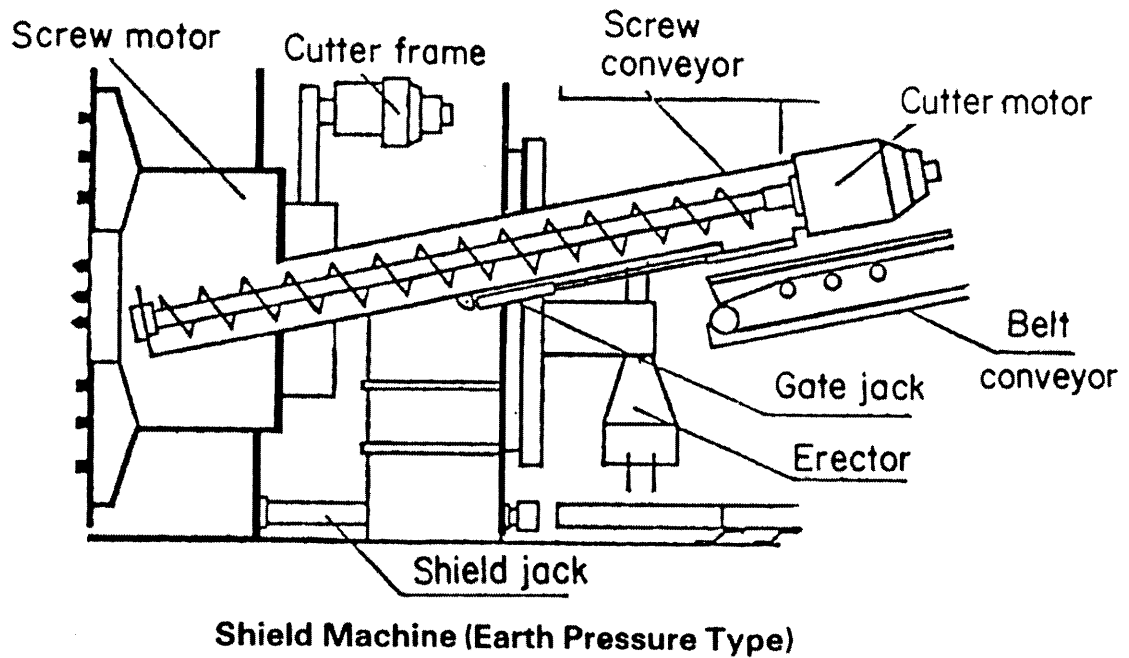


Figure 2.12 Earth Pressure Balance shield introduced by Sato Kogyo (1963)

Table 2-2 Typical advantages of the EPB shield over other shields

Advantages over Slurry Shield	Advantages over Partial-face Shield	Advantages over Open-faced Shield
No separation plant, Economical application in ground with a high percentage of silt and clay	Can excavate a variety of soil conditions below the ground water	Can excavate a variety of soil conditions below the ground water
Can operate in both open mode and earth pressure balance mode	Full face cutter provides a better performance with lower ground loss	No compressed air-lock chamber needed

2.3.2 Excavation

In the EPB shield tunneling technique, a tunnel can be excavated by the shield cutter face. Spoil or excavated soil is taken out through the screw conveyor and belt conveyor as shown in Figure 2.12 and Figure 2.13, respectively from the earth chamber and transported by means of pumping (Figure 2.14) or muck skips pulled by locomotives (Figure 2.15). In general practice, to minimize ground movement, the earth pressure at the cutting face is carefully monitored and controlled as follows:

- 1) Target face pressure for each excavation cycle has to be determined prior to excavation depending on the design alignment and subsurface ground conditions. This target face pressure is used as a control parameter during excavation.
- 2) During excavation, the actual face pressure has to be recorded and controlled and maintained at the target pressure.
- 3) For each excavated ring or each excavation cycle, the target face pressure and the actual face pressure needs to be recorded in the excavation report which will be used as a reference.

The target pressure is used as a control parameter during excavation. As can be seen in Figure 2.16, the shield operator has to closely oversee the excavation in order to ensure that the shield is operated under the predetermined face pressure. Additionally, the shield operators in the shield control room have to monitor all other operational parameters at all time during excavation as shown in Figure 2.17.

It should be noted that if the pumping method is used for muck transport (Figure 2.14), there are some important concerns that need to be considered. In this method, the transport pipe is directly connected to the screw conveyor. The velocity in the transport pipe should be high enough to avoid blockage due to the spoil settling in the pipe, but it should be also low enough to minimize pipe wear. Furthermore, since in the EPB tunneling method, the rate of muck transport has to correspond to the controlled support pressure in front of the earth chamber, the shield operator is required to balance the rate of muck pumping with the shield advance in order to control the face pressure.

Usually, the excavation and shield advancement are carried out simultaneously. As the cutting face cuts the soil in front of the shield, hydraulic jacks behind the shield extend and push against tunnel lining to shove the shield ahead (Figure 2.18 and Figure 2.19). For instance, in the Bangkok Subway (MRTA) project, the shield's jack force or applied thrust force is approximately between 600 and 1000 tons and the stroke of the jack is typically 1.60 m. The careful position control of target pitching, expected horizontal and vertical deviations, and current alignment are also required during shield advancing. Generally, all of these factors are also recorded in every excavation cycle.

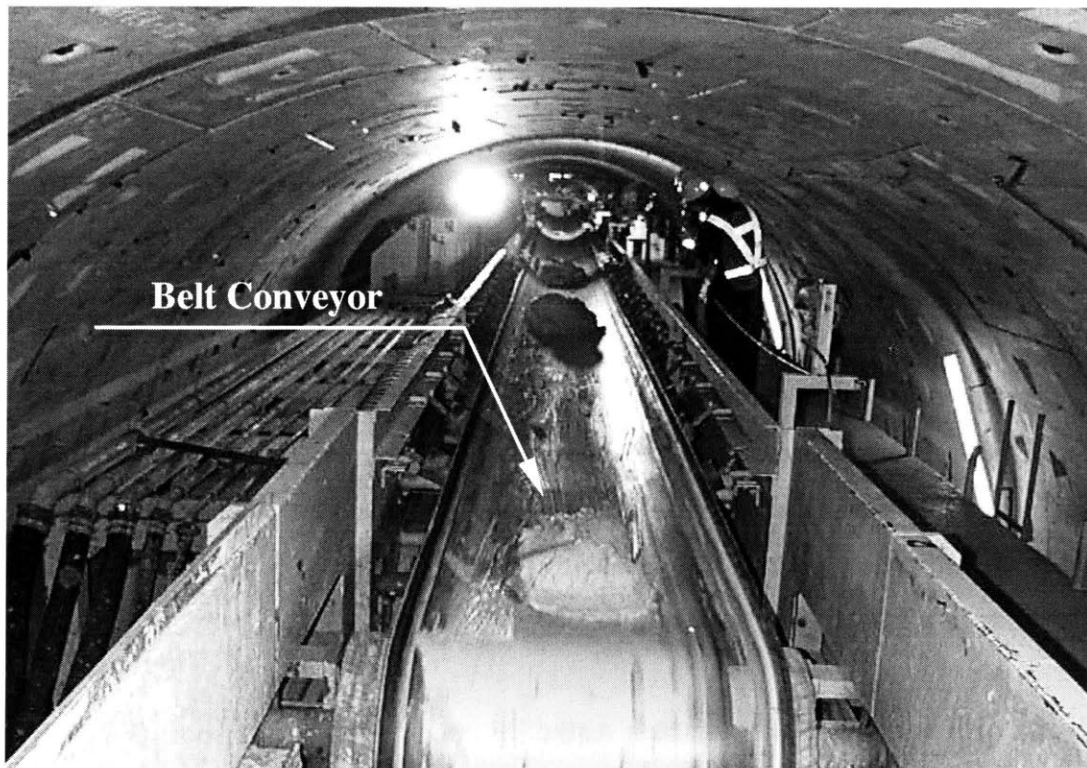


Figure 2.13 Belt conveyor transporting excavated soil from the screw conveyor (Bangkok-MRTA)

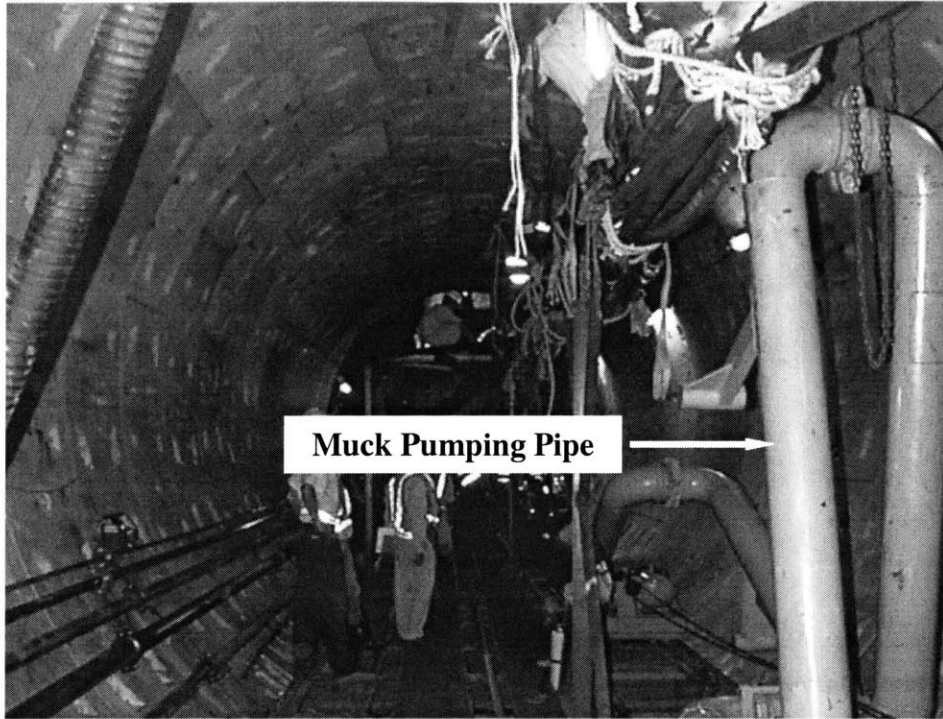


Figure 2.14 Muck pumping pipe connecting directly to screw conveyor (Bangkok-MRTA)



Figure 2.15 Locomotive transporting excavated soil out of tunnel (Bangkok-MRTA)

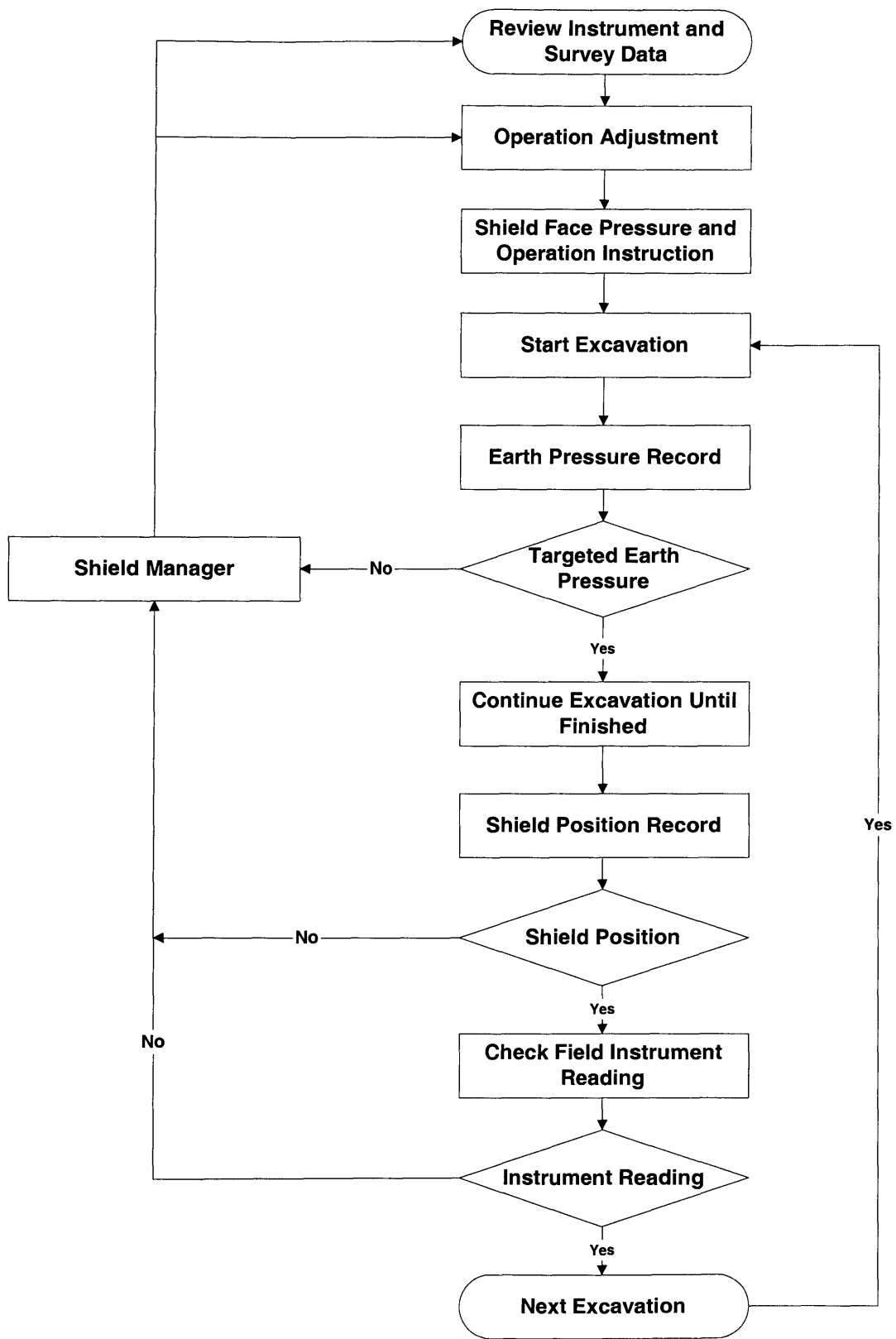


Figure 2.16 Tunnel monitoring work flowchart



Figure 2.17 Shield operators monitoring all operational parameters during excavation

2.3.3 Tunnel Lining

Segmental linings are usually associated with shield tunneling, and they are erected within the protection of a cylindrical tail shield. They can act as a one-pass system, providing both stabilization of the tunnel opening during construction and a permanent lining. Figure 2.20 and Figure 2.21 show the reinforced concrete segmental lining used in the MRTA project. These segments are manufactured and installed to close tolerances. Segmental lining may also be used in two-pass systems, with temporary segments providing only construction stabilization, and a second-pass cast in place concrete lining added for permanent service. Typically, segmental linings are smaller in diameter than the excavated tunnel, because they are erected inside a cylindrical shield that is part of the excavating equipment. The resulting annular void space (Figure 2.22) is usually filled with grout. In wet ground, segmental linings are usually bolted, to compress gaskets to seal against water leakage. In dry ground, unbolted segmental linings may be used. Additionally, in ground with appreciable stand-up time, segmental linings may be expanded by jacking them after they have been cleared by the advancing shield as shown in Figure 2.23.

2.3.4 Segment Erection

The tunnel lining is installed segment-by-segment using an erector located within the shield as shown in Figure 2.24. In the MRTA project, a segmental ring is 1.2 long along the tunnel axis and consists of six reinforced concrete segments for the South Tunnel Section and seven reinforced concrete segments for the North Tunnel Section both including one tapered key-segment. The difference in the number of the segments is due to the differences in segment handling equipment adopted in the North and South sections. Segments are connected using a curve bolt as shown in Figure 2.25 through Figure 2.27.

During excavation, the crew in the tunnel orders segment from the intermediate storage area located on the ground surface (Figure 2.21). The invert segments are normally the

first to be installed. The exact installation sequence is fixed and every change of order means a loss of time in the tunnel. Installing lists which depend on the type of ring and position of installation are established and supplied to an erector-controlling computer. The erector-controlling computer provides information on the optimum centering of the lining ring within the tail, relative to the shield. This is based on the position of the last ring measured after each excavation cycle and the expected position during the next cycle. Precision of the lining installation mainly depends on the steerability of the erector. The erector has to position the lining segments in a ring with a precision of a few millimeters such that the lining ring develops a contact pressure sufficient to compress the gasket between segments. After the installation is finished, the lining position has to be inspected as shown in Figure 2.28.

The segments can be transferred to the erector in two ways: (1) via the invert and (2) via the crown area. In the MRTA project, segments were transferred to the erector via the tunnel invert which requires less equipment than that in the tunnel crown as shown in Figure 2.29.

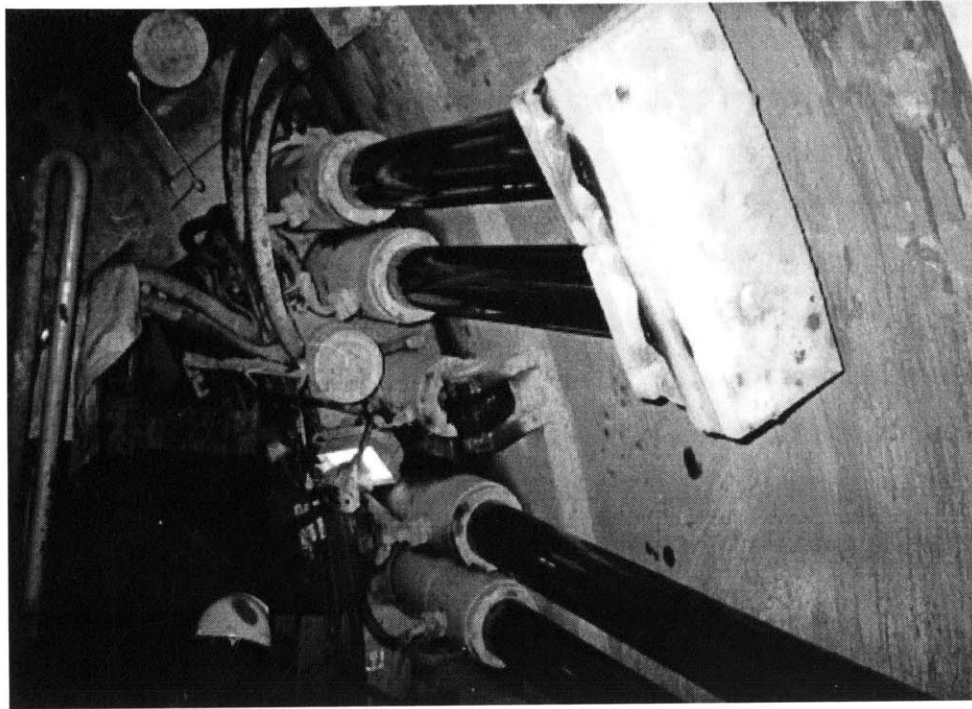


Figure 2.18 Hydraulic jacks behind the EPB shield

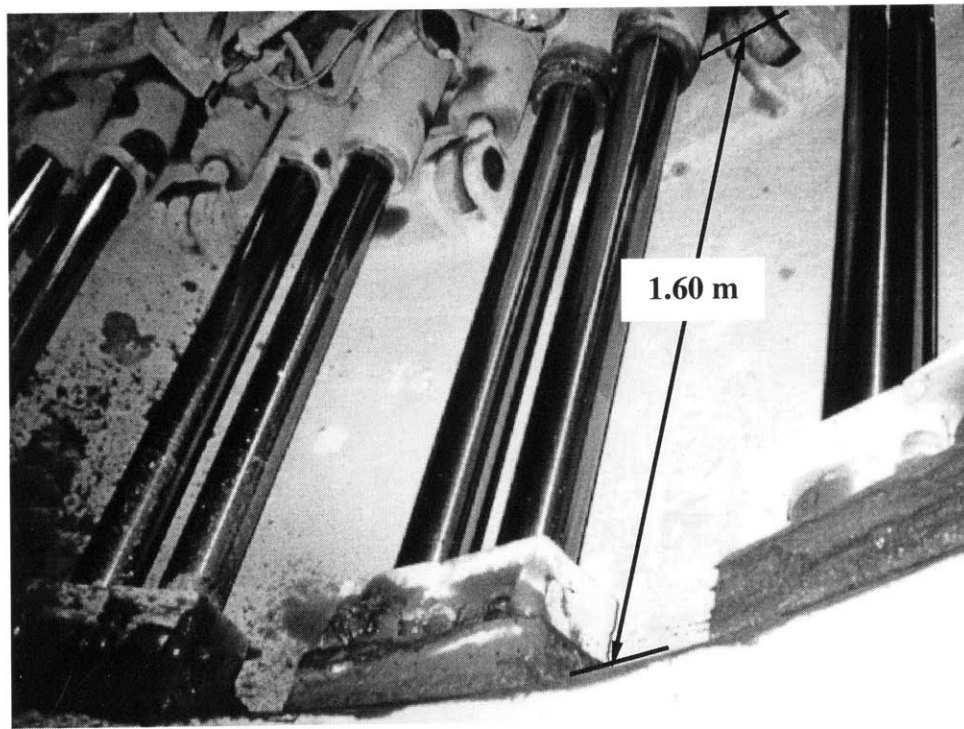


Figure 2.19 Hydraulic jacks push against installed lining during shield advancing



Figure 2.20 The Bangkok MRTA Project, reinforced concrete segmental lining

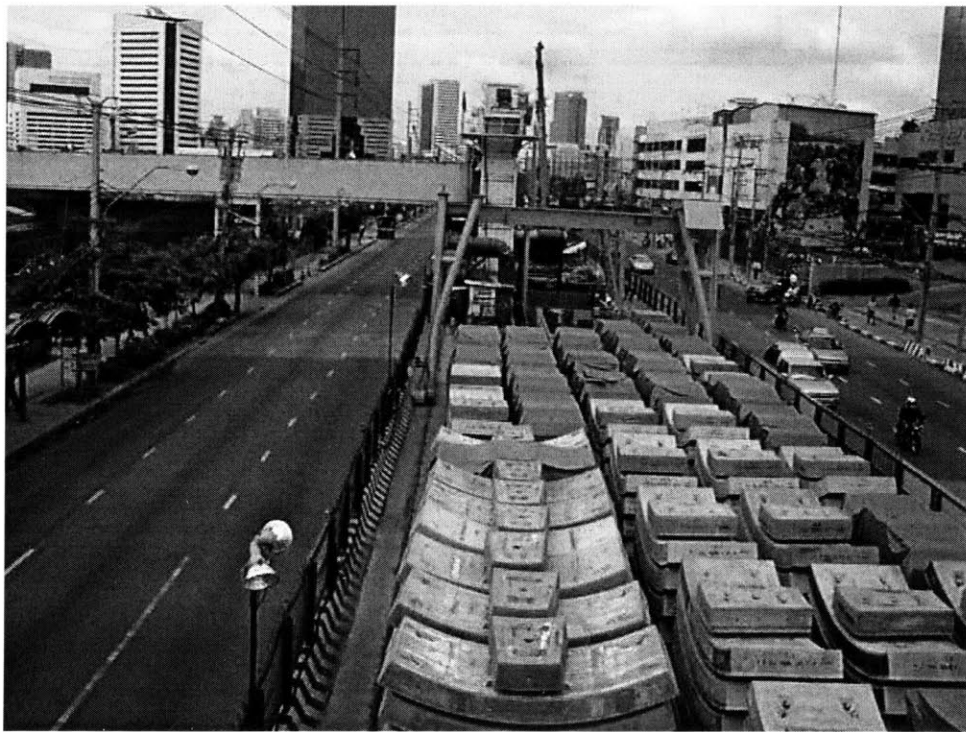


Figure 2.21 Segmental lining storage (Bangkok-MRTA, Thiam Ruam Mit Station)

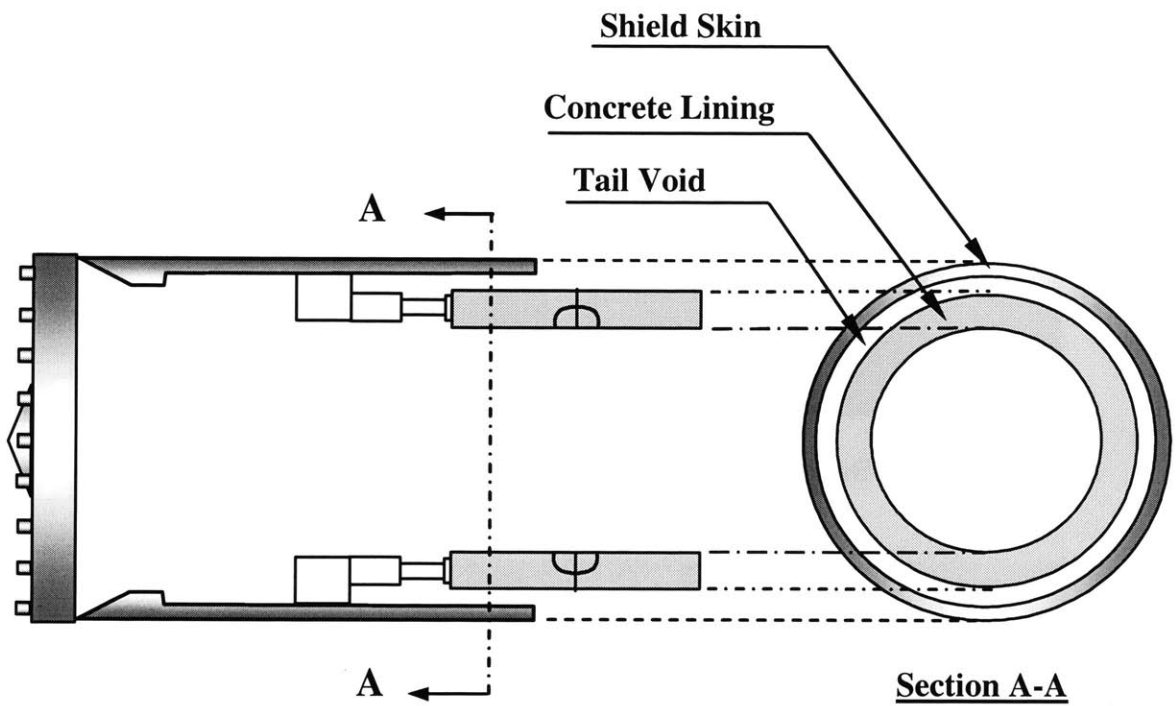
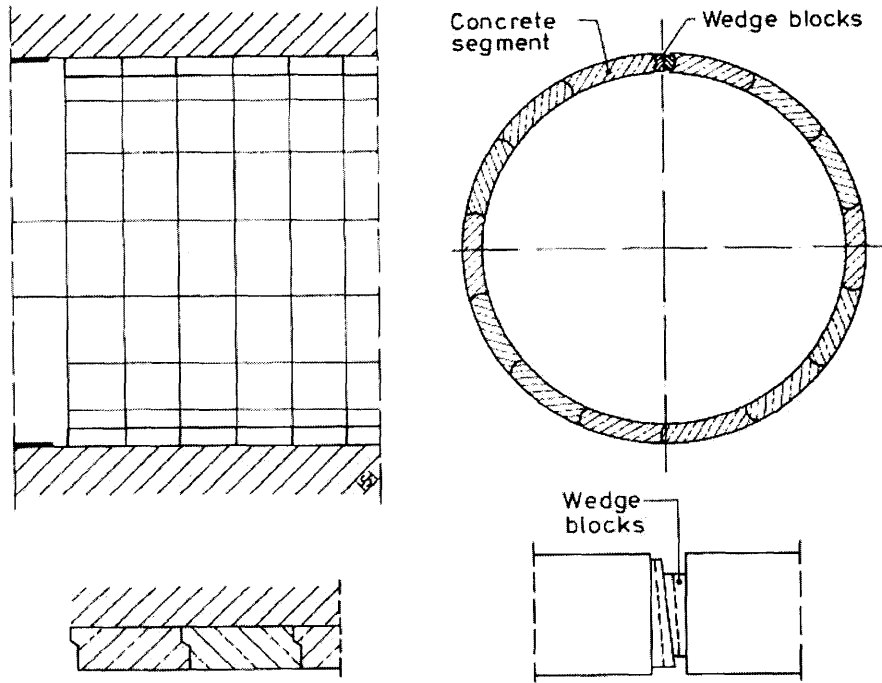
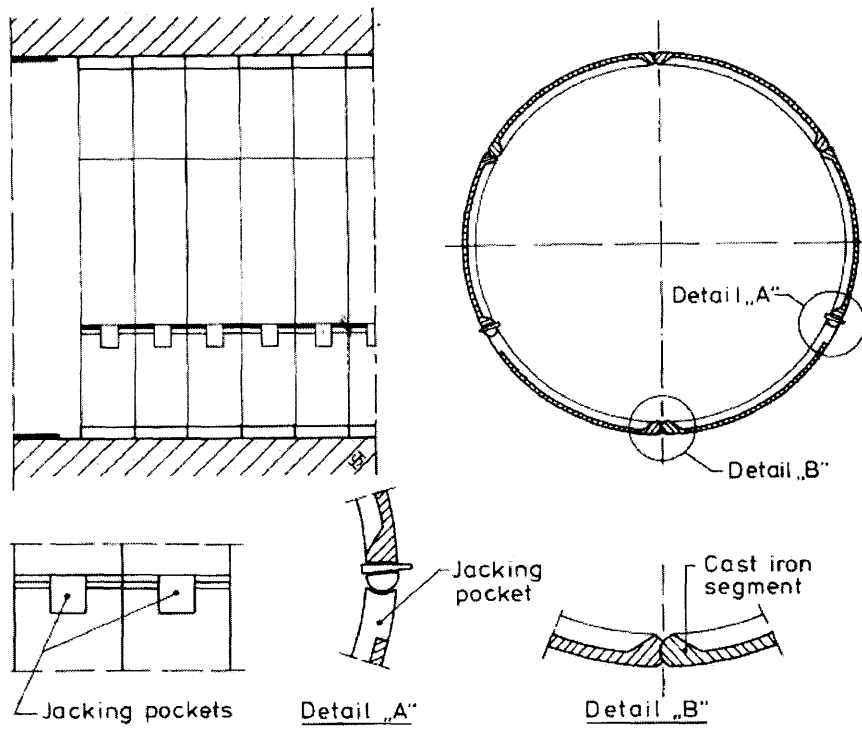


Figure 2.22 Schematic diagram showing a tail void between tunnel lining and the shield



(a) Concrete segment with wedge blocks



(b) Cast iron segment with jacking pockets

Figure 2.23 Expanded segmental lining



Figure 2.24 Erector arm erecting a segment with the designated location

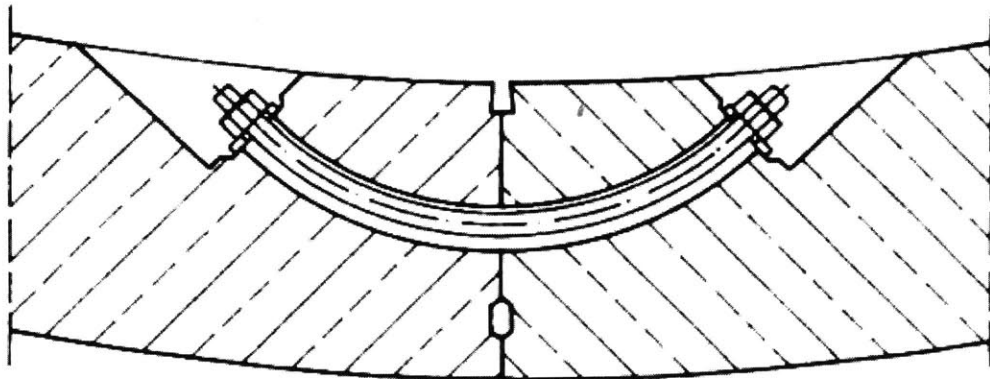


Figure 2.25 Connection of segments with curve bolt

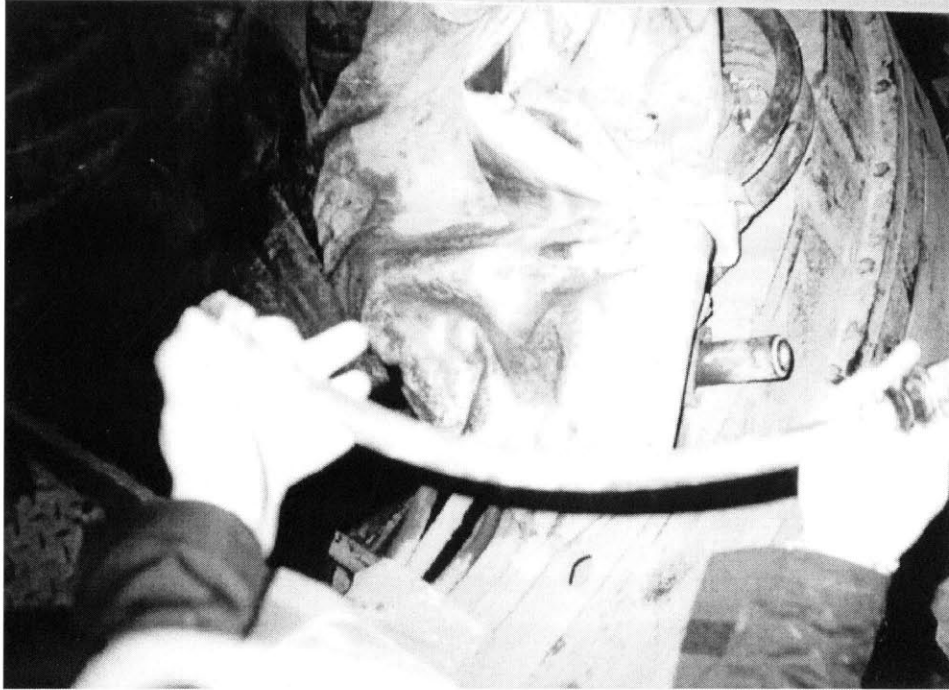


Figure 2.26 Curve bolt



Figure 2.27 Worker securing a curve bolt between segments



Figure 2.28 Worker checking the position of the installed lining ring

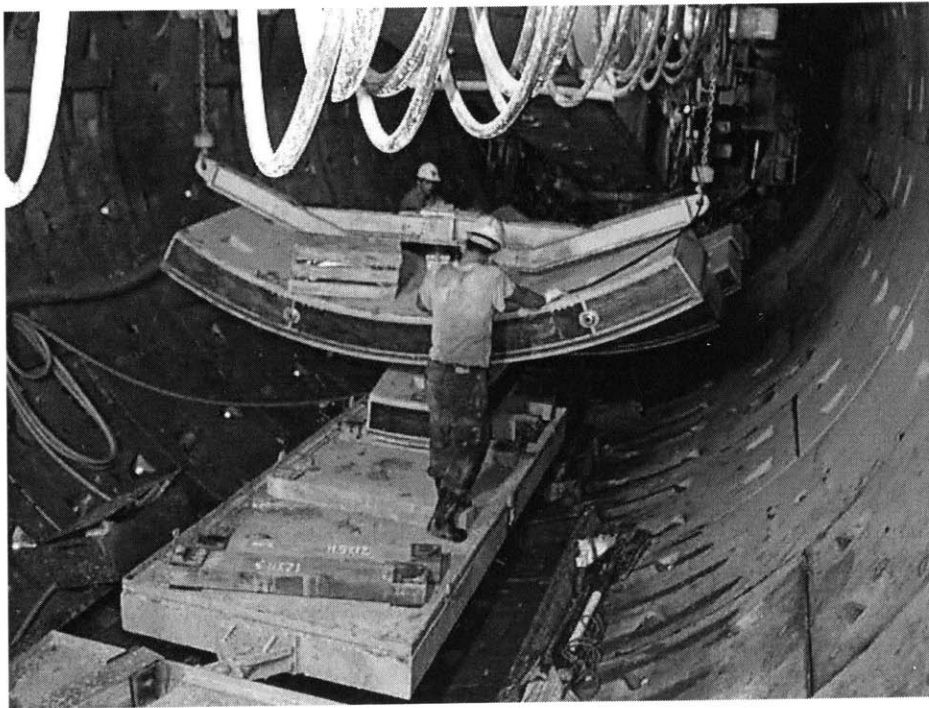


Figure 2.29 Segment transferred to the erector via the tunnel invert

2.3.5 Tail Void Grouting

In all shield tunneling methods, the diameter of the shield is larger than that of the prefabricated lining, first because of the shield skin plate must overlap the lining to permit assembly of the lining rings, and second because clearance must be provided between the outside of the lining and the inside of the tail plate to allow steering the shield around curves and to correct misalignment. As a result, this creates an annulus or “tail void” around the outside of the lining as the shield is jacked forward (see Figure 2.22). Therefore, tail void grouting must be used to minimize ground deformations outside the tunnel.

At the shield tail, there is a tailskin seal used to protect the rear end of the shield against ground water, the surrounding ground, and the support fluid or grout. The tailskin seal separates the shield from the ring annulus and is designed to reliably seal the joint between the tailskin and the segmental lining (see Figure 2.30). It has to withstand the earth pressure, the water pressure, and the grouting pressure all of which can be very high. Originally all sorts of flexible material such as cloth, wood-wool, and rope were used to stuff the joint and counteract loss of compressed air (in the case of compressed air shields) or prevent leakage of grout into the shield. Nowadays, these methods have been replaced by wire brush seals, which are also used in the shields for excavating the subway tunnel in Bangkok. The wire brush seal, which was developed in Japan is firmly mounted on the tail skin as shown in Figure 2.30. For the Kawasaki and Herrenknecht machines used in the MRTA project, there are three rows of wire brush seals. Grease is injected into the chambers between the individual rows and kept at a high pressure to prevent water, ground or grout from infiltrating the sealing area.

The grout is injected through holes in the segments. The holes are fitted with screwed connection pieces and closed by plugs during the ring installation. In the MRTA project, plastic non-return valves were built into the segments. As shown in Figure 2.31, during grouting, grout is injected and flows down from the holes at the tunnel crown so that the grout is able to penetrate into the void by injected pressure and gravity. The injection is

continuously performed under high pressure in the tail void developing behind the shield tail. Note that the back fill grout injection is not only volume controlled (i.e. defined as percent grout filling) but also pressure-controlled, which is measured at the grout pipe or at the concrete segment. In the MRTA project, the pressure is automatically controlled to be as close as possible to 3 bar (300 kPa), which is the design condition of the segmental lining. With this high-pressure injection, the void can be filled in a short time and the grouting material can effectively prevent ground displacements towards the tunnel. Both volume and grouting pressure are monitored and recorded by the tunnel monitoring system at every excavation cycle.

Grouting volume is controlled to ensure that grout fully fills the void. Percent grout filling can be calculated by:

$$\text{Grout Filling (\%)} = \frac{\text{Grout Volume} \times 100}{\text{Estimated Void Volume}} \quad (2-1)$$

In the MRTA project, the grouting material was a combination of two components called material A and material B. Material A was composed of cement, bentonite and water. Material B was an accelerator liquid (sodium silicate). At the tail of the shield, the two components A+B were mixed as shown in Figure 2.32 before being pumped through a segment grout hole (fitted with a non-return valve) to fill the void around the ring.

Secondary grouting is applied to fill remaining cavities around the tunnel and to confirm that the primary grouting is sufficient. For reasons of space, the secondary grouting is carried out only after the shield has advanced 40-120 m. Therefore, in this project, this activity was done within 14 days of ring erection. Generally, the grouting pressure used for the secondary grouting does not exceed 3 bar.

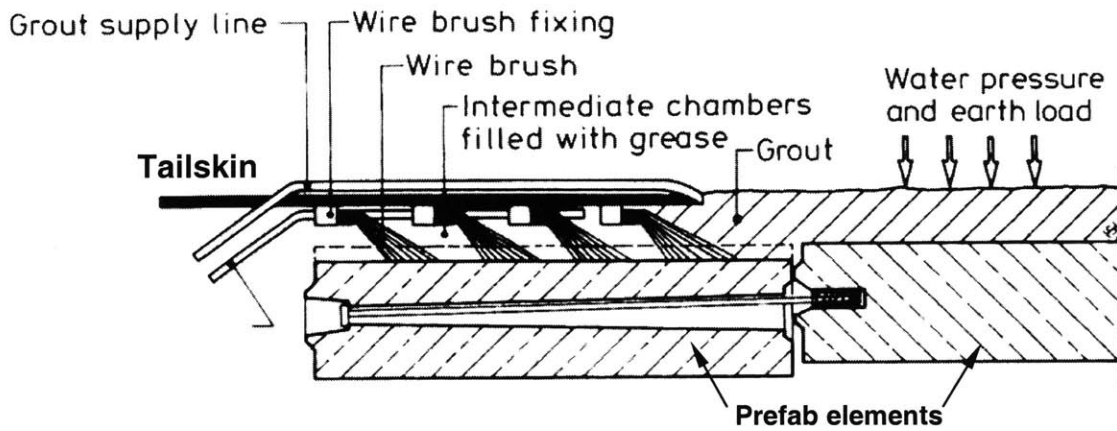


Figure 2.30 Tailskin seal (wire brush seal)

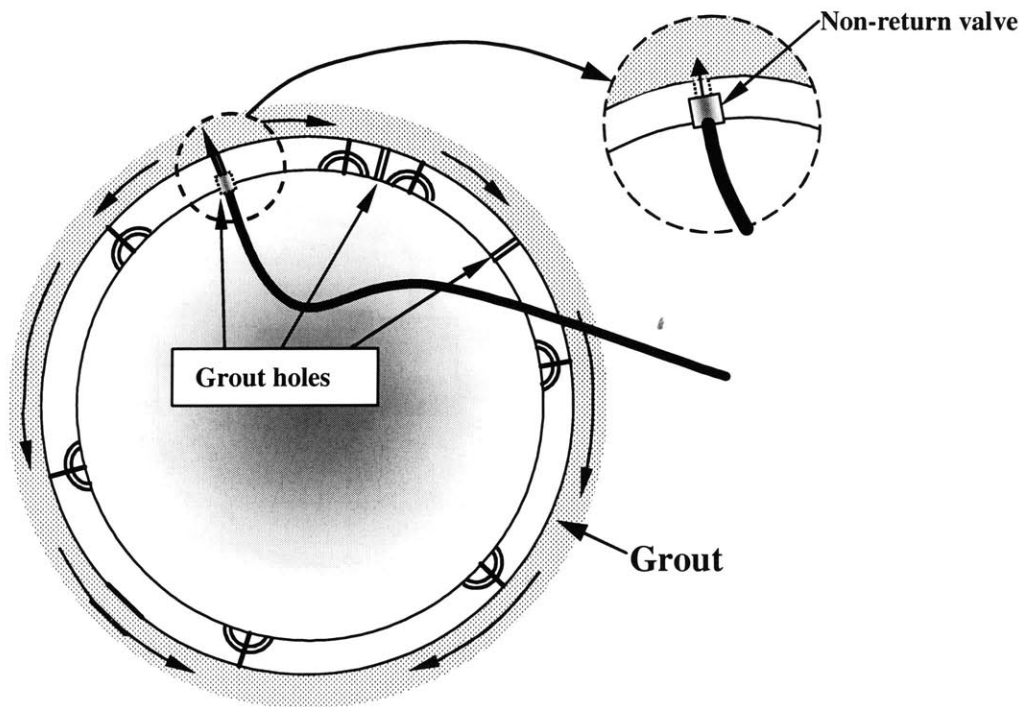


Figure 2.31 Grout injected through grout holes in the segmental lining

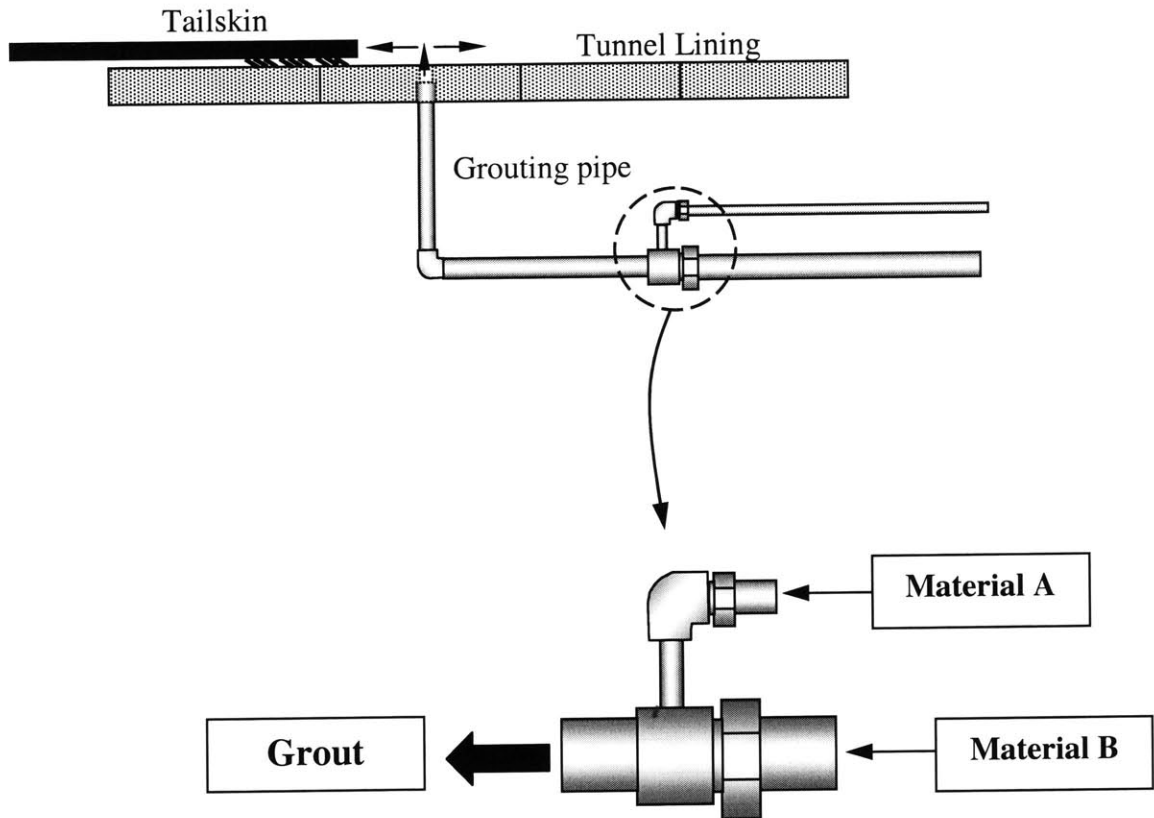


Figure 2.32 Grout as a mixing material between Material A and Material B

2.3.6 Guidance System

Tunnel drives with a shield can never be accomplished without a certain degree of deviation from the intended tunnel axis, and it is essential that the driver is continuously supplied with updated information on the shield's position in relation to the planned tunnel axis in order that corrective action can be taken. Hence, because of the exacting specification concerning accuracy of the tunnel drive and shield steering during excavation, surveying and guidance systems are very important.

The modern positional survey and guidance systems allow one to continuously monitor the shield's position. Figure 2.33 illustrates the components of the shield guidance system. At present, laser based directional control is normally used in tunnel construction. Either a simple laser or a laser theodolite (Figure 2.34) is used to transmit the laser beam. The theodolite has to be installed parallel to the shield axis in a surveying window to be kept free over the entire length of the shield including the back-up system. In order to determine the position of the machine via the laser beam, a target system that allows for roll correction is required. The target of the active electronic laser system is rigidly fixed to the shield (Figure 2.35), and detects the position where the center of the laser beam strikes it, feeding back data on the horizontal and vertical co-ordinates to the system's computer, located at the operator's control position (see Figure 2.36 and Figure 2.37). This system is widely used in shield tunneling around the world. However, the system requires substantial knowledge by the operator.

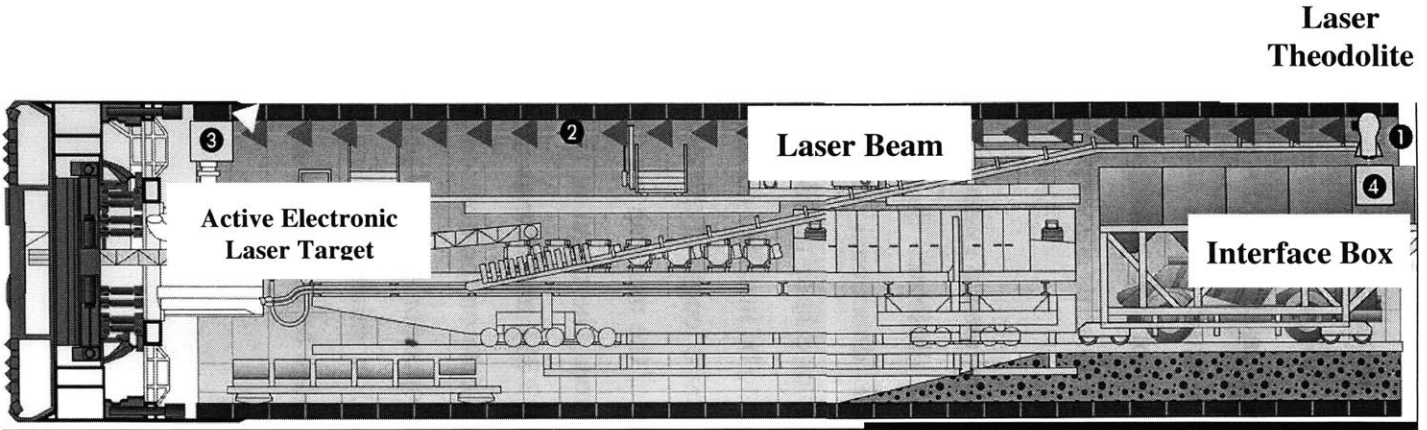


Figure 2.33 Components of the guidance system

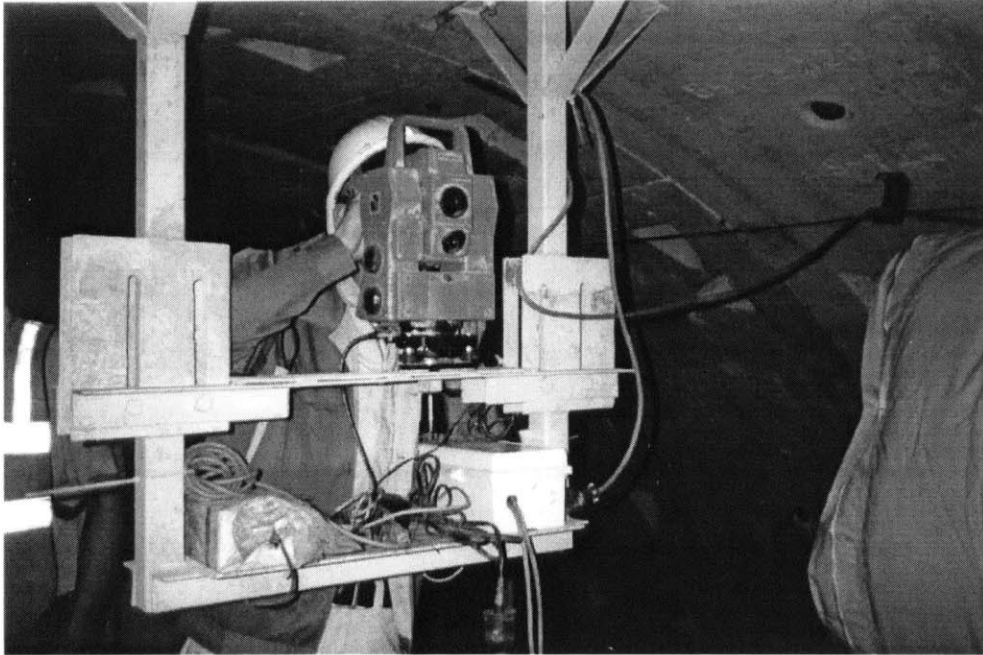


Figure 2.34 Laser theodolite installed at lining ring behind the EPB shield

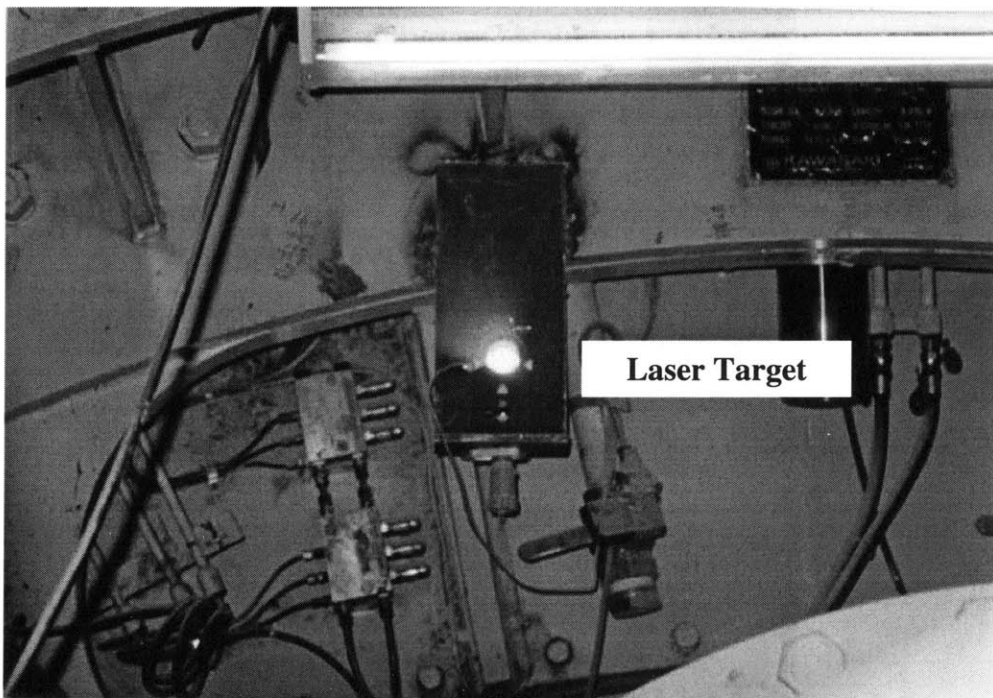


Figure 2.35 Laser target fixed behind the EPB shield

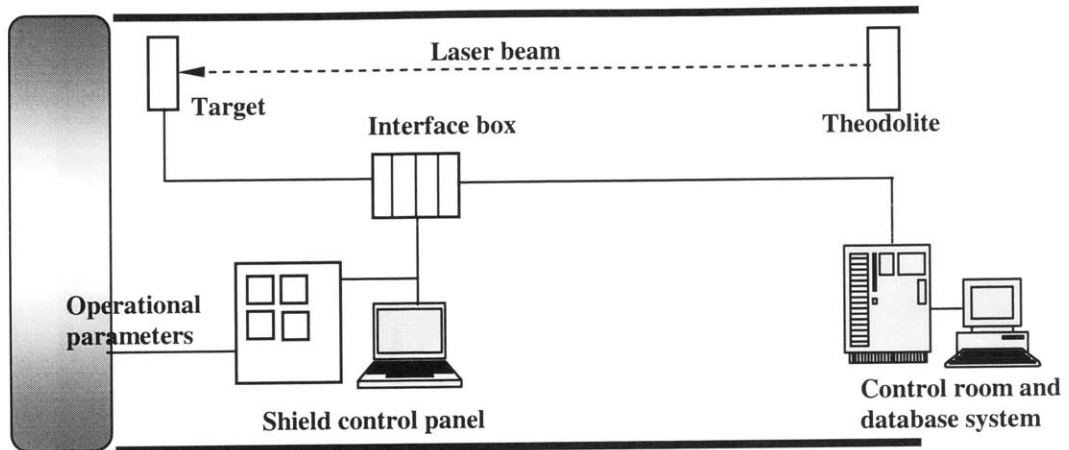


Figure 2.36 Shield driving monitoring system

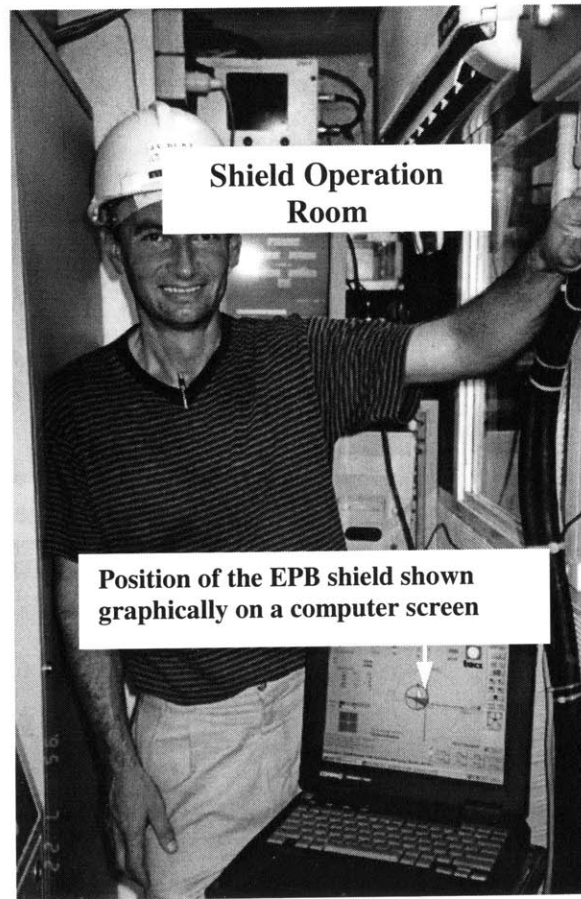


Figure 2.37 Guidance information system in the control room

References

Bickel, J., H., Kuesel, T. R., and King, E., H. (1996). *Tunnel Engineering Handbook*, Chapman & Hall, New York.

Herrenknecht GmbH (1996). *Technical Documentation: Project No. S-142 (Subway Bangkok)*.

Kawasaki Heavy Industries (1998). *Specification Manufacturing: MRTA Initial System Project Underground Structure-South (Joint Venture BCKT)*, submitted to MRTA.

ION Joint Venture (1999). *Method Statement for Excavation for Tunneling: Section II*, submitted to MRTA.

Maidl, B., Herrenknecht, M., and Anheuser, L. (1996). *Mechanised Shield Tunneling*, Ernst & Sohn, Berlin.

Stack, B. (1982). *Handbook of Mining and Tunneling Machinery*, John Wiley & Sons, New York.

CHAPTER 3

Review of Ground Response Induced by Shield Tunneling and Methods of Prediction

3.1 Introduction

The most fundamental ground response to any type of tunneling in soft ground is that the soil moves towards the opening, since this is where the stress relief has occurred. Furthermore, if the soil is under the water table, ground water will migrate toward the opening. Beyond this simple concept, the details of the ground response will vary depending on the type of tunneling technique used. The objective of this chapter is to introduce the fundamentals of the ground response caused by shield tunneling that have been developed to predict and describe ground deformations.

In general, soft ground tunneling causes ground deformations in two ways. First, the deformation, which is directly due to the tunnel excavation; this is the largest and most critical deformation and often characterized by the term “ground loss.” Second, consolidation settlement, which is classified as “long-term settlement,” is caused by increasing the in-situ effective stress around the tunnel. The consolidation settlement usually occurs over a long period of time after the shield passed depending essentially on

soil conditions. In this study, only the ground loss, which is affected by the tunneling practice and occurs during the tunnel excavation, will be discussed.

There are two categories of ground loss. In the first category occurring in the early years of shield development, ground loss might be in a sudden, uncontrolled or catastrophic manner. It is due to running, flowing or squeezing of soil and water influx into the tunnel face as happened in the classical case of Marc Brunel's tunneling underneath the Thames River in 1828 (Figure 3.1), but it can also occur due to flow of soil through the tunnel lining or collapse of an unstable lining. However, after the closed face shield tunneling techniques were introduced, in which the tunnel face is under control by means of compressed air, slurry pressure, or earth pressure applied at the front of the shield, such large catastrophic movements can be prevented. Hence, this is not discussed further.

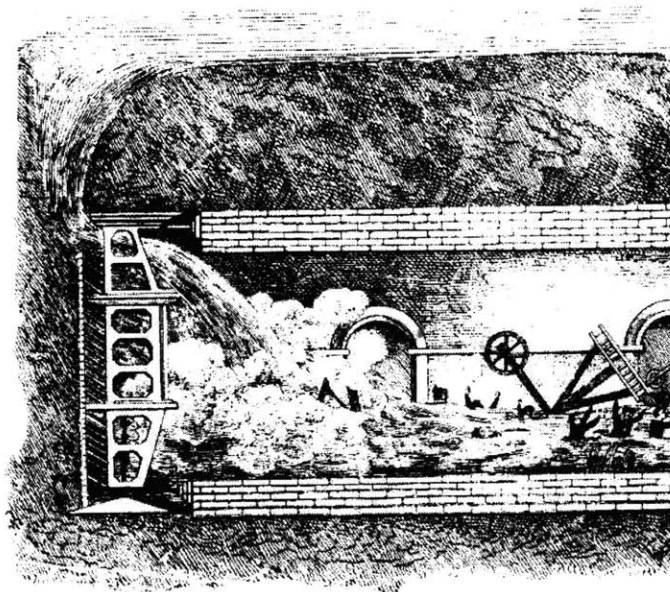


Figure 3.1 The collapse of the tunnel underneath the Thames River in 1828 (Maidl et al. 1996)

The ground loss in the second category is caused by the shield tunneling processes. In Figure 3.2 to Figure 3.6, the principal possibilities for the ground loss are illustrated. Such “regular” ground loss over the shield basically occurs in five different phases:

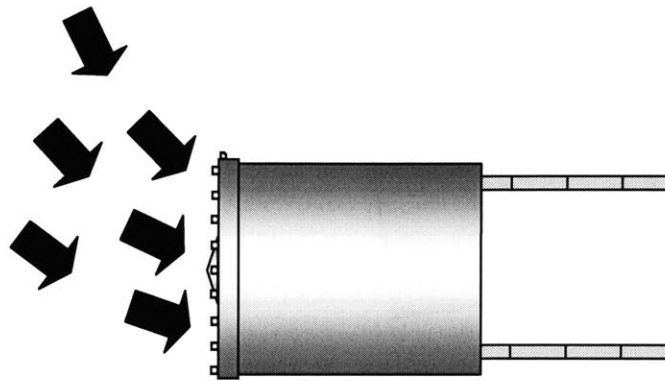


Figure 3.2 Ground loss at the shield face

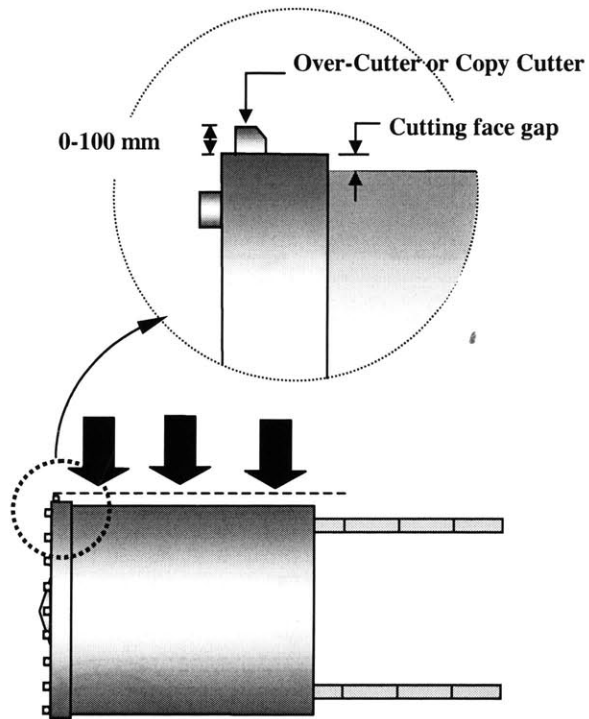


Figure 3.3 Ground loss due to over-cutting

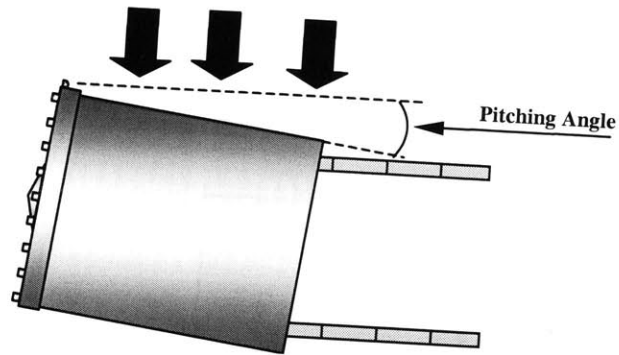


Figure 3.4 Ground loss due to pitching

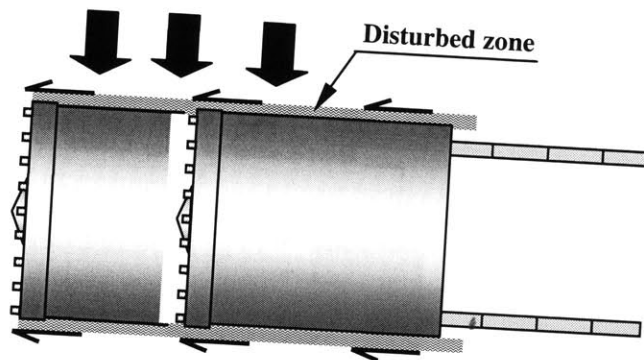


Figure 3.5 Ground loss due to ground disturbance

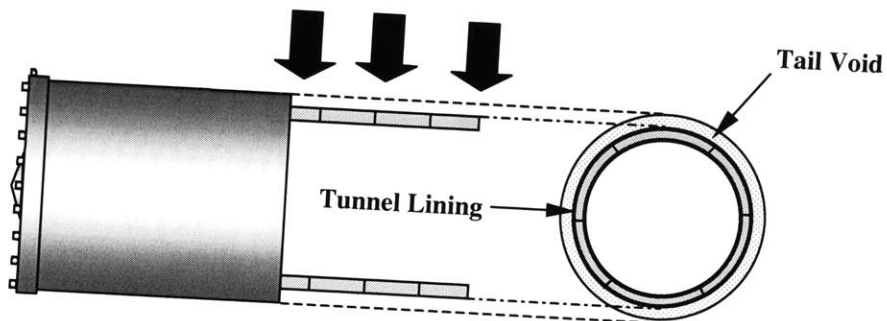


Figure 3.6 Ground loss due to tail void closing

Phase 1: Face loss into the tunnel develops when an open-face shield is used, or if the shield is operated at low support pressure so that the soil is allowed to move towards the face as depicted in Figure 3.2. In this condition, the volume balance is negative, or more volume of soil is removed than is occupied by the shield advance.

Phase 2: Over-excavation outside the tunnel perimeter at the face of the machine that is caused by the presence of over-cutters or copy cutters (extending up to 100 mm outside the perimeter), and teeth on the front of the machine (Figure 3.3).

Phase 3: Plowing or yawing of the machine caused by pitching can cut an ellipse of larger cross-sectional area than the area of the shield (Figure 3.4). At the same pitching angle, a shield with longer length theoretically introduces a larger gap over its shield than a shield of shorter length.

Phase 4: A disturbed or remolded zone around the shield surface due to shoving of the large diameter shield can cause ground movement over the shield body (Figure 3.5).

Phase 5: The tail void after shield passing causes an additional component of ground deformation due to closure of the soil into the gap. The void is created by the difference between the excavated periphery and the outer liner surface (Figure 3.6). One usually tries to eliminate the gap by expanding the lining or by grouting around the lining as it emerges from the tail of the shield, before the soil displaces into the gap.

The magnitude of ground movements that occur from these different phases is mainly influenced by ground conditions, the construction method, and shield operation control. Operation control includes the pressure control at the face, the steering of the shield, penetration rate, and quality of workmanship. Hence, allowing movements into the face of the tunnel, introducing tail void enlargement, greater soil disturbance by poor steering

practices, and slow installation of the liner due to the poor operation all lead to an increase in ground movements.

Ground movement due to ground loss manifests itself at the surface in a trough extending laterally and ahead of the advancing face. Figure 3.7 shows the typical three-dimensional shape of surface settlement trough caused by tunneling in soft ground. However, in the case that less soil volume is excavated and removed than the volume of the shield advance (i.e., the shield is operated to have a positive volume balance), soil would heave (Figure 3.8). This case can be the result of applying too high a support pressure at the shield face.

3.2 Methods of Predicting Ground Deformation

During recent years, much research on the topic of ground deformation caused by tunneling has been conducted. This has led to a much better understanding of the problem. Estimating ground deformation has mainly been approached in the following four ways:

- 1) Stochastic and empirical methods: the mathematical model for predicting the subsidence of a “stochastic medium” was first suggested by Litwinisyn (1956). Later on, Peck (1969) proposed that the surface settlement distribution could be determined empirically using the normal probability curve or Gaussian curve. The design parameters to be used in the “error function” are compiled from previous field measurement in tunnel projects in different soil conditions (Peck, 1969; Cording and Hansmire, 1975). The empirical approach was supported by a study done by O’Reilly and New (1982). In addition, Attewell and Woodman (1982) also adopted the stochastic theory for predicting longitudinal surface settlement.

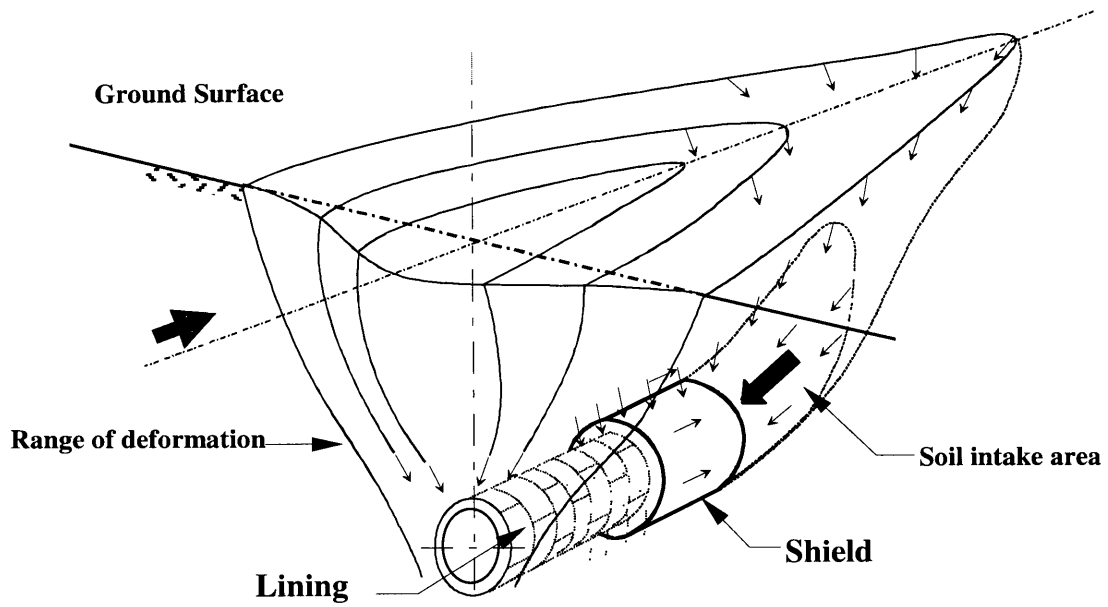


Figure 3.7 Typical ground deformation induced by shield tunneling

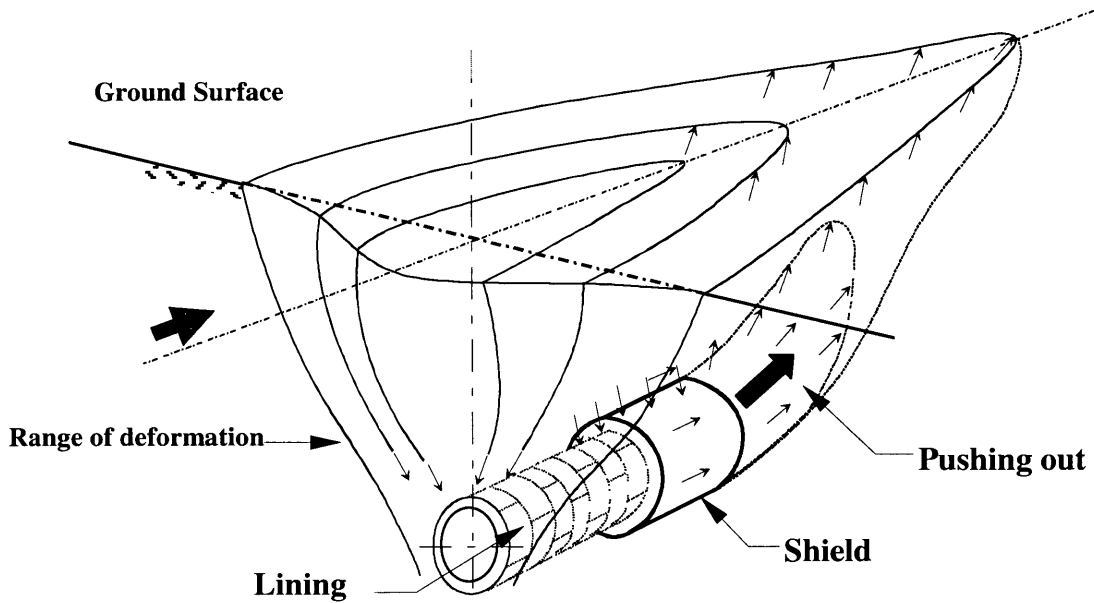


Figure 3.8 Surface heave ahead of the shield due to a positive volume balance

2) Analytical methods: the ground stresses and movements are calculated analytically. Many investigators have described methods based on closed form solutions. Sagaseta (1987) presented a two-dimensional analysis of ground deformations for obtaining the strain field in an initially isotropic and homogeneous incompressible medium (i.e., extending the strain path method of Baligh, 1985 by introducing a stress free ground surface). Verruijt and Booker (1996) first modified an approximate method suggested by Sagaseta (1987) to give the solution for the case of ground loss not only for the undrained case with Poisson's ratio equal to 0.5, but also for arbitrary values of Poisson's ratio. Loganathan and Poulos (1998) modified the solution given by Verruijt and Booker (1996) and neglect the distortion component that results in narrower surface settlement trough. Additionally, Pinto (1997) extended the analytical solution to describe both surface troughs and lateral deformations.

3) Finite element and numerical methods: because of the difficulties involved in formulating suitable analytical solutions, the finite element (FE) numerical method has been increasingly applied to problems in soil and rock mechanics. However, there are still difficulties with the accuracy of material parameters and the fact that a two-dimensional plane strain simulation of a tunnel in soil does not take into account soil movements ahead of the tunnel face (Mair and Taylor, 1997). Furthermore, a constraint regarding finite element analysis is that it is often difficult to acquire the in-situ material properties needed for realistic inputs to the finite element program. Nevertheless, the prediction of ground movement based on finite element or other numerical methods are useful for indicating the general form of a deformation field.

4) Laboratory experiments: model tunnel tests in cohesive and cohesionless materials were conducted to study the mechanism of ground movements and collapse (Atkinson et al., 1975; Atkinson and Potts, 1977; Kimura and Mair, 1981; and Nomoto et al., 1999). Based on the results, it was suggested that the deformation parameters determined in the model tests can be used for estimating shapes of settlement troughs and maximum surface settlements. Moreover, the results of performed tests are also useful for checking the validity of numerical solutions.

3.2.1 Stochastic and Empirical Methods

3.2.1.1 Litwinniszyn (1956)

A stochastic process is one that obeys probabilistic rather than deterministic laws, usually with time as the dominant independent variable. In this stochastic model, the ground is represented by a material composed of numerous equi-sized spheres in three-dimensions or discs in two-dimensions as shown in Figure 3.9. A movement is created at the base of the stacked assemblage by the removal of one sphere. This removal can be regarded as analogous to the inward movement of ground (or ground loss) at a tunnel. The model elements, acted upon by gravity alone, then move according to the laws of probability, leading to an inverted bell-shaped surface settlement trough in the form of a normal probability curve or a Gaussian curve. There are no demands upon any stress-strain properties of the medium, the concern being only with deformation.

From this model, the settlement trough of normal probability form can be expressed as:

$$\delta_v(y,z) = \frac{0.8t}{K_a} \left(\frac{z_o - z}{2a} \right)^{-n} \exp \left[-0.5 \left(\frac{y}{aK_a} \right)^2 \left(\frac{z_o - z}{2a} \right)^{-2n} \right] \quad (3-1)$$

for settlement over a thin tabular opening of width $2a$ and closure thickness t (see Figure 3.10) at a depth z_o , K_a and n are empirical coefficients in the equation and z is the vertical coordinate.

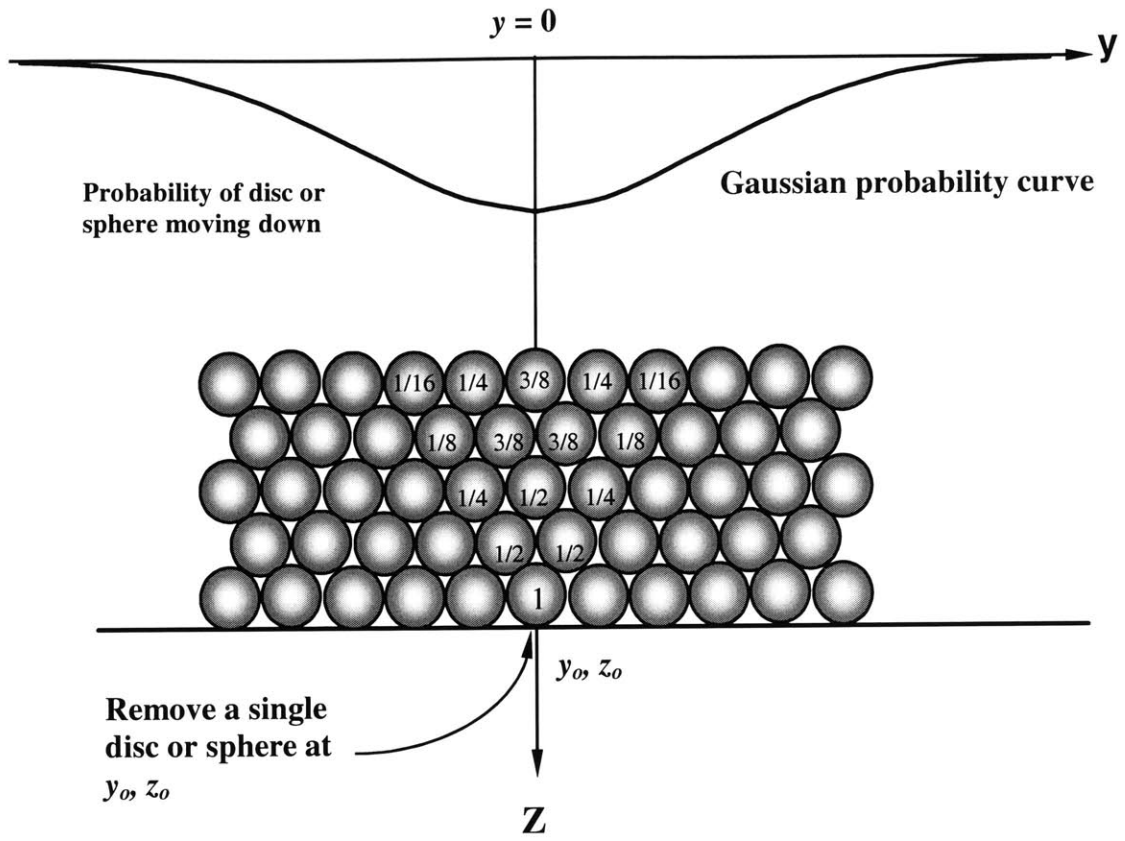


Figure 3.9 The settlement process modeled stochastically (after Attewell, 1978)

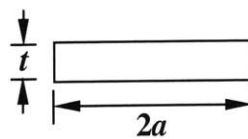


Figure 3.10 Definitions of width $2a$ and closure thickness t

For small strains*, and with respect to three Cartesian axes, there is no volume change; that is

$$\varepsilon_x + \varepsilon_y + \varepsilon_z = 0 \quad (3-2)$$

In the plane strain case (an infinitely long opening in the x direction),

$$\varepsilon_y + \varepsilon_z = 0 \quad (3-3)$$

and so, writing subscripts h and v to denote horizontal and vertical respectively, and if δ_v is the vertical displacement,

$$\varepsilon_h = -\varepsilon_v = -\frac{d\delta_v}{dz} = \frac{n\delta_v}{z_0 - z} \left[\left(\frac{y}{i} \right)^2 - 1 \right] \quad (3-4)$$

Taking tension positive in this case, the inflection point at a distance i from the center, is written as

$$i = aK_a \left[\frac{(z_0 - z)}{2a} \right]^n \quad (3-5)$$

The horizontal displacement δ_h is

$$\delta_h = \int_{-\infty}^y \varepsilon_h dy \quad (3-6)$$

And, as before,

$$\delta_h = -n \frac{y\delta_v}{(z_0 - z)} \quad (3-7)$$

*Continuum mechanics is used since there are many particles

Litwiniszyn (1956) recommends $K_a = 1$ and $n = 0.5$. From the tunneling case history evidence of Peck (1969), n has been allocated a value of 0.8 and values for K_a range from 1 to 1.5. Although data from later investigations and statistical analyses on surface settlement, may suggest different n and K_a values, it is found that settlement curves calculated from the stochastic model and using the above n , K_a values correspond well to those measured over real tunnels in clay soils (Attewell, 1978). However, values for n and K_a are found to be critical when attempting to describe sub-surface settlement profiles in term of stochastic theory. Therefore, the maximum vertical and horizontal displacements can be expressed as:

$$\delta_{v_{\max}} = \frac{0.8t}{K_a} \left(\frac{z}{D} \right)^{-n} \quad (3-8)$$

$$\begin{aligned} \delta_{h_{\max}} &= 0.606 \delta_{\max} \frac{ni}{z} \\ &= 0.242 t n \left(\frac{z}{D} \right)^{-1} \end{aligned} \quad (3-9)$$

where D = tunnel diameter. It is preferable to use the volume loss per unit length, V_t , rather than the “seam” closure thickness, t . From the relation:

$$V_t = Dt \quad (3-10)$$

therefore,

$$\delta_{v_{\max}} = \frac{0.8V_t}{K_a D} \left(\frac{z}{D} \right)^{-n} \quad (3-11)$$

and

$$\delta_{h_{\max}} = \frac{0.242V_t n}{D} \left(\frac{z}{D} \right)^{-1} \quad (3-12)$$

3.2.1.2 Peck (1969)

Based on the available data from many tunnel projects, Peck (1969) observed that the settlement trough over a single tunnel could usually be represented within reasonable limits by the error function or normal probability curve (also known as a Gaussian curve). Basically, Peck (1969) simplified the stochastic solution first proposed by Litwinniszyn (1956). Peck's (1969) solution provides an estimate of the settlements to be expected at varying distances laterally from the centerline of a tunnel. Such information is needed for judging the necessity of underpinning adjacent buildings, or of relocating vital utilities.

The pertinent properties of the normal probability function and its relationships to the dimensions of the tunnel are shown in Figure 3.11. The radius of the tunnel is represented by R , and the depth to the center of the tunnel is represented by z . The maximum ordinate of the normal probability curve is the empirically determined maximum settlement δ_{\max} so that the displacement, δ , at any point is:

$$\delta = \delta_{\max} \exp\left[-\frac{y^2}{2i^2}\right] \quad (3-13)$$

The determination of δ_{\max} will be described below. The points of inflection of the curve are located at a distance i on either side of the centerline. The value of i is, according to the properties of the normal probability curve or the standard deviation, equal to $0.61 \delta_{\max}$.

Values of i have been calculated for tunnels for which reasonably reliable settlement data are available. They are illustrated in the dimensionless plot of i/R against $z/2R$, (Figure 3.12). The plot shows trends and relates the results to soil types. As expected, the greater the depth of tunnel, the greater the width of the settlement trough.

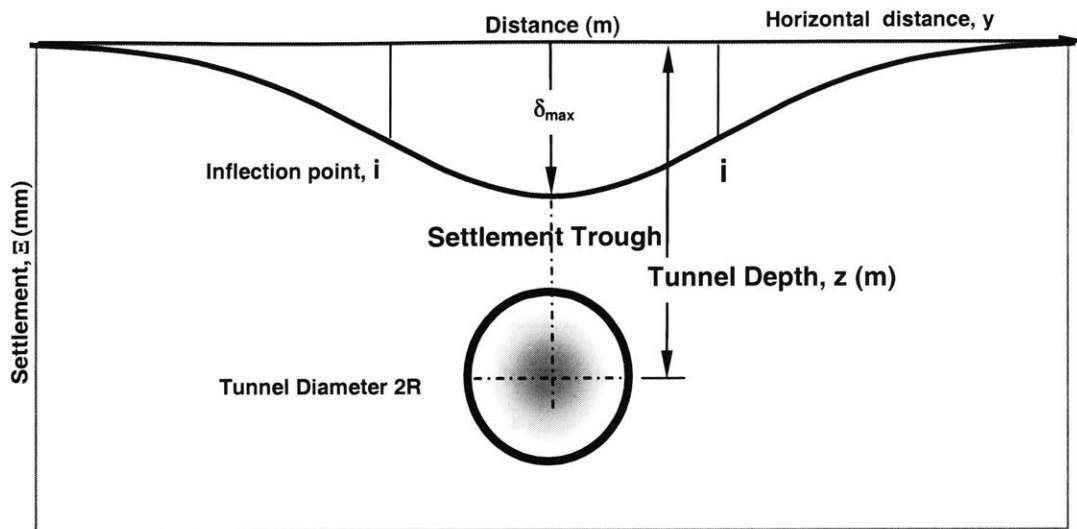


Figure 3.11 Normal probability curve used to describe transverse settlement trough

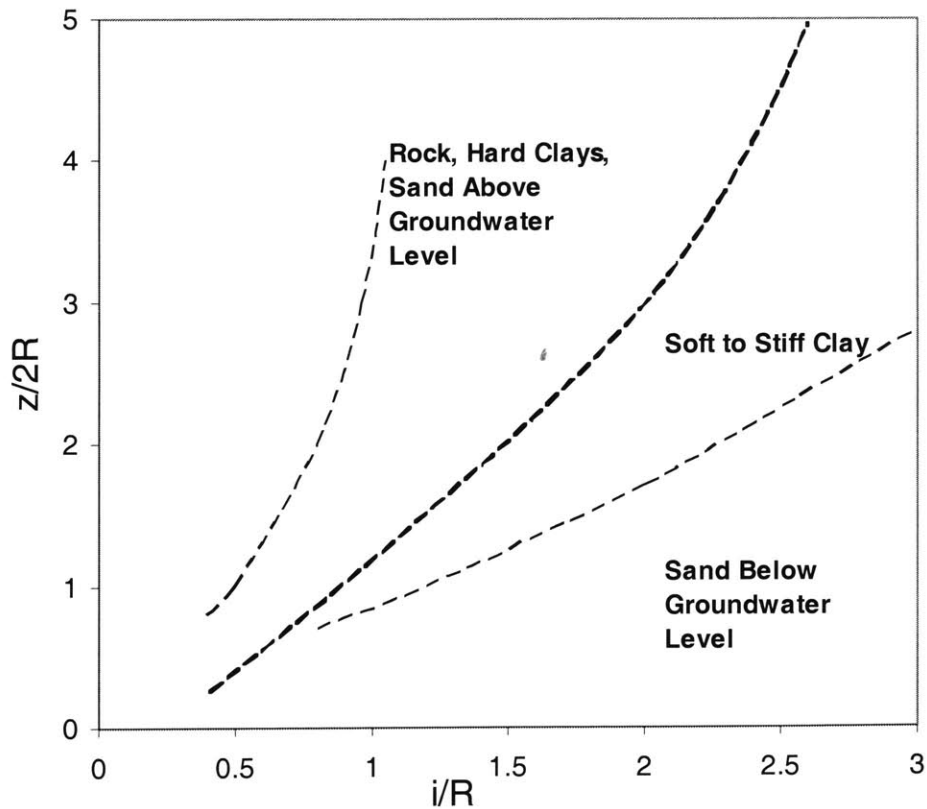


Figure 3.12 Relation between settlement trough width parameter and tunnel depth for different ground conditions (details including data from actual projects are provided in Peck, 1969)

The volume of the settlement trough (i.e., volume per unit length) having the shape of a normal probability curve is:

$$V_s = 2.5i \delta_{\max} \quad (3-14)$$

Based on the field data reported by Cording and Hansmire (1975), the volume of the settlement trough can be related to ground loss into a tunnel. They observed that most of the tunnels in clays developed surface settlement volumes approximately equal to volume of ground loss into the tunnels. Typically, ground loss ($G.L\%$) is expressed as the percentage fraction of excavated area of the tunnel (i.e., for a circular tunnel of diameter D):

$$V_s = \frac{G.L\%}{100} \left(\pi \frac{D^2}{4} \right) \quad (3-15)$$

Hence, δ_{\max} can be determined if volume of ground loss is known.

3.2.1.3 O'Reilly and New (1982)

O'Reilly and New (1982) proposed that ground movements above tunnels can be estimated using empirical methods similar to Peck's (1969), which is based on available case history data. Originally, the formulation reported by O'Reilly and New (1982) was based on a statistical evaluation of field observations of settlement above tabular mine openings (Litwinniszyn, 1956). However, Peck (1969) previously confirmed that this approach also adequately models the shape of the settlement trough caused by tunneling in soft ground.

O'Reilly and New (1982) assumed that all movements in the soil occur along radial paths toward the tunnel axis and that conditions of plane strain constant volume deformation apply. The assumption is supported by data from field measurements and the results of centrifuge tests on model tunnels in soft clay (Figure 3.13). The information available tends to suggest that the flow is directed towards a "sink", which is located at a point somewhat below axis level of the tunnel, perhaps close to the invert level of the tunnel.

The adoption of the radial flow assumption means that the width of the zone of deformed ground decreases linearly with depth below the ground surface. This results in the magnitude of the ground movements increasing linearly with depth below the surface to conform to the plane strain constant volume assumption:

$$i = Kz \quad (3-16)$$

where i is the inflection point (i.e., trough width parameter) at height z above tunnel axis and K is an empirical constant of proportionality which is equal to 0.5 for cohesive or 0.25 for granular soils. Further review of field data suggests that for clay, K varies between 0.4 (stiff clay) and 0.7 (soft, silty clay). For granular materials above the water table K ranges between 0.2 and 0.3. Typical values for parameter K for a range of soil types and tunneling methods are given in Table 3-1.

Table 3-1 Summarized settlement trough data for a range of soils (after O'Reilly and New; 1982)

Ground Conditions	Tunneling Methods	Trough width parameter constant, K	Remarks
Stiff fissured clay	Shield or hand	0.4-0.5	Considerable data available; losses normally 1-2 %
Glacial deposits	Shield in free air Shield with compressed air	0.5-0.6	Compressed air to assist control of ground movements
Recent silty clay deposit ($C_u = 10-40$ kPa)	Shield with compressed air	0.6-0.7	
Granular material above the water table		0.2-0.3	

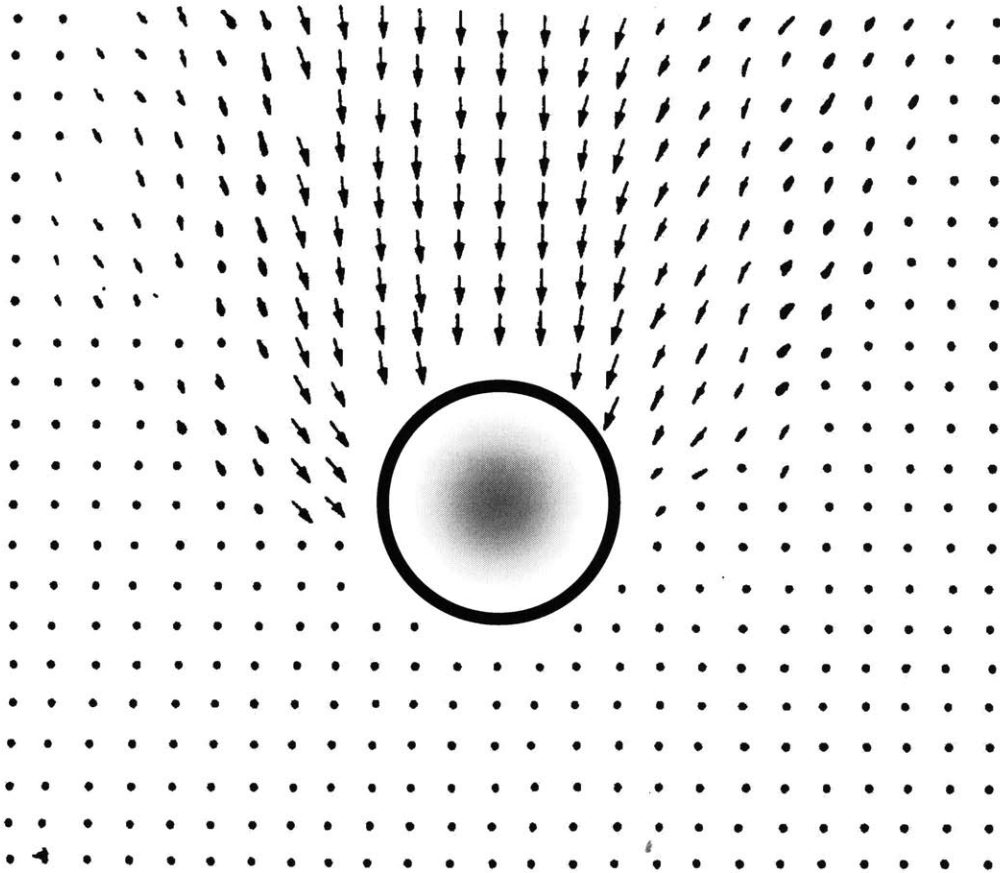


Figure 3.13 Soil deformation around model tunnel in clay (after Kimura and Mair, 1981)

The expression of $i = 0.4z$ to $0.5z$ for tunnels in clay is in agreement with tunnel database (Table 3-2) reported by Mair and Taylor (1997). The trough width parameters or inflection points based on the report are plotted against tunnel depth as illustrated in (Figure 3.14).

Furthermore, the result is reasonably consistent with the findings of Fujita (1981) who examines data from a large number of case histories in Japan for tunnels excavated using varied techniques such as hand mined shield, blind shield, slurry shield, and EPB shield. Fujita (1981) confirmed the conclusion of O'Reilly and New (1982) that the width of the surface settlement profile above tunnels in clays is independent of construction method.

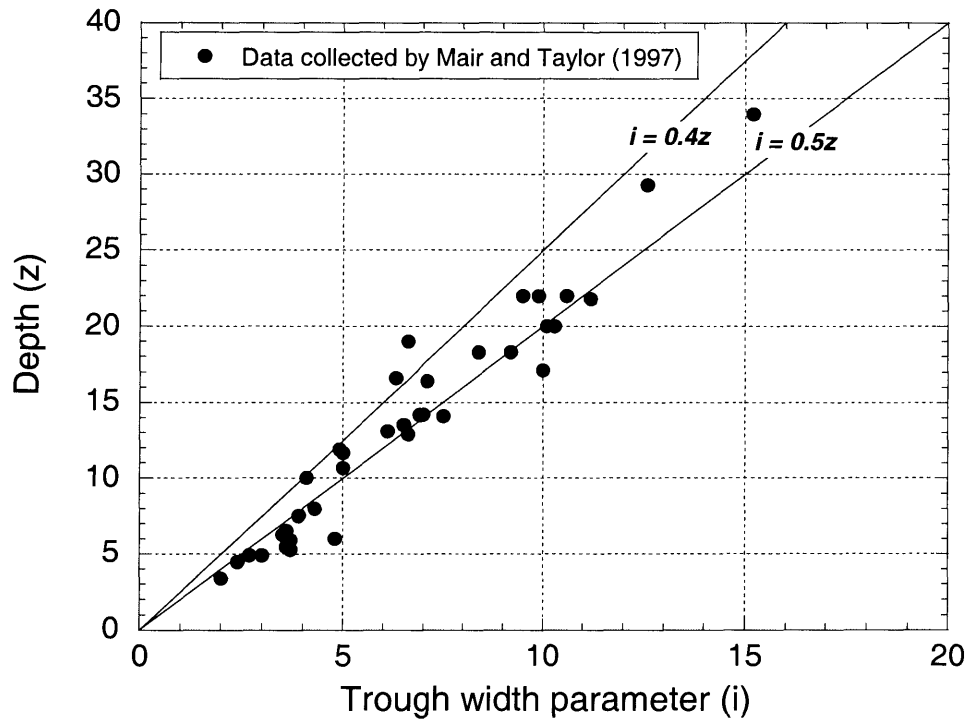


Figure 3.14 Variation in trough width parameter of tunnels in clays

However, the solution given above for cohesive soil is unlikely to be applicable to granular soil, as the assumption that particle displacements well away from the tunnel are directed toward the tunnel axis is not supported by laboratory studies (Cording et al.

1976). Further, the assumption of deformation at constant volume is untenable as some dilation or contraction of granular soils is almost inevitable during deformation. Potts (1976) and Cording et al. (1976) also reported a rapid narrowing with large inward displacements of the settlement trough near the ground surface with the sand funneling down into the void created by the excavation (Figure 3.15 and Figure 3.16). Atkinson et al. (1975) discussed this settlement mode in term of a dilating wedge over the tunnel crown, which develops until collapse occurs on surfaces that propagate vertically upwards from the tunnel haunches.

O'Reilly and New (1982) stated that ground movement in cohesionless soils leads to a deep and narrow settlement trough with high horizontal surface strain when associated with vertical ground strains in excess of 0.5%. Hence, the Gaussian curve cannot always accurately approximate this type of ground movement. These assumptions also correspond to the reports presented by Cording and Hansmire (1975) and Attewell (1978) that, in several case studies particularly in granular materials, the surface settlement trough cannot suitably be represented by a normal probability curve. Therefore, they proposed the alternative settlement trough, which is a triangular wedge. The lateral settlement is simply limited by the shear surfaces that rise from the circumference of the tunnel at an angle β , where $\beta = 45 - \phi/2$ and ϕ is the friction angle of the granular material as shown in Figure 3.17.

Table 3-2 Tunnel database reported by Mair and Taylor (1997)

No.	Source	Location	Ground Condition	Excavation Method	Tunnel Diameter (m)	Depth to Tunnel Axis (m)	δ_{max}	Trough width, i (m)	
1	Hanya (1977)	Japan	Stiff cohesive soil	Slurry shield	7.5	18.3	16	9.2	
1a			Stiff cohesive soil	Slurry shield	7.5	21.8	43	11.2	
1b			Stiff cohesive soil	Shield, hand	10.7	19.0	22	6.6	
1c									
2	Attewell and Farmer (1974)	Green Park, UK	Stiff OC clay	Shield, hand	4.2	29.3	6	12.6	
3	Attewell (1978)	Hebburn, UK	Soft NC clay	Shield, hand	2.0	7.5	8	3.9	
4	Glossop et al. (1979)	Belfast, Ireland	Soft silty clay	Shield, hand	2.7	4.9	17	2.7	
4a			Soft silty clay	Shield, hand	2.7	4.5	20	2.4	
4b									
5	Toombs (1980)	Avonmouth, UK	Soft alluvial deposit	Shield, hand	3.4	6.0	13	4.8	
6	West et al. (1981)	York Way, UK	Stiff OC clay	Hand excavated	4.1	14.1	3	7.5	
7	Attewell (1978)	Tyneside, UK	Soft silty alluvial clay	Shield, hand	4.3	13.5	23	6.5	
8	Muir wood and Gibb (1971)	Heathow, UK	Stiff OC clay (London Clay)	Shield, hand	10.9	12.9	11	6.6	
9	Glossop and O'Reilly (1982)	Haycroft, UK	Soft silty clay	Shield, hand	3.0	5.5	40	3.6	
9a			Soft silty clay	Shield, hand	3.0	6.5	60	3.6	
9b			Soft silty clay	Shield, hand	3.0	8.0	68	4.3	
9c									
11	Eden and Bozozuk (1968)	Ottawa, Canada	Firm OC clay (Leda Clay) sensitive	TBM, rotary	3.0	18.3	6	8.4	
12	Henry (1974)	Grangmouth, UK	Soft-very soft laminated silty clay	Shield, hand	2.45 to 2	10.0	24	4.1	
14	Moretto (1969)	Buenos Aires, Argentina	Soft to firm clay ^{13.1}	Mechanical shield	4.7	16.4	150	7.1	
17	Lake et al. (1992)	Gateshead, UK	Firm clay, laminated	Hand with timber lagging	1.5x1.5	5.3	37	3.7	
19	Hanya (1977)	Japan	Firm cohesive soil	Shield, hand	7.3	16.6	63	6.3	
20	Peck (1969)	Chicago, US	Medium clay (Chicago Leda Clay)	Hand excavated	6.1	11.9	23	4.9	
21	Peck (1969)	Toronto, Canada	Glacial till	Hand excavated	5.3	13.1	9	6.1	
22	O'Reilly and New (1982)	Newcastle, UK	Firm stiff clay, glacial till	Partial face machine	5.2	14.2	8	7.0	
23	O'Reilly and New (1982)	Sutton, UK	Stiff fissured clay	Hand	1.8	17.1	4	10.0	
23a			Firm to stiff weather clay	Hand	1.8	3.4	4	2.0	
23b			Firm to stiff weather clay	Full face micro TBM	1.5	4.9	7	3.0	
23c									
24	O'Reilly and New (1982)	Oxford, UK	Stiff fissured clay	TBM, full face	2.8	11.7	2	5.0	
25	Attewell (1978)	Howden, UK	Stiff boulder clay	Hand excavated	3.6	14.2	11	6.9	
26	Barratt and Tyler (1976)	Regents Park, UK	Stiff OC clay	Shield, hand	4.2	34.0	5	15.2	
26a			Stiff OC clay	Shield, hand	4.2	20.0	7	10.3	
26b									
27	McCaul (1978)	Stockton-on-Tees, UK	Soft to very soft silty clay	Shield, hand	1.3	6.3	44	3.5	
27a			Shield, hand	1.3	5.9	56	3.7		
27b									
28	New and Bowers (1994)	Heathow, UK	Stiff OC clay (London Clay)	NATM	-	22.0	21	9.5	
28a						11.3	22.0	28	9.9
28b						-	22.0	15	10.6
28c						11.3	22.0	27	9.9
28d									
30	Kuwamura (1997)	Chicago, US	Soft to firm silty clay	Shield	7	10.7	18-30	5.0	
31	Shirlaw (1988)	Singapore	Very stiff to hard clay with boulders	NATM	6.0	20.0	6	10.1	

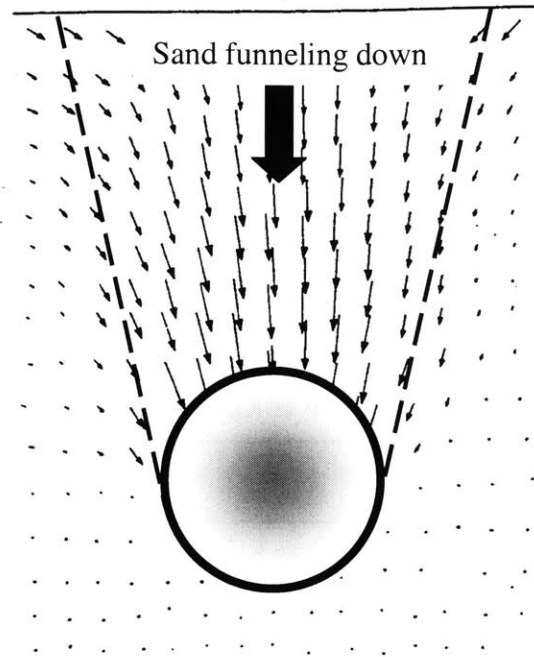


Figure 3.15 Soil deformations around tunnel in sand (after Potts, 1976)

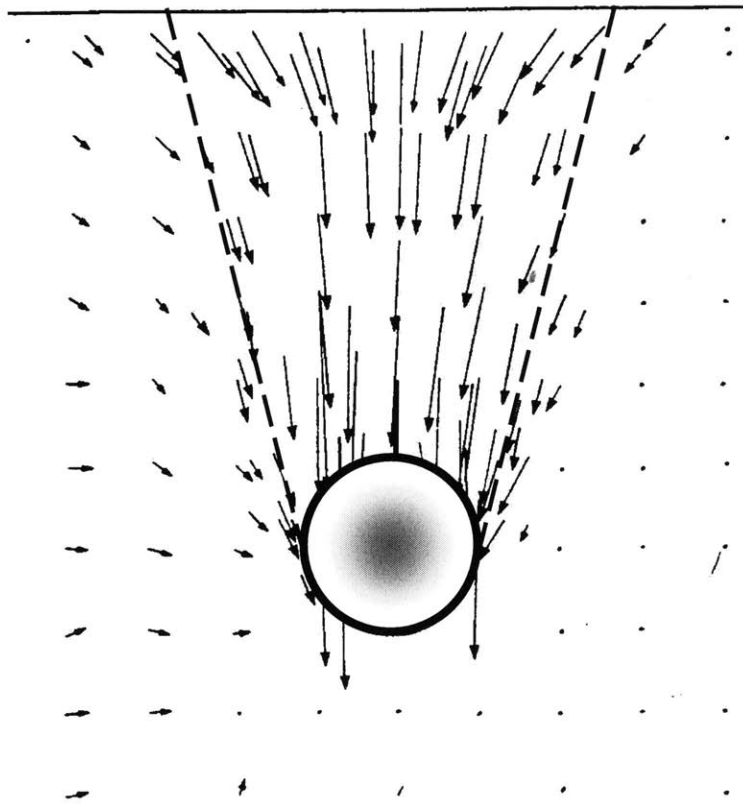


Figure 3.16 Soil deformations around tunnel in sand (after Cording et al., 1976)

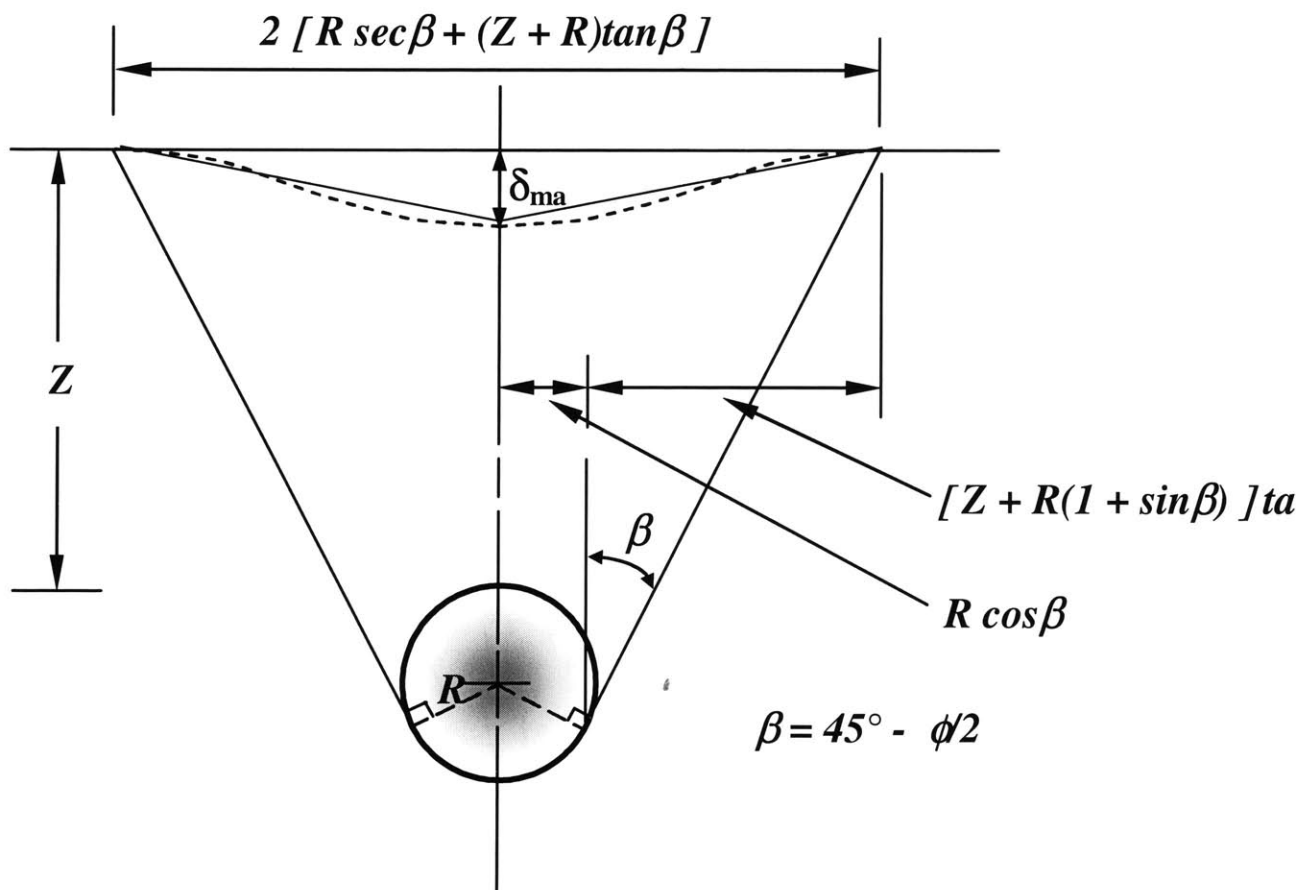


Figure 3.17 Generation of transverse settlement profile in sand (after Cording and Hansmire, 1975)

3.2.1.4 Attewell and Woodman (1982)

Shield tunneling not only induces ground deformation in the transverse direction resulting in a settlement trough, but also ground deformation in the longitudinal direction. This can cause damage to existing structures as illustrated in Figure 3.18. Unfortunately, little research has been devoted to the mechanism of ground settlements occurring in the longitudinal direction.

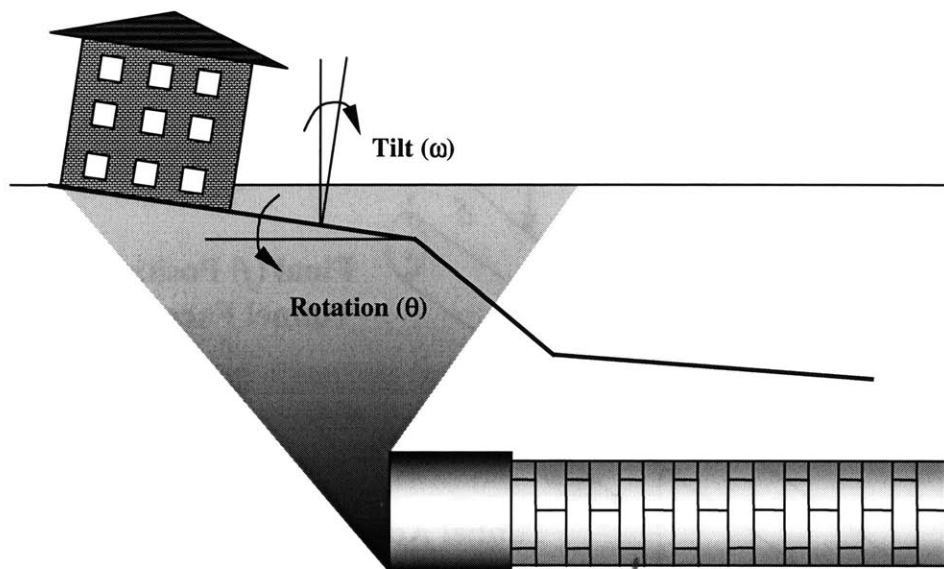


Figure 3.18 Longitudinal surface settlement caused by shield tunneling

Only Attewell and Woodman (1982) proposed an empirical solution for longitudinal surface settlement derived from a modified normal probability equation. They adopted the stochastic theory given by Litwinisyn (1956) as described earlier. However, they stated that the equations are of limited value to practical tunneling. Specifically, in the longitudinal direction, it is necessary to consider a point source of loss at depth z_0 on the line $y = 0$, moving along the x -coordinate axis from x_i to x_f , where ‘ i ’ is used to denote the “initial” or tunnel start point, and subscript ‘ f ’ denotes “final” point as shown in Figure 3.19.

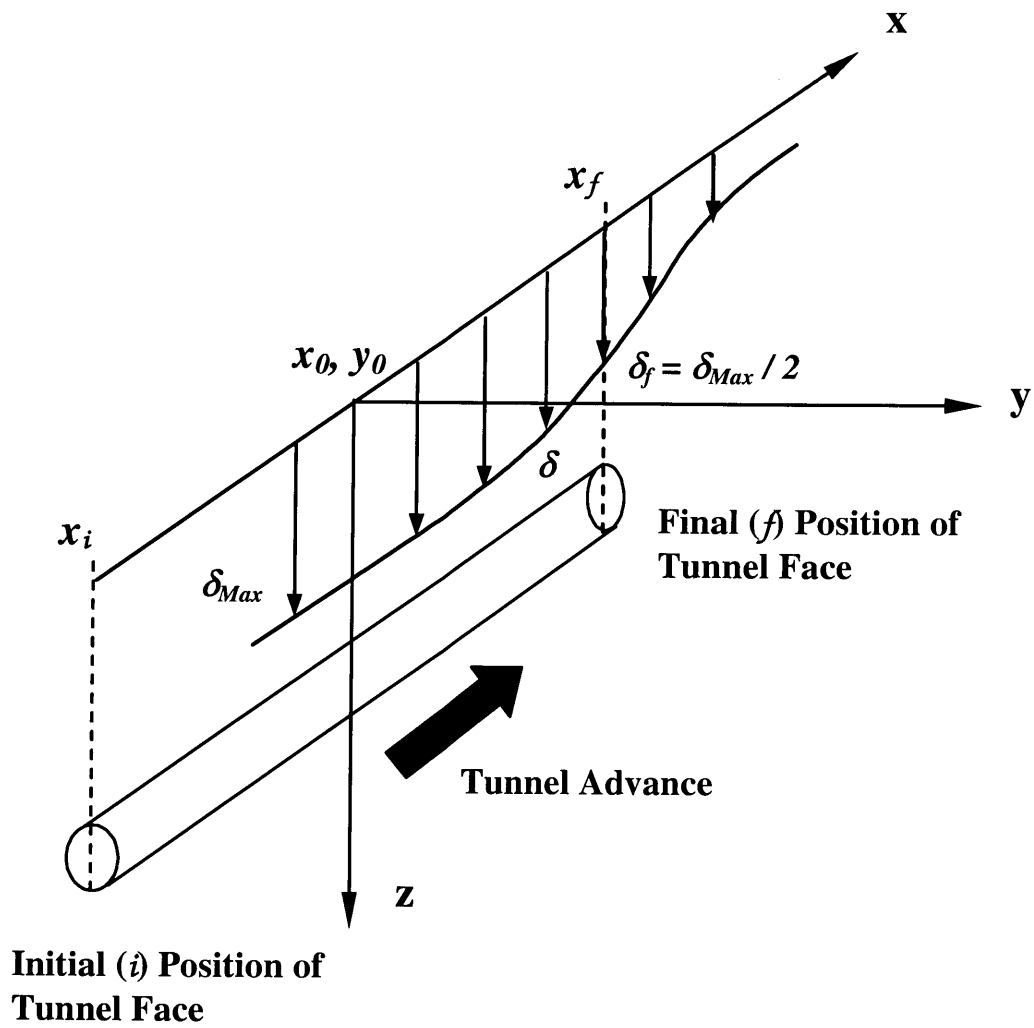


Figure 3.19 Tunnel coordination system for longitudinal surface settlement (after Attewell and Woodman, 1982)

Based on the conditions in Figure 3.19, one can approximate the longitudinal settlement (δ) due to the ground loss into the tunnel:

$$\delta = \frac{V}{\sqrt{2\pi \cdot i^2}} \exp\left[\frac{-y^2}{2i^2}\right] \left\{ G\left(\frac{x-x_i}{i}\right) - G\left(\frac{x-x_f}{i}\right) \right\} \quad (3-17)$$

where,

$G()$ = a probability function provided by Attewell and Woodman (1982).

In particular $G(0) = 0.5$ and $G(\infty) = 1$

V = volume of ground loss that is determined as percent ground loss:
G.L.% x volume of tunnel

i = the transverse horizontal distance between the points of maximum settlement to the “inflection point” that can be determined from the solution by Peck (1969) or O’Reilly and New (1982) as shown in Figure 3.12 and Equation (3-16), respectively

z = depth to tunnel axis

Attewell and Woodman (1982) assumed that 50 percent of maximum surface deformation ($0.5\delta_{\max}$) occurs at the plane of the shield face (Figure 3.20). However, they acknowledged that the assumption is only appropriate for the settlement induced by tunneling in clayey soil as they compared their solution with the settlement occurring in the Jubilee Line Project, which is excavated in London Clay. In addition, they agreed that more three-dimensional deformation data (i.e., in both the transverse and the longitudinal directions) are needed from field measurements in order to provide a basis for modifying and extending their approach.

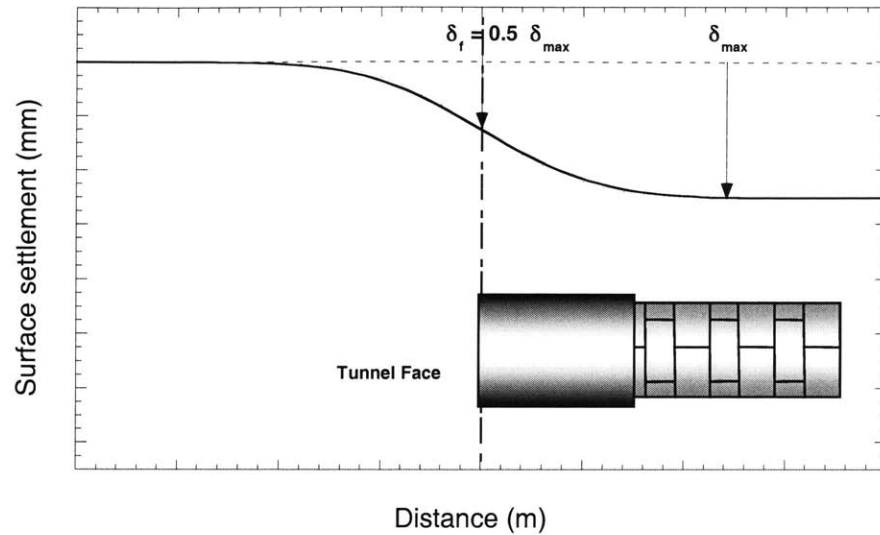


Figure 3.20 Longitudinal surface settlement shape proposed by Attewell and Woodman (1982)

3.2.2 Analytical Solutions

3.2.2.1 Verruijt and Booker (1996)

Verruijt and Booker (1996) proposed an analytical solution for a tunnel in a homogeneous elastic half-space. Their solution is a generalization of a method suggested by Sagaseta (1987) in that it gives the solution of ground loss not only for the incompressible case (i.e., with Poisson's ratio equal to 0.5) but also applicable to arbitrary values of Poisson's ratio, and including the effect of ovalization.

The original solution suggested by Sagaseta (1987) is based on the constraint of incompressible material behaviors (Figure 3.21). First, the undrained ground loss in an infinite space is considered, reducing the tunnel to a point sink (Step 1), with the conditions of incompressibility and spherical symmetry determining a radial field of

displacements, decreasing with the distance to the sink. The surface is considered by using a virtual image technique (Step 2), combined with corrective surface tractions (Step 3), for which elastic solutions for the half space are used.

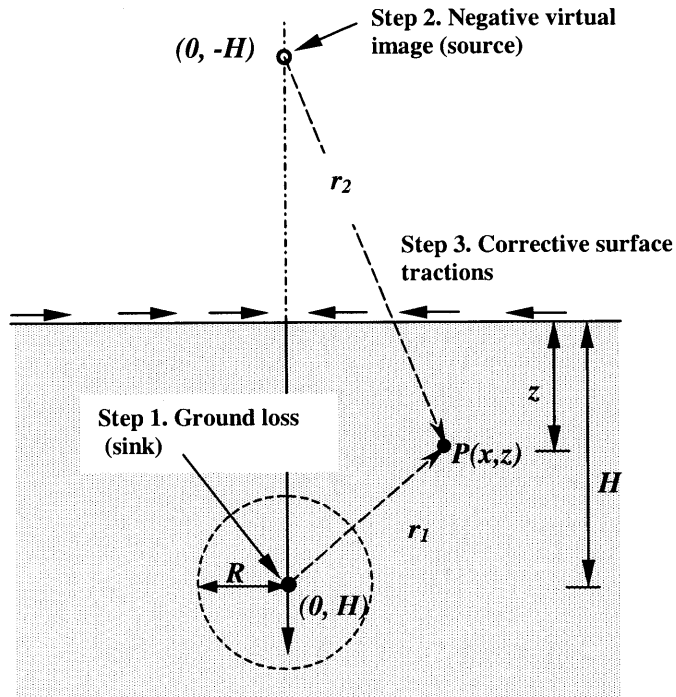


Figure 3.21 Virtual image technique (after Sagasetta, 1987)

From Figure 3.21, a closed form solution presented by Verruijt and Booker (1996) for the estimation of the surface and subsurface ground deformation can be expressed as:

$$U_z = -\varepsilon R^2 \left(\frac{z_1}{r_1^2} + \frac{z_2}{r_2^2} \right) + \delta R^2 \left(\frac{z_1 (kx^2 - z_2^2)}{r_1^4} + \frac{z_2 (kx^2 - z_2^2)}{r_2^4} \right) \\ + \frac{2\varepsilon R^2}{m} \left(\frac{(m+1)z_2}{r_2^2} - \frac{mz(x^2 - z_2^2)}{r_2^4} \right) - 2\delta R^2 h \left(\frac{x^2 - z_2^2}{r_2^4} + \frac{m}{m+1} \frac{2zz_2(3x^2 - z_2^2)}{r_2^6} \right)$$

(3-18)

Where,

- ε = uniform radial ground loss (Figure 3.22)
- δ = long-term ground deformation due to the ovalization of the tunnel lining (Figure 3.22)
- z_1 = $z - H$
- z_2 = $z + H$
- r_1^2 = $x^2 + z_1^2$
- r_2^2 = $x^2 + z_2^2$
- R = tunnel radius
- H = depth to the source
- m = $1/(1-2\nu)$
- k = $\nu(1-\nu)$
- ν = Soil Poisson's ratio

In this solution, Figure 3.22 shows two basic deformation mechanisms of the tunnel namely, a uniform radial displacement (representing, in first approximation, the ground loss that may occur during construction of the tunnel), and the ovalization of the tunnel that is caused by the displacement of tunnel lining. Note that this analytical solution was modified by González and Sagasetta (2001) and they can fit measurement data better than Verruijt and Booker's (1996) solution.

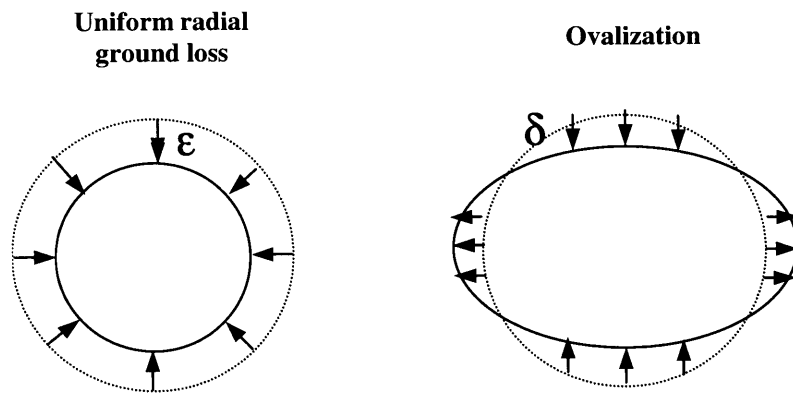


Figure 3.22 Ground loss and ovalization after Verruijt and Booker (1996)

3.2.2.2 Loganathan and Poulos (1998, 1999)

In empirical solutions, the ground loss is obtained by observation and judgment that do not always consider tunneling configuration. In practice, the ground loss values may vary, depending on the tunneling method, tunnel configuration, soil types, etc. The fact that such a variation in empirical observations exists suggests the need for a more logical approach to the estimation of the ground losses and therefore the ground movement prediction due to tunneling. Rowe and Kack (1983) defined the gap parameter g (Figure 3.23) as the magnitude of the equivalent two-dimensional (2D) void formed around tunnel due to the combined effects of the three-dimensional (3D) elastoplastic ground deformation at the tunnel face, over-excavation of soil around the periphery of the shield shield, and the physical gap that is related to the shield, and lining geometry.

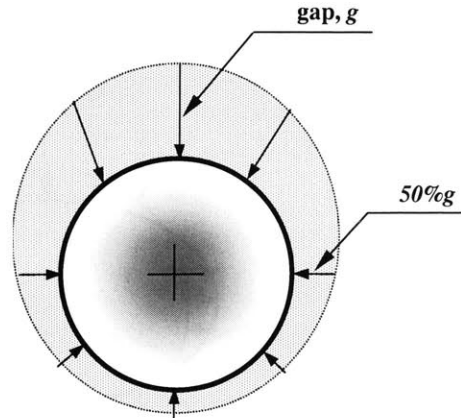


Figure 3.23 Oval-shaped ground deformation around tunnel section

The gap parameter can be estimated using a theoretical method proposed by Lee et al. (1992) as described in Figure 3.24. The undrained gap parameter g can be estimated as:

$$g = G_p + u_{3D}^* + \omega \quad (3-19)$$

Where,

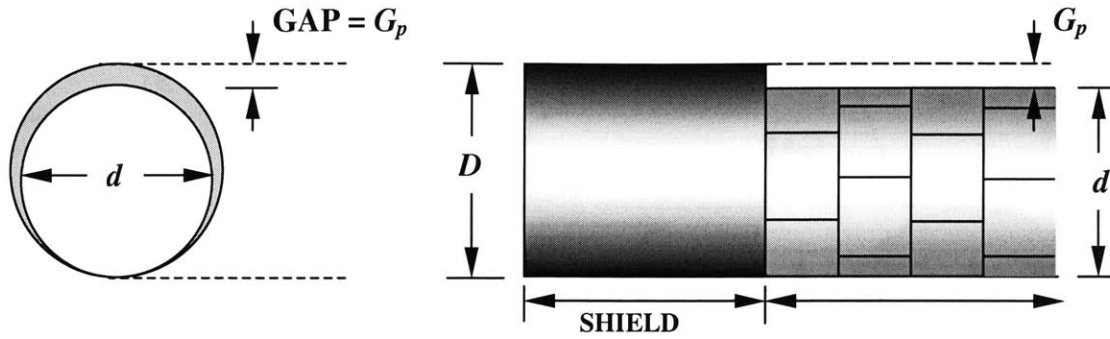
G_p = physical gap ($G_p = 2\Delta + \delta$) that represents the geometric clearance between the outer skin of the shield and the lining as illustrated in Figure 3.25

Δ = thickness of the tail piece

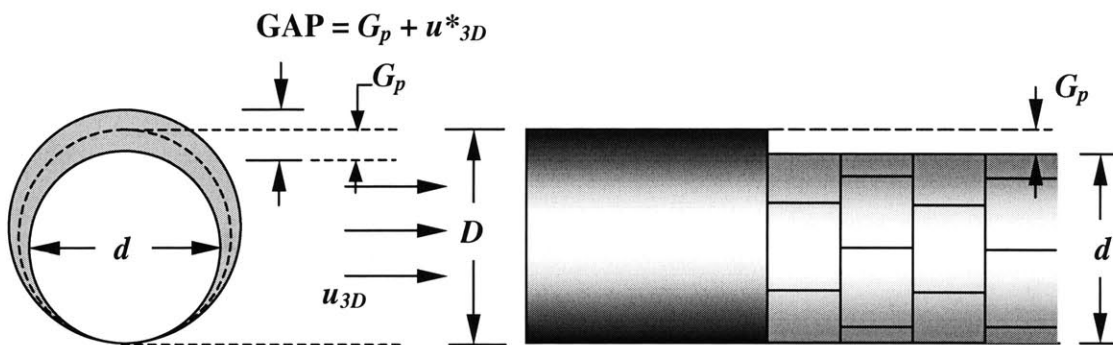
δ = clearance required for erection of the lining

u_{3D}^* = equivalent 3D elastoplastic deformation at the tunnel face

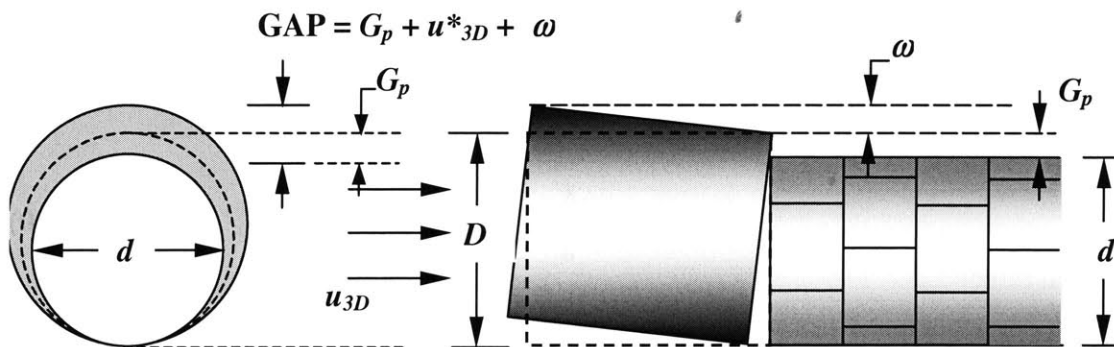
ω = value that takes into account the quality of workmanship.



(a) Tunnel advances in perfect alignment and fully supported at the face



(b) Tunnel advances in perfect alignment but allowing soil movement at the face due to relief of stresses



(c) Tunnel advancement is subjected to all possible sources of "ground loss" Including over-excavation due to alignment and workmanship problems

Figure 3.24 Simulation of ground loss (gap parameter), after Lee et al. (1992)

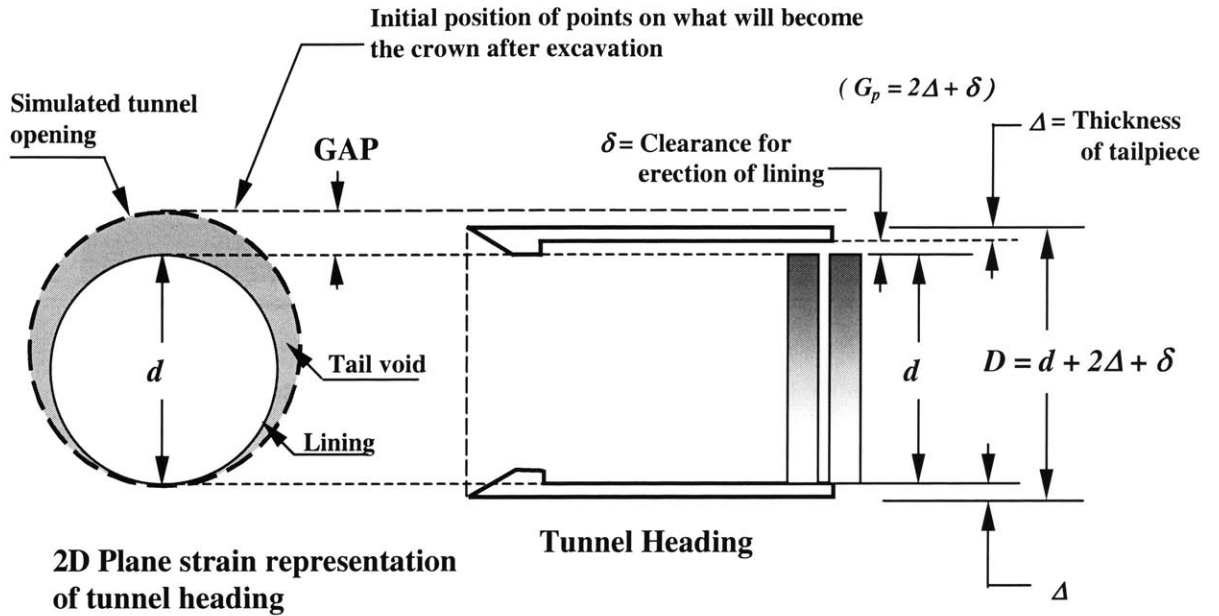


Figure 3.25 Definition of GAP, after Lo et al. (1984) and Lee et al. (1992)

The free field stress state in a given section is modified as the excavation of the tunnel approaches it (i.e., shield arrival). If the net supporting pressure is lower than the free-field stress, then the soil mass will move towards the tunnel face. The volume of soil that intrudes into the tunnel face owing to pressure release at the face will eventually be excavated. The u_{3D}^* component in (3-19) can be defined as:

$$u_{3D}^* = \frac{k}{2} \delta_x \quad (3-20)$$

where,

k = soil-cutter resistance factor

δ_x = tunnel face soil intrusion

Lee et al. (1992) established experimental and elastoplastic analytical relationships for k and δ_x . k is basically a correction factor taking account of the doming effect across the tunnel face and can be expressed as:

$$k = \frac{\text{Volume of non uniform axial intrusion across the tunnel face determined by 3D analysis}}{\text{Volume assuming uniform axial intrusion}} \quad (3-21)$$

They suggested the value of $k = 0.7-0.9$ for stiff to soft clays; $k = 1$ represents a uniform intrusion at the tunnel face. Lee et al. (1992) observed that intrusion of soil near the center of the tunnel face is quite uniform if plastic flow occurs (very soft clay). δ_x is the magnitude of maximum axial intrusion at the tunnel face which can be defined as:

$$\delta_x = \frac{\Omega R P_0}{E} \quad (3-22)$$

where,

Ω = dimensionless displacement factor (Lee et al., 1992)

R = tunnel radius

E = Young's modulus (typically the undrained modulus in an extension mode)

P_0 = total stress removed at the tunnel face

The total stress removed at the tunnel face, P_0 can be expressed as:

$$P_0 = (K_0 P'_v + P_w) - P_i \quad (3-23)$$

where,

K_0 = the coefficient of earth pressure at rest

P'_v = the vertical effective stress at the tunnel springline

P_w = the in-situ pore pressure at the tunnel springline
(i.e., prior to construction of the tunnel)

P_i = the tunnel support pressure (i.e., if tunnel face has no support, $P_i = 0$ and the presence of compressed air or other supporting means causes $P_i > 0$)

All the pressures acting on the tunnel are shown in Figure 3.26.

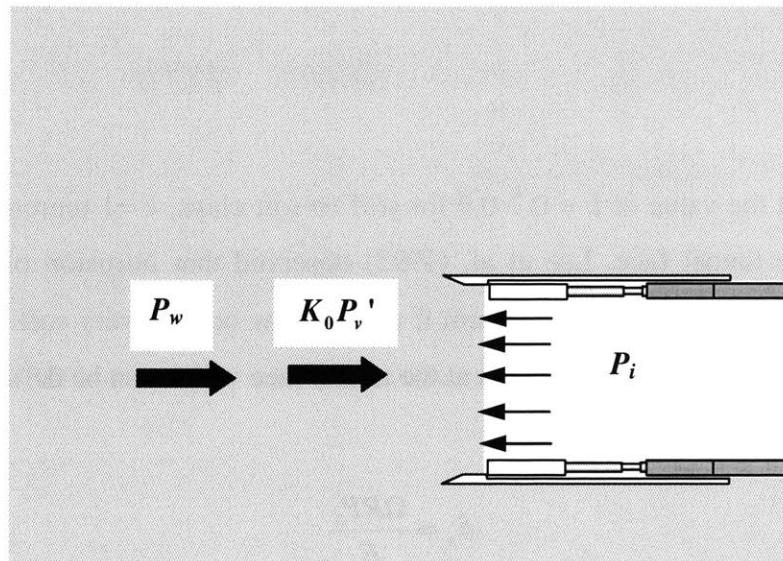


Figure 3.26 Pressures acting on tunnel during excavation

The estimation of the gap parameter using Lee's et al. (1992) method does not consider time-dependent consolidation and creep components. Hence, the equivalent ground loss estimated using the gap parameter is only applicable to the state immediately after passing of the shield. The advantages in using the gap parameter to define the equivalent ground loss parameter are: (1) the various construction methods and tunneling equipment configurations can be considered, and (2) elastoplastic behavior of the soil can be considered.

Loganathan and Poulos (1998) defined the equivalent ground loss ϵ_0 with respect to the gap parameter g as:

$$\varepsilon_0 = \frac{4gR + g^2}{4R^2} \times 100\% \quad (3-24)$$

Where,

R = radius of the tunnel

g = gap parameter estimated using (3-19)

The ground loss and the ground deformation calculations proposed by Verruijt and Booker (1996) are based on uniform radial ground movement around the tunnel (Figure 3.22). However, as pointed out by Rowe and Kack (1983), the radial ground movement is not uniform since the equivalent 2D gap around a tunnel is noncircular but oval-shaped as shown in Figure 3.23. The reasons for the formation of an oval-shaped gap around the tunnel given by Rowe and Kack (1983) are (1) tunnel operators advance the shield at a slightly upward pitch relative to the actual design grade to avoid the diving tendency of the shield, (2) the tunnel lining settles on the ground when the tail is removed, and (3) 3D elastoplastic movement of the soil occurs at the tunnel face.

The equivalent ground loss parameter obtained in (3-24) is further modified to incorporate the non-uniform radial movement of the soil (due to the oval-shaped gap) around the tunnel, which basically influences the deformation pattern of the surrounding soil. The component of the equivalent ground loss parameter $\varepsilon_{x,z=0}$, which causes the surface settlement, may be assumed to be an exponential function that models the nonuniform movement of the soil around the tunnel:

$$\varepsilon_{x,z=0} = \varepsilon_0 B \cdot \exp(-Ax^2) \quad (3-25)$$

where A , B = constants and ε_0 = equivalent ground loss as obtained from (3-24). Constants A and B can be derived based on the boundary conditions as shown in Figure 3.27.

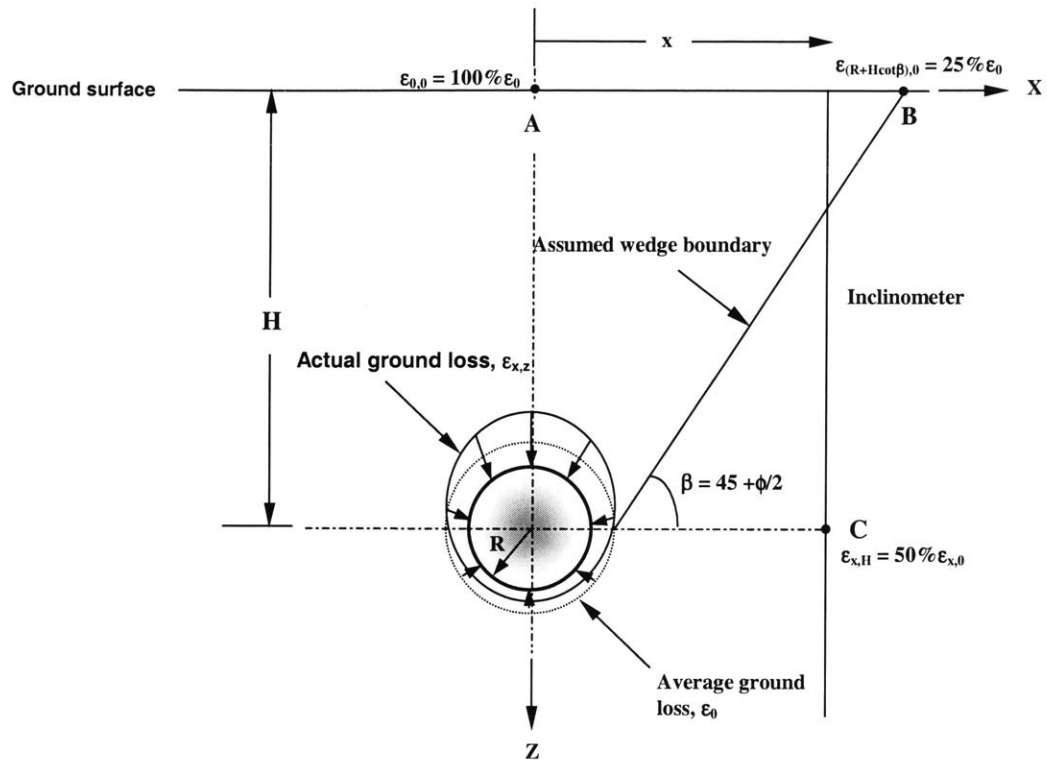


Figure 3.27 Ground deformation patterns and ground loss boundary conditions (after Loganathan and Poulos, 1998)

As shown in Figure 3.28, when the portion of the soil above the tunnel crown touches the tunnel lining, the soil at the side of the tunnel displaces towards the bottom of the tunnel: see also Figure 3.16. Therefore, any upward movement of the soil below the tunnel is limited. Loganathan and Poulos (1998) assumed that when the tunnel lining settles on the bottom of the annulus gap (due to its self-weight), the distance between the crown of the tunnel lining and the crown of the excavated surface, become twice the thickness of the annulus gap (Figure 3.23). This is based on the simple geometric assumption that the void area above the tunnel springline is approximately 75% of the total void area. Thus, they considered that 75% of the vertical ground movement occurs within the upper annulus of the gap around the tunnel as shown in Figure 3.29.

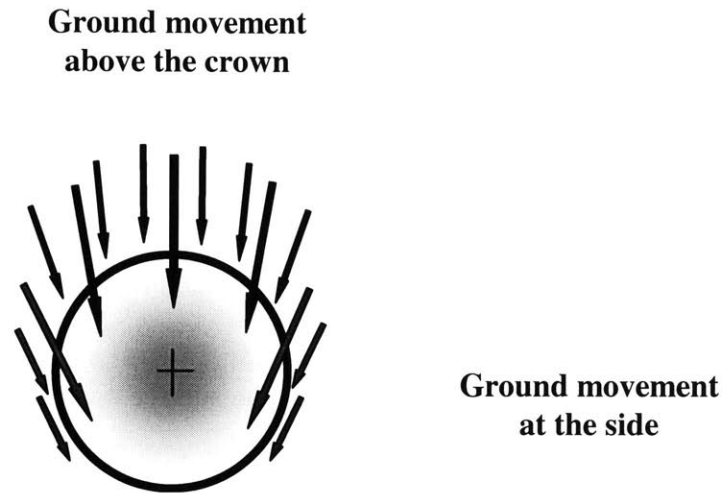


Figure 3.28 Ground movement towards tunnel

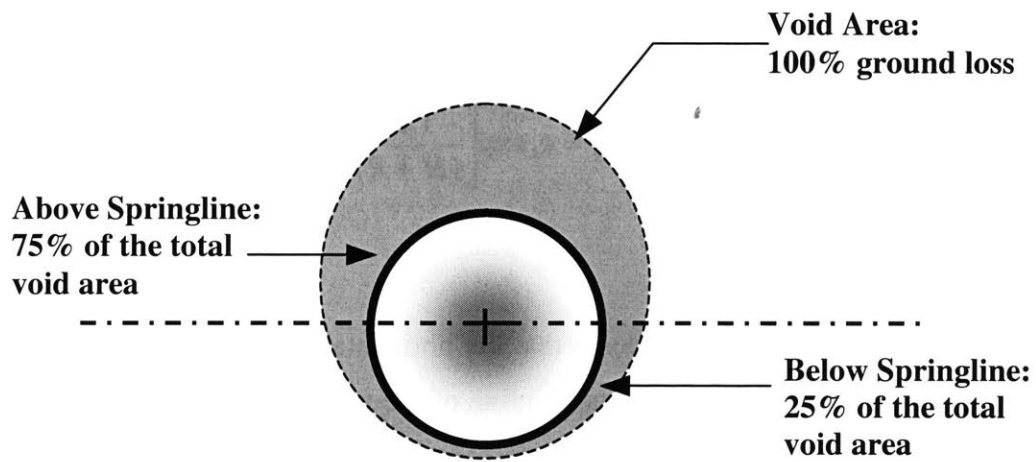


Figure 3.29 Oval-shape ground deformation pattern around tunnel section proposed by Loganathan and Poulos (1998)

The relationship between surface deformation trough width, which is an indirect measure of the ground movement influence zone, and the tunnel depth can be expressed as a horizontal angle β drawn from the springline of the tunnel to the width of the surface deformation trough. From the observations made by Cording and Hansmire (1975), angle β can be defined as $45 + \phi/2$, where ϕ = friction angle. Therefore, for tunneling in undrained conditions, the parameter $\beta = 45^\circ$ and $\cot\beta = 1$.

Based on the assumption stated above, the surface settlement above the tunnel axis is the complete cumulative equivalent ground loss ($100\% \varepsilon_0$) around the tunnel as represented by point A in Figure 3.27, and the surface settlement at the horizontal distance $(R+H\cot\beta)$, which is labeled as point B in Figure 3.27, is the partial cumulative equivalent ground loss ($25\% \varepsilon_0$).

In the case of undrained conditions where $\beta = 45^\circ$ and applying the boundary conditions in Figure 3.27 on (3-25), the equivalent ground loss component that models the nonuniform vertical movement can be derived as:

$$\varepsilon_{x,z} = \varepsilon_0 \exp\left[\frac{-1.38x^2}{(H+R)^2}\right] \quad (3-26)$$

Loganathan and Poulos (1998) considered that the horizontal ground movement into the tail void or gap is at a maximum at the springline of the tunnel and is zero at the crown and the invert of the tunnel. Therefore, the lateral ground movement is symmetrical about the tunnel axis. The lateral movement component is incorporated into the ground loss as:

$$\varepsilon_{x,z} = \varepsilon_{x,z=0} C \cdot \exp(-Dz^2) \quad (3-27)$$

where C and D are constants that are derived based on the boundary conditions described below.

Based on the oval-shaped gap geometry, the magnitude of the horizontal movement at the tunnel springline is approximately half of the vertical movement at the tunnel crown, which causes 75% of the ground movement into the upper annulus of the oval-shaped gap around the tunnel. Thus, the equivalent ground loss component due to the horizontal movement at the horizontal distance x and the depth H ($\epsilon_{x,H}$) labeled as point C in Figure 3.27 is approximately 50% of the equivalent ground loss causing surface deformation ($\epsilon_{x,z=0}$) at the horizontal distance x .

By applying these boundary conditions (Figure 3.27) and substituting (3-26) into (3-27), the modified equivalent ground loss parameter, incorporating the nonlinear ground movement (due to oval-shaped gap) around the tunnel-soil interface, can be written as:

$$\epsilon_{x,z} = \frac{4gR + g^2}{4R^2} \exp\left\{-\left[\frac{1.38x^2}{(H+R)^2} + \frac{0.69z^2}{H^2}\right]\right\} \quad (3-28)$$

Note that if $\delta = 0$, surface settlement troughs predicted using Verruijt and Booker's method are wider than observed values. Therefore, Loganathan and Poulos (1998) modified the analytical solution proposed by Verruijt and Booker (1996) as expressed in (3-18) to accommodate the newly defined ground loss parameter shown in (3-28). Furthermore, ovalization of the tunnel lining is neglected ($\delta = 0$) in their study because they believed that the ovalization only occurs over the long-term, and it is very small. Therefore, by combining (3-18) and (3-28), the modified formula for the prediction of the surface deformation can be expressed as:

$$U_{z=0} = 4(1-\nu)R^2 \frac{H}{(H^2 + x^2)} \frac{4gR + g^2}{R^2} \exp\left[-\frac{1.38x^2}{(H + R)^2}\right] \quad (3-29)$$

Loganathan and Poulos (1998) indicated that the modified analytical solution (3-29) gives a narrower surface settlement trough than the original solution (3-18) provided by Verruijt and Booker (1996).

3.2.2.3 Pinto (1999)

The solution proposed by Sagaseta (1987) did not explicitly consider the presence of the tunnel lining geometry and was classified as a “point solution.” Verruijt (1997) presented an exact solution method for a circular tunnel undergoing a pre-defined wall deformation in elastic ground using methods of complex variables. Pinto (1999) then extended this method by obtaining solutions for the distortion mode shape and introduced the relative distortion ratio of the tunnel (ρ) that can be defined as the ratio of the lining distortion to uniform convergence as follows:

$$\rho = -\frac{u_\delta}{u_\varepsilon} \quad (3-30)$$

where the uniform radial convergence or radial deformation at the tunnel lining, u_ε and distortion deformation, u_δ (Figure 3.30) are given by the following equations:

$$u_\varepsilon = -\frac{p_0 R}{2G} \quad (3-31)$$

$$u_\delta = \frac{q_0 R(3-4\nu)}{2G} \quad (3-32)$$

Where,

p_0 = In-situ average total stress

q_0 = In-situ deviatoric stress

R = Tunnel radius

G = Elastic shear modulus

ν = Poisson ratio

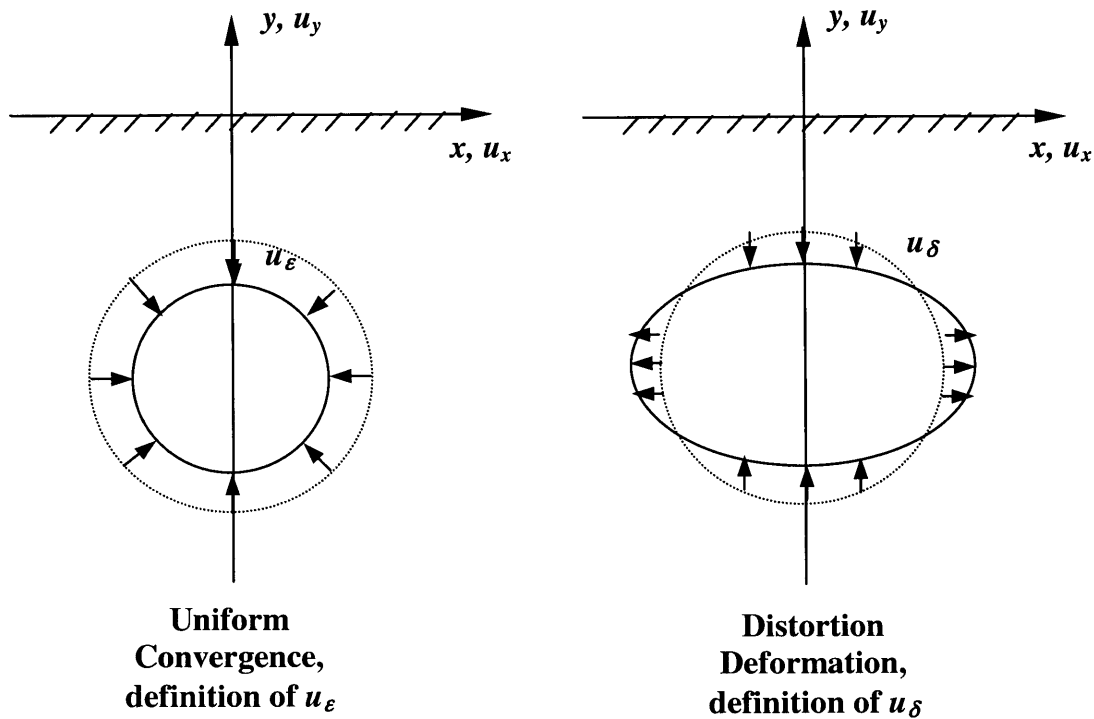


Figure 3.30 Deformation input parameters, u_ϵ and u_δ

In principle, u_ϵ and u_δ can be evaluated by solving equation (3-31) and (3-32), respectively. However, in practice, they are regarded as input parameters that can be assumed regardless of their origin (Pinto, 1999).

The general features of surface deformations are given by:

$$\frac{u_x}{u_\varepsilon} = 4(1-\nu) \frac{R}{H} \frac{x}{H} \frac{-2\rho \left[\left(\frac{x}{H} \right)^2 - 1 \right] + \left[\left(\frac{x}{H} \right)^2 + 1 \right]^2}{\left[\left(\frac{x}{H} \right)^2 + 1 \right]^3} \quad (3-33)$$

$$\frac{u_y}{u_\varepsilon} = 4(1-\nu) \frac{R}{H} \frac{\frac{-2\rho}{3-4\nu} \left\{ \left[\left(\frac{x}{H} \right)^4 - 1 \right] - \frac{1}{4(1-\nu)} \left[3 \left(\frac{x}{H} \right)^2 - 1 \right] \left(\frac{R}{H} \right)^2 \right\} + \left[\left(\frac{x}{H} \right)^2 + 1 \right]^2}{\left[\left(\frac{x}{H} \right)^2 + 1 \right]^3} \quad (3-34)$$

Where,

x = Horizontal coordinate

y = Vertical coordinate

H = Depth to centerline of the tunnel

At the centerline, $x = 0$, u_y^0 as shown in

Figure 3.31, is given by:

$$\frac{u_y^0}{u_\varepsilon} = \frac{4(1-\nu)}{3-4\nu} \frac{R}{H} \left\{ 2\rho \left[1 - \frac{1}{4(1-\nu)} \left(\frac{R}{H} \right)^2 \right] + 3 - 4\nu \right\} \quad (3-35)$$

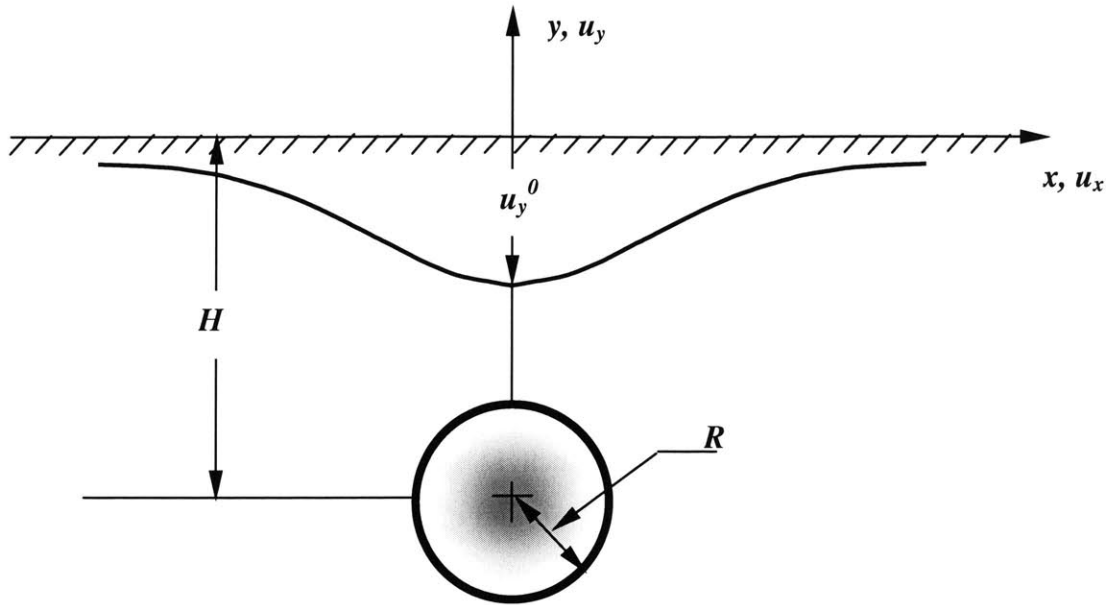


Figure 3.31 Definition of parameters using in ground deformation determination (after Pinto, 1999)

3.2.3 Finite Element and Numerical Methods

At present, two-dimensional (2D) analyses are common. Finite element analyses offer considerable possibilities of modeling many aspects of tunneling. However, it is evident that the development of ground movements around the shield is fully three-dimensional but using 3D analysis for shield tunneling still has problems:

1. The cost and time required for a full 3D analysis, which properly simulates excavation aspects and the 3D geometry, with a realistic non-linear constitutive soil model, are substantial.
2. In shield tunneling, many of the parameters affecting the results are difficult to define, for example tunnel lining properties, degree of soil disturbance, shield advance, tail void size, and soil model parameters.

3. Many analyses of a tunnel section are required for any given project since the geological conditions, tunneling conditions, tunnel alignment geometries, and other related activities change along the tunnel alignment.
4. So far, no constitutive soil model has been proved to be successful at simulating all aspects of soil and tunneling behaviors

All of these reasons still prevail, but considerable progress in FE modeling has been made in recent years.

Three-dimensional finite element analyses such as that described by Lee and Rowe (1991) can be used to predict the spatial 3D ground displacement within the soil mass. However, because of the high cost and processing time associated with this analysis, simplified 2D procedures are often adopted. For the purpose of performing a two-dimensional plane strain analysis, the components of ground loss discussed by Lee et al. (1992) as shown in Figure 3.24 are represented quantitatively in terms of the so-called “gap” parameter as described earlier. Hence, the concept of this method is to simplify the spatial 3-D ground movements due to tunneling into 2-D (plane strain) space. In order to convert the problem dimensions (i.e., from 3D to 2D), the gap parameter needs to be applied to obtain the equivalent volume of ground movements in the transverse section. Specifically, these effects can be approximately incorporated in a 2D plane strain model by assuming a larger excavated tunnel diameter, with the additional volume corresponding to the volume of ground lost over the shield (i.e., volume per unit length of the tunnel) as illustrated in Figure 3.25.

However, in 2D analyses, the predicted settlement troughs tend to be wider than the measured surface settlements, particularly for tunnels in heavily overconsolidated clays. Clough and Leca (1989) suggest that the use of 2D analyses to represent 3D effects is itself one of the reasons for the shape of the settlement trough not being well predicted. Non-linear 2D finite element analyses have been undertaken for NATM construction as noted by Clough and Leca (1989). However, although the 3D analysis for the NATM has some complications, there is no need of simulating the complex movement of the shield.

Akagi and Komiya (1996) described a 3D finite element analysis of an EPB shield tunnel excavated in soft clay, using a critical state soil model. To simulate the advance of a shield machine, they introduced the use of “excavation elements.” These elements are located in front of the cutting head to represent the area of ground disturbance caused by shield tunneling as illustrated in Figure 3.32.

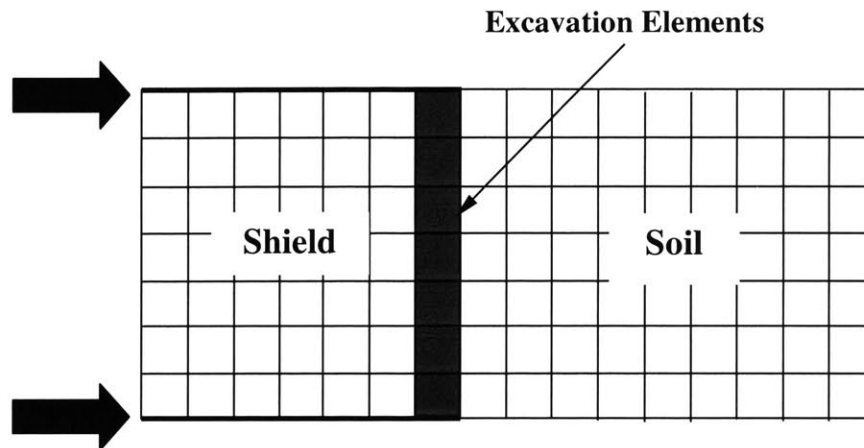


Figure 3.32 Advance of the shield simulated by “excavation elements” (after Akagi and Komiya, 1996)

The predicted results using their 3D model were in good agreement with the field measurement as illustrated in Figure 3.33. However, the shield and its advance were modeled in what clearly is a reasonably sophisticated analysis. Furthermore, the author suggested that, in order to verify the adequacy of the prediction, the model still needs more field measurement to be compared with its result.

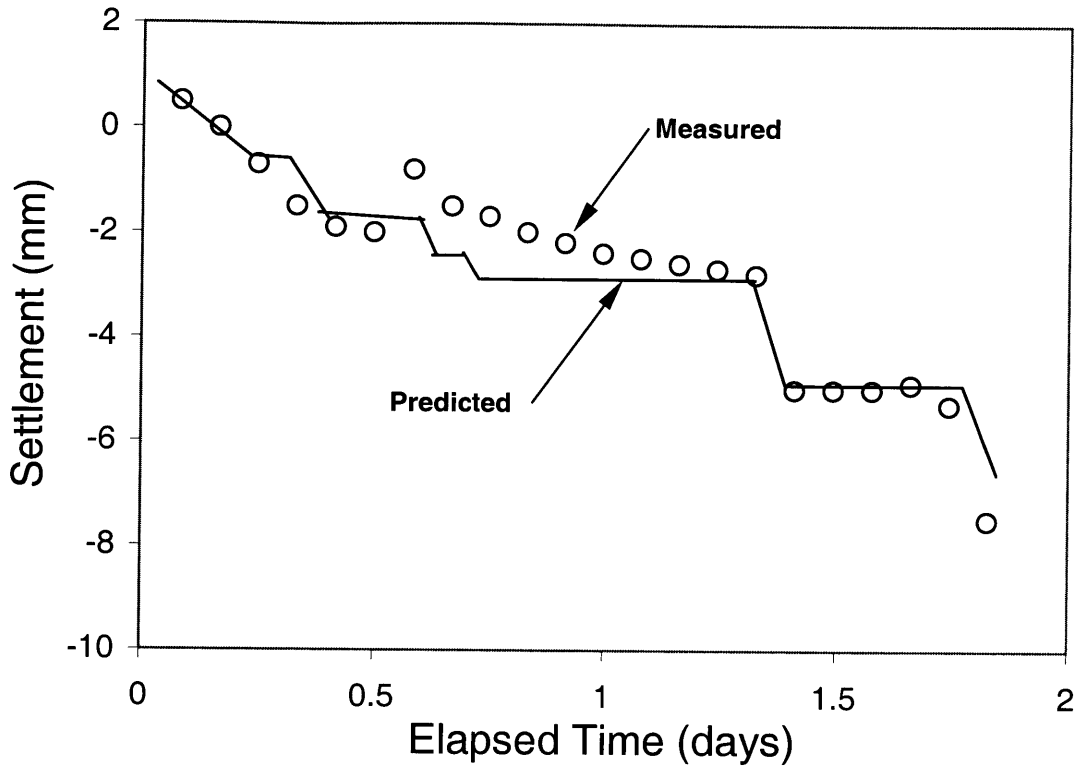


Figure 3.33 Measured data compared with 3D finite element analysis (after Akagi and Komiya, 1996)

Additionally, the major problem with two-dimensional analysis (e.g. plane strain) is that 2D analysis assumes that the end of excavation is far away from the tunnel section being analyzed. Therefore, 2D analysis is inadequate if three-dimensional effects are considered to be significant. For instance, 2D model excludes the possibility of analyzing the excavation-induced stresses at the tunnel face, which is the most critical problem in practice. On the other hand, 3D analysis allows one to conduct a more detailed examination of the near-field stress concentrations that develop around the ends and edges of the excavation. Eberhardt (2001) used a three-dimensional finite-element model, which was based on examples taken from the planned Gotthard base tunnel and the existing Fenster Bedretto in the central Swiss Alps. Although the model intended to simulate tunneling in rock, its procedures are very similar to the model using in soft ground tunneling. The model explored the near-field stress path during the progressive advancement of the tunnel face. The results demonstrated that as the tunnel face

approaches and passed through a unit volume of rock, the spatial and temporal evolution of the three-dimensional stress field encompasses a series of deviatoric stress increases and/or decreases as well as several rotations of the principal stress axis. Such changes to the rock mass condition ultimately influence the near-field tunnel deformation mechanism and mode of failure.

Eberhardt (2001) designed the model using 5200 20-node brick elements assuming symmetry in a plane parallel to the tunnel axis. Element sizes and aspect ratios were minimized near the tunnel boundary and gradually increased outwards. A tunnel diameter of 10 m was used with the outer boundary extending to a distance of 100 m to reduce boundary effects. An overburden of 1,000 m was assumed. To simulate the progressive excavation, two intermediate benches (i.e., an upper bench, followed by the excavation of a lower bench) were used as shown in Figure 3.34. The stress path analysis was performed for each incremental advance of the tunnel face (21 stages in total) using an iterative solver.

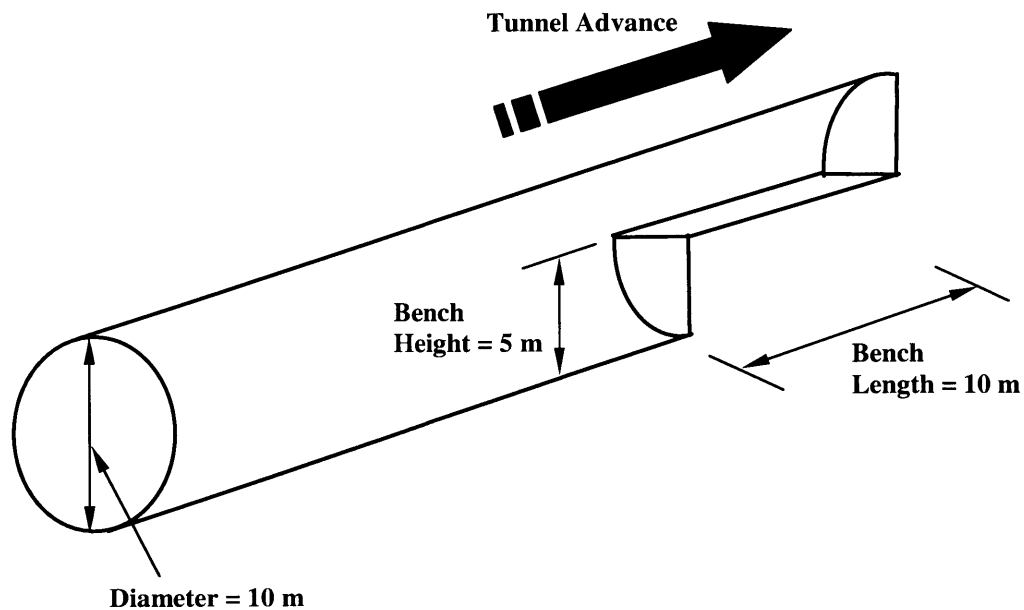


Figure 3.34 Excavation sequencing and tunnel bench dimensions as incorporated into numerical models (Eberhardt, 2001)

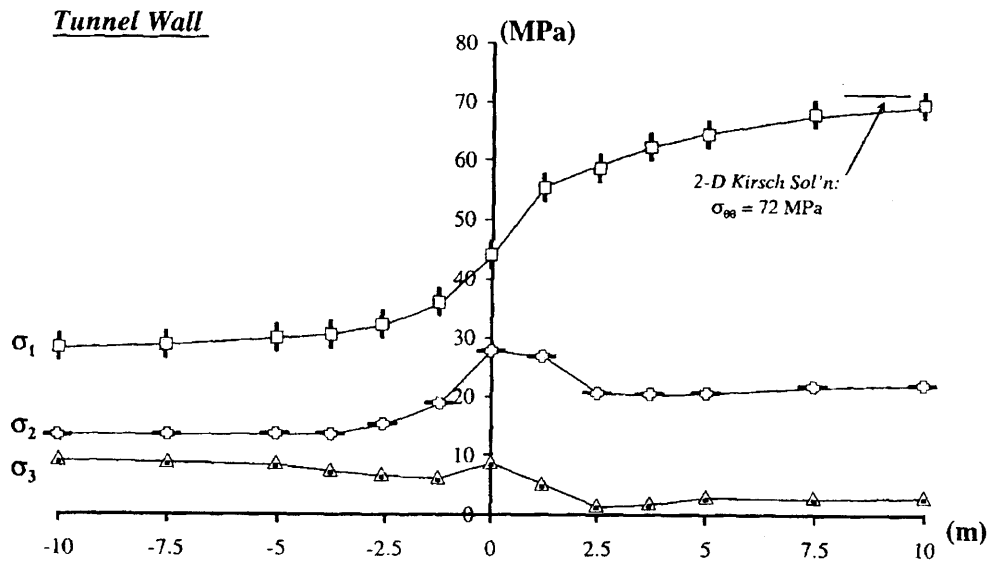
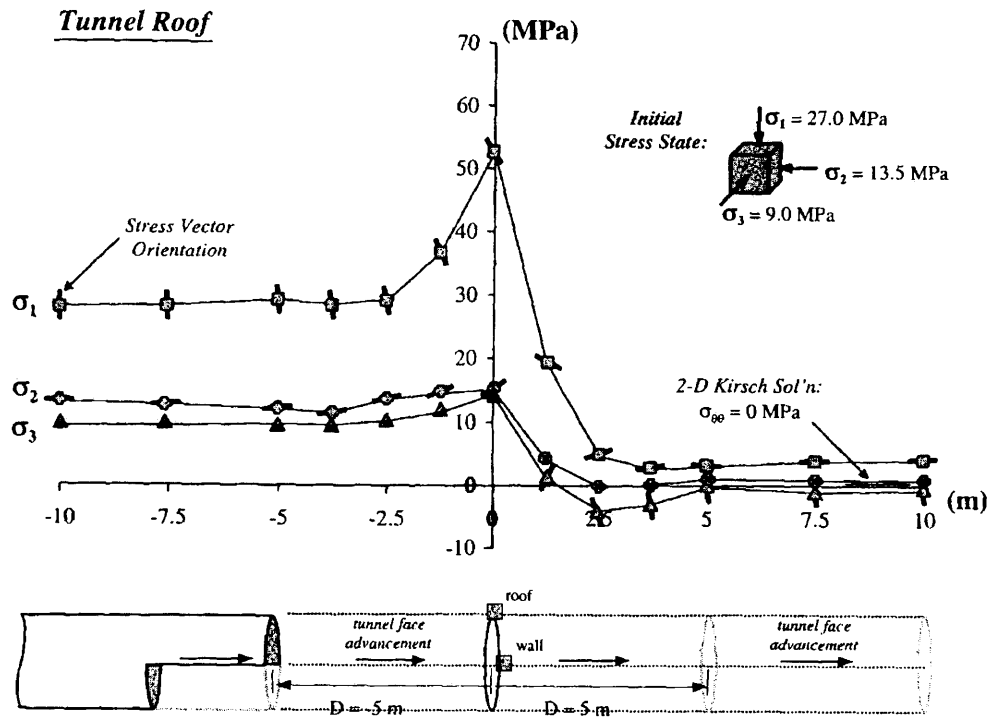


Figure 3.35 Stress path plots of the principal stress magnitudes and orientations at fixed points in the tunnel roof and wall (after Eberhardt,2001)

One of the cases simulated by the 3D model assumes that the initial vertical stress applied in the 3D model is equal to the overburden load with the far-field horizontal stresses, parallel and perpendicular to the tunnel axis. This case is similar to the actual case faced in soft ground tunneling. Additionally, the principal stress, σ_{1i} , was aligned vertically. As a result, Figure 3.35 shows the principal stress magnitudes and orientations, based on the initial stress conditions of this case, for two fixed points relative to the forward sequential advancement of the tunnel face. Based on the result, it was found that stress magnitudes begin to deviate from the far-field initial value as the tunnel face approaches the monitoring sections.

Tunnel roof and wall displacements can be viewed in a similar way. Figure 3.36 shows the total elastic displacement observed at the two fixed monitoring points in the tunnel roof and the walls. Given the vertical orientation of the primary major principal stress, σ_{1i} , the largest displacements are observed in the tunnel roof (crown). As shown on the left-hand side of the plot, displacements begin to accumulate before the tunnel face reaches the fixed monitoring points but are limited due to confinement. Figure 3.36 also provides the direction vectors for the displacements in the tunnel roof. Displacements, both in the tunnel walls and roof, begin by moving towards the approaching tunnel face as it passes by and moves further away from the monitoring points.

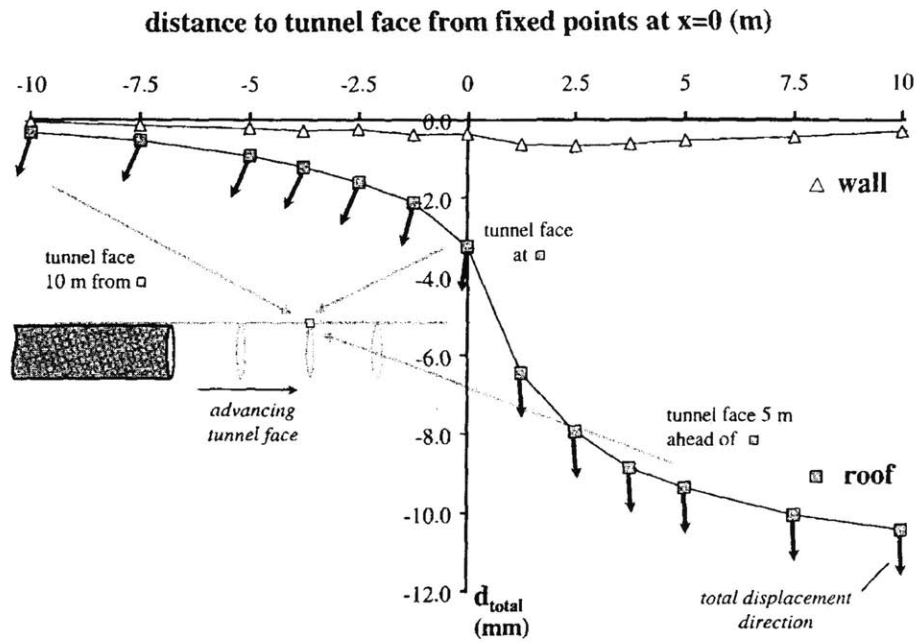


Figure 3.36 Accumulation of deformations with tunnel face advancement for fixed points in the tunnel roof and wall (after Eberhardt, 2001)

3.2.4 Laboratory Experiments

Laboratory experiments on tunnel related deformation involve constructing a scale model of a tunnel of known diameter and depth in different soils. Then, the nature of the soil deformation and strain field can be observed when the tunnel is excavated. This method has been adopted by Atkinson et al. (1975), Atkinson and Potts (1977), Hudson et al. (1976), Kimura and Mair (1981) and Nomoto et al. (1999).

The main purpose for the use of physical models is to demonstrate the way in which soil around a circular cavity, being the most usual soft ground tunnel cross-section, deforms as external pressure is increased and/or internal pressure is reduced. In the other words, deformation behavior of the ground surrounding a tunnel is related to the stress changes within a tunnel during construction. However, a model can hardly reproduce precisely the behavior of a real tunnel during construction, with all details of the methods of excavation and support. The main justification for the laboratory experiments is to provide data for comparison with existing methods for soft ground tunnel design. The model results have also been successfully used to predict the settlements above real tunnels.

3.2.4.1 Atkinson and Potts (1977)

Atkinson and Potts (1977) introduced a centrifuge model for tunneling, which can be accelerated to 75g (i.e., the stresses in the soil around the tunnel were the same as the stresses around a tunnel 75-times larger accelerated in earth's gravity alone). The model tunnel illustrated in Figure 3.37 was constructed in two types of soil: an overconsolidated clay and a dry sand. The clay was kaolin, overconsolidated from a slurry to an overconsolidation ratio of about 4, and the sand was the fraction of Leighton Buzzard sand passing a No. 14 sieve (1.2 mm) and retained on a No. 25 sieve (0.6 mm). Results from the clay can be compared with field results in ground such as the London Clay,

while the behavior of the sand would correspond to that of naturally occurring granular soils above the water table.

The rectangular soil model is contained in a rigid box and uniform surface surcharge stress σ_s can be applied to the top of the model by fluid pressure across a rubber membrane. Note that surface surcharge loading may occur in practice where a tunnel is driven below structures on flexible foundations or when a tunnel is driven through stiff clay or dense sand overlain by a very soft stratum.

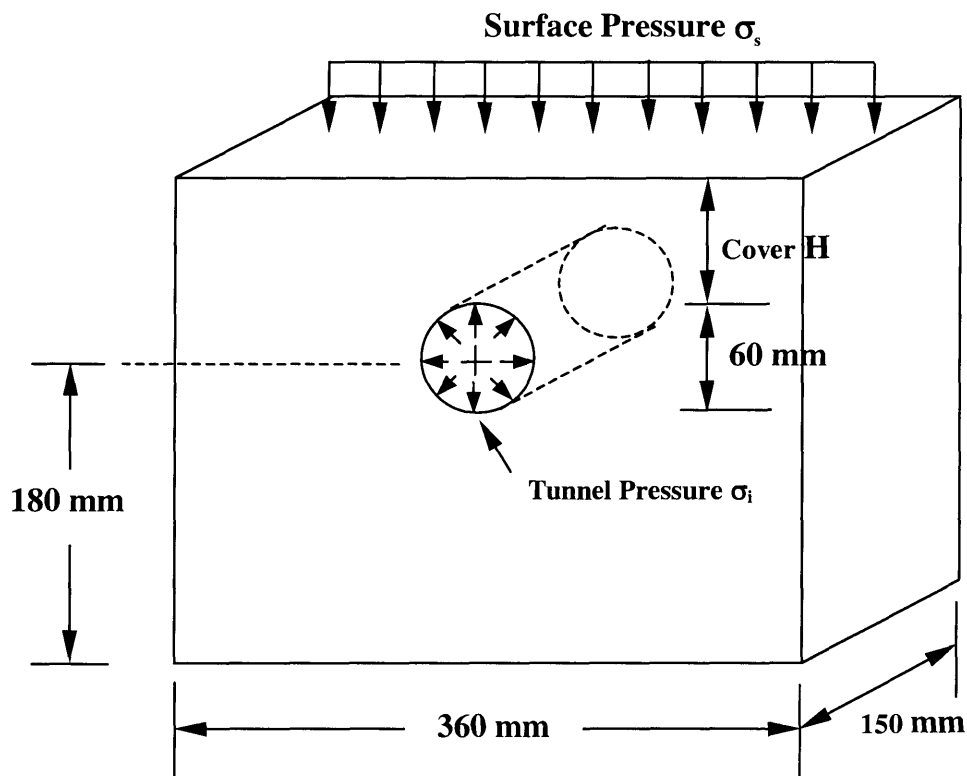


Figure 3.37 Model tunnel tests – boundary conditions and dimensions (after Atkinson and Potts, 1977)

Cylindrical tunnels are driven into the soil using a thin-walled cutter and an internal fluid pressure σ_i applied to the sidewall through another membrane. The tunnel pressure σ_i is the equivalent of an excess air or bentonite pressure at the tunnel face during construction. Because of their design rigidity, the front and back faces of the box impose a condition of plane strain on the soil, the bottom is sufficiently far from the tunnel so that it has no influence on the behavior of the soil around and above the tunnel. The study is therefore mainly concerned with radial ground losses and makes no provision for movements of ground into the tunnel face normal to the plane of section, which will be discussed later.

Two types of tests have been performed. In one series of “static tests” under normal gravitational acceleration, σ_s or σ_i (Figure 3.37) were changed slowly so that any pore pressure arising from the loading was always dissipated and the clay was drained. For the test in sand, the models were accelerated in a large diameter centrifuge so as to increase the stresses due to body-weight forces. Constant accelerations of 75g were applied to induce stresses in the model equal to those in an equivalent structure 75 times larger than the model. The 60 mm diameter tunnel model should therefore have performed in the manner of a 4.5 m diameter tunnel stressed in the earth’s gravitational field. Measurements of local deformations were made by photographic techniques. In some experiments, thin metal tubes were used to line the tunnel in place of thin rubber membranes. Strain gauges were then used to measure the loads in the tubes.

Atkinson and Potts (1977) reported that the magnitude of the surface settlement increases as the crown settles, but the magnitude of i (i.e., distance from the maximum settlement point to the point of inflection, Figure 3.11) for a particular model tunnel will depend on the depth of tunnel, soil characteristics, and the presence of a surface surcharge. For model tunnels in sand without surface surcharge loading, Atkinson and Potts (1977) derived an expression for the point of inflection as

$$i = 0.25(z + R) \quad (3-36)$$

where z is the depth to tunnel axis and R is the tunnel radius. For settlement above tunnels in dense sand and in overconsolidated kaolin, both with surface surcharge loading, the expression is

$$i = 0.125 (3z + R) \quad (3-37)$$

The first equation, if plotted on the graph of i/R against $z/2R$ (Figure 3.38) falls in the area of Peck's (1969) "sand above the water table." The second equation plots within the zone of "soft to stiff clay." Hence, the results obtained from tunnel models are in good agreement with field data. It would seem, however, that one effect of surcharge loading on the subsidence above a tunnel in dense sand is to increase the value of i and, therefore, to increase the width of the settlement trough. This increase in i may be due to the differences in the pattern of deformation near the tunnel when a surface surcharge is applied. For tunnels in overconsolidated clay (stiff clay), the value of i for model tunnels with surface surcharge loading agrees with those obtained from field observations (Figure 3.38).

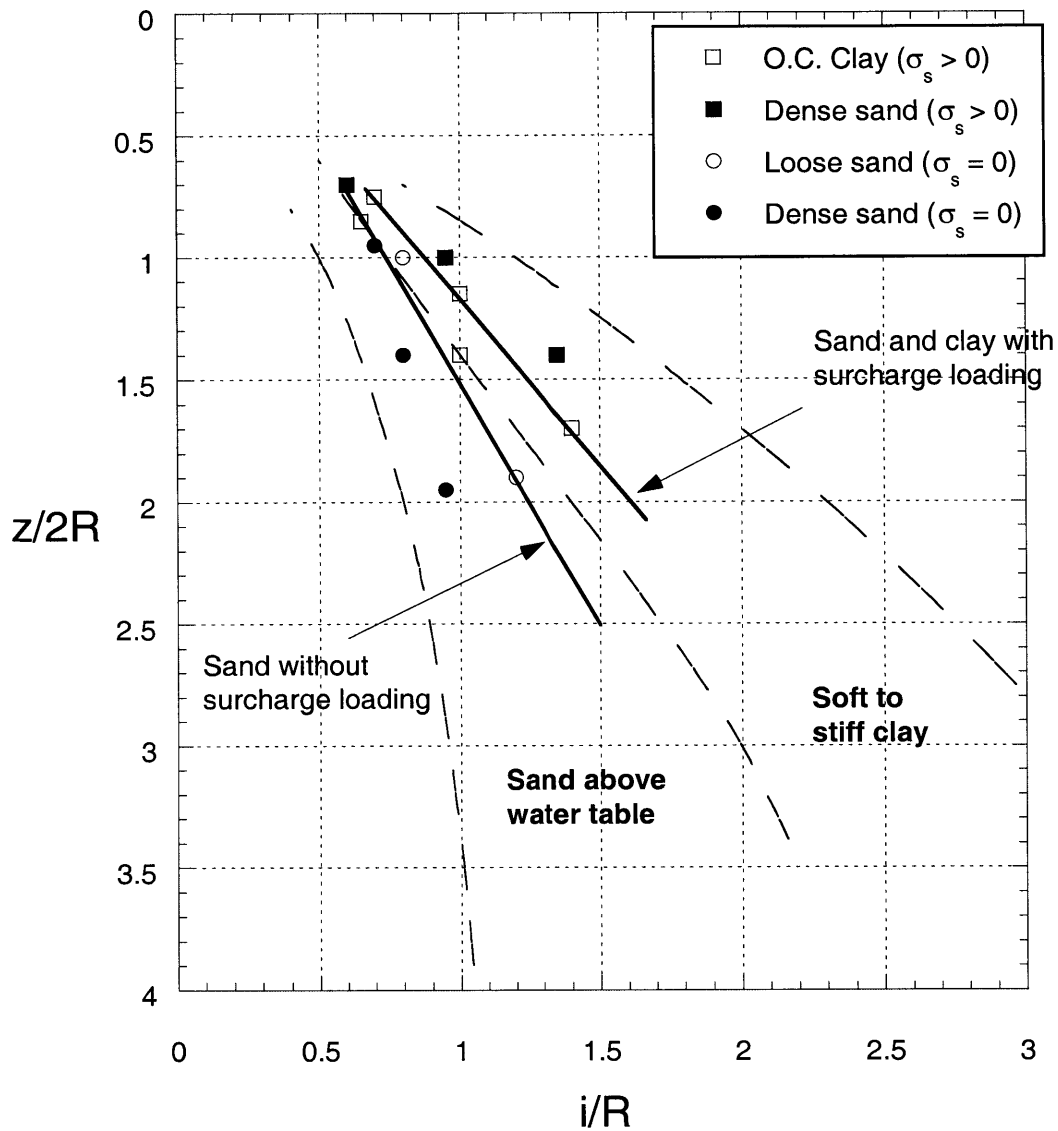


Figure 3.38 Comparison width of settlement trough (i/R) versus dimensionless depth of tunnel ($z/2R$) between Peck (1969)'s field data (dashed lines) and model testing results

3.2.4.2 Kimura and Mair (1981)

Whereas Atkinson and Potts (1977) focused on the ground movement behavior in plane strain (2D) tunnel models, Kimura and Mair (1981) adopted the same testing procedures, but they account for three-dimensional problems of a tunnel heading near the ground surface. Centrifuge tests on model tunnels in soft clay were performed to explore the relationship between the two-dimensional model and three-dimensional model.

In order to investigate the influence of parameters affecting tunnel stability and ground movement, it was necessary to make certain assumptions and create a simplified model of a tunnel under construction. In most instances of soft ground tunneling, the unlined heading can be represented as shown in Figure 3.39, where σ_i is the tunnel support pressure, H is the cover above the crown, D is the tunnel diameter, and L is the distance from the tunnel face to the structural lining. In soft ground, σ_i is often achieved by the use of compressed air or pressurized slurry (i.e., same concept as Atkinson and Potts, 1977).

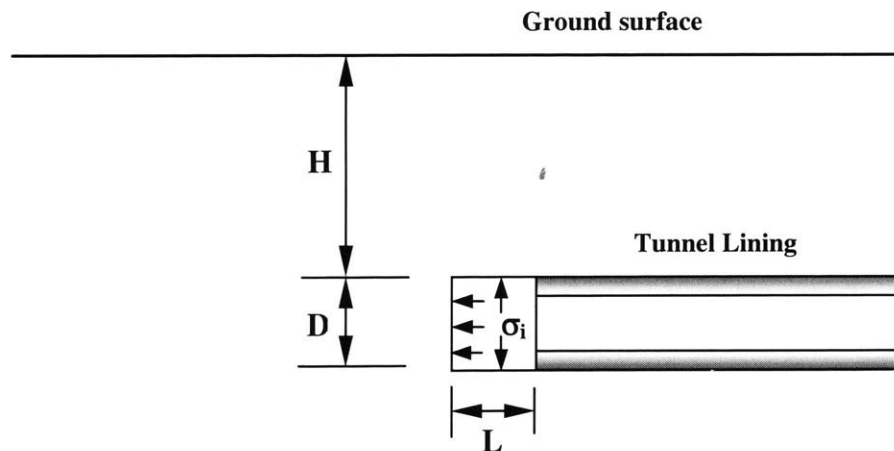


Figure 3.39 Tunnel heading in soft ground (after Kimura and Mair, 1981)

The distance L depends upon the type of tunnel excavation method. If, for example, a tunneling shield is employed, the distance L will be reduced to 0 (i.e., all openings are lined). As explained in the previous sections, the basic tunnel analysis is often two-

dimensional (plane strain). This is believed to be realistic only if the distance L is large as seen in the testing results provided later in this section. For the two-dimensional test series, the experimental techniques and models were exactly the same as the model tunnels introduced by Atkinson and Potts (1977). The schematic of the model is shown in Figure 3.37. For the 3D test series, however, Kimura and Mair (1981) developed a semi-circular tunnel with the plane of symmetry being a greased and almost frictionless interface between a Perspex window and the clay (Figure 3.40). Most of the length of the semi-circular tunnel was lined, so that only the heading of length L was unlined; the ratio L/D was varied from 0 to 3. Kaolin clays with undrained shear strength of 26 kPa were used throughout the test series.

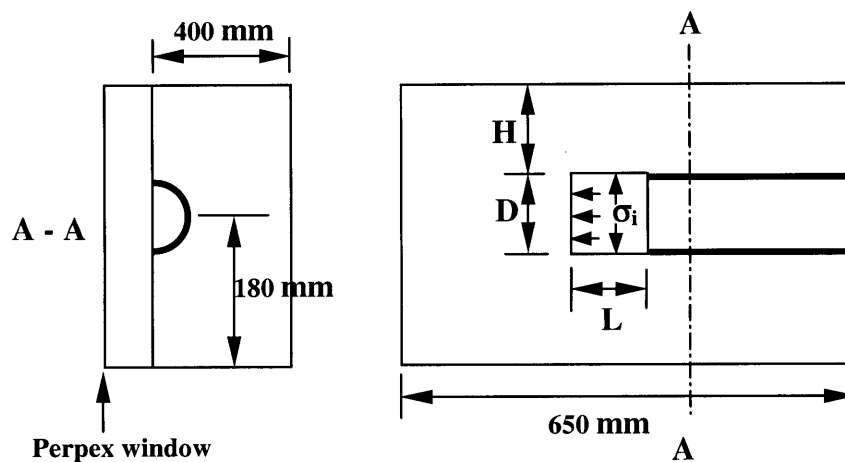


Figure 3.40 Dimension of 3D test series (after Kimura and Mair, 1981)

A result from 2D test series is presented in Figure 3.41. Complete collapse of the tunnel has occurred causing ground movement toward the tunnel. This collapse mechanism leads to the subsidence of ground surface as shown in Figure 3.42. Kimura and Mair (1981) observe that the width of the surface settlement trough is in good agreement with the field data reported by Peck (1969). This result also agrees with the model tunnel test conducted by Atkinson and Potts (1977).

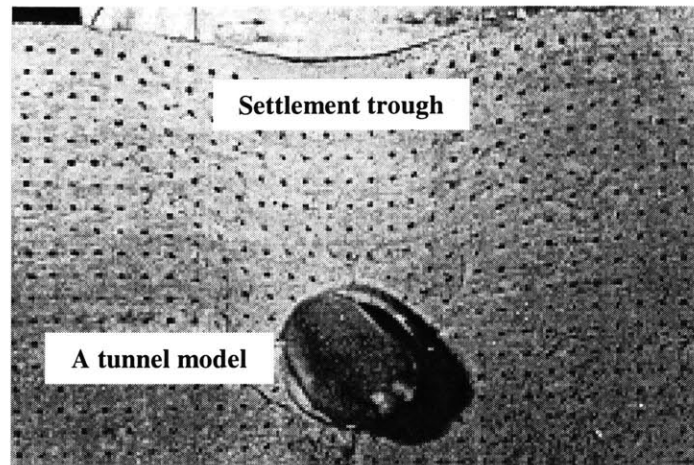


Figure 3.41 View of a typical 2D model tunnel after failure (after Kimura and Mair, 1981)

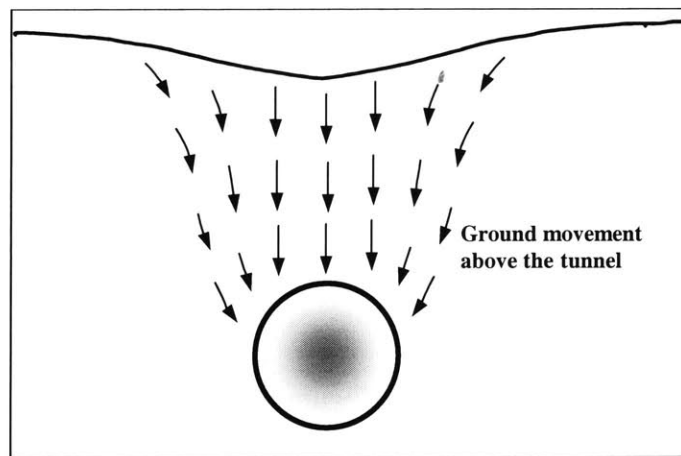


Figure 3.42 Schematic diagram of the failure above the tunnel model

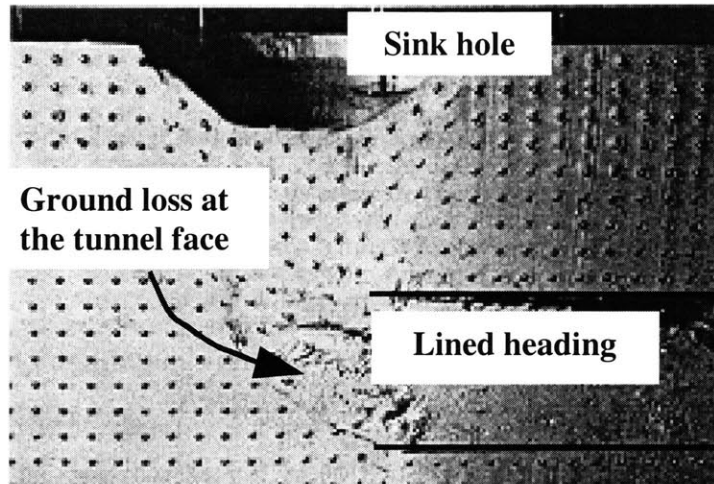


Figure 3.43 Model tunnel heading (3D Test) after failure for lined heading ($L/D = 0$) and $H/D = 1.5$ (after Kimura and Mair, 1981)

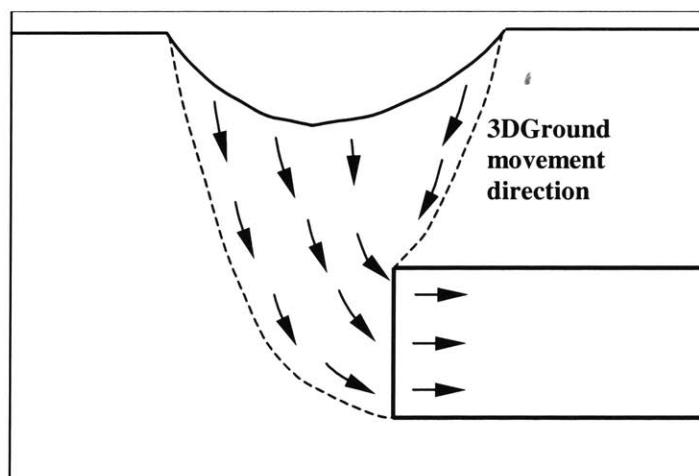


Figure 3.44 Schematic diagram of failure mechanism (see 3D ground movement at the face of the tunnel)

A typical result from the 3D test series after failure is shown in Figure 3.43 and Figure 3.44, in which the cover-to-diameter ratio (H/D) was 1.5 and the length of unlined heading L was zero (i.e., the heading was rigidly supported right up to the face). As can be seen in the figure, the soil moved toward to the tunnel face and caused a depression (a sink hole) at the ground surface. The behavior shows three-dimensional ground movement ahead of the tunnel face.

In contrast, the model shown in Figure 3.45 had a significant portion of unlined heading ($L/D = 2.0$), and it exhibited a mechanism approaching perfectly two-dimensional behavior that the soil movement in the direction of tunnel axis (i.e., ahead of the tunnel face) was very small in comparison to the vertical movements (Figure 3.46). Kimura and Mair (1981) specifically indicated that if the length of the unlined heading is large and the tunnel support pressure is low, ground movement or ground loss into the tunnel tends to exhibit two-dimensional behavior (i.e., soil moves vertically toward the tunnel) rather than three-dimensional behavior (i.e., soil intrudes to the tunnel face).

In conclusion, the centrifuge tests on model tunnels revealed how ground movement characteristics are strongly affected by the tunnel stability. In addition, these results may be helpful to assist the tunnel design and evaluation based on the observed behavior of ground movement.

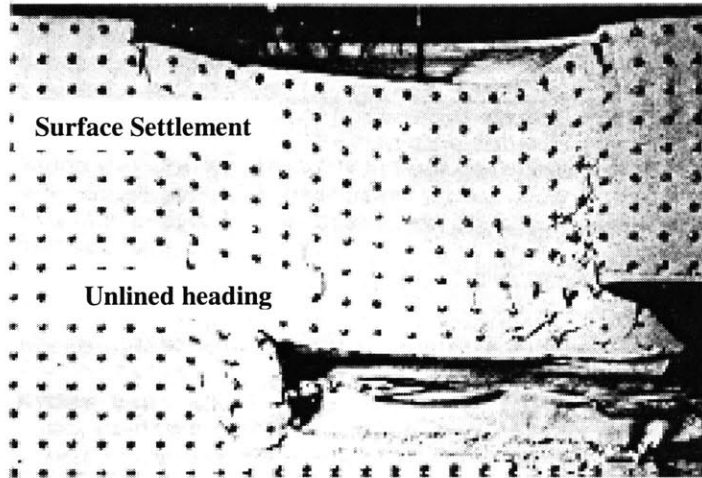


Figure 3.45 Model tunnel heading (3D Test) after failure for unlined heading ($L/D = 2.0$) and $H/D = 1.5$ (after Kimura and Mair, 1981)

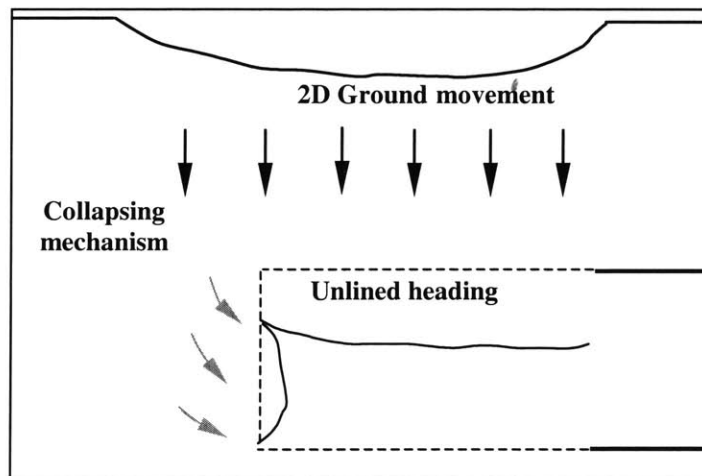


Figure 3.46 Schematic diagram of failure mechanism (see 2D ground movement above the tunnel)

3.2.4.3 Nomoto et al. (1999)

Nomoto et al. (1999) developed a miniature shield machine that can operate under centrifugal accelerations and can simulate the detailed construction processes of closed-face shield advancing and tail void formation. In this test, they used dry Toyoura sands, which have an approximate density (D_r) of 70% and $\phi_{\max} = 42$ degree. Factors examined in this test program are the ratio of cover to diameter (C/D) (i.e., C is overburden cover and D is shield diameter) as shown in Figure 3.47, tail void thickness (v), and construction sequence. A constant centrifugal acceleration of 25g (245 m/s^2) is used with varying overburden cover from 1D to 4D. The test simulates a penetration speed of 15 mm/min and a cutting revolution of 11 rpm. A 2.5 m diameter shield machine at prototype scale is modeled.

The shield test was designed to simulate processes of shield tunneling from cutting to tail void formation. At the beginning, the shield model (Figure 3.47) is thrust through the entrance of the container for 230 mm before it is pulled out to create a tail void of 2 mm. In the real shield tunneling work, the tail void is formed as the forward movement of the shield leaves the gap between the shield periphery and the outer lining surface. In the model, it is difficult to accurately simulate the process. Therefore, the tail void is formed by pulling out the external pipe (Figure 3.48) in the opposite direction to shield movement after completion of the predetermined cutting and thrusting process. Two types of lining with diameter of 96 mm and 98 mm were built for the shield test to allow the formation of two different tail void gaps (i.e., 1 mm and 2 mm): see also Figure 3.48. However, the backfill grouting process was not being incorporated into the shield test since the process is too complicated to be modeled and requires further elaboration (Nomoto et al., 1999).

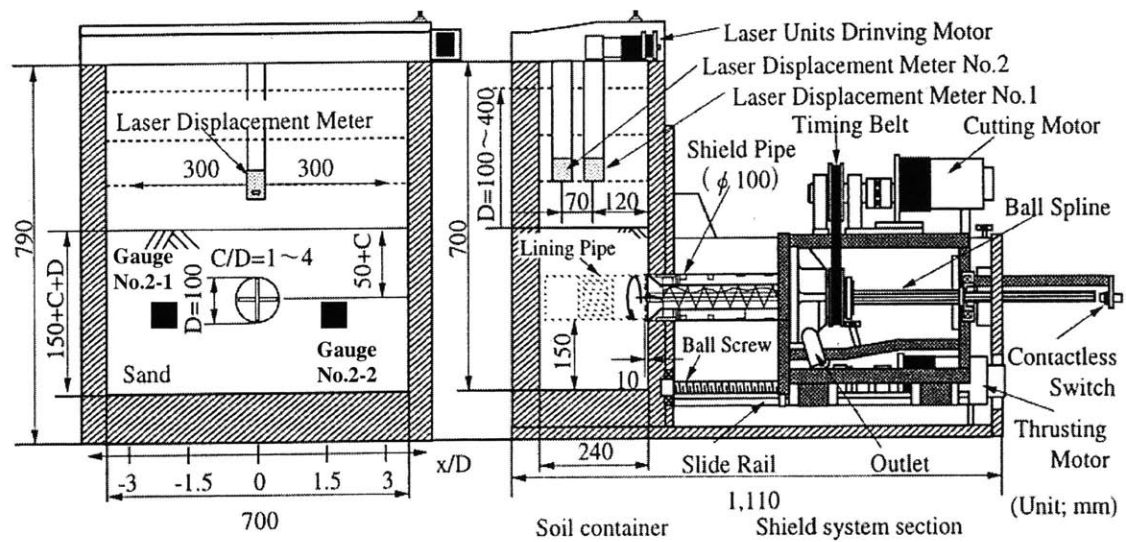


Figure 3.47 Miniature shield tunneling machine for centrifuge test scaled in mm. (after Nomoto et al., 1999)

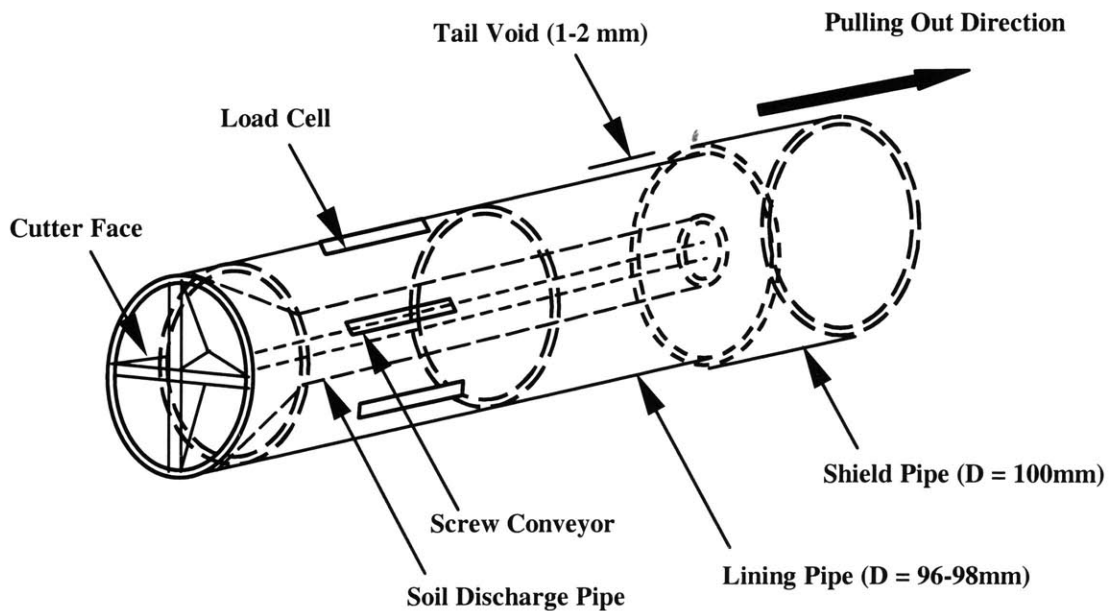


Figure 3.48 The miniature shield and tail void formation process (after Nomoto et al., 1999)

Nomoto et al. (1999) found that the final surface settlement profile induced by the shield test (i.e., including tail void formation) conforms fairly well to the normal probability curve proposed by Peck (1969). Hence, they propose the similar equation as follows:

$$\delta = \delta_{\max} \exp(-\alpha \cdot x^2) \quad (3-38)$$

where, α is a test coefficient. The correlation between the coefficient α for the shield test and the cover to diameter ratio (C/D) can be expressed by the following equation:

$$\alpha = \beta \cdot \left(\frac{C}{D}\right)^{-\gamma} \quad (3-39)$$

where, β and γ are test constants obtained from a series of tests.

The longitudinal surface settlement was also measured by laser displacement meters. Figure 3.49 indicates that the major surface settlement occurs over the shield and after shield passing. At the shield face, very small settlement is measured. The settlement due to tail void closing is the largest fraction of maximum settlement. Compared with the solution proposed by Attewell and Woodman (1982) also shown in Figure 3.49, the result indicates that Attewell and Woodman (1982)'s solution is not valid for shield tunneling with face support (i.e., slurry shield and EPB shield). The solution by Attewell and Woodman (1982) assumes that the surface settlement directly above the tunnel face corresponds to about $0.5\delta_{\max}$ or 50 percent of the maximum settlement after the shield passed as shown in Figure 3.20. However, this hypothesis is only applicable for tunnels using open face shield method but not suitable for EPB and slurry shield tunneling techniques where the major part of settlement, can occur after the shield face passed depending on operational practices (more details are provided in Chapter 7).

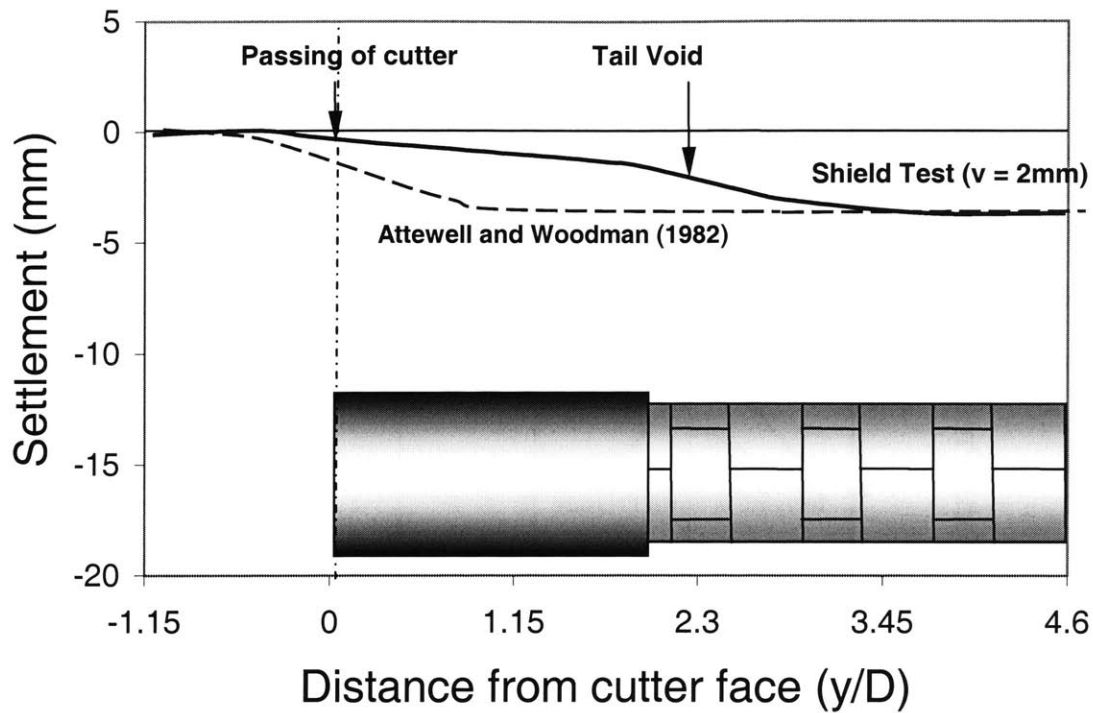


Figure 3.49 Surface settlement profile from the shield test with void thickness, $v = 2$ mm (after Nomoto et al., 1999)

Nomoto et al. (1999) also studied the earth pressure behavior around the shield. The earth pressure was measured by two pressure gauges installed in the model (i.e., gauges No. 2-1 and 2-2) as depicted in Figure 3.47. They found that the earth pressure starts to increase as the cutting operation commences and reaches the maximum level when the cutter is passing the measurement point before declines gradually during shield passing (Figure 3.50). Note that the simulated tail void gap (v) = 1 mm and the earth cover = $2D$ (i.e., D = diameter of the shield) in this test. A centrifuge acceleration of $25g$ was selected. During the tail void formation process, the earth pressure measured in gauge No. 2-1 and 2-2 (see also Figure 3.47) drops and then stabilizes at an earth pressure level which can be lower than the initial level as shown in Figure 3.50. Nomoto et al (1999) proposed that the initial increase is due to the soil arching in the front of the tunnel excavation and the sudden drop of earth pressure is the result of local plastic yield around the shield.

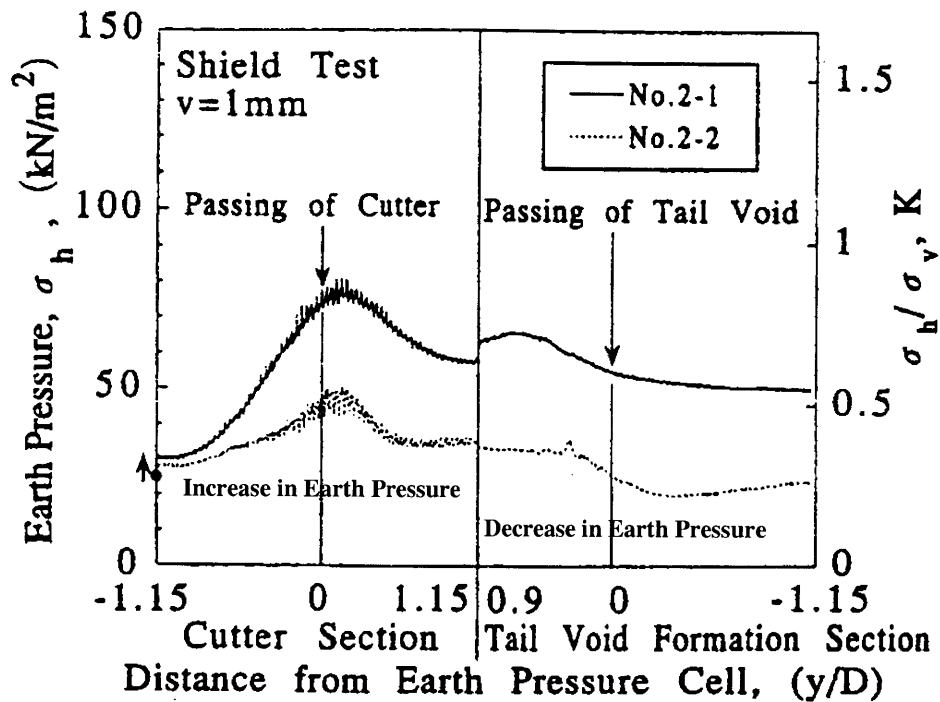


Figure 3.50 Earth pressure measurement results (after Nomoto et al., 1999)

3.3 Summary

1. Based on the literature, it has been concluded that the normal probability curve remains most widely used for fitting to transverse settlement troughs. Therefore, in real world practice, it is appropriate to use the empirical solution given by Peck (1969) and the parameter (K) introduced by O'Reilly and New (1982) to determine the surface settlement trough induced by tunneling. However, the limitation of empirical methods is that they require knowledge of the maximum settlement (δ_{max}) which can be obtained from instrumentation reading only after shield passing or can be predicted from estimated ground loss (G.L.%). Since the maximum settlement depends on all five components of ground loss (i.e., face loss, over-excavation, pitching, ground disturbance, and tail void

closure), predicting the magnitude of ground loss is extremely difficult especially in EPB tunneling. Hence, to predict the surface settlement profile correctly, one still needs other means to determine the maximum settlement, or needs “good judgment” in the selection of an appropriate value of ground loss. This requires consideration of such aspects as the tunneling techniques, operation control, tunnel alignment, and ground conditions.

2. For the longitudinal surface settlement, the solution provided by Attewell and Woodman (1982) assumes that 50 percent of maximum surface deformation ($0.5\delta_{\max}$) is coincident with the plane of the shield face (Figure 3.20) which is valid only for open-face shield. However, the assumption is not true in the case of closed-face shields. Based on the results of centrifuge tests simulating ground response due to closed-face shield tunneling (i.e., slurry shield and EPB shield) performed by Nomoto et al. (1999), the settlement in the plane of the shield face was smaller than $0.5\delta_{\max}$ (see also Section 3.2.4.3).

3. Providing a more theoretical basis than the empirical solutions, the analytical solution proposed by Verruijt and Booker (1996) in most cases cannot match field measurements. This analytical solution was modified by González and Sagaseta (2001) and they can fit measurement data better than Verruijt and Booker’s (1996) solution. However, using the solution, one may need to go through a trial and error process in order to select the suitable uniform radial parameter, ε and ovalization parameter, δ as shown in (3-18). Loganathan and Poulos (1998), (1999) therefore modified the solution of Verruijt and Booker (1996) by neglecting δ and adopting “gap parameter” (Lo and Rowe, 1982) in order to provide more realistic model of shield tunneling. As a result, their model gives a narrower surface settlement trough than the original solution. Although their prediction curve fits well some case history results, the solution still requires selecting the “gap parameter” as a function of the actual physical gap, a virtual deformation parameter at the face and a workmanship factor to match the actual settlement curve. All of these factors are empirical parameters, which are not constant and vary section-by-section depending on the shield operation practice as well as the ground conditions.

4. Although the prediction of ground movement based on finite element or other numerical methods are useful for indicating the general form of the settlement, they also have significant limitations. 2D analyses are not realistic for modeling three-dimensional behavior of shield tunneling and still cannot achieve good predictions of the settlement trough. 3D finite element analyses are adopted to improve these limitations (however, the cost and time required for the full 3D analysis are substantial). Furthermore, the 3D models cannot replicate all aspects of shield tunneling behavior, which is very complex. Hence, in practice, the use of the finite element method is still relatively limited.

5. All the laboratory models confirm the solution proposed by Peck (1969) that the surface settlement trough conforms to the normal probability curve. Only the inflection points or width parameters from the tests are somewhat different. The centrifuge tests on model tunnels done by Kimura and Mair (1981) reveal how ground movement characteristic is strongly affected by the tunnel stability. The ground movement due to the face loss manifests itself at the surface in a sinkhole extending from ahead of the shield to over of the shield (Figure 3.44). Nomoto et al. (1999) introduced a miniature shield tunneling machine in a centrifuge test. More advanced than other tests, their test did show the ground movement mechanism in the longitudinal direction as the shield advances. However, even their sophisticated model cannot simulate the entire shield tunneling process. The factors such as pitching angle and tail void grouting, which also contribute to the degree of the surface settlement, were not modeled. Thus, the physical models can be only used to confirm assumptions and to provide an overall picture of ground movement mechanism. Note that the models have limitations in that they still cannot precisely reproduce the behavior of a real tunnel during construction with all details of the tunneling methods of excavation and support which are very complicated especially in EPB tunneling.

6. Most of research has concentrated on the transverse settlement trough. Based on the field data, the empirical solution provided by Peck (1969) incorporated with proposed trough width parameter by O'Reilly and New (1982) is appropriate and the most used in practice for predicting surface settlement trough caused by shield tunneling. Although the

surface settlement in the longitudinal direction is critical and affects existing structures not less than that in the transverse direction, little research has been conducted in this area. Only Attewell and Woodman (1982) proposed an empirical solution to predict the longitudinal settlement. The solution is applicable to the settlement induced only by open-face shield. The use of the solution in the case of EPB tunneling method has not been studied yet. Therefore, a further study is required to understand the ground response caused by EPB tunneling. However, to fulfill the study goal, extensive field observation and instrumentation data are necessary. Some case histories of EPB tunneling are discussed in the next chapter.

References

- Akagi, H. and Komiya, K. (1996). "Finite Element Simulation of Shield Tunneling Processes in Soft Ground". *Proc. Int. Symposium on Geotechnical Aspects of Underground Construction in Soft Ground*, London, Balkema, pp. 447-452.
- Atkinson, J. H., Brown, E. T., and Pottss, D. M. (1975). "Collapse of Shallow Unlined Tunnels in Dense Sand". *Tunnel & Tunneling*, May 1975, pp. 81-87.
- Atkinson, J. H. and Pottss, D. M. (1977). "Subsidence above Shallow Tunnels in Soft Ground". *Proc. ASCE Geotechnical Engineering Division*, Vol. 103, GT 4, pp. 307-325.
- Attewell, P. B. and Farmer, I. W. (1974). "Ground Deformations resulting from Shield Tunneling in London Clay". *Canadian Geotech. J.*, Vol. 11, No. 3, pp. 380-395.
- Attewell, P. B. (1978). "Ground Movements caused by Tunneling in Soil". *Proc. Int. Conf. on Large Movements and Structures (ed. J. D. Geddes)*, Pentech Press, London, pp. 812-948.
- Attewell, P. B. and Woodman J. P. (1982). "Predicting the Dynamics of Ground Settlement and its Derivatives caused by Tunneling in Soil". *Ground Engineering*, Vol. 15, No. 8, pp. 13-22 and 36.
- Baligh, M. M. (1985). "Strain Path Method". *Journal of Geotechnical Engineering*, ASCE, Vol. 111, GT9, pp. 1108-1136.

- Clough, G. W. and Schmidt, B. (1981). "Design and Performance of Excavations and Tunnels in Soft Clay". *Soft Clay Engineering*, Elsevier, pp. 569-634.
- Clough, G. W. and Leca, E. (1989). "With Focus of Use of Finite Element Methods for Soft Ground Tunneling". *Review Paper in Tunnels et Micro-Tunnels en Terrain Meuble-du Chantier a la Theorie*, Paris, pp. 531-573.
- Cording, E. J., and Hansmire, W. H. (1975). "Displacements around Soft Ground Tunnels". *General Report 5th Pan American Conference on Soil Mechanics and Foundation Engineering*, Buenos Aires, Session IV, pp. 571-632.
- Cording, E. J. et al. (1976). "Displacement around Tunnels in Soil". *Report to US. Department of Transportation prepared at the University of Illinois at Urbana-Champaign*, DoT-TST-76T-22.
- Cording, E. J., Brierley, G. S., Mahar, J. W., and Boscadin, M. D. (1989). "Controlling Ground Movements during Tunneling". *Art and Science of Geotechnical Engineering at the Dawn of the 21st Century*, Prentice-Hall, Ch. 25, pp. 477-505.
- Eberhardt, E. (2001). "Numerical Modelling of Three-Dimensional Stress Rotation Ahead of an Advancing Tunnel Face". *International Journal of Rock Mechanics & Mining Sciences*, Vol. 38, pp. 499-518.
- Fujita, K. (1981). "On the Surface Settlement caused by Various Methods of Shield Tunneling". *Proc. 11th Conf. on Soil Mechanics and Foundation Engineering*, Vol. 4, pp. 609-610.
- Gonzalez, C. and Sagaseta, C. (2001). "Patterns of Soil Deformations around Tunnels. Application to the Extension of Madrid Metro". *Computer and Geotechnique*, Vol. 28, pp. 445-468.
- Hudson, J. A. et al. (1976). "Understanding Ground Movements caused by Tunneling". *Proc. of Conf. on Underground Engineering*, Paper No. D21G11, London.
- Kimura, T. and Mair, R. J. (1981). "Centrifugal Testing of Model Tunnels in Soft Clay". *Proc. 10th Int. Conf. of Soil Mechanics and Foundation Engineering, Stockholm*, Vol. 1, pp. 319-322.
- Lee, K. M. and Rowe, R. K. (1991). "An Analysis of Three-Dimensional Ground Movements: the Thunder Bay Tunnel". *Canadian Geotech. J.*, Vol. 28, pp. 25-41.
- Lee, K. M., Rowe, R. K., and Lo, K. Y. (1992). "Subsidence owing to Tunneling. I: Estimating the Gap Parameter". *Canadian Geotech. J.*, Vol. 29, pp. 929-940.
- Litwinski, J. (1956). "Application of the Equation of Stochastic Processes to Mechanics of Loose Bodies". *Arch. Mech. Stosow*, Vol. 8, pp. 396-411.

- Lo, K. Y., Ng, M. C., and Rowe, R. L. (1984). "Predicting Settlement due to Tunneling in Clays". *Proc. Geotech '84 – Tunneling in Soil and Rock*, ASCE, Atlanta, Georgia, pp. 47-76.
- Lo, K. Y., Ng, R. M., and Rowe, R. K. (1984). "Predicting Settlement due to Tunneling in Clays". *Proc. Tunneling in Soil and Rock*, Geotech III Conf., ASCE, Reston, VA, pp. 48-76.
- Loganathan, N. and Poulos, H. G. (1998). "Analytical Prediction for Tunneling-Induced Ground Movements in Clays". *Journal of Geotechnical and Geoenvironmental Engineering*, ASCE, Vol. 124, No. 9, pp. 846-856.
- Loganathan, N. and Poulos, H. G. (1999). "Tunneling Induced Ground Deformations and their Effects on Adjacent Piles". *Proc. of 10th Australian Tunneling Conference*, Melbourne, pp. 241-250.
- Maidl, B., Herrenknecht, M., and Anheuser, L. (1996). *Mechanised Shield Tunneling*, Ernst & Sohn, Berlin.
- Mair, R. J. and Taylor, R. N. (1993). "Prediction of Clay Behavior around Tunnels using Plastic Solution". *Proc. Worth Memorial Symposium*, Oxford, 1992, Thomas Telford, pp. 449-463.
- Mair, R. J. and Taylor, R. N. (1997). "Bore Tunneling in the Urban Environment". Theme Lecture, Plenary Session 4, *Proc. 14th Int. Conf. of Soil Mechanics and Foundation Engineering*, Hamburg, Vol. 4, pp. 2353-2385.
- Nomoto, T., Imamura, S., Hagiwara, T., Kusakabe, O., and Fujii, N. (1999). "Shield Tunnel Construction in Centrifuge". *Journal of Geotechnical and Geoenvironmental Engineering*, ASCE, Vol. 125, No. 4, pp. 289-300.
- O'Reilly, M. P. and New, B. M. (1982). "Settlement above Tunnels in the United Kingdom – Their Magnitude and Prediction". *Tunneling 88*, London, pp. 231-241.
- Peck, R. B. (1969). "Deep Excavations and Tunneling in Soft Ground". *Proc. 7th Int. Conf. on Soil Mechanics and Foundation Engineering*, Mexico City, State of the Art Volume, pp. 225-290.
- Pinto, F. (1999). "Analytical Methods to Interpret Ground Deformations due to Soft Ground Tunneling". SM Thesis, MIT, Cambridge, MA.
- Potts, D. M. (1976). "Behavior of Lined and Unlined Tunnels in Sand". Ph.D. Thesis, University of Cambridge.
- Rowe, R. K. and Kack, G. J. (1983). "A Theoretical Examination of the Settlements induced by Tunneling: Four Case Histories". *Canadian Geotech. J.*, Vol. 20, pp.299-314.

Rowe, R. K. and Lee, K. M. (1992). "Subsidence owing to Tunneling. II. Evaluation of a Prediction Technique". *Canadian Geotech. J.*, Vol. 29, pp. 941-954.

Sagaseta, C. (1987). "Analysis of Undrained Soil Deformations due to Ground Loss". *Geotechnique*, Vol. 37, No. 3, pp. 301-320.

Shirlaw, J. N., Doran, S. and Benjamin, B. (1988). "A Case Study of Two Tunnels Driven in the Singapore 'Boulder Bed' and in Grout Coral Sands". *Engineering Geology and Underground Movements*, Geological Society Engineering Geology Special Publication, No. 5, pp. 93-103.

Verruijt, A. and Booker, J. R. (1996). "Surface Settlements due to Deformation Tunnel in an Elastic Half Plane". *Geotechnique*, Vol. 46, No. 4, pp. 753-756.

Verruijt, A. (1997). "A Complex Variable Solution for a Deforming Circular Tunnel in an Elastic Half Plane". *International Journal for Numerical and Analytical Methods in Geomechanics*, Vol. 21, pp. 77-89.

CHAPTER 4

Case Histories of Shield Tunneling

4.1 Introduction

Although Earth Pressure Balance (EPB) shields have been used for many decades, very little information exists about the actual mechanism of shield-ground interaction. The ground response mechanism induced by EPB tunneling is difficult to understand. This is so because to study the ground response requires not only reliable ground deformation measurements in the field but also operational records of the shield. Therefore, until now, very few studies on EPB tunneling are available.

The objectives of this chapter are: (1) to observe the overall mechanism of the ground response induced by EPB tunneling based on case histories of shield tunneling projects around the world and (2) to determine factors influencing the ground settlement and to study how they affect the settlement. Relatively comprehensive deformation measurements and shield operational parameters recorded from the shield tunneling cases are presented in this chapter. It should be noted that not only cases using EPB shields, but also cases using slurry shields are studied here since both methods have similar effects on the ground settlement.

4.2 Washington Metropolitan Area Transit Authority Project (WMATA)

Between 1986 and 1988, several projects were undertaken for the Washington Metropolitan Area Transit Authority (WMATA) using EPB shields. Leca (1989) and Clough and Leca (1993) reported the contracts known as F3 and F4 that were located on the southeast extension of Washington Metro, at the crossing of the Anacostia River and the Navy yard (Figure 4.1). Subsurface conditions for the F3 and F4 tunnels were variable and complex, and the water table was consistently located above the tunnel crown. The soil at the sites was layered, consisting of soft organic clays, stiff clays, and uncemented sands (Figure 4.2). In some areas, the tunnels were excavated exclusively in one of the layers, but often the face of the tunnel encountered two and more layers. Particularly challenging conditions arose where the tunnel crown was in the sands, and the invert in stiff clays.

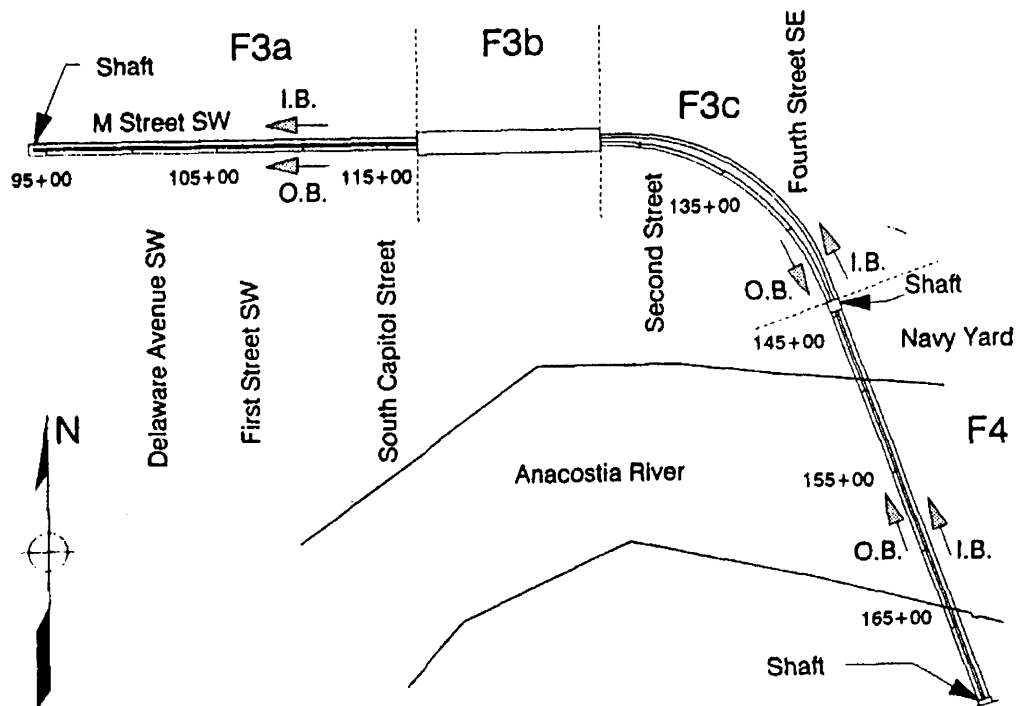


Figure 4.1 Plan view of tunneling project (after Clough and Leca, 1993)

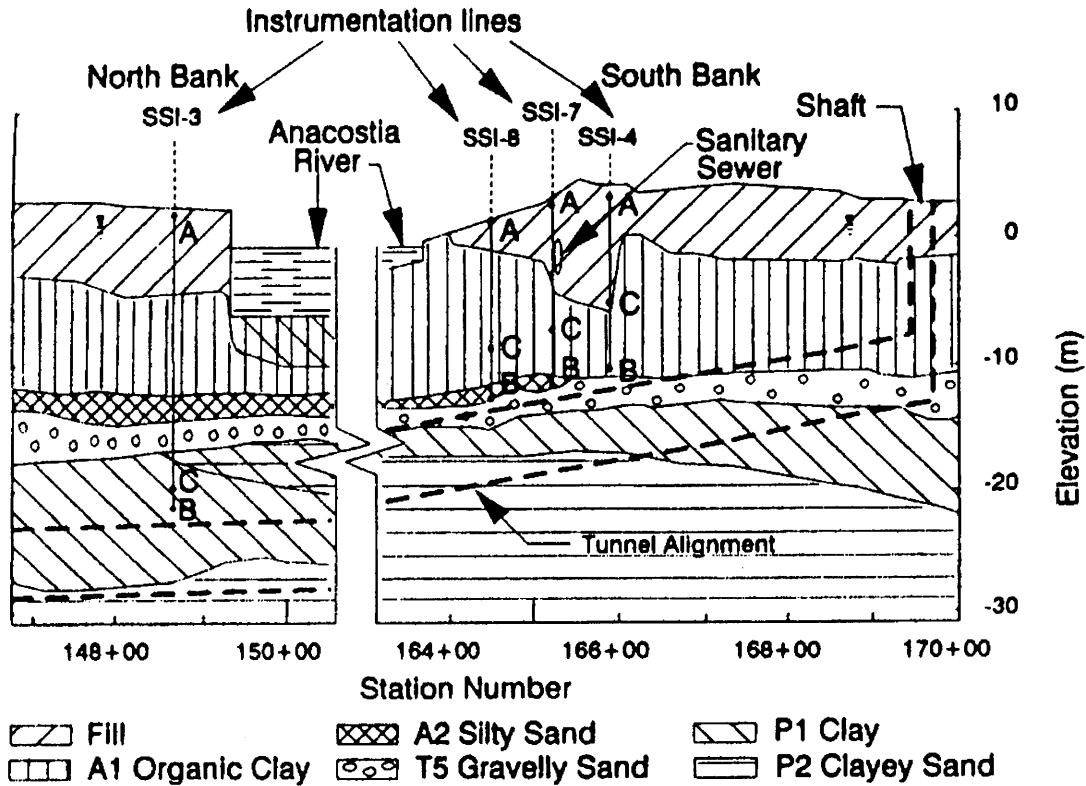


Figure 4.2 Soil profile on F4 project (after Clough and Leca, 1993)

Table 4-1 Average engineering properties of soils on F3 and F4 projects

Soil Layer	Soil Type	Soil Classification	γ (kN/m ³)	w (%)	LL	PI	D_r (%)	S_u (kPa)
F	Fill		20	-	-	-	-	-
A1	Organic Clay	OH	15.7	69	82	43	-	24-53
T1(A)	Silty Clay	CL	-	-	-	-	-	120-168
T1(F)	Silty Clay	CL	-	-	-	-	-	29-38
T5	Gravelly Sand	GP-GM	18.8	25	-	-	50	-
P1	Clay	CH	20.3	22	-	-	-	144-335
P2	Clayey Sand	SM-SC	18.6-19.3	21	-	-	50-70	-

The F4, F3a, and F3c projects (i.e. excluding F3b) were 1.7 km long and consisted of twin circular tunnels of 5.74 m diameter. A soil profile along the F4 project is shown in Figure 4.2. It is typical of the conditions found in the F3 and F4 sites, and it is characterized by layered soils with a water table located at a depth of 1 m. The tunnel depths ranged between 13 and 29 m. The letters: A, B, and C shown in the figure represent locations of monitoring levels of extensometers. Four typical soil layers were identified on the project as described in Table 4-1.

Two EPB shields were used to excavate tunnels in the F3 and F4 projects: a Hitachi shield (Japanese Manufacturer) for contract F4 and F3a, and a Lovat shield (Canadian Manufacturer) for F3c. The Hitachi machine (Figure 4.3) was a refurbished machine and 7.23 m long. The spoil was removed from the chamber by a ribbon screw conveyor, which was designed to allow boulders up to 60 cm in diameter to be passed and evacuated. The pressure in the chamber was controlled by the opening width of the discharge gate and the rotation speed of the screw conveyor as shown in Figure 4.3. The Lovat machine (Figure 4.4) was 6.31 m long. In this shield, the confining pressure at the face and mucking operation were controlled by a muck ring. The muck ring consists of a circular chamber behind the cutting wheel, where the excavated ground is confined and squeezed through two discharge gates. The opening of gates can be adjusted to control the rate of muck discharge and the confining pressure applied at the face. The theoretical tail void is 156 mm for the Hitachi machine and 127 mm for the Lovat machine.

Instrumentation of the projects included subsurface and surface settlement markers. In addition, shield operation factors such as muck counts (spoil volume), thrust pressures, and support pressures were recorded after each excavation cycle for each lining ring. The ground movements observed in the project are shown in Figure 4.5 to Figure 4.8. As reported in all cases, the settlement started about one diameter (5.74 m) in front of the shield face and became almost constant one diameter behind the tail. Clough and Leca (1993) suggested that there were two major sources of settlement: (1) face intake and (2) tail void closure. They observed that the large amount of face intake was related to the presence of the sand layer at the tunnel crown in the SSI-4, SSI-7, and SSI-8 sections as

can be seen in Figure 4.5 to Figure 4.7, respectively. This was in contrast to the SSI-3 section (Figure 4.8) where the tunnel was entirely in a clay layer and the measured ground movement in front of the shield was much smaller. In addition, Clough and Leca (1993) pointed out that large face intakes were caused by the shield that was operated at low face pressures.

However, if one takes a detailed look at the settlement curve in Figure 4.5, it can be observed that the settlement curve continues to develop significantly over the shield body during the shield advance. This indicates that there is a mechanism affecting the settlement over the shield body. Categorizing major sources of the settlement into two regions namely, the settlement ahead of the shield as face intake and the settlement after shield passing as tail void closure is not appropriate since the settlement over the shield body is also important. Instead, the total settlement should be divided into 3 main zones namely, (1) in front of the shield; (2) over the shield body; and (3) after shield passing.

To show how much of the settlements occurred in each zone, they are plotted as shown in Figure 4.9 to Figure 4.12. The figures indicate that the extent of the settlements measured at the ground surface in each zone vary section-by-section. In the SSI-4 section (Figure 4.9) where the crown of the tunnel is largely located in gravelly sand (see also Figure 4.2), all zones indicated the same portion of the settlements which, by the way, are greater than at the other measurement sections. In section SSI-7, the settlement after shield passing dominates the overall settlement (Figure 4.10). On the other hand, the settlement in front of the shield is smallest in section SSI-3 (Figure 4.12) while the settlement over the shield represents the major settlement portion in SSI-8 (Figure 4.11).

Evidently, the extent of the settlement occurring in each zone is affected by a combination of many factors such as ground conditions (i.e. type of soil, and ground water level) and shield operational parameters (i.e. face pressure, penetration rate, grouting quality), which typically vary section-by-section during excavation.

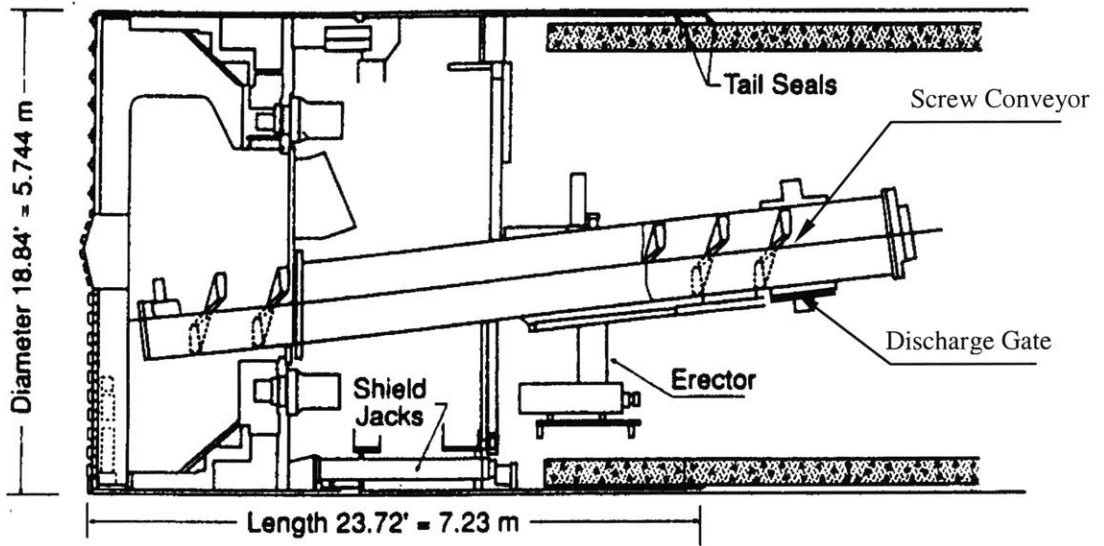


Figure 4.3 Hitachi machine used on F3a and F4 projects (after Leca, 1989)

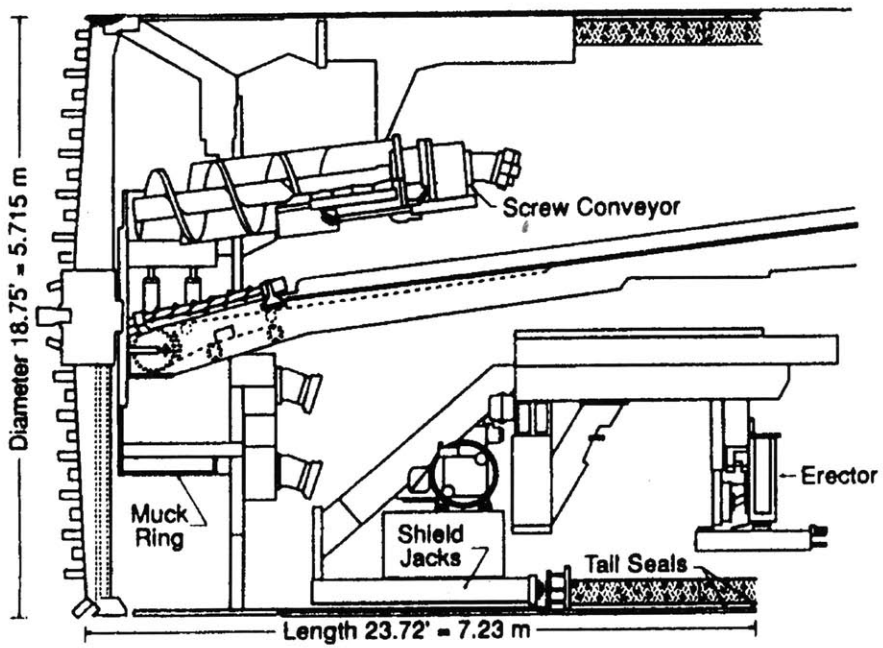


Figure 4.4 Lovat machine used on F3c project (after Leca, 1989)

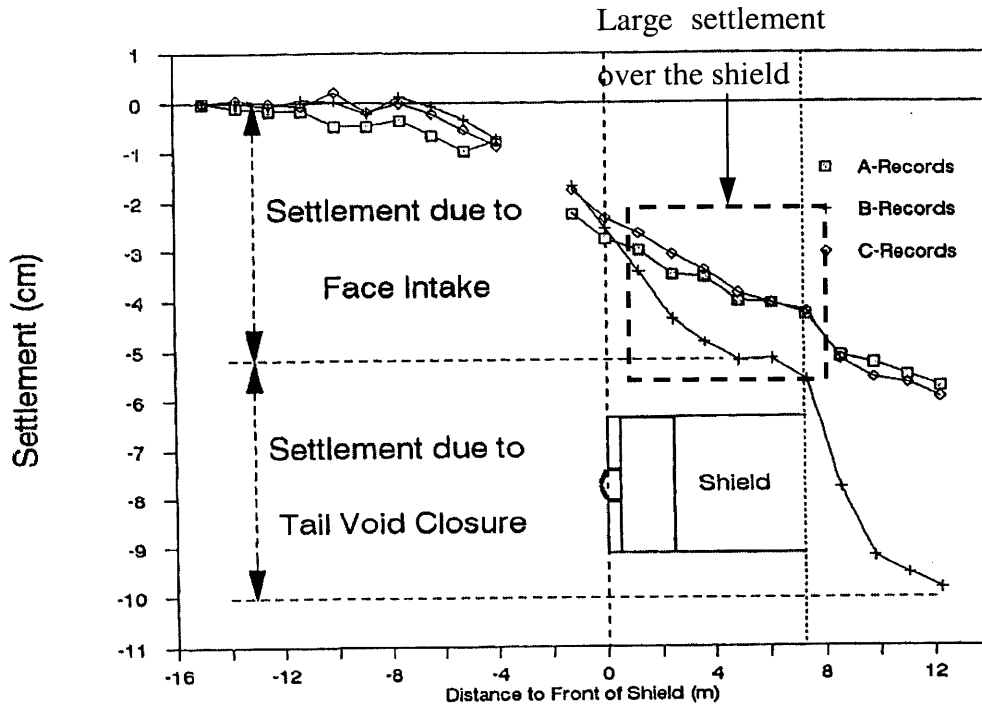


Figure 4.5 Surface settlement vs. shield position at SSI-4

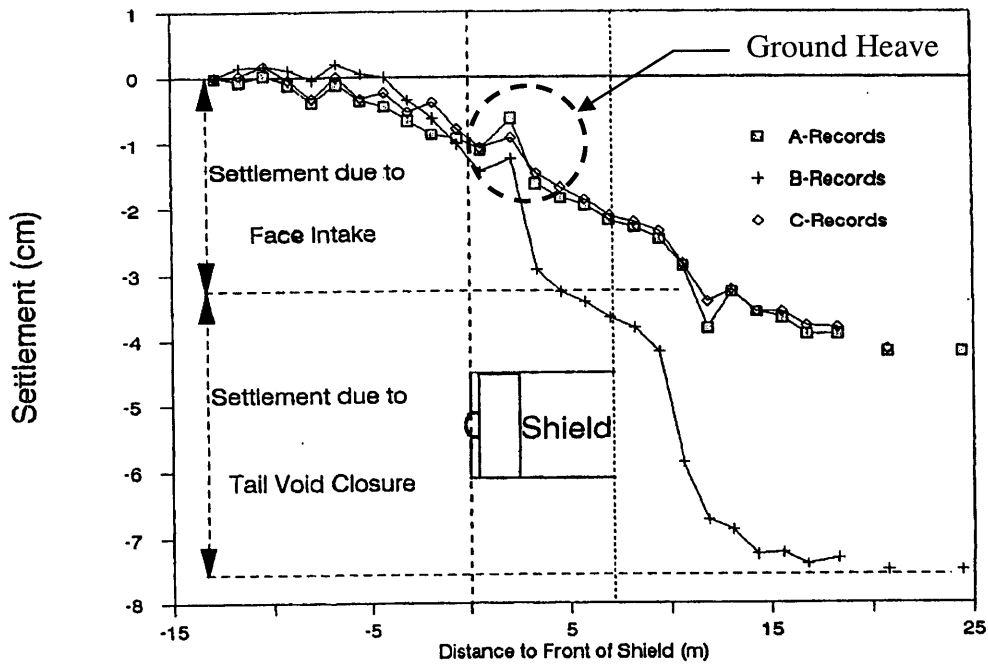


Figure 4.6 Surface settlement vs. shield position at SSI-7

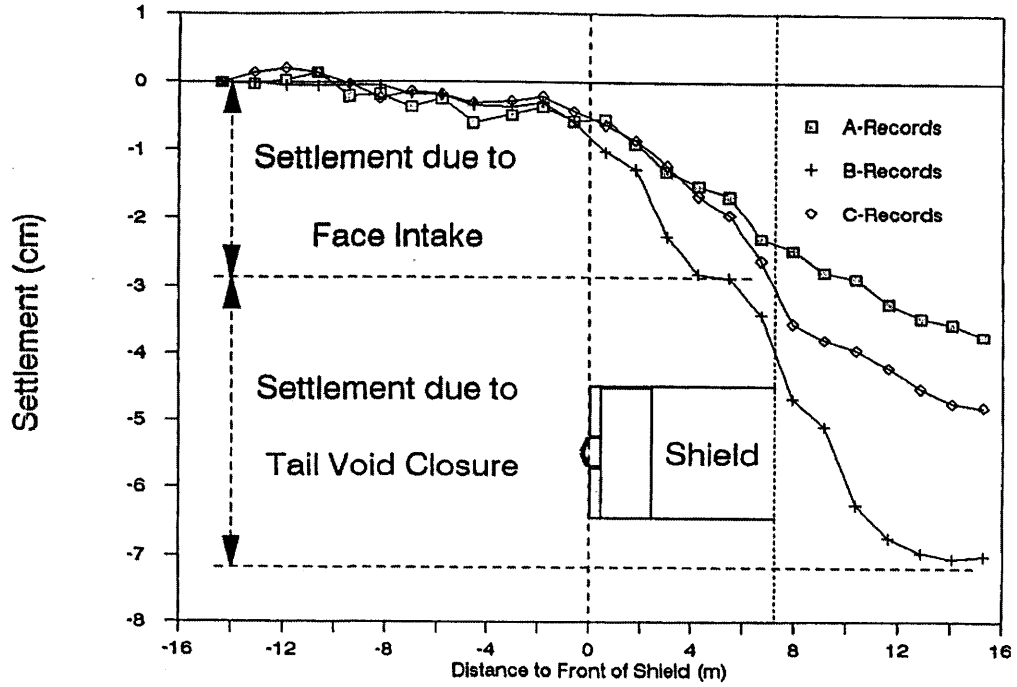


Figure 4.7 Surface settlement vs. shield position at SSI-8

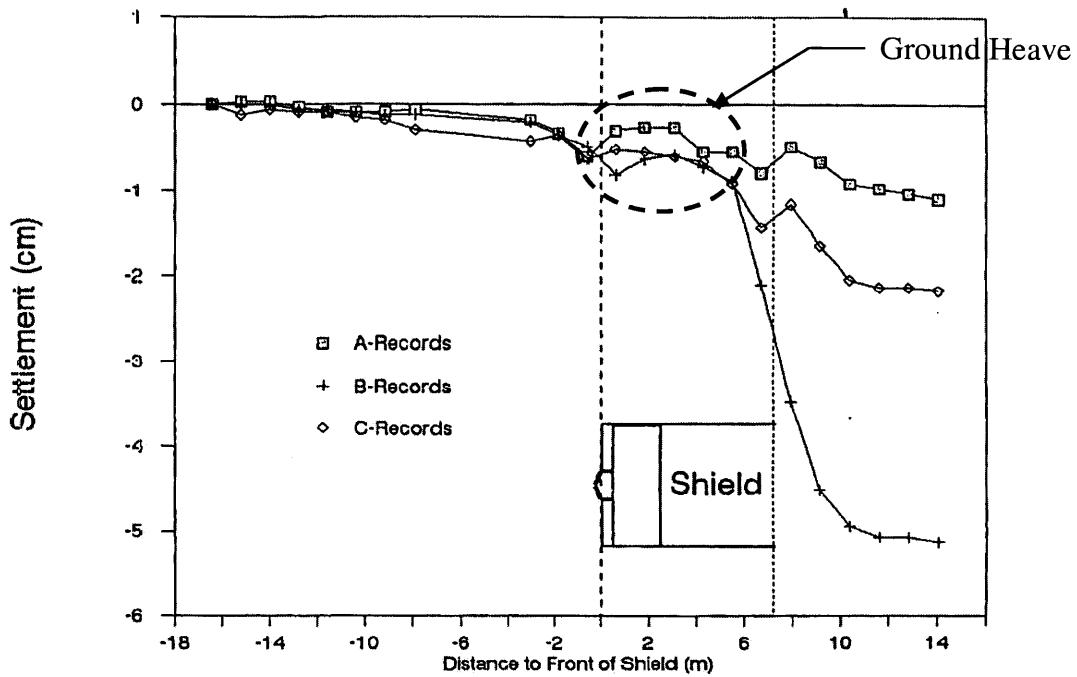


Figure 4.8 Surface settlement vs. shield position at SSI-3

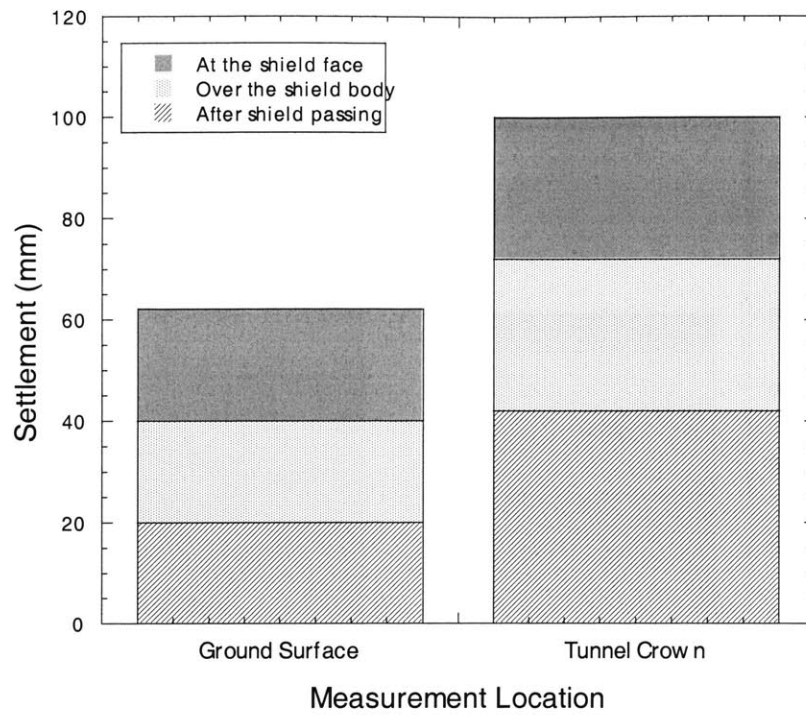


Figure 4.9 Settlements at different zones measured at SSI-4

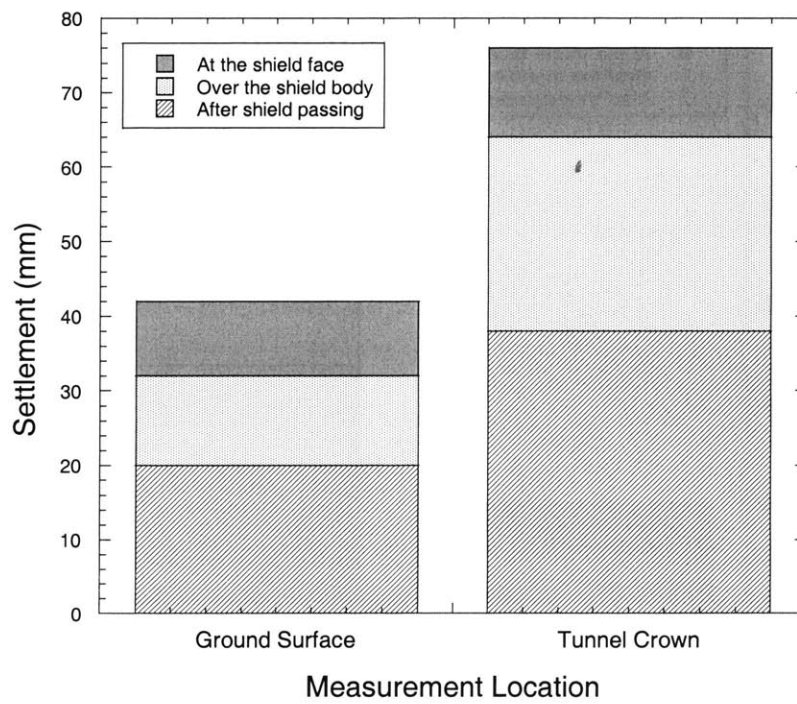


Figure 4.10 Settlements at different zones measured at SSI-7

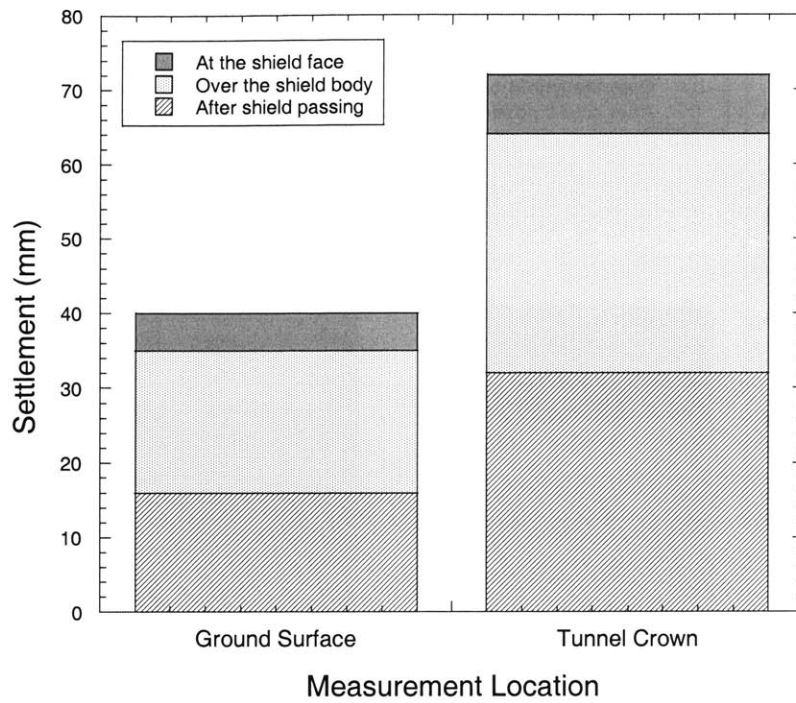


Figure 4.11 Settlements at different zones measured at SSI-8

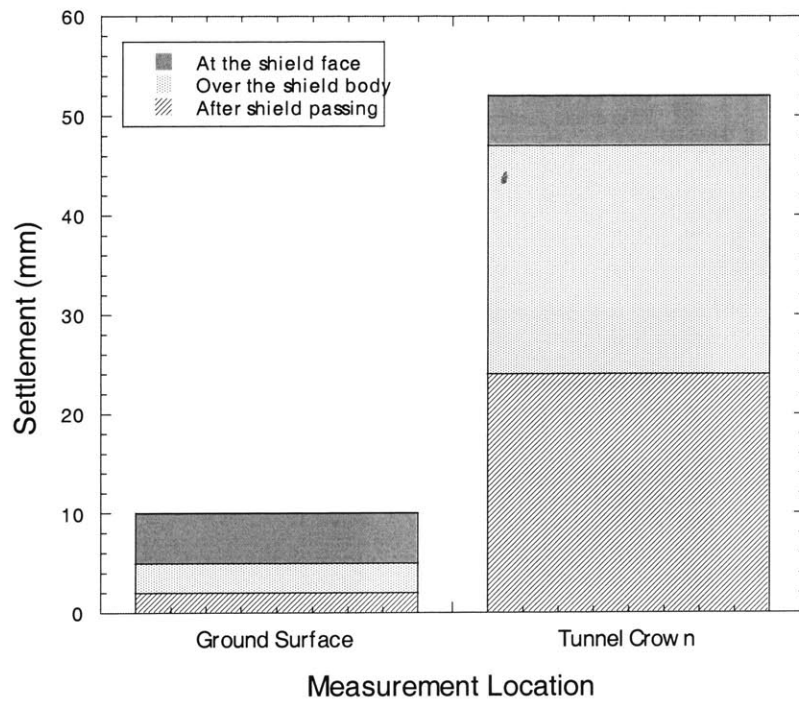


Figure 4.12 Settlements at different zones measured at SSI-3

Soil type appears to have a significant effect on the magnitude and the pattern of surface settlements. For example, the section where the tunnel encountered sand or gravel layers, measured surface settlements are much larger than in the section where the tunnel was excavated entirely in the clay layer. Additionally, the settlement ahead of the shield also becomes a major portion of the whole settlement. This is in agreement with Leca (1989) who found that severe problems with ground movement occurred each time mixed ground conditions were encountered, i.e., where a hard clay material existed in the lower part of the face and a sand layer was found at the tunnel crown. As a result, the EPB shields were unable to properly control ground movements. Furthermore, the presence of hard ground caused the machine progress to slow down, and allowed large amounts of running sands in the crown to move into the machine.

Grouting quality also plays a vital role for controlling ground movements after shield passing. The settlements measured after shield passing are relatively constant at the crown (i.e. 25-40 mm) regardless of soil type and tunnel depth. This probably is a result of tail void grouting that proves to be efficient in limiting the ground movement towards the gap.

As can be seen in settlement monitoring diagrams (Figure 4.5 to Figure 4.8), in some cases, small relative ground heave was observed over the shield as shown in Figure 4.6 and Figure 4.8. The heaves are possibly affected by the shield position or pitching angle during the excavation as will be discussed later.

4.3 Taipei Rapid Transit Systems (TRTS)

Dietz (1994), Moh et al. (1996), and Ju. et al. (1999) reported on the excavation of the initial network of the Taipei Rapid Transit Systems (TRTS), which consists of six lines namely, the Mucha, Tamshui, Hsintien, Nankang, Panchiao, and Chungho lines, with a total of 79 stations and total length of 86.8 km as shown in Figure 4.13. The project included 21 km of bored tunnels for which EPB shields with an outer diameter of 6.05

meter were used. The typical subsurface condition of the project was a thick layer of alluvium, the so called “Sungshan Formation,” which consisted of silty sand (SM) and silty clay (CL) as illustrated in Figure 4.14.

In Contract 201A of the Tamshuei Line (Dietz, 1994), where the site lies close to the main railway station in the town center (see also Figure 4.13), EPB shields manufactured by Herrenknecht (Figure 4.15) were used. The shields have all the standard equipment as described in Chapter 2. Specifically, the steel shield skin has an external diameter of 6.09 m and a length of 5.47 m, including the tail. The face pressure is monitored by pressure cells installed in the earth chamber. Caused by many factors including the learning curve of the tunnel crew, the initial drive of the shield was very slow namely, less than 5 m per day. Large settlements were also found in this initial drive. After the shield excavated 50 m of the tunnel, the back-up systems were installed behind the shield; from this moment on, the shield significantly increased its performance while settlement was minimized. Operating with two shifts, the advance rate increased up to a maximum of 16 m per working day. Evidently, the distance of the shield from the launching station appears to be an indirect factor influencing surface settlements as it represents the learning curve since the tunnel crews gain experience as the shield excavates for some distance leading to the better performance. Ju et al. (1999) also reported that in the same section (Contract 201A) there were a few major collapses on the ground surface, which occurred either during launching of the shield from a shaft or during arrival (breakthrough) of the shield into the shaft. Although ground treatment was routinely carried out as depicted in Figure 4.16, substantial settlements were typically measured in such locations. Additionally, in a very permeable layer where the ground water level was located above the tunnel invert, water leakage towards the tunnel became a critical problem during tunneling.

In the TRTS project, the tunnel was excavated mostly in a silty clay layer as shown in Figure 4.14. Based on the tunneling records, the typical face pressure measured in the front chamber was maintained between 180 and 200 kPa which is very high relative to the tunnel depth. Moh et al. (1996) reported typical ground deformations (on a semi-log

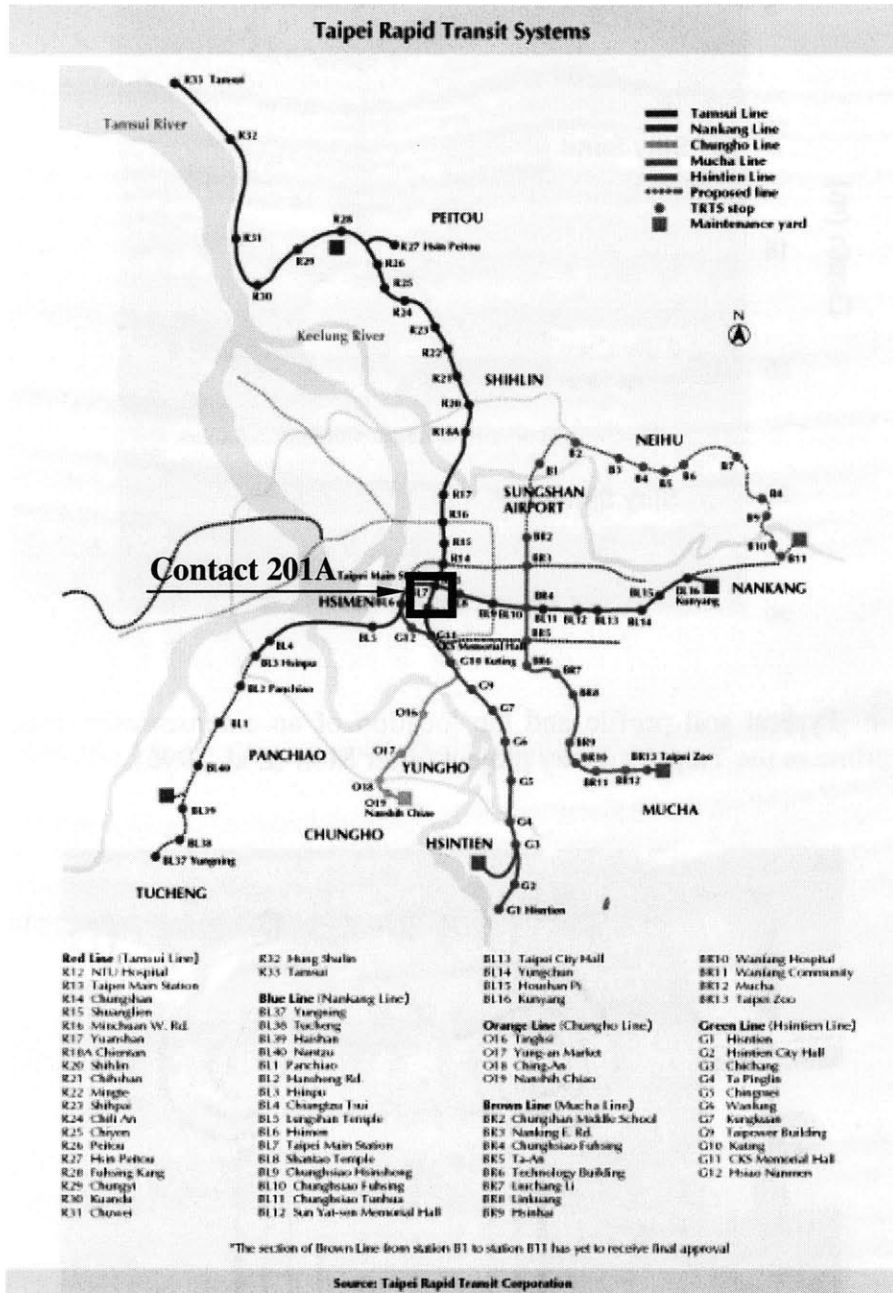


Figure 4.13 Initial network of Taipei Rapid Transit System

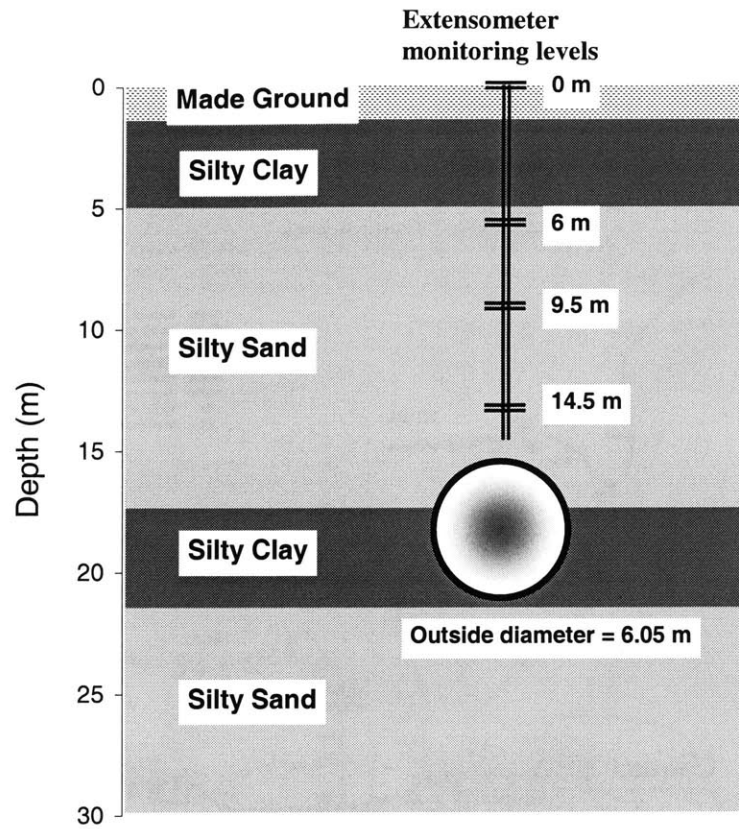


Figure 4.14 Typical soil profile and the location of an extensometer installed above tunnel centerline in the Taipei subway project (after Moh et. al, 1996)

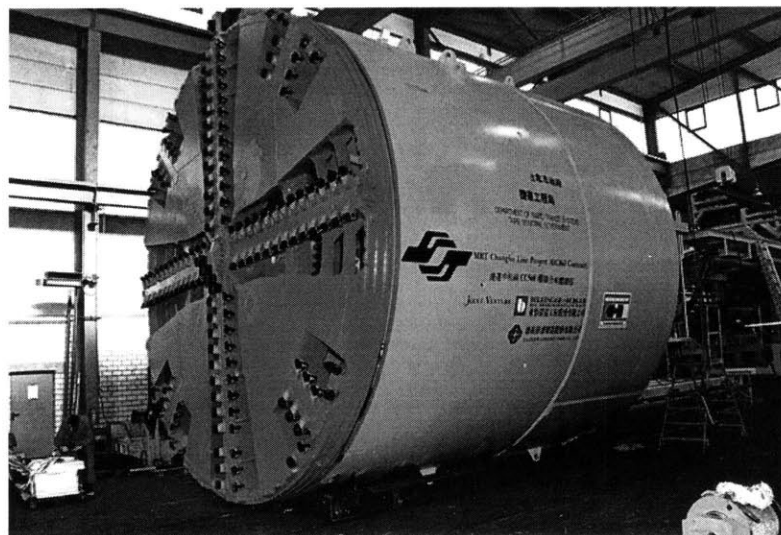


Figure 4.15 The Herrenknecht EPB shield with 6.09 m diameter used in the TRTS project

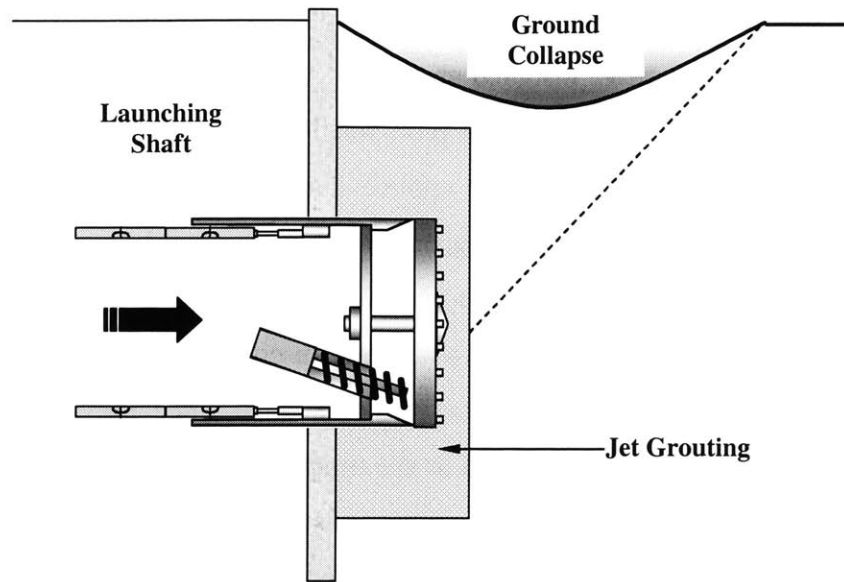


Figure 4.16 Ground collapse during launching of the shield

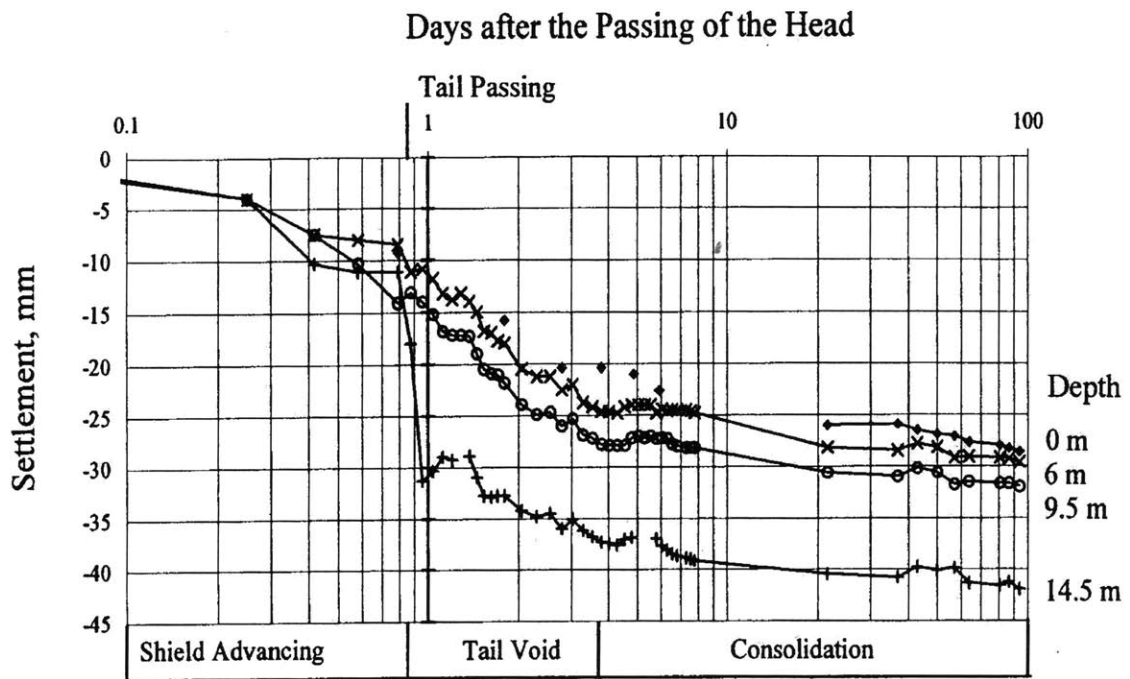


Figure 4.17 Ground deformation above tunnel in Taipei (after Moh et al, 1996)

scale) above the tunnel as shown in Figure 4.17. The ground deformations were measured from an extensometer installed above the tunnel centerline as shown in Figure 4.14. As can be seen in the deformation plot, relative large settlements still occurred, although high supporting pressures were applied during excavation. This suggests that maintaining high face pressure does not guarantee that the shield operators can achieve small settlements. Moh et al. (1996) also pointed out that the largest portion of ground settlements occurred after shield passing and was caused by tail void closure (but very few settlement data were obtained in this project). Also since the settlement curves provided by Moh et al. (1996) are plotted in the time scale not in the distance scale (i.e. position of the shield relative to the measurement section), it is impossible to distinguish the settlement occurring in each zone precisely. Hence, one still cannot verify that the largest part of the settlement only took place after shield passing.

4.4 San Francisco Clean Water Project

Clough et al. (1982), Finno (1983), and Finno and Clough (1985) reported on the tunnel project, known as the N-2 contract, which is located on the northeastern portion of the San Francisco Peninsula several blocks from the waterfront and San Francisco Bay (Figure 4.18). The project was the first tunnel excavated using an EPB shield in the U.S. The shield had a diameter of 3.7 m and was used to drive the 915 m long tunnel. Clough et al. (1982) reported that the tunneling project was a challenge because, in addition to the existing structures, which were not to be disrupted: (1) there was an average of only 9.1 m of cover; (2) the tunnel section was in a soft layer of sediments overlain by a rubble fill of indeterminate quality; (3) the ground water table was about 4.6 above the crown; (4) numerous wooden piles, some abandoned and some still supporting active sewers, passed through the tunneling section; and (5) a high pressure water line, which remained active, was located near the surface only 1.5 m off the tunnel center line.

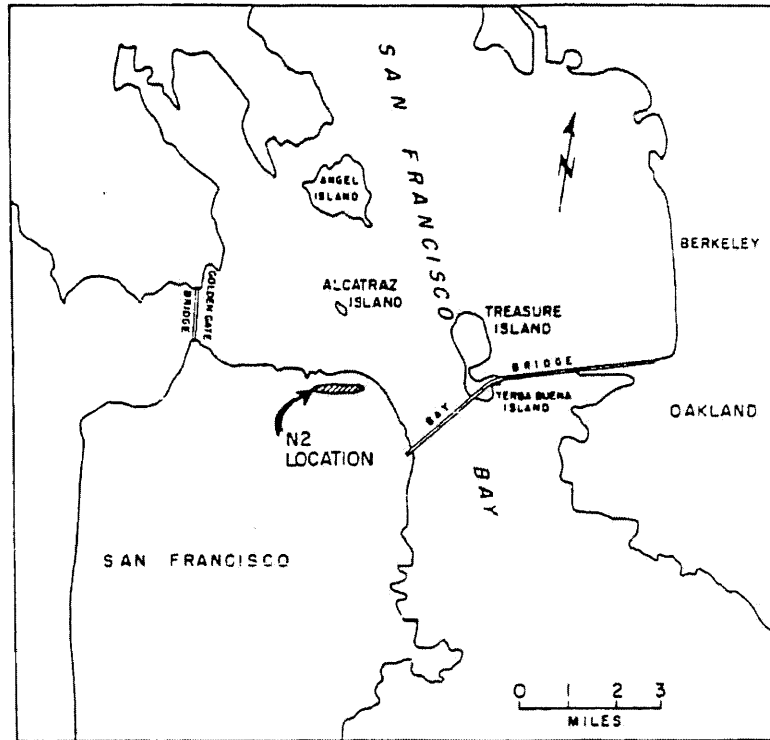


Figure 4.18 The location of the San Francisco Clean Water Project (N-2 project)

Figure 4.19 shows the subsurface conditions of the N-2 project. The major portion of the profile consists of an average of 6.1 m of rubble fill underlain by 9.1 m of soft sediment, known locally as the Bay Mud. A stratum of colluvial and residual sandy clay is found below the Bay Mud. The tunnel was excavated entirely within the Recent Bay Mud except near the western terminus, where the tunnel invert encountered the clayey sand layer. The overlying fill consists of randomly dumped rock fragment, dune sand, Bay sediment, and rubbish. The Bay Mud along the tunnel alignment is made up of silt and lean clay with some beds of fine sand. The clay is normally consolidated except near the top of the stratum where it has been lightly overconsolidated by desiccation. The data from unconsolidated-undrained (UU) triaxial tests suggest that the undrained shear strength of the Recent Bay Mud is about 24.3 kPa just below the fill and increases approximately at 0.63 kPa/m with depth.

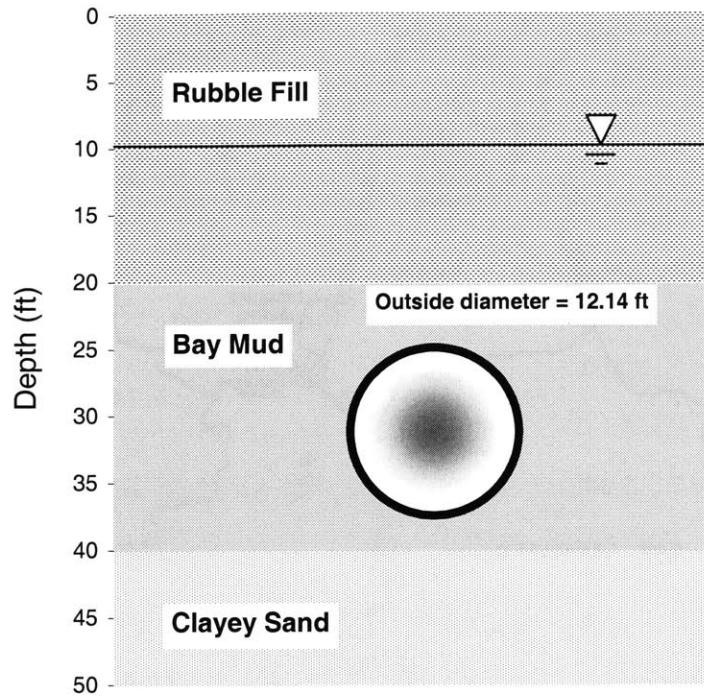


Figure 4.19 Subsurface condition of the N-2 project

The EPB shield (Figure 4.20), designed for the N-2 project, was manufactured by Mitsubishi (Japanese Manufacturer). The shield has an outside diameter of 3.7 m and is 5 m long. Its major components are the rotating cutterhead, spoil chamber immediately behind the cutterhead, screw conveyor, hydraulic jacks, liner erector arm, and tail seals. The earth pressure balancing process was controlled by the shield operator. The operator monitored the excavation process using a series of gages, which provide information as to cutter torque, thrust force, screw conveyor speed, and cutterhead rotation as previously discussed in Chapter 2. The condition of the muck in the chamber was tracked with readings of an earth pressure cell located on the bulkhead at the rear of the earth chamber as shown in Figure 4.20. For the N-2 project, Finno (1983) stated that it was common practice to operate the EPB shield so that the screw conveyor removed a volume of soil that was slightly less than that of the shield advance. The shield operator intended to produce an initial small heave of the soil to compensate the subsequent settlement due to tail void closure.

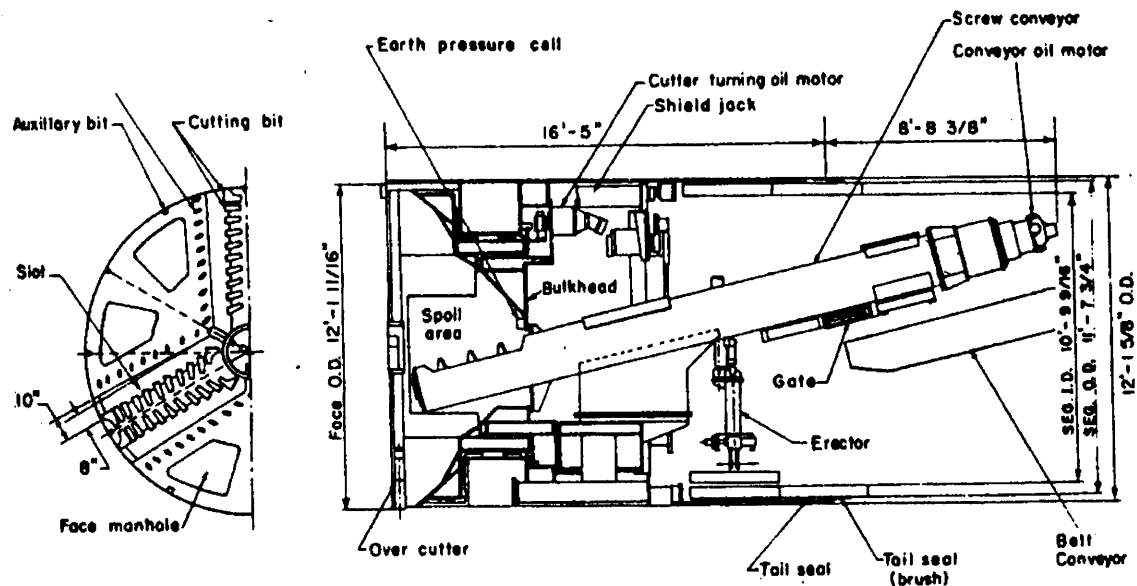


Figure 4.20 Section of the Mitsubishi Earth Pressure Balance Shield used in N-2 project

With a three-shift, five-day-a-week operation, the average rate of the shield progress for the entire job was 9.1 m per day (Clough et al., 1983). The maximum daily rate reached 30.3 m per day. During most of the tunneling, the shield was operated on a pitch of 0.5 percent above grade. However, in some sections, the pitch was temporarily increased to 1.3 percent above designed grade. Earth pressures measured by the earth pressure cells were relatively constant. In the N-2 project, the tail void was grouted using a sand, bentonite and water mix (Finno, 1983). Grout was injected into the tail void under pressures of 201-310.5 kPa (i.e. 2-3 bar) four to six rings behind the shield. In addition, no problems with ground water were encountered during the excavation although the tunnel crown was under the water table.

Clough et al. (1983) observed that the advance of the EPB shield at the N-2 site led to initial outward movements from the shield as shown in Figure 4.21. These movements were primarily lateral and were largely confined to the Bay Mud immediately to the side of and in front of the shield. Displacements increased rapidly as the shield approached the measurement section. This type of ground movement is in contrast to the conventional

open-faced shield where inward movements toward the shield face would be expected. The magnitude of the heave appears to correlate directly with the level of the earth pressure measured inside the earth chamber of the shield. Clough et al. (1983) also observed that the earth pressure increased where the shield encountered wooden piles, apparently due to partial clogging of the screw conveyor by pile fragments, which did not allow for an expeditious removal of the spoil.

Additionally, large or more variable (oscillating) settlements were measured in the early part of the EPB shield tunnel. This phenomenon has been also observed in many other shield tunneling projects such as the BART Subway Project (Kuesel, 1972), the Thunder Bay Tunnel Project (Ng, 1984), TRTS Project (Ju et al., 1999), and the Bangkok Subway Project (Maconochie and Suwansawat, 1999). It was suggested that the inexperience of tunnel crews at the early stages of excavation significantly contributed to the phenomenon.

The differences in the final lateral displacement response at the measurement sections appear to correlate relatively well with the measured earth pressure. Where the face pressures were high as shown in the Sections 3 and 4 (Table 4-2), initial outward heaves occurred which were large enough to exceed the subsequent previous inward movements. Note that the lateral movements were measured by inclinometers 15-30 days after shield passing. In the case of initial outward movement at the Sections 1 and 2 where the face pressures were low, the initial outward movements were small relative to the inward movement due to tail void closure so that the inclinometers recorded inward movement after shield passing. The high face pressure at the Sections 3 and 4 is apparently caused by cutting through old wooden pile. Clough et al. (1983) observed that the largest inward movement occurred at Section 2 and appears to be induced by the large tail void created there since the shield was pitched above its designed grade to the greatest extent at that location.

For the surface settlement, small vertical soil heaves occurred as the shield approached the instrumentation section as shown in Figure 4.22. After shield passing, the ground

began to settle and continued for about 40 days. A maximum settlement of 1.2 in. (30 mm) was reached at this time. Clough et al. (1983) suggested that the large downward movements which developed after shield passing were caused by tail void closure. However, in this case, consolidation due to soil disturbance might play an important role after shield passing, since the ground still continued to develop a significant settlement even more than 10 days after shield passing. Maximum surface settlements were measured at 150 locations along the tunnel alignment, and total earth pressure in the chamber was recorded for each advance or every excavation cycle (i.e. every 1 m of the drive). The values of earth pressure, recorded as the shield approached the location of each settlement point, are averaged and plotted versus the corresponding the maximum settlement at the point in Figure 4.23. The trend of the field data may indicate that lower earth pressures are generally associated with the higher settlement values. As the support pressure increases, the surface settlement decreases.

Finno (1983) concluded that the source of ground losses during tunneling can be associated with various phases of the construction sequence. Losses at the ground surface can be expressed as a sum of the ground losses associated with each of the zones: (1) into the face of the shield; (2) over the shield; (3) into the tail void; and (4) occurring over time after construction is completed. Finno (1983) also found that the consolidation settlement in this case appears to be a major source of the total settlement since excess pore water pressure was induced during shield passing and it took a long period of time to dissipate.

Table 4-2 Comparison between face pressure and lateral displacement

Section	Face Pressure (kPa)	Max. lateral displace. during shield passing (mm)	Max. lateral displace. after shield passing (mm)	Note
1	40	12.7	-10.16 (inward)	
2	40	15.24	-12.7 (inward)	High pitching angle
3	100	81.28	58.42 (outward)	Wooden pile fraction
4	80	71.12	30.48 (outward)	Wooden pile fraction

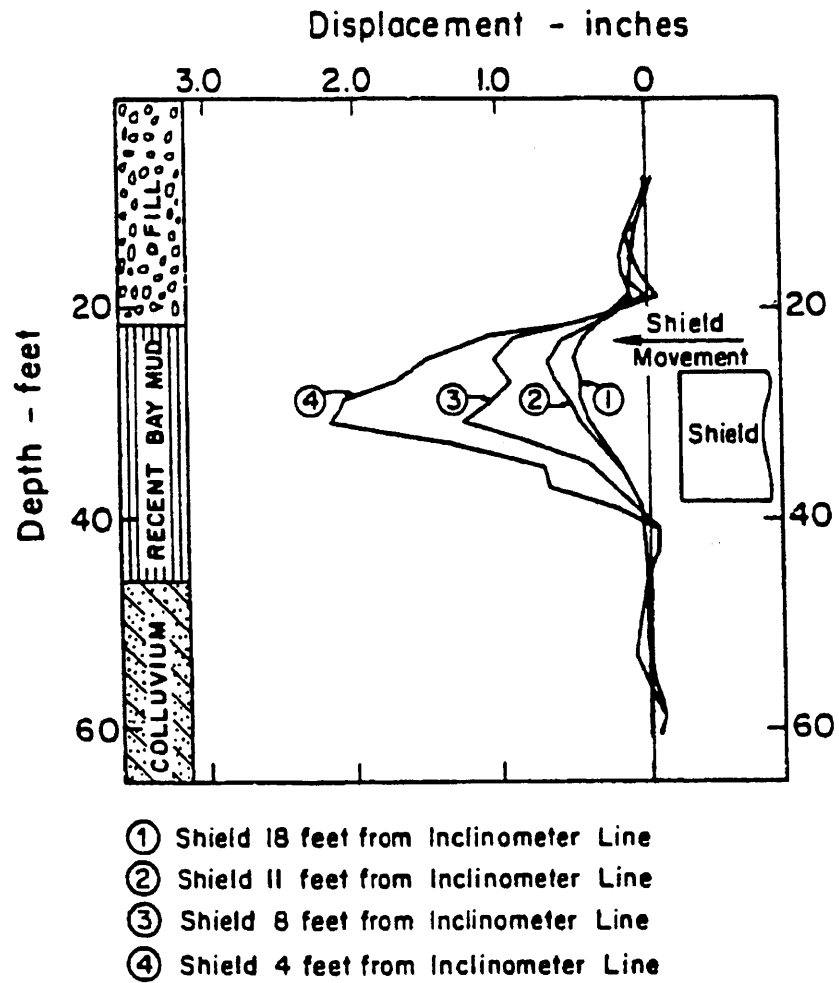


Figure 4.21 Lateral displacement in the front of advancing shield (after Clough et al. 1983)

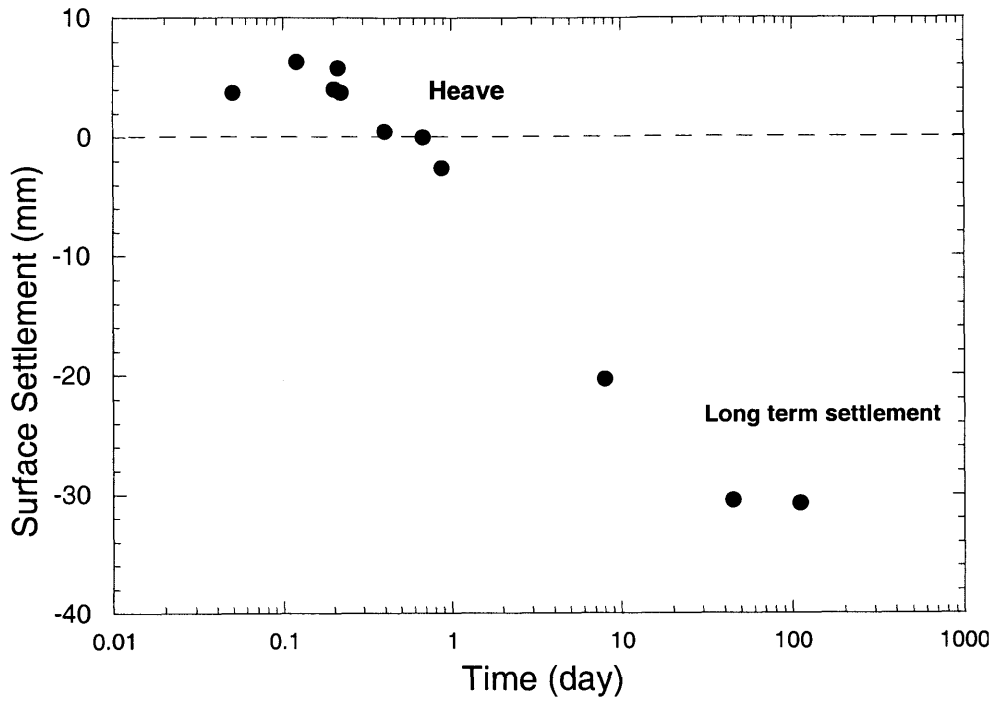


Figure 4.22 Surface settlement measured from N-2 tunnel project

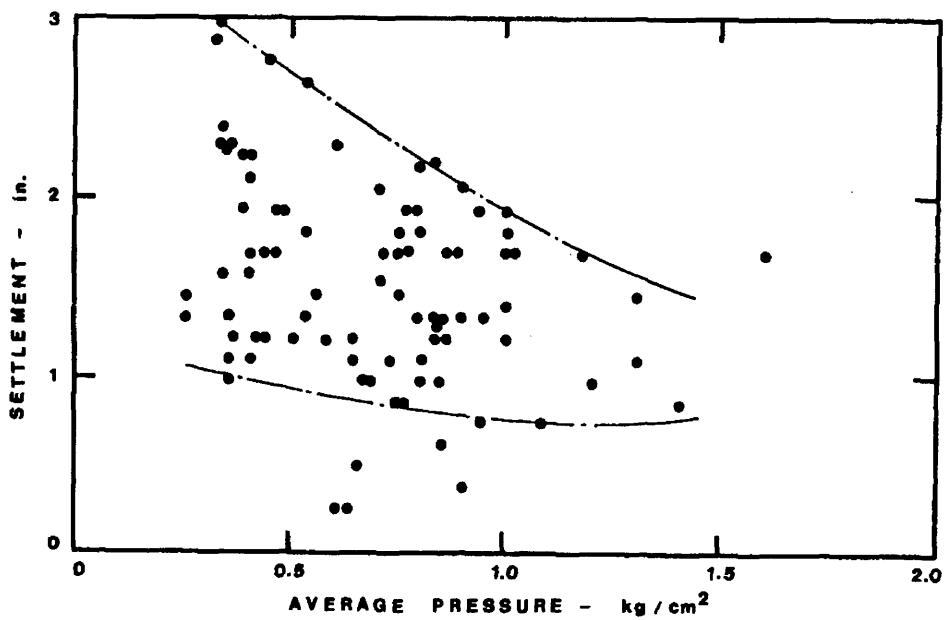


Figure 4.23 Surface settlement versus average earth pressure recorded at N-2 project (after Finno and Clough, 1985)

4.5 Fukuoka City Subway Project

Matsushita et al. (1995) reported the performance of a large slurry shield used in the tunneling of the subway underneath Fukuoka, Japan. The shield was a 10 m diameter slurry shield that excavated the tunnel at a depth of 8 m to 16 m. Most of the tunnel alignment was excavated within a decomposed granite soil layer overlain by Holocene and Pleistocene deposits that mainly consist of sands. The tunnel alignment and soil profile are shown in Figure 4.24. In this case, two sections were selected for monitoring the ground response induced by shield tunneling. The first section (No.1) was located close to the launching shaft where the tunnel was approximately 15 m from the surface. The second section was located at the point where the shield was driven up slope approaching the end of the tunnel (No. 2). From instrumentation readings, it was found that there are three zones of settlement. The first zone is a small ground settlement in front of the shield. The second zone is the settlement over the shield body and the final settlement zone occurred after shield passing. Specifically, the settlement began ahead of the shield and continued to develop as the shield approached the section.

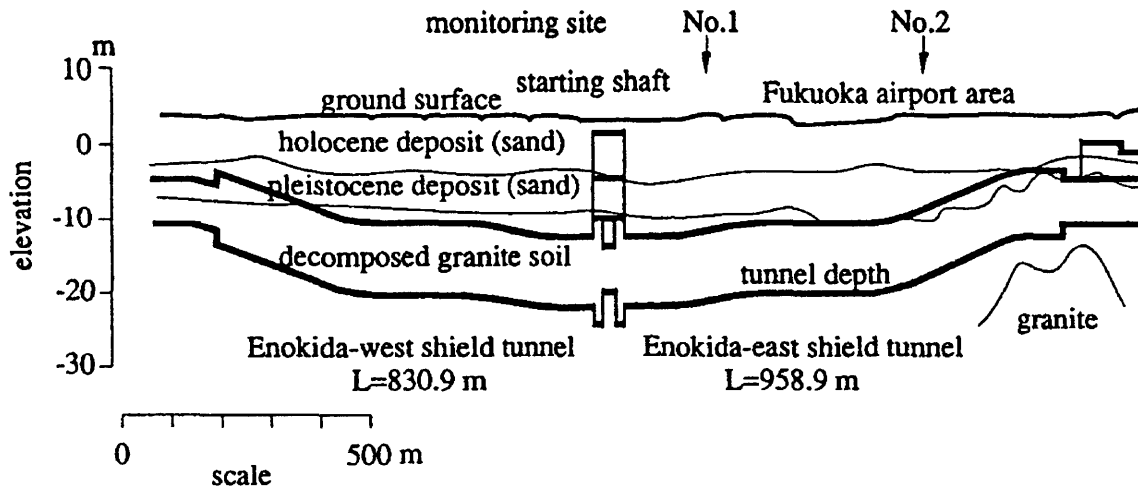


Figure 4.24 Tunnel alignment and soil profile of the Fukuoka subway (after Matsushita et al., 1995)

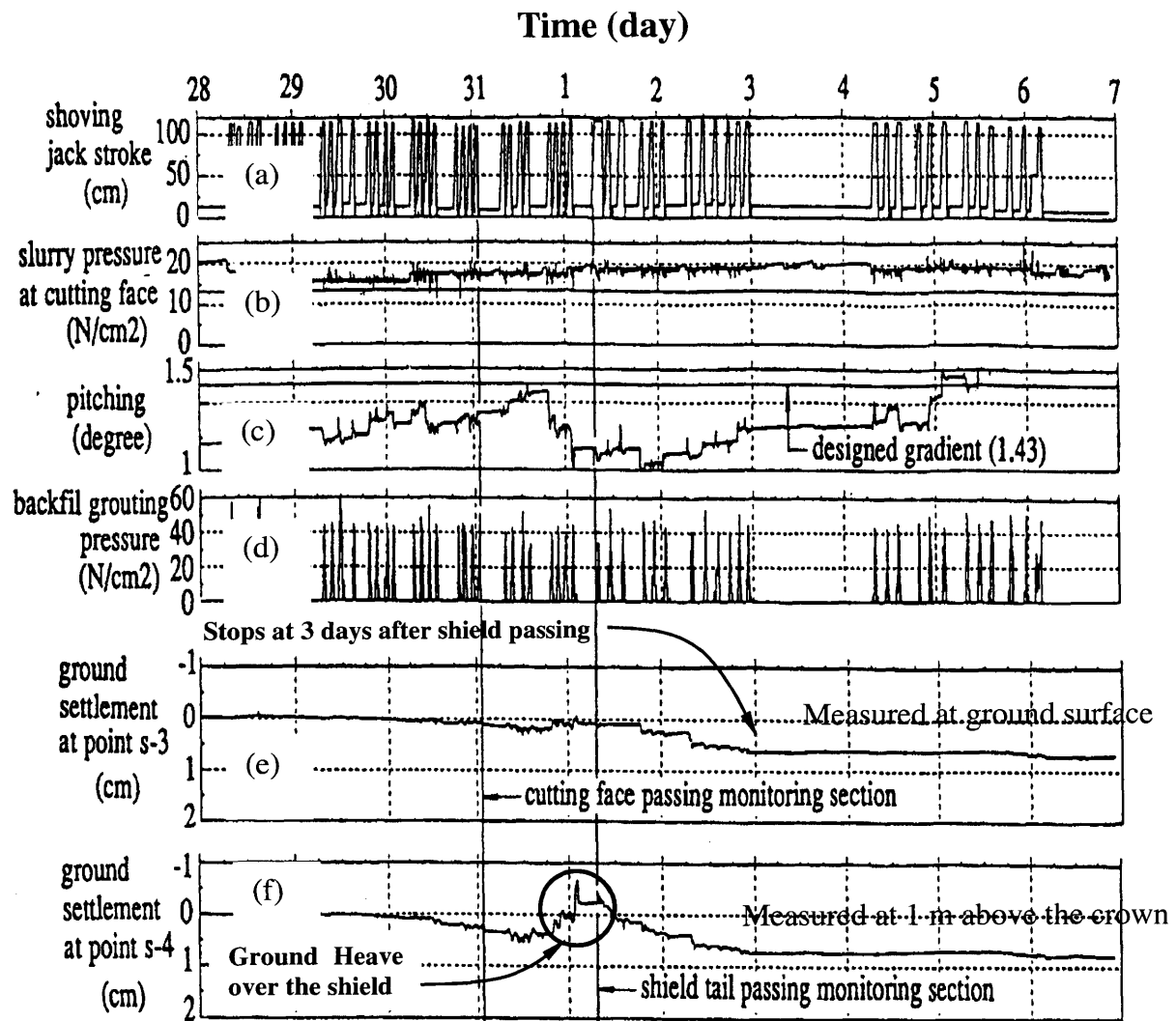


Figure 4.25 Observed ground settlement and operation record (after Matsushita et al., 1995)

In this project, shield operational factors such as slurry pressures, pitching angles and grouting pressures were also recorded during shield passing in Section No. 2 and compared with the ground settlement as shown in Figure 4.25. The records done by Matsushita et al. (1995) are very useful for determining what factor dominates the ground movement during each zone of the settlement. From the figure, the settlement prior to shield passing increased as the shield approached the section. Only 5 mm of the surface settlement was measured in the plane of the shield face (Figure 4.25e). Matsushita et al. (1995) suggested that slurry pressure applied to stabilize the tunnel face highly affected surface settlements. For example, it was found that the settlement, while the shield approached the measurement section, decreased in proportion to slurry pressure as shown in Figure 4.26.

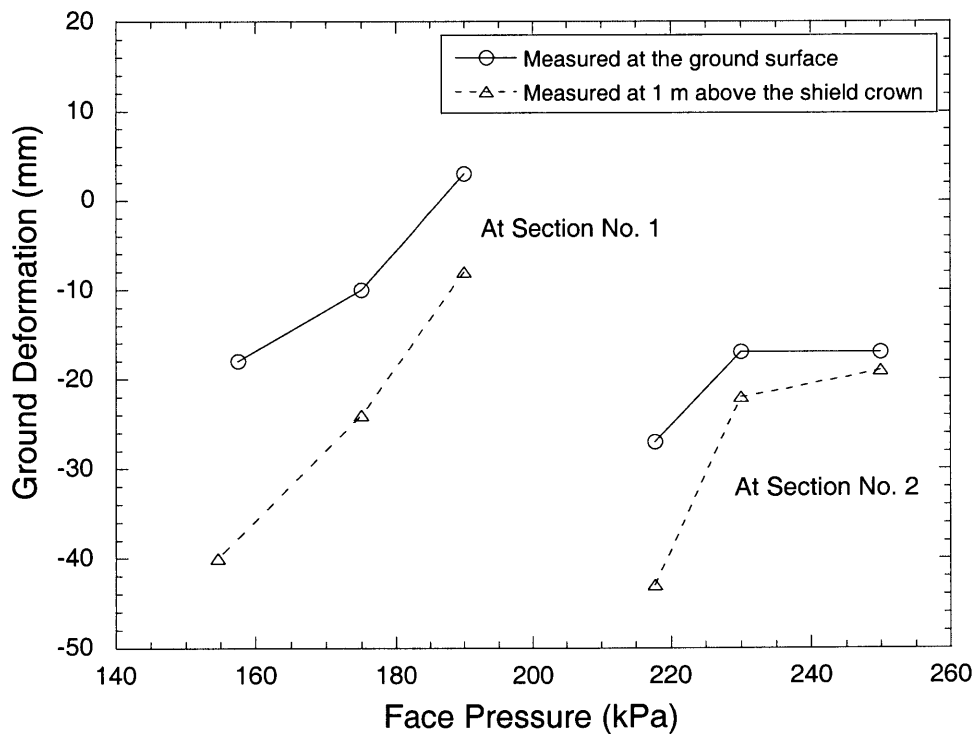


Figure 4.26 Slurry pressure versus settlement (after Matsushita et al., 1995)

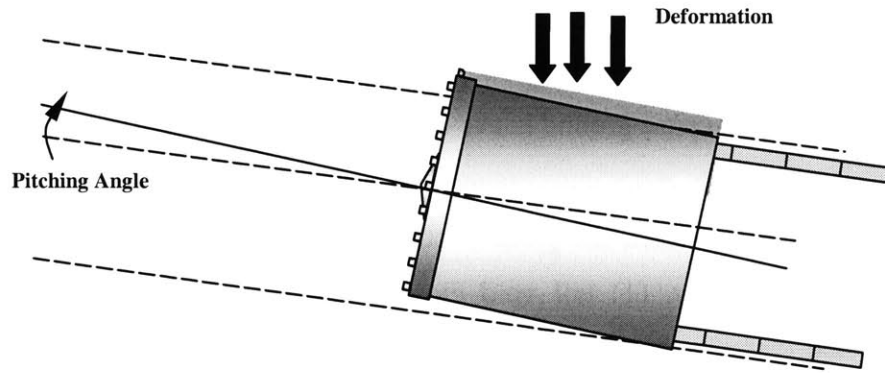


Figure 4.27 Pitching angle causing the ground deformation

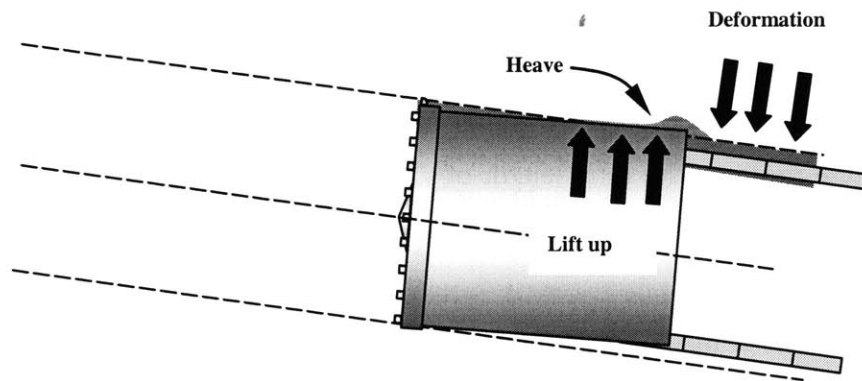


Figure 4.28 Temporary lifting causing the ground heave

Matsushita et al. (1995) also pointed out that the ground movement over the shield was caused by the position of the shield at the section and noticed that there are two types of the shield position related to the settlement: first, the inclination of the shield relative to longitudinal direction represented by pitching angle (Figure 4.27) and second, the temporary lifting of the shield tail caused by shoving jacks (Figure 4.28). As a result, the lift up of the shield can cause ground heave over the shield as shown in Figure 4.25f.

As observed from the project, the ground settlement after shield passing was caused by two main factors namely, (1) tail void closure and (2) ground disturbance (i.e. the surrounding soil disturbed by shoving the large diameter shield). The authors suggested that tail void grouting under a constant pressure substantially reduces the final zone of ground settlement. The ground settlement is less than 1 cm and it did not develop further after 3 days after shield passing as can be seen in Figure 4.25e and Figure 4.25f. This observation is also in agreement with the settlement pattern observed in the Washington Metropolitan Area Transit Authority Project (WMATA) as described earlier.

4.6 Milan Subway Project

Chiorboli and Marcheselli (1996) examined the performance of an EPB shield of 8.03 m in diameter for the excavation of the Milan subway project in Italy. Figure 4.29 shows the location of the project. The total length of the tunnel excavated by the EPB shield was close to 4 km and the overburden varied from 4 m to 16 m with an average of 8 m.

The Milan subsoil is made up of fluvioglacial sandy and gravely alluvial deposits with dense to very dense sand deposits and gravel. Since the project was located in an urban area, surface settlements induced by the EPB tunneling were a major concern. Hence, a large number of settlement markers were installed along the tunnel alignment and instrument readings were regularly checked twice a day when the shield was arriving and passing. Subsequently, the reading frequency decreased as the shield excavated the tunnel 200 m away from the instrumentation section since the ground deformation stopped to

develop further. In Figure 4.30, based on the data given by Chiorboli and Marcheselli (1996), operational factors of the shield including face pressure, penetration rate and tunnel depth were plotted against the surface settlement after shield passing. In this case, the face pressures are normalized by tunnel depth to give a meaningful parameter called “face pressure ratio” which can be defined as:

$$\text{Face Pressure Ratio (kPa/m)} = \frac{\text{Face Pressure (kPa)}}{\text{Tunnel Depth (m)}} \quad (4-1)$$



Figure 4.29 Milan Subway Project

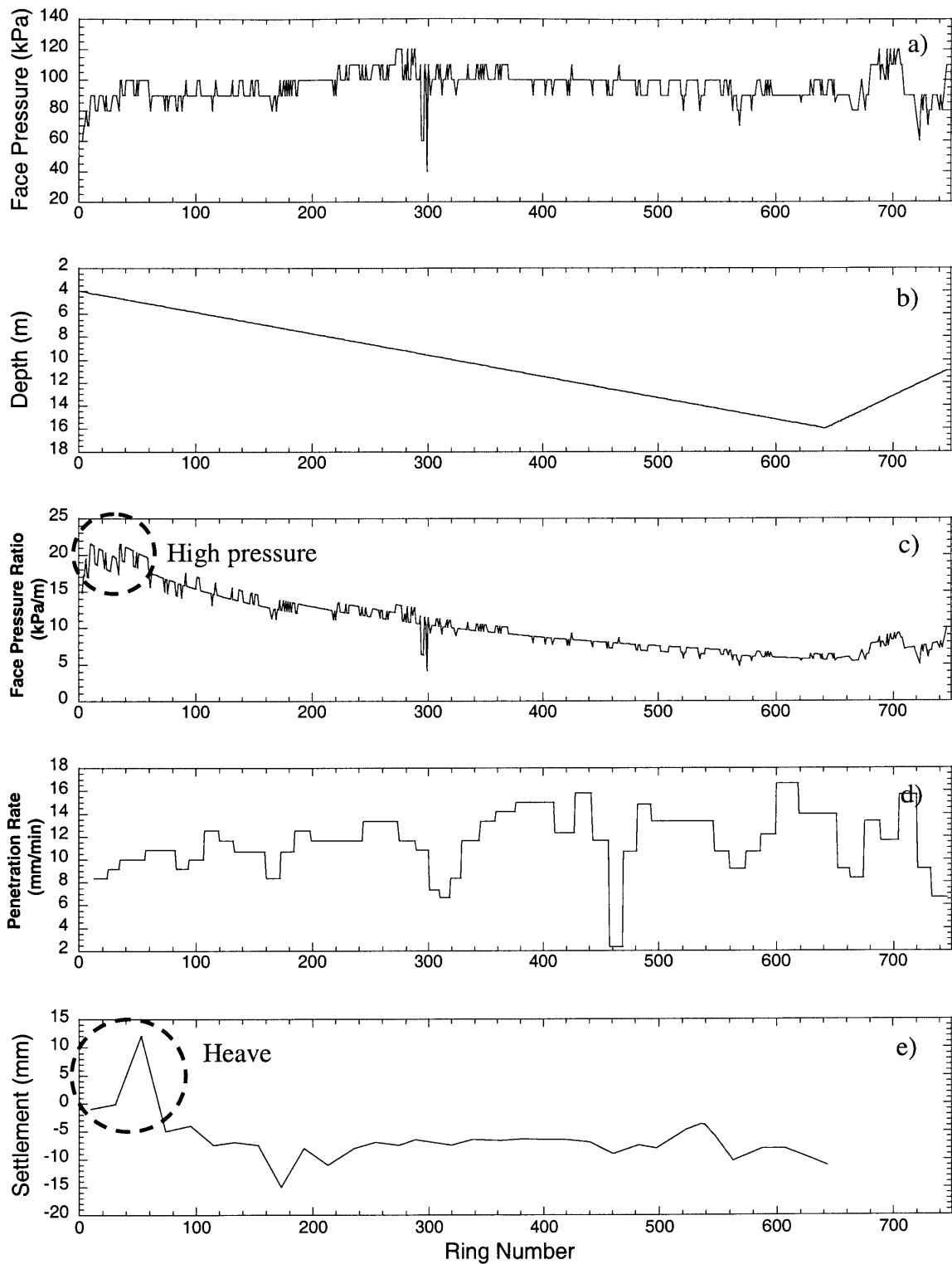


Figure 4.30 Operational factors and the surface settlement measured at the Passante Ferroviario of the Milan project (after Chiorboli and Marcheselli, 1996)

The face pressure ratio is a very useful parameter for comparing the face pressure to the settlement. For example, before the face pressures are normalized, the pressures appear to be constant at the entire tunnel alignment (Figure 4.30a). However, overburden pressures which are directly related to tunnel depths should be also taken into the account. After the face pressures were normalized by the tunnel depth, the face pressure ratio indicates a significant change of the face pressure along the tunnel alignment (Figure 4.30c). In the initial drive, the face pressure ratio was very high (i.e. up to 21 kPa/m at 5 m from the surface). As a result, the surface heave was observed as shown in Figure 4.30e.

Chiorboli and Marcheselli (1996) also suggested that the operational factors showed a clear effect on the settlement. For instance, they observed that if the face pressure is too small, large surface settlements would be observed. On the other hand, surface heave occurs when the pressure is too high. The authors also stated that the largest portion of the surface settlement appeared to occur in the plane of the shield face, which is associated with the low face pressure.

Penetration rate or advance rate is the another factor recorded during the excavation. The authors suggested that slow advancement or stopping the excavation can cause substantial settlement. To verify their observation, influencing factors, which are face pressure, penetration rate and tunnel depth are plotted against measured surface settlements as shown in Figure 4.31 through Figure 4.33.

As can be seen in Figure 4.31, at a high face pressure ratio (i.e. more than 19 kPa/m), the observed surface heave was as high as 12 mm, while at lower levels of the face pressure ratio (12-15 kPa/m), the settlements are between 5 mm and 15 mm. However, the relationship between the face pressure and the surface settlement is still not clear. Additionally, Chiorboli and Marcheselli (1996) observed that large settlements are subjected to low penetration rate of the shield. However, as can be seen in Figure 4.32, no clear relationship between the penetration rate applied during excavation and the surface settlement can be established statistically. Figure 4.33 also shows no correlation between the tunnel depth and the surface settlement.

Evidently, although the factors are considered to be major factors affecting the surface settlement, it is difficult to establish the relationships with the ground settlement. This is due to the impossibility to separate one effect from others since all factors influence the surface settlement at the same time. Therefore, a clear trend between a specific factor and the surface settlement cannot be found.

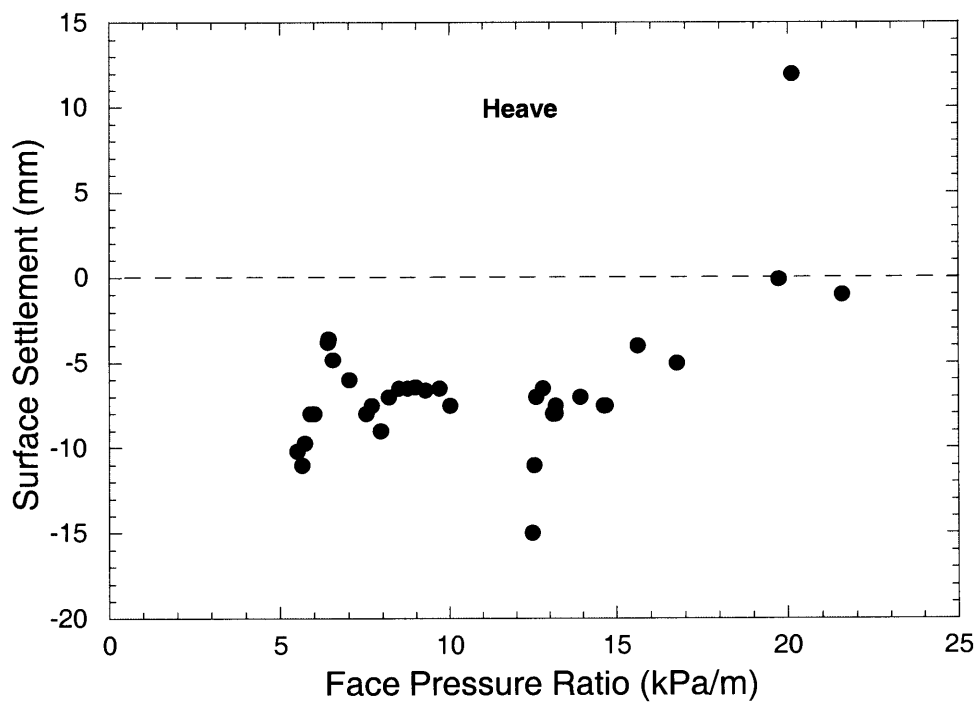


Figure 4.31 Face pressure ratio versus surface settlement

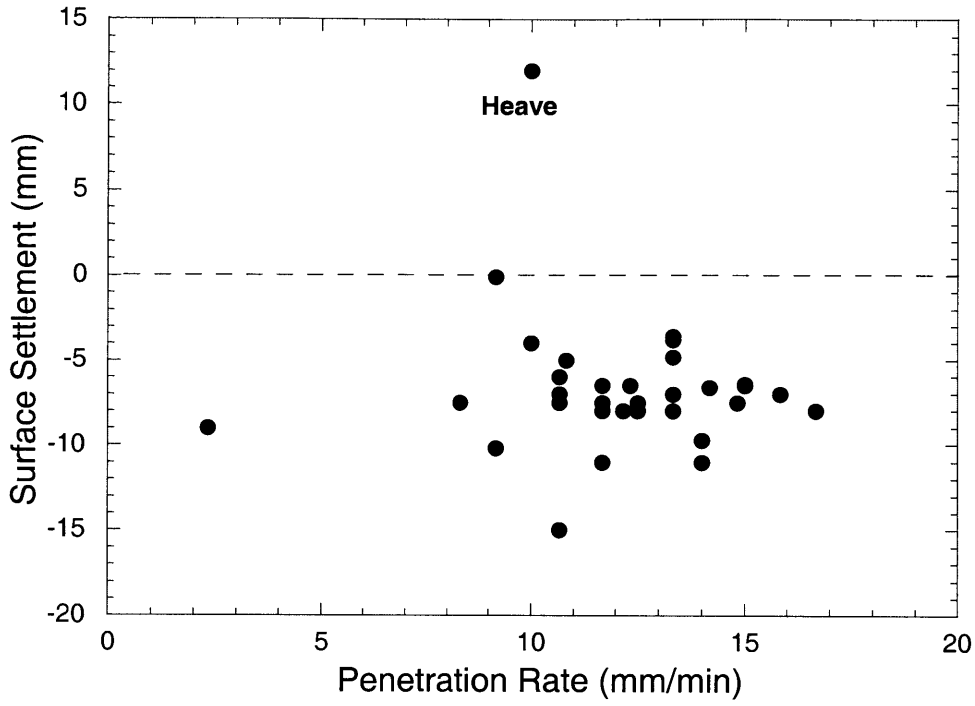


Figure 4.32 Penetration rate versus surface settlement

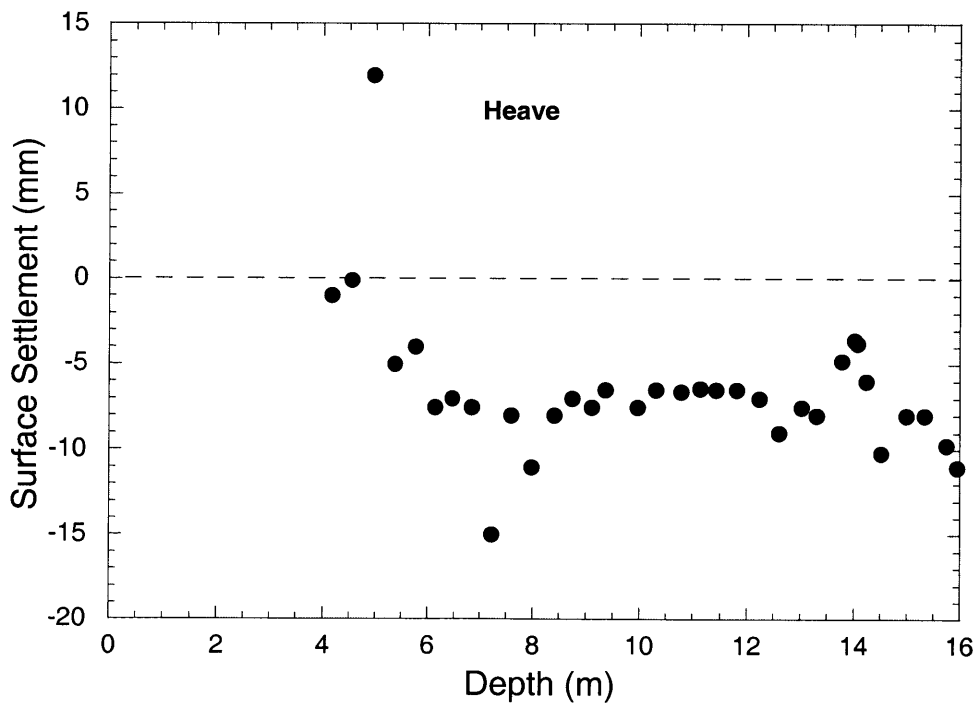


Figure 4.33 Tunnel depth versus surface settlement

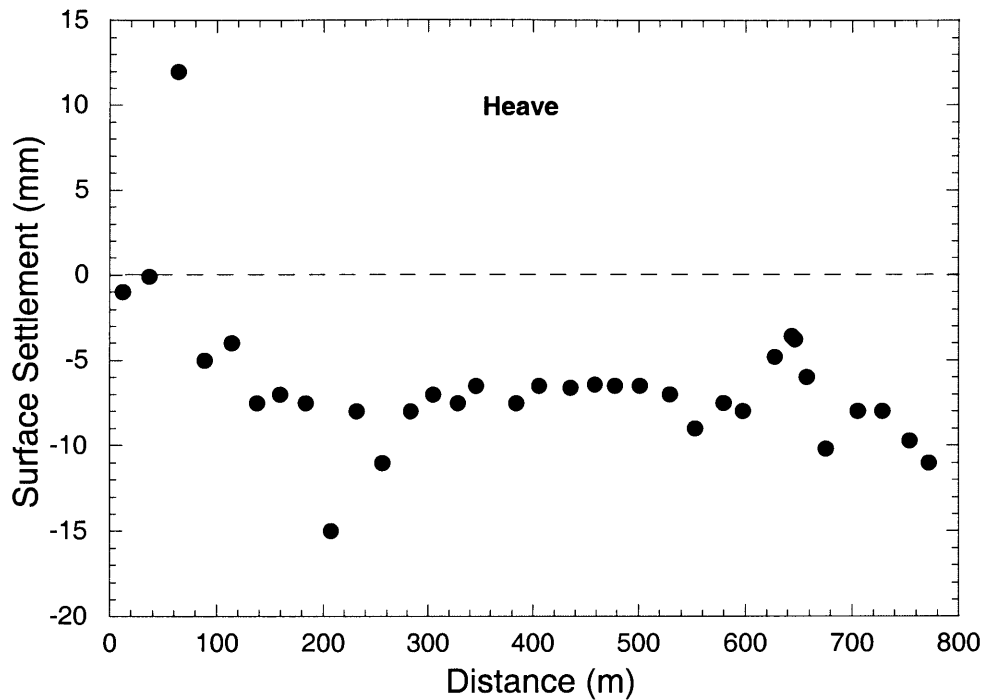


Figure 4.34 Distance from launching station versus surface settlement

4.7 Summary

1. Based on the case histories, the surface settlement can be divided into three major zones: (1) the settlement in front of the shield, (2) the settlement over the shield body, and (3) the settlement after shield passing. The magnitude of the settlement in each zone depends upon many factors including geological conditions, shield operational parameters (i.e. face pressure, penetration rate, pitching angle, and grouting quality), and tunnel geometry (i.e. depth and distance from launching station). The combination of effects caused by these factors makes the EPB tunneling problem very complex to understand.
2. In all cases presented in this chapter, geological conditions obviously have a significant effect on the performance of EPB shields and the magnitude of surface settlements. If the tunnel were excavated entirely in a sand layer under high ground water

level, substantial ground movements at the shield face would be expected. Additionally in mixed-face condition especially if a sand layer is found at the tunnel crown, large settlements were also observed. In contrast, tunneling entirely within a clay layer is found to cause less settlement.

3. The face pressure appears to be one of the critical factors affecting the magnitude of surface settlements particularly in the first zone (i.e. in front of the shield) and the second zone (i.e. over the shield body). As observed by Clough et al. (1983), Matsushita et al. (1995), and Chiorboli and Marcheselli (1996), large surface settlements were found when the shield was operated at low face pressure. In contrast, applying very high face pressure may cause heave on the ground surface as indicated in the San Francisco and the Milan projects. In case of tunneling within normally consolidated soft material (such as Bay Mud in San Francisco), heave on the ground surface was often followed by large consolidation settlements over time after shield passing.

4. The penetration rate also contributes to surface settlements as Chiorboli and Marcheselli (1996) suggested that the lower the penetration rate, the greater the surface settlement. However, not much information about this factor is available. Therefore, the relationship between the penetration rate and surface settlements is still questionable.

5. The position of the shield in terms of the pitching angle during excavation was found to be associated with the settlement over the shield body as observed by Matsushita et al. (1995) in the Fukuoka City subway project. They also suggested that the temporary lifting of the shield tail caused by the shoving jack could cause ground heave over the shield.

6. Grouting quality in terms of grouting pressure and percent grout filling is also very essential in reducing surface settlements particularly in the last zone (i.e. after shield passing). In the cases of the WMATA project and the Fukuoka City subway project, the settlements attributed to tail void closure were significantly reduced by grouting. As a

result, surface settlements found after shield passing in the projects are very small and about the same in all sections.

7. The distance from the launching station was also found to affect shield performances and the magnitude of surface settlements. Ground collapse or substantial settlement often occurred at the beginning of the tunnel drive in the TRTS project (Ju. et al., 1999), although ground improvement was performed. As the shield excavated for some distance, smaller surface settlements were observed. Additionally, large settlements or more variable settlements were measured in the early stages of EPB tunneling. All of this is due to the effect of the learning curve of tunnel crews during excavation in that they gained experience as the shield excavated the tunnel for some distance.

8. There is still a controversy regarding which of the factors mentioned above causes the most significant settlement in EPB tunneling. Some reports suggested that it should be the tail void closure since in some cases, the largest portion of surface settlements occurred after shield passing (Moh et al., 1996 and Clough et al., 1982). However, others argued that in the modern EPB shield methods, backfill grouting was adopted and proved that it can successfully prevent the settlement caused by tail void closure (Matsushita et al., 1995). Additionally, in the cases where high quality grouting was performed, the settlement after shield passing is found to be constant regardless of ground conditions (Leca, 1989 and Matsushita et al., 1995). The latter group of researchers pointed out that face pressure and ground disturbance during shield passing may induce larger surface settlements than those caused by tail void closure.

9. A major problem in studying the EPB tunneling method and its effect on surface settlements is that extensive instrumentation data and continuous observation of operational factors have not often been available such that information on some essential factors is missing.

References

- Clough, G. W., Sweeney, B. P., and Finno, R. J. (1982). "Measured Soil Response to EPB Shield Tunneling". *Journal of Geotechnical Engineering*, Vol. 109, No. 2, pp. 131-149.
- Clough, G. W. and Leca, E. (1993). "EPB Shield Tunneling in Mixed Face Conditions". *Journal of Geotechnical Engineering*, Vol. 119, No. 10, pp. 1640-1656.
- Chiorboli, M. A. and Marcheselli, P. P. (1996). "Analysis and Control of Subsidence due to Earth Pressure Shield Tunneling in Passante Ferroviario of Milano". *Proc. of Int. Conf. on North American Tunneling '96*, Balkema, Rotterdam, pp. 97-106.
- Finno, R. J. (1983). "Response of Cohesive Soil to Advanced Shield Tunneling". Ph.D. Thesis, Stanford University, Ca.
- Hwang, R. N. and Moh, Z-C. (1996). "Pore Pressures induced in Soft Ground due to Tunneling". *Proc. of Int. Symp. On Geotechnical Aspects of Underground Construction in Soft Ground*, Balkema, Rotterdam, pp. 695-700.
- Ju, D., Moh, Z-C., and Hwang, R. N. (1999). "Soft Ground Tunneling for Taipei Rapid Transit Systems". *Proc. of the 3rd Conf. on Geo-Engineering for Underground Facilities*, ASCE, pp.610-621.
- Kuesel, T. R. (1972). "Soft Ground Tunnels for the BART Project". *Proc. of 1st Rapid Excavation Tunneling Conference*, Chicago, Vol. 1, pp. 287-313.
- Leca, E. (1989). "Analysis of NATM and Shield Tunneling in Soft Ground". Ph.D. Thesis, Virginia Institute and State University, Blacksburg, Va.
- Maconochie, D. and Suwansawat, S. (1999) "Bangkok MRTA: Chaloem Rachamongkhon Line". *Tunnel & Tunneling International*, November 1999, pp.19-22.
- Matsushita, Y., Hashimoto, T., Iwasaki, Y., and Imanishi, H. (1995). "Behavior of Subway Tunnel driven by Large Slurry Shield". *Proc. of Int. Conf. on Underground Construction in Soft Ground*, Balkema, Rotterdam, pp. 253-256.
- Moh, Z-C., Hwang, R. N., and Ju, D. H. (1996). "Ground Movements around Tunnels in Soft Ground". *Proc. of Int. Symp. On Geotechnical Aspects of Underground Construction in Soft Ground*, Balkema, Rotterdam, pp. 725-730.
- Ng, R. M-C. (1984). "Ground Reaction and Behavior of Tunnel in Soft Clays". Ph.D. Thesis, the University of Western Ontario, London, Ontario, Canada.

CHAPTER 5

The Chaleom Ratchamongkhon Line, Bangkok MRTA Project

5.1 Project Background

The Chaleom Ratchamongkhon Line (formerly known as the Initial System Project or the Blue Line) is the first phase of an integrated transportation plan for Bangkok, to be implemented in conjunction with other schemes, by the Metropolitan Rapid Transit Authority (MRTA). The project of 20-kilometers twin tunnels originates at Bangkok's Hua Lumphong railway station and ends at Bang Sue railway station as shown in Figure 5.1. This distance covers one of the most heavily congested areas of the city. Each of the twin tunnels is 6.3 meters in outer diameter and 5.7 meters in inner diameter.

The Southern half of the project involves construction of a twin bored tunnel subway from the inter-city railway terminal at Hua Lamphong near the Chao Praya river eastwards for 5 kilometers beneath the busy Rama IV road to the Queen Sirikit National Convention Center, then 4.5 kilometers north beneath Asoke and Ratchadaphisek roads ending at Rama IX station with a connecting line to the depot. The Northern section of the subway continues from Rama IX station for 4.5 kilometers north along Ratchadaphisek road to Lat Phrao road then turns west to Chatuchak park and finally terminates beneath the Bang Sue yards of the State Railway of Thailand. The tunnel axis

level is typically between 16 and 23 meter below the ground surface. Each section is approximately 10 kilometers long and includes 9 underground stations.

The major civil works are being implemented under two principal designs and construct contracts. A contract for the South section was let to a joint venture consisting of Bilfinger & Berger Bauaktiengesellschaft, Ch. Karnchang Public Co. Ltd., Kumagai Gumi Co. Ltd. and Tokyu Construction Co. Ltd. (BCKT) in November 1996. The North contract was let to the ION Joint Venture comprising Italian Thai Development Public Co. Ltd., Obayashi Corporation and Nishimatsu Construction Co. Ltd. in August 1997. These contracts are supervised by the Construction Supervision Consultant (CSC1) comprising a consortium of Louis Berger Inc., Lahmeyer International GMBH, Sverdrup Civil Inc., Sea Consult Engineering Co. Ltd., Arun Chaiseri Consulting Engineers Co Ltd, Roge Consultant Co. Ltd, Project Planning Services Co. Ltd. and P.U. Associates Co Ltd. The MRTA's project management consultant (MPMC) was engaged by MRTA at the outset to assist and advise MRTA with the implementation of these civil works contracts and other track work, lift and escalator, depot and concessionaire contracts. BCKT appointed Sindhu Maunsell Consultants to provide design services in the civil, structural, geotechnical, architectural and mechanical and electrical disciplines in conjunction with Philip Schuetz for tunneling services. ION appointed Ove Arup and Partners (Thailand) assisted by Geoconsult tunneling services.

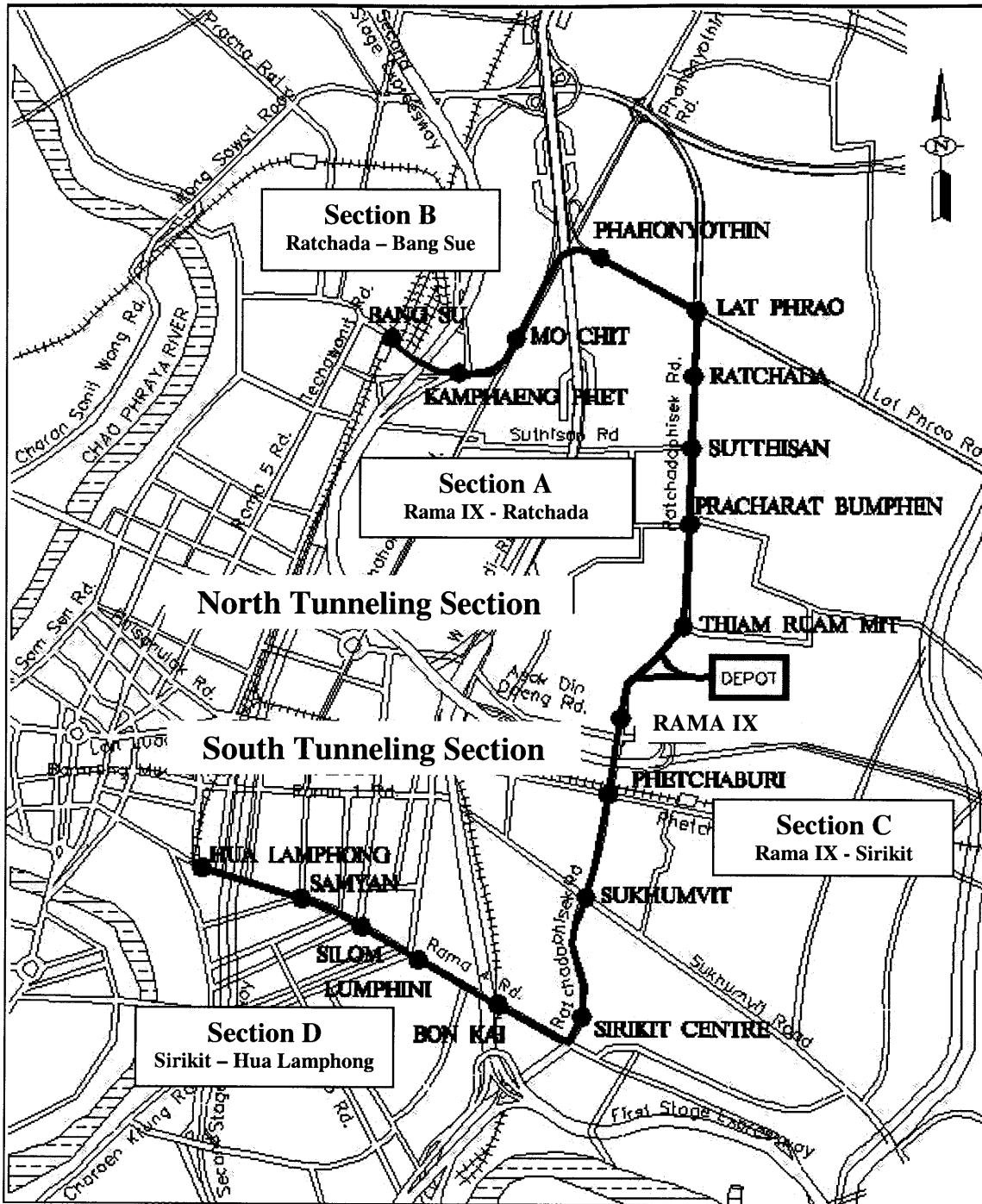


Figure 5.1 MRTA Chalerm Ratchamongkhon Line

5.2 Geological Background

5.2.1 Introduction

Bangkok is a city of approximately 10 million people lying in the Chao Praya delta plain. Its topography is low and flat being approximately 0.5 to 1 meter above sea level. Extensive field explorations and laboratory programs were carried out by contractors (Ove Arup and Partner Int., 1998 and Sindhu Maunsell, 1997). Interpretative results will be summarized in this section. Subsurface conditions along the MRTA project can be subdivided into the North Tunnel section and the South Tunnel section as described earlier. For the North section (i.e. from Thiam Ruam Mit station to Bang Sue station), the soil profile is very uniform with soft clay underlain by stiff clay along the tunnel alignment (Figure 5.2). In this tunneling section, a horizontal-twin tunnel is excavated mostly within the stiff clay layer (i.e. about 15-25 m below ground surface). For the South section (Figure 5.3), most of the tunnel alignment is also located within a stiff clay layer. However, in some part of the route, tunnels are stacked so that the lower tunnel is excavated in a sand layer.

5.2.2 Geographical Setting

The center part of Thailand comprises the Chao Phraya Plain, which extends northwards from the Gulf of Thailand for a distance of 500 km to the Northwest Highlands. The plain, on average, is some 100 km wide and stretches from the Tanaosri Mountain Range in the west to the Khorat Plateau in the east. The major drainage system of the plain is the Chao Praya River and its tributaries. This plain has been filled with alluvial, deltaic, and shallow marine sediments during the Pleistocene (i.e. 2 million to 15,000 years Before Present, BP) and Holocene (i.e. 15,000 years BP to Present). The plain can be subdivided into the Lower Central Plain to the south and the Upper Central Plain to the north. The Lower Central Plain with Bangkok is an extensive alluvial plain which contains material deposited in a more coastal environment than the predominantly fluvial deposits of the Upper Central Plain. The geological map of Thailand is shown in Figure 5.4.

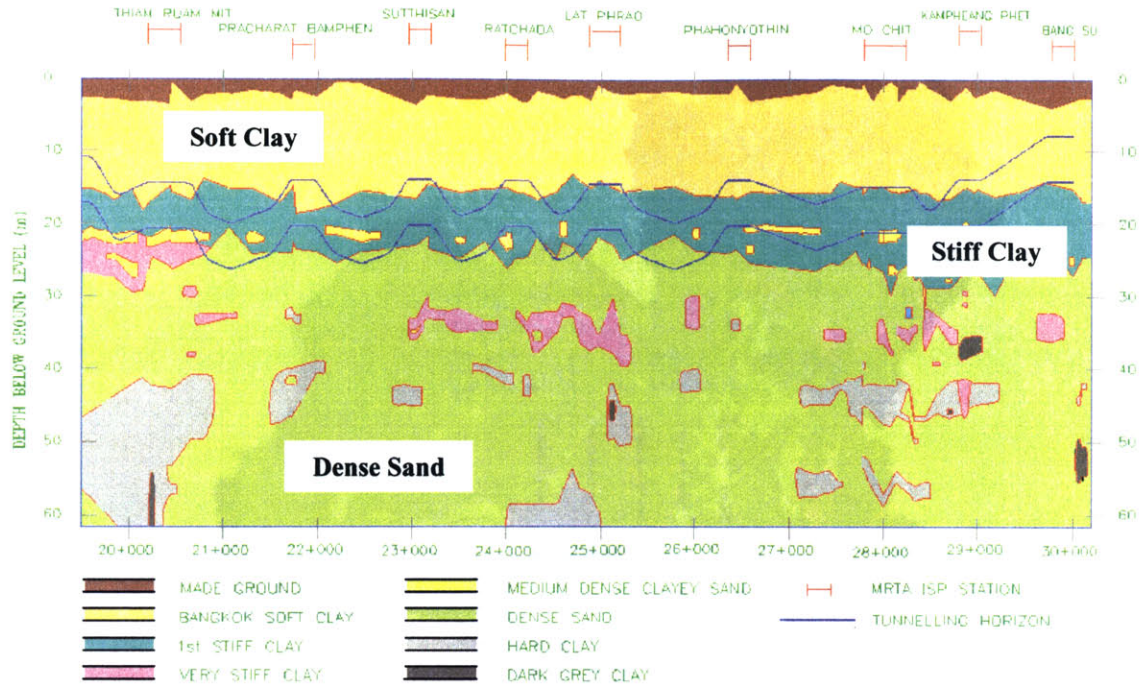


Figure 5.2 Soil profile of the North Tunnel section

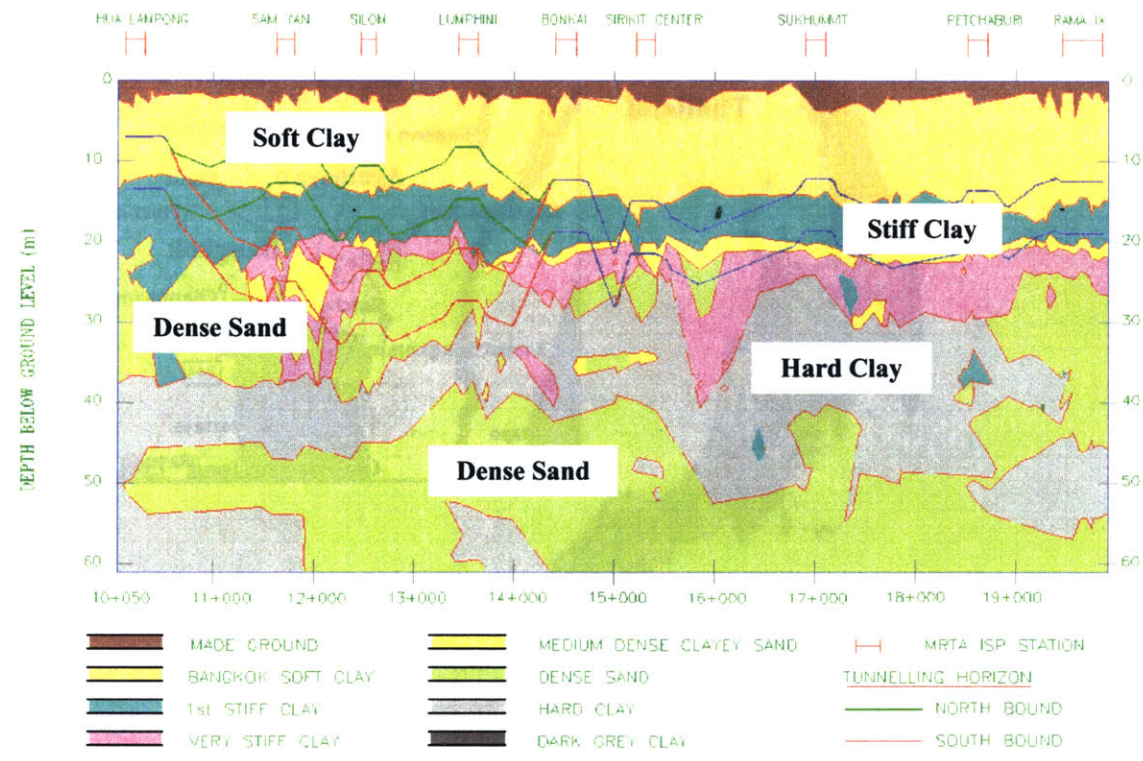


Figure 5.3 Soil profile of the South Tunnel Section

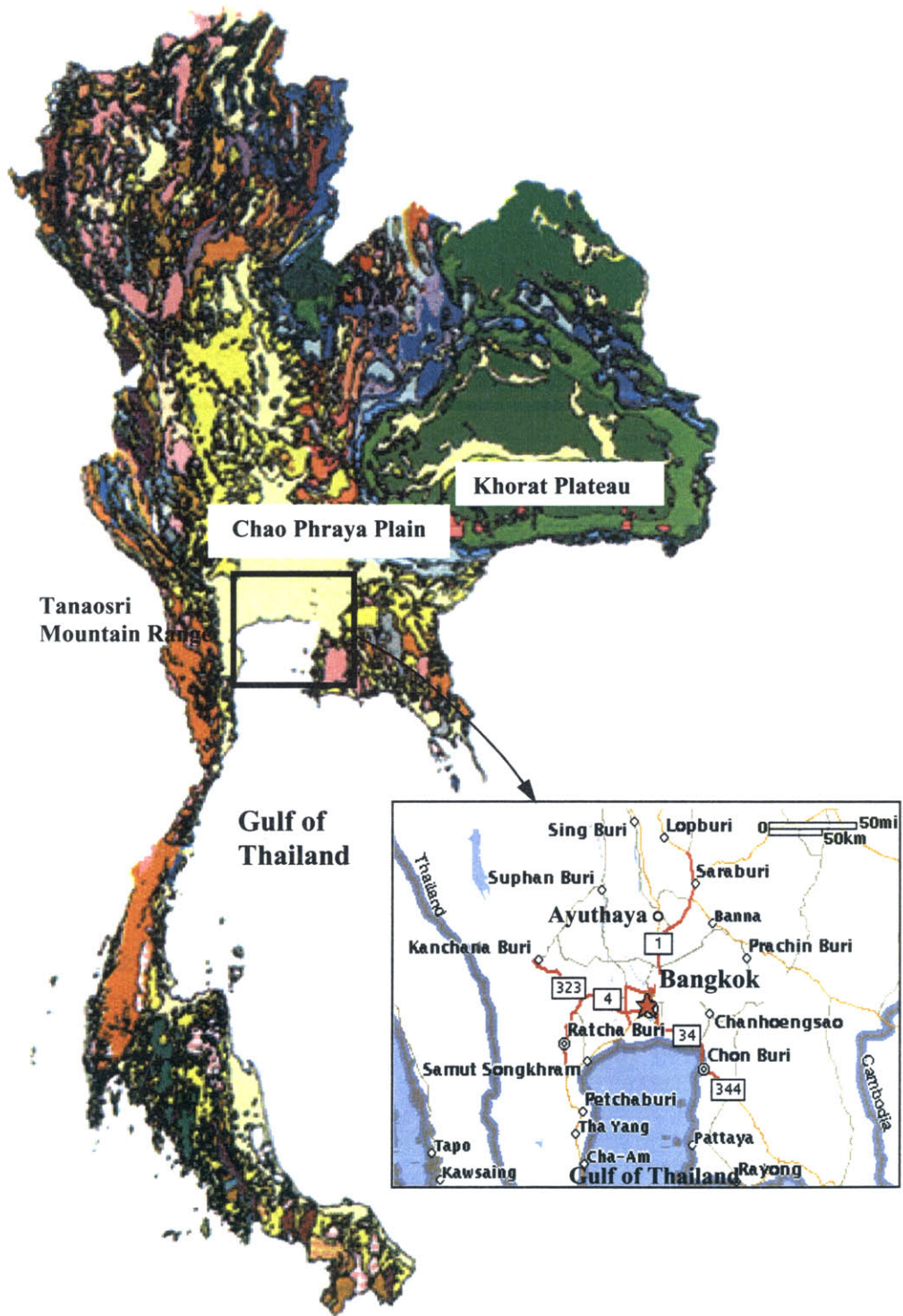


Figure 5.4 Geological map of Thailand (Scale 1:10,000,000)

5.2.3 Bedrock Geology

The Central Plain and Gulf of Thailand are located within a north-south trending structural depression, which was generated by fault block tectonics during the Tertiary Period (i.e. 64 million years BP to present). A fault zone is known to follow the line of the Chao Phraya River with its upthow on the east side forming the Bang Poo Horst and the downthrow to the west forming the Saladaeng Graben (Rau and Nutalaya, 1981). The exact profile to the bedrock is unknown but its level is thought to vary between 550 and 2000 m below ground level. A number of boreholes have been drilled to bedrock and these indicate a variety of basement rock types including gneiss and quartzite.

5.2.4 Drift Deposits

The tectonic basin was continuously filled during the Pliocene periods with clastic sediments consisting of, in the north, alluvial sand and gravels interbedded with floodplain silts and clays progressing seaward into deltaic deposits and marine clays. The distribution of these deposits depends on fluctuations of the sea level resulting from glacial and interglacial periods and from tectonic movement. In the Lower Central Plain eight principal aquifers have been identified in the upper 550 m of sediments. These consist of sands and gravels with clay inclusions separated by relatively impermeable clay layers laid down during sea transgressions. These clay layers may be discontinuous and it is understood that the aquifers are interconnected.

In the late Pleistocene the sea invaded the central plain during, which period the First Stiff Clay was deposited. The sea regressed between about 45,000 to 14,000 years BP leaving the First Stiff Clay exposed to the subaerial processes of desiccation and oxidation. The surface of the First Stiff Clay was also dissected by streams, which formed broad shallow valleys, which are evident near the Gulf of Thailand and further north near Ayuttaya (i.e. a province located at the north of Bangkok). This indicates that some erosion has taken place, which resulted in some of the overconsolidation that is known to

have affected the stratum. The amount of erosion is disputed but it is probable that further overconsolidation results from the processes of weathering and desiccation.

The sea made its last transgression over the central plain as far as Ayuthaya (see Figure 5.1) between approximately 14,000 and 3,000 years BP, during which time the Bangkok Soft Clay was deposited. Since the retreat of the sea, the exposed surface of the Bangkok Soft Clay has been subjected to desiccation. This has resulted in a stiffer weathered crust, which can be up to 4 m thick. A distinct unconformity exists between the base of the Bangkok Soft Clay and the underlying First Stiff Clay. It has been proposed that the First Stiff Clay derives its strength from a combination of desiccation and, to a lesser extent, erosion. The Bangkok Aquifer system and the upper soil profile are presented in Table 5-1 and presented graphically in Figure 5.5.

Table 5-1 Typical soil profile beneath Bangkok

Depth (m)	Strata and Description
0-15	Bangkok Soft Clay
15-25	First Stiff Clay
25-70	Bangkok Aquifer
70-120	Phrapradaeng Aquifer
120-160	Nakhonluang Aquifer
160-250	Nonthaburi Aquifer
250-300	Sam Khok Aquifer
300-350	Phayathai Aquifer
350-450	Thonburi Aquifer
450-550	Paknam Aquifer

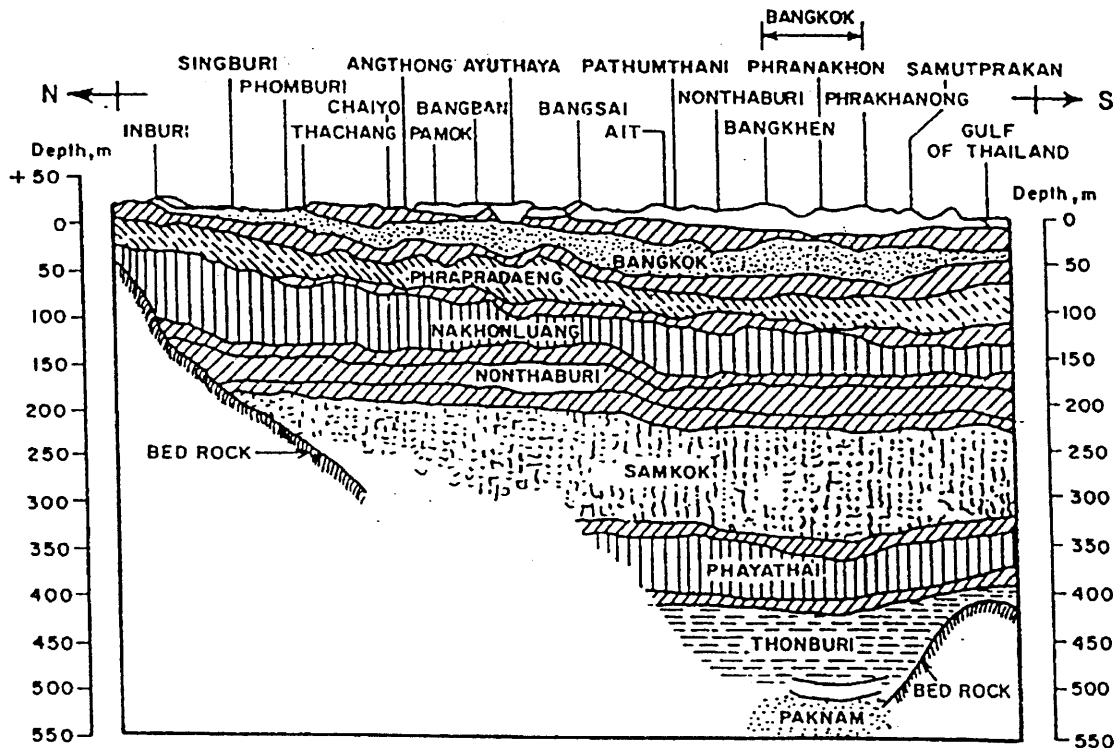


Figure 5.5 System of Aquifers under the Chao Phraya Plain

5.2.5 Hydrology

Pumping of ground water from the aquifers listed in Table 5-1, for both domestic and industrial purposes, has reduced the piezometric head beneath the southern part of the Chao Phraya Plain. The depression in ground water level was initially centered on Bangkok, but as industry moved out of the city, and pumping increased in the industrial areas to the south and east of the city, the piezometric levels in these areas became depressed at the same time as those in Bangkok recovered.

There are two main effects of the depression in the water tables. First, the localized depression of the water table has caused migration of ground water from the surrounding areas, which has allowed saline water from the Gulf of Thailand to infiltrate the aquifers.

This is one of the reasons for the high chloride contents within the ground water at some locations. Secondly, the reduction in pore pressure has caused consolidation of the substrata leading to significant long-term ground settlement across the region.

Large-scale exploitation of ground water commenced in the early 1950's when the daily pumping rate was 8,400 m³/day. The rate increased rapidly to 1,300,000 m³/day in 1983 at which time measures were introduced to control the amount of extraction. Pumping rates stabilized until the control measures were lifted in 1987 after which the daily rate was approximately 1,500,000 m³/day. These pumping rates are totals for the areas of Bangkok, Samutprakan, Nonthaburi and Pathumthani (i.e. surrounding provinces of Bangkok), however the concentration of the pumping appears to have moved from Bangkok into the surrounding provinces.

The most productive aquifers are the Phrapradaeng, Nakhonluang, and Nonthaburi Aquifers. The aquifers below this are being developed. The Bangkok Aquifer has a high salinity and is therefore not extensively exploited. The effect on the Bangkok Aquifer of this pumping has been to lower the piezometric levels within the aquifer by underdrainage through connection with the aquifers below. Beneath the site of the MRTA the piezometric levels were reduced from what would have originally been a hydrostatic profile from near the ground level (i.e. before any pumping occurred), to a level of about 23 m below ground level by 1979. The piezometric level in the Bangkok Aquifer does not appear to have changed from this level between 1979 and the present day. The First Stiff Clay and Bangkok Soft Clay above are underdrained near their base, however, because of replenishment from the surface and its relatively low permeability, the Bangkok Soft Clay has a hydrostatic profile from near ground level to approximately 10 m below ground level (Figure 5.6).

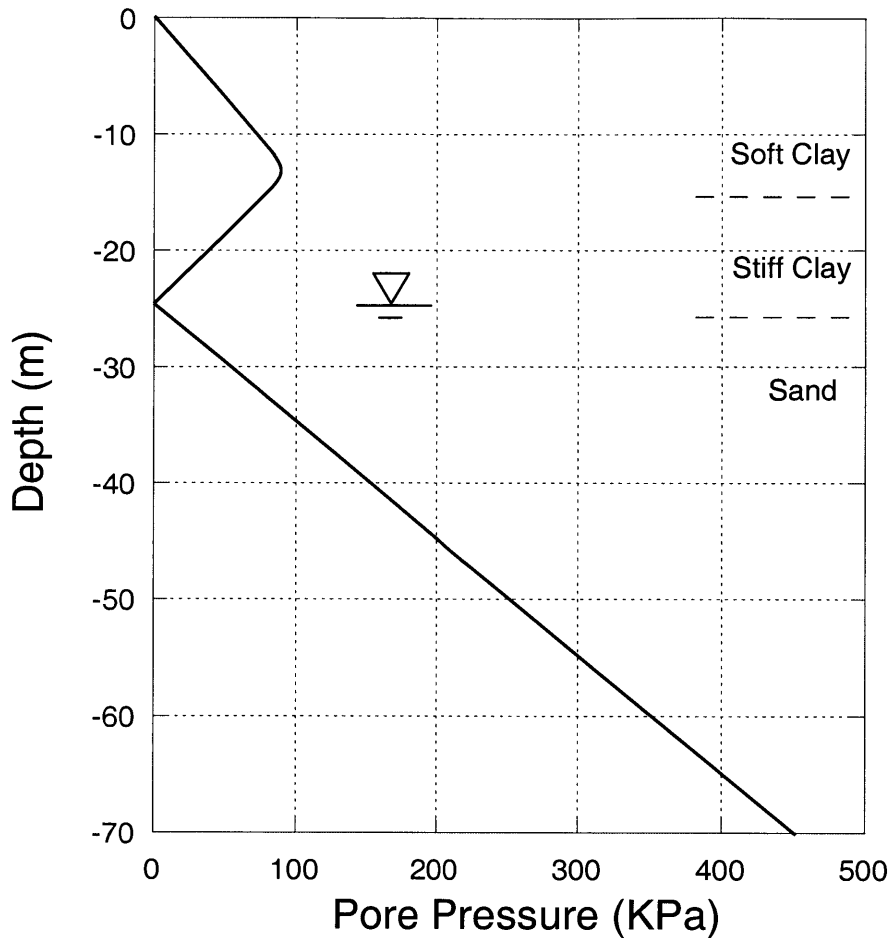


Figure 5.6 Typical pore water pressure profile in Bangkok

In Figure 5.7 and Figure 5.8, the piezometric levels in the aquifers underlying the Bangkok Aquifer measured over the period 1979 to 1990 show that water levels beneath Bangkok have risen while the levels to the east of the city have dropped. The piezometric pressure in the Phrapradaeng Aquifer beneath the Bangkok Aquifer at the site of the MRTA has risen during this period from approximately 31 to 24 m below ground level. Conversely around the industrial town of Lad Krabang some 30 km to the east of the city, the level has moved from approximately 20 m to 40 m below ground level. Over the same period the piezometric levels in both the Nakhonluang and Nonthaburi Aquifers have also risen from approximately 43 m to 34 m below ground level beneath the MRTA site.

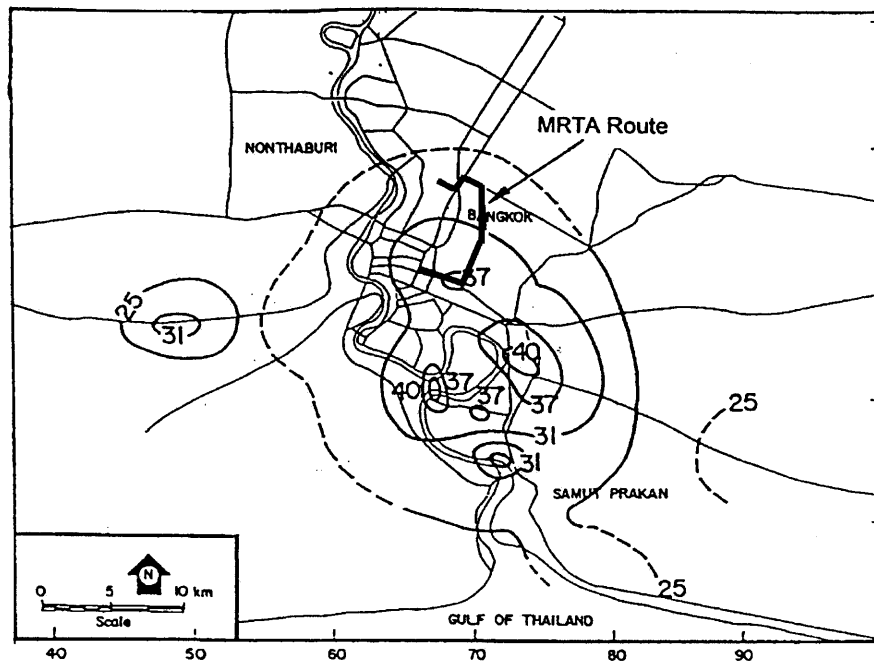


Figure 5.7 Piezometric Levels (meter from the ground surface) in the Phra Pradaeng Aquifer in 1979

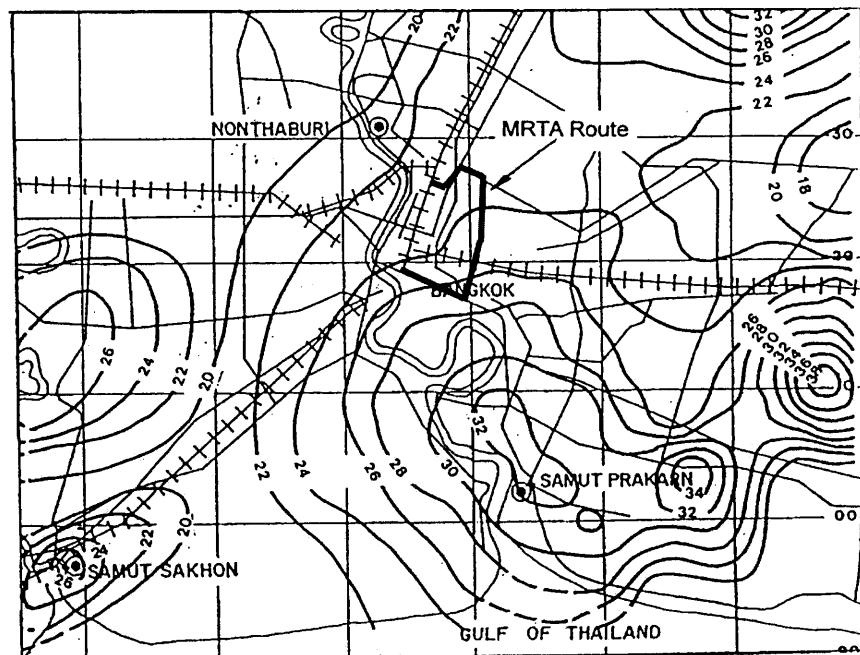


Figure 5.8 Piezometric Levels (meter from the ground surface) in the Phra Pradaeng Aquifer in 1990

5.2.6 Consolidation Settlement

The extraction of ground water has lead to significant consolidation settlement within the substrata. Prinya et al. (1989) suggested that up to 1.6 m of surface subsidence has occurred in the Bangkok area between 1933 and 1987 with approximately 800 mm to 1000 mm occurring at the MRTA site (Figure 5.9).

The annual rates of the consolidation settlement were between 40 and 150 mm/year in 1978, reducing to between 25 and 75 mm/year in 1984 (Ove Arup and Partner Int., 1998). The smaller settlements occurred to the south and west of the MRTA route. The subsidence rate has diminished further since about 1984 to approximately 15 mm/year. Ramnarong and Buapeng (1991) reported a settlement rate of 8 to 12 mm/year in 1989. This reduction in rate is probably due to the restriction of groundwater extraction as discussed earlier, and the subsequent rise in piezometric pressures in the aquifers below the Bangkok Aquifer. Additionally, deep datum points have been installed at various depths from which the settlement at different levels within the sub-strata has been measured. The annual settlement rates in the vicinity of the MRTA route in 1981 and 1996 are summarized in Table 5-2.

Table 5-2 Subsidence Rates beneath Bangkok in 1981 and 1996

Depth below Ground Level	Annual Settlement Rates in 1981	Annual Settlement Rates in 1996
	Typical Range (mm/year)	Typical Range (mm/year)
1 m	50 to 165	10 to 20
10 m	No Data	3 to 18
20 m	20 to 150	0 to 17
50 m	No Data	No Data
200 m	0 to 25	0 to 15
400 m	0 to 65	0

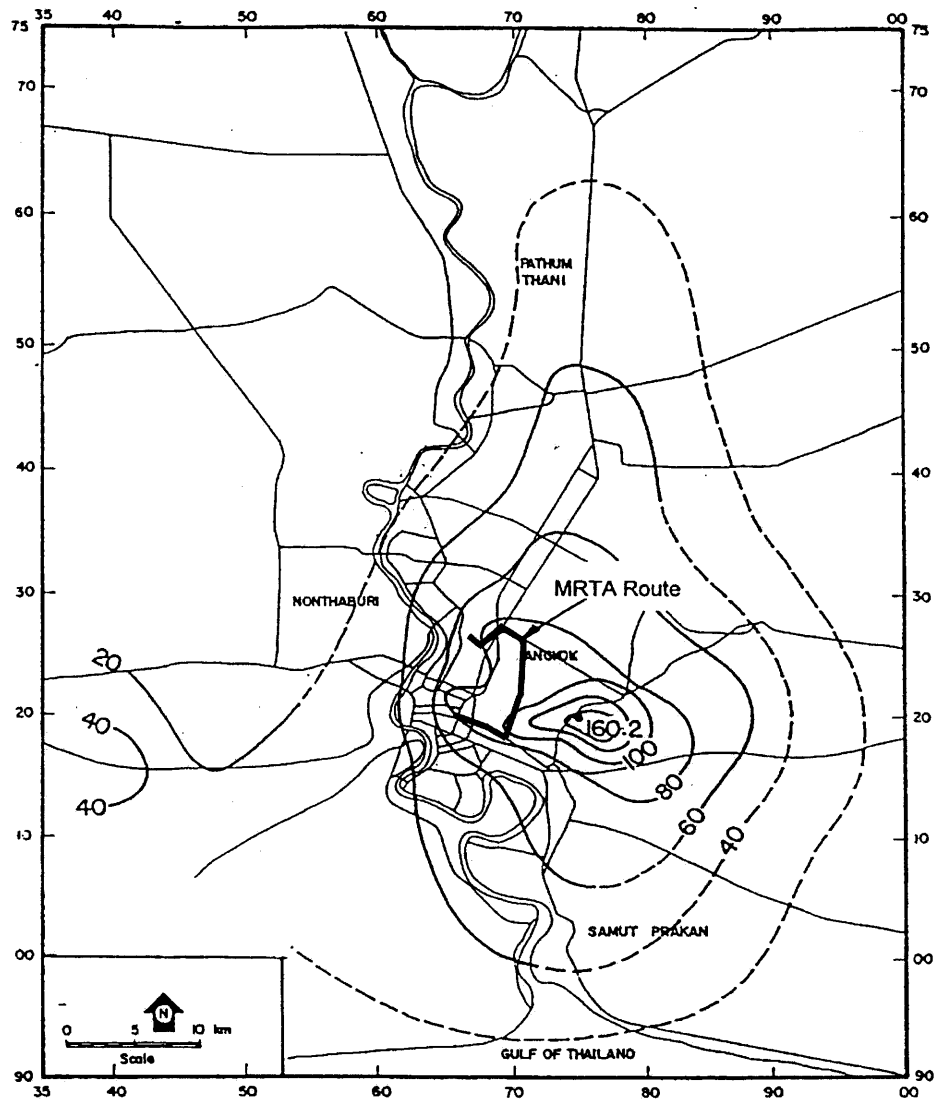


Figure 5.9 Total ground surface subsidence in centimeters between 1933 and 1987 (after Prinya et al., 1989)

Data from the four settlement monitoring stations with settlement pins installed at depth in the vicinity of the MRTA route indicate that compression of the Bangkok Soft Clay may have been between about 2 mm and 15 mm/year in 1996. It is not possible from the data available to determine the rates of settlement in the strata beneath this. However, as stated above it seems likely that there is very little movement at a depth of 200 m and below.

The piezometric pressures in the Bangkok Aquifer have been relatively stable at 22-24 m below the ground surface over the period 1979 to 1997. The ground settlement monitored over this period is likely to be principally due to consolidation of the clay overlying the Bangkok Aquifer. The rate of settlement monitored in 1996 at 20 m below ground level appears to be only some 10% of that monitored in 1981 and, given no further decrease in piezometric level within the Bangkok Aquifer, it can be expected that this reduction in settlement rate may continue in the future.

5.3 Subsurface Conditions

Based upon comprehensive field exploration and laboratory tests conducted by contractors of the North and South sections of the MRTA project, this section presents an interpretation of the data. Geotechnical design parameters are also presented for each soil stratum.

5.3.1 Made Ground (Fill)

The type and thickness of Made Ground encountered along the length of the tunnel alignment varies considerably depending on the land usage in a particular area. For most of the tunnel route located within dense city areas, Made Ground typically consists of road construction materials such bituminous materials, concrete, sands, gravels and laterite fill materials, which were found to be up to 4 m thick. In the park area of the North section, the surface material was found to be topsoil, which consisted of turf and silty clays with rootlets up to 1.3 m thick.

Relatively few samples of the Made Ground were obtained in the MRTA project. SPT(N) values varying between 2 and 9 were measured in granular fill material indicating loose to very loose deposit. Given the variable nature of the material, it is recommended that following parameters are adopted as listed in Table 5-3.

Table 5-3 Typical design parameters of Made Ground

Parameter	Made Ground
Bulk Density	18 kPa
Undrained Shear Strength	N/A
Effective Shear Strength	$C' = 0, \phi' = 25$
Stiffness	$E' = 5000$ kPa
Poisson Ratio	0.3

5.3.2 Bangkok Soft Clay

The Bangkok Soft Clay was deposited in marine conditions at the delta of the rivers in the Chao Phraya Plain. It is generally described as a soft dark gray clay, which in some boreholes becomes medium stiff with depth, with a trace of sand. The upper layers of this deposit have been subject to oxidation and desiccation, which produced, in some areas, a stiffer crust, which is described as a brownish gray sandy or silty clay of medium to stiff consistency. The stiffer crust can be up to 4 m thick. In addition, pockets of shell debris, rootlets and organic matter occur in the Bangkok Soft Clay and appear to be more abundant in the upper 6 m of the deposit.

The base of the soft clay is subject to underdrainage caused by water extraction from the underlying aquifers. This has reduced the porewater pressure within the deposit below hydrostatic beneath approximately 8-10 m from the surface and increased the effective stress and undrained shear strength below this depth. The strength and consolidation characteristics of the clay are dependent on its stress history. In the MRTA project, preconsolidation pressures have been determined from the results of laboratory oedometer tests conducted on relatively undisturbed soil samples. Based on the tests, high

OCRs (i.e. about 2-6) were found in the upper 5 m of the deposit, which are consistent with overconsolidation most probably resulting from near surface desiccation. Beneath the crust, the OCR values generally range between 1 and 2 with a typical value of about 1.2. Table 5-4 summarizes typical global design parameters for the Bangkok Soft Clay as discussed above.

Table 5-4 Typical design parameters for the Bangkok Soft Clay

Parameter	Crust (where present)	Bangkok Soft Clay
Unit Weight	16-18 kN/m ³	16 kN/m ³
PL	20-40%	20-40%
LL	55-90%	55-90%
LI	0-0.5	0.5-1.0
PI	30-50%	30-50%
Water Content	30-50%	50-80%
Clay Content	35-85%	35-85%
S _u	15-30 kPa	20 + 3.5(z-7) <i>z begins at 7 m from surface</i>
E _u	6,250 kPa	6,250 + 900(z-7) kPa
φ'	23	23
K _o	1	0.75
OCR	2-6	1.2
k	N/A	3 x 10 ⁻⁹ m/s

5.3.3 First Stiff Clay

The First Stiff Clay is generally described as a stiff to hard light brownish or greenish gray, grayish brown or yellowish brown silty clay. It often becomes a sandy clay towards the base of the stratum. Micro fissuring with small polished surfaces was noted in some samples. Large planar fissures with polished slickensided surface were also found. Black staining was noted on some of the large fissures. Occasional limestone concretions were found particularly near the top of the stratum.

Occasional bands of medium dense yellowish brown clayey fine sand up to 2 m thick were encountered near the base of the stratum particularly in Thiam Ruam Mit station of the North section (Figure 5.2) and along the Rama IV road. (Figure 5.1) of the South

section (Figure 5.3). These materials reflect the prevailing marine and deltaic depositional environments, which fluctuated with gradual encroachment and retreat of the sea during the Pleistocene period. The First Stiff Clay was at times during its deposition exposed and subjected to the processes of erosion, desiccation, and chemical weathering before burial by subsequent deposits. These processes have dictated the nature of the clay. Desiccation and the effects of erosion have resulted in some overconsolidation and may be responsible for the fissuring that has been noted. Chemical weathering and leaching may have lead to the cementing of concretion, which were observed. The effect of these processes will vary with location and depth, as different areas will have been exposed at different times. In comparison with the Bangkok Soft Clay very few data have been published on the First Stiff Clay. Table 5-5 summarizes typical design parameters for the First Stiff Clay.

Table 5-5 Typical design parameters for the First Stiff Clay

Parameter	Above 20 m	Below 20 m
Unit Weight	19 kN/m ³	19 kN/m ³
PL	25-40%	15-25%
LL	60-80%	30-50%
LI	-0.25 to 0.4	-0.25 to 0.4
PI	30-50%	15-30%
Water Content	25-40%	15-25%
Clay Content	85%	20%
S _u	78 kPa at 13 m to 120 kPa at 20 m	120 kPa
E _u	43,000 kPa at 13 m to 52,800 kPa at 20 m	52,800 kPa
φ'	26	26
K _o	0.65	0.65
OCR	1.65	1.65
k	1 x 10 ⁻⁹ m/s	1 x 10 ⁻⁹ m/s

5.3.4 Bangkok Aquifer

The Bangkok Aquifer, which underlies the First Stiff Clay, is the upper most aquifer of a series of eight aquifers identified beneath the Chao Phraya Delta (Figure 5.5). It was

deposited in alluvial and deltaic environments and consists, along the North tunnel alignment as shown in Figure 5.2, of sands with discontinuous bands of clay generally less than 5 m thick, although at the southern end of the route in the area of Thiam Ruam Mit station more substantial clay deposits were found. Occasional zones of a softer Dark Grey Clay were also found within the Bangkok Aquifer. The clay horizons vary both vertically and laterally in extent.

In the South Tunnel Section (Figure 5.3), unlike the North section, two main sequences of Bangkok Aquifer were found. First, a significant thickness of dense sand beneath the First Stiff Clay layer was found with variations between Hua Lumphong to Sam Yan, Silom to Lumpini and generally north of Phetchaburi. This sequence below the First Stiff Clay is a typically more uniform and horizontally layered of dense sand, hard clay, dense sand and hard clay (see Figure 5.3). In the second section, between Sirikit and Phetchaburi (see also Figure 5.3), the first sand layer is absent being substituted by a very stiff grayish brown to light brown silty clay, which separates the First Stiff clay and a thickened section of the Second Hard Clay layer. Between Sam Yan and Silom stations a zone of interbedded sands and clays form a wide channel deposit. The base of the Bangkok Aquifer is taken as the third hard clay layer at about 70 m below the ground surface. The following tables summarize typical design parameters for the soils of Bangkok Aquifer.

Table 5-6 Typical design parameters for the Dense Sand

Parameter	Dense Sand
Unit Weight	20 kN/m ³
Clay Content	< 35%
ϕ'	36
OCR	1.5
K_o	0.5
k	1×10^{-7} m/s

Table 5-7 Typical design parameters for the Second Hard Clay

Parameter	Hard Clay
Unit Weight	20 kN/m ³
PL	22
LL	55
LI	-0.21 to 0.24
PI	33
Water Content	15-30%
S _u	150 kPa at 20 m to 200 kPa at 40 m 200 kPa (>40 m)
E _u	82,500 kPa at 20 m to 100,000 kPa at 40 m 100,000 kPa (> 40 m)
φ'	23
OCR	1*
K _o	0.8
k	2 x 10 ⁻⁹ m/s

*assumed value

5.4 Tunneling of the MRTA Project

5.4.1 Earth Pressure Balance (EPB) Shield

A total of eight Earth Pressure Balance (EPB) shields were used for tunneling of the entire project. As described earlier, the project of 20-kilometers is divided into 2 main tunnel sections namely, the North Tunnel Section and the South Tunnel Section. The North Tunnel Section in turn is composed of Tunneling Sections A and B, whereas the South Tunnel Section is divided into Tunneling Sections C, and D. All of this is shown in Figure 5.1. Each of four sections used two shields for excavating northbound and southbound tunnels.

For Section A in the North Tunnel Section, two machines (i.e. No. 1 and No. 2) operated by Nishimatsu were driven northward from Thiam Ruam Mit station to Ratchada

station. Obayashi operated the other two machines (i.e. No. 3 and No. 4) which excavated the twin tunnels from Ratchada station to Bang Sue station known as Section B. For the South Tunnel Section, two machines (i.e. No. 5 and No. 6) were launched from Rama IX station and driven southward to Sirikit station in Section C, which was excavated by Kumagai Gumi. The last section is Section D starting at Sirikit station to Hua Lumphong station. This section was excavated by Bilfinger & Berger using two EPB shields, which were refurbished from the machines used in Taipei Rapid Transit Systems (Figure 4.15). Six EPB machines (i.e. No. 1 to No. 6) were the same model manufactured by Kawasaki (Figure 5.10) and the other two (i.e. No. 7 and No. 8) were Herrenknecht machines (Figure 5.11). All of the shields had very similar specification as shown in Figure 5.12. The details of each shield are provided in Table 5-8. The details of tunnelling progress were also given in Maconochie and Suwansawat (1999).

The tunneling conditions principally involve excavation in stiff to hard clay, which is self-supporting, and dense fine silty sand as the drives become deeper between stations. Although six of the eight machines are Kawasaki, they are operated differently by each of the operators and have slightly different specifications as detailed in Table 5-8. The machines are all high speed capable of up to 10 cm per minute cutting speed. They can operate in dual mode but typically have been operated with slurry injection using polymers or bentonite to control the consistency of the clays as the moisture content of the stiff clay is close to the plastic limit. Specification Details are provided in Kawasaki (1998) and Herrenknecht (1996). The drive sequence and driving schedule relative to the excavation progress of the stations is summarized in Table 5-9.

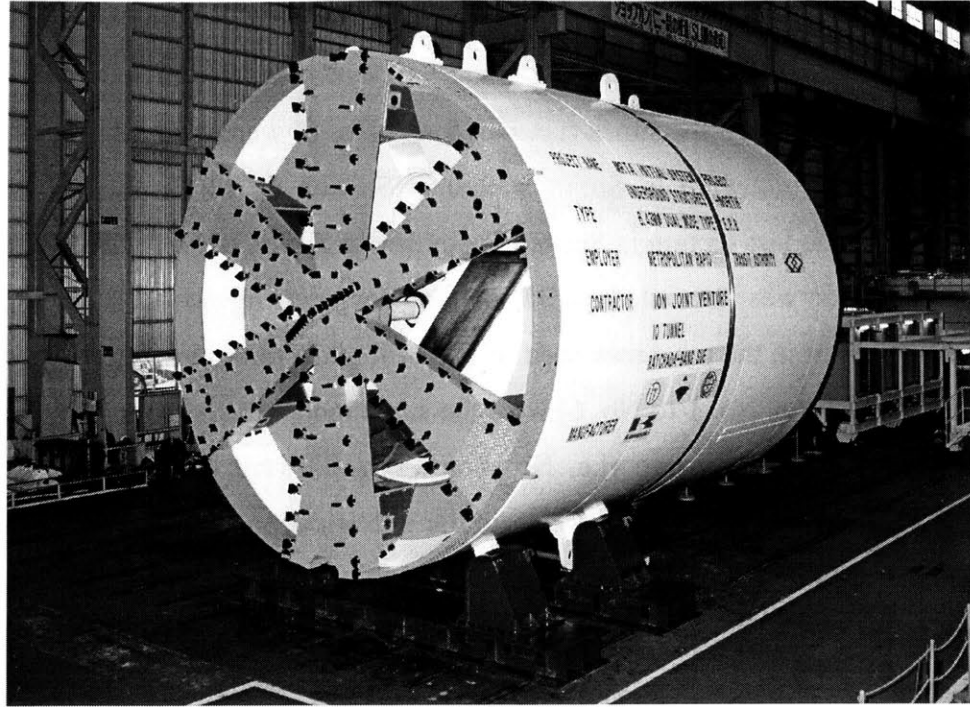


Figure 5.10 Kawasaki EPB Shield (the model used in Sections A, B, C)

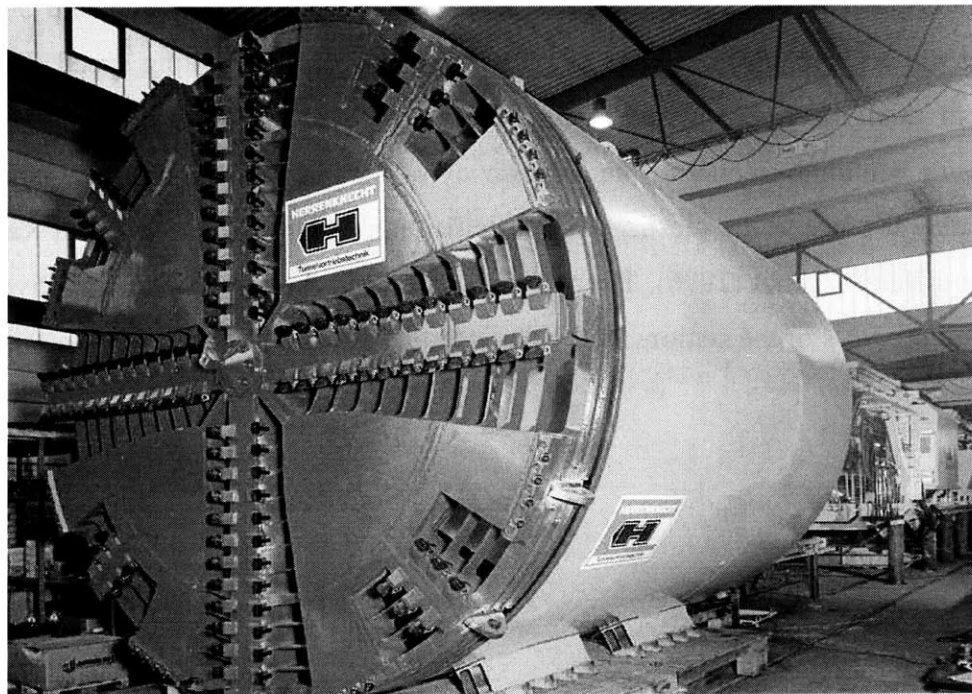
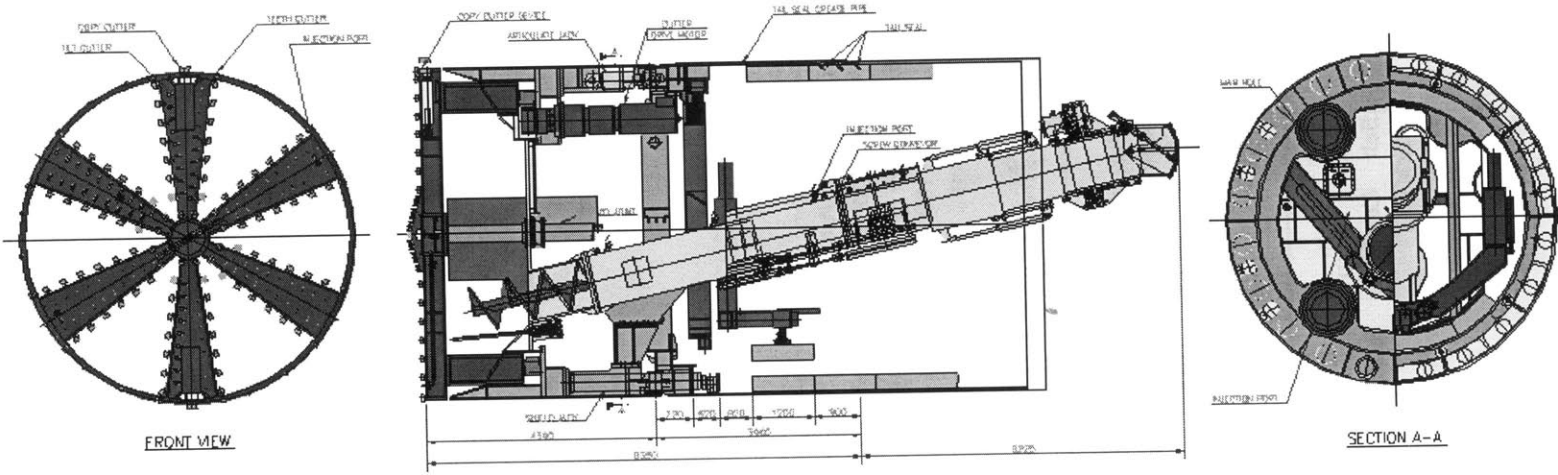


Figure 5.11 Herrenknecht Earth Pressure Balance Shield used in Section D



SHIELD BODY	
OUTER DIAMETER	46470mm
OVERALL LENGTH	46350mm
SHIELD JAW	300 x 1400 x 100kg/cm ² FWD
CONCRETE JACK	175 x 1050 x 200kg/cm ² FWD
CONCRETE ANGLE	2°
MIN. RADIUS OF CURVE	200m

OUTER DISK	
TYPE	FLAT FACE CUTTING TYPE
OUTER DIAMETER	46470mm
THICKNESS	27.5mm
EXTENDING TUBOULE	Ø27.5mm x 4m
ELECTRIC MOTOR	1000mm x 1000mm x 4000W
EXTENDING BAR	TELESCOPIC BAR 3000mm x 100mm
ARTICULATED JACK	23 T x 1000 x 200kg/cm ²

SEGMENT ERECTOR	
TYPE	SPINE DRIVEN TYPE
ØE AND W/ØØP	1400000-2
EXTENSION TUBOULE	27.5mm
EXTENSION TUBOULE	10.000m
THICKNESS	24mm x 100mm x 3mm
EXTENSION SHOCK	16.7.750mm
SLIDE SHOCK	W/1000 x 1000 x 100mm

SCREW CONVEYOR	
RADIUS OF CURVE DIAMETER	46300mm
SCREW LENGTH	Ø = 21 x 100m
ROTATION	Ø = 10 x 100kg/cm ²
SCREW TYPE	Ø = 10 x 100kg/cm ²

RETRACTABLE HOPPER	
SLIDE SHOCK	11.000mm

	POWER UNIT					
	FOR SHIELD JACK	FOR ERECTOR	FOR COPY-OUTLET	FOR SCREW CONVEYOR		FOR COPY-OUTLET
HYDRAULIC PRESSURE	15000psi / 110MPa	2100psi / 150MPa	2100psi / 150MPa	15000psi / 110MPa	15000psi / 110MPa	15000psi / 110MPa
WORKING PRESSURE	200 kg/cm ²	270 kg/cm ²	270 kg/cm ²	140 kg/cm ²	140 kg/cm ²	140 kg/cm ²
SCREW SPEED	2 - 145 r/min	32 r/min	32 r/min	245 r/min	245 r/min	245 r/min
ELECTRIC MOTOR	750 x 1500000 W	37 x 1500000 W	37 x 1500000 W	75 x 1500000 W	75 x 1500000 W	15.0 x 1500000 W
SLURRY	1	1	1	2	1	1

Figure 5.12 Specification of the Earth Pressure Balance Shield used in the MRTA project (manufactured by Kawasaki)

Table 5-8 Comparison of EPB shields used in the MRTA project

EPB Shield	1 & 2	3 & 4	5 & 6	7 & 8
Section Route	A North TRM – Ratchada	B North Ratchada – Bang Sue	C South Rama IX - Sirikit	D South Sirikit - Hua Lampong
Operator	TRM – Rama IX, Depot Nishimatsu	Obayashi	Kumagai Gumi	Bilfinger & Berger
Specification	Kawasaki	Kawasaki	Kawasaki	Herrenknecht
Manufacturer	Kawasaki	Kawasaki	Kawasaki	Herrenknecht
Shield Diameter	6.43 m	6.43 m	6.43 m	6.46 m
Typical Face Pressure	50 kPa	180 kPa	200 kPa	180 kPa
Cutting wheel dia. Not including copy cutter	6.43 m	6.43 m	6.43 m	6.48 m
Over-excavation Gap	6.5 cm	6.5 cm	6.5 cm	9 cm
Max. Copy Cutter Stroke	10 cm	10 cm	10 cm	N.A.
Overall Length	8.35 m	8.35 m	8.33 m	6.19 m
Articulation Number	1 (4.39/3.94)	1 (4.39/3.94)	1 (4.39/3.94)	1 (3.275/2.915)
Number of Jacks	20 x 200 tonne	20 x 200 tonne	40 x 100 tonne	40 x 100 tonne
Total Thrust Force	35630 kN	35630 kN	35630 kN	28300 kN
Cutter head drive	4 x 180 Kw electric motors	4 x 180 Kw electric motors	4 x 180 Kw electric motors	8 hydraulic motors powered by 4 x 160 Kw electric pumps
Opening Ratio of cutter face	60 %	60 %	60 %	42 %
Grouting				
Type of Grouting	Thixotropic cement / bentonite	Thixotropic cement / bentonite	Thixotropic cement / bentonite	Bentonite, cement + Fly Ash
Typical Pressure	2.5 bar	2 bar	2 bar	>3 bar
Typical Quantities	1.8 m ³ /m	1.8 m ³ /m	2.2 m ³ /m	N.A.
Typical Grout Filling Ratio	120 %	120 %	120 %	150%
Muck Removal Operation	Screw Conveyor, Belt Conveyor & Muck Car	Screw Conveyor & Pumping	Screw Conveyor, Belt Conveyor & Muck Car	Screw Conveyor, Belt Conveyor & Muck Car
Max. Screw Conveyor	312 m ³ / hr	312 m ³ / hr	312 m ³ / hr	200 m ³ / hr
Max. Belt Conveyor	150.0 m ³ / hr	-	-	-
Max. Pumping Rate	-	150.0 m ³ /hr	-	-
Typical Slurry	2.5 m ³ / m	13.0 m ³ / m	N.A.	11.0 m ³ / m
Additive Volume				
Typical Excavated Soil Volume	45.0 m ³ / m	55.0 m ³ / m	N.A.	51.0 m ³ / m

Table 5-9 Drive sequence of the EPB shields

EPB Shield	1 & 2	3 & 4	5 & 6	7 & 8
Section Route	A North	B North	C South	D South
Operator	Nishimatsu	Obayashi	Kumagai Gumi	Bilfinger & Berger
Tunnelling Start Date	SB 23-Apr-99 NB 30-Apr-99	SB 16-Feb-99 NB 19-Mar-99	NB 9-Jun-99 SB 25-Jun-99	SB 24-July-99 NB late August 1999
Section Length (SB & NB)	6871 m, 1290 m, 631	4292 m, 2819 m, 2459 m	7466 m	9888 m
TBM / Station interface	Station excavation incomplete, move TBM between drives except as noted	Station excavation incomplete, move TBM between drives except as noted	Skid TBM thru completed station boxes S8, S7	Skid TBM thru completed station boxes S5, S4, S3, S2
Driving Sequence Refer Figure 1	NB:- TRM→Ratchada drive thru PRA, SUT TRM→DEPOT Rama IX→TRM SB:- TRM→Ratchada TRM→Rama IX	RAT→Phahonyothin drive thru Lat Phoa Bang S→KamPP Mo C→Phahonyothin Mo C→KamPP	Rama IX→Sirikit	Sirikit→Hua Lumphong
Best week	199 rings from both machines	231 rings from both machines	164 rings from both machines	167 rings from one machine
Best Day	41 rings	43 rings	35 rings	33 rings
Alignment	Twin Tunnels 18 m apart	Twin Tunnels 18 m apart	Twin Tunnels 12-18 m apart (<2 m in Asoke Rd.)	Twin & Stacked Tunnels
Maximum Cover	22 m	22 m	20 m	27 (SB), 22 (NB)
Minimum Cover	15 m	8 m	13 m	8 m
Minimum horizontal Curve Radius	200 m	190 m	300 m	200 m
Maximum Gradient	+ /- 4 %	+ /- 2 %	+ /- 2 %	+ /- 3 %
Geological Conditions	Stiff Clay & dense fine sand	Stiff Clay & dense fine sand	Mostly in Stiff Clay Layer	SB:-Stiff Clay & sand NB:-Soft – Stiff Clay
Max. Water Level above Invert	7 m	7 m	10 m	9 m
Location of highest Water pressures	Thiam Ruam Mit - Pracharat Bumphen	Lat Phrao – Phahonyothin	Sukhumvit – Sirikit	Silom – Sam Yan

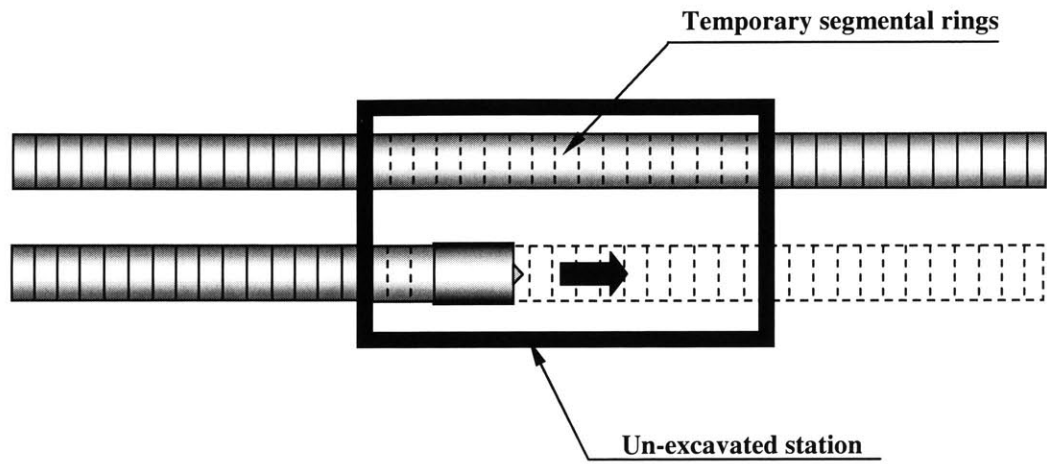
5.4.2 Tunneling Methodology

Generally, the North Section's approach was to start tunneling as early as possible and drive through the launching station prior to their excavation. The North contract (i.e. Tunneling Sections A and B) was awarded one year after the South contract (i.e. Tunneling Sections C and D). Hence, to achieve the promised schedule, contractors had to start the tunneling work before the excavation of stations had been completed. For example, in Section A, the EPB shield driving from Thiam Ruam Mit station progressed from a launch shaft inside the north end of the station to Pracharat Bamphen station, through each diaphragm end wall and the un-excavated station as shown in Figure 5.13a and similarly at Sutthisan station until its arrival at Ratchada station, which had by that time been fully excavated and the base slab constructed. Temporary segmental lining rings were used as the shield excavated within the un-excavated station box. These segmental rings were then removed during the excavation of the station. Tunnel drive sequences of Tunneling Sections A and B are shown in Figure 5.14 and Figure 5.15, respectively.

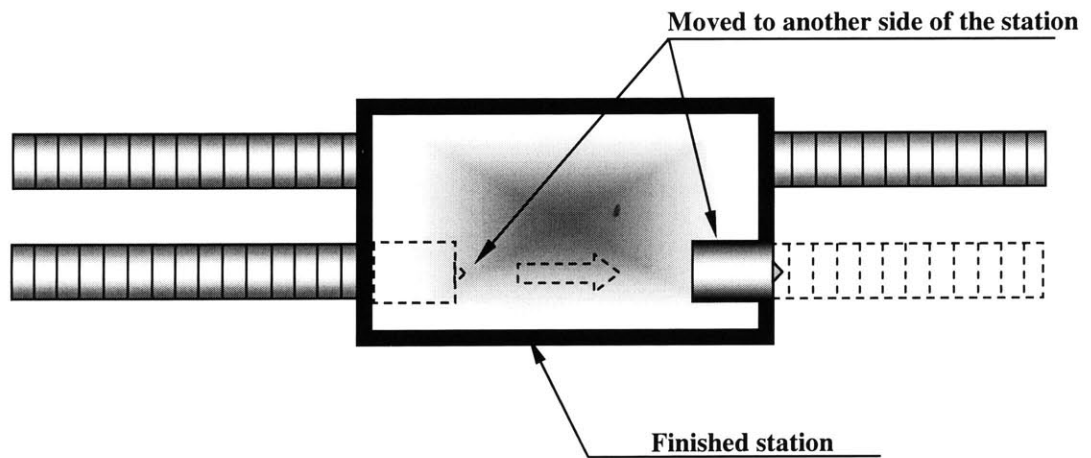
Note that EPB shields were designed to be able to grind through diaphragm walls in the North Tunnel Section as shown in Figure 5.18 and Figure 5.19. The remaining drives with these two shields involved single drives between stations and retrieval from within the completed station. As shown in Figure 5.15, the drives by Obayashi (Section B) from the north end of Ratchada station to Phahonyothin station involved tunneling through the incomplete Lat Phrao station. The shields had to be disassembled and moved to Bang Sue station to be re-launched for the excavation of the tunneling section between Bang Sue and Kamphaeng Phet. This was primarily due to: (1) the delays in underpinning work between Phayonyothin and Mo Chit stations, and (2) the delays in occupation of one end of the site at Kamphaeng Phet station in Chatuchak market resulting in the shield's being unable to drive through the incomplete station.

By contrast, in the South Tunnel Section (see Figure 5.16 and Figure 5.17), where the station work started earlier, it was possible to complete intermediate station excavation in advance of the shields. The South contractors started tunneling later but avoided an extra length of

temporary tunnel by not having to tunnel through un-excavated station boxes. In the case of Section C (see Figure 5.16) the shield cut through the station end walls and was skidded through the station to the far end where tunneling re-commenced as shown in Figure 5.13b. For Section D (see Figure 5.17), with Herrenknecht machines (Shields No. 7 and No. 8), the diaphragm wall was broken out by hand as shown in Figure 5.20 and Figure 5.21. This approach required the construction of large blocks of ground treatment by jet grouting to stabilize the ground and permit safe entry and launching of the shield at the stations. As also observed in other early shield tunneling projects (Chapter 4), generally, the surface settlements near the launch shafts were higher due to the minimal cover to the soft clay and the slower initial penetration rates arising from the temporary back up arrangements while the shields were launched.



(a) North Tunneling Section (Sections A and B)



(b) South Tunneling Section (Sections C and D)

Figure 5.13 Tunneling procedures of the North and the South sections

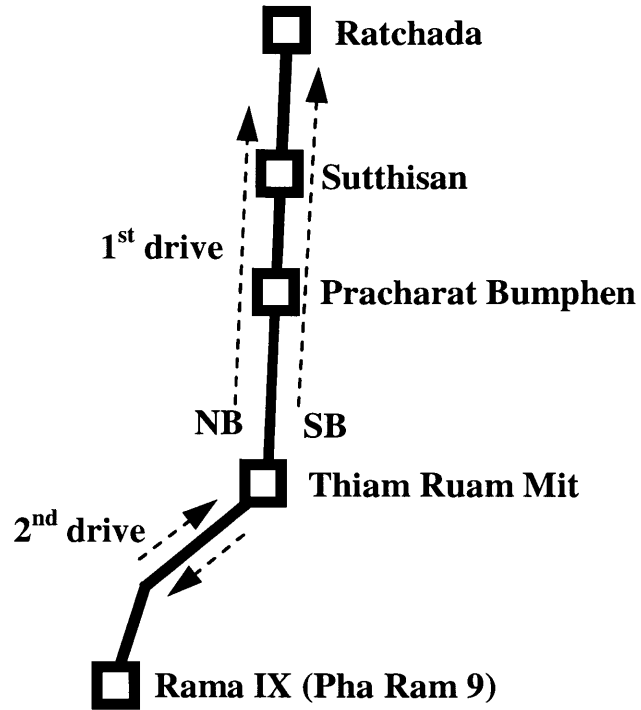


Figure 5.14 Tunnel drive sequence of Section A (North Section)

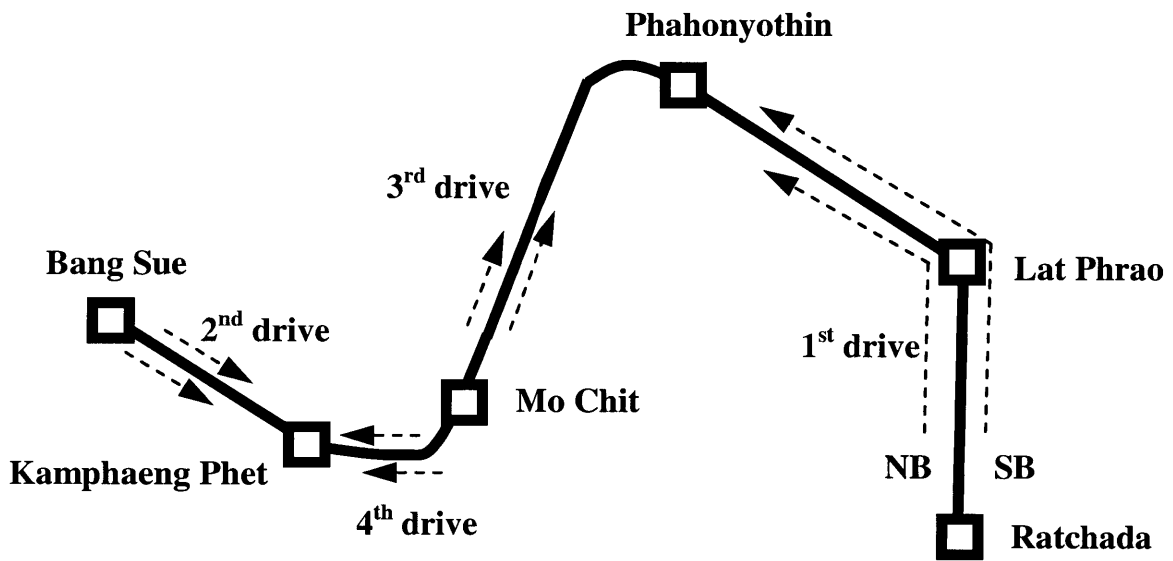


Figure 5.15 Tunnel drive sequence of Section B (North Section)

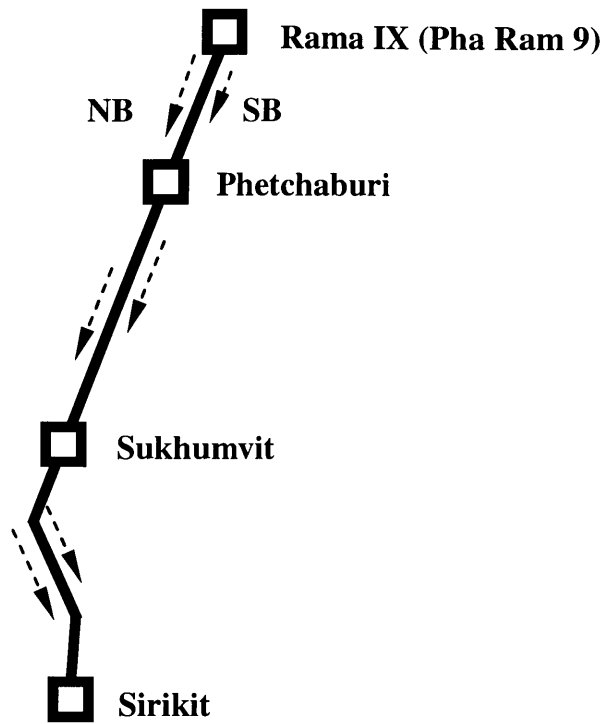


Figure 5.16 Tunnel drive sequence of Section C (South Section)

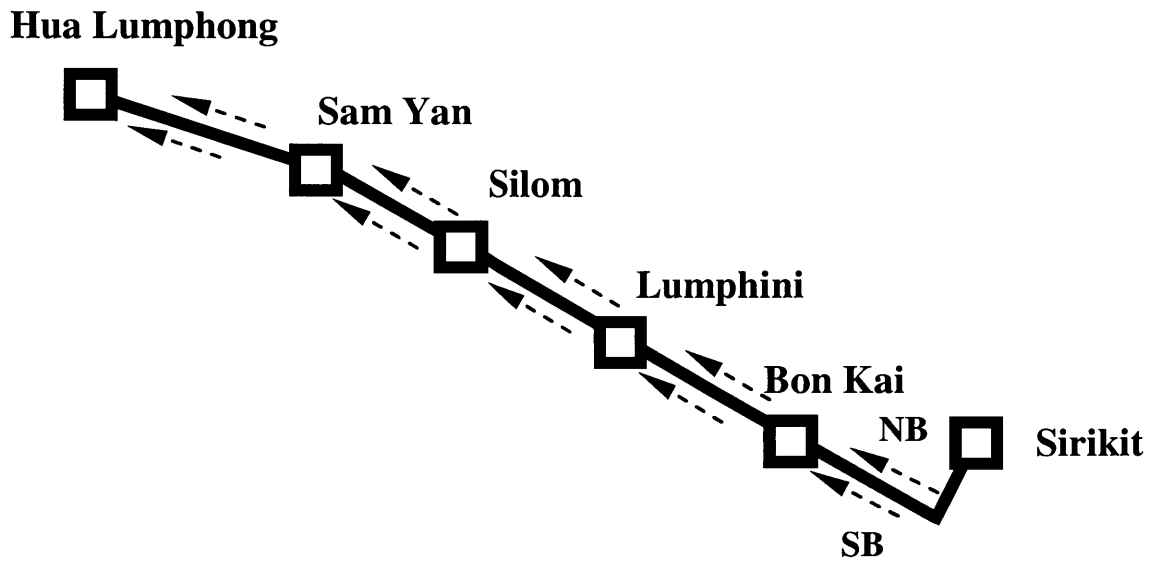


Figure 5.17 Tunnel drive sequence of Section D (South Section)



Figure 5.18 Diaphragm wall prepared for shield cutting through in Ratchada station (North Tunnel Section)

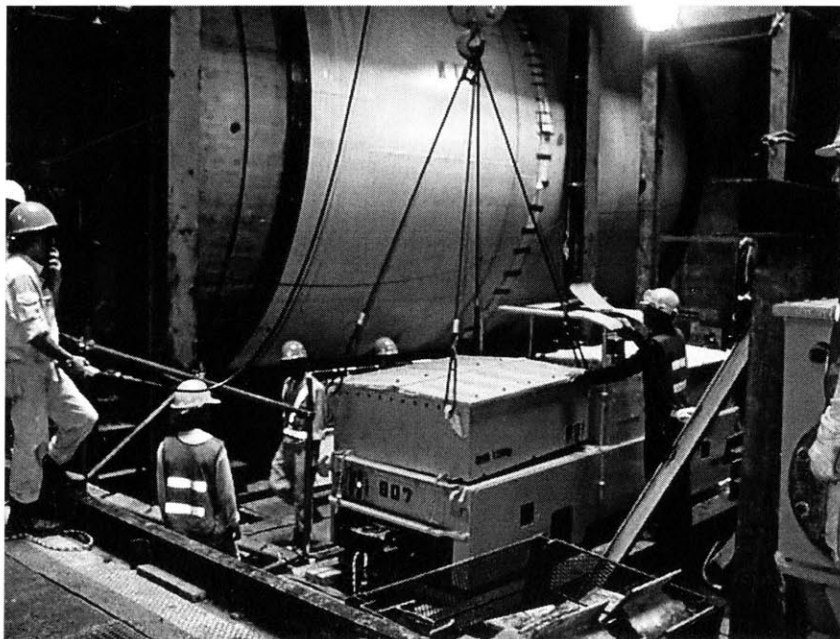


Figure 5.19 EPB shield cutting through the diaphragm wall

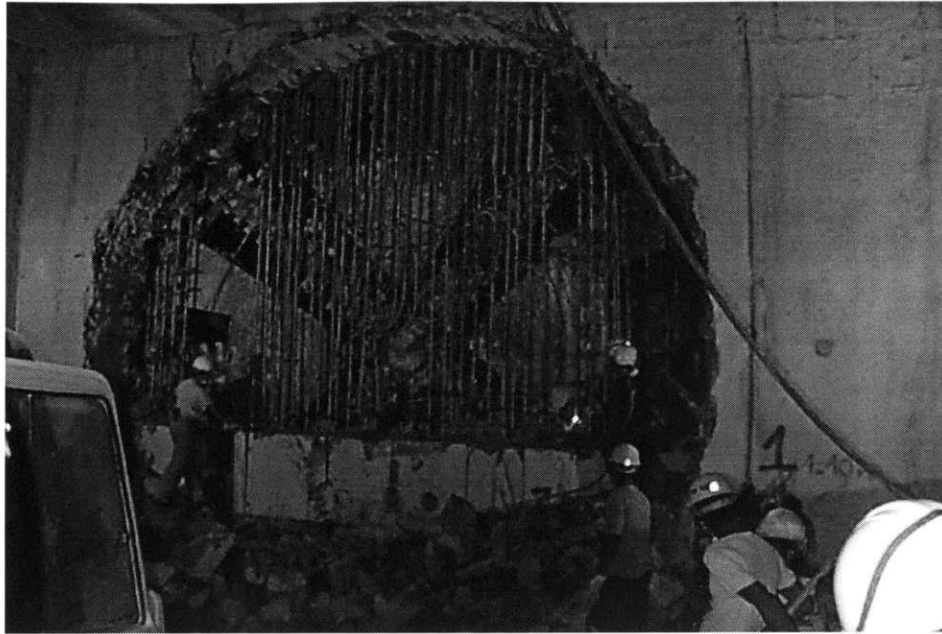


Figure 5.20 Breakthrough at Lumphini station (South Tunnel Section)

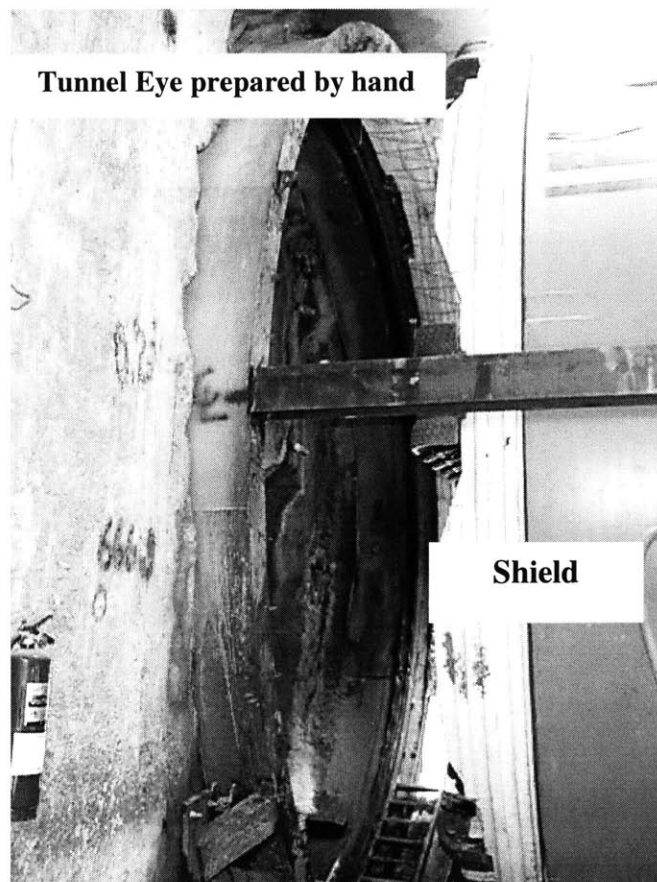


Figure 5.21 Breakout at Sirikit station (South Tunnel Section)

5.5 Tunnel Drive Details

5.5.1 Tunneling Section A

In Section A, the 6.30 m outer diameter twin-tunnel was excavated underneath Ratchadaphisek road (Figure 5.22), an eight-lane road, which is located in the north region of Bangkok. The distance between the axes of the twin tunnels was as wide as 15-20 m. The tunnel drive sequence is shown in Figure 5.14. Nishimatsu launched two EPB shields from a temporary start shaft inside Thiam Ruam Mit station (Figure 5.28) in April 1999. The southbound shield was launched first and followed by the northbound shield such that the first shield was about 100-150 meters (i.e. about 2 working weeks) ahead of the second shield. Backup equipment was initially fitted within the upper two levels of the launch shaft with umbilical cables and hoses linked to the machines. Each drive progressed 60 rings before the backup equipment was transferred to the tunnel. The tunnel drive commenced in stiff clay, which changed to largely dense fine sand as the depth increased between stations. The machines were operated at low face pressure with injection of water into the cutter chamber to maintain consistency within the screw conveyer. Face pressures of typically 50 kPa were used resulting in surface settlements from both shields. The spoil was transported by skips to a tipping hopper at the launch shaft. A vertical conveyer was used within the shaft.

Prior to completion of the drives through to the south end of Ratchada station, excavation of the Thiam Ruam Mit station was completed and the base slab cast as shown in Figure 5.23. The connecting diaphragm wall was broken out to ease the tunneling logistics in the shaft area. This shaft then served the drives between Thiam Ruam Mit station and Rama IX station and the depot approach with muck trains traveling through the station. Both shields were required to tunnel through several lines of driven piles remaining after two canal bridges (Figure 5.22) were underpinned as shown in Figure 5.24. The general procedure was to slowly grind through the piles and then once past the bridge stop the machine and inspect the face and remove any tangled reinforcing wire, which hadn't been removed through the screw conveyer. A small block of jet grouted ground improvement (see Figure 5.25) was

constructed ahead of tunneling in the crown of the tunnel to facilitate the planned inspection. These machines were also required to negotiate jet grouted zones around the cross passage connections to two incomplete intervention shafts which will be used as emergency exits, entrances for rescuers, and ventilation shafts (see also Figure 5.27). Both southbound and northbound drives were temporarily delayed for about 5 weeks during the tunneling through of Sutthisan station to undertake repair of the seals which had started to leak soil into the main bearing.

Four instances of significant loss of ground occurred in this section during shield operation. The first incident occurred during entry of the face (i.e. earth chamber) to examine the bearing seals before Pracharat Bamphen station. The second incident resulted from running the shield with zero face pressure or fully open mode. The third incident was due to an inexperienced operator failing to advance the shield during rotation of the cutter wheel especially during the initial drive. The other ground loss occurred when attempting to re-start the machine in the shallow drive towards the depot after a stoppage due to a failure of the screw conveyor. Difficulties were encountered in steering during the re-start. These problems resulted in significant surface settlement of more than 100 mm. Apart from the third incident, breaking two large high pressure water mains beneath Ratchadaphisek road, which were quickly repaired, the other incidents resulted in minimal disruption at the surface. Best performances are summarized in Table 5-9.

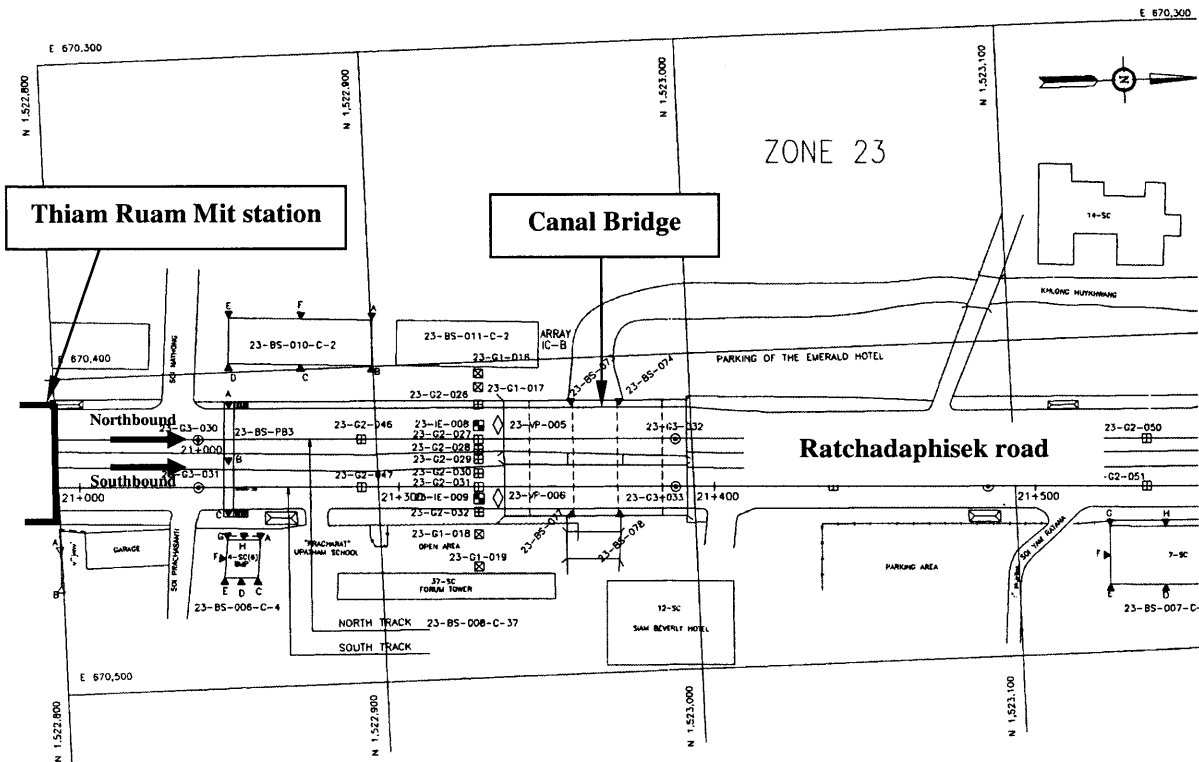


Figure 5.22 Map of Tunneling Section A showing the initial drive from Thiam Ruam Mit station

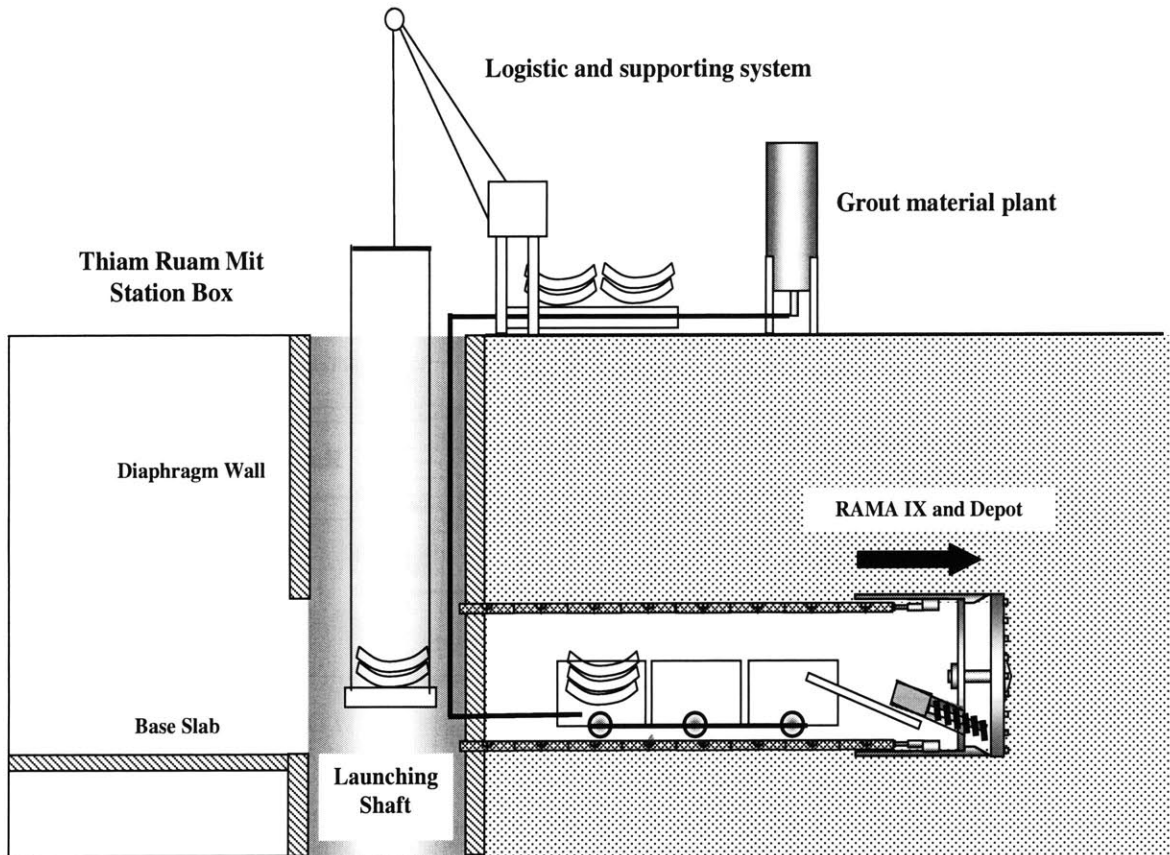


Figure 5.23 Schematic diagram of the initial drive of Section A showing station box, launching shaft and supporting system located in the ground surface

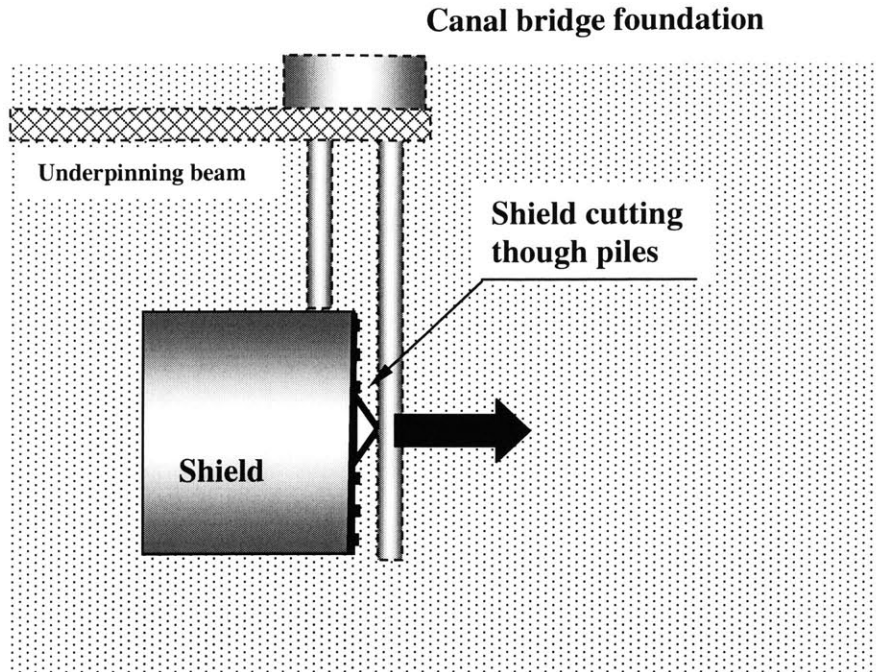


Figure 5.24 Shield cutting through piles of an underpinned canal bridge

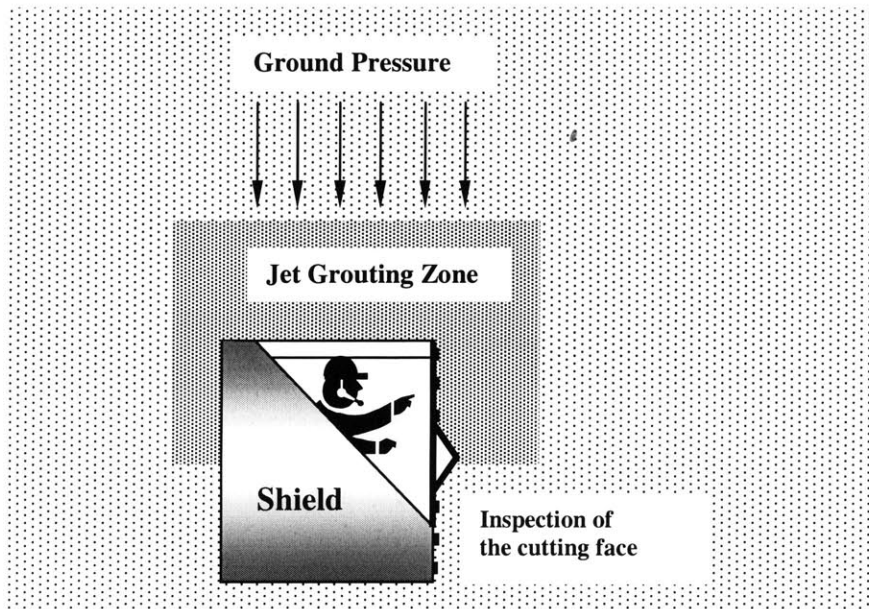


Figure 5.25 Jet grouting zone providing stability during the inspection of the shield's cutting face

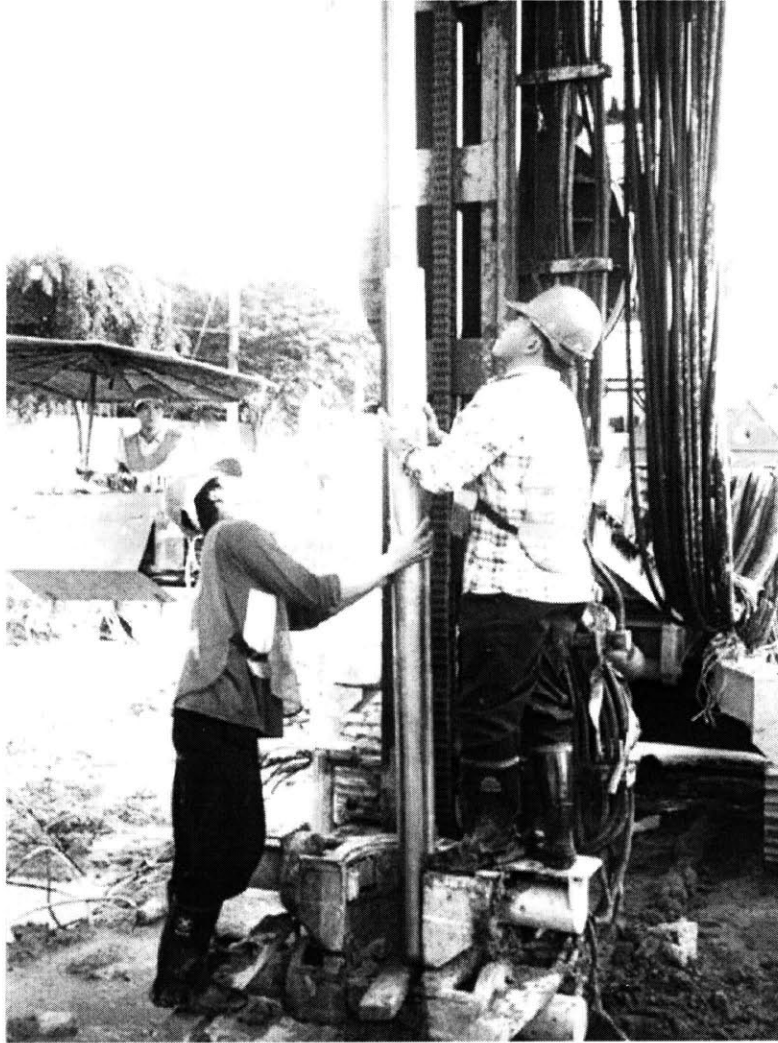
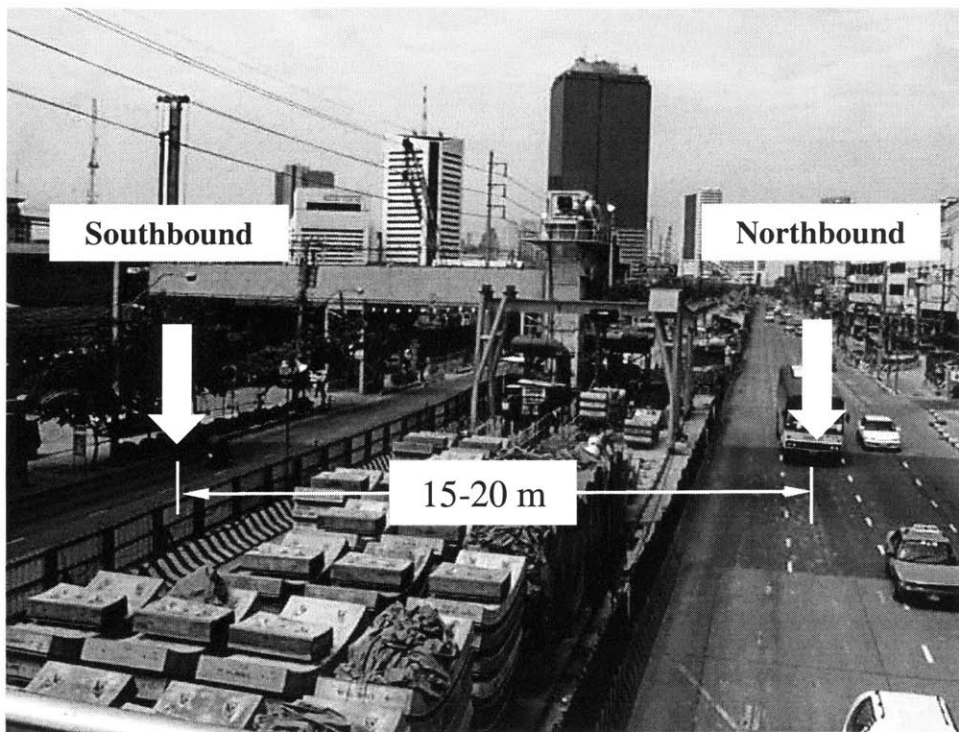


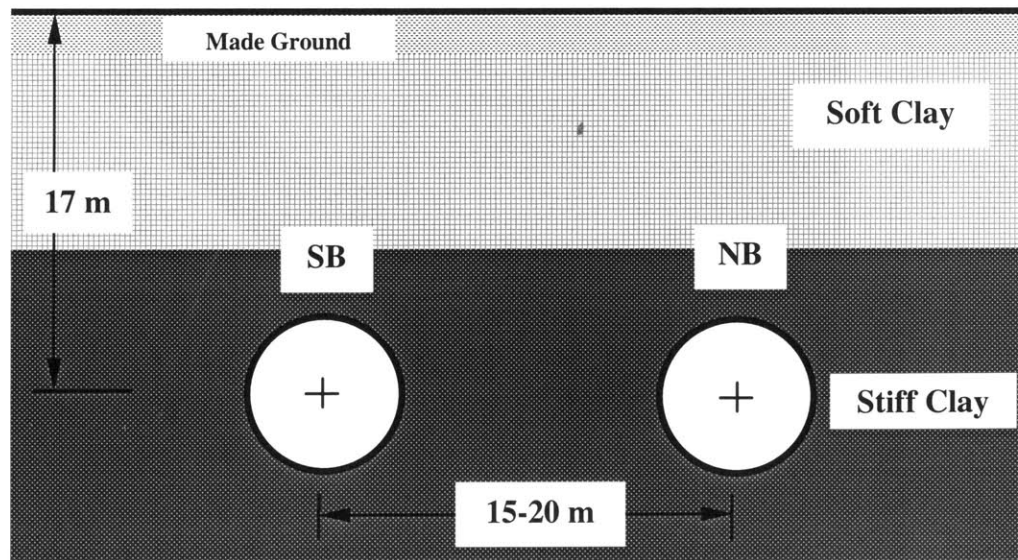
Figure 5.26 Workers installing grouting pipe used for soil improvement or grouting zone



Figure 5.27 Intervention shaft during construction



(a) Location of Thiam Ruam Mit station in Ratchadaphisek road



(b) Typical tunnel profile of Section A

Figure 5.28 Thiam Ruam Mit station and typical tunnel alignment

5.5.2 Tunneling Section B

The southbound tunnel drive was started from a launch shaft formed from a partitioned section within the Ratchada station box (see the map in Figure 5.1) in February 1999. A second shield started the northbound drive approximately 100 m behind the first in March. The backup equipment was assembled on the surface with umbilical hoses and cables powering the initial drive of the SB tunnel of 98 rings to beyond the previously underpinned Khlong Naem Kaew bridge piles (see Figure 5.29). While the cutters were being inspected after cutting through the 30 cm thick driven piles, the backup equipment was shifted into the tunnel. The initial drive of the NB tunnel was limited to 53 rings, which was the minimum requirement to install the backup equipment in the tunnel and launch shaft. The Kawasaki EPB shields were designed to grind through the fiberglass rod reinforced concrete of the diaphragm wall and the small diameter redundant bridge piles at Khlong Naem Kaew which were only lightly reinforced. Each machine also had to contend with the bored pile foundations of a pier of the Lat Phrao road overpass (Figure 5.29). Two piers were underpinned in advance and a new steel box girder beam was installed supported by new barrettes constructed on either side of each running tunnel. Each machine was stopped for a period of approximately ten days while a crew broke out the more heavily reinforced 80 cm diameter piles by hand in a chamber in which the roof was supported by a zone of jet grout previously created from the surface around the redundant piles. Face conditions of hard clay beneath the jet grout layer required minimal support. These EPB shields continued through Lat Phrao Station installing temporary rings, which were subsequently broken out during station excavation. Before each intersection with the diaphragm wall, Obayashi provided a small jet grout layer to inspect the cutting wheel and change the cutters where necessary. A 450 mm diameter pipe was also installed inside each end of the station box in a bore-hole from the surface to provide ventilation of the face during cutter pick inspection, to facilitate a wire drop survey of the alignment and to provide future access for invert concrete supply. Both tunnels advanced to Phahonyothin station beneath the relative narrow corridor (Figure 5.32) provided by Lat Phrao road avoiding pedestrian bridge piled foundations at two locations. A slight delay incurred at the midpoint of the drive grinding through the previously constructed jet grout treatment zones adjoining the cross passages (at the time not constructed) for the ventilation Shaft No.6. These two machines were retrieved from a

reception shaft prepared within the end of the incomplete Phahonyothin station for subsequent re-installation at Bang Su station. Prior to re-commencement at Bang Su, both machines had their main bearings completely stripped, cleaned and the bearing seals replaced. From Bang Su the machines drove back to Kamphaeng Phet Station in December 1999 followed by Mochit to Phahonyothin stations and then Mochit to Kamphaeng stations.

In terms of surface settlement control, the most challenging sections involved tunneling beneath some railway warehouses, and the two level overpass adjacent to Phahonyothin station. The initial advance after launching was typically up to 40 rings per week, where relatively large surface settlements were observed. Once the backup equipment was installed, Obayashi consistently achieved 80 rings per week. The shields were operated entirely in the EPB mode, in which applied face pressures were maintained at approximately 200 kPa with polymer injected into the cutter chamber to condition the generally stiff clays for pumping back to the service shaft.

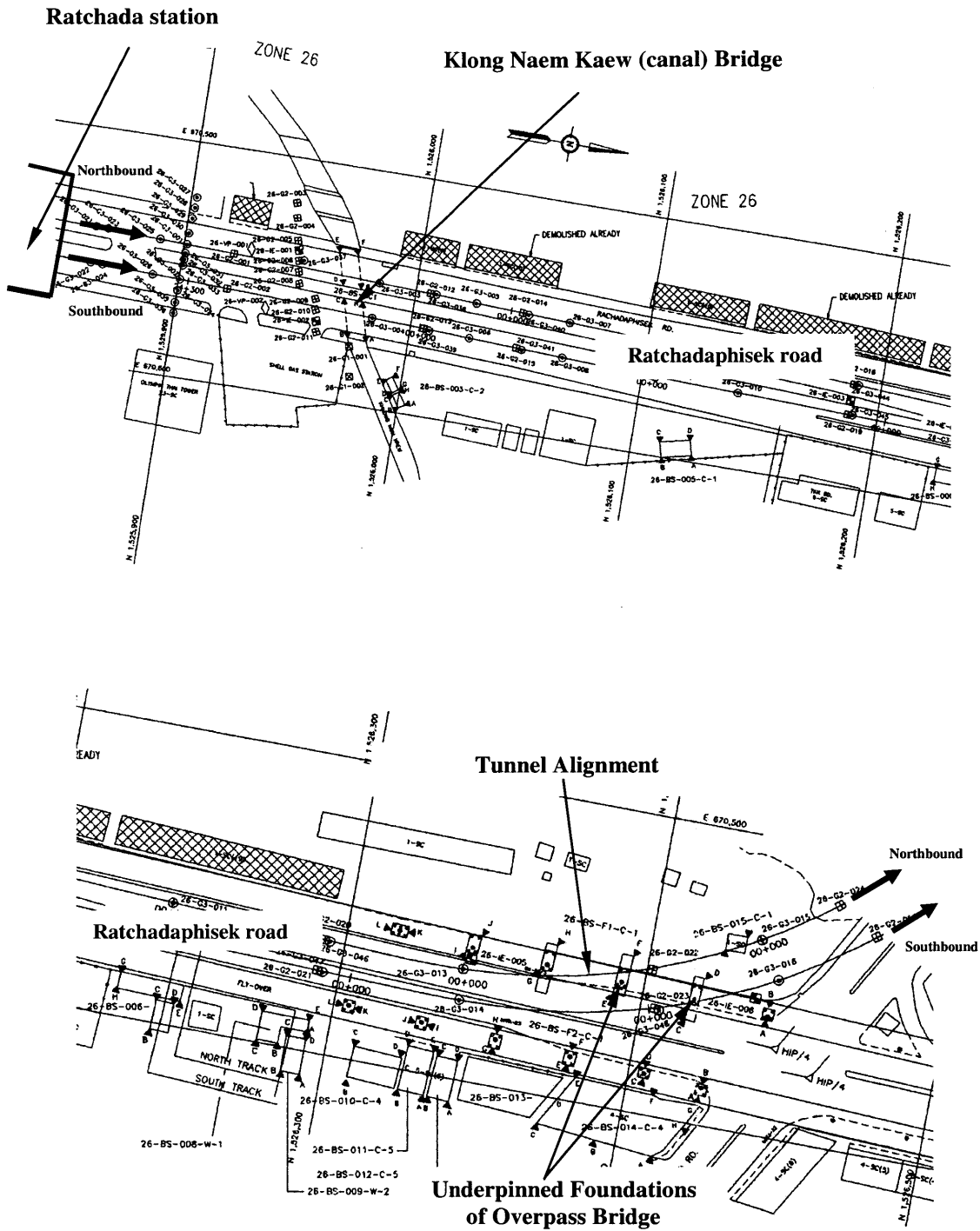
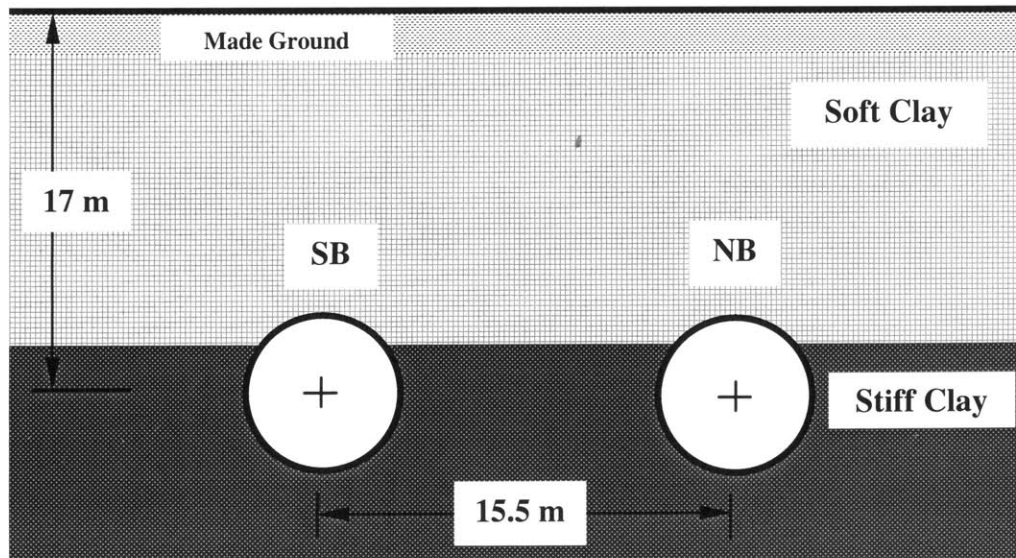


Figure 5.29 Map of Tunneling Section B showing the initial drive from Ratchada station



(a) Location of Ratchada station in Tunneling Section B



(b) Tunnel section underneath Ratchada station

Figure 5.30 Ratchada station and the tunnel alignment in Section B

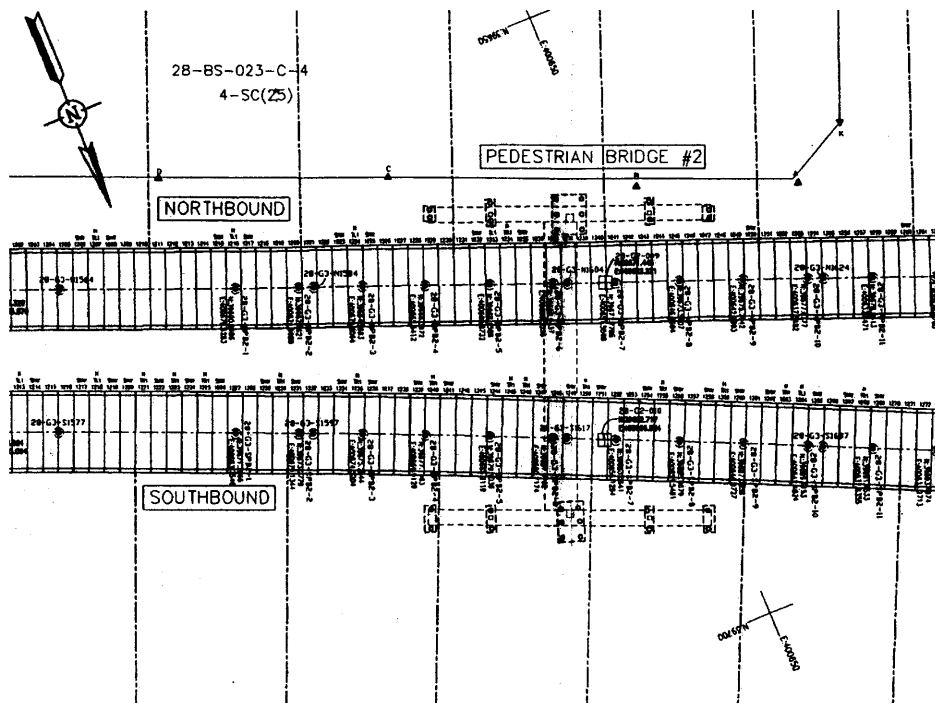
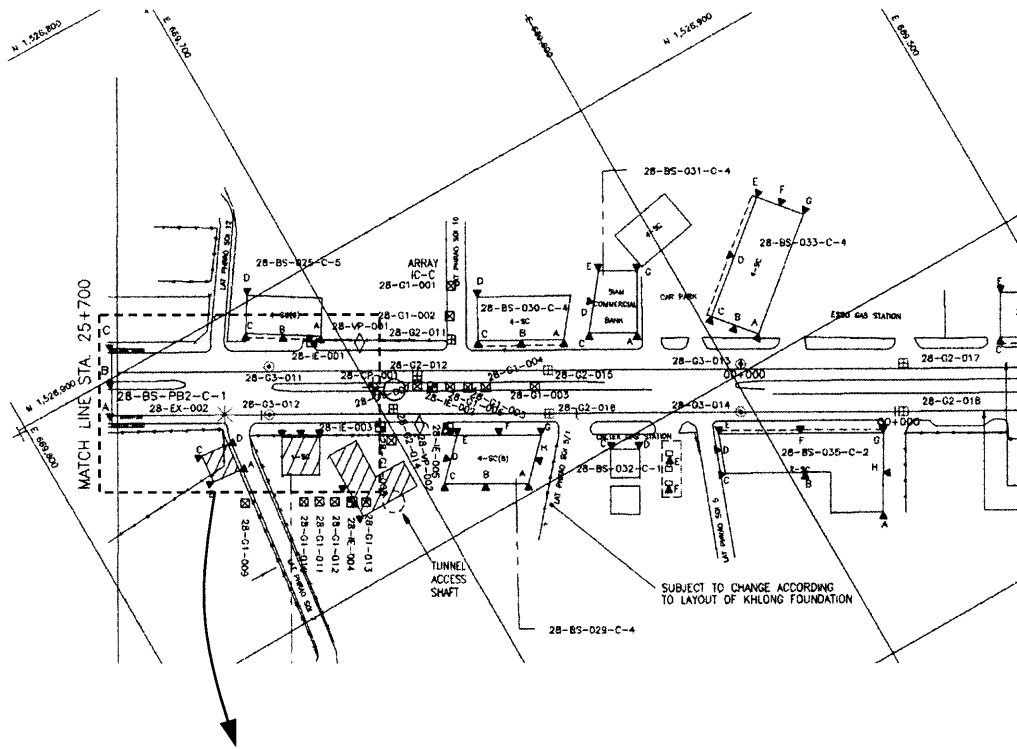


Figure 5.31 Tunnel Section B from Lat Phrao station to Pahonyothin station

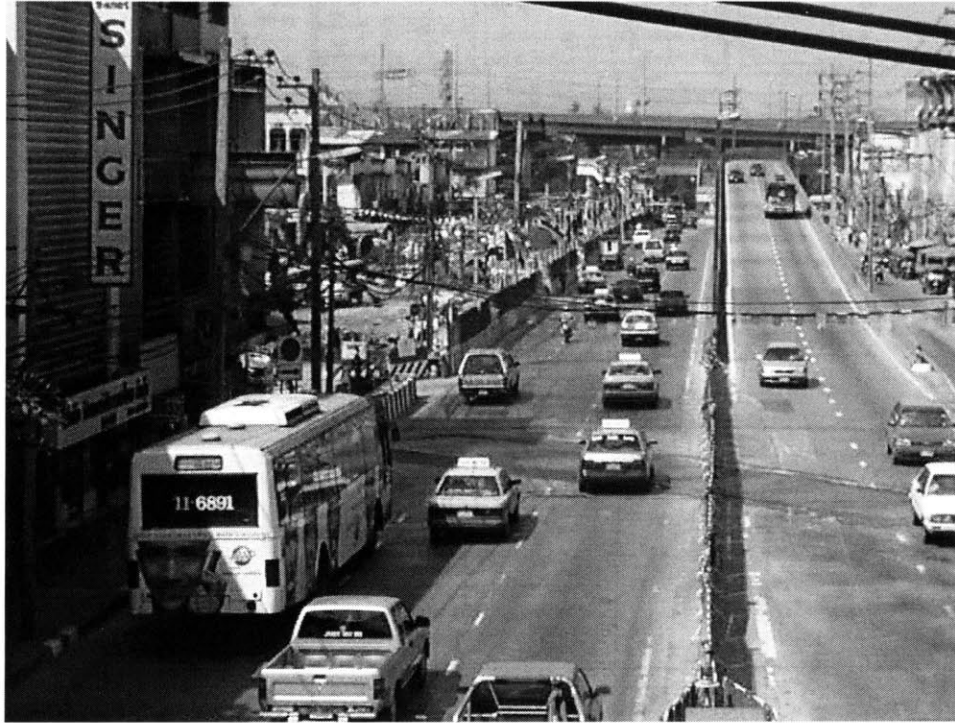


Figure 5.32 Location of Section B from Lat Phrao station to Phahonyothin station

5.5.3 Tunneling Section C

Two Kawasaki EPB shields were launched from a structurally complete Rama IX station (see Figure 5.16) in June 1999 heading south towards Petchaburi station beneath Ratchadaphisek road. Figure 5.33 illustrates the location of Rama IX station and the tunnel section. These two shields differed slightly from the Nishimatsu and Obayashi shields with respect to the shove rams, a cutter motor, a ring former and a double man lock as a contingency for compressed air working as detailed in Table 5-8. The shields, complete with backup equipment, were installed in the Rama IX station soon after the base slab was cast. Initial surface settlements of approximately 30 mm, recorded close to the station, were reduced when the face pressure was increased. Additionally, surface heave was observed due to very high face pressure because of a trial and error process. The shields successfully passed through the back filled holes left after the removal of redundant driven piles of Khlong Sam Sen bridge soon after crossing Rama IX road. The northbound shield cut through the Petchaburi station diaphragm wall (Figure 5.36) at the end of August and was followed soon after by the machine on the SB drive. Typically, progress rates of 80 rings per week were achieved with a best week of 111 rings from one shield.

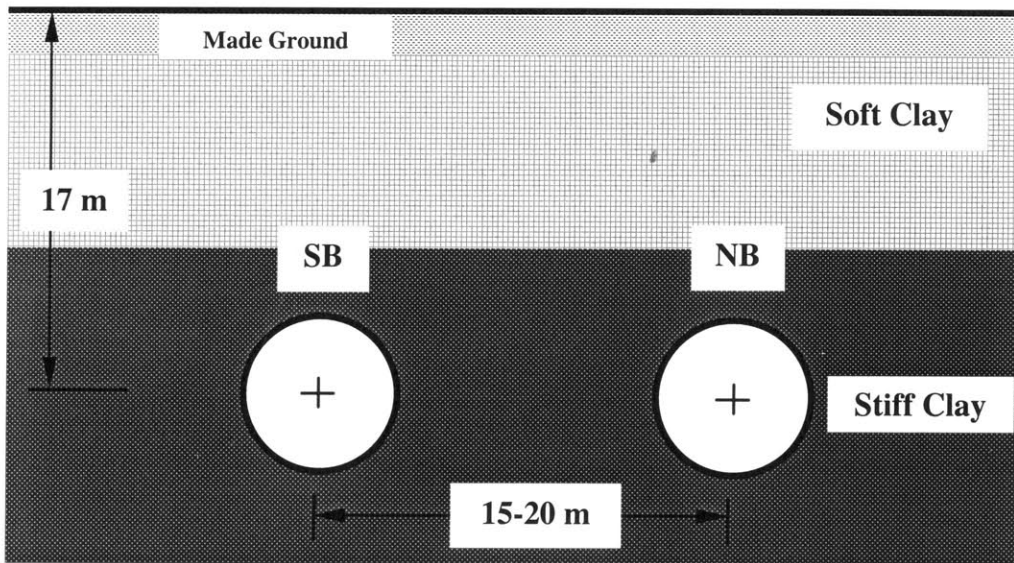
Soon after re-launching from the completed Petchaburi station, the shield passed the Khlong Saen Saep bridge piles (Figure 5.35), which were removed following re-construction of the bridge (see the tunneling alignment in Figure 5.34, and the tunnel section in Figure 5.35). The North bound shield suffered a bearing seal failure beneath the south abutment of the bridge which necessitated stopping the machine for 7 weeks beneath the southern bridge approach span. The seals were replaced in situ by Kawasaki (Figure 5.37). The machine subsequently reached Sukhumvit station without further incident. The SB shield was similarly affected soon after passing the same bridge requiring similar repairs. From Phetchaburi station to Sukhumvit station, the EPB shields had to drive underneath Asoke road, one of the most congested areas in Bangkok. Since Asoke road is very narrow, the distance between the southbound and the northbound tunnel is very small (see the tunnel alignment in Figure 5.38, and the tunnel section in Figure 5.39). Furthermore, many existing buildings were located very close to the tunnel alignment. Hence, the surface settlement

became a major concern. All of this made this tunneling drive one of the most challenging sections in the South Tunnel section.

The EPB shields continued from Sukhumvit to Sirikit stations generally successfully but with a significant ground loss incident attributable to hurriedly conceived ground stabilization for two tunnel sumps. A low strength concrete diaphragm cut-off wall was installed in saturated sand below the tunnel invert to facilitate subsequent tunnel invert sump construction. At Sukhumvit station (Figure 5.40), the diaphragm wall panels were constructed ahead of tunneling and extended below the tunnel invert but also above the tunnel to within a few meters of the surface. When the NB shield cut through these walls, the tail skin of the shield was trapped between the upper and lower sections of diaphragm wall (see Figure 5.41) due to large settlements arising from over-excavation. In the case of the NB drive, the settlements were significant and very high shove forces were required to free the shield. In the following SB drive, the settlements were limited due to rigorous control of the face pressure and the shield negotiated the diaphragm walls without incident. Typical face pressures of 150 to 250 kPa resulted in a minimum surface settlement of typically 10 to 15 mm. Both tunnels passed beneath spans of two expressway bridges and the existing elevated railway, which crossed the alignment with no adverse effects to the foundations or the spans.



(a) Rama IX station



(b) Tunnel section underneath Rama IX station

Figure 5.33 Rama IX area and typical tunnel alignment

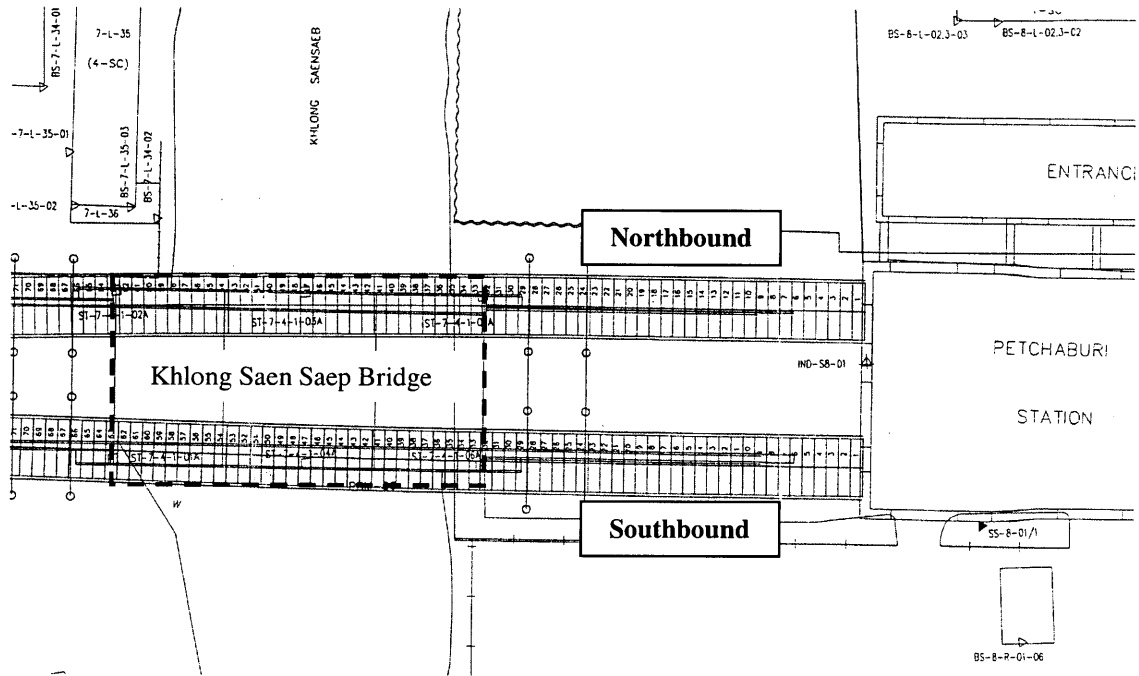
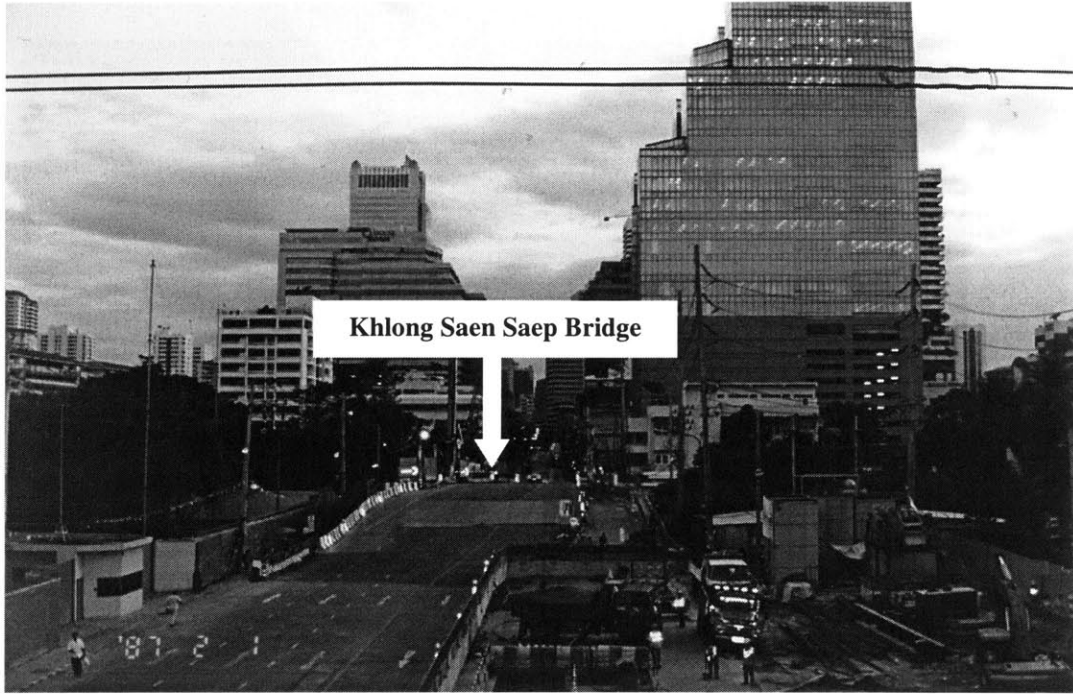
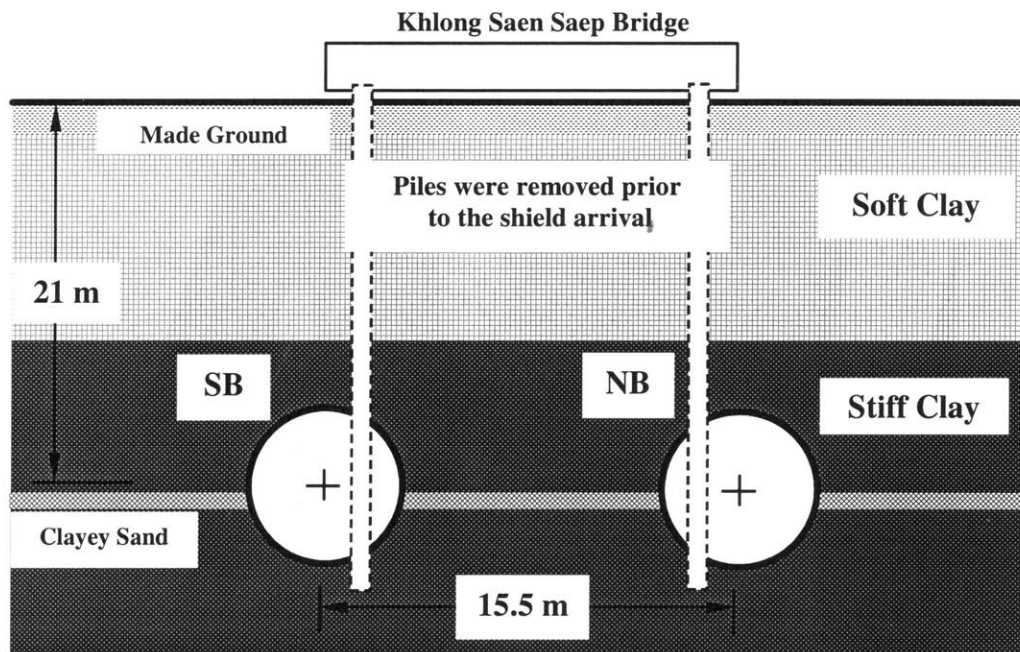


Figure 5.34 Alignment of Tunnel Section C showing the initial drive from Petchaburi station to Sukhumvit station and Khlong Saen Saep Bridge



(a) Khlong Saen Saep bridge ahead of the Phetchaburi station



(b) Tunnel section underneath Phetchaburi station

Figure 5.35 Phetchaburi station and tunnel alignment

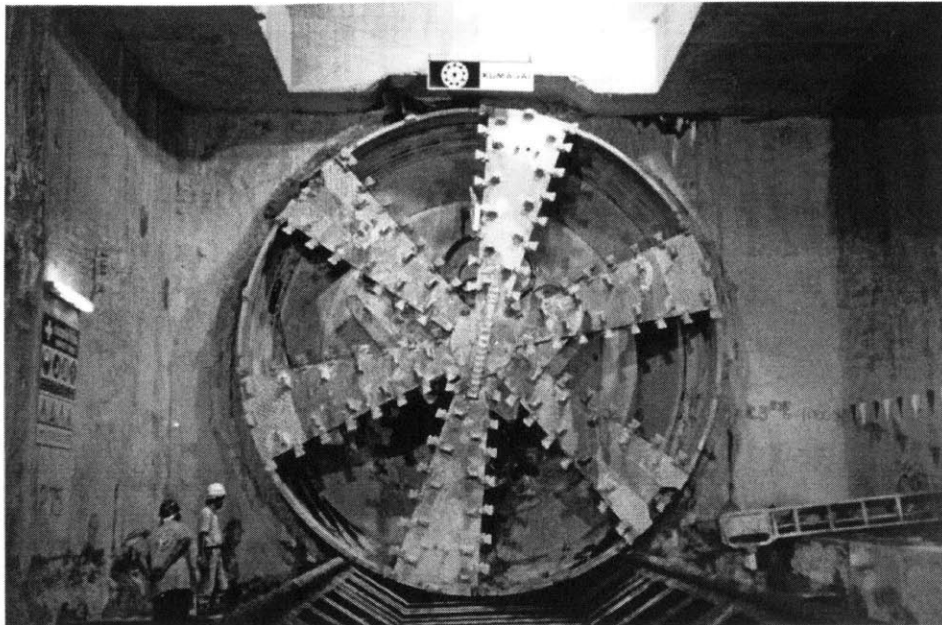


Figure 5.36 Breakthrough of the northbound shield at the Phetchaburi station diaphragm wall (Section C)

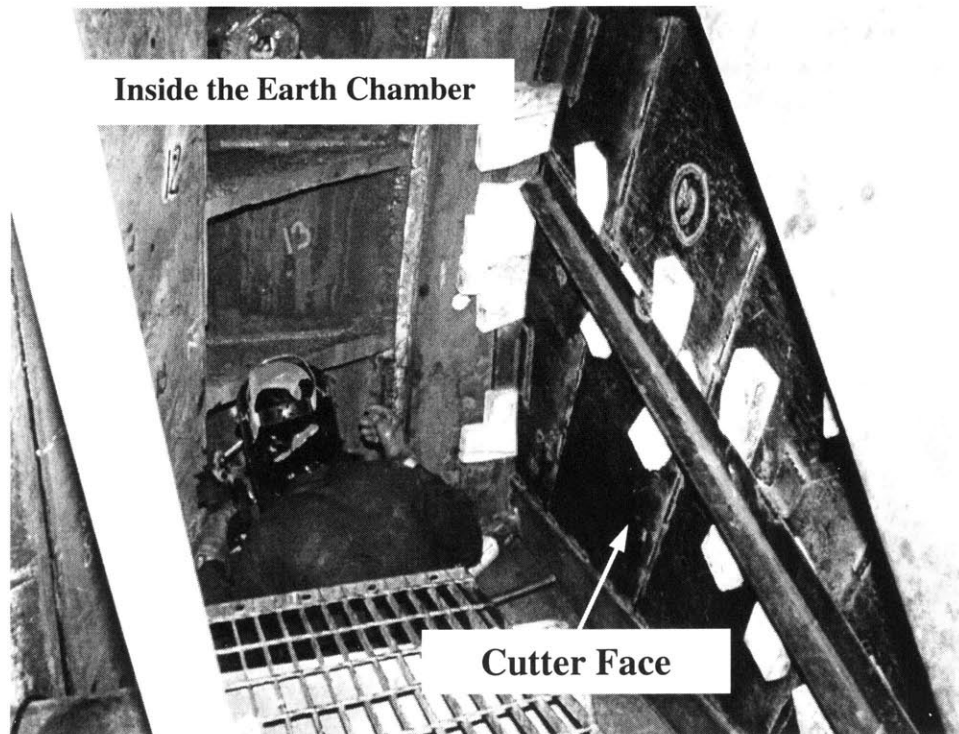


Figure 5.37 Worker fixing the bearing seals inside the earth chamber of the northbound shield (Section C)

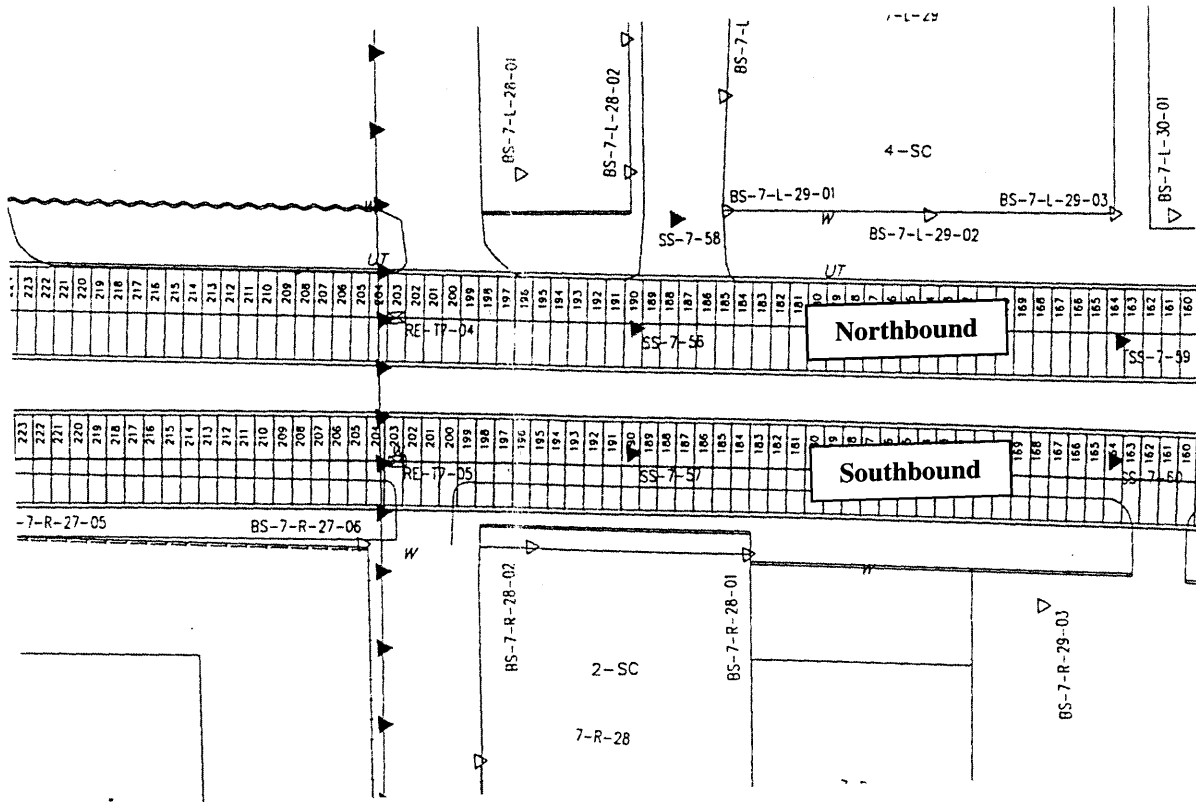
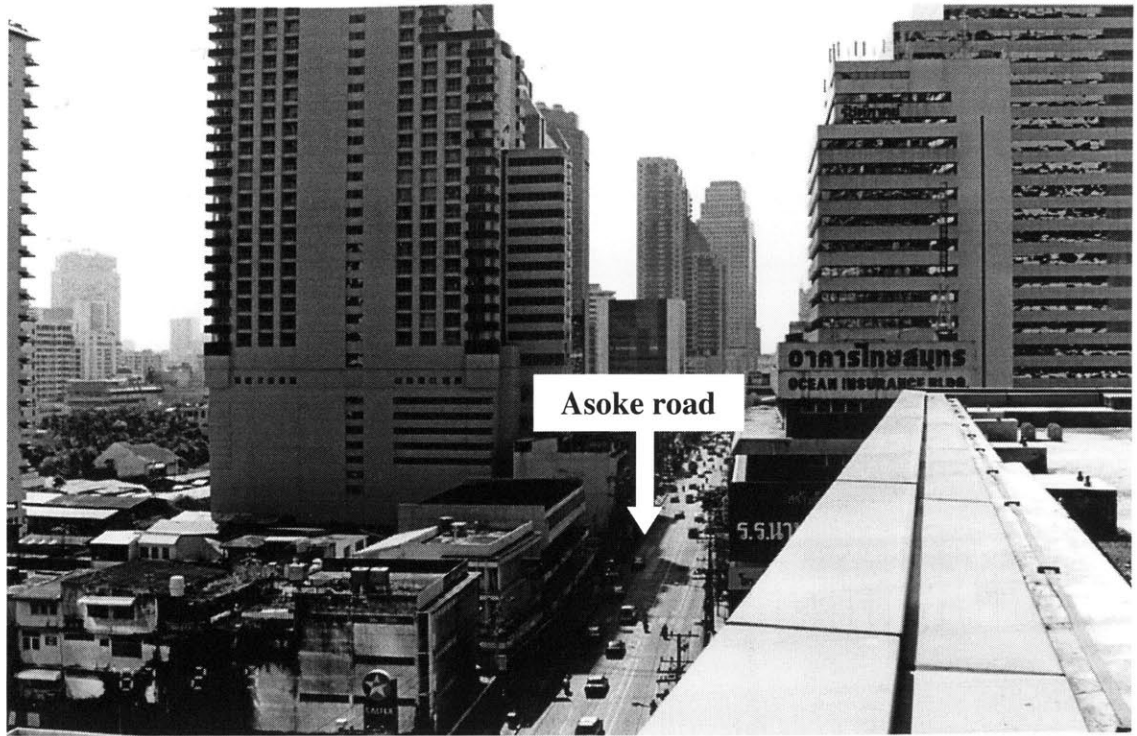
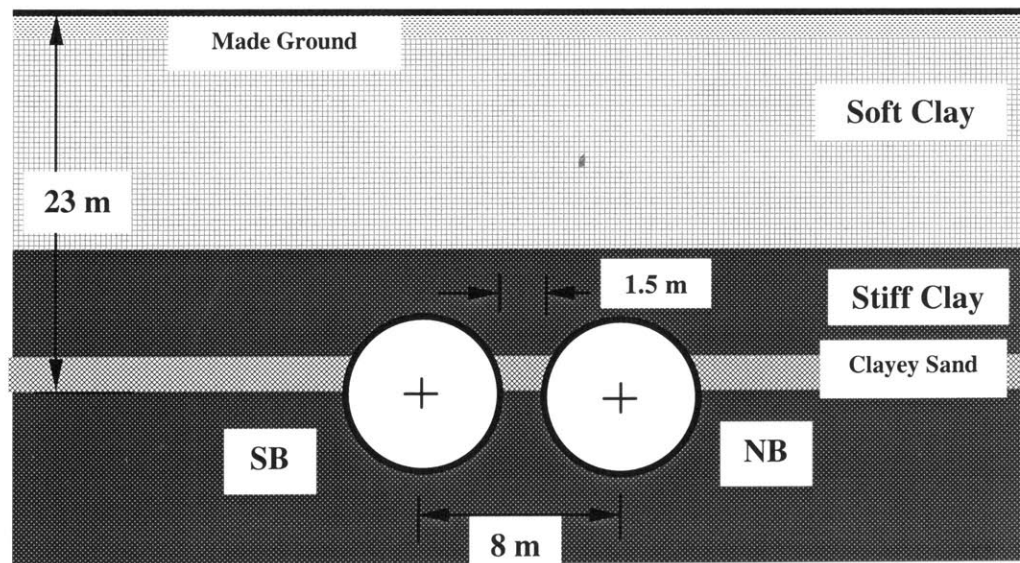


Figure 5.38 Tunnel alignment along Asoke road (between Phetchaburi and Sukhumvit stations)

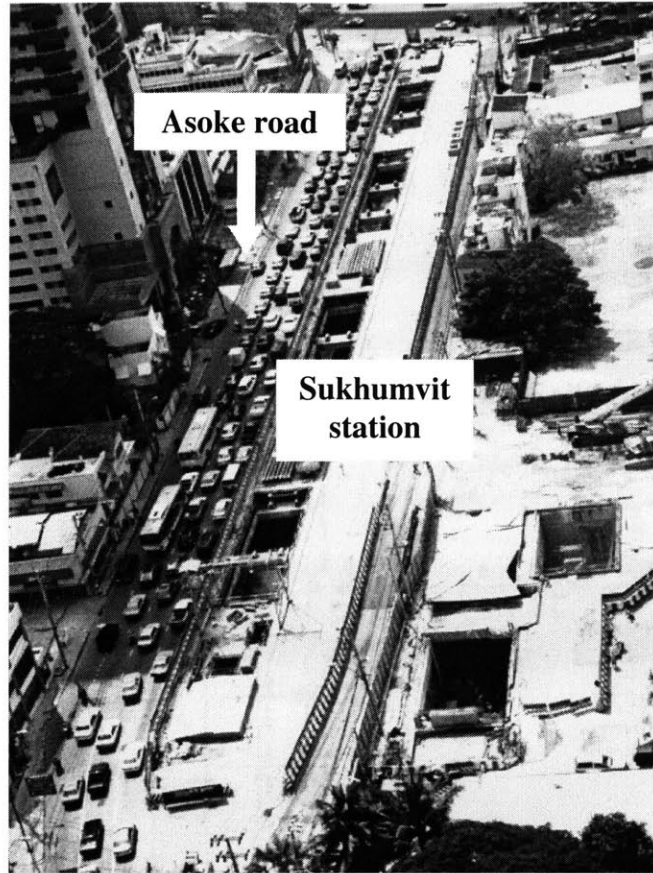


(a) Asoke road connecting between Phetchaburi and Sukhumvit stations

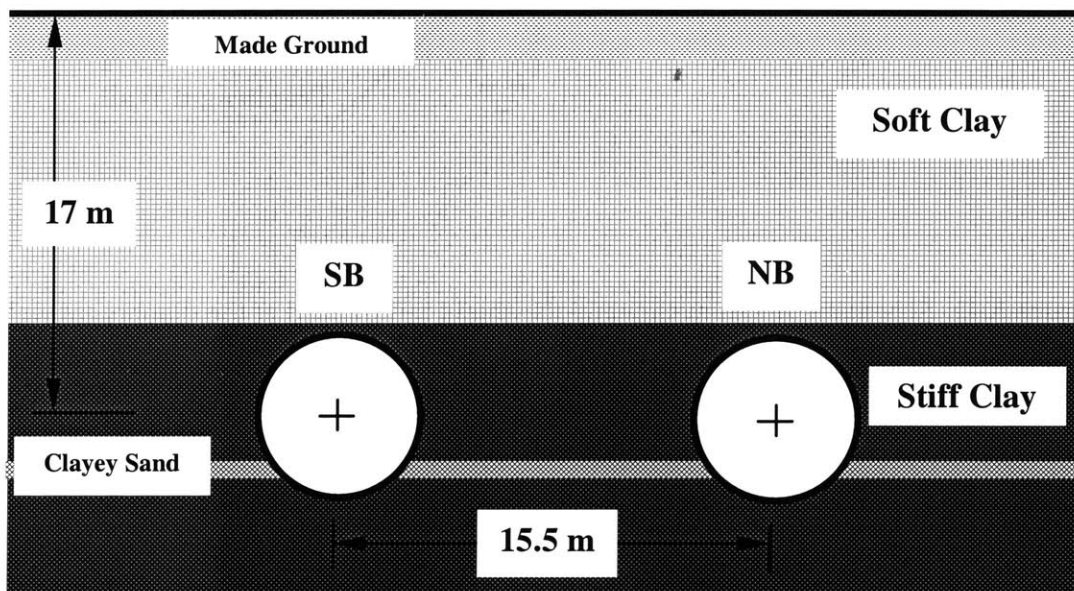


(b) Tunnel section underneath Asoke road

Figure 5.39 Location and tunnel section of the tunnel drive under Asoke road (between Phetchaburi and Sukhumvit stations)



(a) Location of Sukhumvit station



(b) Tunnel section underneath Sukhumvit station

Figure 5.40 Sukhumvit station and tunnel alignment

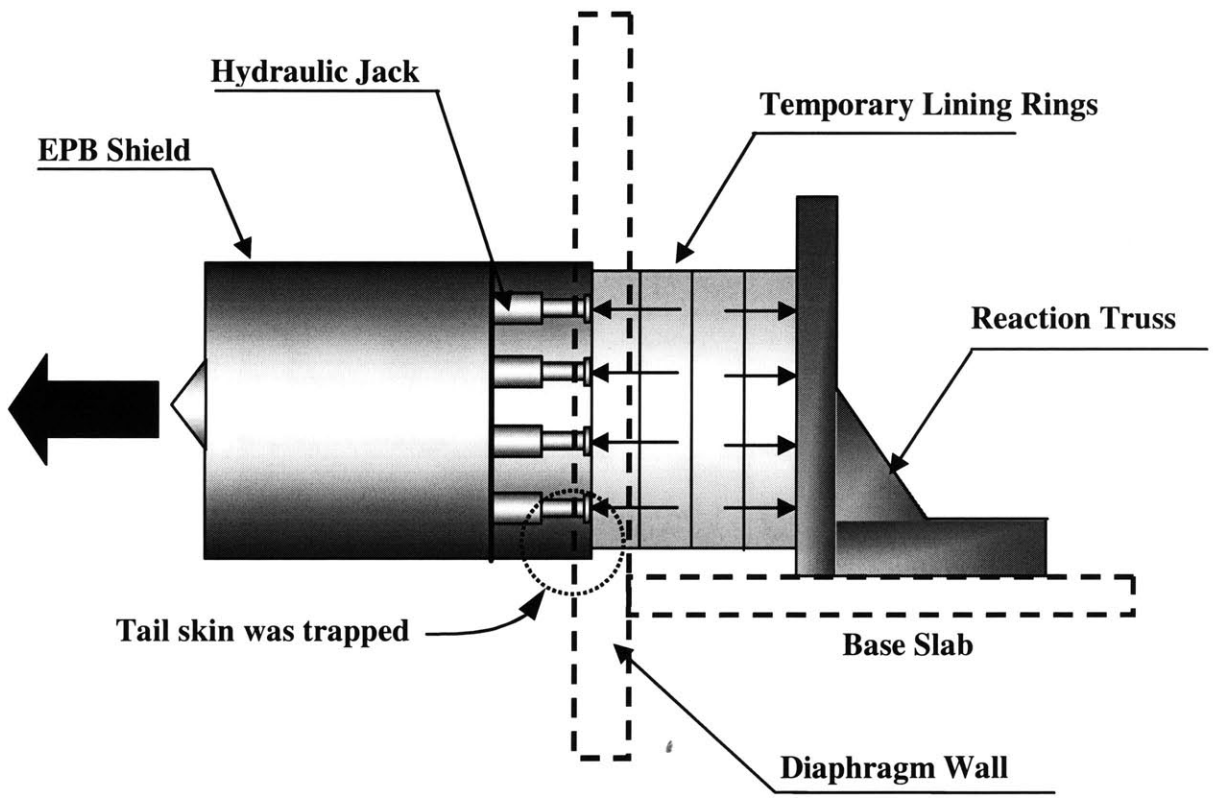


Figure 5.41 Schematic diagram showing the shield tail trapped at the diaphragm wall

5.5.4 Tunneling Section D

At Sirikit station, Bilfinger & Berger launched two re-conditioned Herrenknecht EPB shields previously used on the Taipei MRT project with the backup equipment for the shields fully installed within the station box from the outset as shown in Figure 5.42. The tunnel drive sequence of Section D is shown in Figure 5.17. The Southbound tunnel machine was launched from the southern end of the partially completed Sirikit station in July and the northbound tunnel drive in late August 1999. Both shields commenced tunneling in a 200 m radius curve on a 3% down gradient in order to pass close beneath a 2.5 m diameter water supply tunnel in Rama IV road (Figure 5.43). The shields initially pumped the spoil back to the shaft but this was changed a little earlier than scheduled to transport by skips due to the harder than expected nature of the clays encountered after about 150 rings. The tunnels passed beside bored piled foundations of a new fly-over bridge being constructed by the Bangkok Municipal Authority at the Ratchadaphisek - Rama IV intersection. The shields were skidded through completed station boxes at Bon Kai, Lumpini, Silom, Sam Yan and retrieved at Hua Lamphong. Between the midpoint of Lumpini and Bon Kai to near Hua Lamphong stations, the northbound tunnel is stacked above the southbound tunnel so that the northbound tunnel crown is located in the Soft Clay layer and the southbound tunnel has to be excavated within the sand layer as shown in Figure 5.45.

At several locations, the tunnels passed within 1.5 m of actively loaded piles of an overpass abutment and a 22 story hotel, where the tunnels were stacked vertically above each other. The lower southbound tunnel was excavated first and followed by the upper northbound tunnel. Surface settlements at these critical locations were kept to less than 15 mm. The most challenging section was located 50 m beyond Sam Yan station, where the tunnels passed close under and above a 3.6 m diameter high pressure water supply tunnel as shown in Figure 5.48. This tunnel could not be taken out of service during tunneling as it supplied approximately one third of Bangkok with water. After careful analysis, engineers established a permissible settlement value of the water tunnel of 8 mm for the lower SB drive. In order to stay below this value, the septum between the two tunnels was reinforced in advance with horizontal mini piles drilled from the station. A precision horizontal drill was used for this purpose. Careful attention to face pressure control enabled the shield to quickly transit the

critical zone without incident. Extensometers were installed to monitor the water tunnel settlement and a horizontal electrolevel inclinometer was installed alongside the horizontal mini piles. Unfortunately, the results were inconsistent and could not be relied upon at the critical time. The NB shield successfully passed 1.2 m above the water tunnel without incident.

Two significant ground loss incidents occurred along the Rama IV road section. The first during the approach of the deeper SB machine into Lumphini station, where the face changed very suddenly from hard clay to sand and difficulties were encountered in balancing the face pressure (Figure 5.46). The second incident occurred during the entry of the SB shield through the jet grout treatment zone and diaphragm wall at Silom station where the tunnel was at maximum depth (Figure 5.47). The in situ face conditions comprised saturated fine sand with the water table slightly above the crown. Besides the grouting, there were two other measures used to prevent the ground water intrusion. First, a 2 m thick low strength concrete block had been cast inside the station (Figure 5.47). Second, sand bags were used to control the water and sand flow beneath the shield (see also Figure 5.47). However, a settlement trough of approximately 25 cm developed on the surface over a width of about 10 m. Extensive high pressure grouting of the area adjacent to the tunnel and jet grouting stabilized the affected area and limited the settlement of the adjacent 20 story building to a safe recorded magnitude of less than 4 mm.



Figure 5.42 Backup equipment installed behind the SB shield inside Sirikit station

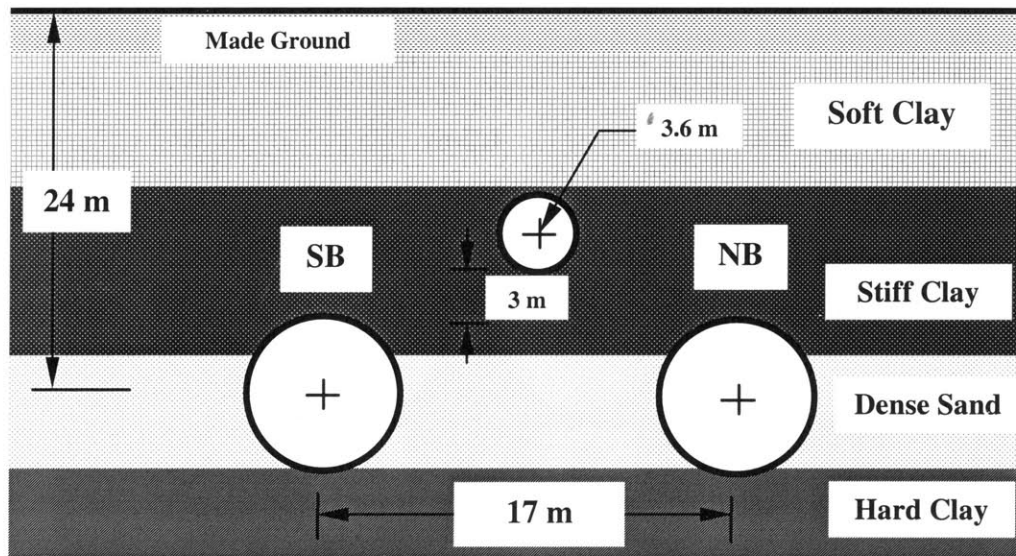
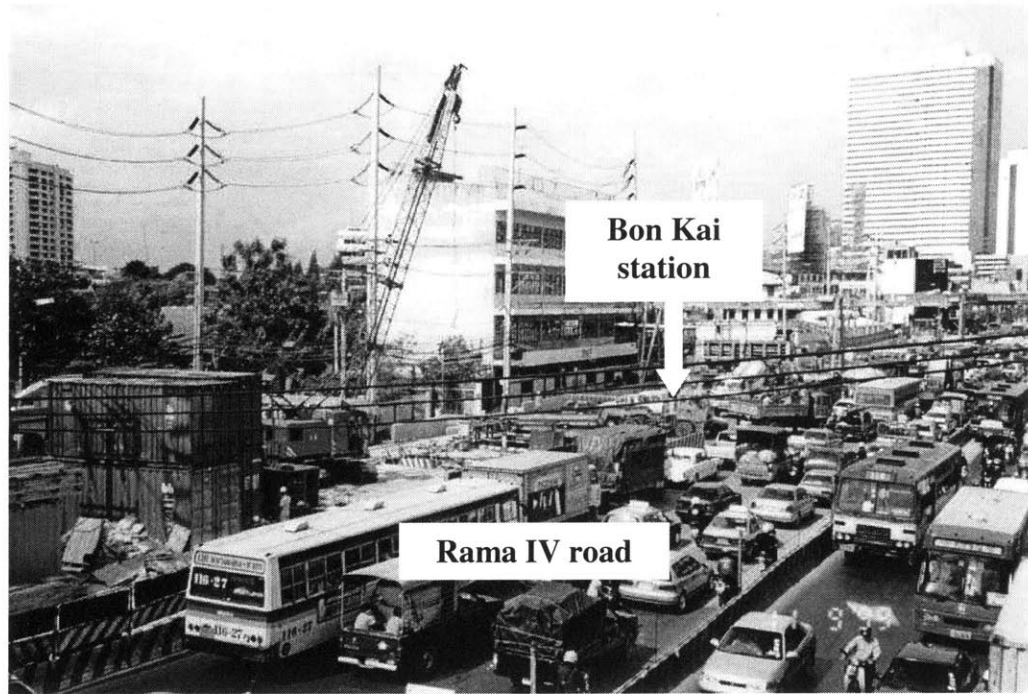
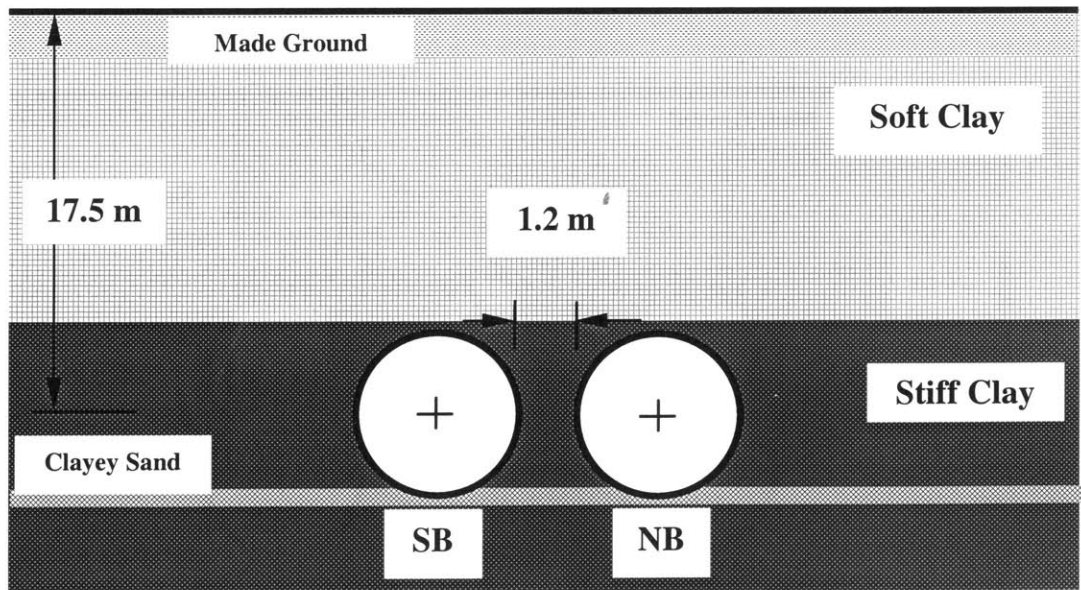


Figure 5.43 Tunnel alignment from Sirikit station to Bon Kai station

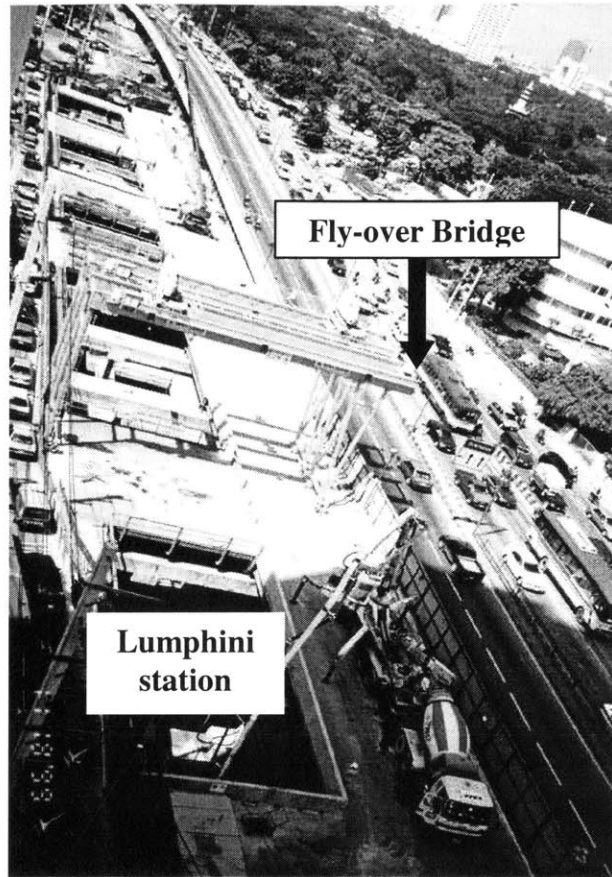


(a) Location of Bon Kai station

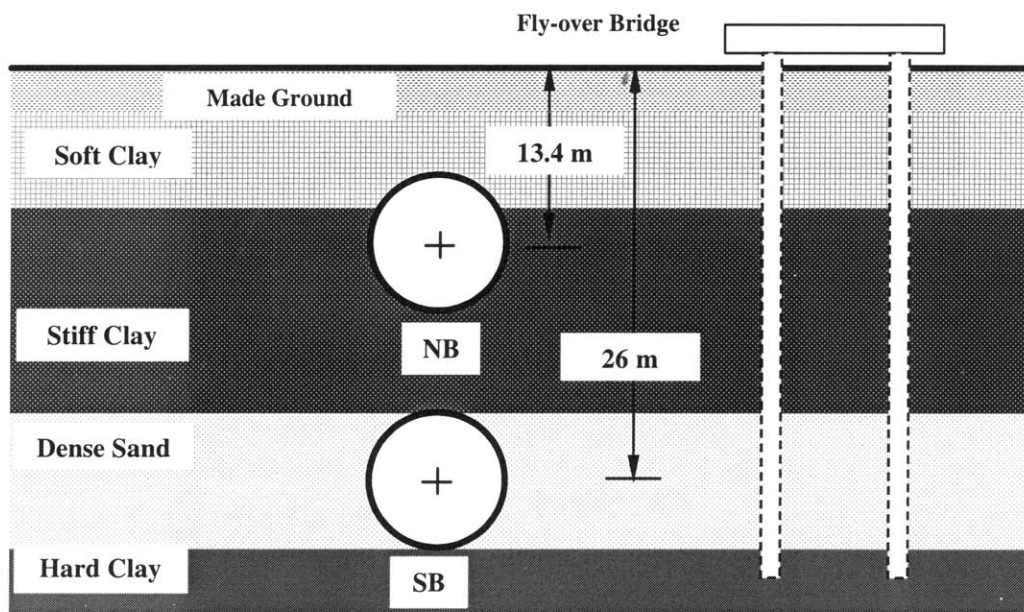


(b) Tunnel section underneath Bon Kai station

Figure 5.44 Bon Kai station and tunnel alignment



(a) Location of Lumphini station



(b) Tunnel section at Lumphini station

Figure 5.45 Lumphini station and tunnel alignment

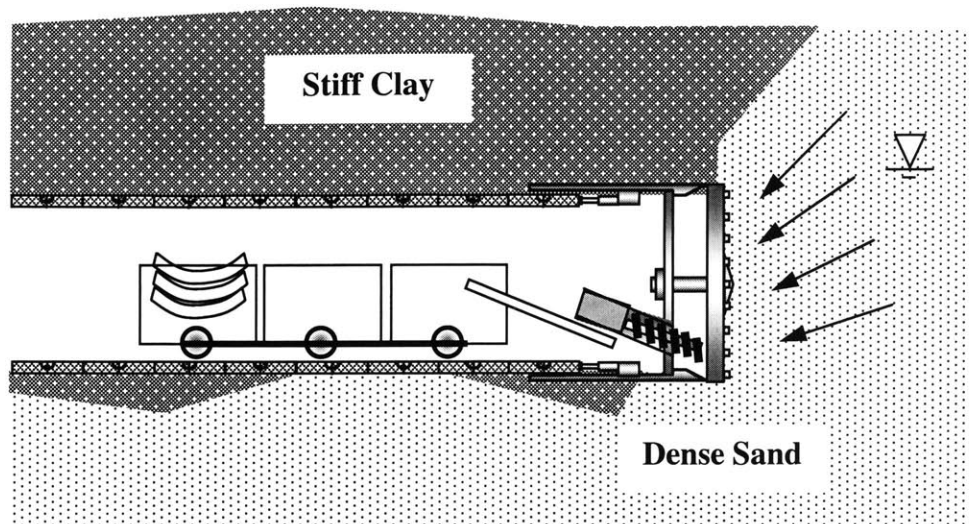


Figure 5.46 Ground loss as the SB shield encountering a sand layer under Rama IV road

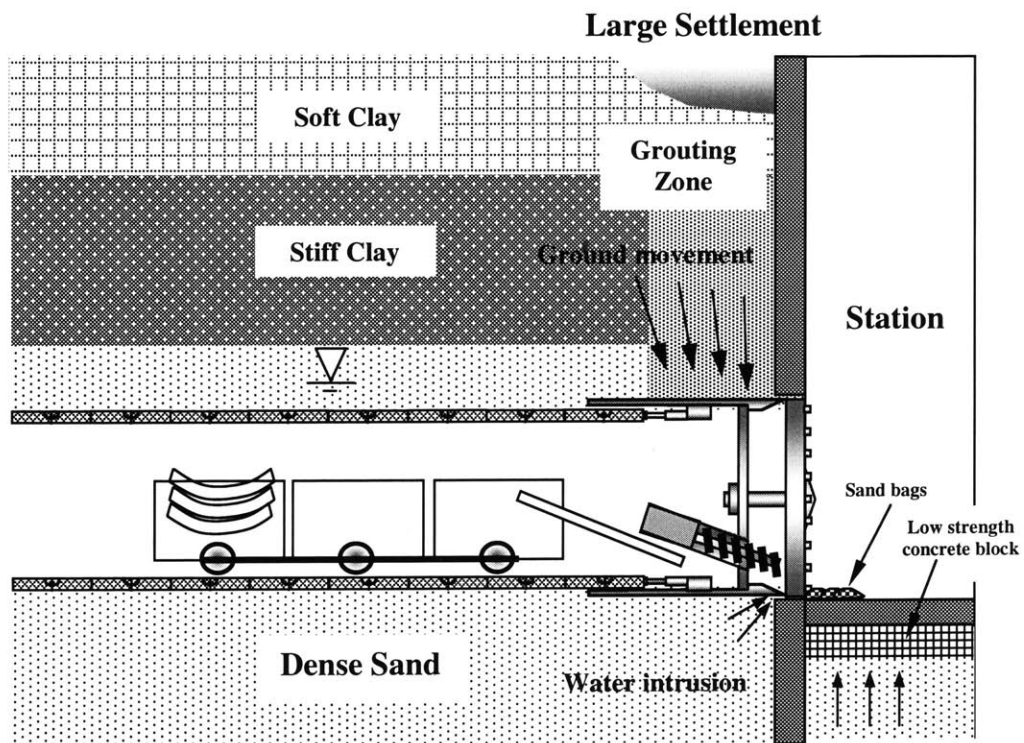


Figure 5.47 Ground loss occurring as the SB shield approaching Silom station

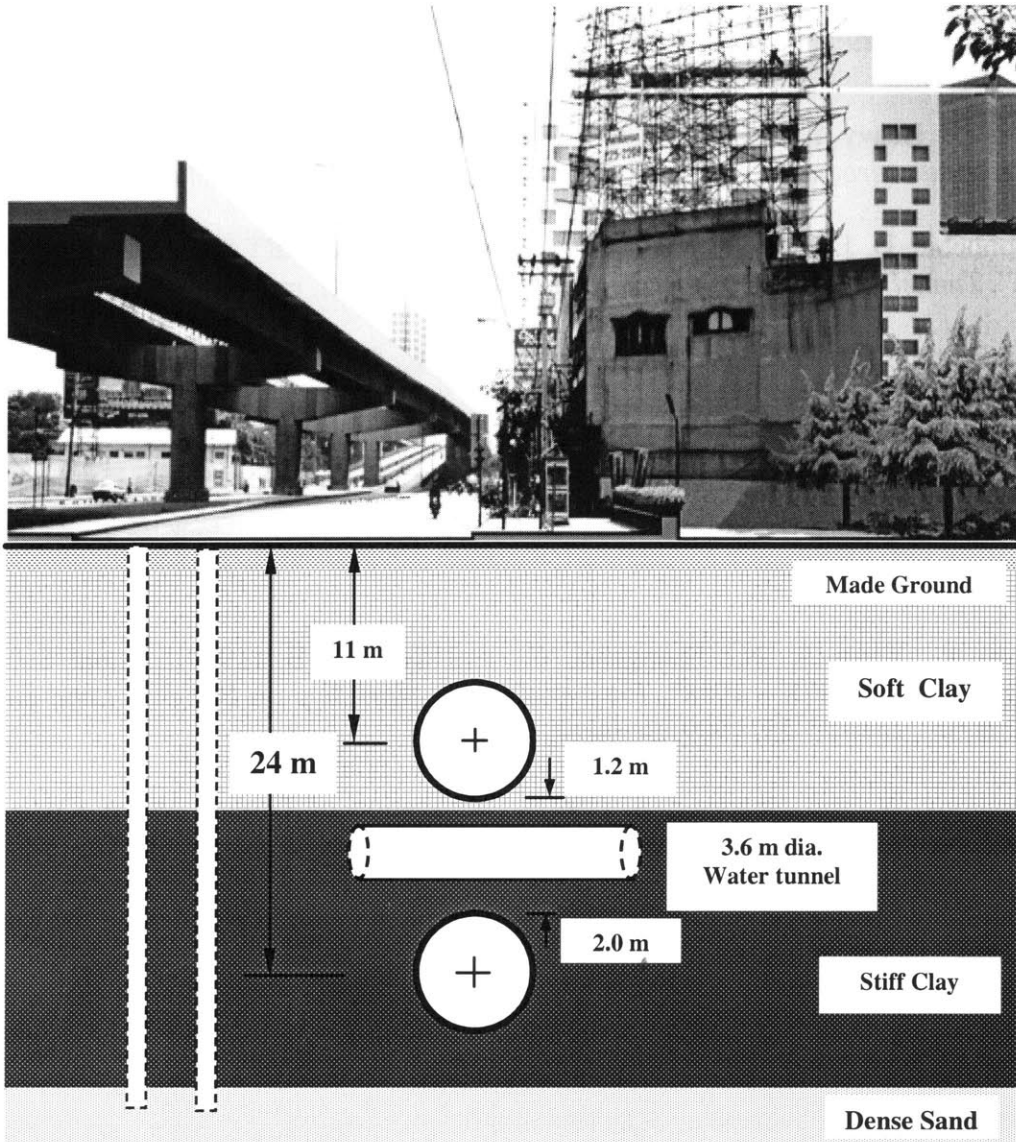


Figure 5.48 Tunnel alignment at Sam Yan station

References

- Herrenknecht GmbH (1996). *Technical Documentation: Project No. S-142 (Subway Bangkok)*.
- Kawasaki Heavy Industries (1998). *Specification Manufacturing: MRTA Initial System Project Underground Structure-South (Joint Venture BCKT)*, submitted to MRTA.
- Maconochie, D. J. and Suwansawat, S. (1999). "Bangkok MRTA: Chaloem Ratchamongkon Line". *Tunnel & Tunneling International*, November 1999, pp. 19-22.
- Maconochie, D. J., Suwansawat, S., and Chang, C. C. (2001). "Tunneling for the Chaloem Ratchamongkon Line in Bangkok". *Proc. 2001 of Rapid Excavation and Tunneling Conference*, Society for Mining, Metallurgy, and Exploration, Littleton, Colorado, pp. 113-129
- Ove Arup and Partner Int. (1998). *Interpretative Geotechnical report*, submitted to MRTA, Vol. 1.
- Prinya, N., Yong, R. N., Thongchai, C., and Somkid, B. (1989). "Land Subsidence in Bangkok during 1978 – 1988". *Presented at the Workshop on Bangkok Land Subsidence – What Next?*, June 22-23, 1989, Bangkok, Thailand.
- Ramnarong, V. and Buapeng, S. (1991). "Mitigation of Ground Water Crisis and Land Subsidence in Bangkok". *Journal of Thai Geoscience*, Vol. 2, pp. 125-137.
- Rau, J. L. and Nutalaya, P. (1981). "Chloride Contamination in Aquifers of the Central Plain, Thailand". *Geotechnical Engineering*, Vol. 12, p. 123.
- Sindhu Maunsell (1997). *Geotechnical Interpretation Report*, submitted to MRTA.

CHAPTER 6

Computerized Database Management

6.1 Introduction

As discussed in preceding chapters, tunneling in urban environments is very challenging and ground movements induced by tunneling are major concerns during excavation. Based on the case histories (Chapter 4), one realizes that many factors such as geological conditions, shield operation, tunnel geometry affect surface settlements. Therefore, to understand the complicated behavior of ground-shield interaction, all geological data, instrumentation records, tunneling data, surveying records, and daily activity updates have to be systematically collected and managed.

During the initial year of research, observation and data collection were conducted at the MRTA project while the eight EPB shields were excavating the tunnels. In this context, a computerized database system was assembled using all information collected from the MRTA project. The database contains monitoring results that include all shield operational records and field instrumentation readings. The database system consists of different hierarchic levels as illustrated in Figure 6.1. The main database provides linkages to sub databases (e.g., 2nd and 3rd levels), and within main databases. Input data were associated with the lining ring number along the tunnel alignment.

The main advantage of this computerized database is that it does not only serve as a data management tool, but can also be used for studying of the ground-shield interaction by providing:

1. Records of operational parameters along the tunnel alignment
2. Instrumentation readings
3. Tunnel alignment coordinates
4. Instrumentation layouts
4. Geological conditions

Hence, this computerized database is useful for the study of the EPB tunneling method and ground deformations (moreover, later on in this thesis, Artificial Neural Networks (ANN) will be incorporated with this database to determine the maximum surface settlement after shield passing).

6.2 Instrumentation Database

Using a spreadsheet software, Microsoft EXCEL, the information collected from each tunneling section was entered into a series of files section-by-section. In each tunneling section, an instrumentation database contains a main file (main database) allowing one to link to any instrumentation file as shown in Figure 6.2. The database file is divided into five worksheets based upon types of information as follows:

1. Surface settlement markers (Figure 6.3)
2. Arrays of surface settlement markers (Figure 6.4)
3. Extensometers (Figure 6.5)
4. Inclinometers (Figure 6.6)
5. Piezometers (Figure 6.7)

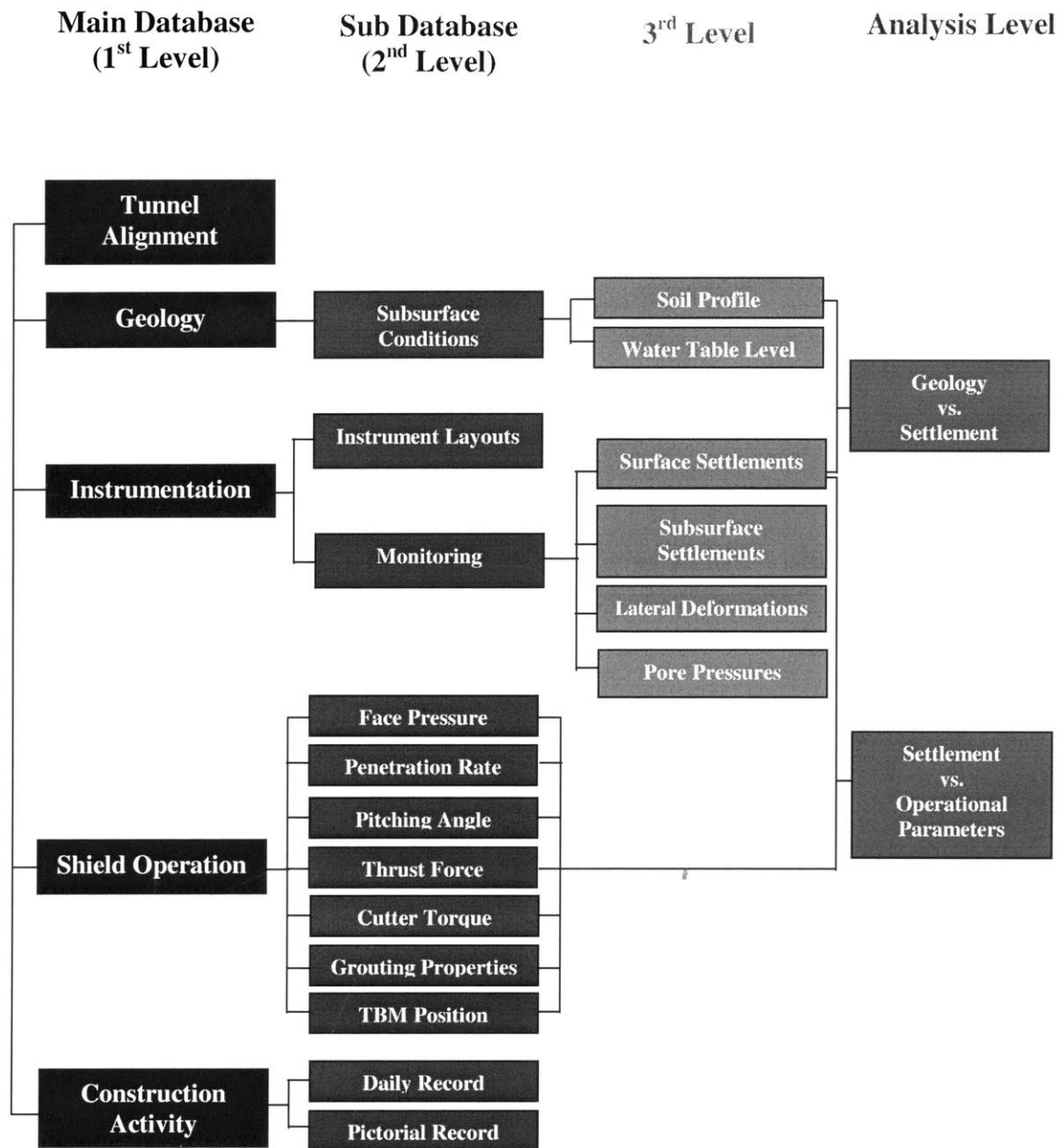


Figure 6.1 Structure of the computerized database system for EPB tunneling in the MRTA project

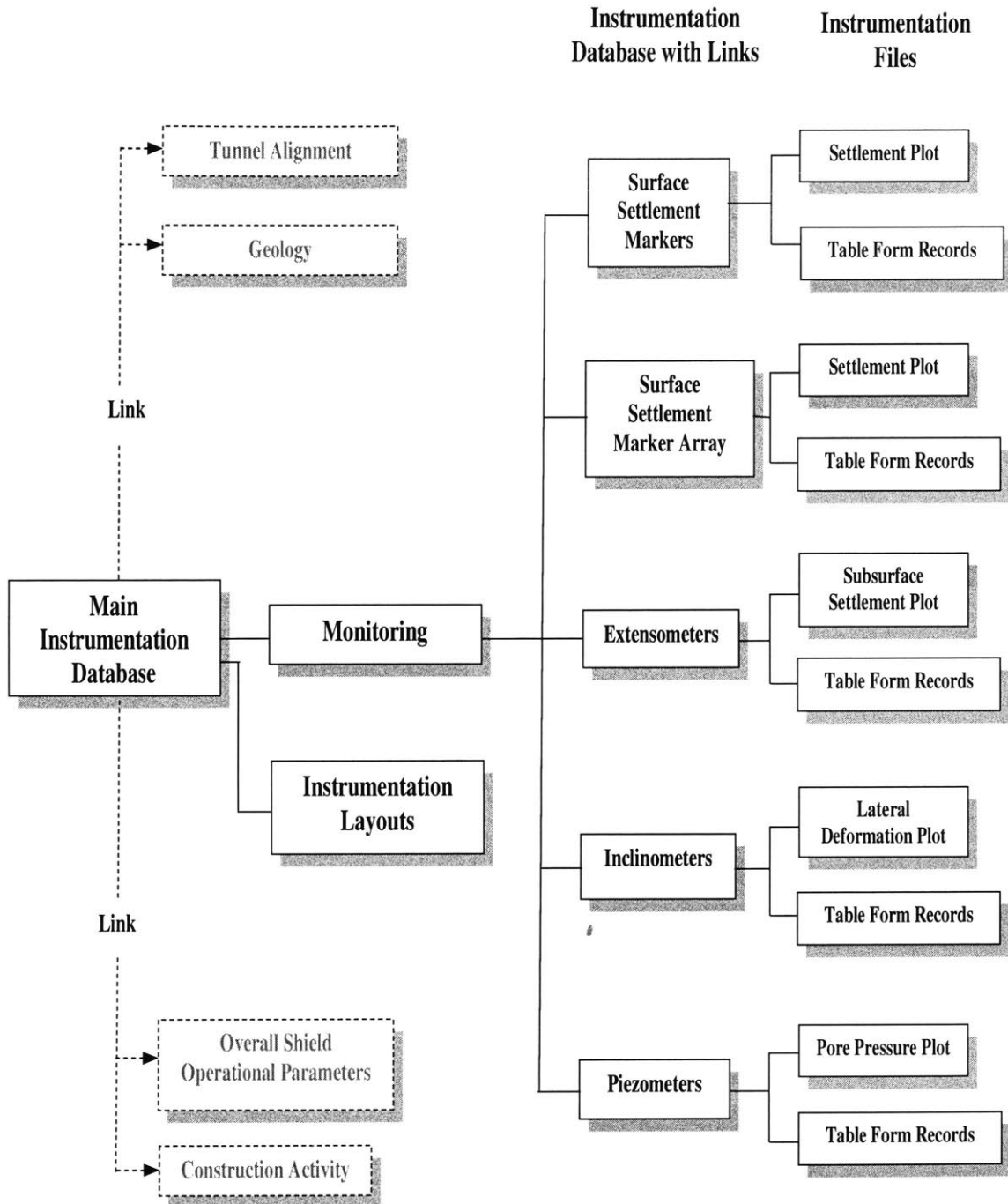


Figure 6.2 Structure of main instrumentation database and its links

Surface Settlement Marker Database

Zone 23 Thiam Ruam Mit (ST12) - Pracharat Bumphen (ST-13)

[Click Here to Link to the Overall Shield Operational Records and Instrumentation Layout](#)

[Tunneling Section](#)

[Shield Records](#)

[Layout](#)

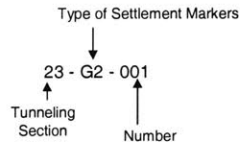
Settlement Markers

[Click Here to Link to the Tunneling Data in the location](#)

Type	Ring Number	Shield Passing Date	Max. Settlement (mm)	Average Face Pressure (kPa)	Depth (m)	
23-G3-001-002 Settlement	23-G3-001	28N	14-May-99	-44.4	70	18.269
	23-G3-002	28S	3-May-99	-60.5	40	18.269
23-G2-001-002 Settlement	23-G2-001	49N	22-May-99	-31.3	60	18.631
	23-G3-002	49S	7-May-99	-51.4	30	18.631

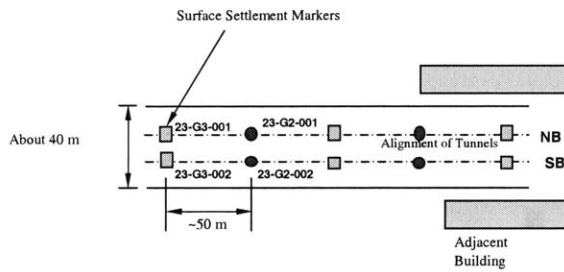
[Click Here to Link to the Settlement Data and Plot](#)

Note:
Type



Ring Number

The number of the segmental ring located in the plane of the instrumentation location
The database goes from lower to higher numbers of rings
(i.e. following the shield drive)



Shield Passing Date Date when the shield passed the instrumentation location

Max. Settlement (mm) The maximum surface settlement measured after shield passing

Average Face Pressure (kPa) The average face pressures recorded during shield passing

Depth (m) Depth to tunnel axis

Figure 6.3 Surface settlement maker database and its links

Surface Settlement Marker Array Database

[Click Here to Link to the Overall Shield Operational Records and Instrumentation Layout](#)

Zone 23 Thiam Ruam Mit (ST12) - Pracharat Bumphen (ST-13)

[Shield Records](#)

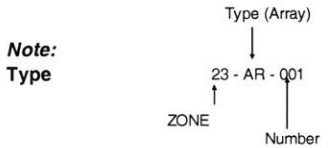
[Layout](#)

[Click Here to Link to the Tunneling Data in the location](#)

Settlement Arrays

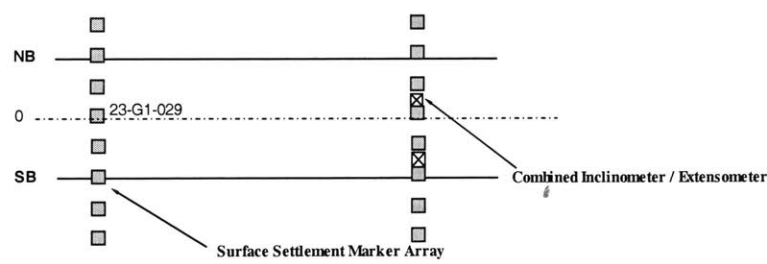
Type		Ring Number	Distance	Shield Passing Date	Max.Sett.(mm)	Depth (m)
23-AR-001 Layout Settlement Trough	23-G1-016				-53.88	22
	23-G1-017		-24.5			
	23-G2-026		-18.5			
	23-G2-027		-7.8			
	23-G1-028	603N	-4.5	19-Aug-99		
	23-G2-029		-1.2			
	23-G2-030		3.3			
	23-G2-031	613S	7.8	29-Jul-99		
	23-G2-032		15.5			
	23-G1-018		22.5			
	23-G1-019		32			

[Click Here to Link to the Settlement Data and Plot](#)



Ring Number The number of the segmental ring located at the instrumentation location

Distance 0 = Centerline of the twin tunnels



Shield Passing Date Date when the shield passed the instrumentation location

Max.Settlement (mm) The maximum surface settlement measured after shield passing

Depth (m) Depth to tunnel axis

Figure 6.4 Surface settlement marker array database and its links

Extensometer Database

[Click Here to Link to the Overall Shield Operational Records and Instrumentation Layout](#)

Zone 23 Thiam Ruam Mit (ST12) - Pracharat Bumphen (ST-13)

[Shield Records](#) [Layout](#)

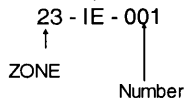
[Click Here to Link to the Tunneling Data in the location](#)

Extensometers						
Type	Ring Number	Shield Passing Date	Sensing Ring	Elevation (m)	Max.Deformation (mm)	Dist. from C.L.(m)
23-IE-001 Deformation	83N	16-Jun-99	23-DATUM01	72.261	3.9	3.5
			23-ME-01/01	73.191	0.4	
			23-ME-01/02	76.218	1.4	
			23-ME-01/03	79.319	0.9	
			23-ME-01/04	82.408	-12.1	
			23-ME-01/05	85.507	-19.1	
			23-ME-01/06	88.597	-18.6	
			23-ME-01/07	91.672	-19.1	
			23-ME-01/08	94.779	-18.6	

[Click Here to Link to the Deformation Data and Plot](#)

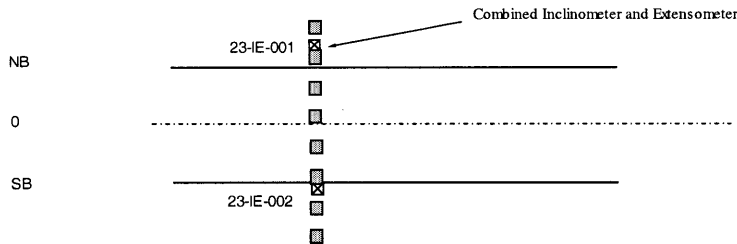
Combined Inclinator and Extensometer

Note:
Type



Ring Number

The number of the segmental ring located at the instrumentation location



Shield Passing Date

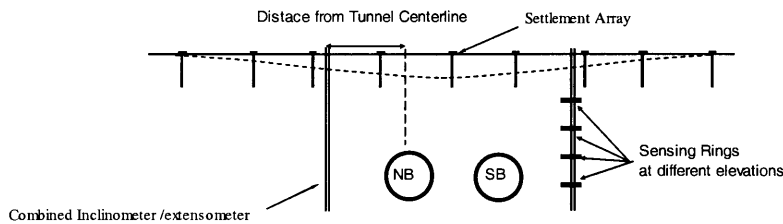
Date when the shield passed the instrumentation location

Sensing Ring

The magnetic rings installed at different depths to monitor subsurface deformation

Elevation (m)

Elevation of each ring sensing location



Max.Deformation (mm)

Maximum subsurface deformation measured from each sensing ring after shield passing

Dist. From C.L. (m)

Distance from tunnel centerline

Figure 6.5 Extensometer database and its links

Inclinometer Database

[Click Here to Link to the Overall Shield Operational Records and Instrumentation Layout](#)

Zone 23 Thiam Ruam Mit (ST12) - Pracharat Bumphen (ST-13)

[Shield Records](#)

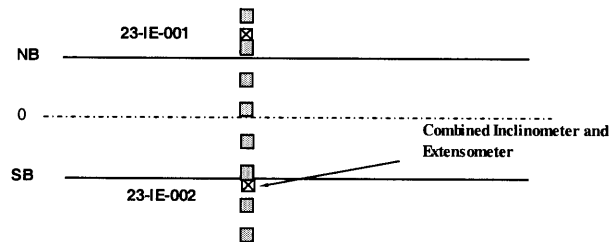
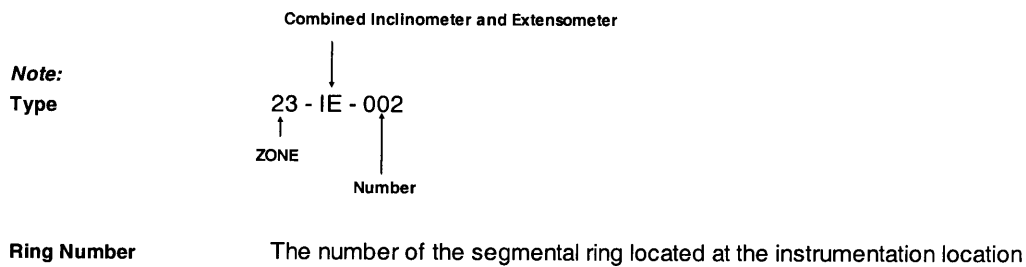
[Layout](#)

[Click Here to Link to the Tunneling Data in the location](#)

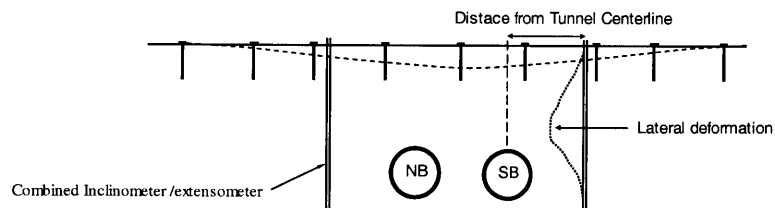
Inclinometers

Type	Ring Number	Shield Passing Date	Max. Deformation (mm)	Dist. from C.L. (m)	Depth (m)
23-IE(incl)-002 Deformation	83S	29-May-99	8.65	3.5	19.4

[Click Here to Link to the Deformation Data and Plot](#)



Shield Passing Date Date when the shield passed the instrumentation location



Max. Deformation (mm) Maximum lateral deformation measured with the inclinometer

Dist. From C.L. (m) Distance from tunnel centerline

Depth (m) Depth to tunnel centerline

Figure 6.6 Inclinometer database and its links

Piezometer Database

[Click Here to Go to the Overall Tunneling Operation Record](#)

Zone 23 Thiam Ruam Mit (ST12) - Pracharat Bumphen (ST-13)

[Shield Records](#)

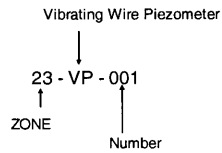
[Click Here to Link to the Tunneling Data in the location](#)

Piezometers

Type		Ring Number	Shield Passing Date	Max. Pore Pressure (kPa)	Average Face Pressure (kPa)	Grouting Pressure (bar)	Dist. From C.L.(m)
23-VP-001~002	23-VP-001	74N	15-Jun-99	23	90		4
Pore Pressure	23-VP-002	74S	27-May-99	4.57	80		4

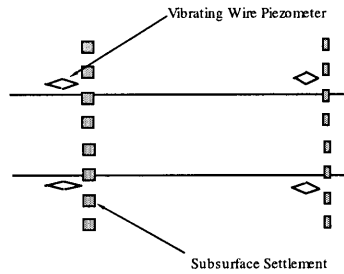
[Click Here to Link to the Deformation Data and Plot](#)

Note:
Type



Ring Number

The number of the segmental ring located under instrumentation location



Shield Passing Date

Date when the shield passed the instrumentation location

Max.Pore Pressure (kPa)

Maximum pore pressure after shield passing

Average Face Pressure

The average face pressures recored during shield passing

Dist. From C.L. (m)

Distance from tunnel centerline to the instrumentation

Figure 6.7 Piezometer database and its links

Information regarding each instrument includes an identification number, the installation location (i.e. over northbound or southbound tunnel), the tunnel ring number in the plane in which the instruments are located, the shield passing date and the maximum deformation or pressure (i.e., in the case of piezometers) after shield passing. Making use of the hyperlink function (originally used for web browsing) provided by the spreadsheet program, one can access target instrumentation files (i.e. 3rd level) from the main file.

6.3 Operational Parameter Database

Operational parameters recorded for every excavation cycle are entered into shield operation files. The operational parameters included:

1. Face Pressure (Figure 6.8)
2. Penetration Rate (Figure 6.9)
3. Pitching Angle (Figure 6.10)
4. Thrust Force (Figure 6.11)
5. Cutter Speed (Figure 6.12)
6. Grouting Pressure (Figure 6.13)
7. Grout Filling (Figure 6.14)
8. Time-position (Figure 6.15)

Note that these operational parameters in the database can be in table form and graphical form.

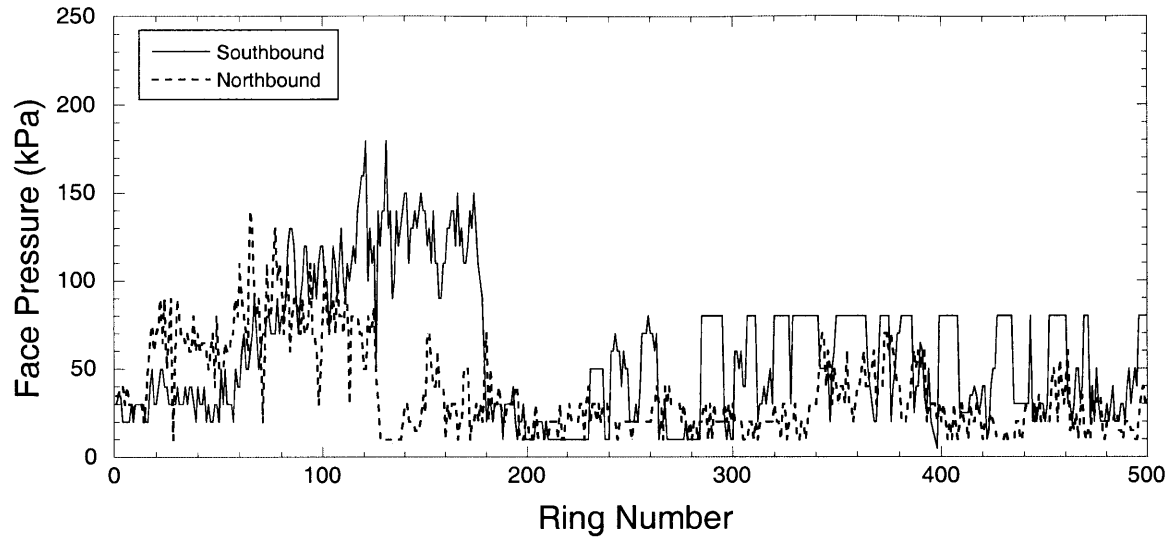


Figure 6.8 An example of face pressure records

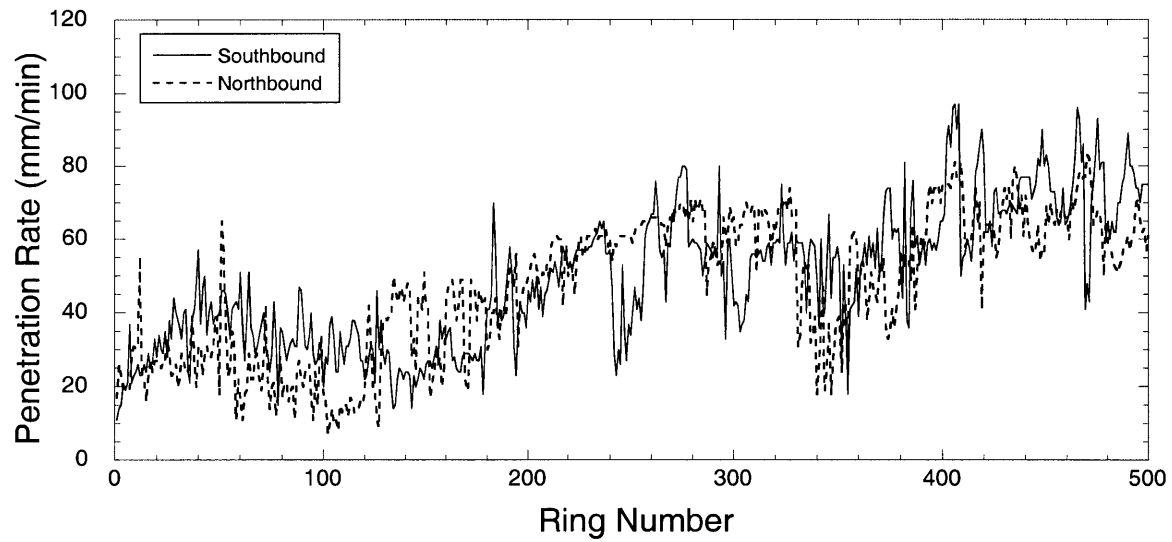


Figure 6.9 An example of penetration rate records

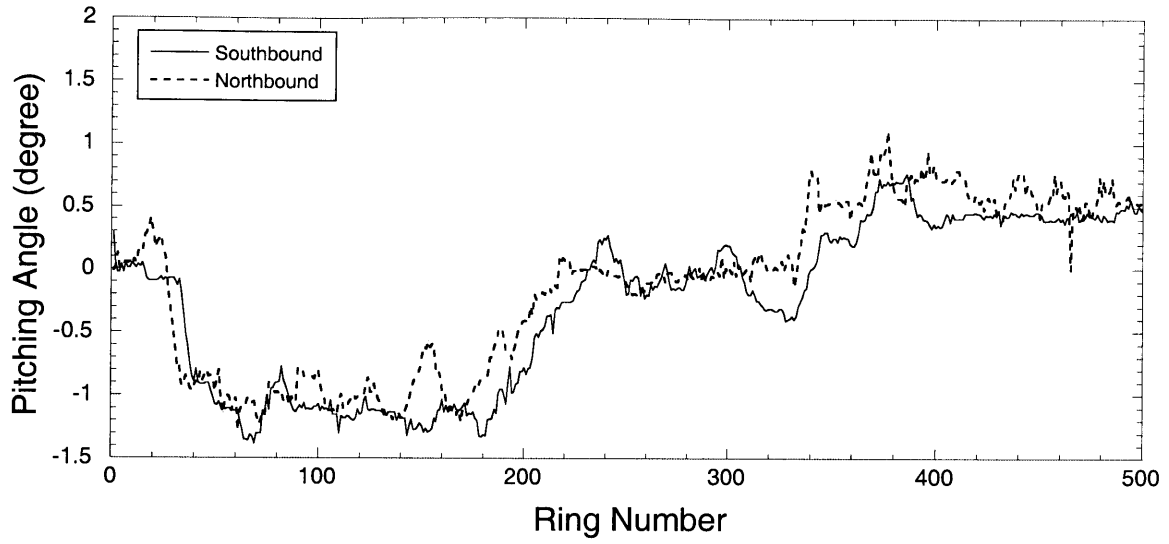


Figure 6.10 An example of pitching angle records

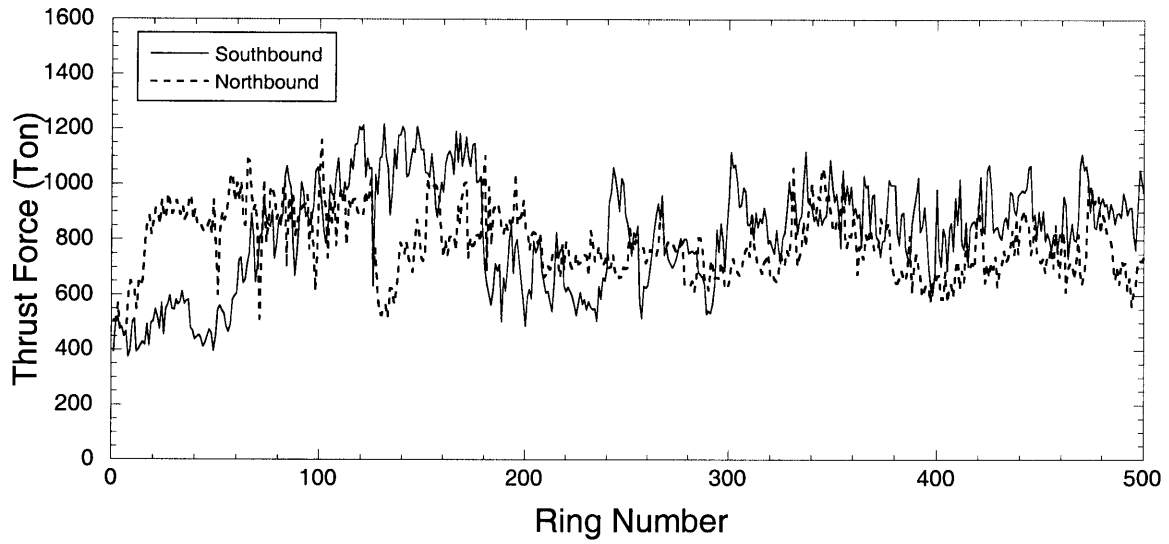


Figure 6.11 An example of thrust force records

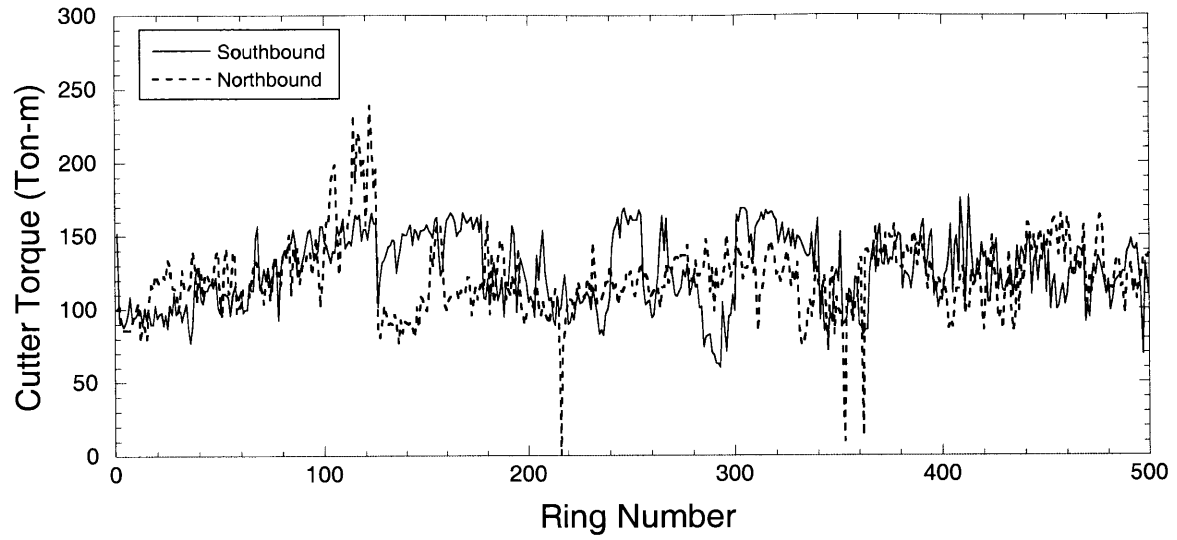


Figure 6.12 An example of cutter torque records

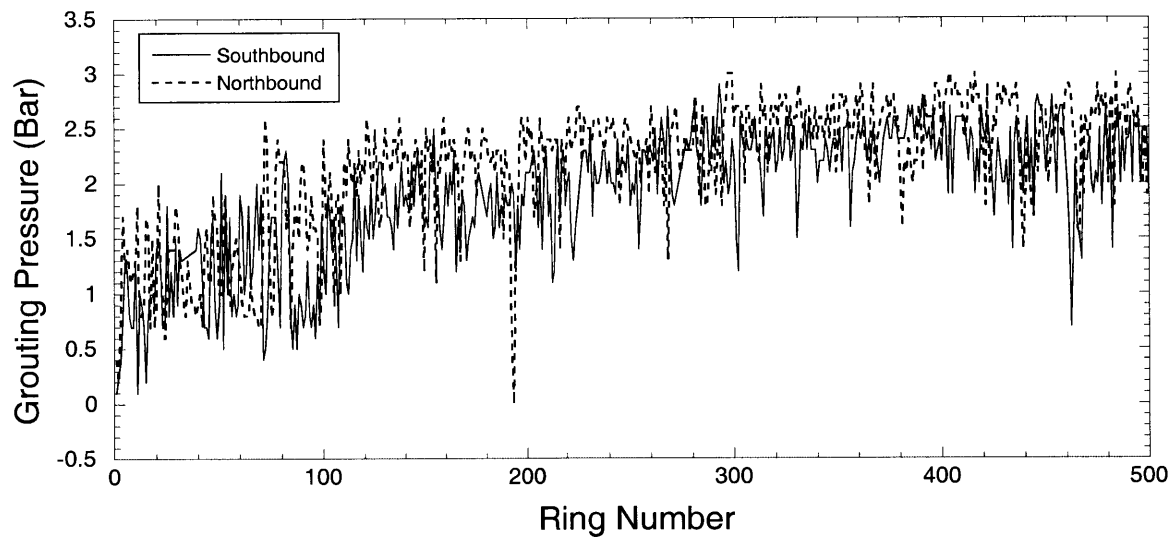


Figure 6.13 An example of grouting pressure records

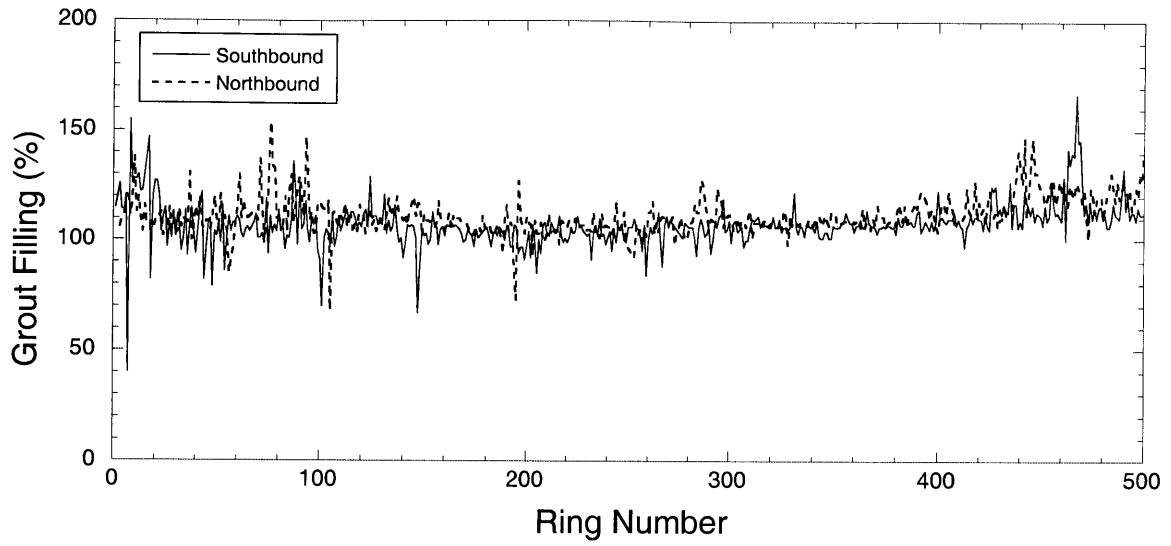


Figure 6.14 An example of grout filling records

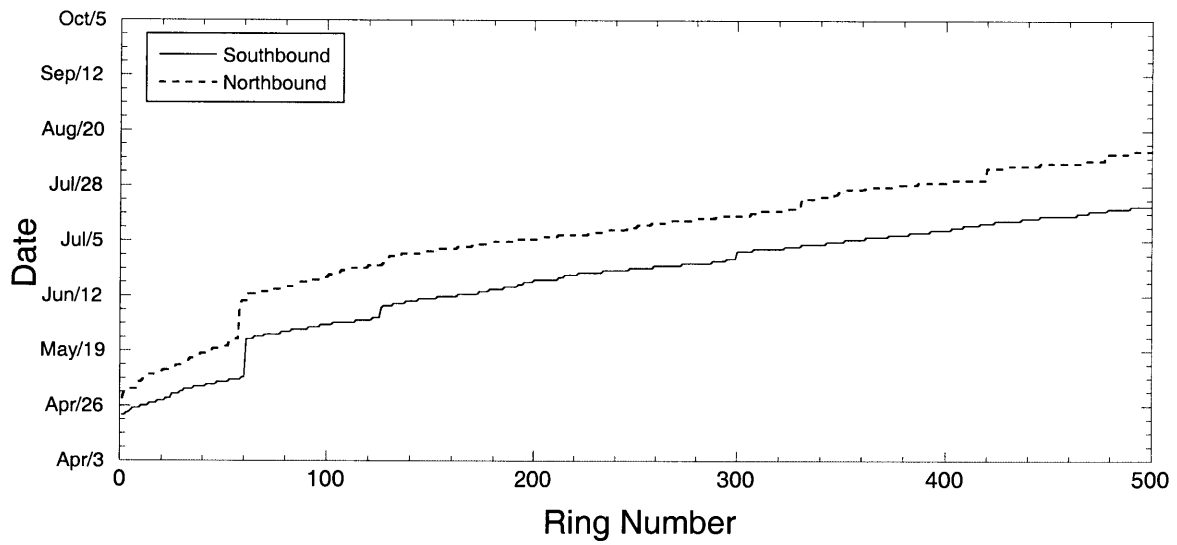


Figure 6.15 An example of time-position records

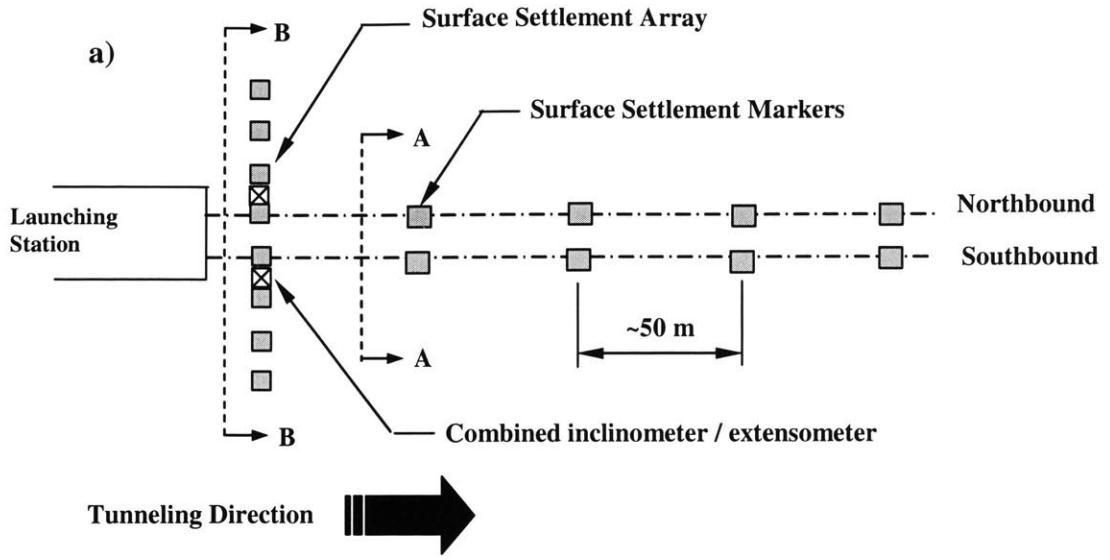
CHAPTER 7

Analysis of Observed Ground Response to EPB Tunneling on the MRTA Project

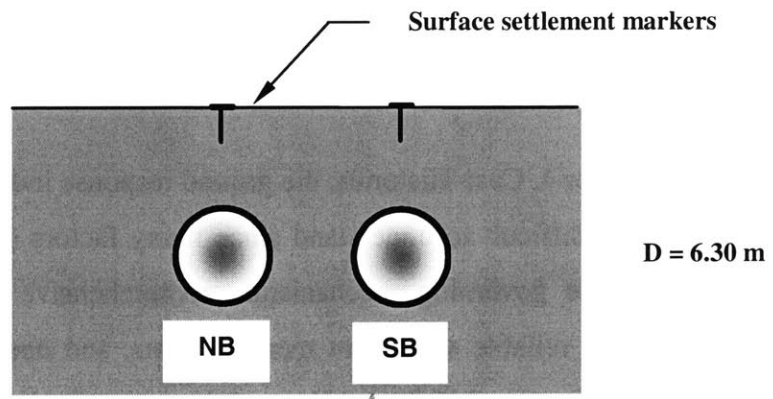
7.1 Introduction

As reviewed in Chapter 4, Case Histories, the ground response induced by EPB tunneling is very complex and difficult to understand since many factors are involved. All agree that to understand the governing mechanisms, comprehensive information including geological conditions, reliable settlement measurements, and operation records of EPB shields are needed. In the MRTA project, due to comprehensive arrangement of instrumentation both in the field and in the shields, the information is available so that the effect of tunneling variables on the development of ground deformations can be studied.

In this chapter, there are two objectives: (1) to evaluate the behavior of ground movements associated with EPB shield tunneling in the MRTA project and (2) to investigate effects of EPB shield operational parameters on ground movements. Measurement results recorded from various types of instrumentation installed in the project including settlement markers, settlement arrays (i.e. multiple settlement markers in the transverse direction), extensometers, and inclinometers are presented in this chapter.



b) Section A-A



c) Section B-B

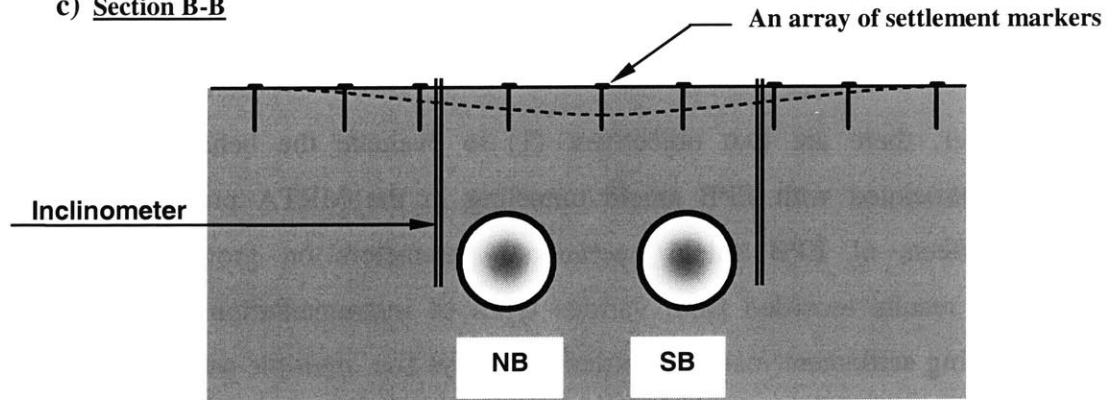


Figure 7.1 Schematic diagram of typical instrumentation locations in the MRTA project

7.2 Surface Settlements

In the MRTA Project, large amounts of surface settlement markers and settlement arrays were installed to measure surface settlements during excavation. Typically, surface settlement markers were installed approximately at 50 meters intervals along the tunnel alignment as shown in Figure 7.1. The primary objective of the measurements with settlement markers is to measure maximum surface settlements above the tunnel centerline. Additionally, since readings were taken over time covering a period between before shield approaching and after shield passing, surface settlement markers also allow one to observe longitudinal surface settlement profiles and to study how they develop during shield passing.

In the transverse direction, arrays of settlement markers were installed to measure settlement troughs developing during and after shield passing. Most of the arrays were located close to launching stations or at the beginning of tunneling drives (Figure 7.1). Basically, the layout of arrays is to concentrate the instrumentation above the tunnel alignment because this is where contractors wanted to check on surface settlements and adequately distant from the alignment to determine a zone of influence. Thus, the main objectives of surface settlement array measurements are: (1) to measure the extent of surface settlement troughs developing during excavation, (2) to observe the shape of settlement troughs and the magnitudes of the deformation. Consequently, results from the instrumentation provide engineers with useful information to design appropriate measures for preventing damage to existing structures induced by EPB tunneling. Note that monitoring frequencies adopted in the MRTA project depended upon shield position. For example, readings were taken every day before and after shield passing but increased to higher frequency (i.e. every 2-4 hours) during shield passing in order to capture the development of surface settlements.

This section begins with the analysis of longitudinal surface settlement profiles measured in different tunneling sections (i.e. Sections A, B, C, and D). Additionally, surface settlement troughs and lateral deformations are also observed and analyzed. In all cases,

effects of operational parameters are studied to determine if a relationship between these parameters and the ground movement exists.

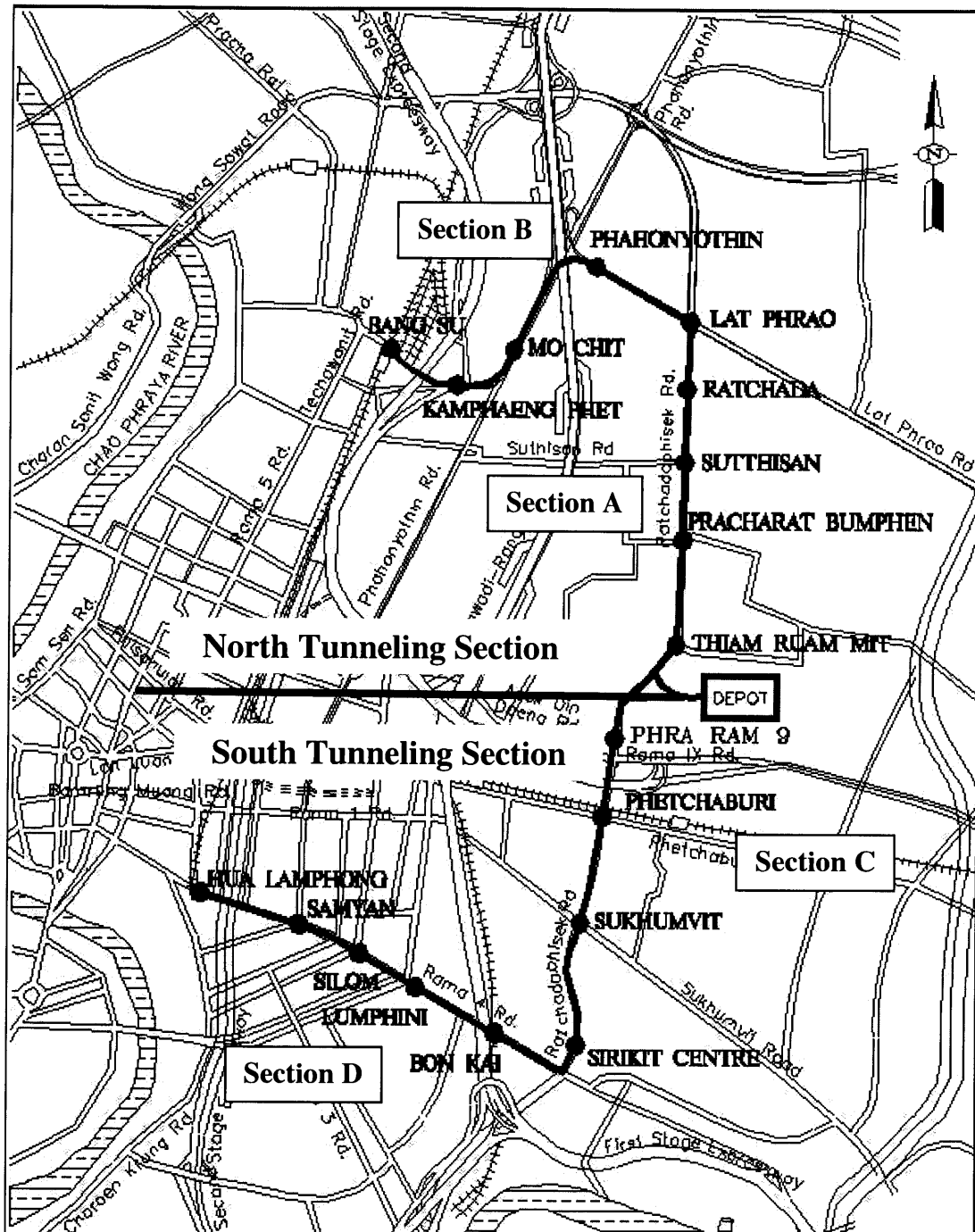


Figure 7.2 MRTA Chaloem Ratchamongkhon Line

7.2.1 Longitudinal Surface Settlements

7.2.1.1 Settlements in Section A

Section A is a part of the North Tunneling Section as shown in Figure 7.2, the detailed description of which can be found in Chapter 5. Figure 7.3 shows subsurface conditions between Thiam Ruam Mit and Pracharat Bumphen stations. This tunnel drive is selected as a case study for Section A since: (1) it is the first tunneling drive of Section A so that effects of the initial drive on settlements can be observed, and (2) large amounts (more than in other sections) of field instrumentation were installed in this section. Note that only the first tunnel (the southbound tunnel) is studied since, in this chapter, only the impact of the first shield on ground deformations is considered. Most of the tunnel in this section was excavated within the stiff clay layer. The only exception is half way between the stations where the tunnel invert was located within the dense sand layer.

The Earth Pressure Balance shield used in this section was operated by controlling the amount of excavated soil that was extracted from the face by a screw conveyor. Basically, the shield face was supported by the excavated soil held in the front chamber at a controlled pressure. The face pressure was used as a control parameter during the excavation process as described in Chapter 2. This pressure was monitored by pressure cells installed inside the earth chamber. Based on face pressures observed during the excavation, this tunneling section can be divided into three particular zones, namely: (1) *initial drive zone*, (2) *pressure building up zone*, and (3) *pressure loss zone* as shown in Figure 7.4.

At the beginning of the excavation, the Earth Pressure Balance shield was assembled behind the northern diaphragm wall of the Thiam Ruam Mit station. Before the SB shield was launched, a so called “Tunnel Eye” was prepared on the diaphragm wall for the shield to cut through as illustrated in Figure 7.5. Note that typical diaphragm walls were reinforced by steel rods. However, the Tunnel Eye that the EPB shield cut through was reinforced with fiberglass rods so that the shield was able to grind through the wall.

Not only were the wall and launching position prepared at this stage, a reaction truss was also installed for the shield to push against (Figure 7.6).

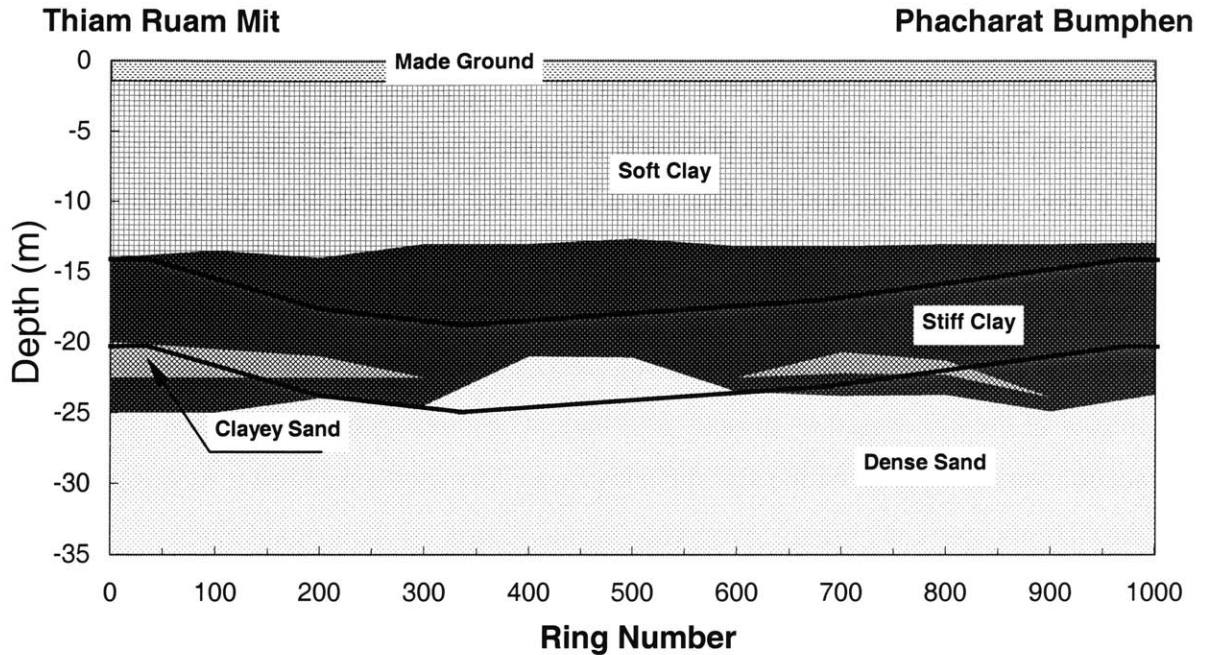


Figure 7.3 Subsurface conditions of tunneling section (southbound) between Thiam Ruam Mit and Pracharat Bumphen (Section A)

Since the space in the launching shaft was very limited, back-up equipment for the shield was initially fitted within the upper two levels of the launch shaft with umbilical cables and hoses linked to the machine. The drive progressed 60 rings before the back-up equipment was transferred to the tunnel. After the pre-launching processes were finished, the shield then started to cut through the diaphragm wall (Figure 7.7). It was shoved slowly until all of the body had passed through the wall. The beginning of the tunnel excavation is known as the initial drive zone. The term “*initial drive zone*” was used to describe a range of a shield drive from the beginning of the tunnel excavation where the shield still requires temporary supports as shown in Figure 7.8 and Figure 7.9 to the distance where no temporary support is needed and the back-up equipment can be set up in the tunnel. Typically, the initial drive zone approximately ranges from 70 m to 120 m. (i.e. 60-100 lining rings or excavation cycles); with the actual length depending on the

support equipment and operation procedure of each shield. After the shield reached the end of the initial drive zone, it stopped. The temporary rings and the reaction truss were removed. Back-up equipment was then set up behind the shield. The equipment train normally requires a free space of up to 100 m behind the shield as shown in Figure 7.10. In some tunneling sections, the initial drive zone can be as long as 120 meters.

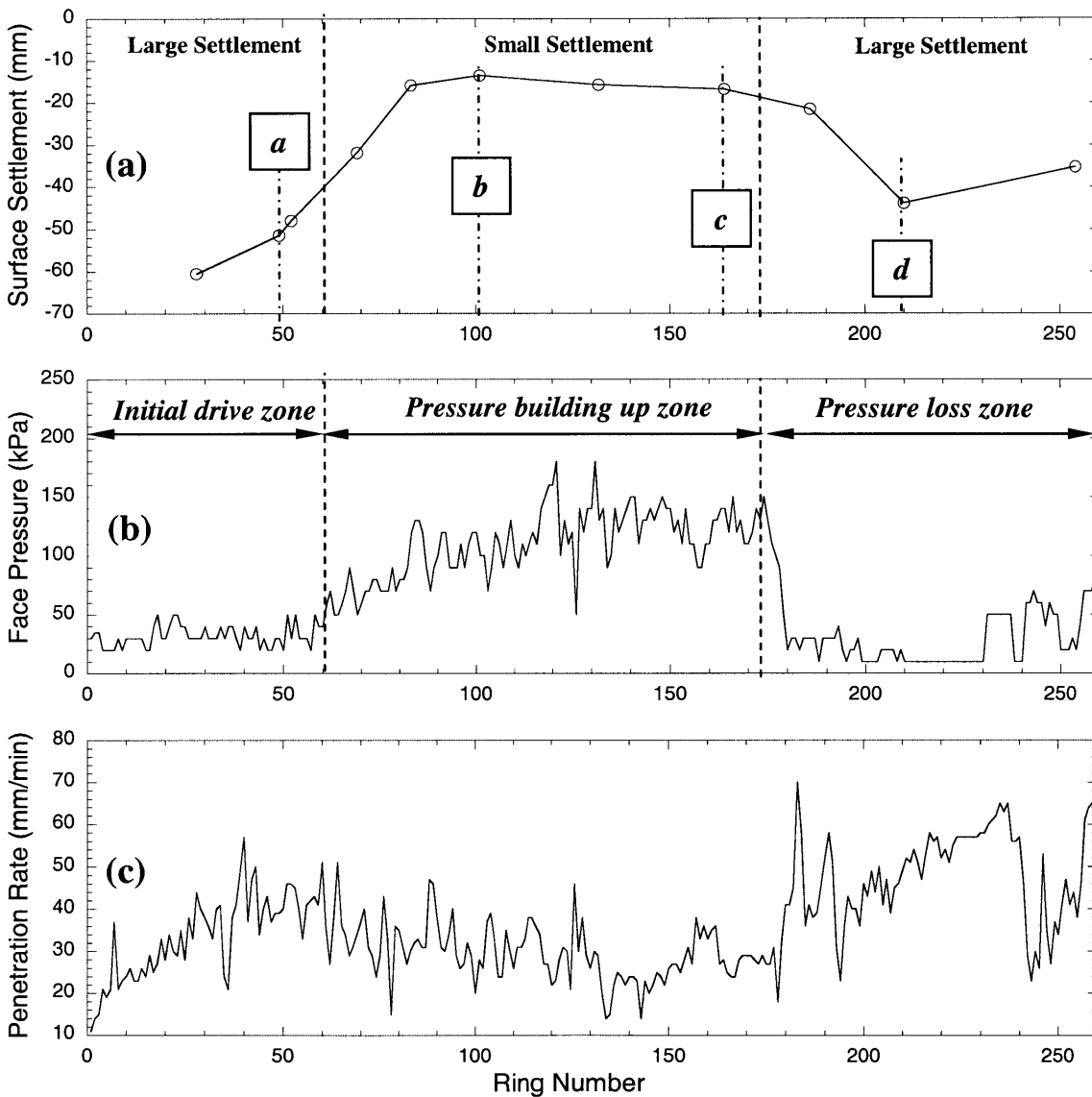


Figure 7.4 Maximum surface settlements, face pressures, and penetration rates recorded between Thiam Ruam Mit and Pracharat Bumphen stations (Section A)

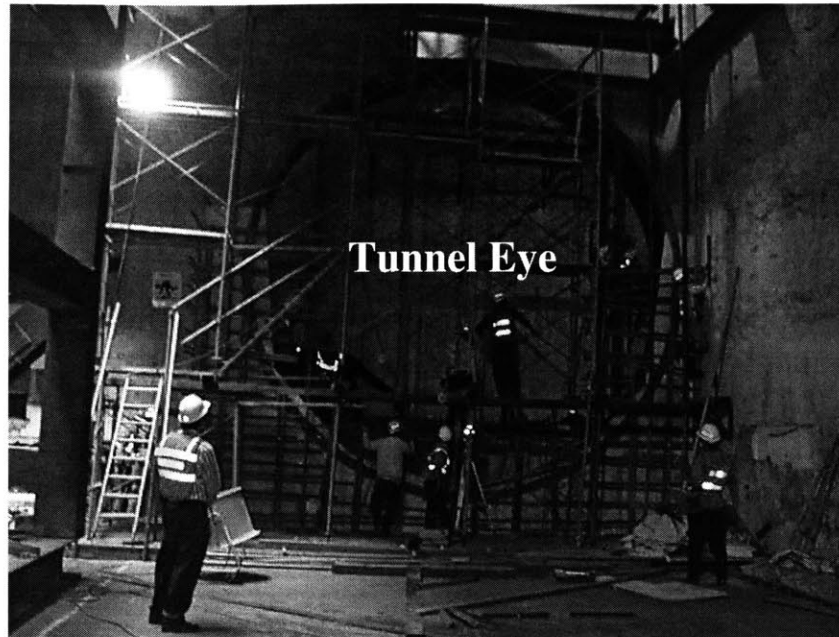


Figure 7.5 “Tunnel Eye” prepared before launching the shield (Thiam Ruam Mit station)

During excavation, the thrust force induced by hydraulic jacks (i.e. 20 to 40 hydraulic jacks used to shove an EPB shield) can be normally as high as 4000 tons. Hence, a large number of installed lining rings were needed to withstand the induced shear stress before the temporary supports can be removed. In Section A, the initial drive was ended at the lining ring no. 60 or 72 meters from the launching station. Within this zone, the shield could not apply very high thrust since the temporary lining rings were not designed to withstand very high thrust load. High face supporting pressure could not be developed at the beginning, as the thrust force is proportional to the face pressure so that only 30-60 kPa pressure was recorded within this zone. As a result, the surrounding ground deformed towards the face of the shield (see also Chapter 3).

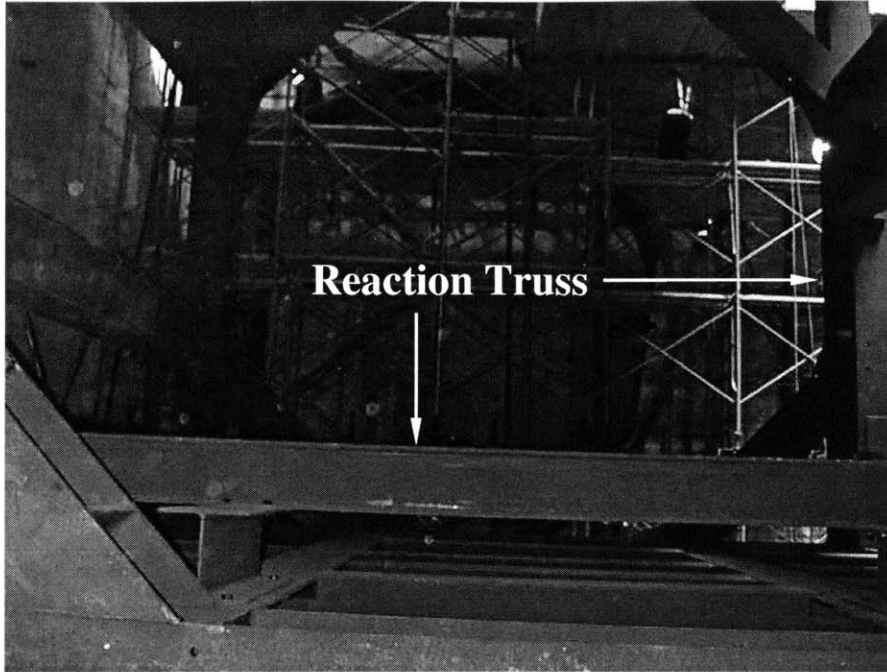


Figure 7.6 Reaction truss installed to support the initial drive (Thiam Ruam Mit station)

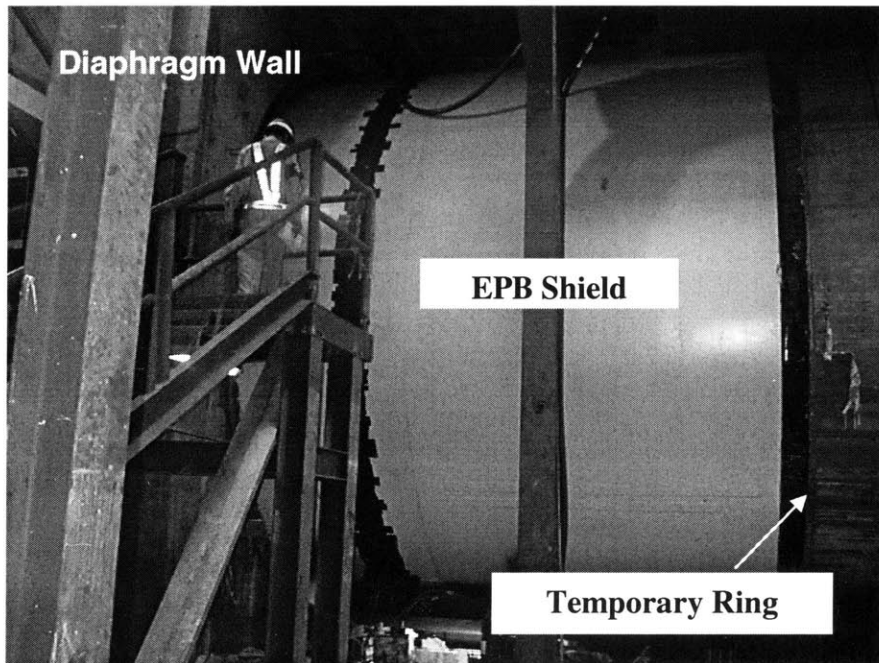


Figure 7.7 The shield launching through the diaphragm wall (Thiam Ruam Mit station)

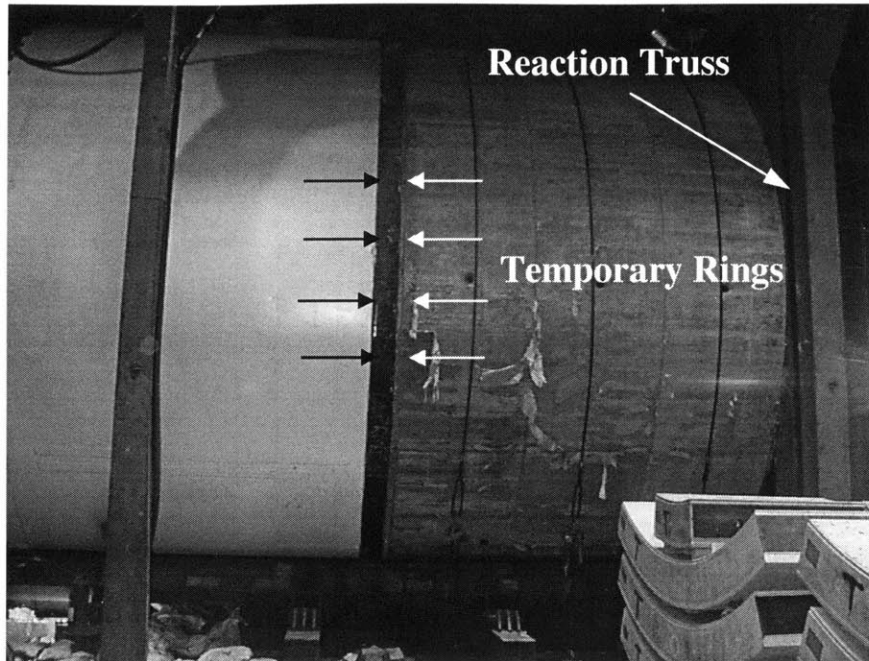


Figure 7.8 Temporary lining rings (Thiam Ruam Mit station)

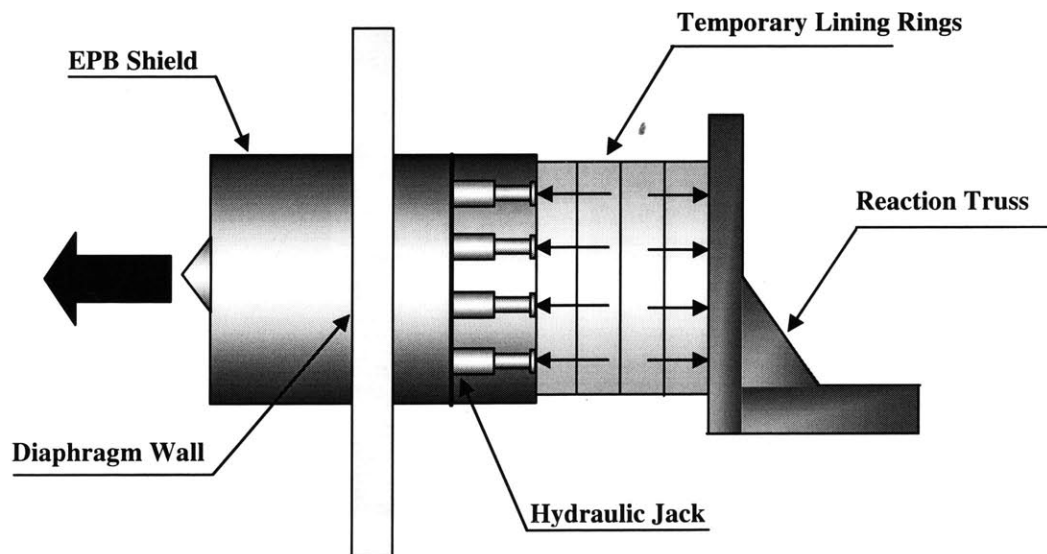


Figure 7.9 Schematic diagram of the initial shield drive



Figure 7.10 Back-up equipment train (Sirikit station)

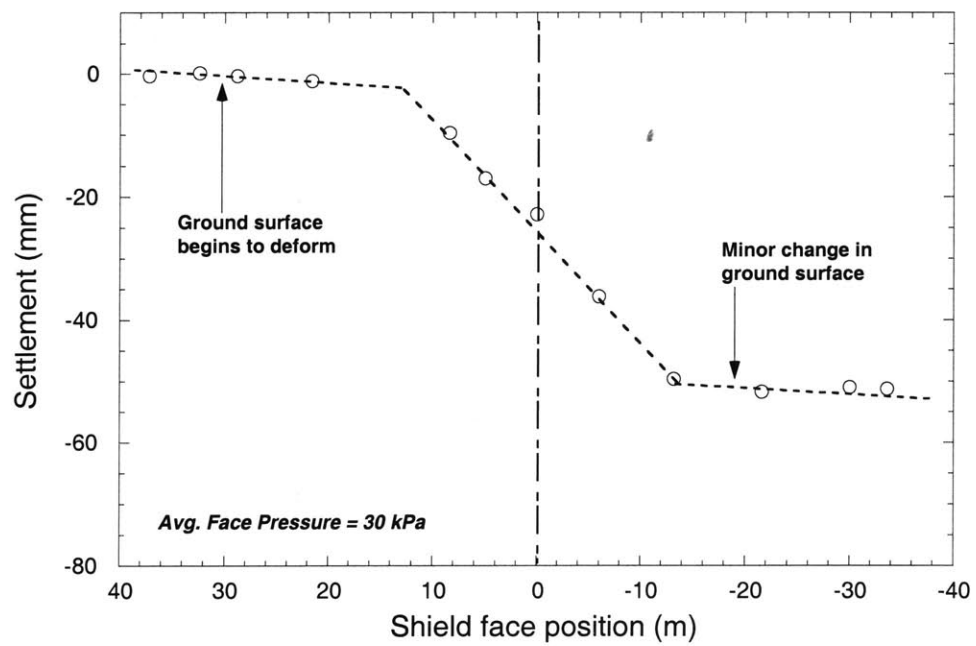


Figure 7.11 Longitudinal surface settlements measured in the initial drive zone (Ring No. 49-southbound)

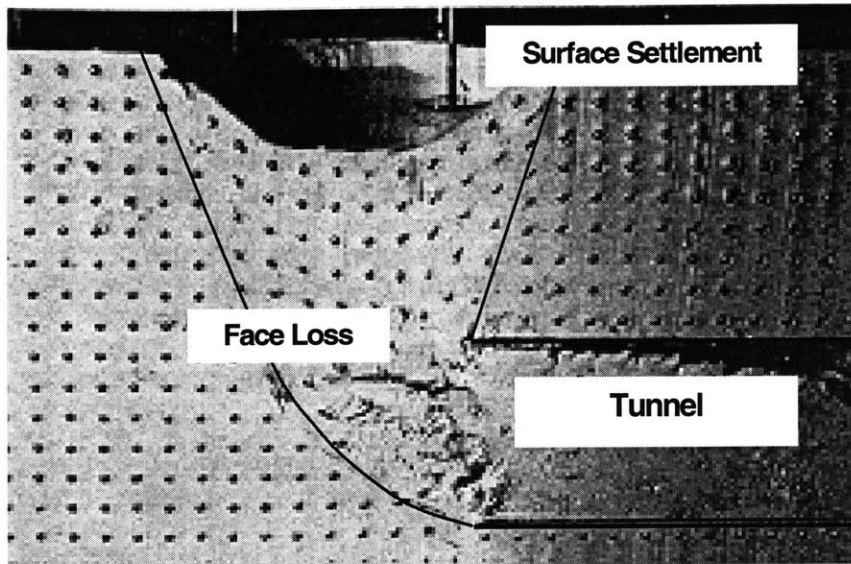


Figure 7.12 Failure mechanism at a tunnel face during a centrifuge test done by Kimura and Mair (1981)

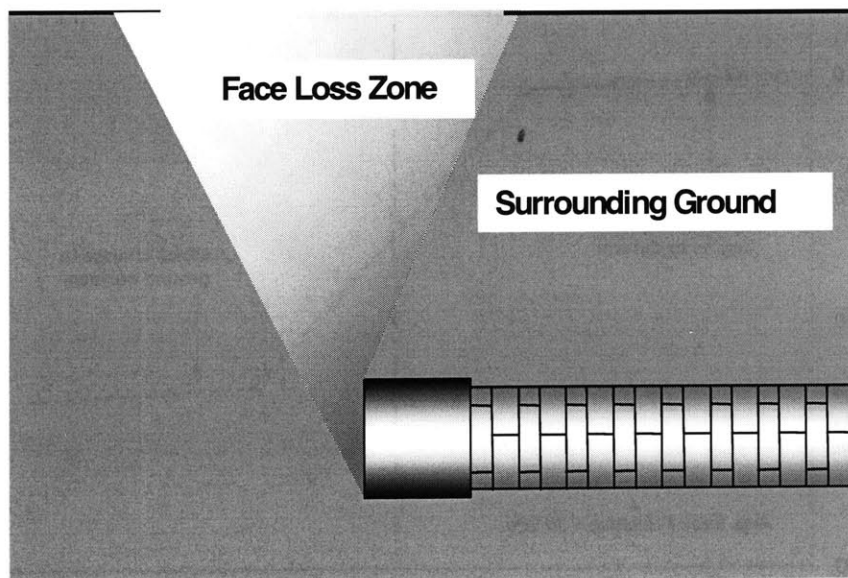


Figure 7.13 Schematic diagram of ground deformation at the shield face

To allow a clearer relationship to be established between surface settlements and tunneling, settlement data were plotted against the shield face position as shown in Figure 7.11. As can be seen from the figure, the ground surface began to deform about 30 meters ahead of the shield. As the shield advanced close to the measurement section, larger settlements developed and accelerated over the shield body. Subsequently, the settlement ceased after the shield arrived at 15 m. behind the measurement section. The settlement was measured at the ground surface over the lining ring no. 49 labeled “*a*” in Figure 7.4a. As the shield passed the section, the average face pressure was only 30 kPa. As can be seen in Figure 7.11, large surface settlements occurred while the shield approached the measurement section particularly in the plane of the shield face. This observation is in agreement with laboratory experiment results shown in Figure 7.12 reported in earlier studies (i.e. Kimura and Mair; 1981, and Atkinson and Potts; 1977) in which ground tended to move towards the tunnel face in the centrifuge test. This ground movement manifested itself at the ground surface causing the large surface settlement. The ground movement zone had a shape like a triangular wedge, the so called “face loss impact zone” as shown in Figure 7.13 (see also Chapter 3).

Note that the above mentioned test was based upon open-face shield simulation not Earth Pressure Balance (EPB) type shields as used in the MRTA project. However, at low applied face pressure, the EPB machine appeared to behave similarly to the open-faced shield, which allows the ground to move towards its face. Additionally, large settlements significantly extend over the shield body but ceased about 15 m. (i.e. 2-shield diameter) behind the face. Subsequently, beyond this point, the settlement showed a small change after shield passing.

After the SB shield was driven 72 m away from the launching station and 60 segmental rings were installed, the shield was stopped, equipment backup trains were set up, and all temporary supports were removed. This was the end of the initial drive and the shield then resumed the excavation again. From this moment on, the SB shield was able to increase the face pressure up to 180 kPa (Figure 7.4a). To investigate the relationship between surface settlements and the shield progress, locations “*b*” and “*c*” (see Figure

7.4a) were selected for investigation. Average face pressures during shield passing were 100 and 120 kPa for locations “*b*” and “*c*”, respectively. The operation is in the “earth pressure balance mode,” where surface settlements can be minimized by adjusting the face pressure equal to the surrounding earth pressure during excavation.

Surface settlements versus the shield face position in locations “*b*” and “*c*” are plotted in Figure 7.14 and Figure 7.15, respectively. In the figures, the maximum settlements were 13 mm at location “*b*” and 11 mm at location “*c*.” Obviously, both sections have less settlement than section “*a*” (~50 mm), where low face pressure was applied. This confirmed the assumption made previously that the face pressure applied during shield passing has a significant effect on the magnitude of surface settlements.

Typically, shield operators need to drive the shield under a controlled face pressure to minimize the surface settlement. Accidentally, after ring No. 177 was completed, one of four cutter drive motors broke causing a problem in the cutter face in that it could not rotate at the desired pressure and letting the face pressure level to drop dramatically (i.e. “pressure loss zone” in Figure 7.4b). Within this zone, large surface settlements were observed. Point “*d*” in Figure 7.4a indicates the observation point at ring No. 208 in the pressure loss zone. As plotted in Figure 7.16, the maximum settlement is 35 mm which is much greater than the settlements measured in points “*b*” and “*c*”, where the shield was operated in the earth pressure balance mode. Not only does the ground indicate large settlements over the shield but it also experiences large ground movements ahead of the shield. This ground response is also similar to what was observed at point “*a*” (Figure 7.11). Nevertheless, in all cases, the patterns of the longitudinal surface settlement are very similar.

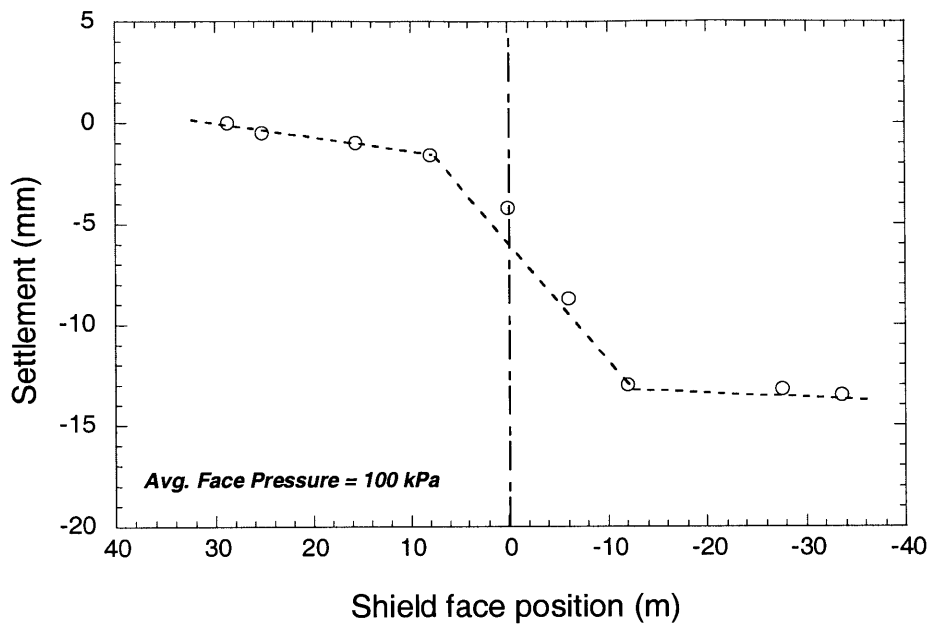


Figure 7.14 Longitudinal surface settlement profile measured at location “b” (Ring No. 101-southbound)

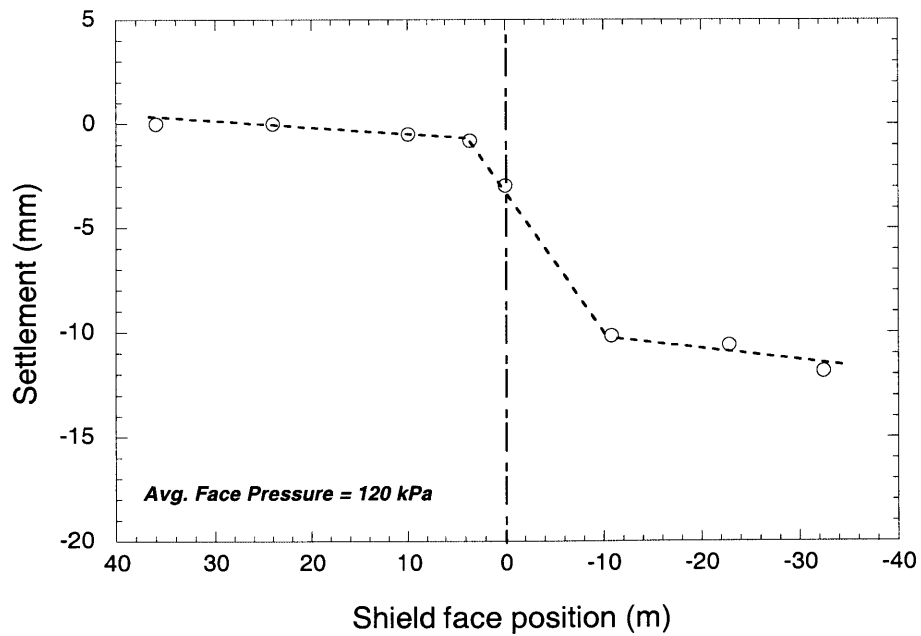


Figure 7.15 Longitudinal surface settlement profile measured at location “c” (Ring No. 164-southbound)

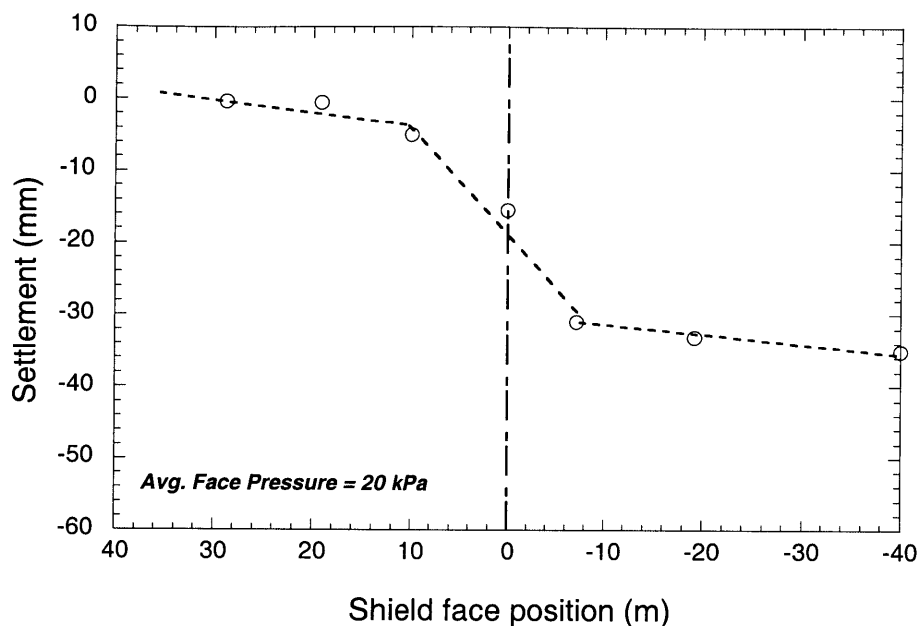


Figure 7.16 Longitudinal surface settlement profile measured at location “*d*” (Ring No. 208-southbound)

Based on these observations, surface settlements induced by EPB tunneling can be divided into three zones regardless of face pressure level namely, (1) Zone 1, (2) Zone 2, and (3) Zone 3 as shown in Figure 7.17. The first zone originates approximately 30 m ahead of the shield, where the ground surface begins to deform. The surface settlement then continues to develop as the shield advances close to the measurement section. About 10 m in front of the shield, the surface settlement significantly increases and accelerates over the shield body. This stage of the surface settlement creates a clear inflection point separating “Zone 1” and “Zone 2”. As observed in Section A, the surface settlement in Zone 2 is the largest portion of overall settlement induced by the EPB shield. After the shield tail passes the measurement section (i.e. about 15 m from the shield face), the settlement development begins to slow down; this is the beginning of Zone 3. The surface settlement in this final zone stops about 30 m after shield passing.

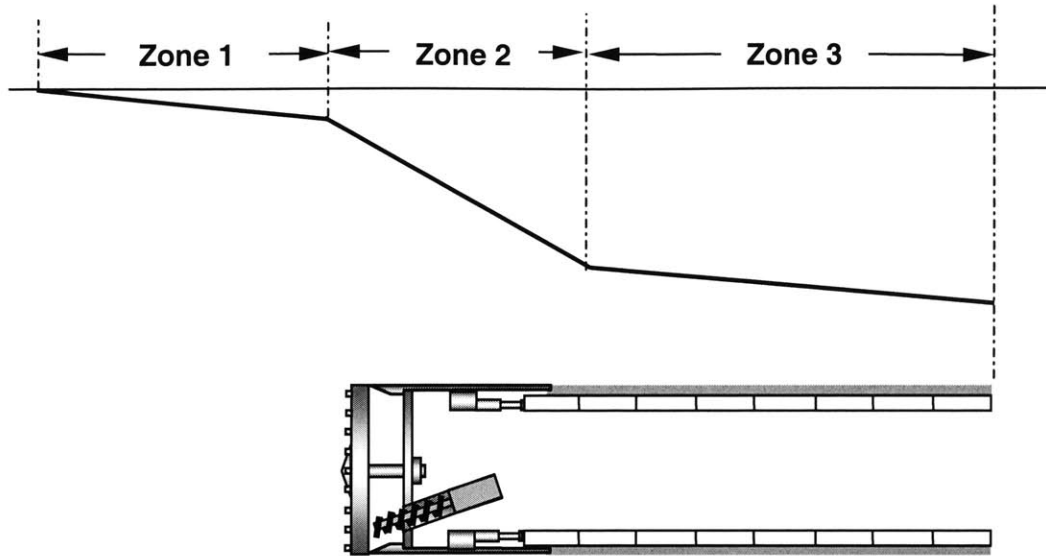


Figure 7.17 Schematic diagram of a typical longitudinal surface settlement profile

7.2.1.2 Settlements in Section B

Soil conditions of the tunnel in Section B are very similar to those of Section A, where most of the tunnel alignment was excavated within the stiff clay layer. Figure 7.18 shows subsurface conditions of the tunneling section between Ratchada and Lat Phrao stations. This tunnel drive is selected as a case study for Section B for the same reasons as was done in Section A (i.e. the first tunneling drive and large amounts of field instrumentation). Note that only the southbound tunnel is considered. Surface settlements measured in this section were recorded along the tunnel alignment as shown in Figure 7.19a. At the beginning of the tunnel drive, relatively large settlements were observed even though the shield was operated at high face pressures (i.e. 150-200 kPa). This phenomenon had been found in most of tunneling sections in the MRTA project and in the case histories discussed in Chapter 4.

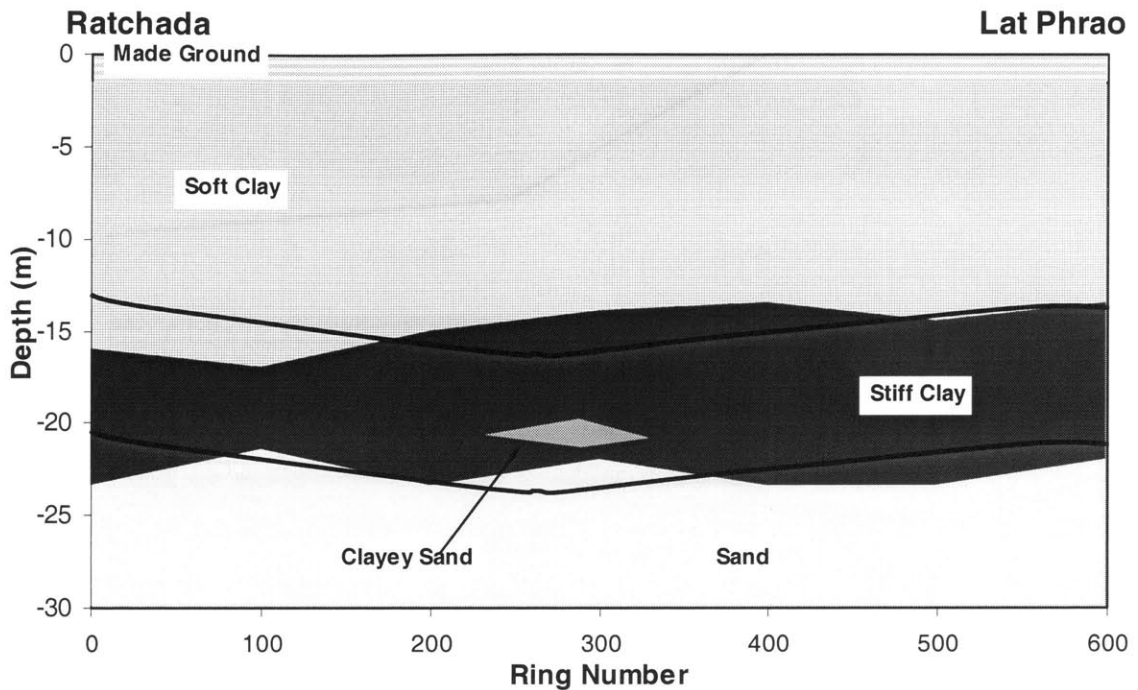


Figure 7.18 Subsurface conditions of tunneling section (southbound) between Ratchada and Lat Phrao stations (Section B)

One of the factors that affect the ground response in the early stages of excavation is the inexperience of the tunnel crews. Furthermore, if one takes a detailed look at the shield penetration rates plotted in Figure 7.19c, it was found that the shield was driven at only 10-30 mm/min at the beginning of the excavation. In particular, between rings No. 80 – 100, the penetration rate was very low (i.e. less than 5 mm/min in some sections). Unlike other tunnel sections, Obayashi who operated the shield adopted a pipe transport technique instead of muck locomotives (Figure 7.20). This technique required the rate of pumping to be related to the shield advance/penetration rate or vice versa as described in Chapter 2. Hence, this becomes a limitation in this tunneling section in that the shield cannot be shoved at high penetration rates.

Evidently, such a low penetration rate was found to be associated with large surface settlements measured over the shield, particularly at ring No. 86 as shown in Figure

7.19a. To explore the behavior of ground response during shield passing, surface settlements recorded over the ring No. 86 were plotted against the shield position as shown in Figure 7.21. The shape of the longitudinal surface settlement is similar to that of Section A with three distinct zones. Particularly Zone 2, settlement over the shield body is also the largest portion of the settlement. The surface settlement in Zone 1 appears to be relatively large (i.e. 11 mm at the transition point between Zone 1 and Zone 2), while the surface settlement in Zone 3, where the shield already passed the section has the smallest settlement. Based upon this observation, although the shield was operated at high face pressures during excavation in Section B, the surface settlements were still large as long as the penetration rate was very low. This suggests that penetration rate may also be a factor affecting the magnitude of surface settlements.

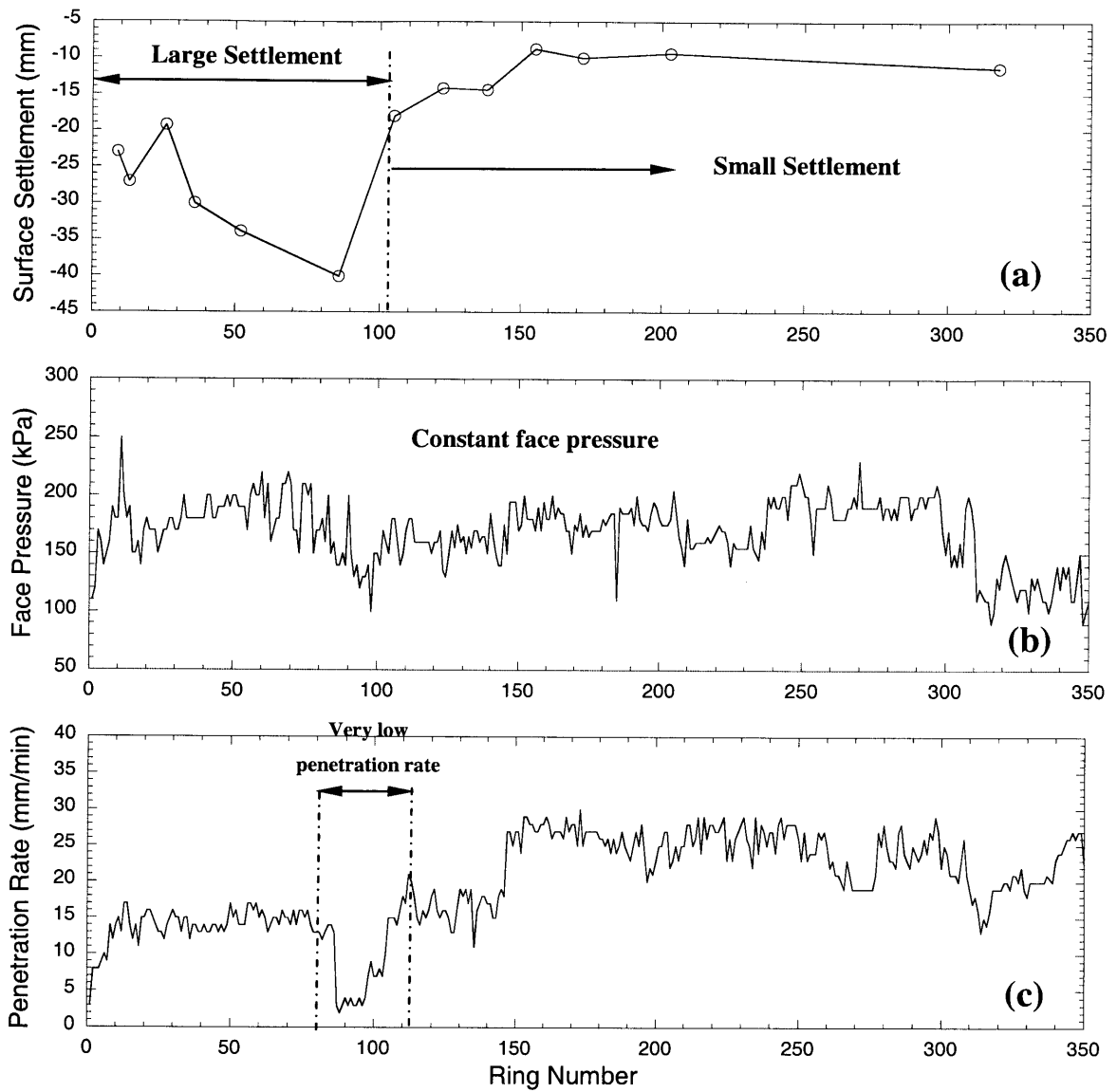


Figure 7.19 Maximum surface settlements, face pressures, and penetration rates recorded between Ratchada and Lat Phrao stations (Section B)

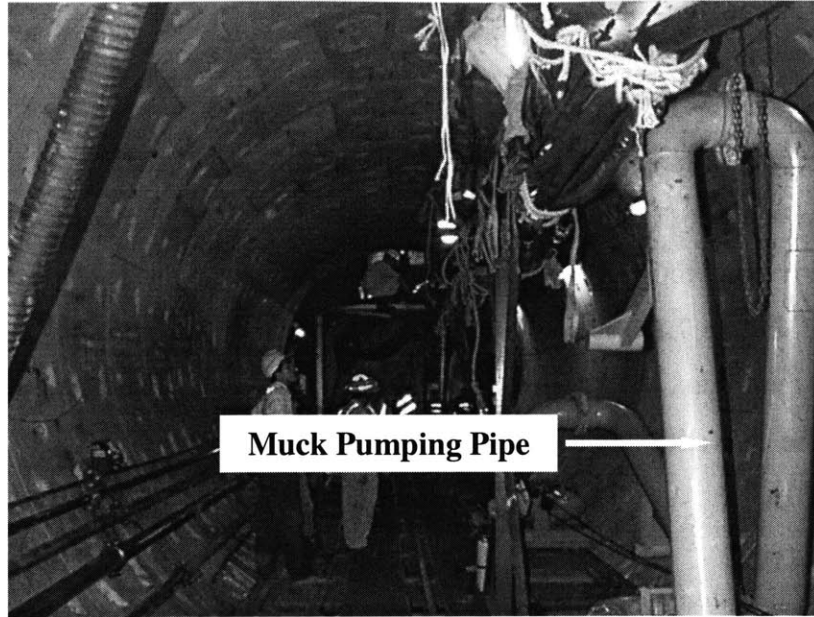


Figure 7.20 Muck pumping pipe used in Section B

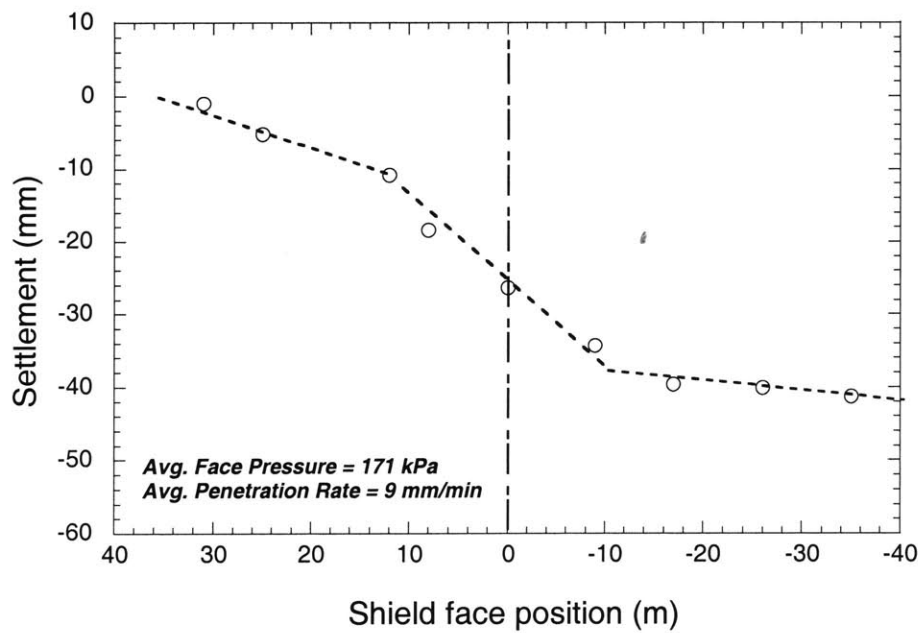


Figure 7.21 Longitudinal surface settlement profile measured over southbound ring No. 86-southbound in Section B

7.2.1.3 Settlements in Section C

Section C excavated by Kumagai Gumi is a part of the South Tunnel Section (see Figure 7.2). Unlike other sections, the northbound shield was launched first. The northbound tunneling drive between Rama IX to Phetchaburi stations is used as a case study since it was the first drive of Section C so that the initial drive effects on surface settlements can be investigated. Figure 7.22 shows the subsurface conditions of the tunneling section. As can be seen in the figure, most of the tunnel alignment was excavated entirely within the stiff clay and the very stiff clay layers.

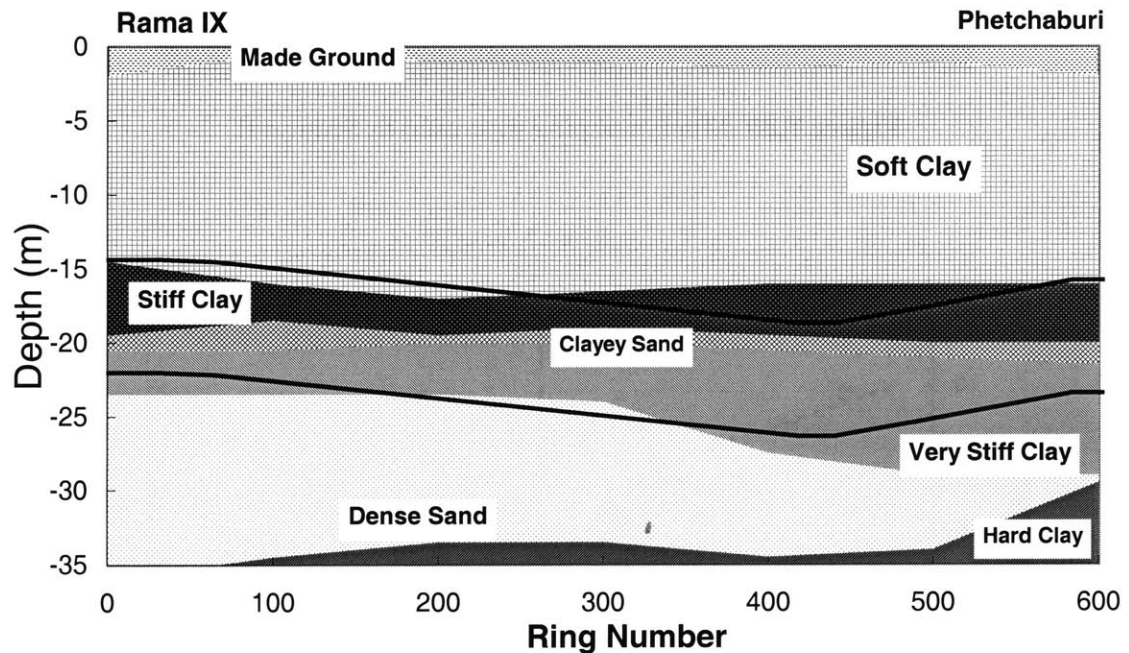


Figure 7.22 Subsurface conditions of tunneling section (northbound) between Rama IX and Phetchaburi stations (Section C)

The shield used in this section is also manufactured by Kawasaki and is very similar to the machines used in Sections A, and B. However, each shield was operated differently depending upon each contractor's practices. Maximum surface settlements and operational parameters were also measured here along the tunnel alignment as shown in Figure 7.23. As can be seen in Figure 7.23b, very high face pressures were applied at the early stage of the excavation causing significant ground heave. Additionally, the applied

face pressure was oscillated in the initial drive because the shield operator was determining an optimum pressure balance mode by trial and error.

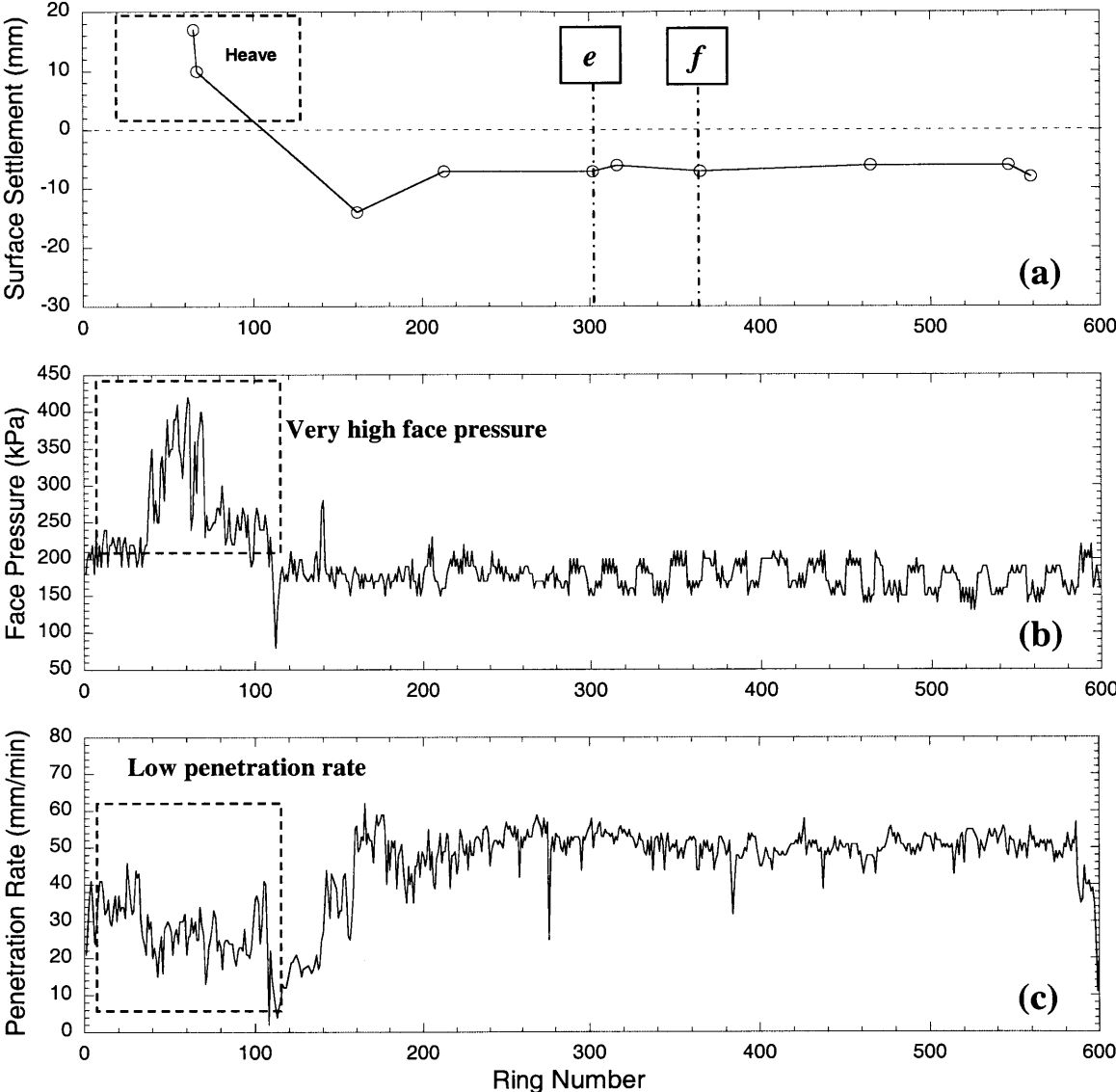


Figure 7.23 Maximum surface settlements, face pressures, and penetration rates recorded between Rama IX to Phetchaburi stations (Section C)

Unlike Section B, although penetration rates recorded in the initial drive were relatively low (Figure 7.23c), the ground surface did not settle but heaved instead. It seems that the effect of very high face pressure dominated the behavior of ground response at this location. After the shield excavated the tunnel for a distance and the shield operators succeeded in obtaining an optimum operation, relatively constant face pressures and penetration rates were recorded. The shield operation is associated with small and relatively constant settlements measured along the tunnel alignment as shown in Figure 7.23a. This is again the “earth pressure balance mode” where the EPB shield can achieve low surface settlements during excavation.

To investigate the relationship between the ground response and the advancement of the shield, surface settlements were plotted against the distance from the shield face as shown in Figure 7.24 and Figure 7.25. As can be seen in the figures, the ground began to deform 30-40 m ahead of the shield. However, as the shield approaches the measurement sections at a distance of 3-5 m in front of the shield, the ground experienced a small heave before it subsided over the shield body. If one makes a detailed observation of the face pressures recorded in these sections, it was found that the applied pressure was relatively high during shield passing. Furthermore, penetration rates were also high (Figure 7.23c). Hence, the combination of these factors may have caused heave.

Based on the observation of Tunneling Section C, the face pressure and the penetration rate have impacts on the magnitude of surface settlements. It was found that if the face pressure is very high, ground heave will be observed regardless of the penetration rate. If the face pressure is low and the penetration rate is also low, relatively large settlements will be observed. Finally, if medium level face pressure and high penetration rate are used, some surface settlements will be found.

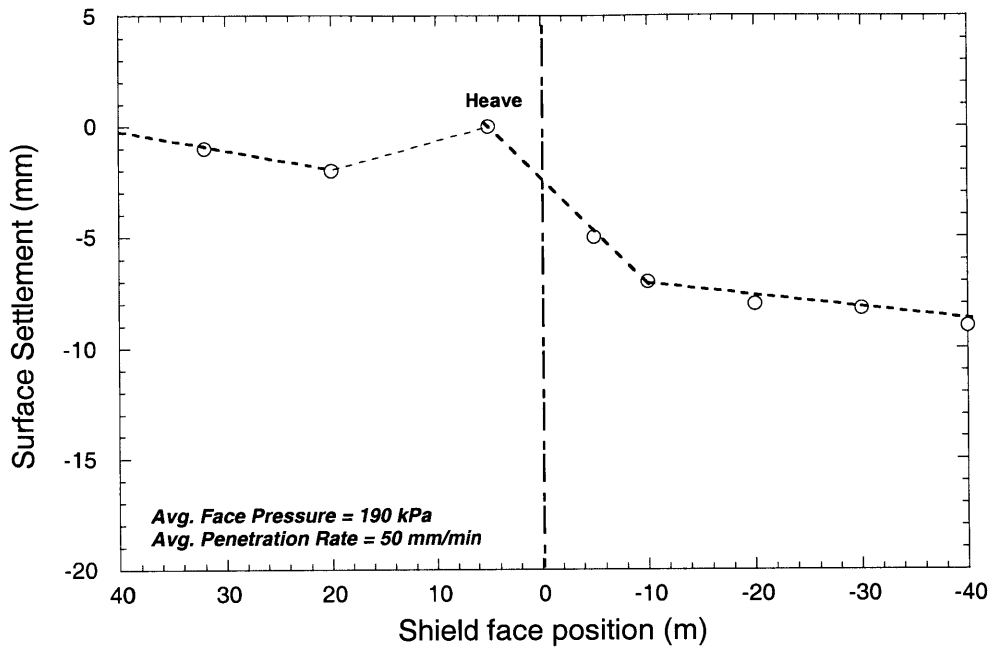


Figure 7.24 Longitudinal surface settlement profile measures at location “e” (Ring No. 303-northbound)

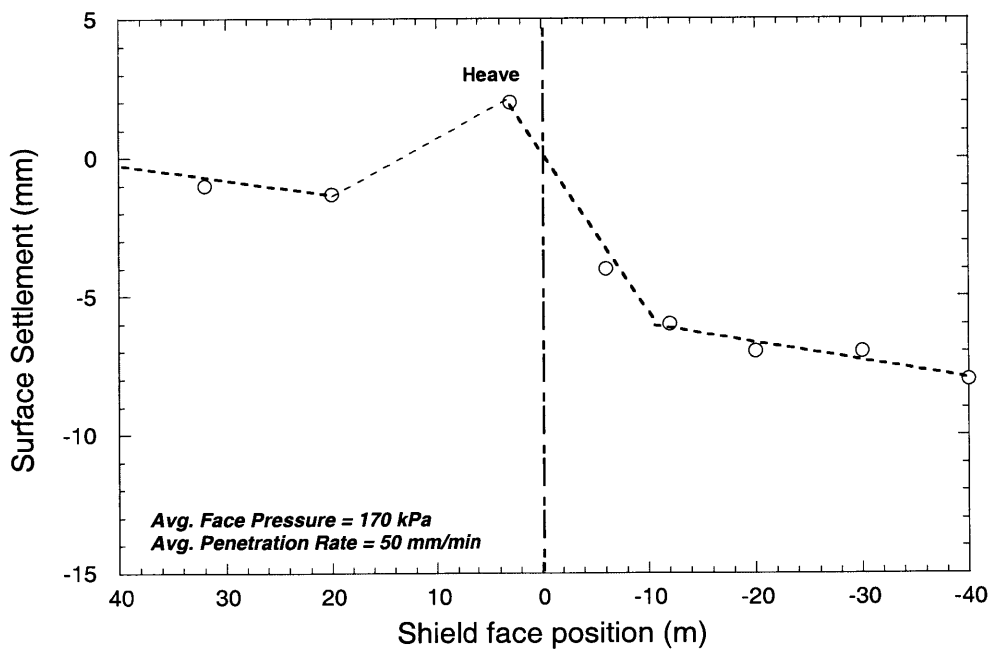


Figure 7.25 Longitudinal surface settlement profile measures at location “f” (Ring No. 366-northbound)

7.2.1.4 Settlements in Section D

In Section D, the tunnel between Sirikit station and Bon Kai station is used as a case study since it was the first tunneling drive of the section and large amounts of instrumentation were installed. Two EPB shields were driven southward to excavate the twin-tunnel underneath Rama 4 road, one of the busiest roads in Bangkok. The southbound tunnel was excavated first and followed by northbound tunnel approximately one month later. Therefore, only the southbound tunnel is considered here. Although the EPB shields are manufactured by Herrenknecht, not Kawasaki as used in Sections A, B, and C, the models are not very different.

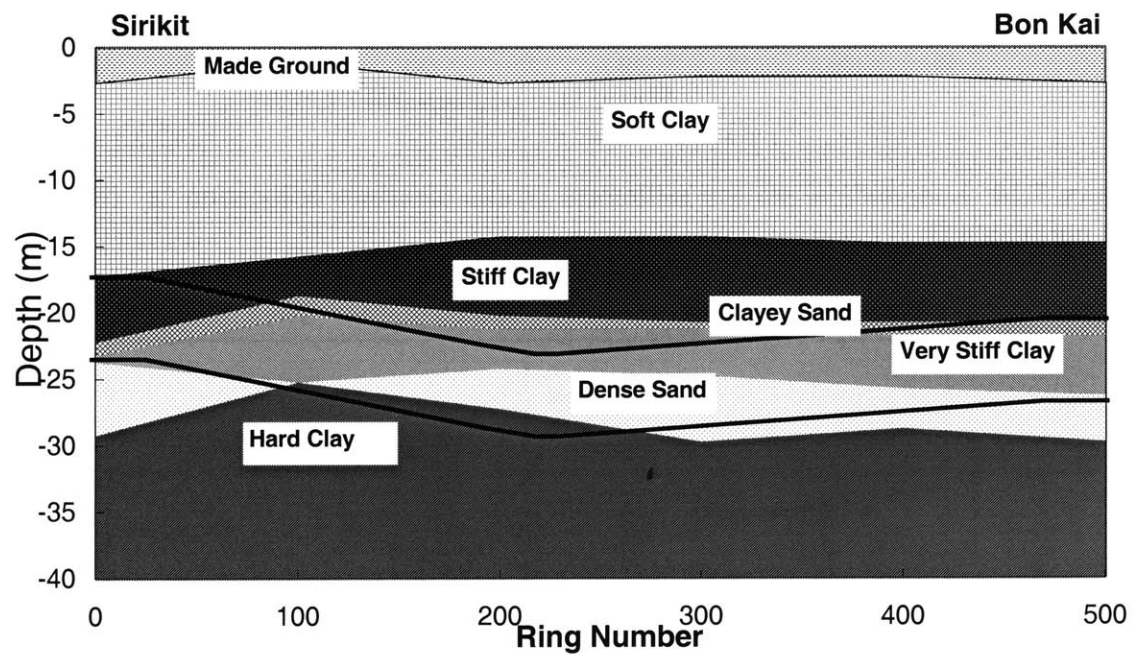


Figure 7.26 Subsurface conditions of tunneling section (southbound) between Sirikit and Bon Kai stations (Section D)

In the early portion of the excavation, the southbound tunnel was located in the stiff to very stiff clay layers. However, as the tunnel was excavated deeper to the mid half of its alignment, the tunnel was also located within the dense sand layer, which is overlain by the clay layers (Figure 7.26). As in the other sections, surface settlement markers were installed along the tunnel alignment to measure the maximum and the development of

surface settlements during excavation. Furthermore, unlike other sections where instrumentation plans concentrated largely on the measurement of surface settlements, extensometers were installed along the tunnel route in both the southbound and northbound tunnels to monitor subsurface settlements of the ground immediately above the tunnels in Section D (Figure 7.27). Because some parts of the tunnels were excavated under a 2.8-m diameter water main tunnel and under a very congested area in Bangkok, vast amounts of instrumentation were used to monitor surface and subsurface ground movements that could possibly damage the adjacent structures. Hence, the reading frequency adopted in the instrumentation plan was also higher; readings were taken every 2-4 hours instead of twice a day during shield passing to ensure that adjacent structures were safe. Consequently, detailed ground deformations presented in this section benefited from this comprehensive instrumentation plan.

Figure 7.28a shows maximum surface settlements measured along the southbound tunnel in Sirikit-Bon Kai tunneling section. Operational parameters including face pressure, penetration rate, and grouting pressure were also recorded as shown in Figure 7.28. As can be seen in the figure, substantial surface settlements occurred within the initial drive zone, where the shield still needed temporary supports as explained earlier. Within this zone, the learning curve of the crew may play an important role as well as operational parameters. For instance, Figure 7.28b shows low face pressures observed in the initial drive. After the initial drive (i.e. segmental ring number 80 or 96 meters away from the launching station), the shield developed greater face pressure that was built up to greater than 200 kPa. Obviously, in the pressure build up zone, smaller surface settlements were observed. However, based upon many case histories described in Chapter 4, it should be noted that to minimize the surface settlement, shield operators not only have to control the shield face pressure under an earth pressure balance mode, but at the same time, have to control other operational parameters such as penetration rate and grouting pressure as well. Otherwise, it is unlikely that the minimum surface settlement can be achieved. In other words, this suggests that other operational parameters are significant and also affect the ground response. As can be seen in Figure 7.28, in the early stage of excavation, penetration rates are relatively low (Figure 7.28c). Hence, the combination of low face

pressures and low penetration rates may also contribute to large surface settlements observed at the initial drive.

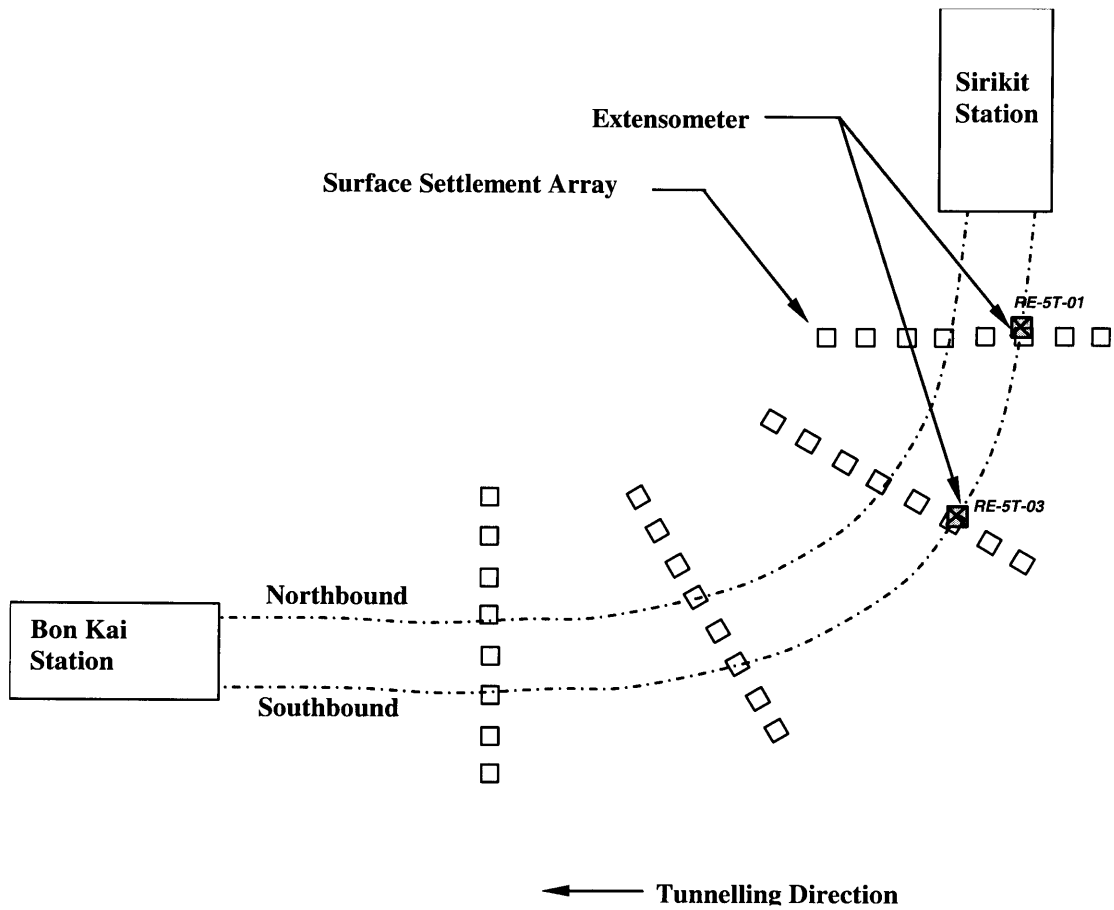


Figure 7.27 Instrumentation layout of the tunneling section from Sirikit to Bon Kai stations

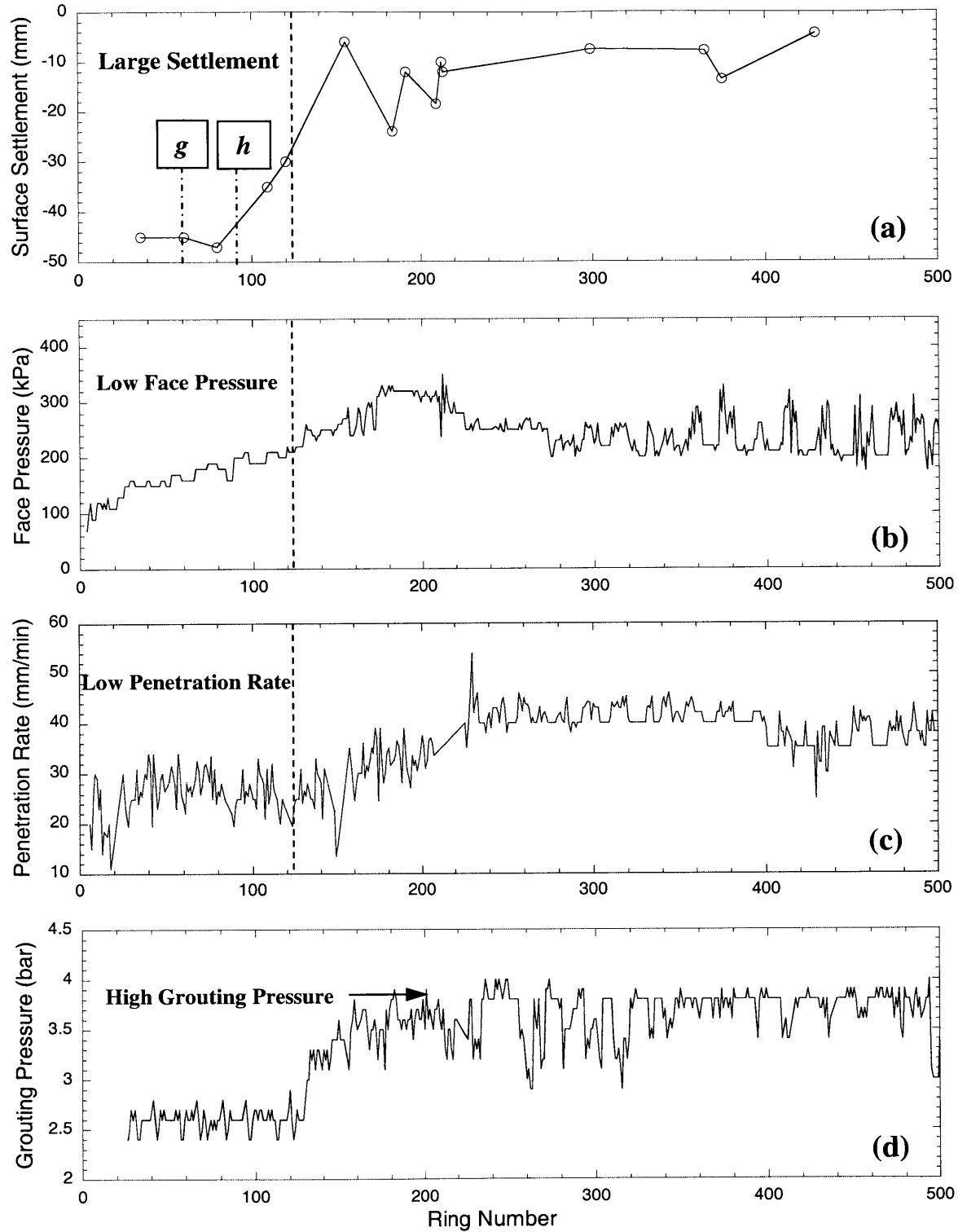


Figure 7.28 Maximum surface settlements and operational parameters recorded from southbound tunnel of Sirikit - Bon Kai tunneling section

To allow a clearer relationship between the shield operation and the ground response to be established, data observed from deep subsurface settlement measurements are analyzed. Figure 7.27 shows the locations of extensometers RE-5T-01 and RE-5T-03 installed to monitor subsurface settlements during excavation of the southbound tunnel. Within the initial drive zone, extensometer RE-5T-01 was located above ring no. 60 marked as “g” in Figure 7.28a. The instrument recorded the development of ground movements over the shield as shown in Figure 7.29. As expected, large ground deformations were found over the shield crown at the monitoring depth of 15.3 m from the ground surface, and the magnitude of ground deformation decreases with decreasing monitored depth. If one takes a detailed look at the settlement curves, it was found that the ground began to subside approximately 10 meters ahead of the shield face and its deformation accelerated substantially over the shield body. The deformation then increased only slightly after the shield tail passed and no significant settlements were observed about 30 m after shield passing. Large ground settlements occurring ahead and over the shield may result from low face pressures and low penetration rates applied during shield passing (see Figure 7.28). Measurements were also made with extensometer RE-5T-03 which was installed over the southbound tunnel ring No. 91, marked as “h” in Figure 7.28a. Subsurface settlements measured with this extensometer also indicated very large settlements over the shield body as plotted in Figure 7.30. However, the magnitude of settlements is lower than that in measurement section “g” where lower face pressures and penetration rates were applied.

Although very large ground deformation developed over the shield body as shown in both measurement sections, the development appeared to slow down considerably as sharp inflection points of settlement curves were observed over the shield tail. Tail void grouting was performed at the segmental lining right behind the shield as shown in Figure 7.31 and Figure 7.32. Evidently, this caused the inflection in the settlement curve. Note that tail void closure is a component causing ground deformation because of the gap between lining and ground (see also Section 3.1). For the MRTA project, the outer diameter of the tunnel is 6.3 meters but the shield outer diameter is 6.43 meters so that, at least, a tail gap of 6.5 cm was created after shield passing. If no grouting was adopted to

fill the void, the deformation in Zone 2 would extend further as illustrated in Figure 7.33a. However, tail void grouting was usually done and further ground movement over the tunnel could be prevented as shown in Figure 7.33b. It should be also noted that the grouting pressure applied during excavation is very high in this tunneling section. Practically, the grouting pressure should be maintained above 2 bar but less than 3 bar as adopted in Sections A, B, and C. However, unlike other sections, the grouting pressure was maintained at over 2.5 bar or even as high as 4 bar in Section D.

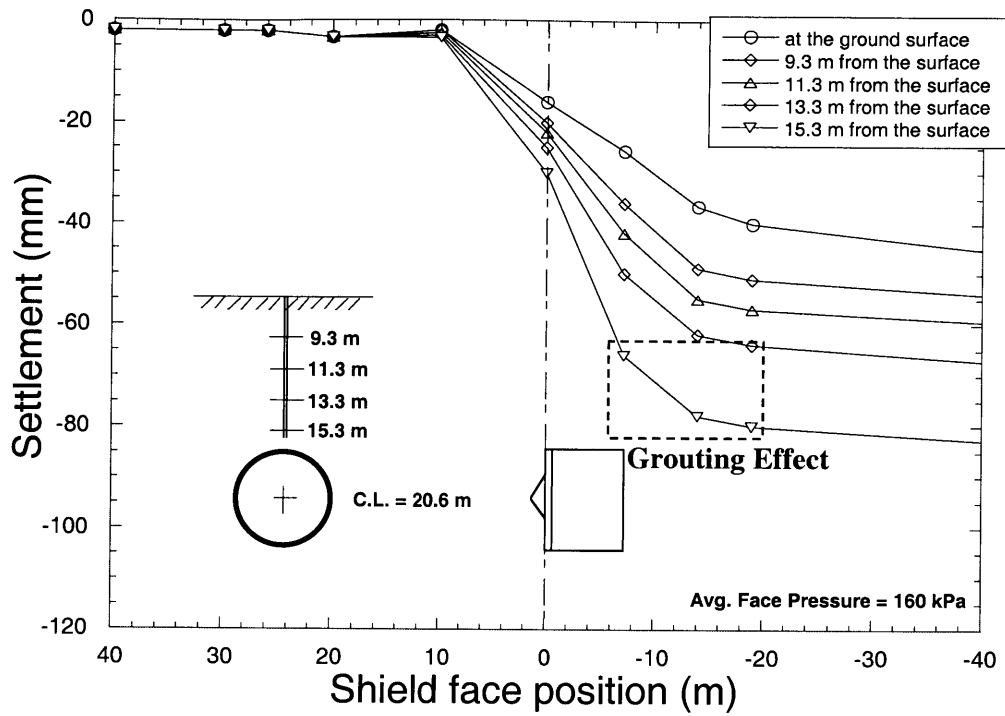


Figure 7.29 Subsurface settlements measured on RE-T5-001 (SB no.61)

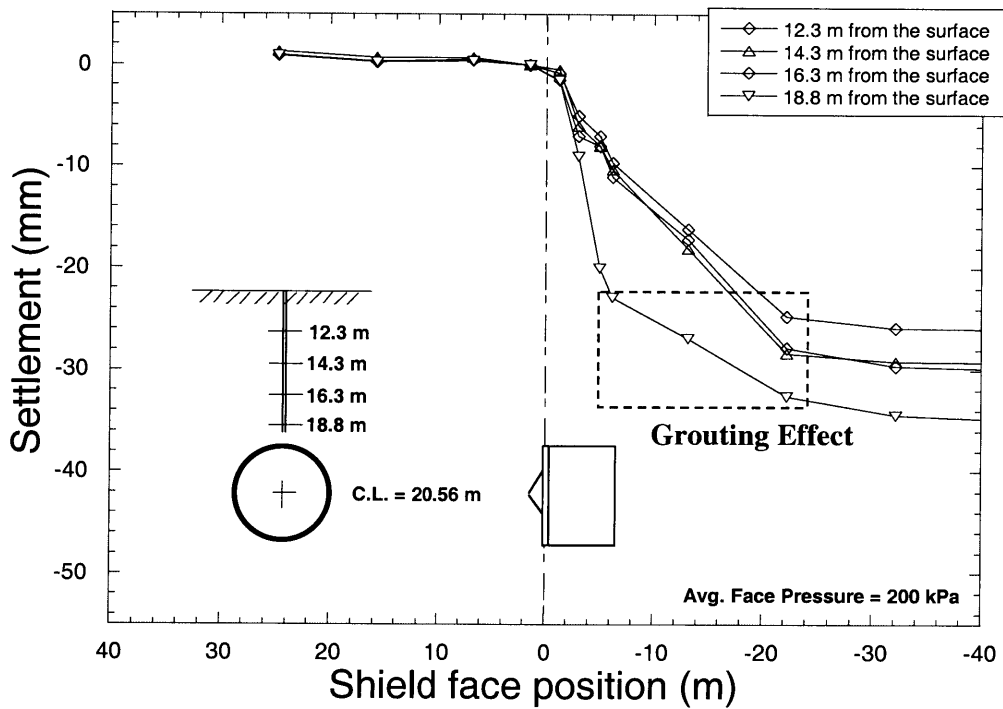


Figure 7.30 Subsurface settlements measured on RE-T5-003 (SB no. 91)



Figure 7.31 Grout hole at the segmental lining (MRTA project)

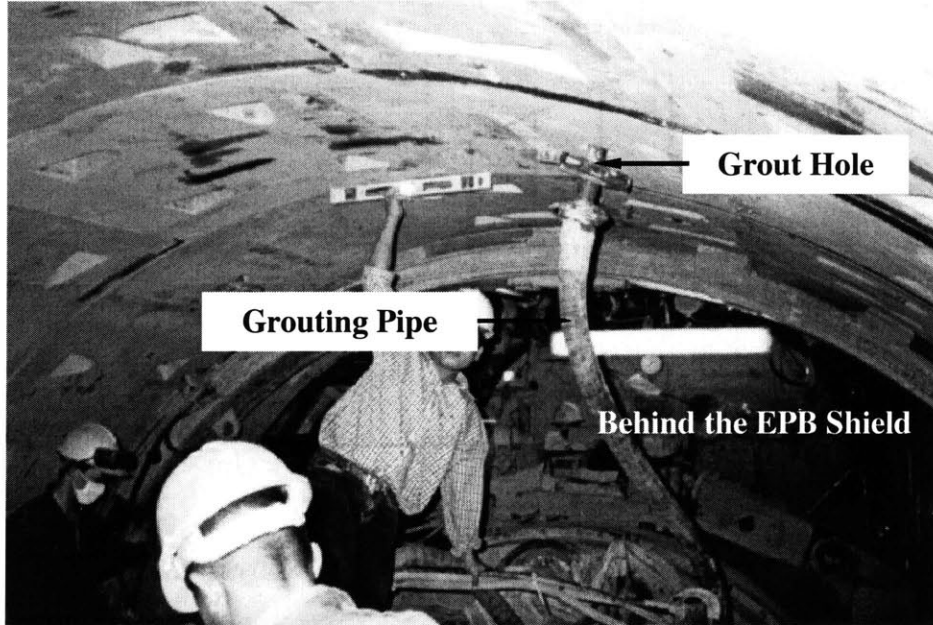
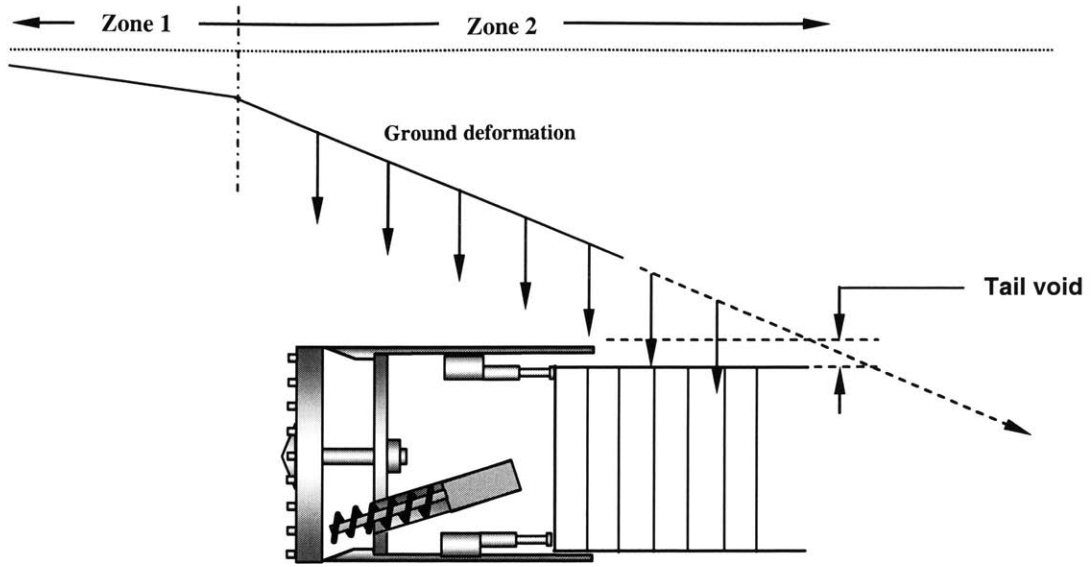
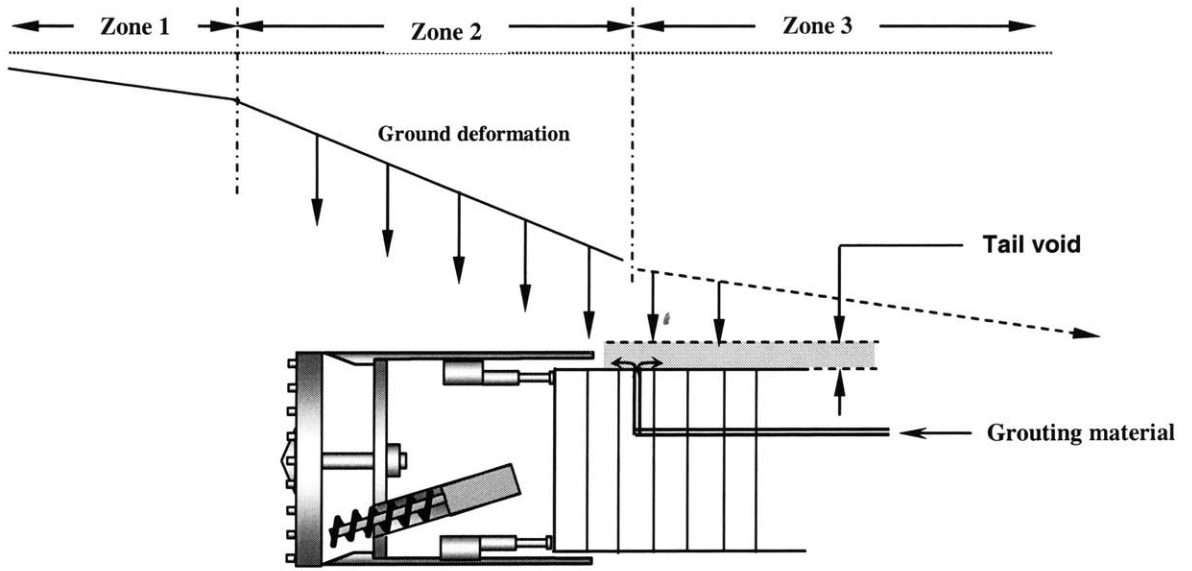


Figure 7.32 Tail void grouting performed behind the shield after segmental linings are completely installed (MRTA project)



(a) Without tail void grouting



(b) With tail void grouting

Figure 7.33 Effect of tail void grouting on ground settlement

7.2.2 Transverse Surface Settlements

As shown in the previous section, EPB tunneling generates settlements at the ground surface. The magnitude of the settlements depends upon many factors, and it is very difficult to predict. Based on several case histories and the observation of the MRTA project, surface settlements not only developed longitudinally as affected by the shield advance but are also distributed in the transverse direction causing a depression trough at the ground surface. In the MRTA project, transverse settlements were measured by settlement marker arrays installed over the tunnel alignment. Results of the measurement are shown in Figure 7.34 to Figure 7.55. Note that the discussion in this section refers to settlement troughs above a single tunnel. The second tunnel effects will be discussed in Chapter 8.

As can be seen in these figures, most of surface settlement troughs are very symmetric with respect to the tunnel centerline. Since the Gaussian curve or normal probability function is the most popular approach used for modeling the shape of surface settlement troughs induced by tunneling (Mair and Taylor, 1997), it is attempted to describe the settlement troughs measured in the MRTA project in this manner. As a matter of fact and as shown in Figure 7.34 through Figure 7.55, the Gaussian curves do fit the settlement troughs very well. As earlier discussed in Chapter 3, the settlement curve can be empirically and fully characterized by the maximum settlement (δ_{max}) and the trough width parameter/distance (i), which is obtained from the best fit of the Gaussian curve to the observed data. The surface settlement δ at a distance y from the tunnel centerline can be determined by the following equation (see also Section 3.2.1.2):

$$\delta = \delta_{max} \exp\left[-\frac{y^2}{2i^2}\right] \quad (7-1)$$

The two most popular methods used for estimating surface settlement trough width (i) are: (1) Peck (1969)'s solution and (2) O'Reilly and New (1982)'s solution. Both

solutions use the Gaussian curve to fit transverse settlement data points by adjusting the trough width parameter (i). Their recommended trough width parameter is based upon observations of many case histories as also described in Chapter 3. In this study, both solutions are investigated to determine the validity of the empirical methods in the MRTA project where EPB tunneling technique was used.

First, trough width parameters obtained by fitting the measured surface settlement data points with the Gaussian curves are plotted with the Peck (1969)'s empirical curve as shown in Figure 7.56. As can be seen, most of the data fall within the "Sand below ground water level" zone rather than "Soft to stiff clay" zone in which most of the tunnel alignment in the MRTA project located. The finding suggests that Peck (1969)'s empirical recommendation is not suitable for this case.

Figure 7.57 shows the data plotted with $i = Kz$ lines recommended by O'Reilly and New (1982). Most of the data are located within the range bounded by $i = 0.4z$ and $i = 0.6z$. This is in agreement with the conclusion of O'Reilly and New (1982) that for most cases, $i = 0.5z$ irrespective of whether the tunnel is in soft or stiff clays. Only one point is located between $i = 0.4z$ and $i = 0.3z$ lines. The data for this point was measured above the tunnel centerline where the shield encountered a sand layer (Figure 7.55). As can be seen in that figure, the Gaussian curve can fit the data well, but the trough is much narrower compared to the troughs where the tunnel was excavated in the stiff clay layer. Previous laboratory tests done by Potts (1976) and Cording et al. (1976) suggested that the Gaussian curve is unlikely to be applicable to granular materials. Instead, a rapid narrowing with large inward displacements of the settlement trough near the ground surface with the sand funneling down into the void created by the tunneling would be expected as described in Chapter 3. However, the results of the tests were only based upon a case in which a tunnel is excavated entirely in and underneath a whole layer of sand not in stratified soil conditions where stiff and soft clay layers overlie the sand layer as in the MRTA project.

Case histories with field observations of surface settlement profiles above stratified soils where the tunnel is excavated in sands overlain by clay layers (e.g., Ata, 1996 and Atahan et al, 1996) also indicate wider settlement troughs than would be obtained if the tunnels were excavated entirely in sands. Hence, in the case where the tunnel is excavated within the sand layer overlain by clay layers, the trough width parameter is slightly greater than $i = 0.3z$ (i.e. $i = 0.35z$ for the point shown in Figure 7.57). Furthermore, the study done by Mair and Taylor (1997) suggested that based on many collected data obtained from tunnels in sands, trough width parameters fall within the bound of $i = 0.25z$ and $i = 0.45z$, with a mean line of $i = 0.35z$ and no significant difference between tunnels below or above the water table, contrary to the suggestion by Peck (1969).

In the MRTA project, it should be noted that all surface settlement troughs were measured 3 days after shield passing or about 30 m. behind the shield face. This is the point classified as the maximum settlement (δ_{max}) after which there is no significant change in the magnitude of surface settlements as discussed in the previous section. Additionally, in this study, we consider the ground response only affected by the EPB shield (i.e. during and immediately after shield passing) not by consolidation settlements (i.e. long term settlement). The long term settlement may have an effect on the surface settlement trough as reported by Mair and Taylor (1997) in that additional post-construction settlements due to consolidation may cause wider settlement troughs.

In Figure 7.58, the trough width parameters obtained where the tunnel was excavated in clay layers in the MRTA project are plotted together with the data from tunnels in clays collected by Mair and Taylor (1997). Although, the reference data were based on various types of tunneling including slurry shield, mechanical shield, open shield, and NATM, most of the data show no apparent influence of the tunneling method and were bounded between $i = 0.4z$ and $i = 0.6z$. Only some points are out of the bounds. It was suggested that the width of the surface settlement trough above tunnels in clays only depends on tunnel depth not on the tunneling method. Hence, if the maximum surface settlement (δ_{max}) is known, using the Gaussian function with the recommended trough width parameter can make it possible to predict the settlement trough induced by tunneling.

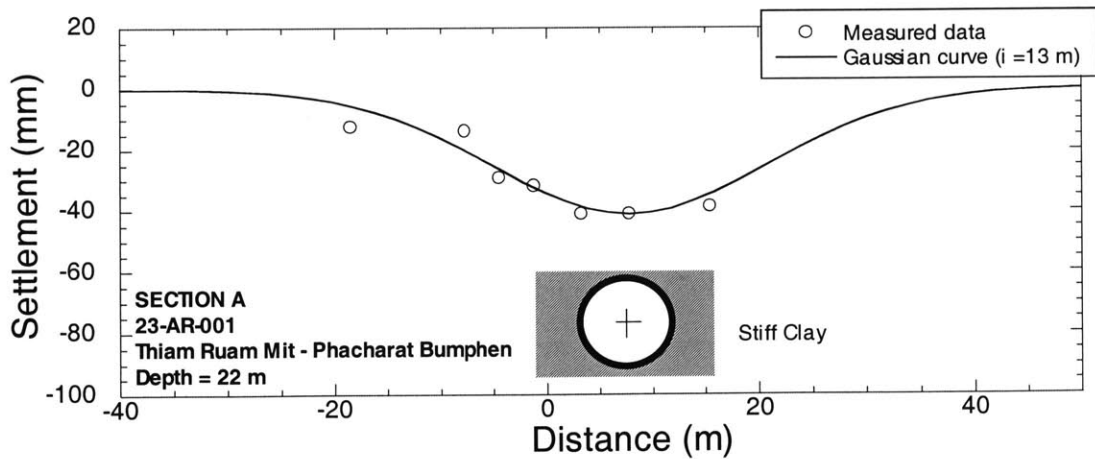
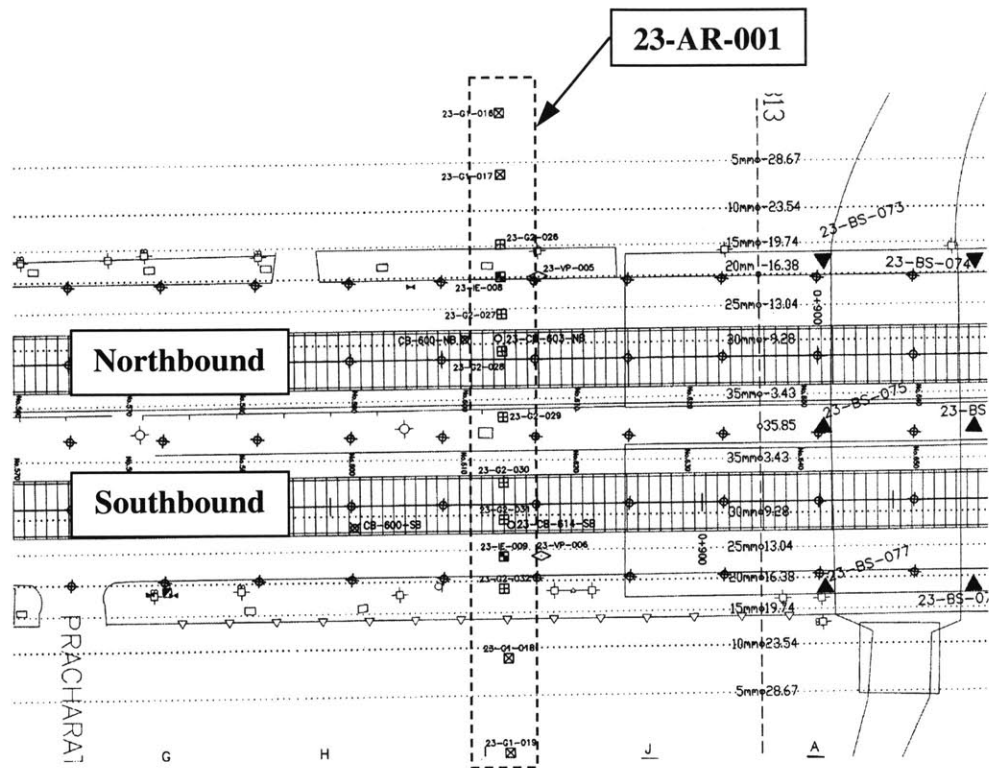


Figure 7.34 Surface settlement trough measured on 23-AR-001 (southbound tunnel-Ring no.613) and the instrumentation layout

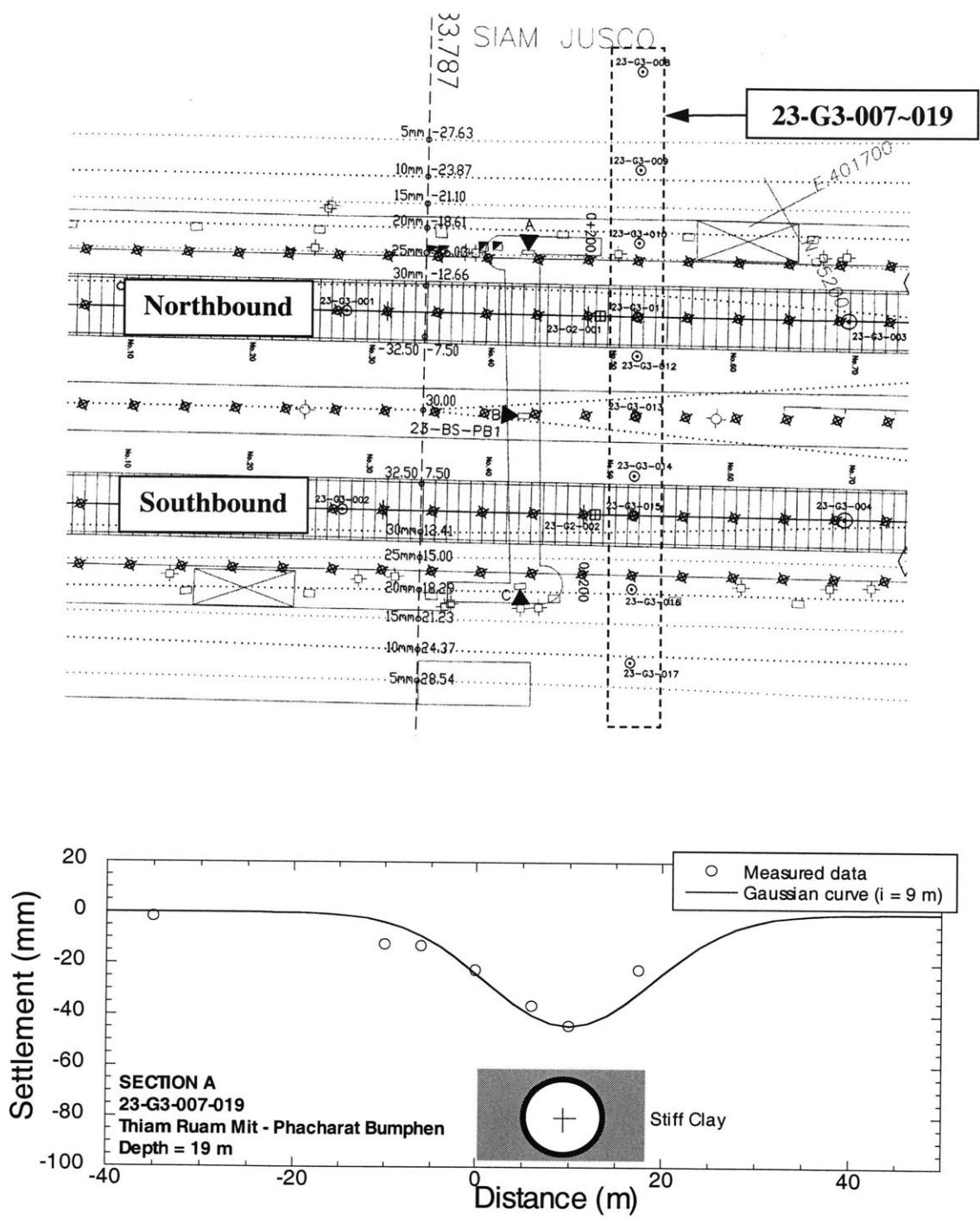


Figure 7.35 Surface settlement trough measured on 23-G3-007-019 (southbound tunnel-Ring no.52) and the instrumentation layout

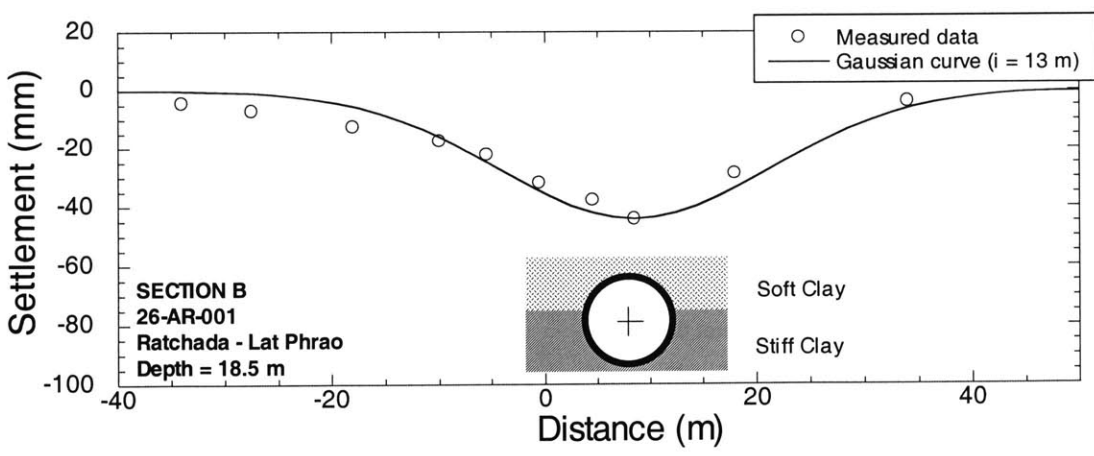
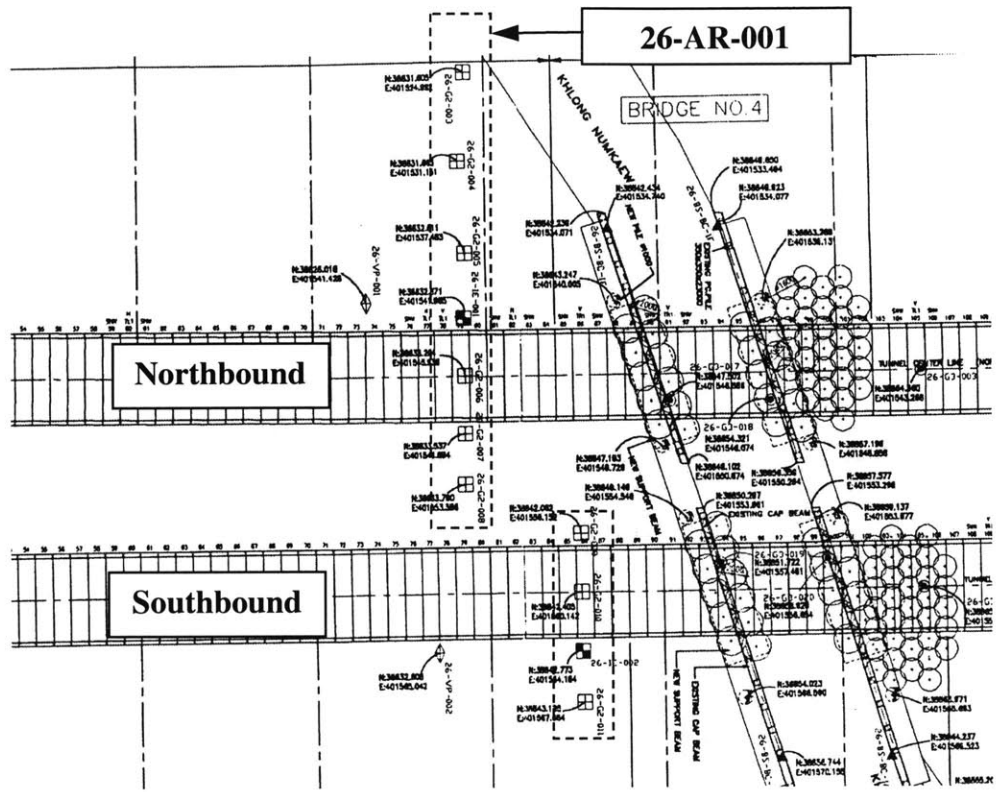


Figure 7.36 Surface settlement trough measured on 26-AR-001 (southbound tunnel-Ring no.86) and the instrumentation layout

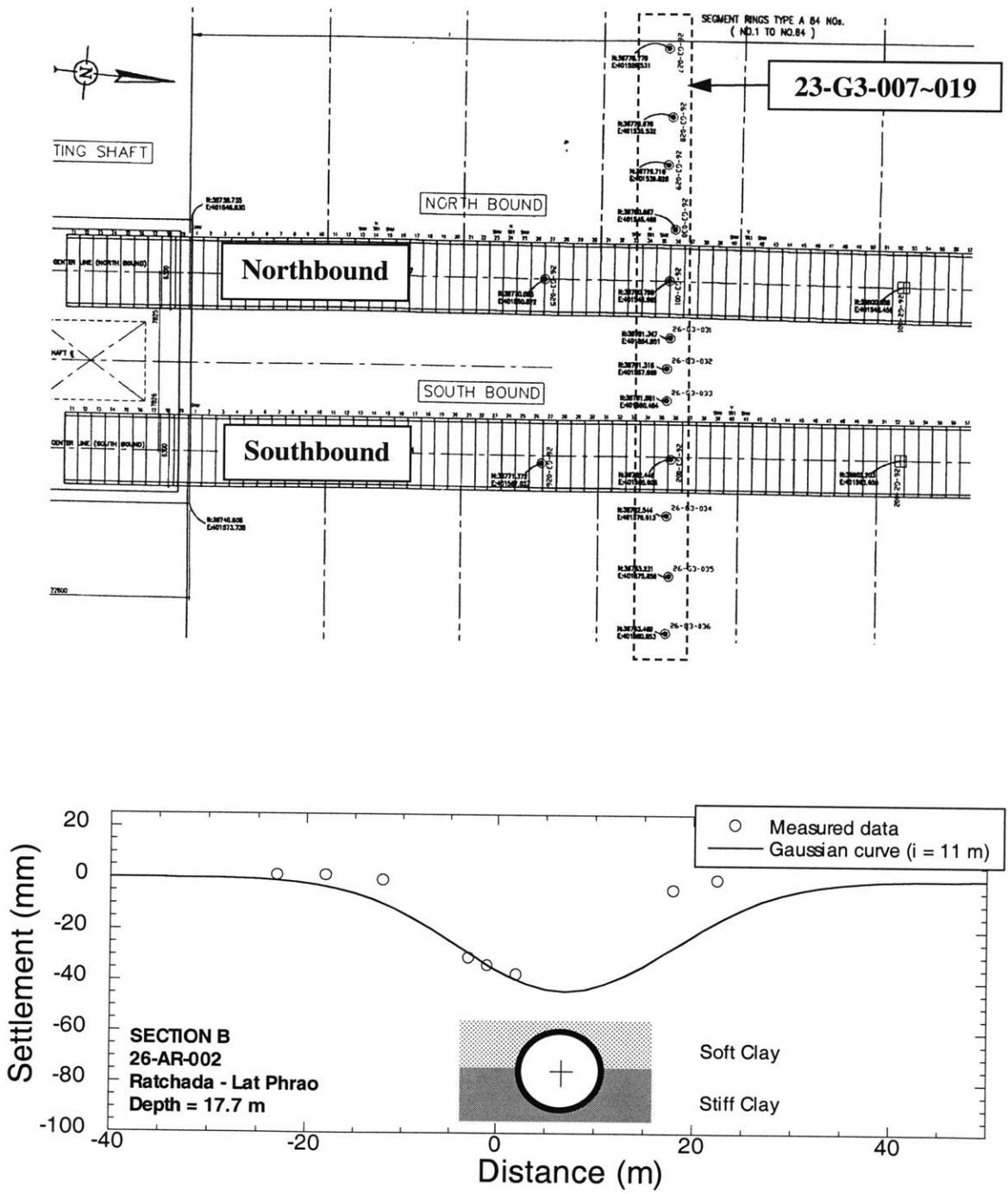


Figure 7.37 Surface settlement trough measured on 26-AR-002 (southbound tunnel-Ring no.36) and the instrumentation layout

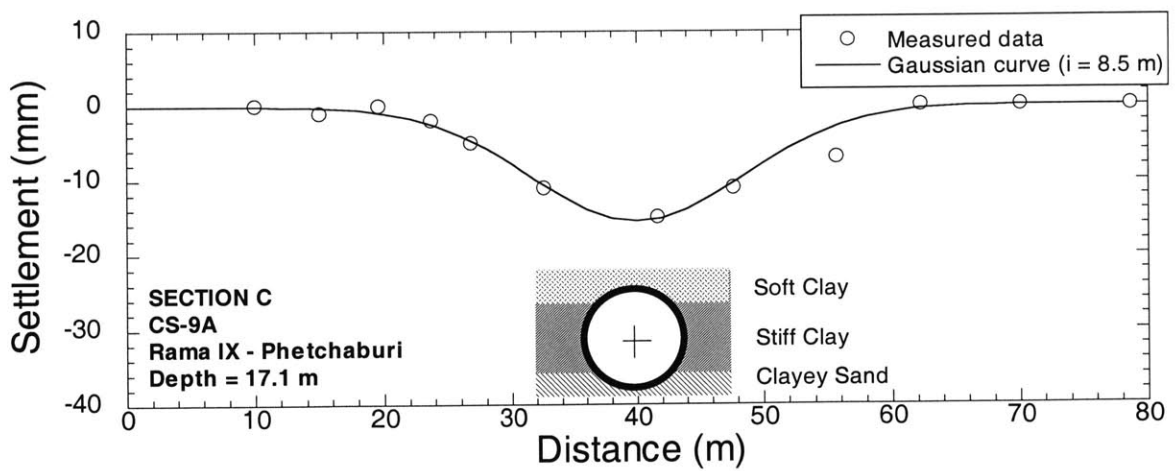
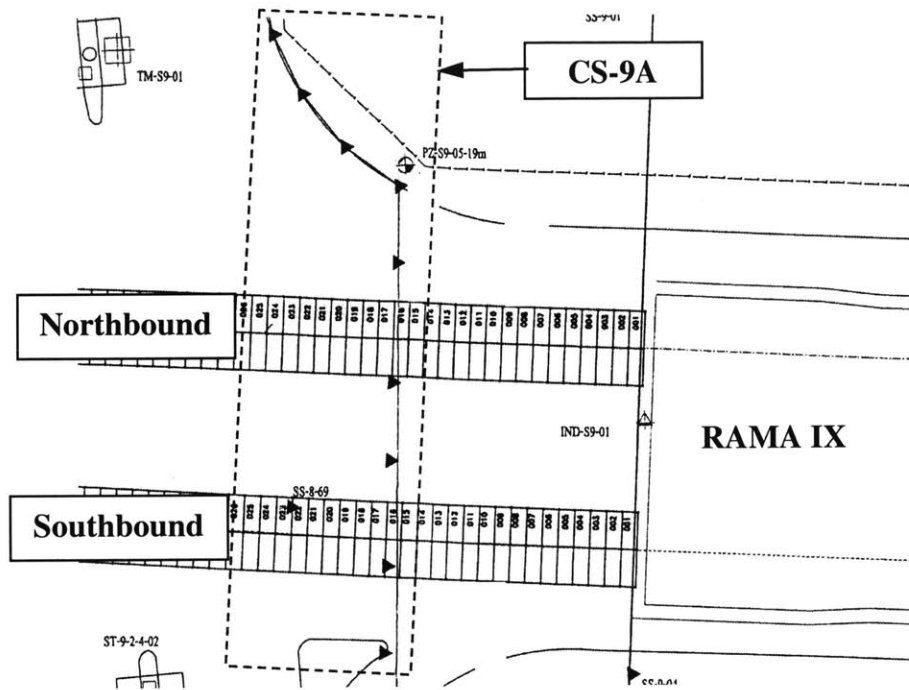


Figure 7.38 Surface settlement trough measured on CS-9A (northbound tunnel-Ring no.16) and the instrumentation layout

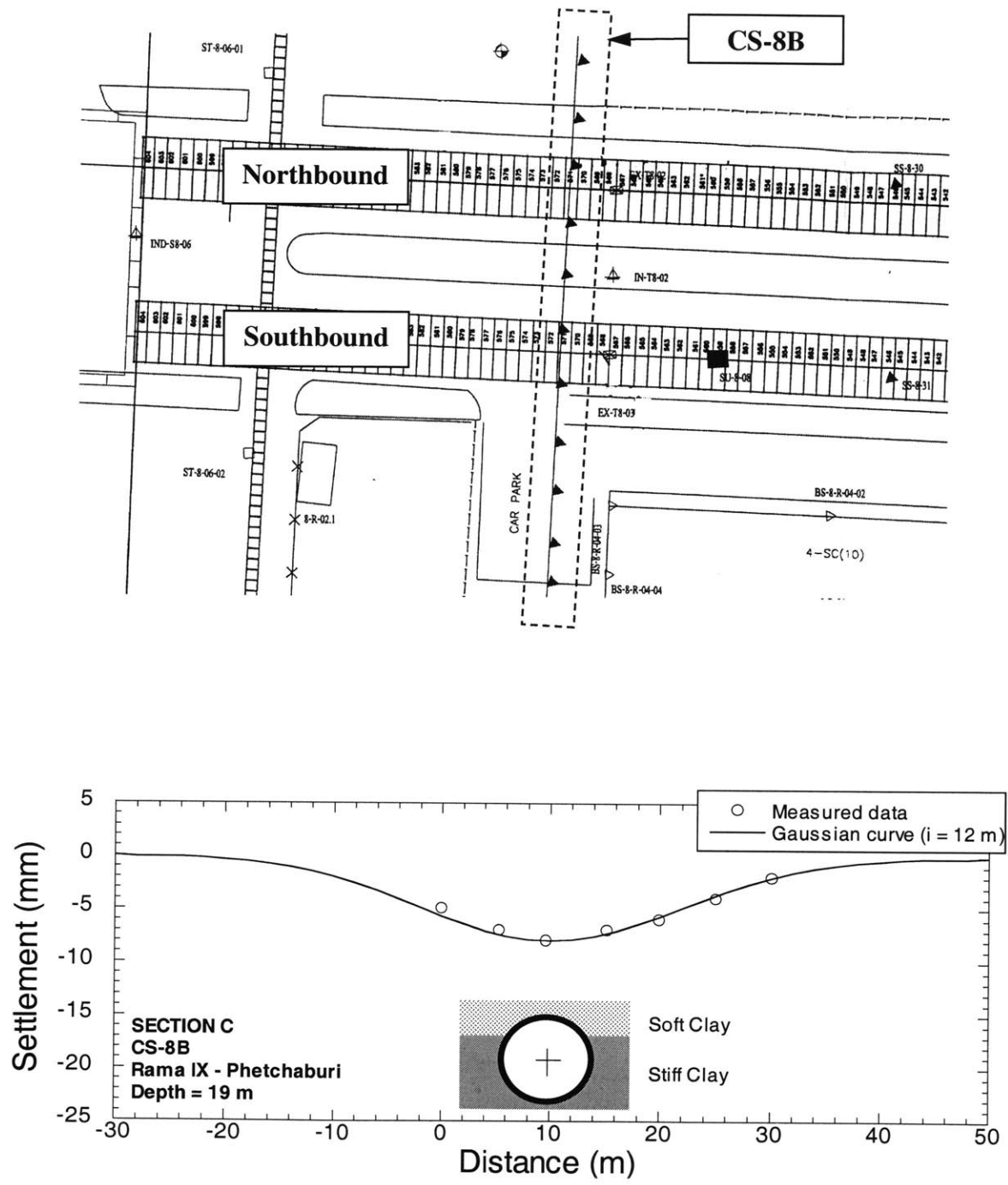


Figure 7.39 Surface settlement trough measured on CS-8B (northbound tunnel-Ring no.571) and the instrumentation layout

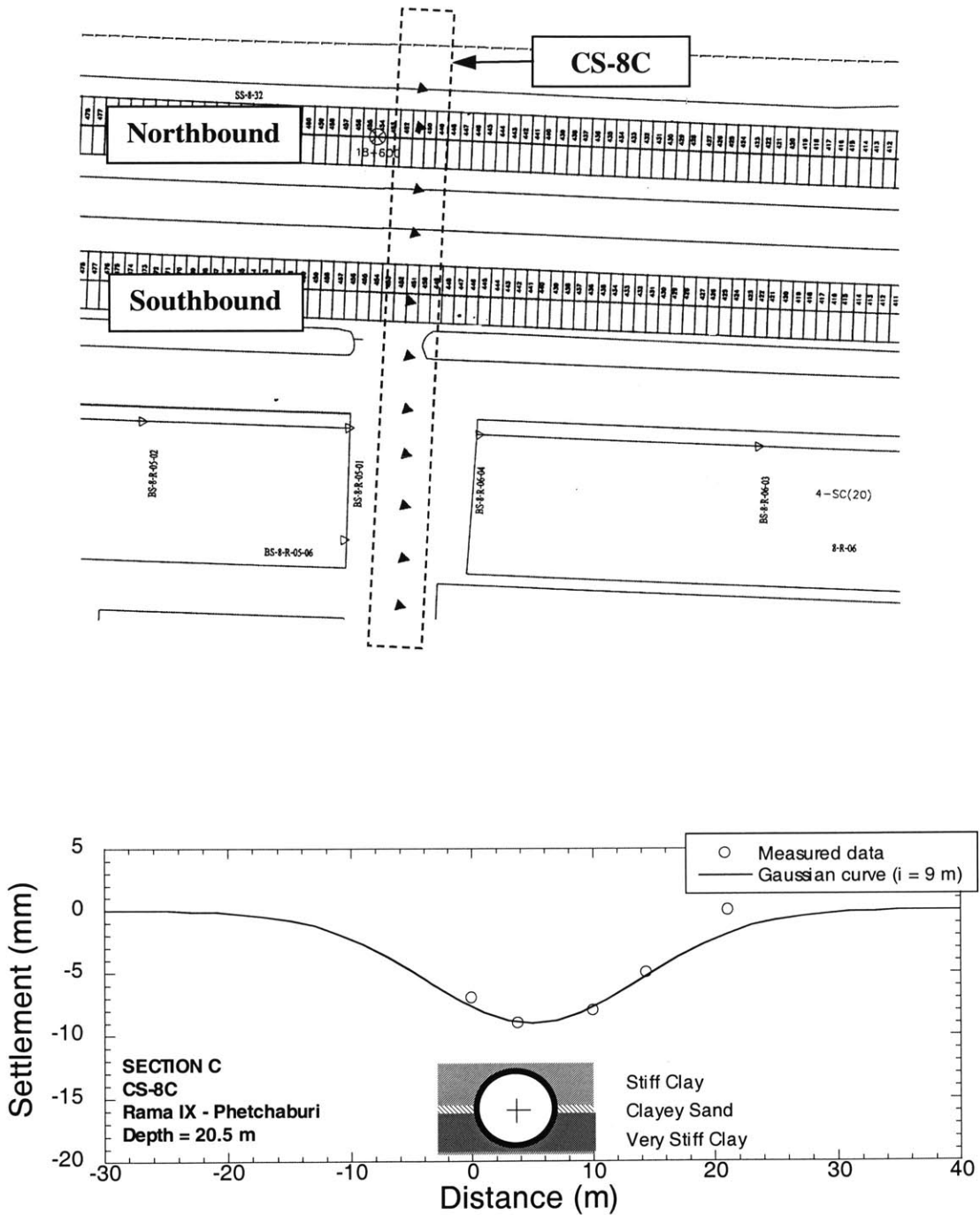


Figure 7.40 Surface settlement trough measured on CS-8C (northbound tunnel-Ring no.451) and the instrumentation layout

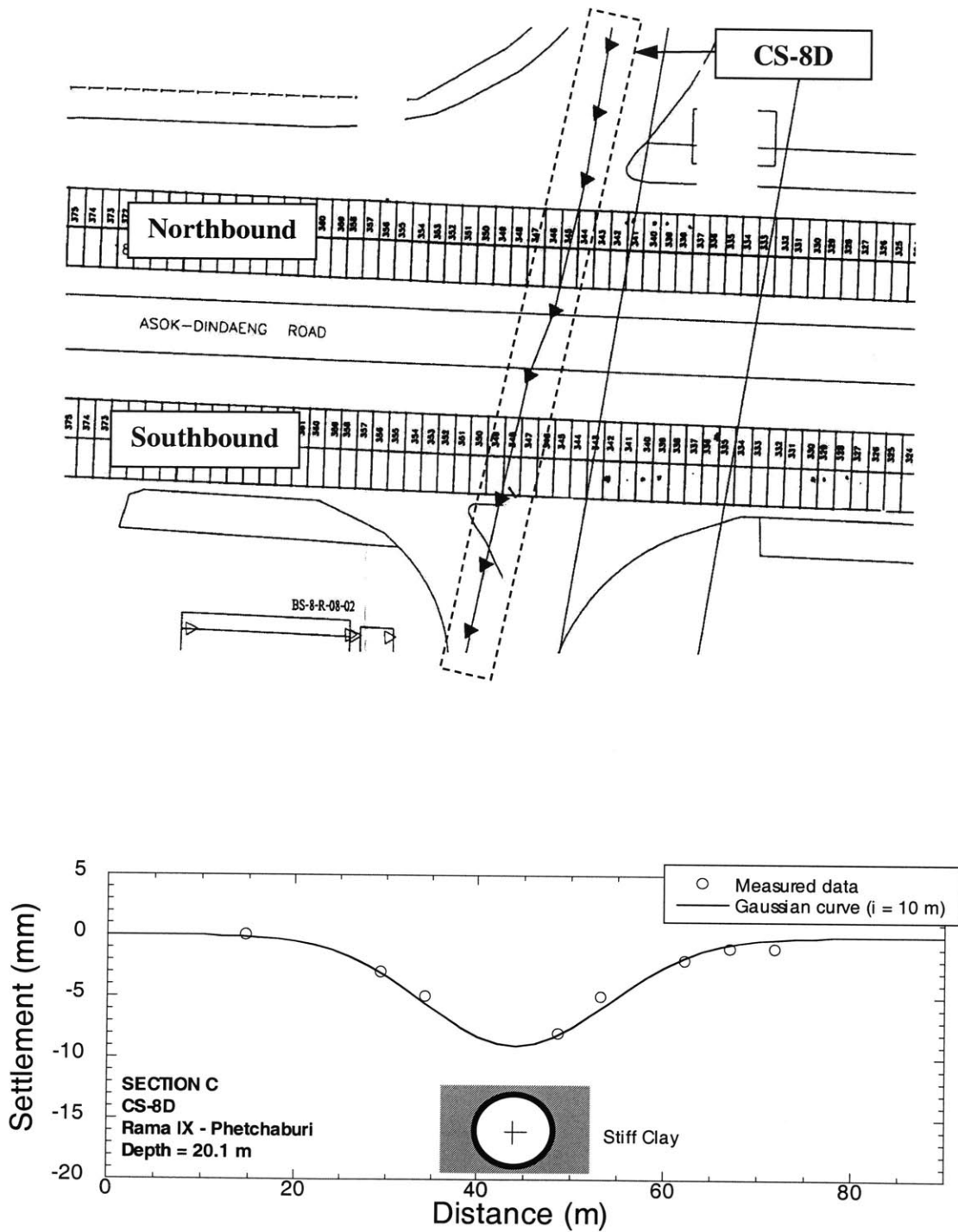


Figure 7.41 Surface settlement trough measured on CS-8D (northbound tunnel-Ring no.345) and the instrumentation layout

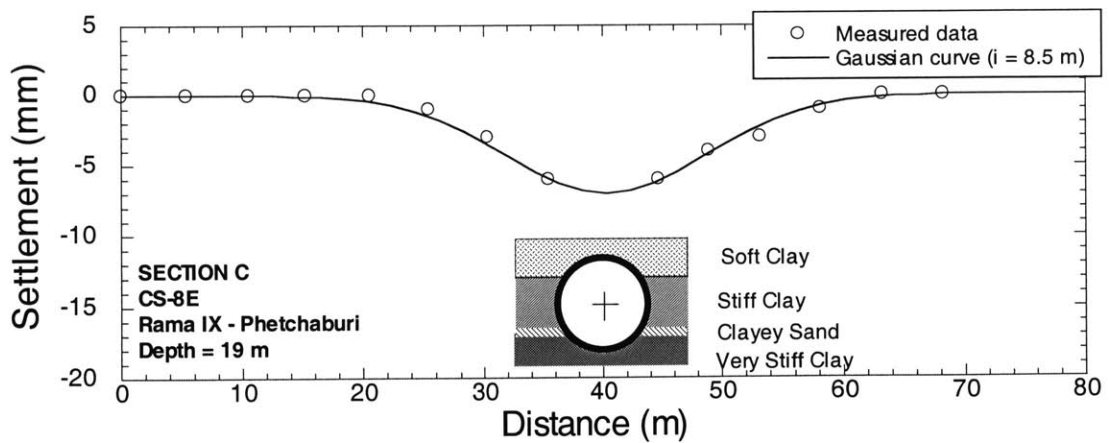
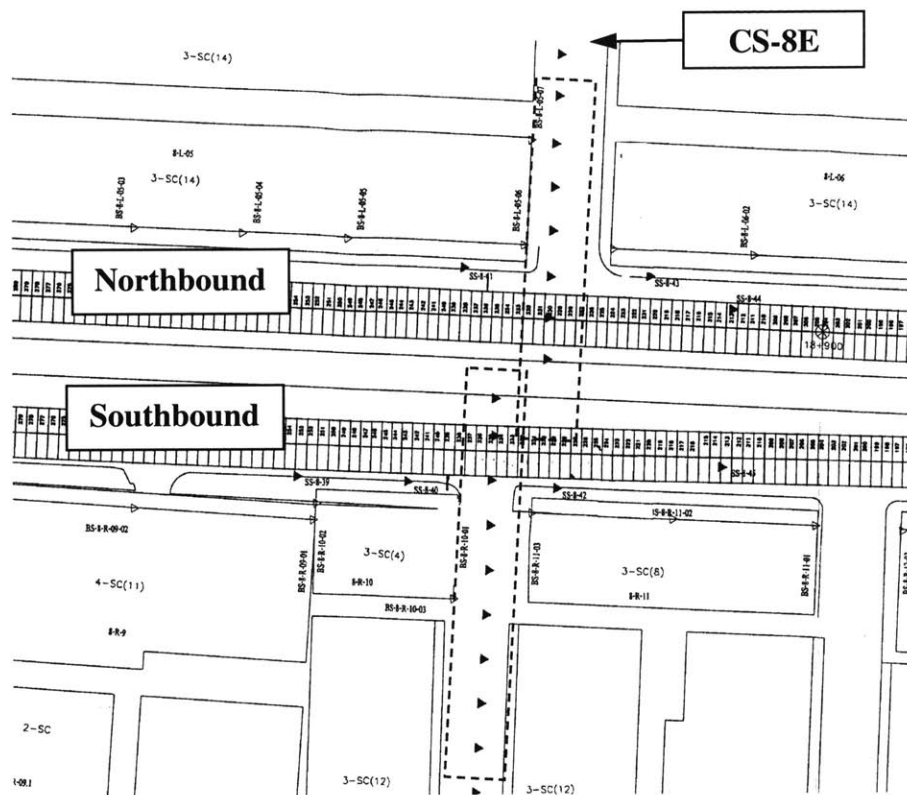


Figure 7.42 Surface settlement trough measured on CS-8E (northbound tunnel-Ring no.230) and the instrumentation layout

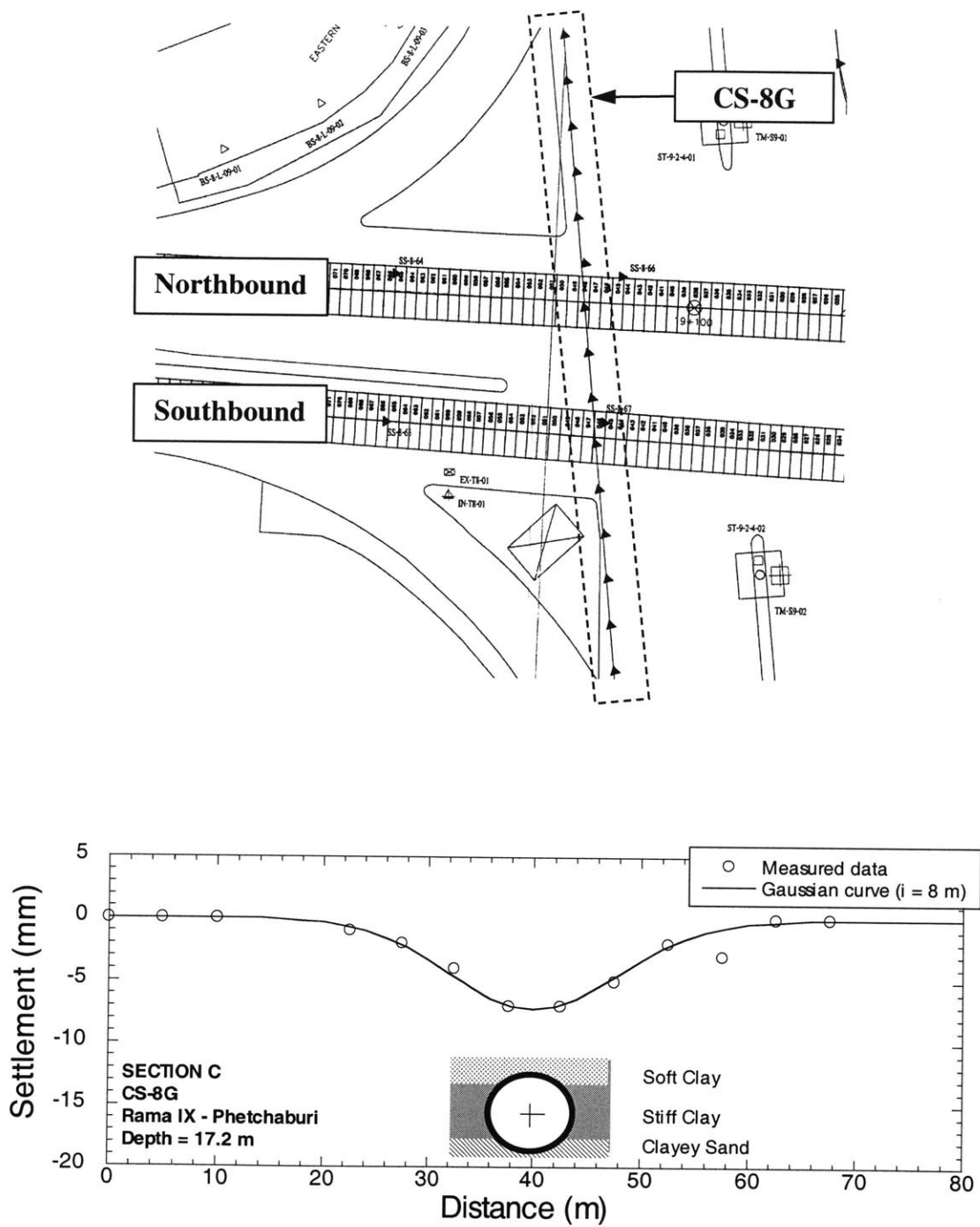


Figure 7.43 Surface settlement trough measured on CS-8G (northbound tunnel-Ring no.48) and the instrumentation layout

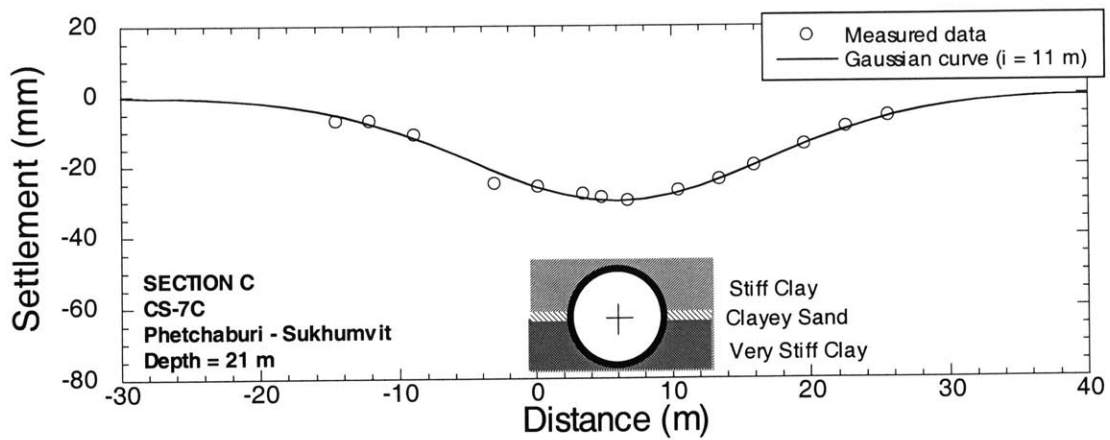
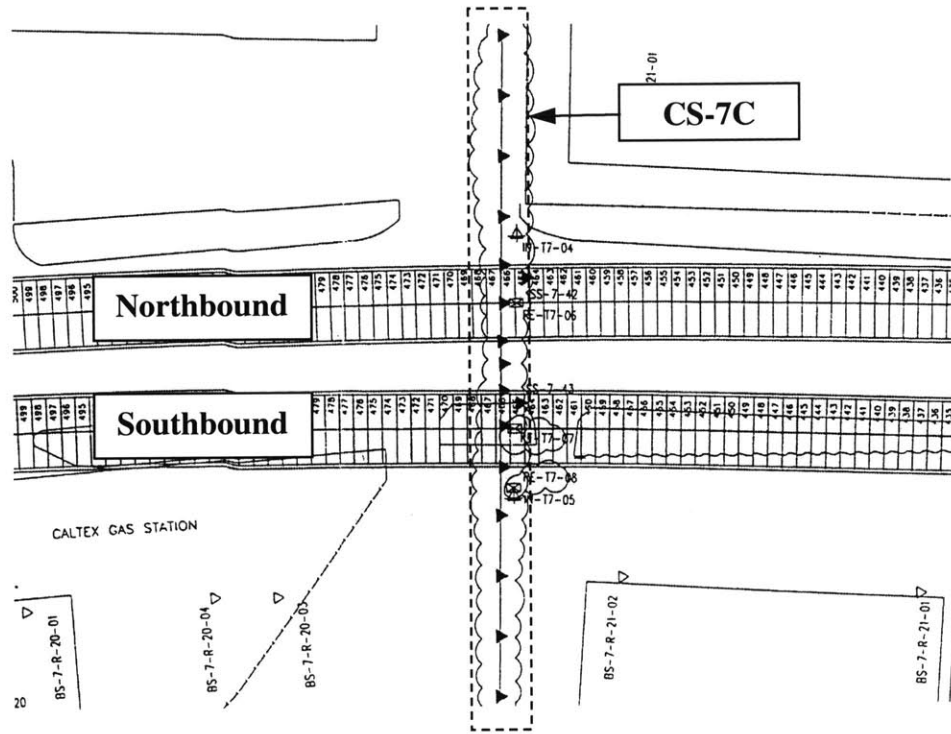


Figure 7.44 Surface settlement trough measured on CS-7C (northbound tunnel-Ring no.466) and the instrumentation layout

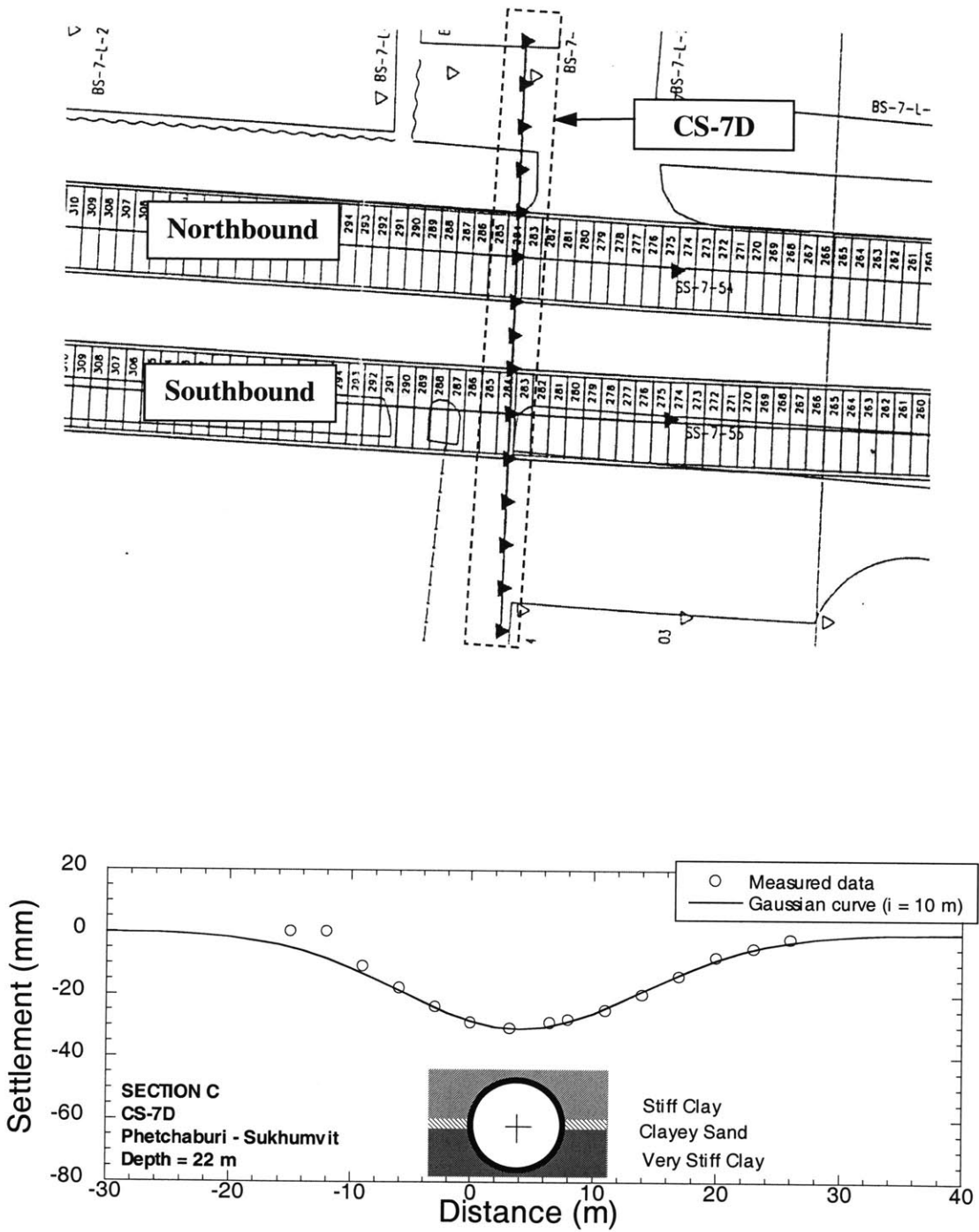


Figure 7.45 Surface settlement trough measured on CS-7D (northbound tunnel-Ring no.284) and the instrumentation layout

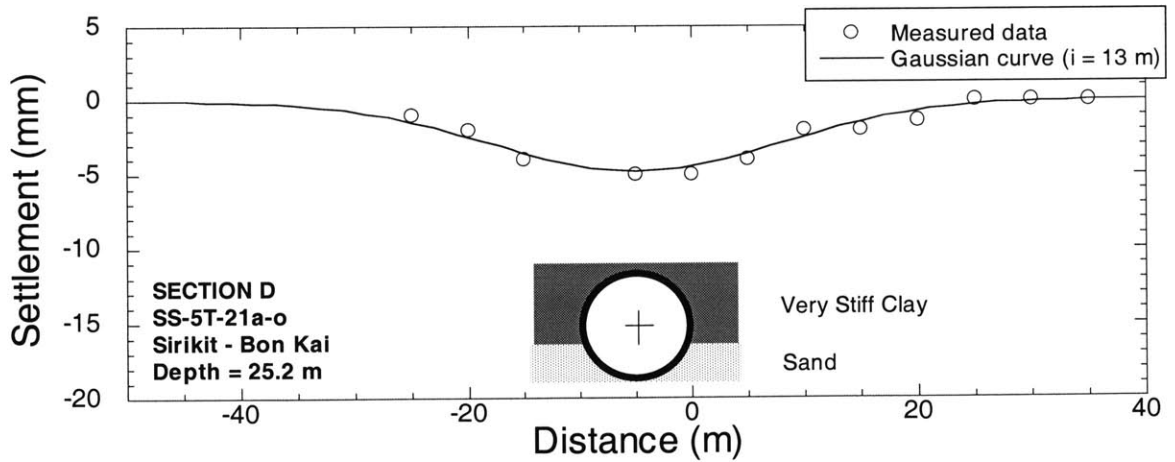
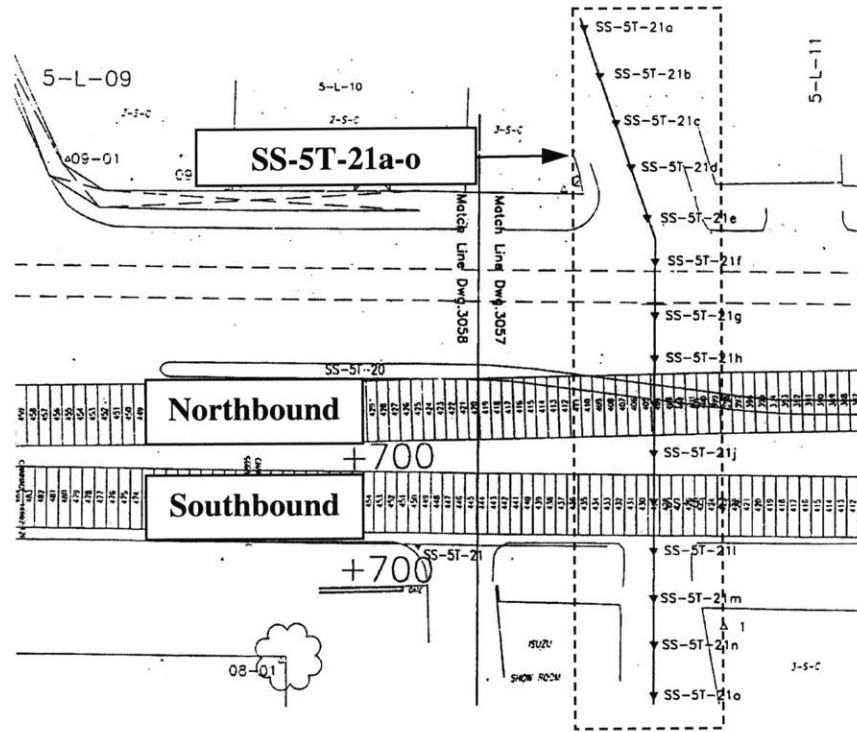


Figure 7.46 Surface settlement trough measured on SS-5T-21a-o (southbound tunnel-Ring no.429) and the instrumentation layout

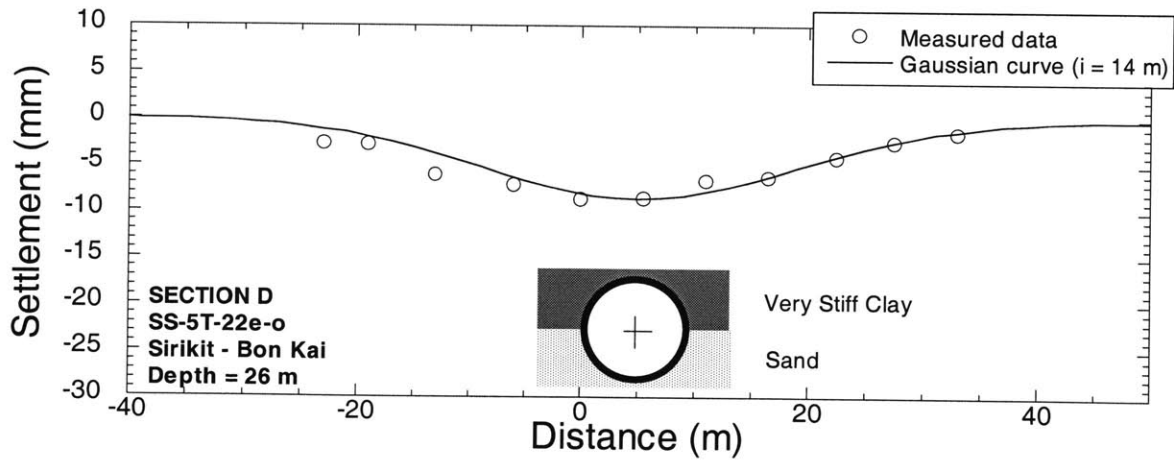
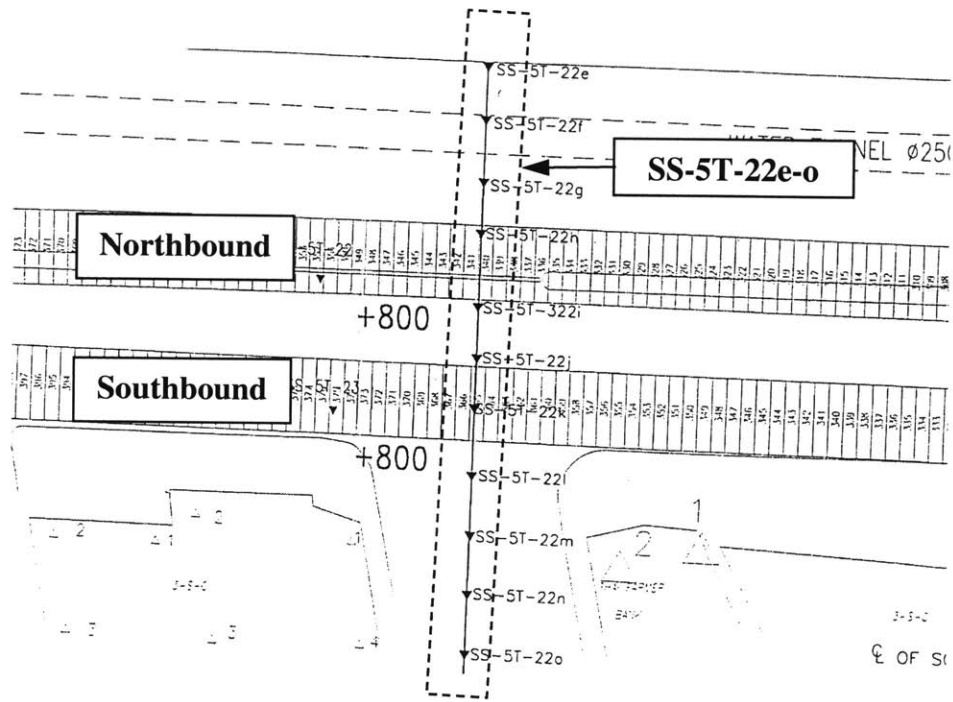


Figure 7.47 Surface settlement trough measured on SS-5T-22e-o (southbound tunnel-Ring no.365) and the instrumentation layout

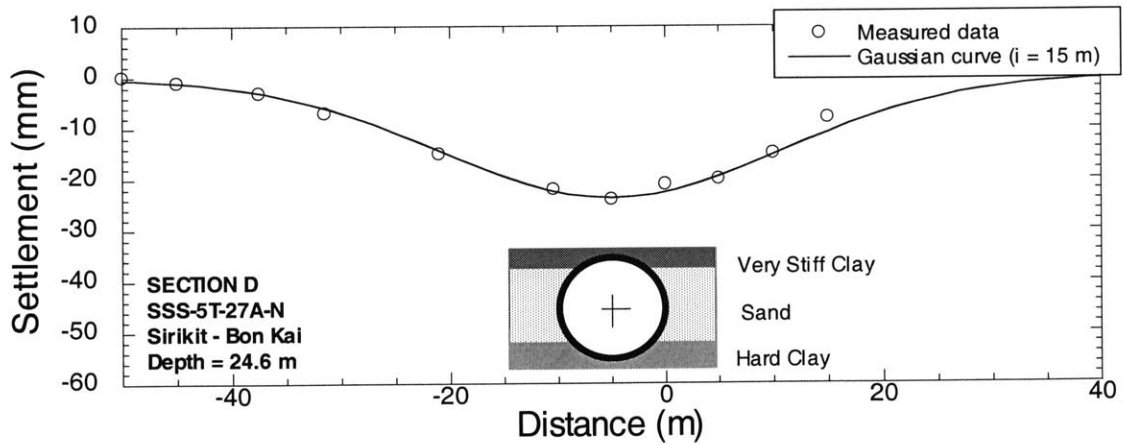
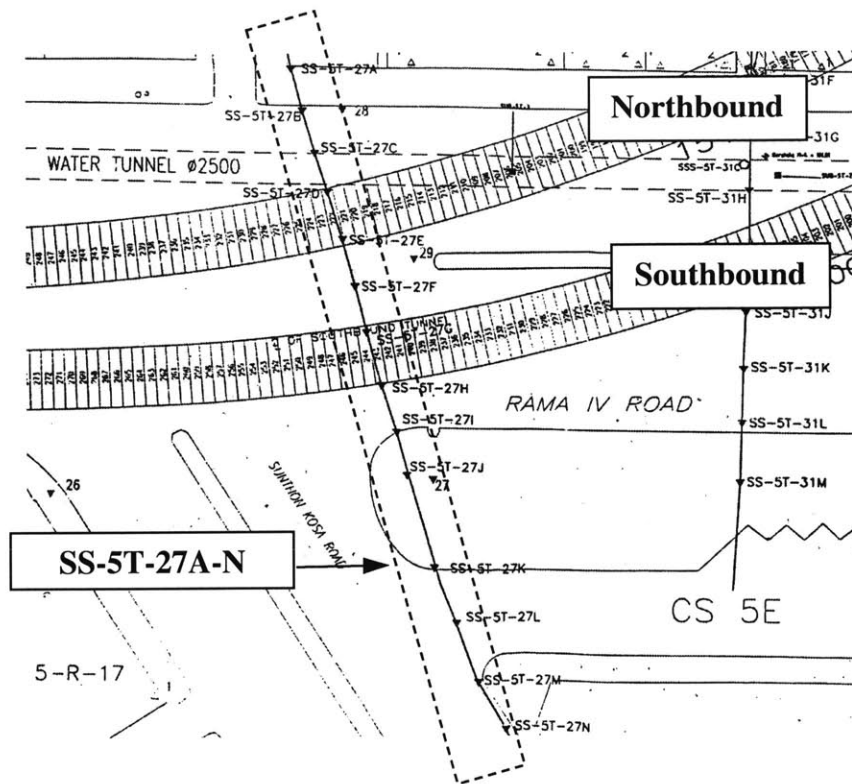


Figure 7.48 Surface settlement trough measured on SS-5T-27A-N (southbound tunnel-Ring no.243) and the instrumentation layout

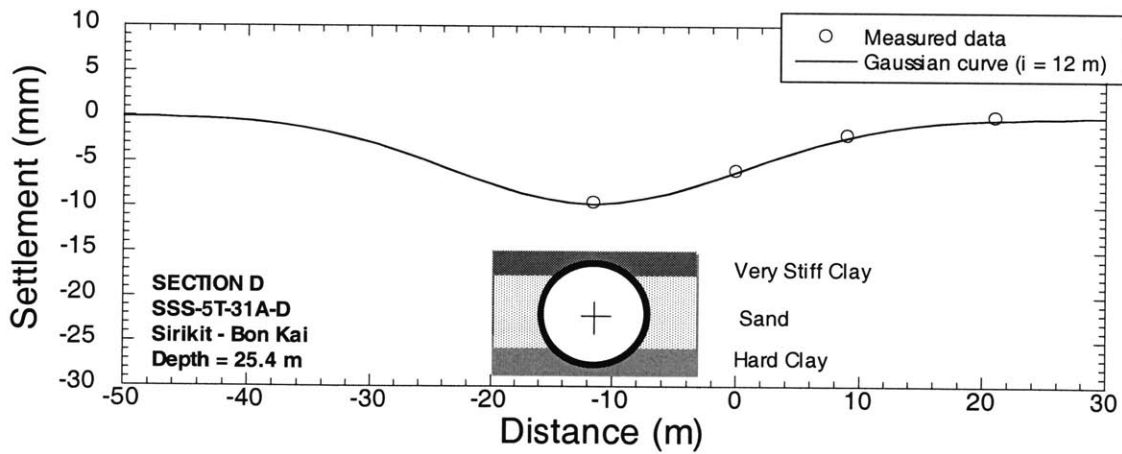
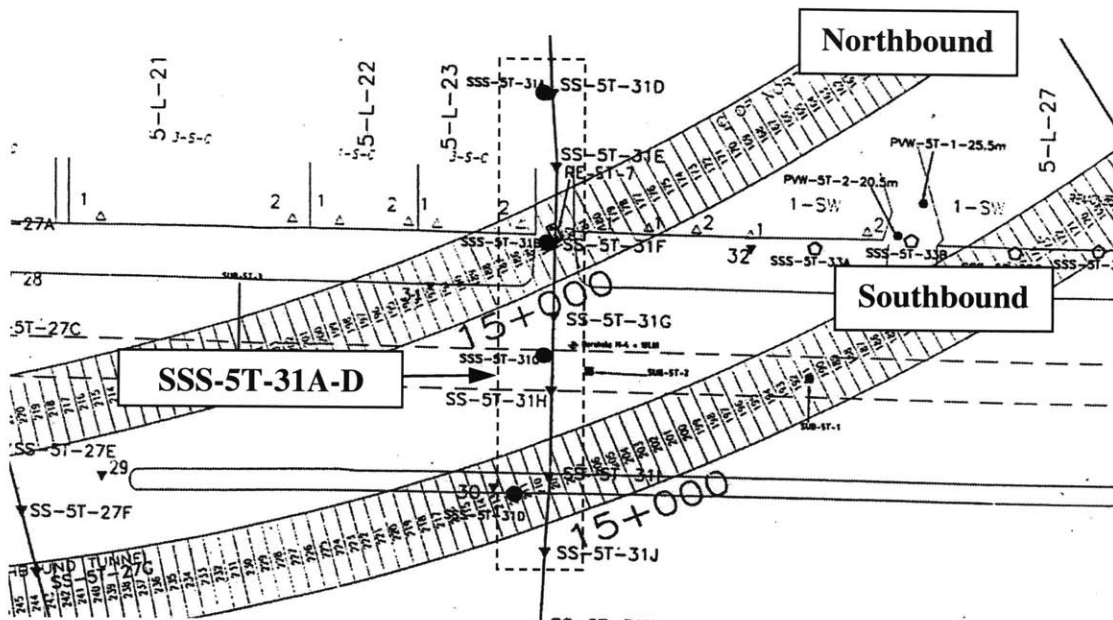


Figure 7.49 Surface settlement trough measured on SSS-5T-31A-D (southbound tunnel-Ring no.212) and the instrumentation layout

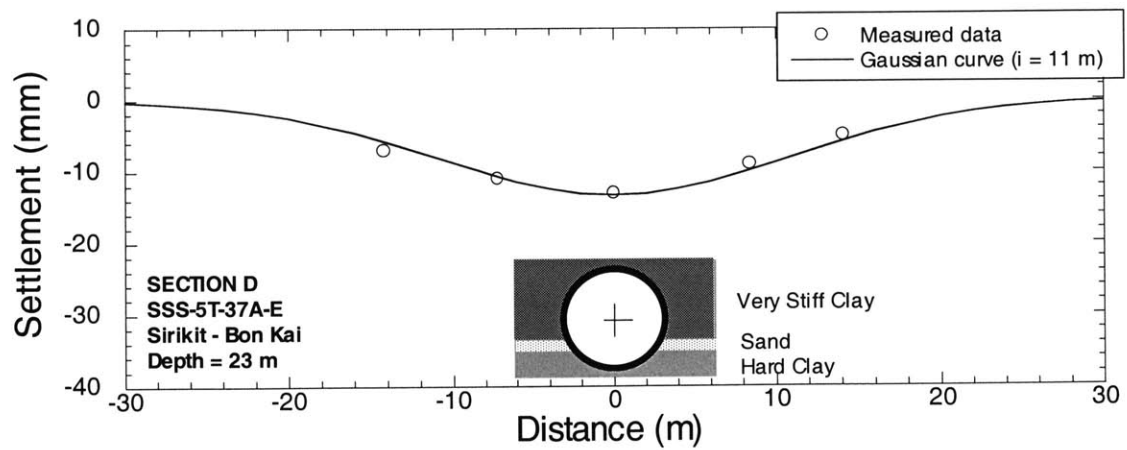
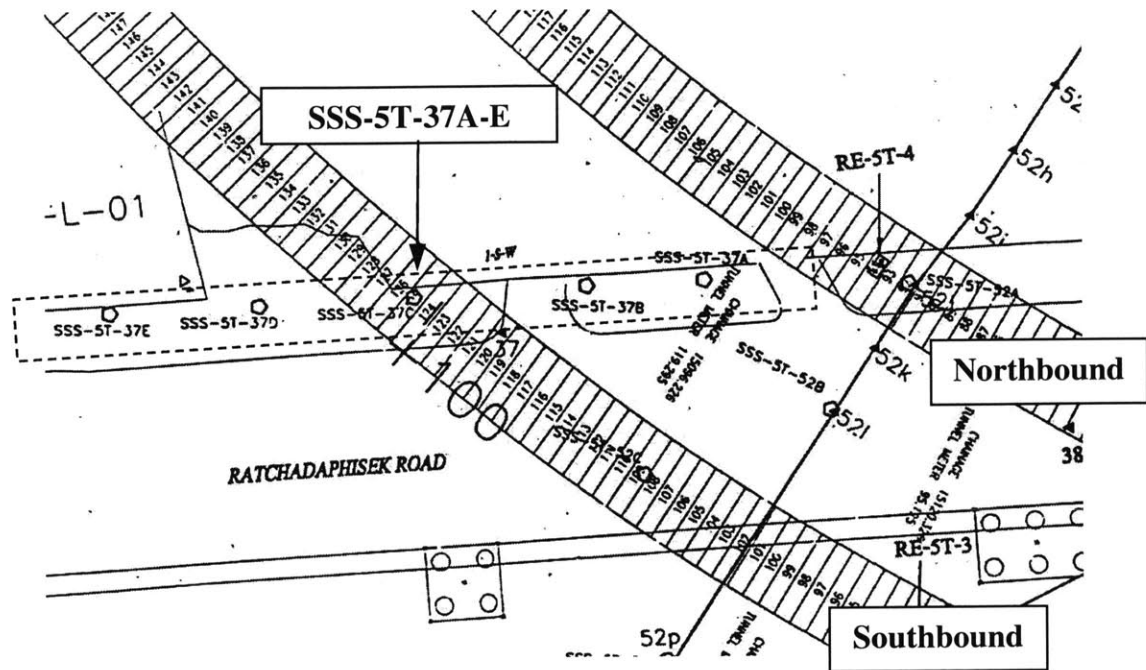


Figure 7.50 Surface settlement trough measured on SSS-5T-37A-E (southbound tunnel-Ring no.125) and the instrumentation layout

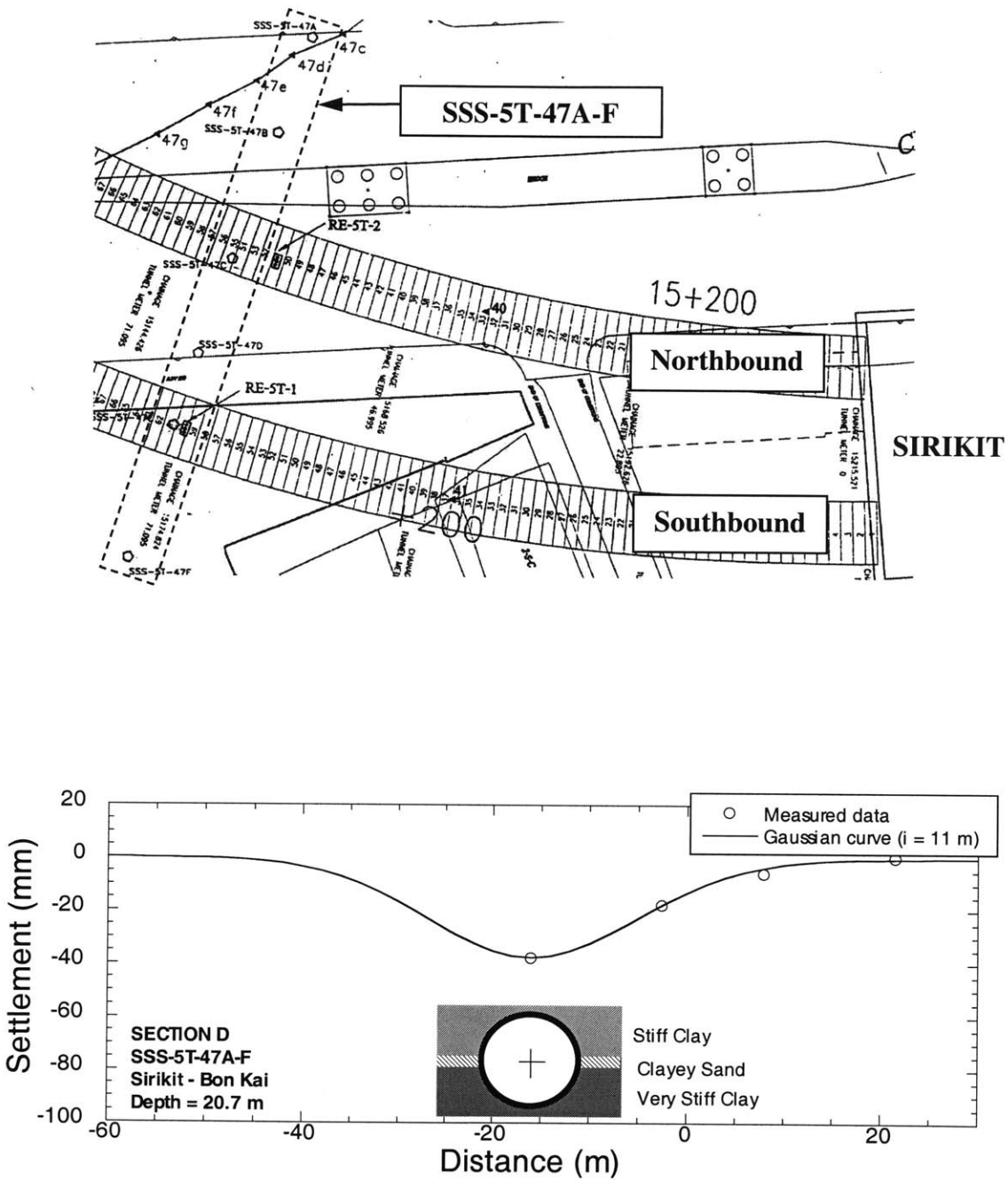


Figure 7.51 Surface settlement trough measured on SSS-5T-47A-F (southbound tunnel-Ring no.61) and the instrumentation layout

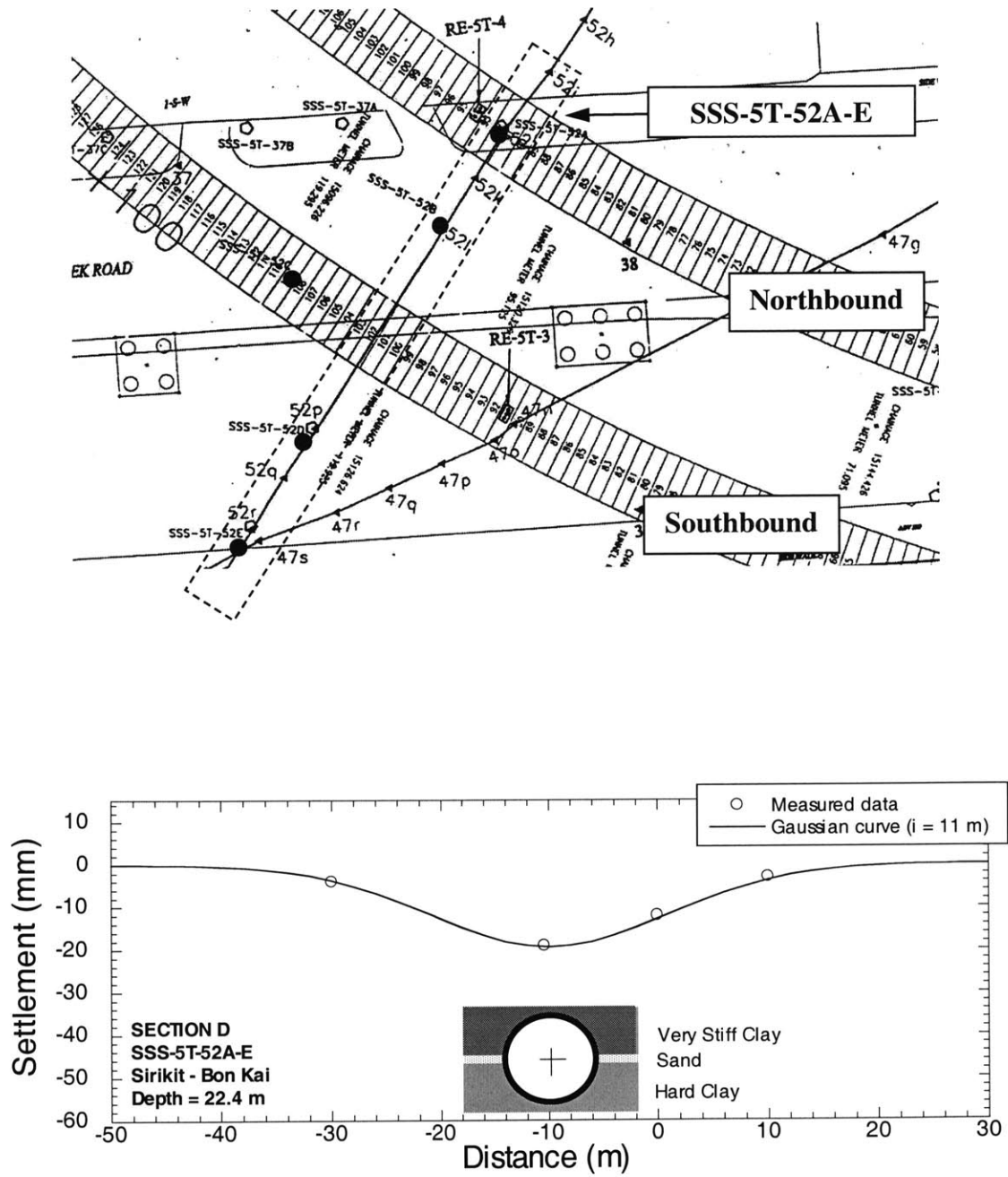


Figure 7.52 Surface settlement trough measured on SSS-5T-52A-E (southbound tunnel-Ring no.102) and the instrumentation layout

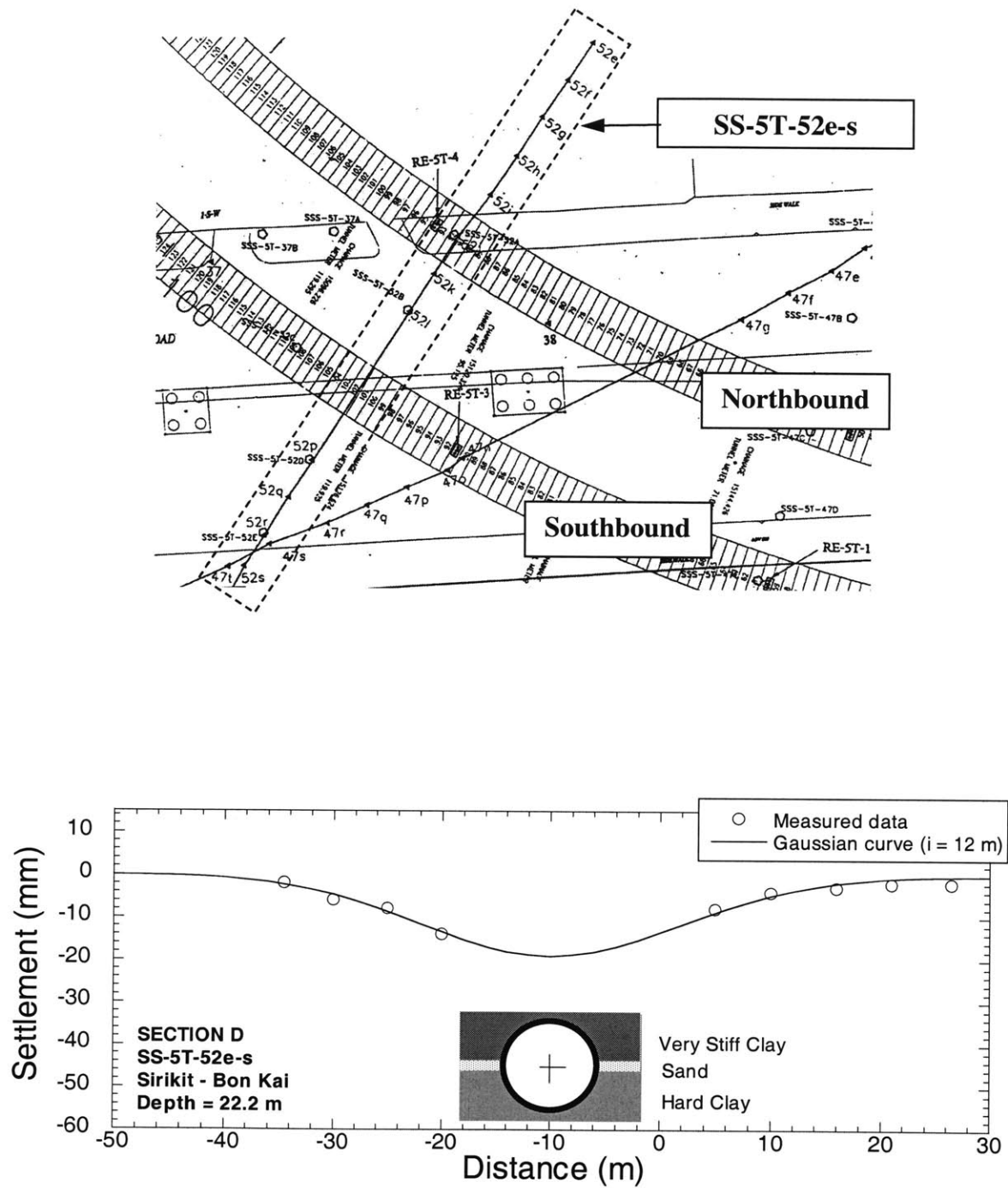


Figure 7.53 Surface settlement trough measured on SS-5T-52e-s (southbound tunnel-Ring no.102) and the instrumentation layout

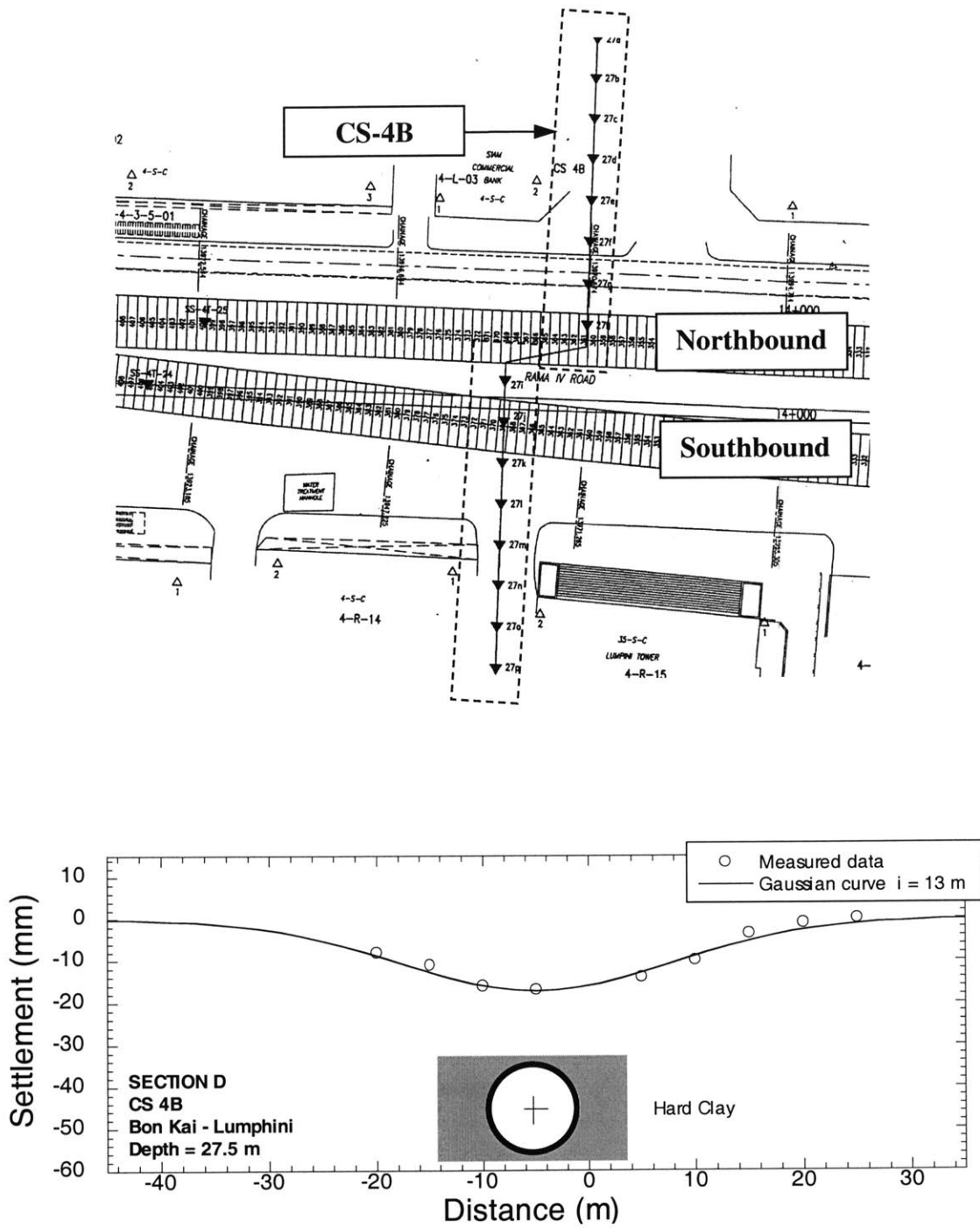


Figure 7.54 Surface settlement trough measured on CS-4B (southbound tunnel-Ring no.369) and the instrumentation layout

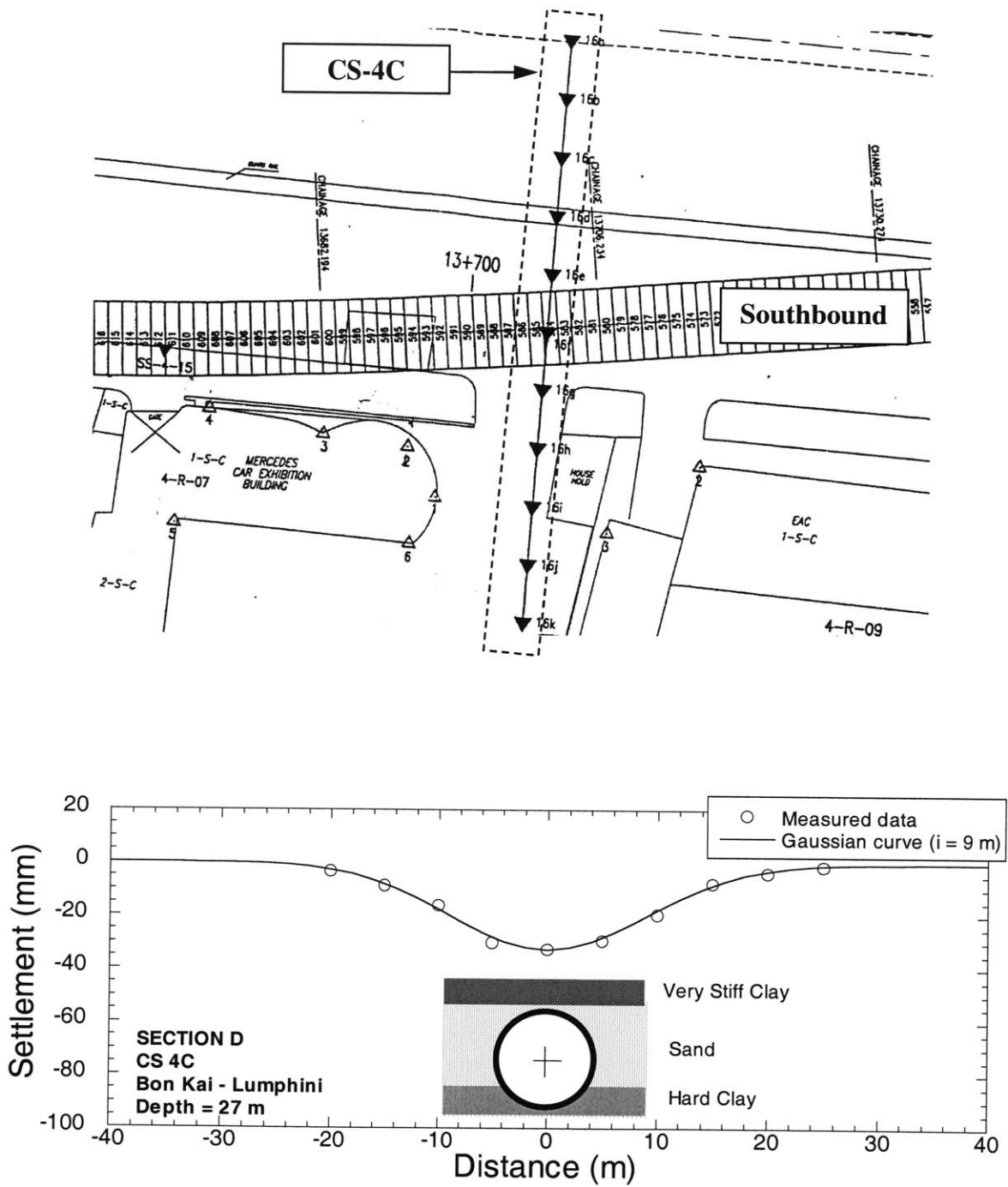


Figure 7.55 Surface settlement trough measured on CS-4C (southbound tunnel-Ring no.584) and the instrumentation layout

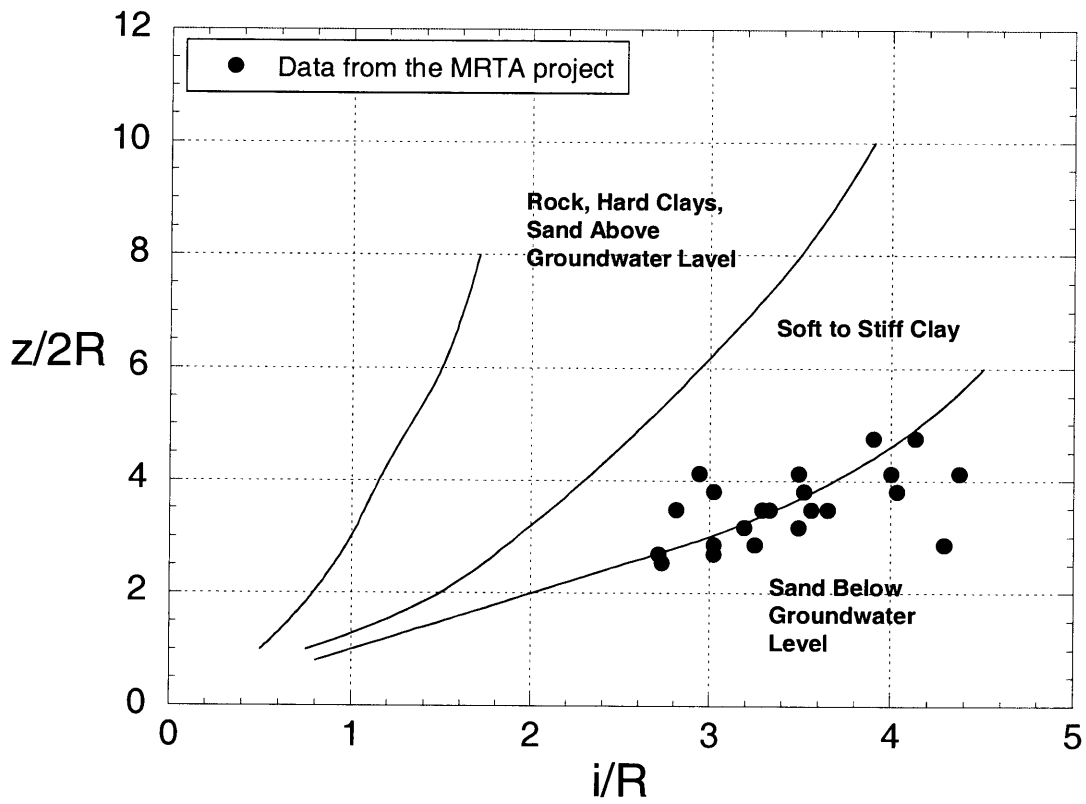


Figure 7.56 Observed settlement trough parameters from the MRTA project in Peck's (1969) empirical chart

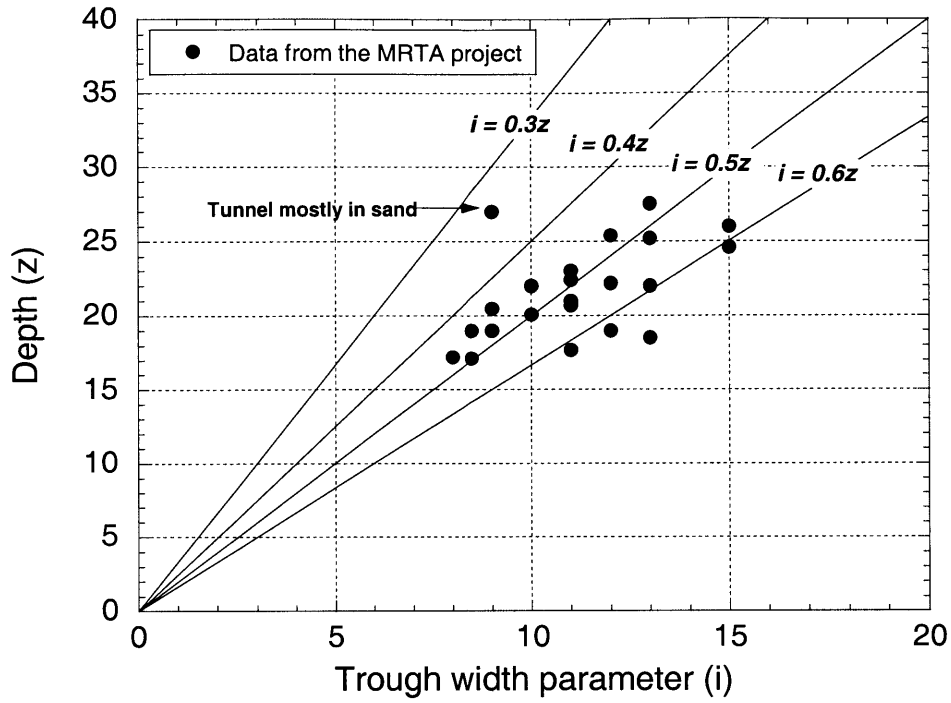


Figure 7.57 Observed settlement trough parameters from the MRTA project compared with the parameter recommended by O'Reilly and New (1982)

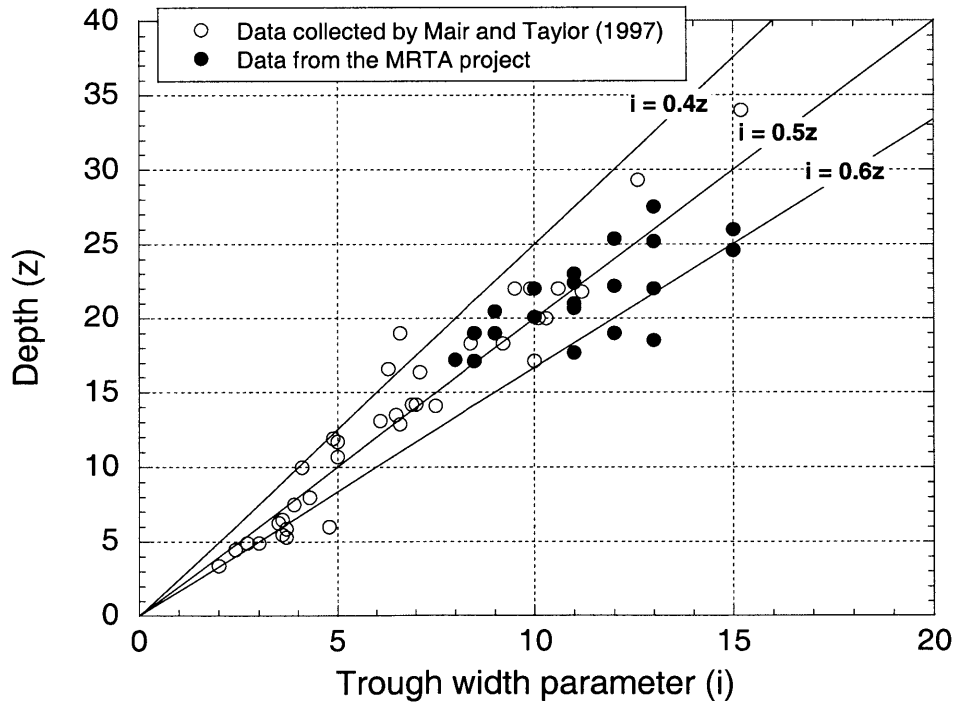


Figure 7.58 Observed settlement trough parameters from the MRTA project (only tunneling in clays) together with case history data collected by Mair and Taylor (1997)

7.3 Lateral Ground Deformations

In the MRTA project, inclinometers were installed along the side of the tunnel alignment to measure lateral ground deformations during excavation as illustrated in Figure 7.1c. Lateral deformations measured along the length of the inclinometer casings and their layouts are shown in Figure 7.59 to Figure 7.64 (for the layout of the overall tunnel route refer to Figure 7.2). As can be seen from Figure 7.59 to Figure 7.64, all inclinometers indicated a very similar pattern of lateral ground deformations, which can be divided into two distinct sections: (1) above the tunnel crown and (2) below the tunnel crown or at the level of the tunnel springline. Above the tunnel crown, the ground deformed towards the tunnel. In contrast, the ground experienced outward movements as the shield passed the measurement sections at the level below the tunnel crown.

To allow a clearer relationship to be established between the lateral ground deformation and EPB shield tunneling, readings measured at inclinometer IN-T7-04 are analyzed (see the instrumentation layout in Figure 7.64 and lateral deformations in Figure 7.65). Figure 7.65 shows deflections in the direction perpendicular to the tunnel axis that were measured with the inclinometer IN-T7-04 during the excavation of the northbound tunnel from Phetchaburi to Sukhumvit stations, which is a part of tunneling in Section C. The inclinometer was located 2.35 m from the tunnel periphery and measurement readings were taken at high frequency (i.e. every 2 hours) in order to capture the development of ground response to the shield advance. Note that the deflections were measured relative to the shield position as illustrated in Figure 7.66.

Above the tunnel crown, three zones can be identified in the lateral ground response to tunneling namely; “Zone 1” as the shield approaches the measurement section; “Zone 2” as the shield is passing the section; and “Zone 3” after shield passing. This classification is identical to that of the longitudinal surface settlement as described in Section 7.2.1. In Zone 1, the ground begins to deform towards the tunnel, when the shield is about 16 m (i.e. 2D) away from the section. The deflection continues to develop as the shield advances to the inclinometer (i.e. point A to point C as shown in Figure 7.66). During

shield passing (points C - F), which is classified as “Zone 2”, the deflection still continues to develop and accelerate significantly. The maximum (inward) lateral deformations measured on the inclinometer are plotted in Figure 7.67. As can be seen in the figure, the ground response is similar to the longitudinal surface settlement profile in that the deformation in Zone 2 (points C – F) is the largest portion of the overall lateral deformation. After shield passing and tail void grouting is performed, the deflection development begins to slow down (points F – H). Evidently, this again confirms the previous finding that the largest ground movement occurs during shield passing.

Below the tunnel crown, the ground shows outward movements as shown in Figure 7.65. As the shield approached the section represented by point C (see also Figure 7.66), the ground began to deform outward (Figure 7.65). The deflection then continued to develop while the shield was passing the section. When the shield tail was located in the plane of the inclinometers (i.e. point E), the ground experiences a substantial increase in the outward deformation as shown in Figure 7.65 and Figure 7.67. At this point, the inclinometer is very close to the ring No. 466 where the tail void grouting is performed. The outward lateral deflection continued to increase until the shield is beyond the section for about 8 m (i.e. point F). In this area (i.e. points E – F), the grout material was injected at approximately 2.5 bar. Beyond this point, no significant ground response was measured (points G – H).

Based upon the observation of the ground response relative to the shield position, it can be suggested that the grouting pressure has an effect on the ground movement. As can be seen in Figure 7.68, the ground deformation model test conducted by Kimura and Mair (1981) indicates that large inward ground movements occur over the tunnel crown and expand to the ground surface creating a dilating wedge zone. As a result, the inclinometer would record the lateral deformation as the ground deforms towards the tunnel. In contrast, at the level lower than the tunnel crown, no ground movement was observed. However, it should be noted that this model test was attempted to simulate the ground movement induced only by opening so that effect of operational parameters were not considered.

As measured in inclinometers at the level above the tunnel crown, the tail void grouting effectively prevented further ground movements towards the void above the tunnel. In contrast, at the level below the tunnel crown, where no inward ground movements were expected (see Figure 7.68), the observed data showed the development of a prominent outward pattern in the plane of the tunnel springline. This outward deflection increased rapidly when the tail void grouting was performed and continued about 4-5 rings after shield passing. To visualize this behavior, Figure 7.69 demonstrates the effect of the grouting on lateral ground movements. The tail void grouting creates a pressure pushing the lateral ground at the tunnel springline outward. To investigate the relationship between the grouting pressure and the maximum outward lateral deformation, observed data are tabulated in Table 7-1. The grouting pressure is normalized by the distance between inclinometer and tunnel periphery in order to show a clearer effect of the grouting on the ground response. The normalized factors calculated in Table 7-1 are plotted against outward deflections in Figure 7.70. Although there is significant scatter, large outward movements appear to be associated with high grouting pressures. In other words, it can be suggested that the higher the grouting pressure, the larger the outward ground movement measured by the inclinometers.

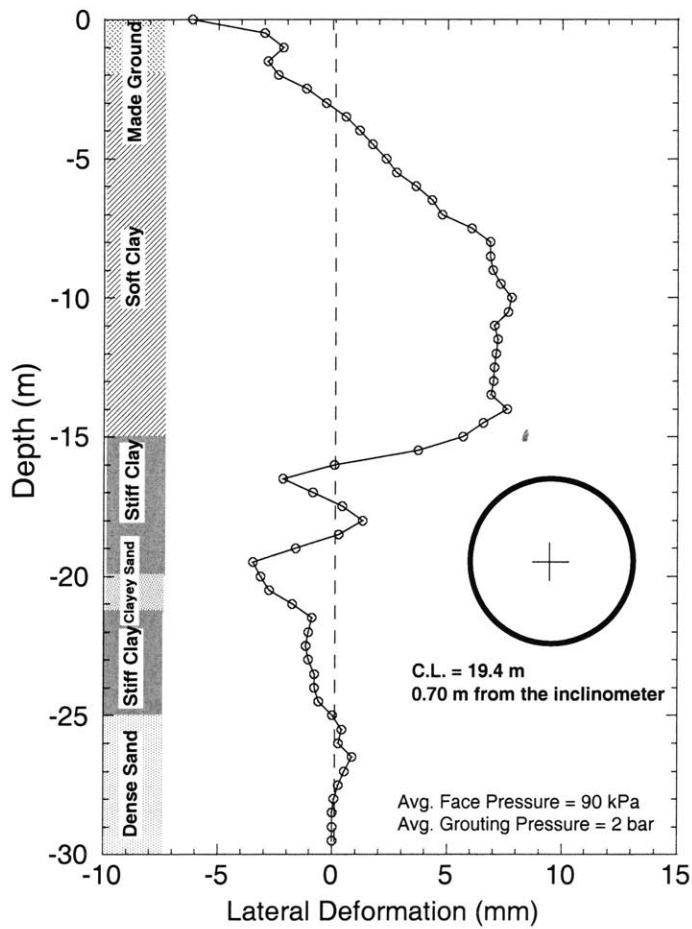
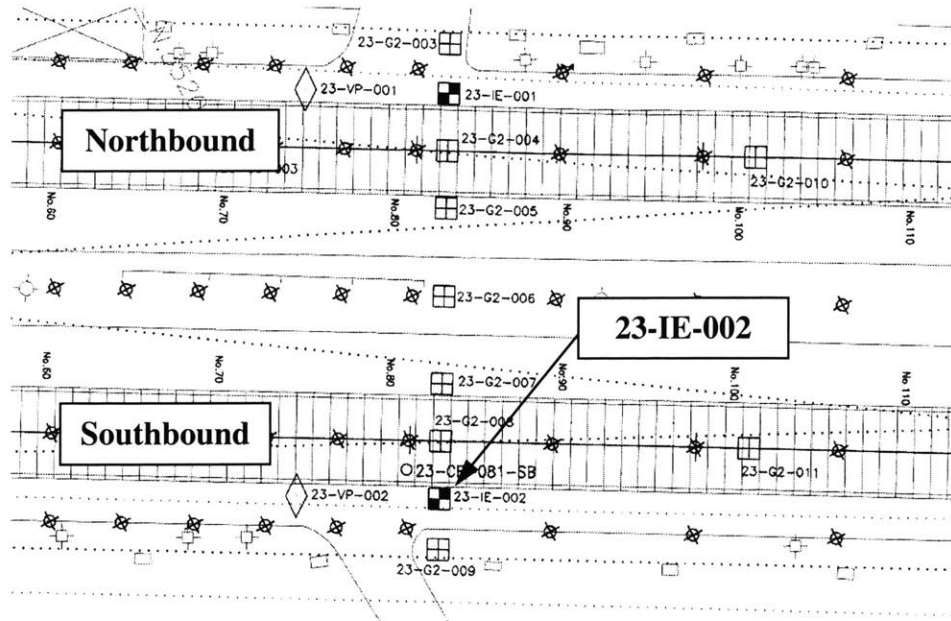


Figure 7.59 Lateral deformation measured on 23-IE-002 after shield passing (SB) in Section A (Thiam Ruam Mit – Pracharat Bumphen) and the instrumentation layout

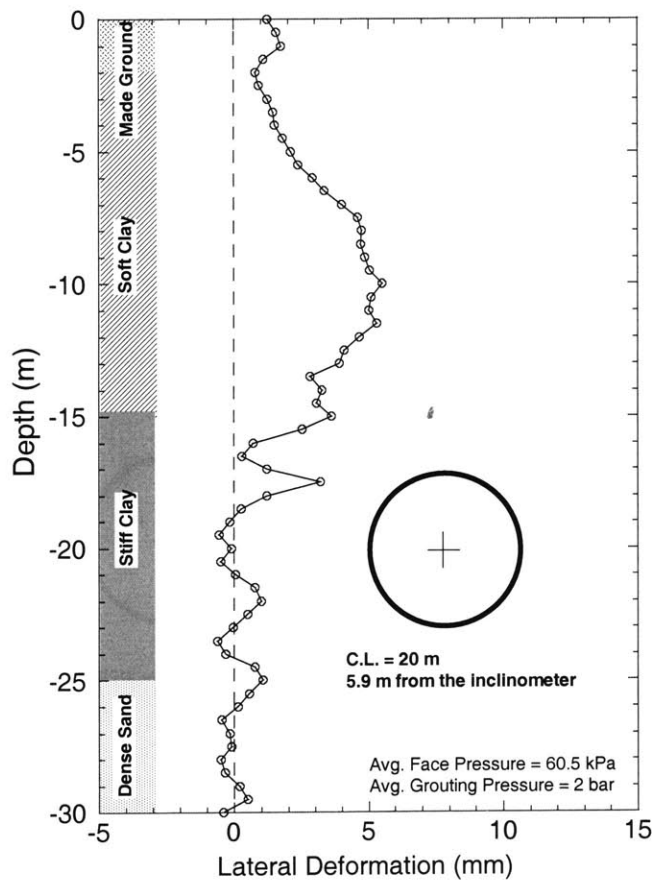
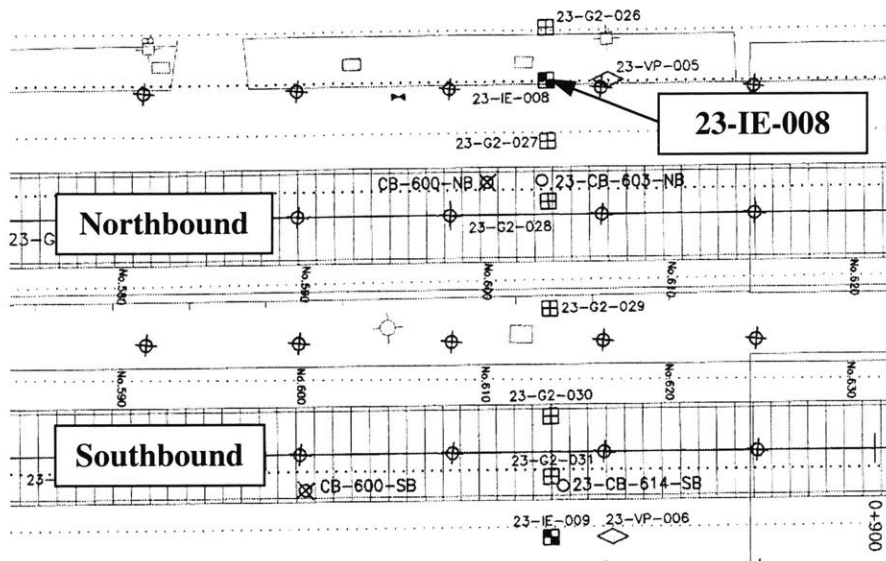


Figure 7.60 Lateral deformation measured on 23-IE-008 after shield passing (NB) in Section A (Thaim Ruam Mit – Pracharat Bumphen stations) and the instrumentation layout

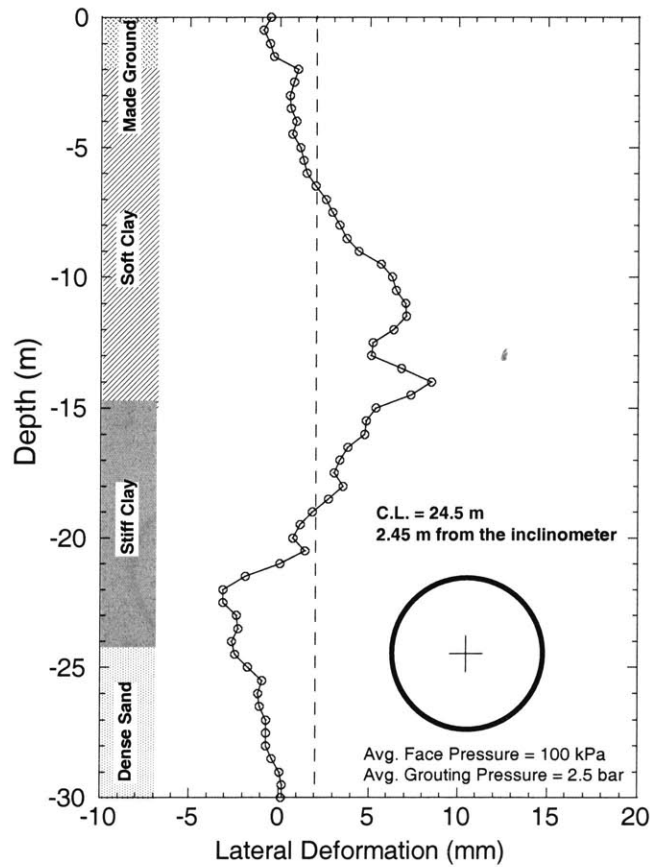
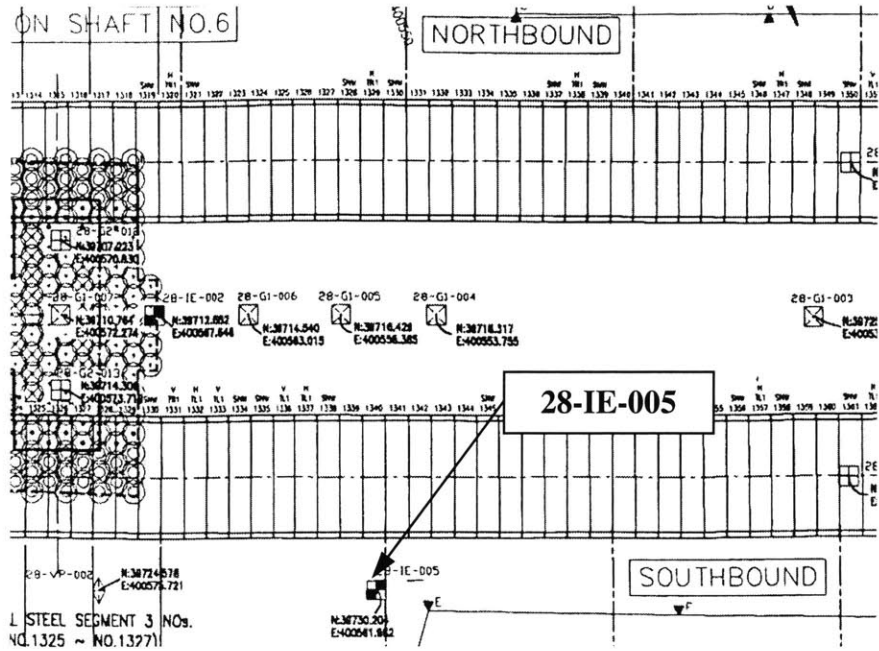


Figure 7.61 Lateral deformation measured on 28-IE-005 after shield passing (SB) in Section B (Lat Phrao – Phahoyothin stations) and the instrumentation layout

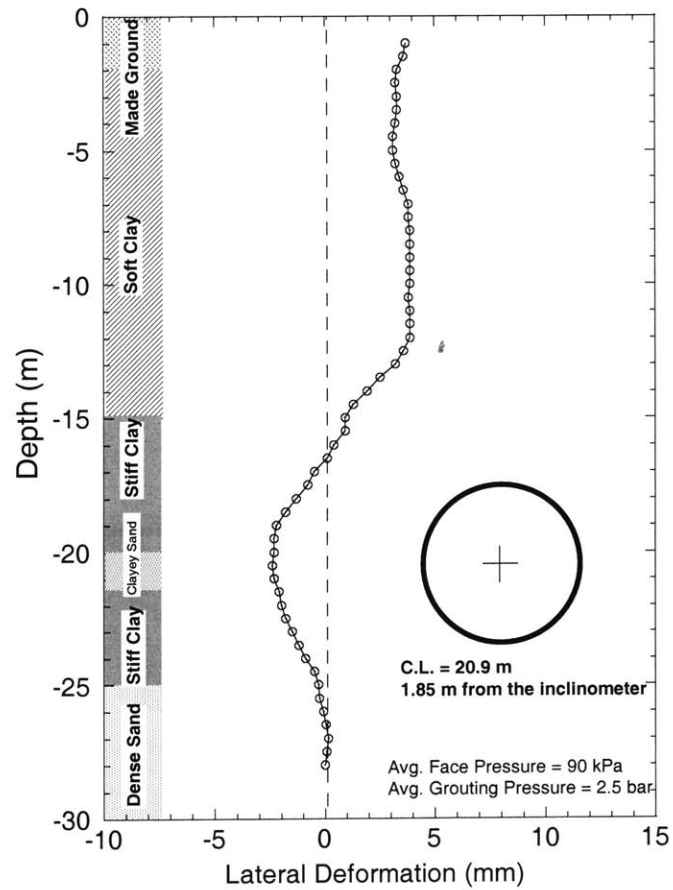
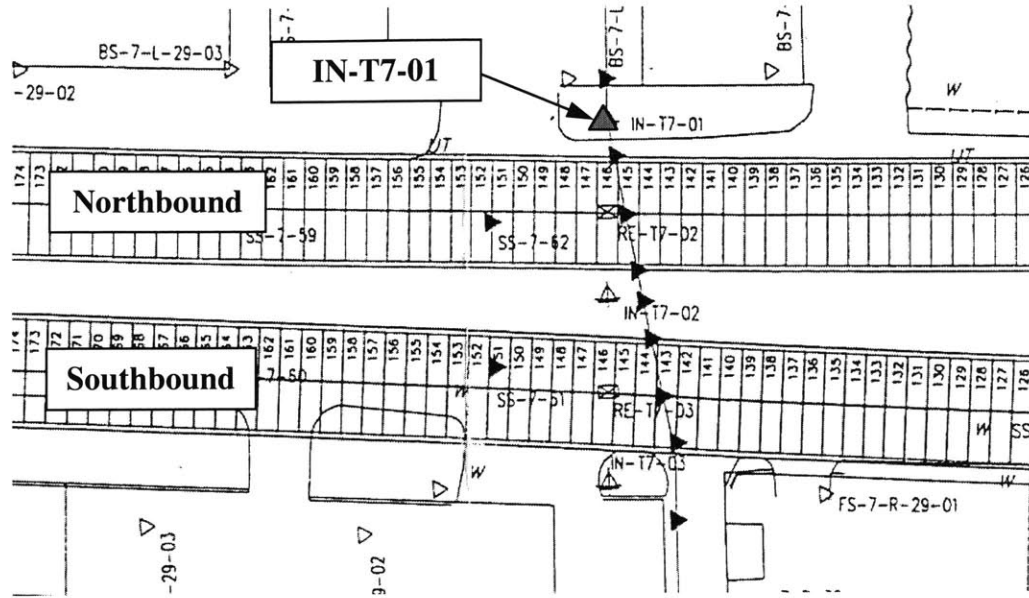


Figure 7.62 Lateral deformation measured on IN-T7-01 after shield passing (NB) in Section C (Phetchaburi –Sukhumvit stations) and the instrumentation layout

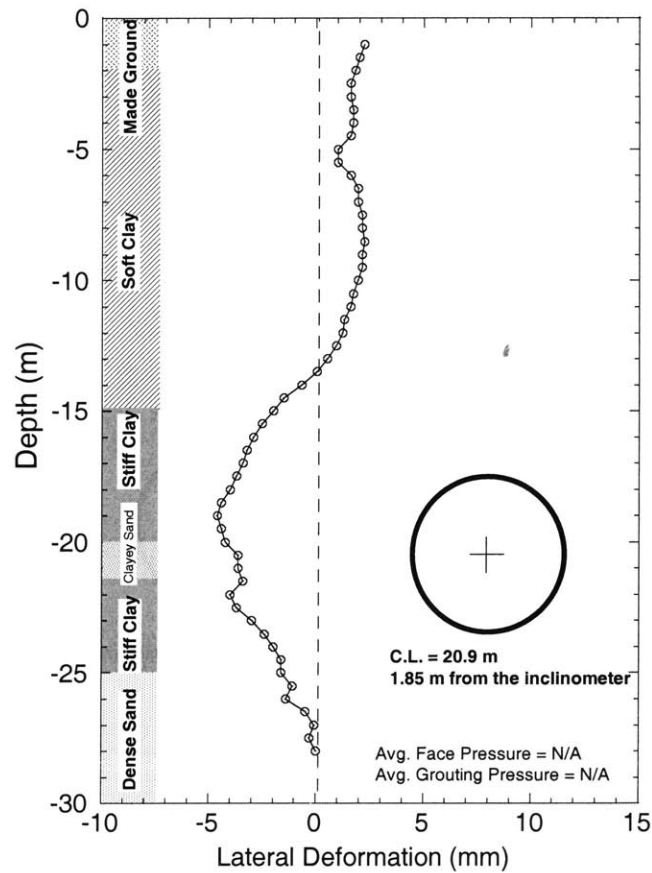
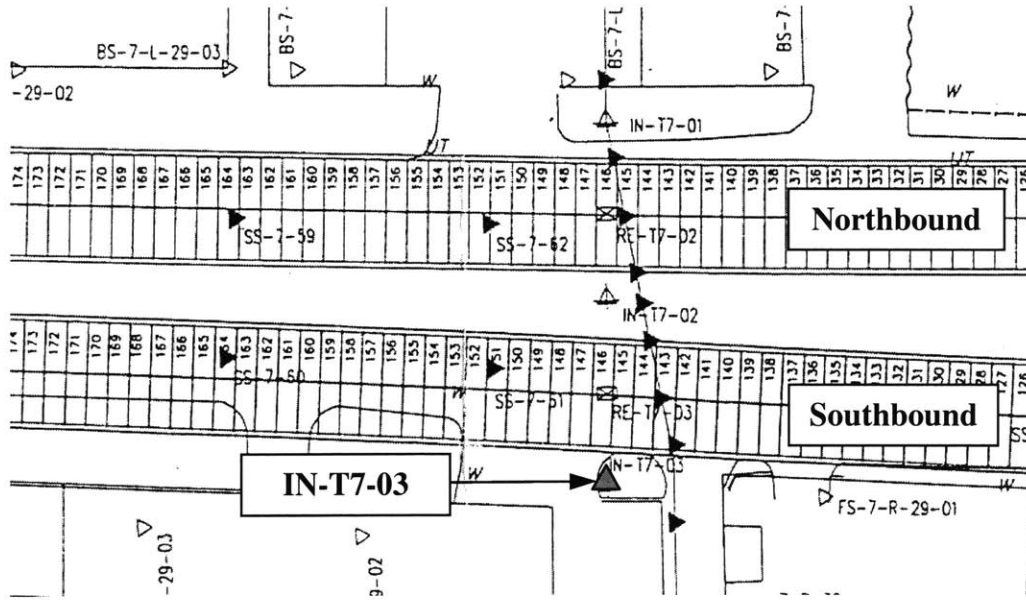


Figure 7.63 Lateral deformation measured on IN-T7-03 after shield passing (SB) in Section C (Phetchaburi – Sukhumvit stations) and the instrumentation layout

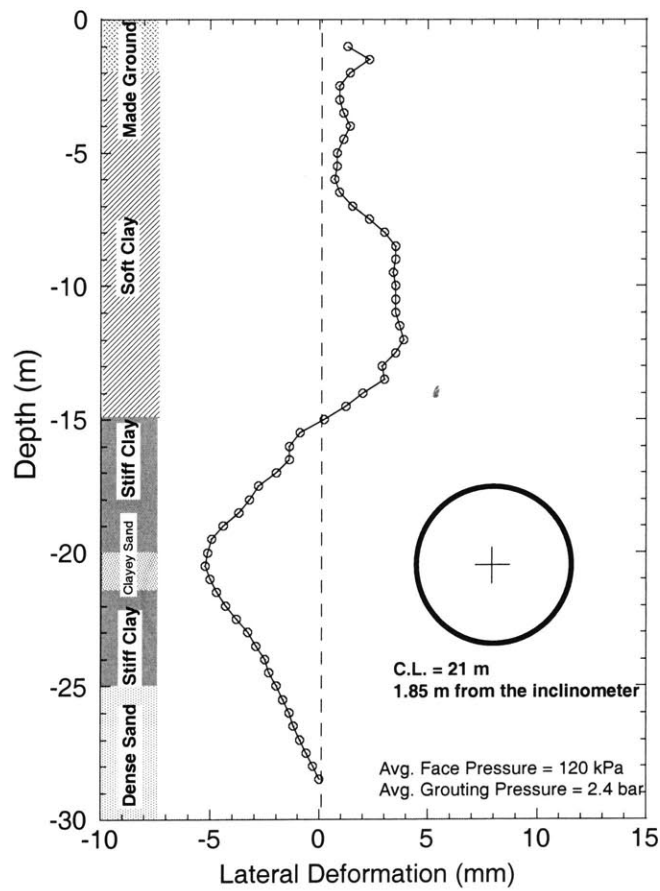
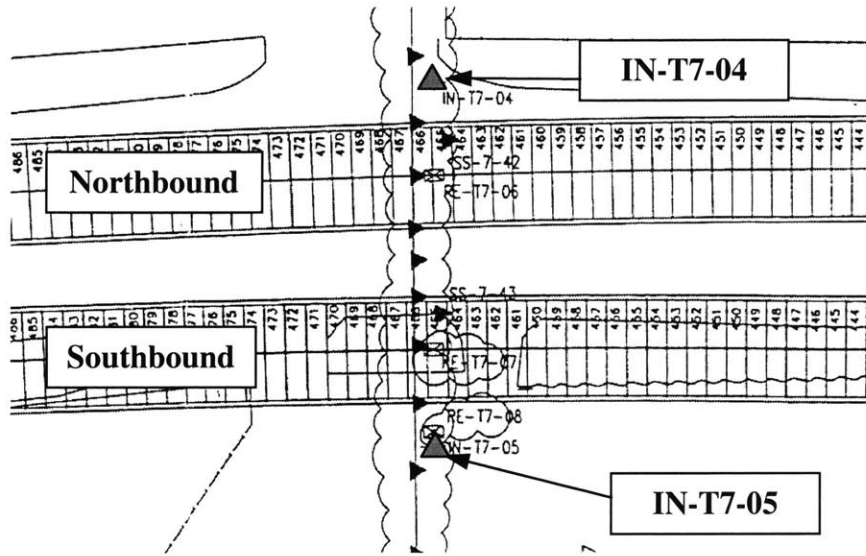


Figure 7.64 Lateral deformation measured on IN-T7-05 after shield passing (SB) in Section C (Phetchaburi –Sukhumvit stations) and the instrumentation layout

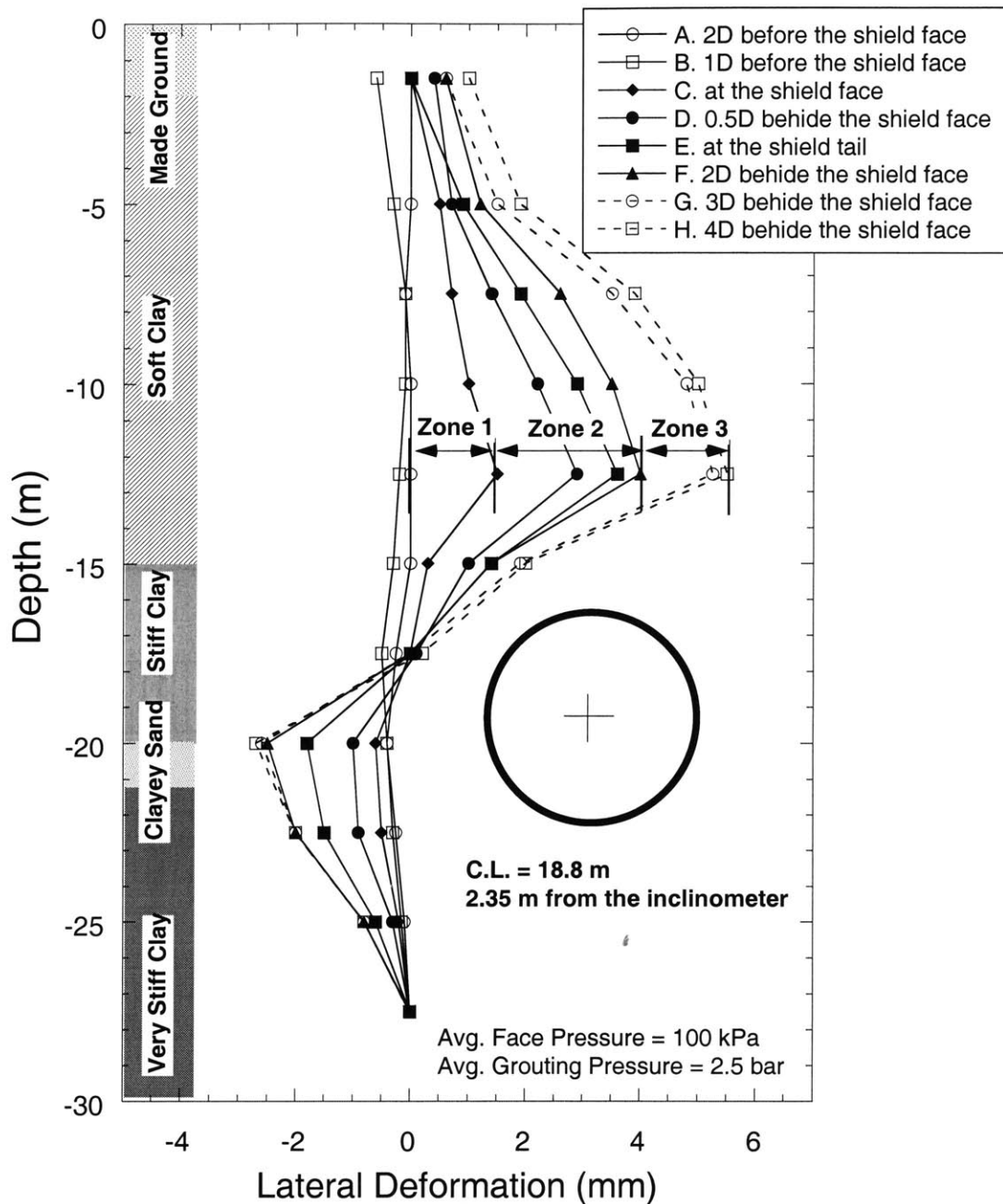


Figure 7.65 Lateral deformation measured on inclinometer IN-T7-04 during excavation of the northbound tunnel in Section C (Phetchaburi –Sukhumvit stations)

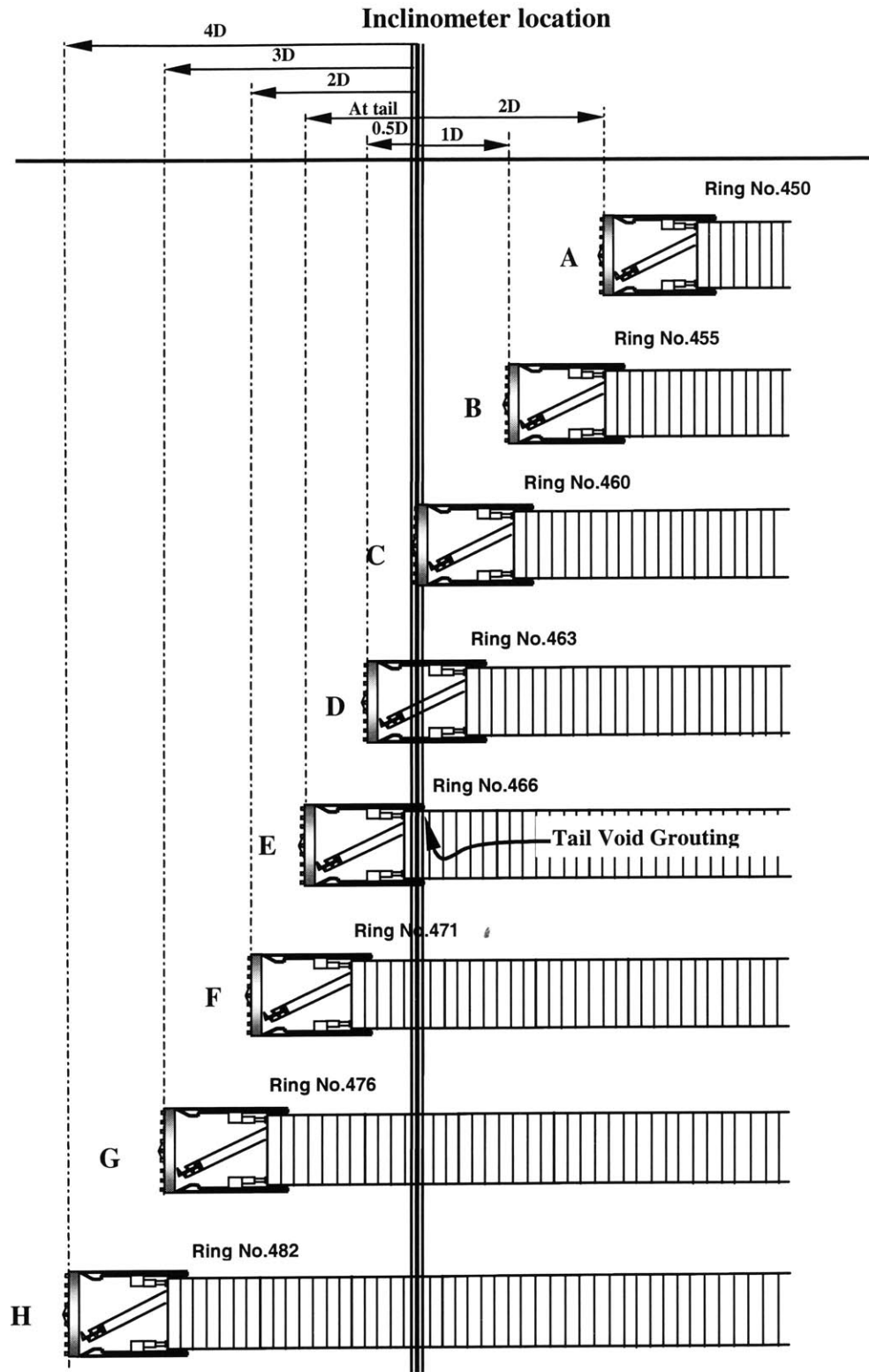


Figure 7.66 Schematic diagram of the shield position relative to the inclinometer location in Figure 7.65

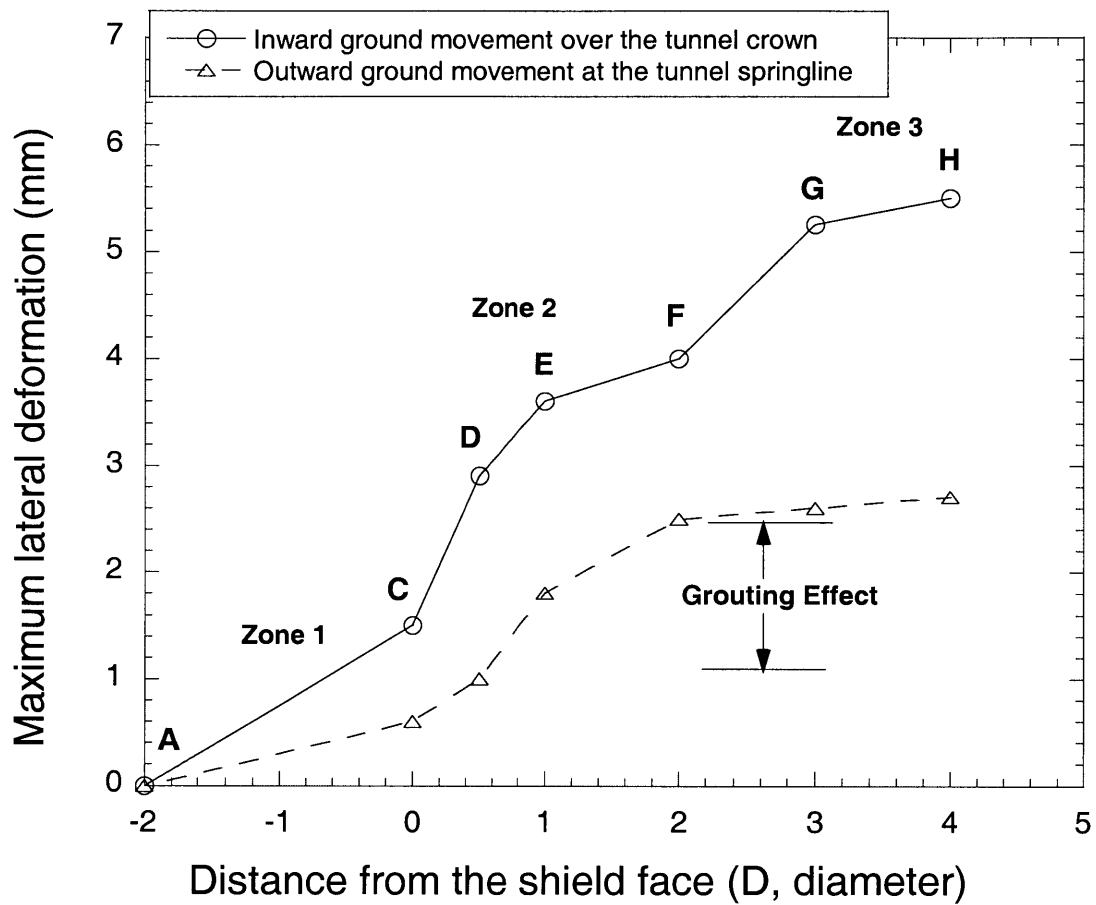


Figure 7.67 Maximum lateral deformations relative to the shield position

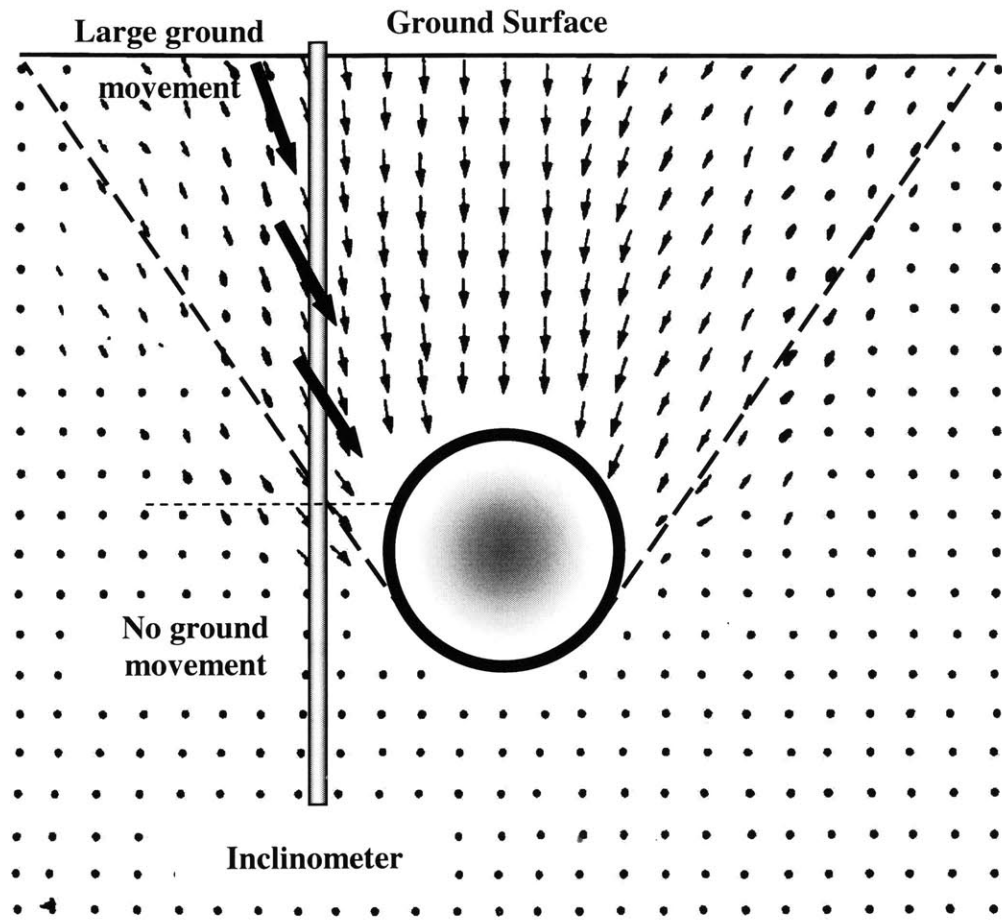


Figure 7.68 Soil deformation around model tunnel in clay (after Kimura and Mair, 1981) and the effect on the inclinometer

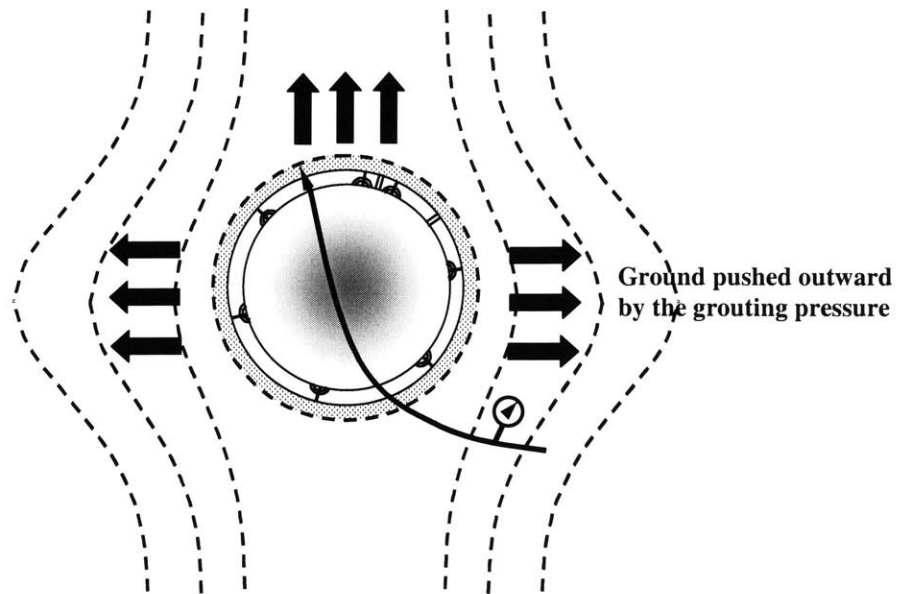


Figure 7.69 Schematic diagram of the effect of tail void grouting on the ground response

Table 7-1 Grouting pressures and maximum outward lateral deformations measured in the MRTA project

Inclinometer	Grouting pressure (bar)	Distance from tunnel periphery (m)	Grouting Pressure / Dist. From tunnel (bar/m)	Max. outward lateral deformation (mm)
23-IE-002	2	0.7	2.86	-3.45
23-IE-008	2	5.9	0.34	-0.5
26-IE-002	1.5	0.9	1.67	-3.7
28-IE-005	2.5	2.45	1.02	-3.1
IN-T7-01	2.5	1.85	1.35	-2.4
IN-T7-04	2.5	2.35	1.06	-2.7
IN-T7-05	2.4	1.85	1.30	-5.2

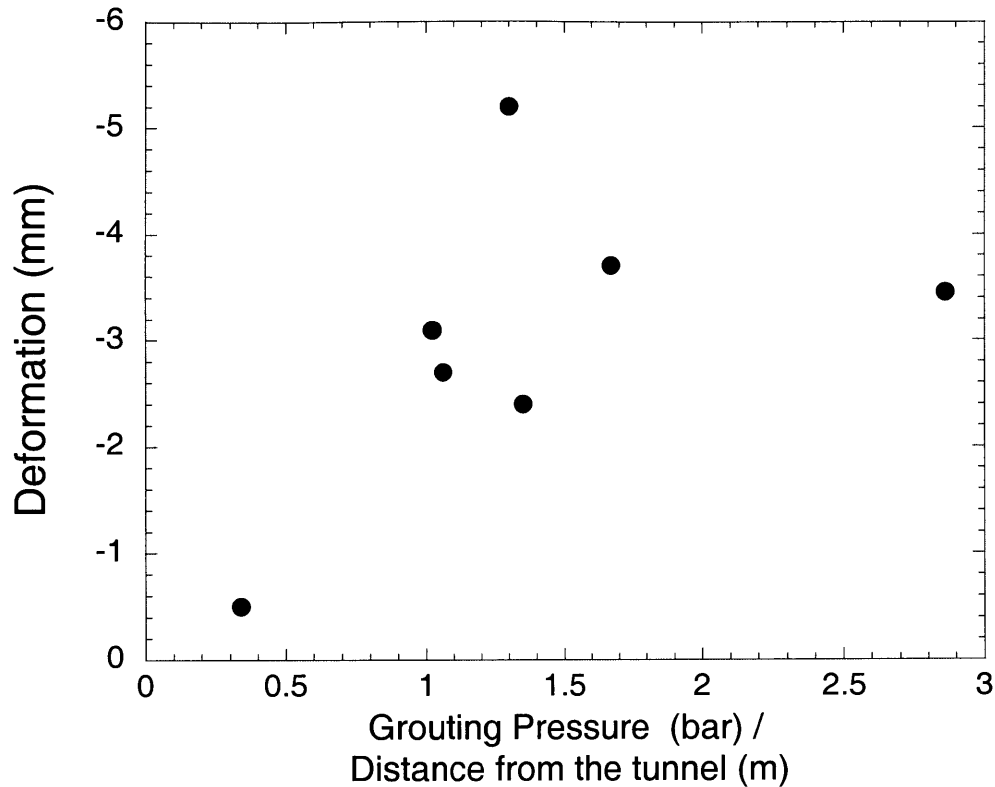


Figure 7.70 Relationship between the grouting pressure and lateral deformations

7.4 Summary

1. Based upon observations, in most cases, surface settlements induced by EPB tunneling can be divided into three zones regardless of soil conditions namely, Zone 1, Zone 2, and Zone 3. Zone 1 originates ahead of the shield where the ground begins to deform. However, it should be noted that in the case of very high face pressures and high penetration rates, the ground might experience heave ahead of the shield in Zone 1. Zone 2 initiates a short distance in front of the shield face and develops significantly over the shield body. Also regardless of soil conditions, Zone 2 was found to be the largest portion of overall settlements. The final zone, Zone 3, begins after shield passing and after the tail void grouting has being performed.

2. Operational parameters affect the magnitude of surface settlements within each zone. Large settlements found in Zone 1 are associated with low face pressure and low penetration rates. In contrast, if applied face pressures and penetration rates were very high, less surface settlements or even ground heave occurred in Zone 1. Face pressure and penetration rate also affect settlements in Zone 2 during shield passing. However, settlements occurred in Zone 3 were mainly influenced by tail void grouting.

3. The Gaussian curve or normal probability function was found to be a good approximation of the surface settlement trough above the tunnel. The trough width parameter (i) selection recommended by O'Reilly and New (1982), in which i is approximately between $0.4z$ and $0.6z$ for tunnels in clays and i is about $0.35z$ for tunnels in sands, was found to be useful as it was in good agreement with field data. This estimation can help engineers to determine the configuration of the settlement trough and to ascertain how far away the settlement would be expected.

4. Two distinct portions were observed in lateral deformation curves as measured with inclinometers. The first portion is the deformation above the tunnel crown, where the ground tends to deform towards the tunnel. The largest development of inward deformation occurs during shield passing similar to the behavior of Zone 2 in the longitudinal surface settlement. In contrast, at the level below the crown; the ground deformed outward during shield passing. It was found that this mechanism was affected by tail void grouting. Additionally, the magnitude of outward deformations appeared to correspond to the magnitude of the applied grouting pressure.

References

Kimura, T. and Mair, R. J. (1981). "Centrifugal Testing of Model Tunnels in Soft Clay". *Proc. 10th Int. Conf. of Soil Mechanics and Foundation Engineering, Stockholm*, Vol. 1, pp. 319-322

Mair, R. J. and Taylor, R. N. (1997). "Bore Tunneling in the Urban Environment". Theme Lecture, Plenary Session 4, *Proc. 14th Int. Conf. of Soil Mechanics and Foundation Engineering, Hamburg*, Vol. 4, pp. 2353-2385.

O'Reilly, M. P. and New, B. M. (1982). "Settlement above Tunnels in the United Kingdom – Their Magnitude and Prediction". *Tunneling 88*, London, pp. 231-241.

Peck, R. B. (1969). "Deep Excavations and Tunneling in Soft Ground". *Proc. 7th Int. Conf. on Soil Mechanics and Foundation Engineering, Mexico City, State of the Art Volume*, pp. 225-290.

CHAPTER 8

Effect of the Second Tunnel on the First Tunnel

8.1 Introduction

In recent years, many tunneling projects have been built in congested urban environments which often involve the tunneling of twin tunnels in close proximity to each other. Additionally, in many cases, the new tunnel is often excavated adjacent to existing tunnels. Hence, in the design of new tunnels, it is crucial to understand the interaction mechanism of the twin tunnels and their effect on the surrounding ground. Furthermore, from the structural engineering point of view, one needs to ensure that excessive bending moments or displacements are not developed in the lining of the tunnel which is built first.

In Chapter 7, ground response and surface settlements induced by EPB shields were observed and analyzed based on the response induced by the first tunnel only. In the MRTA project, twin tunnels, namely northbound (NB) and southbound (SB) were excavated (see Figure 5.1). In Tunneling Sections A, B, and D, the southbound tunnel was excavated first and followed by the northbound tunnel. Only in Section C (i.e. Kumagai Gumi Section), the northbound tunnel was excavated first. Tunnel drive sequences were shown in Figure 5.14 through Figure 5.17. Typically, the second shield was launched two weeks after the first shield so that the interference between two tunnels can be minimized and experience gained during excavation of the first tunnel can be

adopted in the second tunnel. Details of tunneling drives are provided in Chapter 5. As reported by several authors, ground response due to twin tunnels was found to be more complicated than the ground response induced by a single tunnel. Furthermore, the interaction between the first tunnel and the second tunnel can become very significant in lining design.

In this present chapter, three issues are investigated. First, the development of surface settlement troughs induced by twin tunnels excavated side-by-side is studied. Additionally, the effect of operational parameters on the magnitude and shape of the settlement troughs will be also explored. Second, the method proposed by Peck (1969) to describe the settlement troughs caused by twin tunnels will be reviewed in order to verify whether it is applicable for the case of twin tunnels excavated by the EPB technique. This will lead to an improved solution used for describing the surface settlements. Furthermore, the lining behavior of the first tunnel that is affected by the approaching second shield will be also investigated. Third, since in most tunneling drives in Tunneling Section D of the MRTA project (see also Chapter 5), the tunnels were stacked vertically on top of each other, surface settlements developing as a result of the first- and the second shield passages will be studied for this case also.

8.2 Settlements above Twin Tunnels excavated Side-by-Side

It has been observed by several authors in many tunneling projects that surface settlement troughs caused by twin tunnels appeared to have a variety of shapes. Unlike the case of a single tunnel where symmetric surface settlement troughs were likely to be observed as shown in Figure 8.3a (see also Section 7.2.2), surface settlement troughs observed over twin tunnels can be symmetric with respect to the mid-point between the two tunnels or shifting towards either side as shown in Figure 8.3b. However, settlement troughs could be also asymmetric (Figure 8.3c).

Based on observations on the Chicago subway tunnels, Peck (1969) suggested that the settlement curve over twin tunnels is likely to be asymmetric. He pointed out that the loss of ground associated with the second tunnel was larger than that due to the first tunnel so that the greater settlement was found towards the first tunnel. However, Peck (1969) also proposed that in the case where twin tunnels are close enough together, a single symmetric settlement trough would be observed. Therefore, the Gaussian function (equation 3-13) could be applied for describing the settlement trough. Using the same charts shown in Figure 3.10 and Figure 3.11, one can estimate the trough width parameter (*i*) by replacing the radius R with $R' = R + d/2$, where d is the distance between centerlines of the twin tunnels (see Figure 8.3). As a result, the settlement curve can be calculated using the equation (3-13). However, it is very important to note that Peck's (1969) observation was based on open-faced shields with compressed air which is quite different from the case of EPB shield tunneling where complex operational parameters are involved. As discussed earlier in Chapters 5 and 7, ground responses induced by EPB shield tunneling were significantly affected by how the EPB shield was operated. To estimate the magnitude of surface settlements, operational parameters recorded in the shield should be considered. Furthermore, in the case of surface settlements caused by the twin tunnels, a complex combination of several other factors may be involved including operational parameters of both shields, the time interval between the first shield- and the second shield arrivals, and the distance between two tunnels. Thus, Peck (1969)'s assumption is may not be applicable to EPB shield tunneling.

Several other authors studied the shape of surface settlement troughs over twin tunnels. Cording and Hansmire (1975) observed ground movements occurring over twin tunnels of the Washington D.C. Metro project. They suggested that the asymmetric trough shape after the second shield passing may be caused by the interference between the two tunnels. This interference increased as the pillar width between two tunnels decreased. However, it should be noted that this tunneling project also used open-faced shields instead of EPB shields. Shirlaw et al. (1988) observed asymmetry of settlement troughs caused by EPB tunneling of twin tunnels in the Singapore MRT. Nevertheless, their

observations were based on settlement monitoring alone, which did not include shield operational parameters recorded from the first- and the second shields.

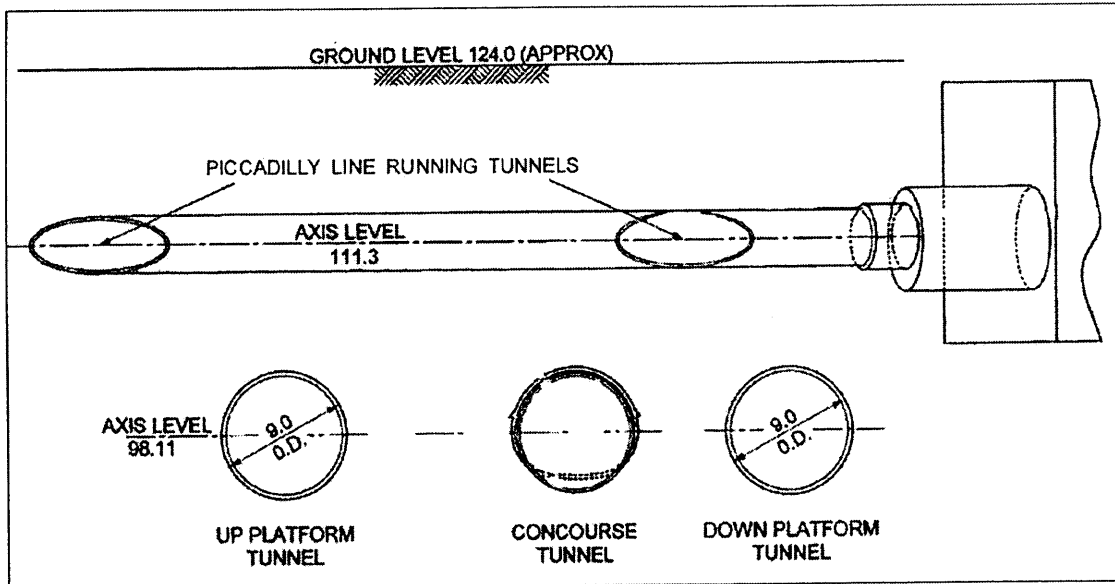


Figure 8.1 Plan and Cross section at London Heathrow Central Terminal Area

Cooper et al. (2002) investigated surface settlement troughs observed during excavation of three tunnels crossing below parallel existing tunnels at London Heathrow Central Terminal Area station (Figure 8.1). Measurements above the existing Piccadilly Line inner tunnel were made and the resulting settlement troughs are shown in Figure 8.2. From Figure 8.2, it is clear that the central concourse tunnel which is constructed first produces a symmetric, albeit somewhat shifted settlement trough. On the other hand, the two outer (Upline, Downline) tunnels produced very asymmetric settlement troughs. However, it should be noted that no EPB tunneling was used in the tunneling section.

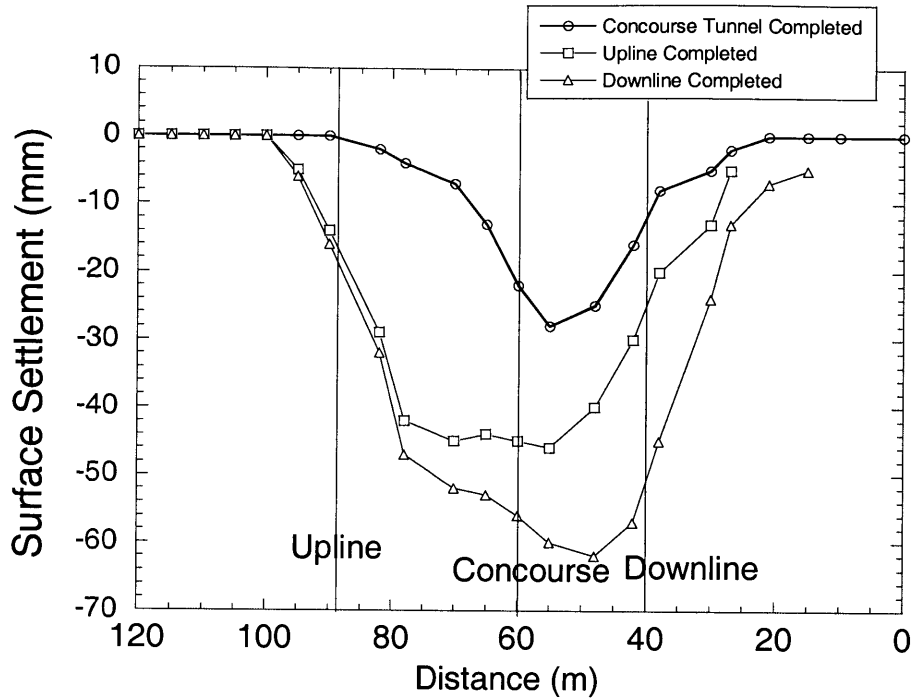


Figure 8.2 Surface settlements observed during construction in the Piccadilly Line Inner tunnel (after Cooper et al., 2002)

In the MRTA project, arrays of surface settlement markers were used to measure surface settlements. Figure 8.4 through Figure 8.18 show development of ground surface settlements during excavation of the first tunnel and the second tunnel which were measured in settlement arrays (see instrumentation layouts in Figure 8.5 through Figure 8.19). Note that the instrumentation readings were generally done on a daily basis. But to show a clear development of the surface settlement, selected data were plotted. In most cases, the ground surface begins to subside during the first shield passing and the settlement continues to develop further for approximately 3-4 days or 30 meters after the shield passed the section (see also Section 7.2.1). The details of the surface settlement development relative to the shield position in the longitudinal direction were discussed in Chapter 7.

As can be seen in Figure 8.4 through Figure 8.18, when the second shield approached the instrumentation section (i.e. an array of surface settlement markers), surface settlements develop again. The development appears to continue until one week after second shield

passing, and after this only insignificant change was found in the settlement troughs. However, in the case measured on CS-8G (Figure 8.18), surface heave was observed during the second shield passing. This phenomenon is due to applying very high face pressure during excavation.

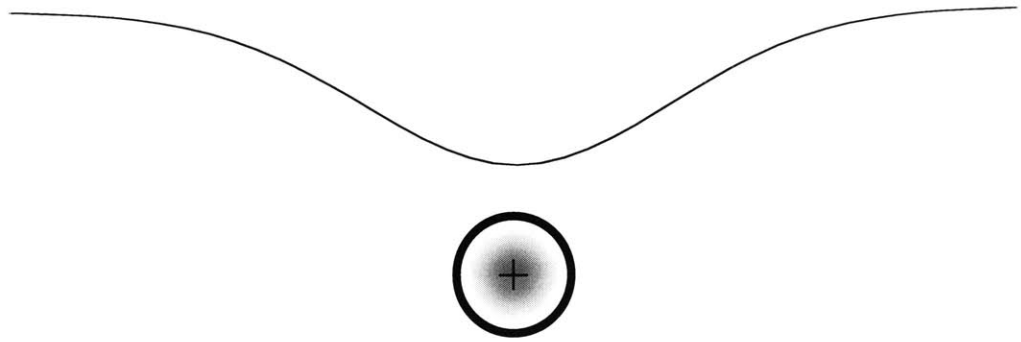
If one takes a detailed look at the surface settlement troughs measured one week after the second shield passing illustrated in the figures, it was found that there are two distinct shapes namely, symmetric and asymmetric. As can be seen in Figure 8.4 through Figure 8.14, the settlements after the second shield passing appear to be relatively symmetric in that each side of the trough is quite identical. Note that this observation is only based on eye judgment which is not perfectly precise. On the other hand, asymmetric shapes were observed in the instrumentation sections shown in Figure 8.16 and Figure 8.18.

Additionally, for the first time, operational parameters were recorded in every excavation cycle in the MRTA project. Hence, one can investigate how EPB shields were operated as they passed the instrumentation sections. In Figure 8.4 through Figure 8.18, the major operational parameters namely face pressure, penetration rate, grouting pressure and percent grout filling are plotted together with the surface settlement troughs. In most cases, each contractor typically operated the northbound shield and the southbound shield similarly, as can be seen when comparing the operational parameters in Figure 8.4 through Figure 8.14; these are the curves in which fairly symmetric settlement troughs may be observed. On the other hand, at section 23-G3-007-019 (Figure 8.16) and section CS-8G (Figure 8.18), where asymmetric settlement troughs were observed, the northbound and southbound shields were operated differently.

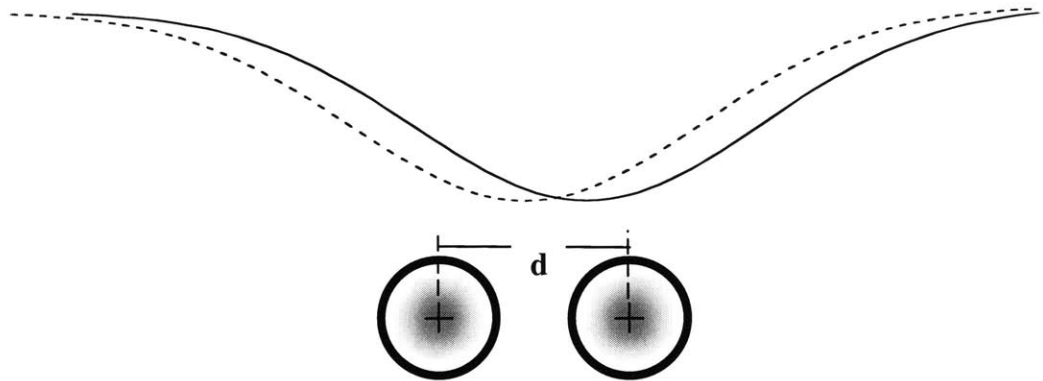
In section 23-G3-007-019 (Figure 8.16), the southbound shield approached the measurement section first. Large surface settlement (i.e. $\delta_{\max} = 40$ mm) was recorded mainly due to a very low face pressure and low percent grout filling (i.e. only 100% or less). However, when the northbound shield passed, the settlements did not show a significant further development even one week after shield passing. As recorded during the northbound shield passing, the face pressure is much higher than that of the

southbound shield (i.e. the first shield). Moreover, the grout filling applied during passing the section is normally above 120%.

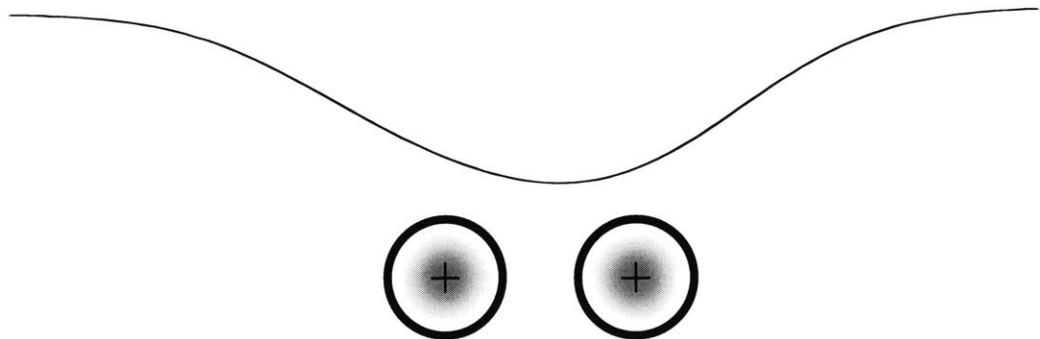
At section CS-8G (Figure 8.18) where the northbound shield arrived first, small surface settlement was observed (i.e. only 5 mm one week after shield passing). This is probably due to operating the shield in an earth pressure balance mode with the optimal face pressure of 200 kPa. The grouting pressure and percent grout filling was sometimes higher than usual. However, as the southbound shield approached the section, surface heave was observed over the 2nd tunnel. Furthermore, even though one week after the 2nd shield passing; the surface heave still remained as shown in Figure 8.18. This phenomenon is associated with very high face pressure recorded in the southbound shield during passing the section. The pressure is as high as 390 kPa, which is twice the lateral earth pressure in that depth. As a result, instead of ground movements forwards the tunnel, the shield pushed the ground outwards causing heave on the ground surface. The surface settlement trough measured one week after the second shield passing is very asymmetric such that the ground surface subsides over the northbound tunnel, but surface heave was found over the southbound tunnel. Thus, based on this observation, one may suggest that asymmetric surface settlement troughs are always associated with significant differences in operational parameters between the first and the second shields. In other words, this assumption can be related to earlier case histories observed by Peck (1969), as operational parameters are different, ground losses into the tunnel are also different and the magnitude of surface settlements induced by the first and the second shields should be also different. Hence, the total settlement as a combination of settlements caused by the shields would be asymmetric.



(a) Symmetric settlement trough over a single tunnel



(b) Symmetric settlement trough (can be offset) over twin tunnels



(c) Asymmetric settlement trough over twin tunnels

Figure 8.3 Definitions of surface settlement trough

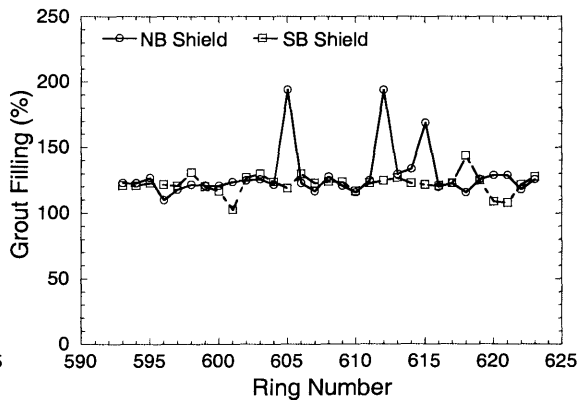
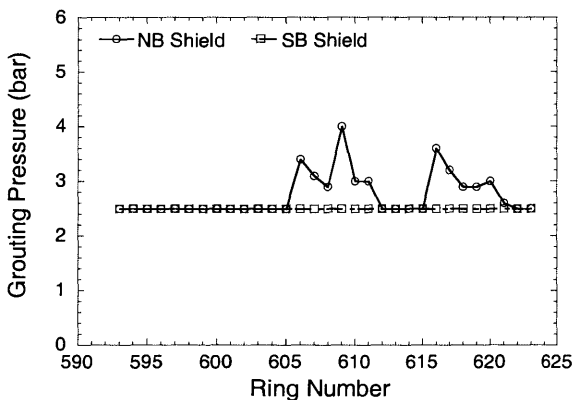
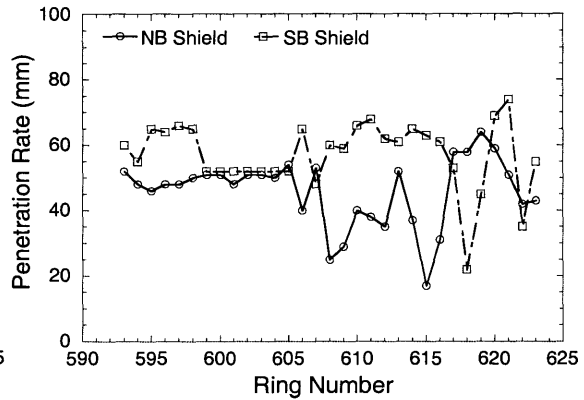
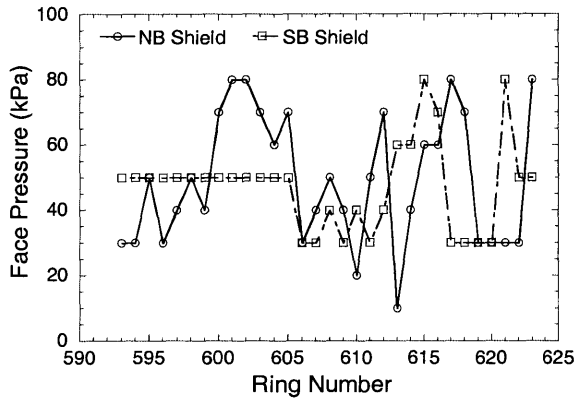
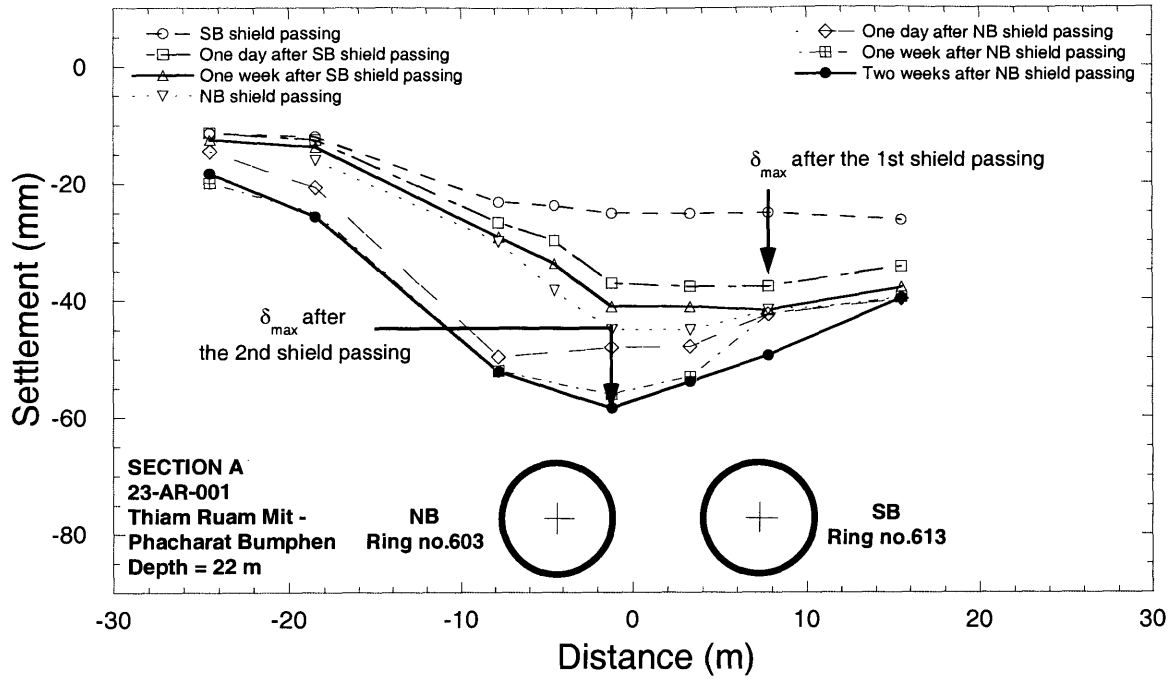


Figure 8.4 Surface settlement troughs measured in 23-AR-001 and operational parameters recorded from NB and SB shields as they pass the measurement section

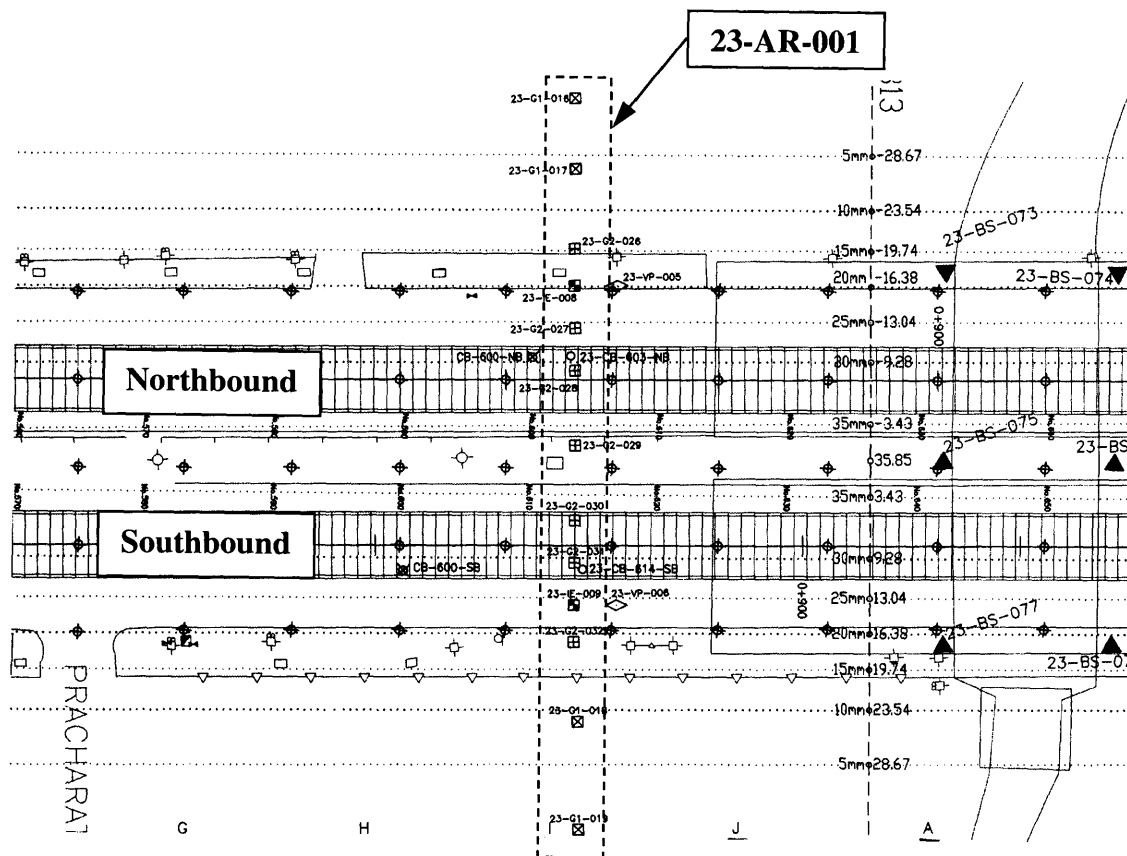


Figure 8.5 Layout of the settlement array 23-AR-001

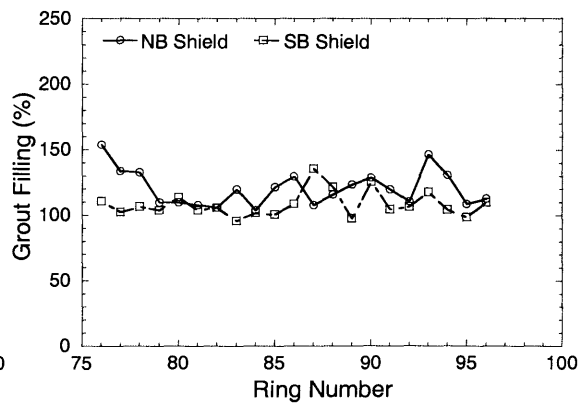
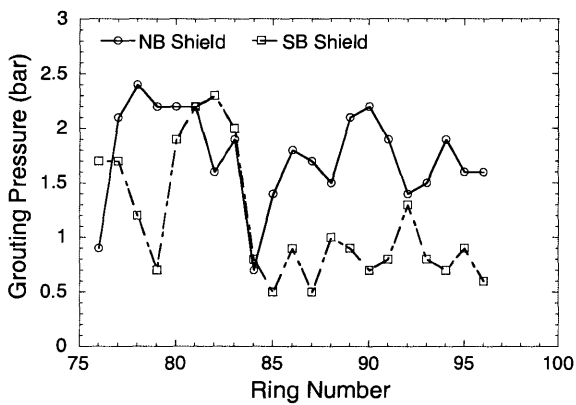
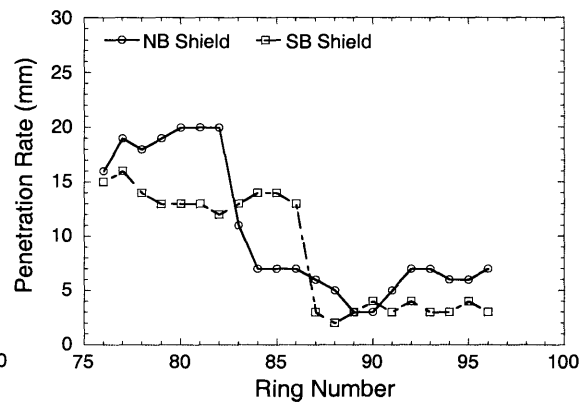
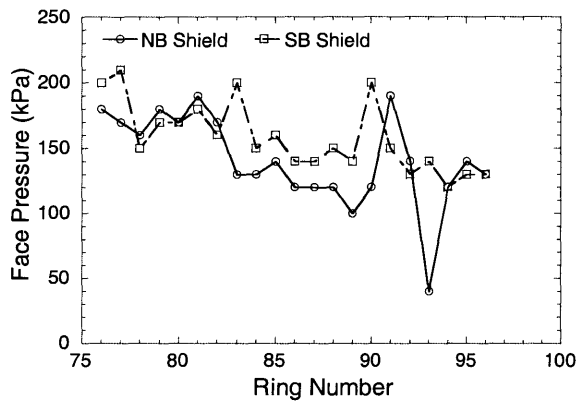
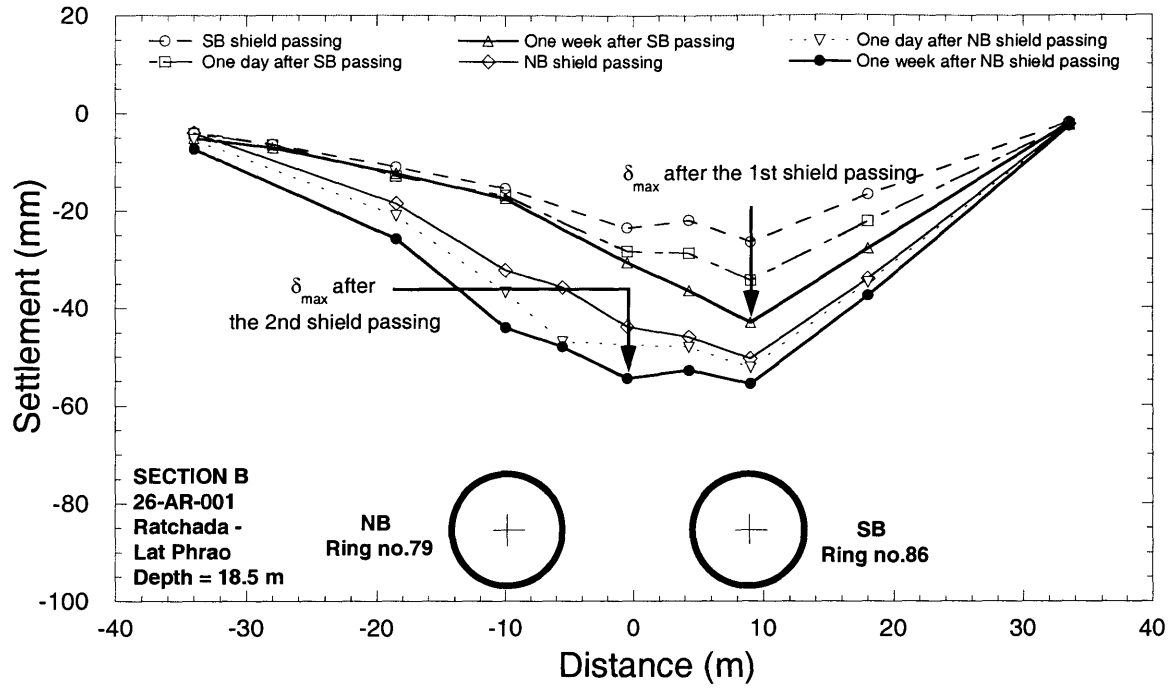


Figure 8.6 Surface settlement troughs measured in 26-AR-001 and operational parameters recorded from NB and SB shields as they pass the measurement section

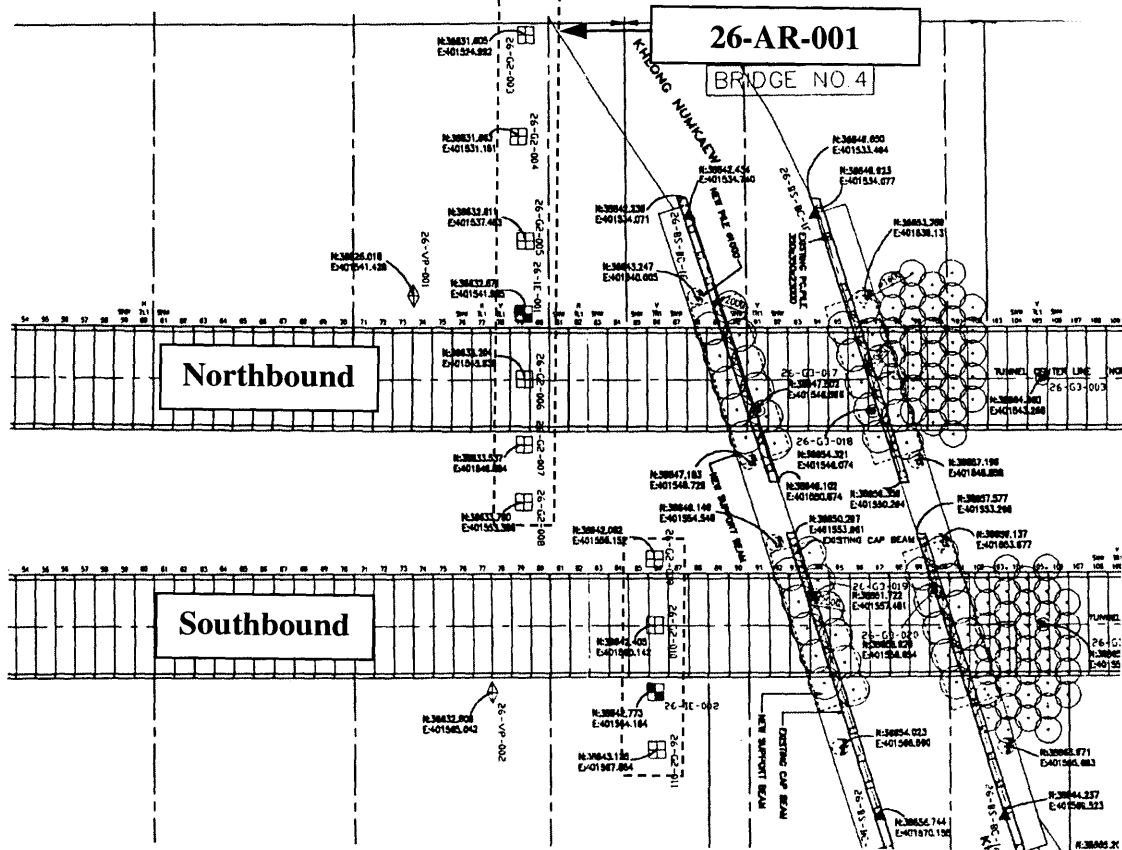


Figure 8.7 Layout of the settlement array 26-AR-001

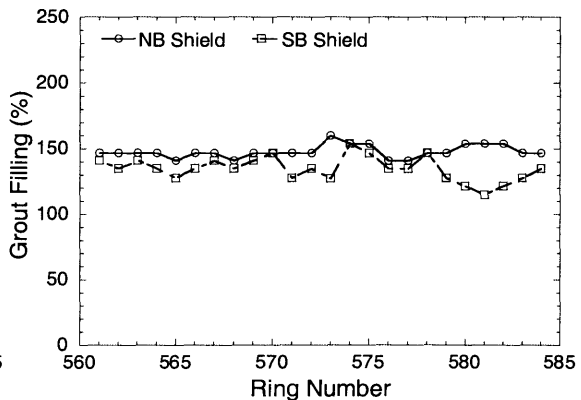
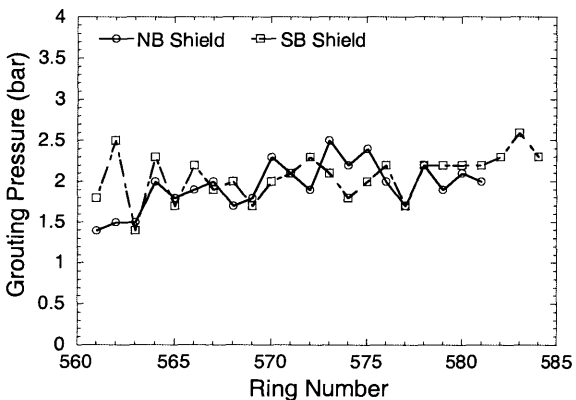
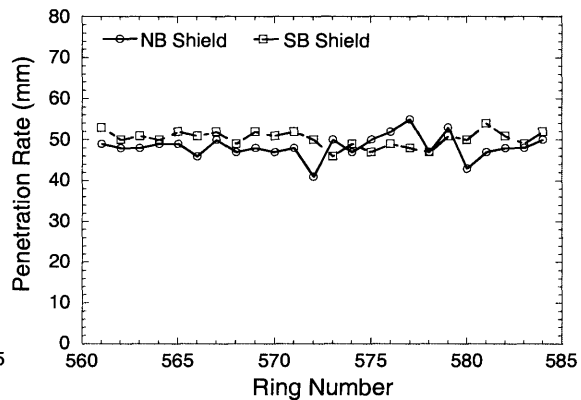
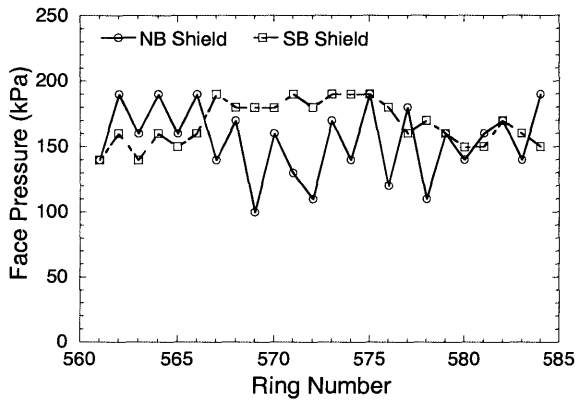
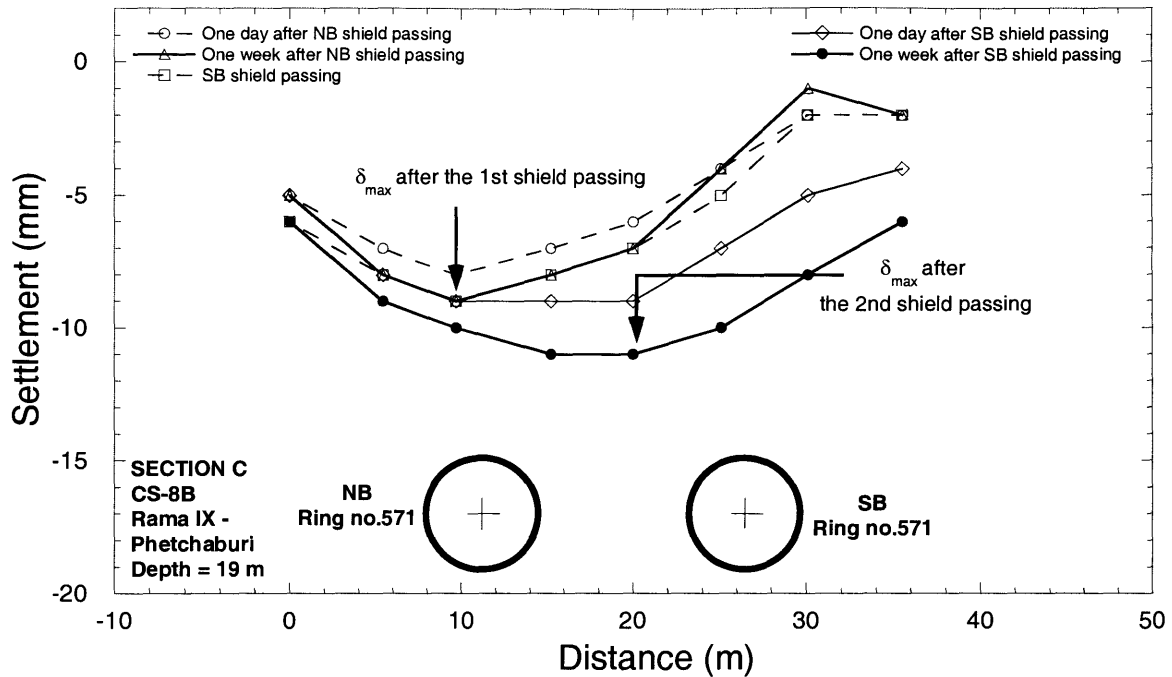


Figure 8.8 Surface settlement troughs measured in CS-8B and operational parameters recorded from NB and SB shields as they pass the measurement section

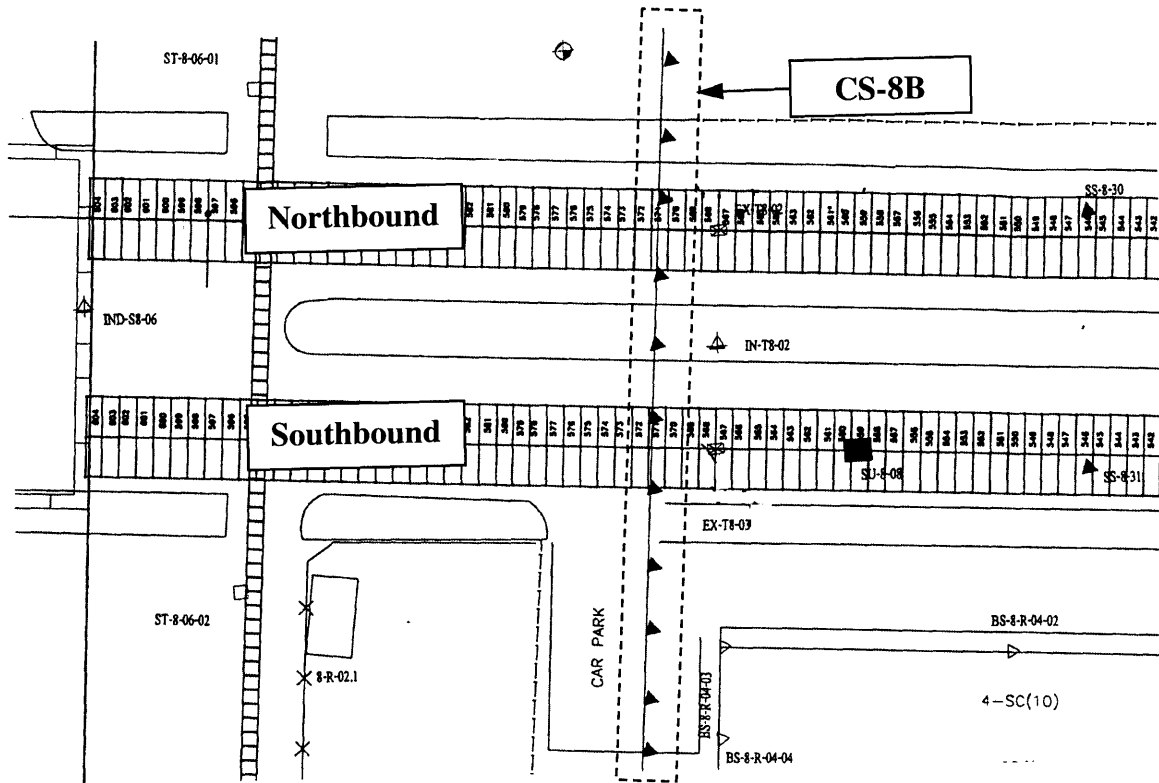


Figure 8.9 Layout of the settlement array CS-8B

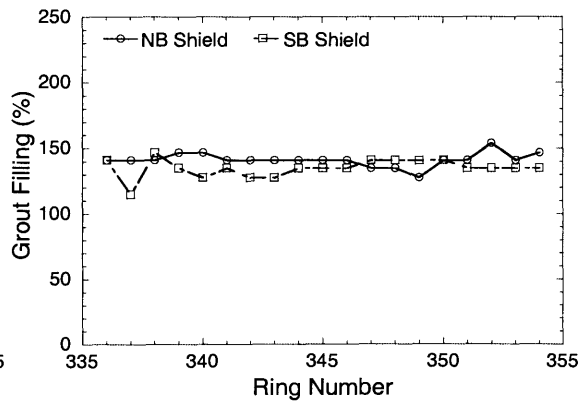
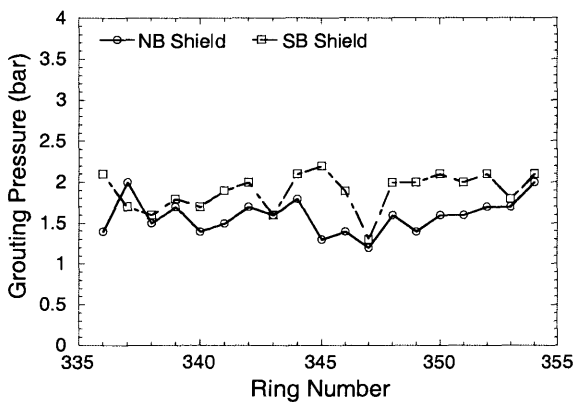
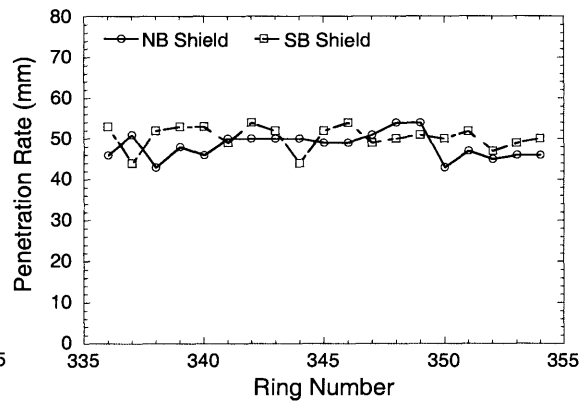
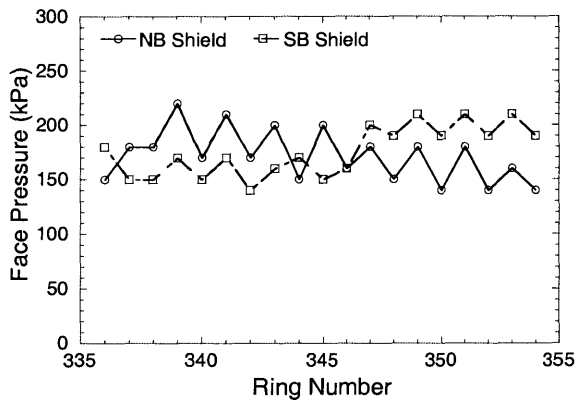
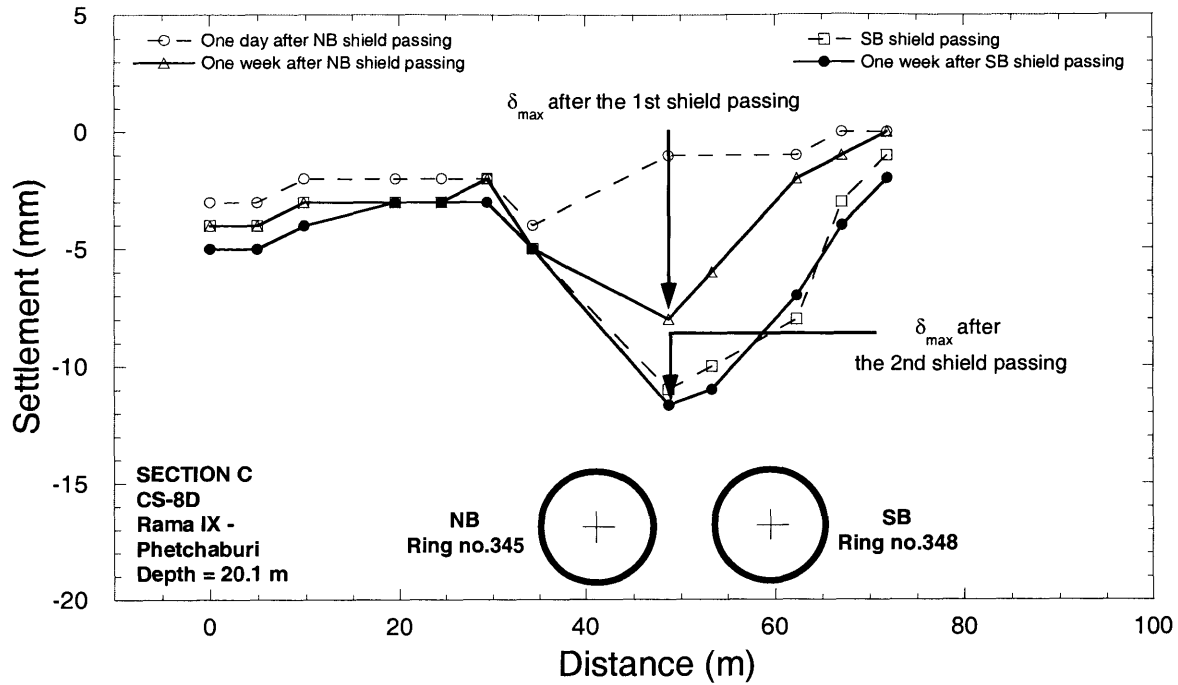


Figure 8.10 Surface settlement troughs measured in CS-8D and operational parameters recorded from NB and SB shields as they pass the measurement section

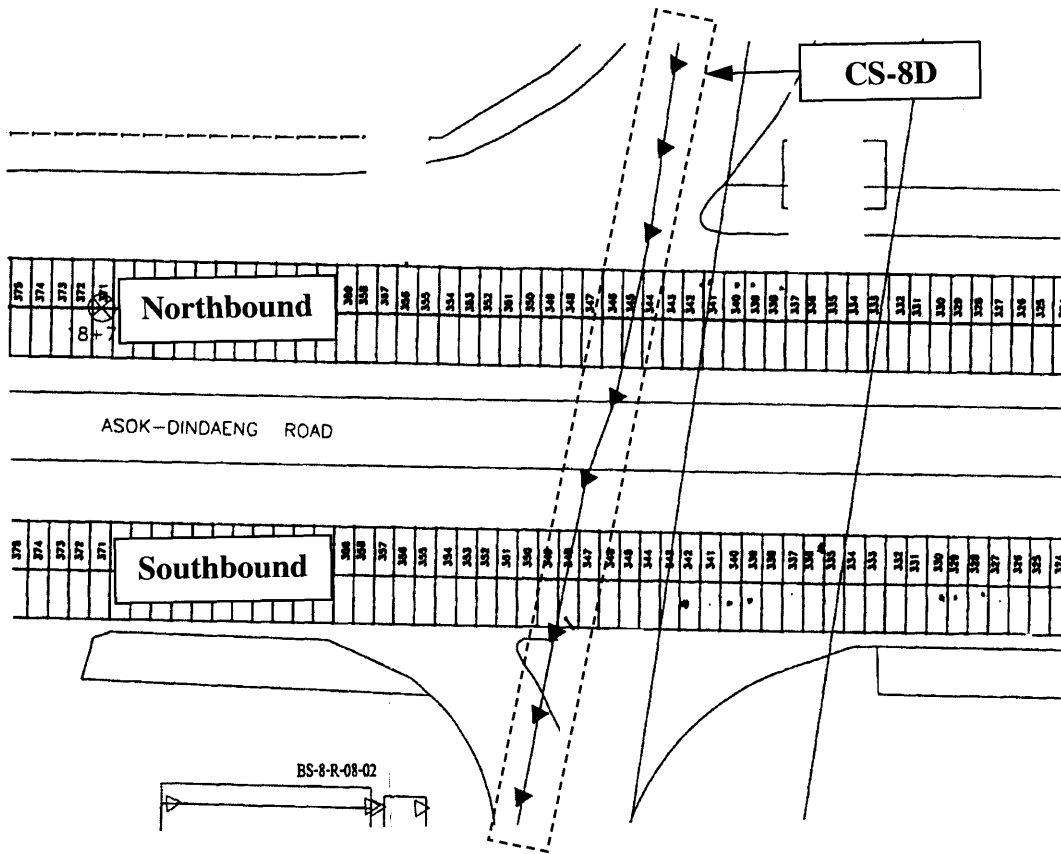


Figure 8.11 Layout of the settlement array CS-8D

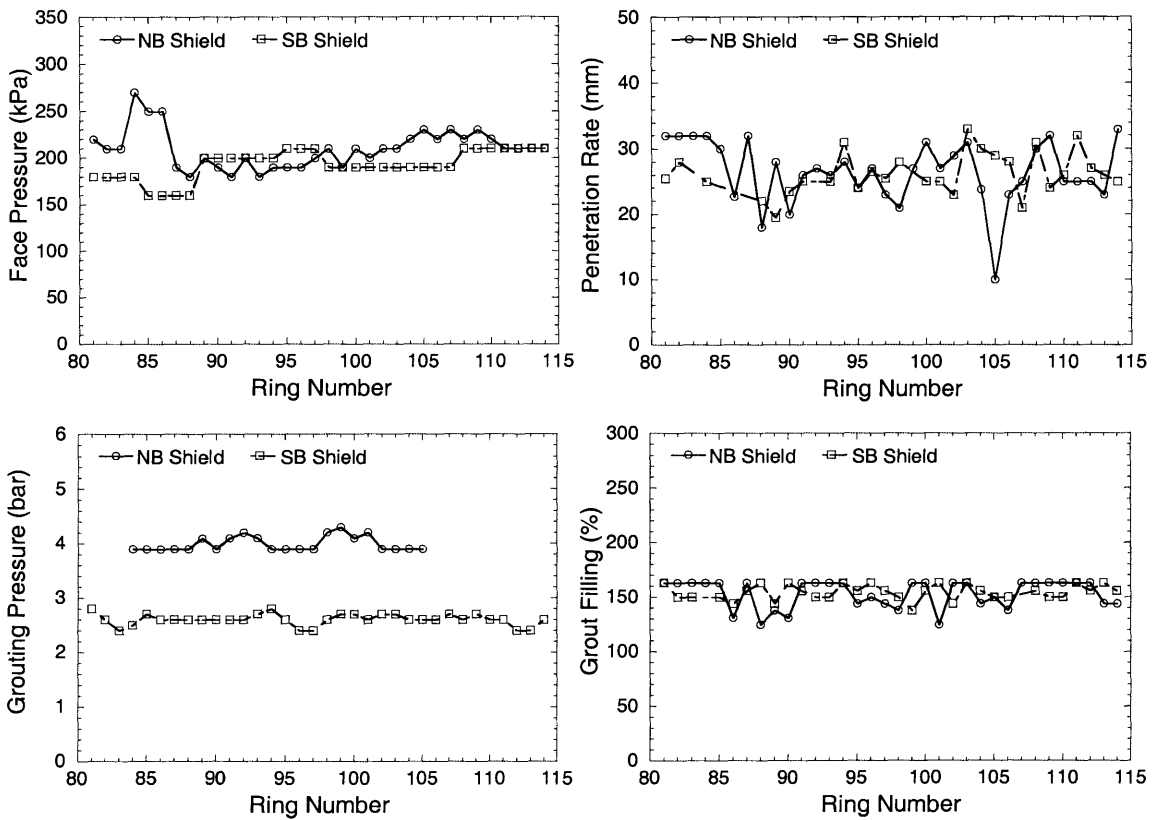
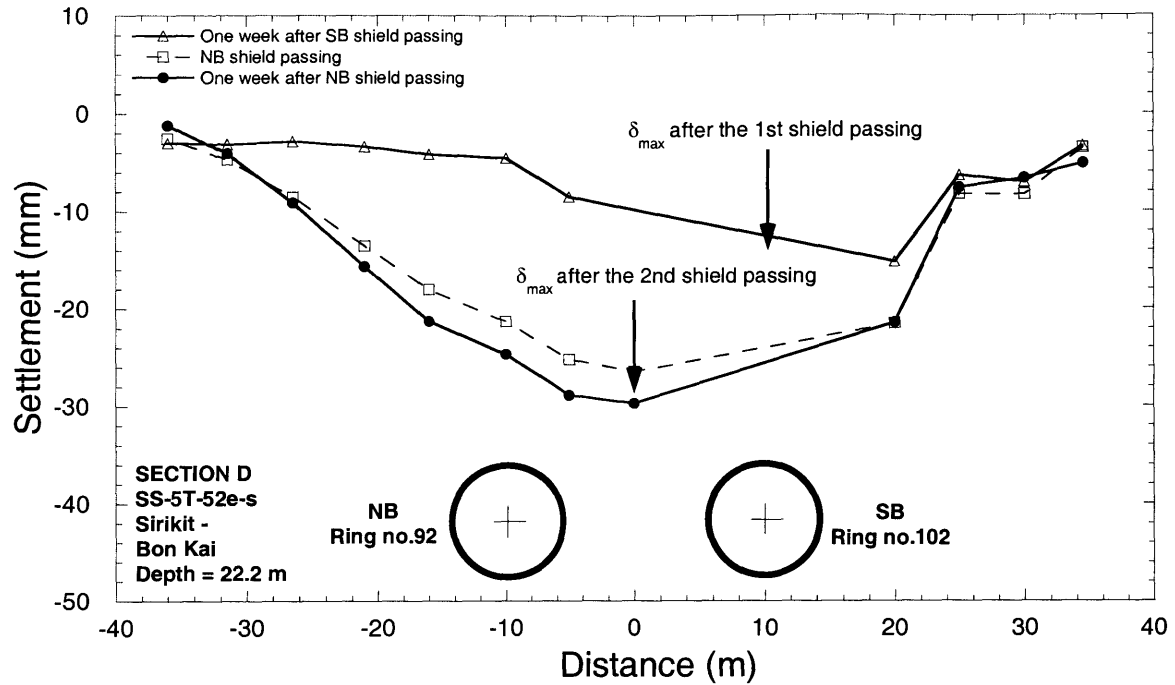


Figure 8.12 Surface settlement troughs measured from SS-5T-52e-s and operational parameters recorded from NB and SB shields as they pass the measurement section

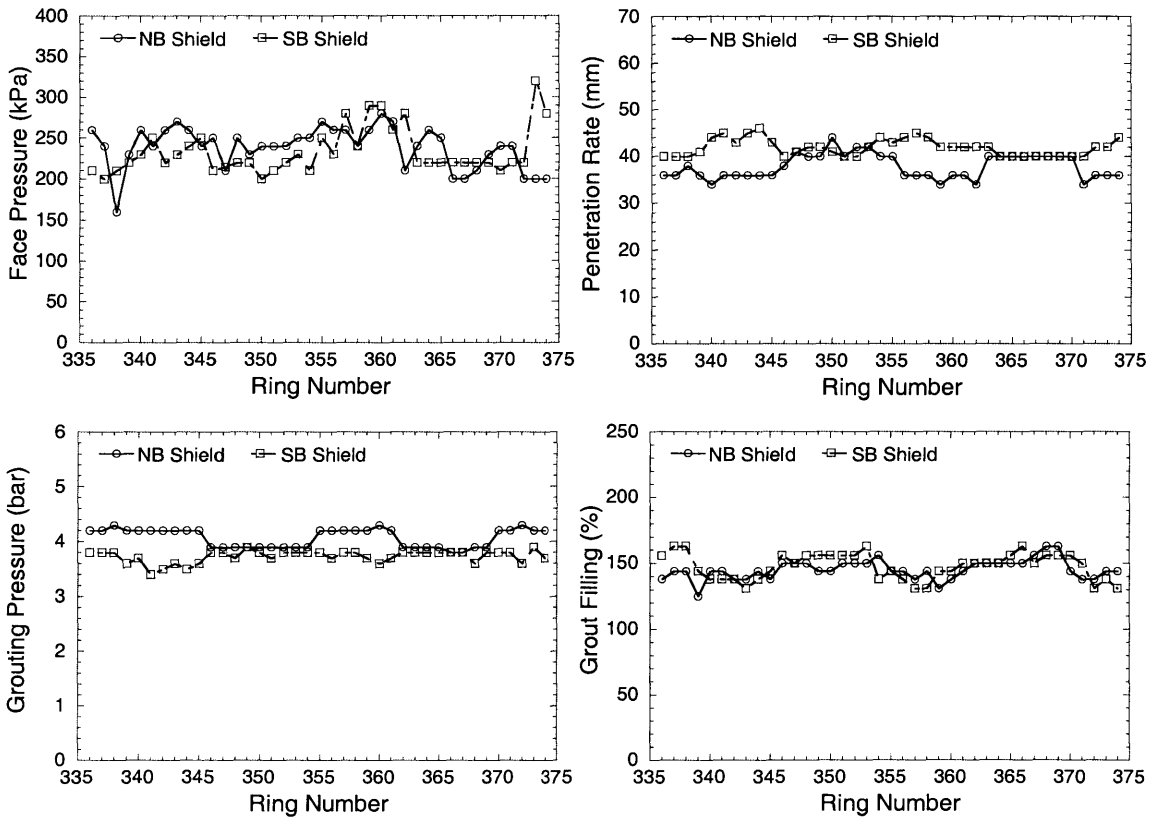
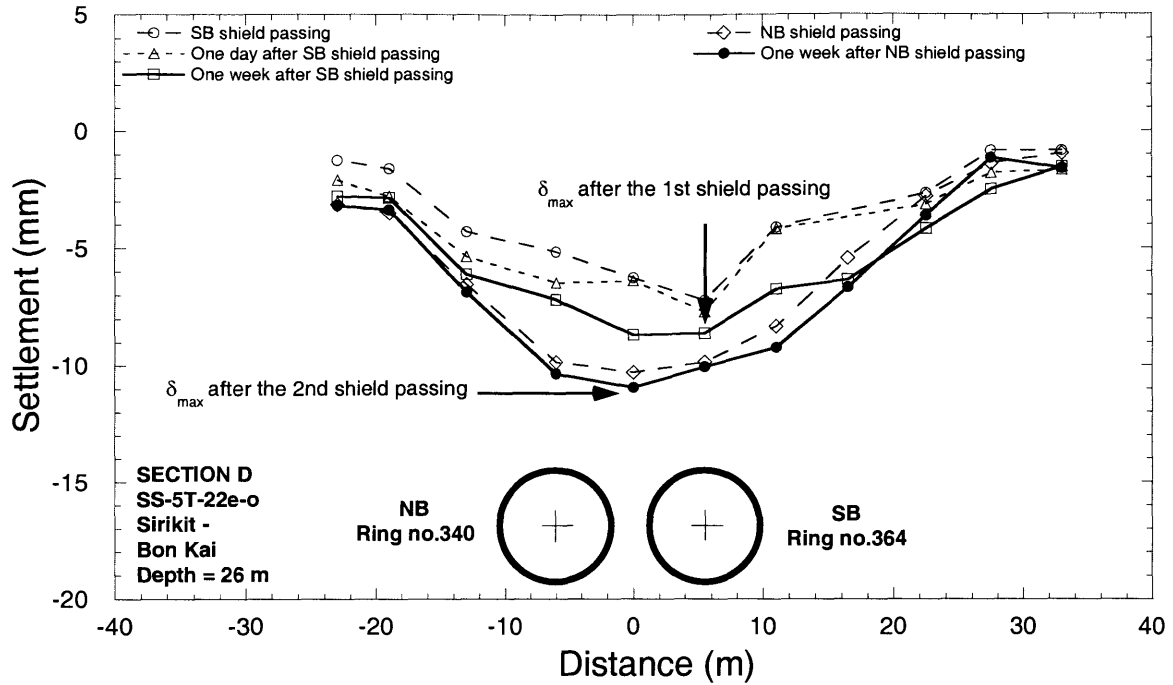


Figure 8.14 Surface settlement troughs measured from SS-5T-22e-o and operational parameters recorded from NB and SB shields as they pass the measurement section

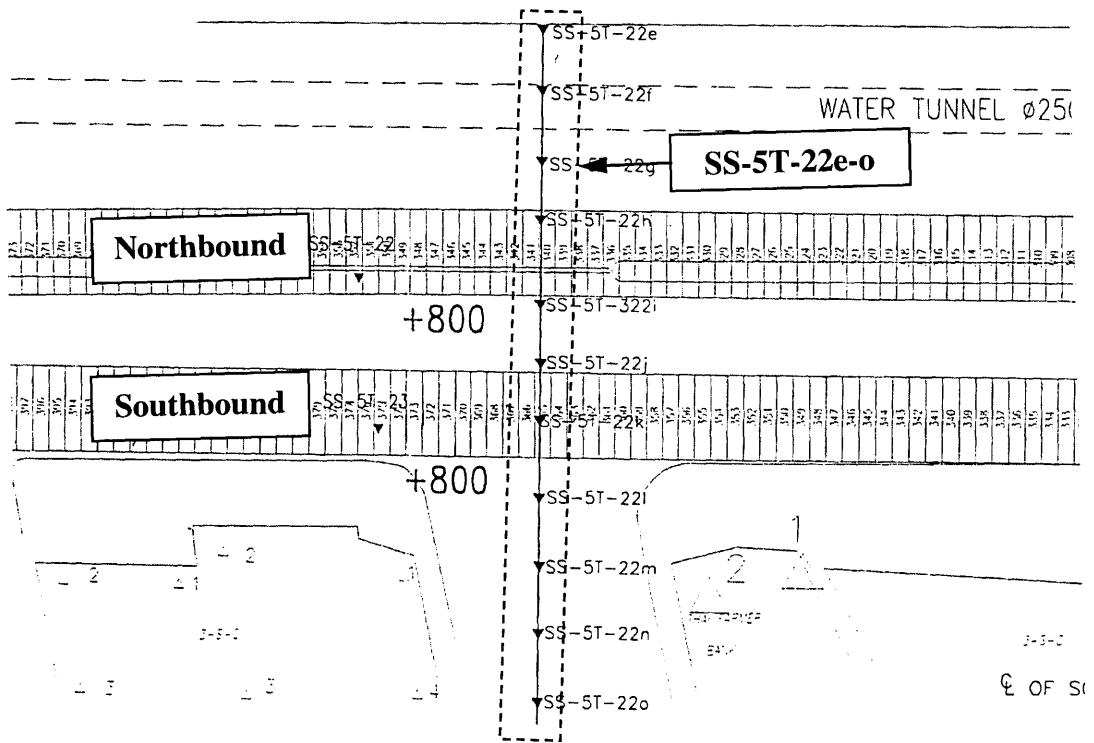


Figure 8.15 Layout of the settlement array SS-5T-22e-o

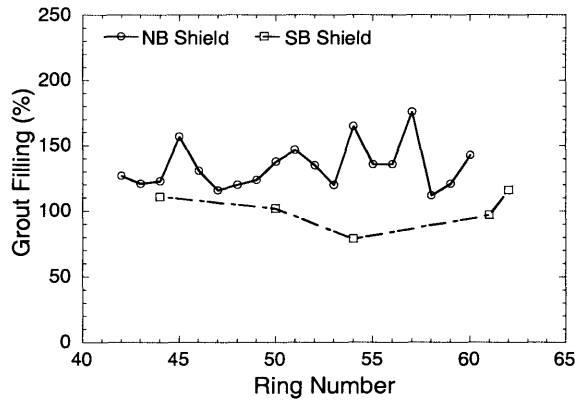
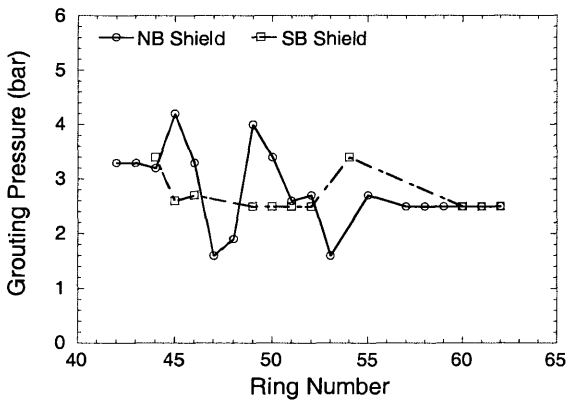
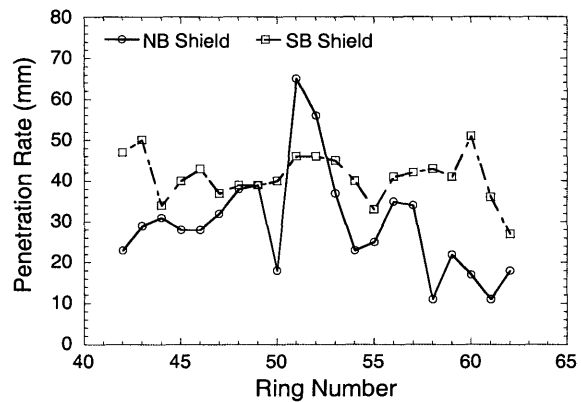
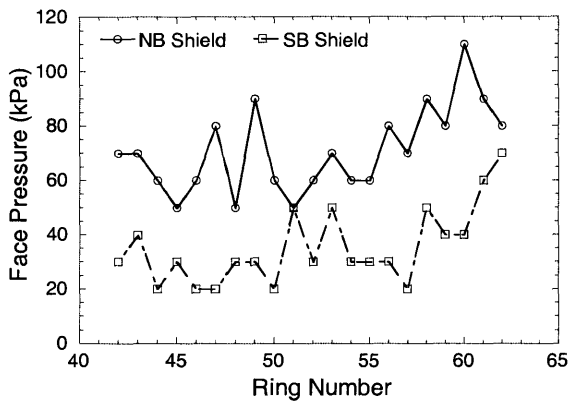
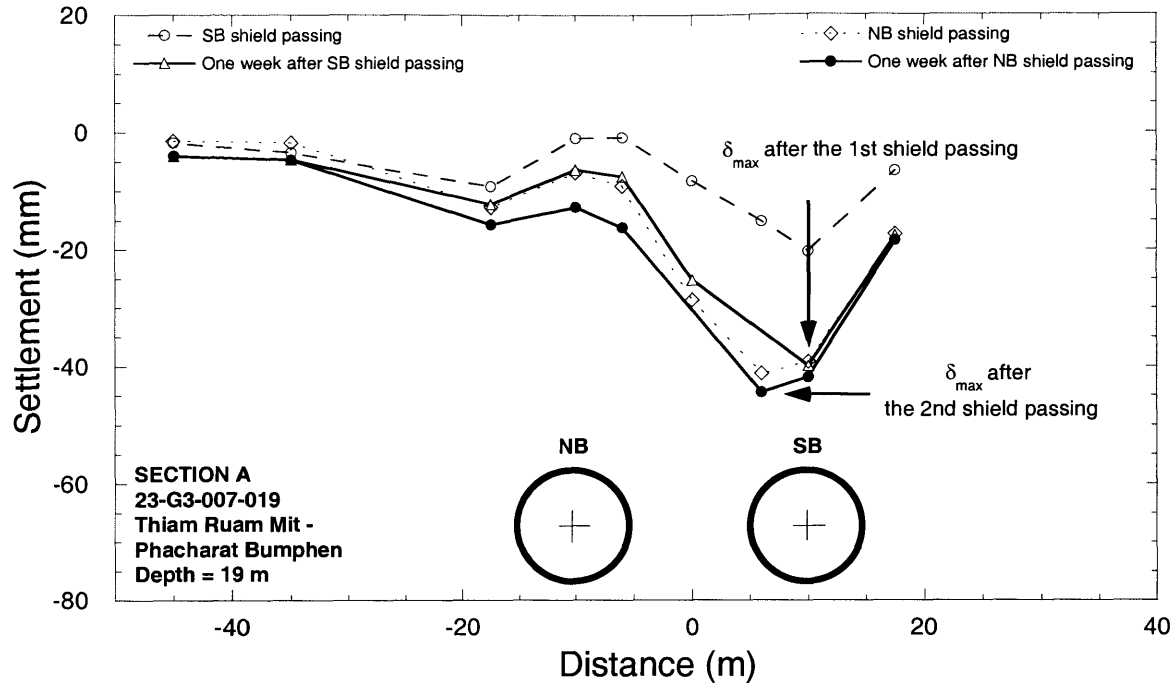


Figure 8.16 Surface settlement troughs measured from 23-G3-007-019 and operational parameters recorded from NB and SB shields as they pass the measurement section

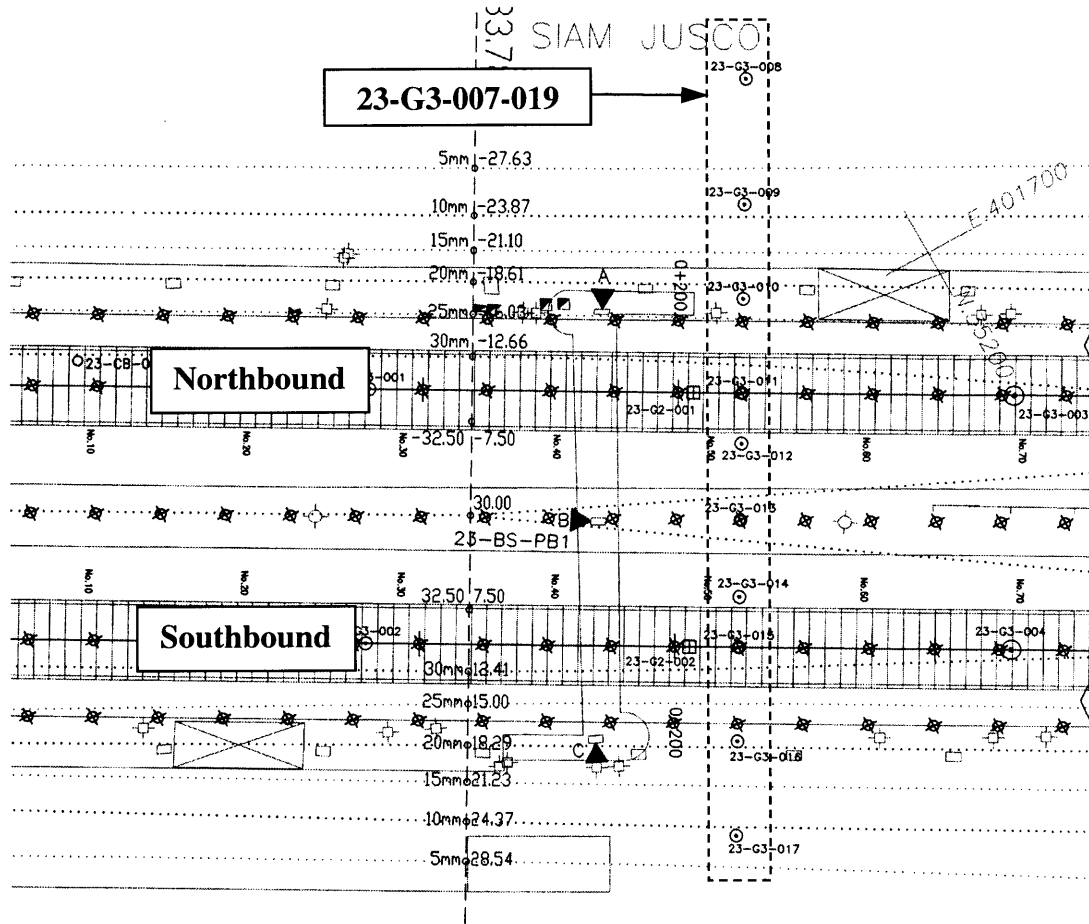


Figure 8.17 Layout of the settlement array 23-G3-007-019

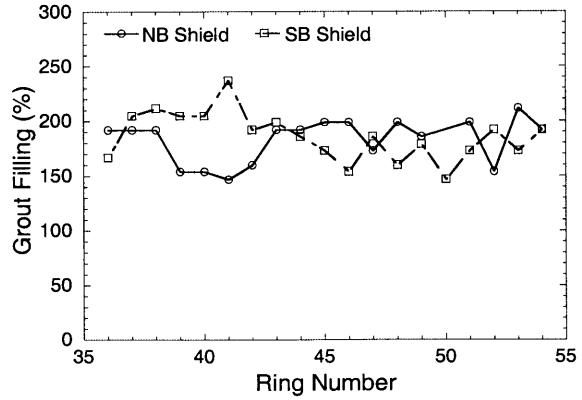
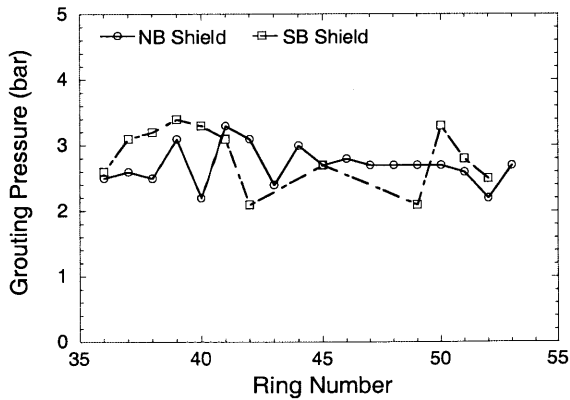
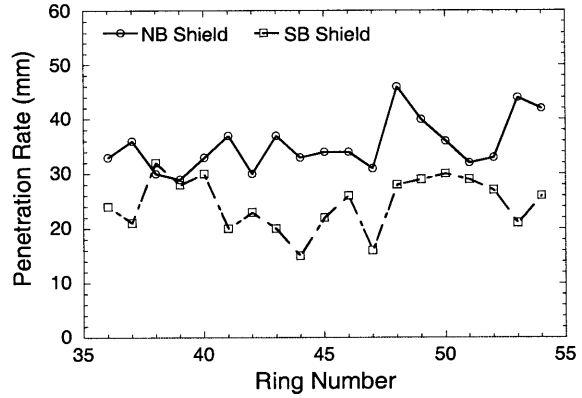
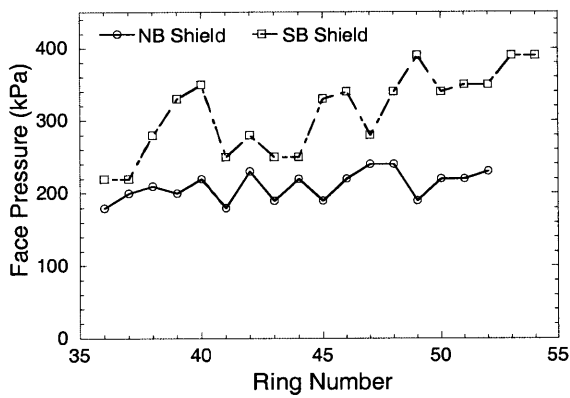
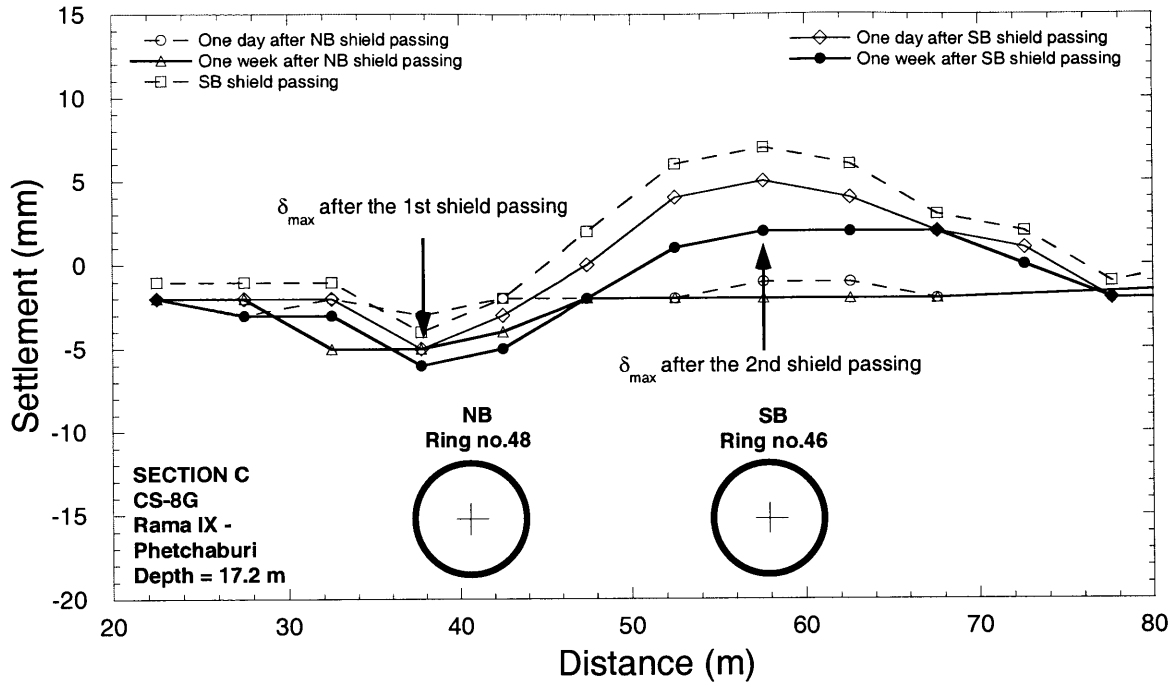


Figure 8.18 Surface settlement troughs measured from CS-8G and operational parameters recorded from NB and SB shields as they pass the measurement section

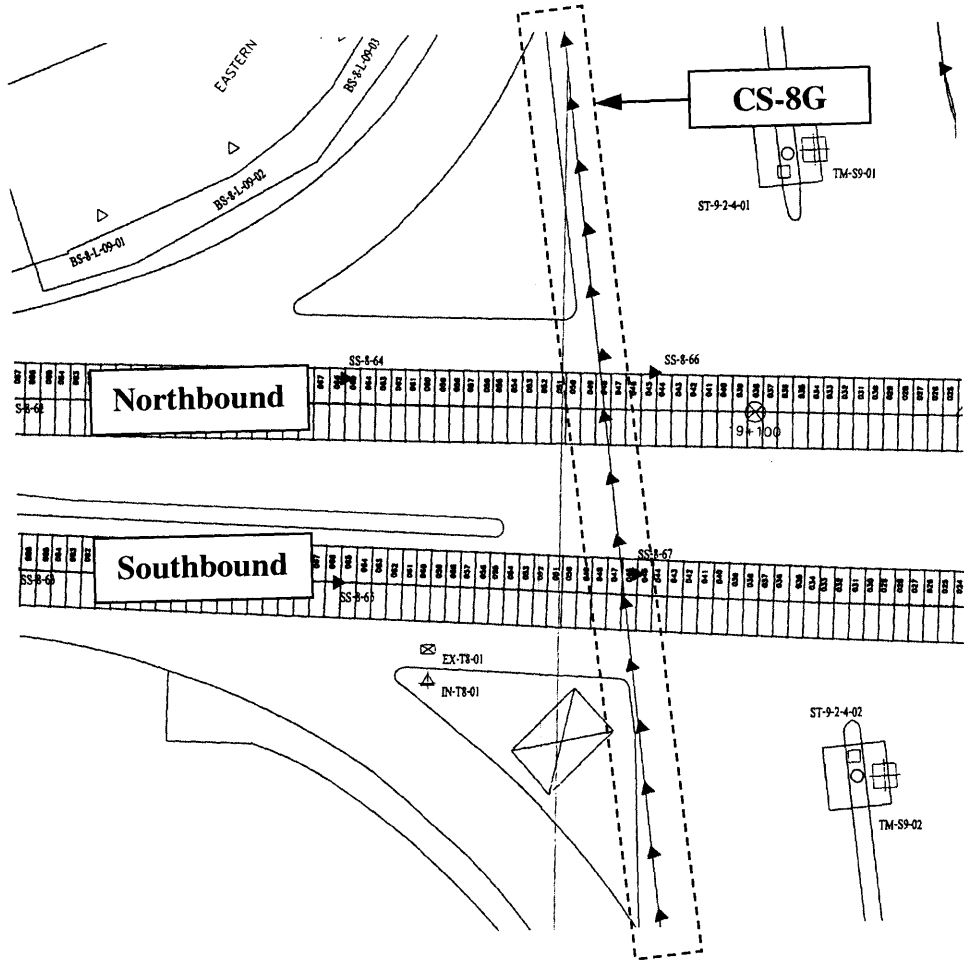


Figure 8.19 Layout of the settlement array CS-8G

8.3 Comparison with Predictive Methods

As discussed earlier in Chapter 7, a settlement trough caused by tunneling of a single tunnel can be described by Gaussian curve or normal probability function (Peck, 1969). By knowing the maximum surface settlement (δ_{max}), transverse settlement data can be fitted by adjusting trough width parameter (i). As the function was applied to fit all surface settlement data after the first shield passing, it was found that the Gaussian curve was able to describe settlement troughs very well (see Section 7.2.2). Additionally in all cases, settlement troughs are symmetric in which the maximum settlement (δ_{max}) was observed over the centerline of the tunnel (Figure 8.3a). Therefore, by selecting an appropriate trough width parameter, one can use the Gaussian function to estimate an entire settlement trough. However, it should be noted that this applies to the first tunnel only. For twin tunnels, this approach needs to be evaluated.

8.3.1 Symmetric Curve over the Twin Tunnels

In this section, the Gaussian function will be used to describe settlement troughs induced by twin tunnels to investigate whether the model is valid for multi tunnels. Settlement data recorded with the instrumentation shown in Section 8.2 are used in this section except for the settlement data recorded in section CS-8G (Figure 8.18) which ground heave was observed. In Figure 8.20 through Figure 8.26, the settlement data measured after the first shield- and second shield passing as shown in the previous section are plotted together with Gaussian curves created by varying the trough width parameter (i) until the best fit is obtained. As can be seen in the case of the settlement troughs measured *after the first shield passing*, Gaussian curves do fit well and the troughs are symmetric with respect to the first tunnel centerline. The results confirm that the assumption of the Gaussian function is appropriate for a single tunnel as expected.

As recommended by Peck (1969), the Gaussian function can be also applied to twin tunnels by assuming that the maximum settlement (δ_{max}) occurs over the mid-point between the two tunnels. However, in most cases (Figure 8.20 through Figure 8.26), it

was found that to obtain a good fit for settlement data measured after the second shield passing, the Gaussian curve has to shift towards the first tunnel. This means that the maximum settlement (δ_{max}) does not exactly occur at the mid-point between the two tunnels but occurs at a location towards the first tunnel. The shifted Gaussian curves are called “offset Gaussian curve,” as shown in Figure 8.20 through Figure 8.26. This observation is in agreement with the observation made by New and Bowers (1993). This phenomenon was also mentioned by Peck (1969) who said that larger settlement is likely to occur towards the first tunnel.

New and Bowers (1993) suggested that Gaussian curves can be used to describe settlement troughs caused by twin tunnels by introducing a new offset parameter (a) into the Gaussian function:

$$\delta = \delta_{max} \exp \left[-\frac{(y-a)^2}{2i^2} \right] \quad \mathbf{8-1}$$

The equation allows one to offset the Gaussian curve to fit measured data, with the value of the offset parameter (a) equal to the offset distance (i.e. towards the first tunnel). It should be noted that the offset parameter (a) can be obtained only by trial and error. Hence, this technique is not an ideal solution for predicting surface settlement troughs. In the next section, a normalization and superposition technique will be introduced. In cases of twin tunnels, this technique can be used to describe surface settlement troughs better than other previous solutions.

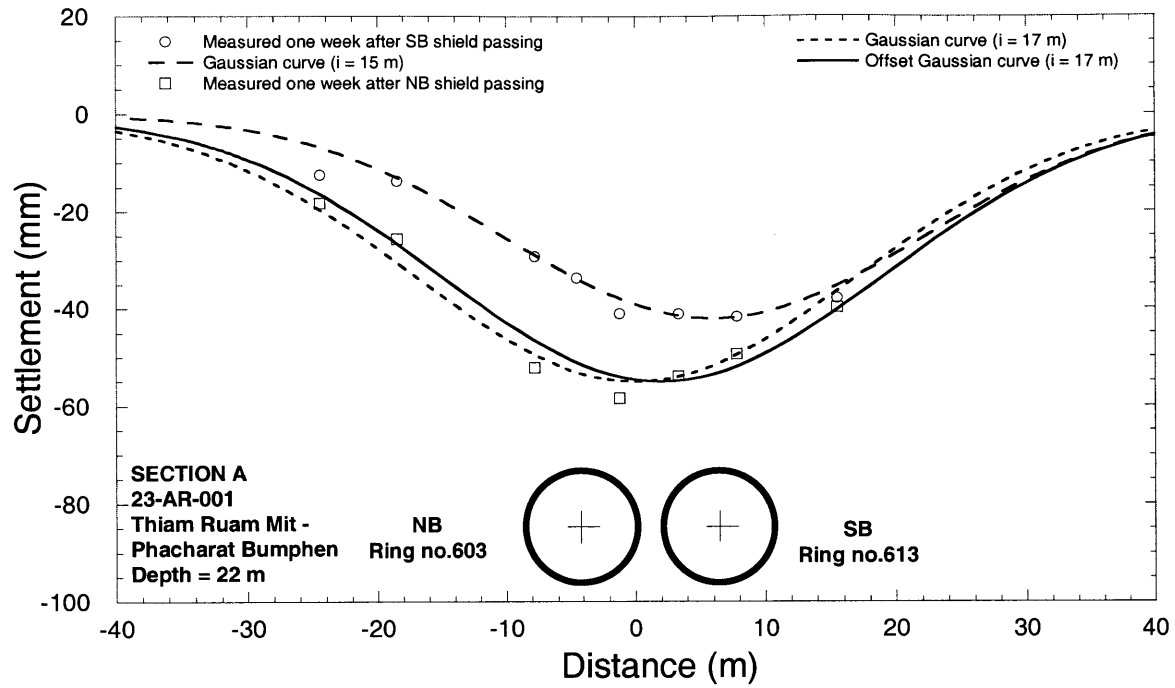


Figure 8.20 Surface settlements measured in 23-AR-001 and settlement troughs described by Gaussian curves

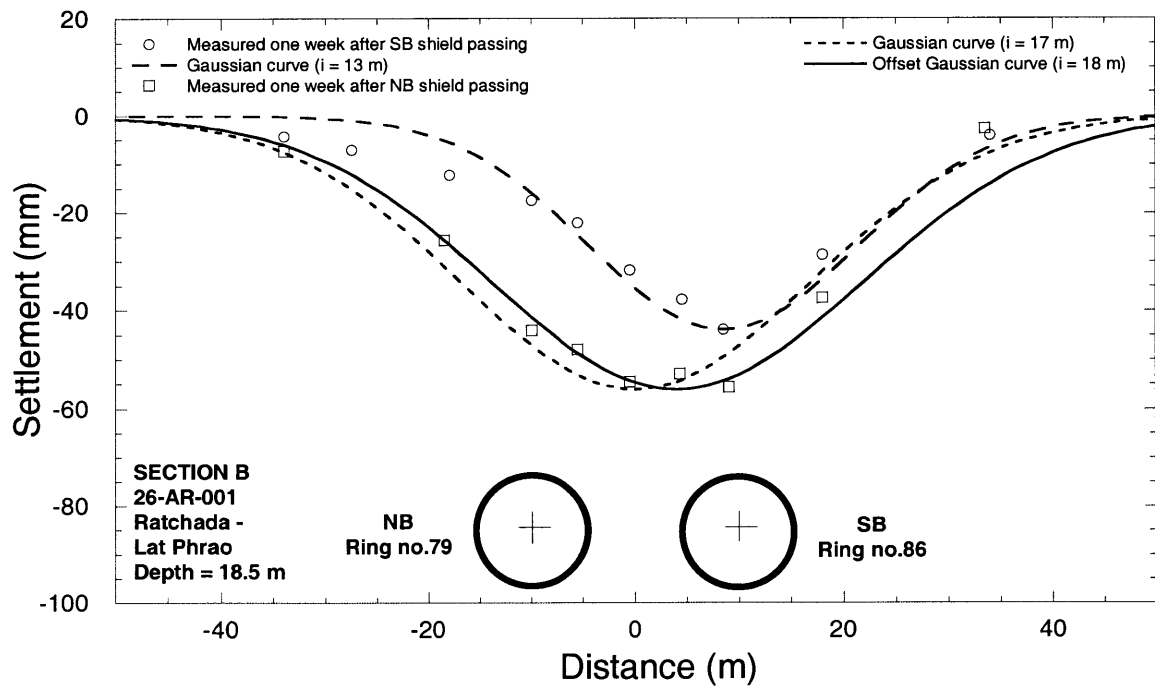


Figure 8.21 Surface settlements measured in 26-AR-001 and settlement troughs described by Gaussian curves

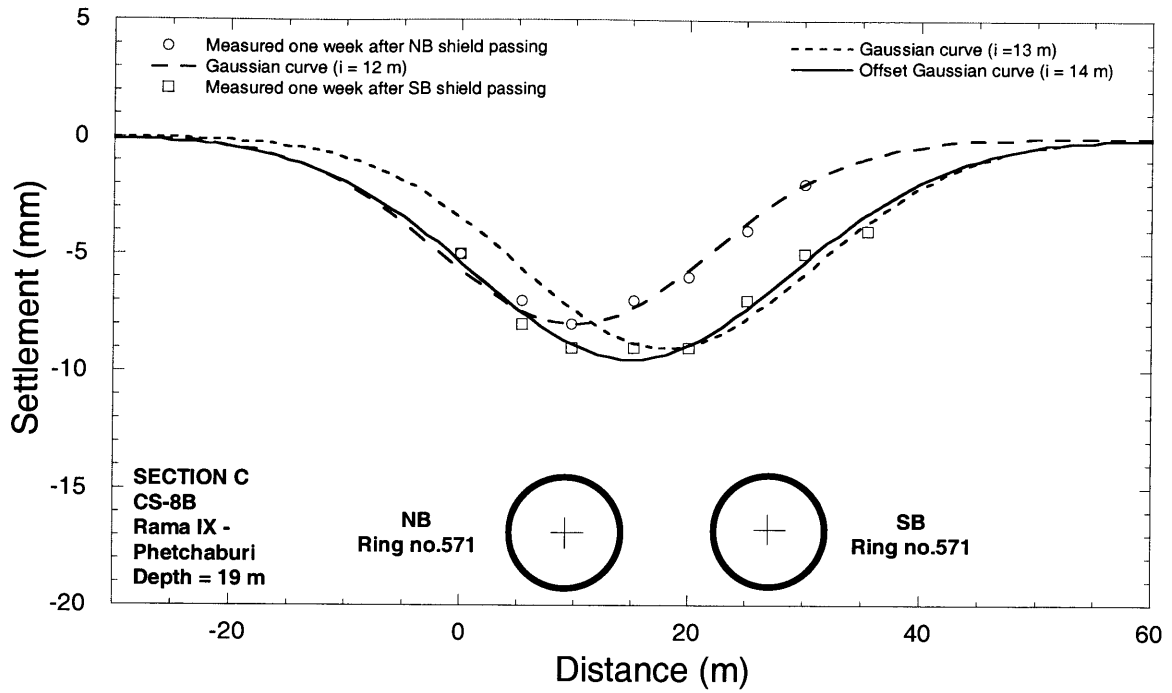


Figure 8.22 Surface settlements measured in CS-8B and settlement troughs described by Gaussian curves

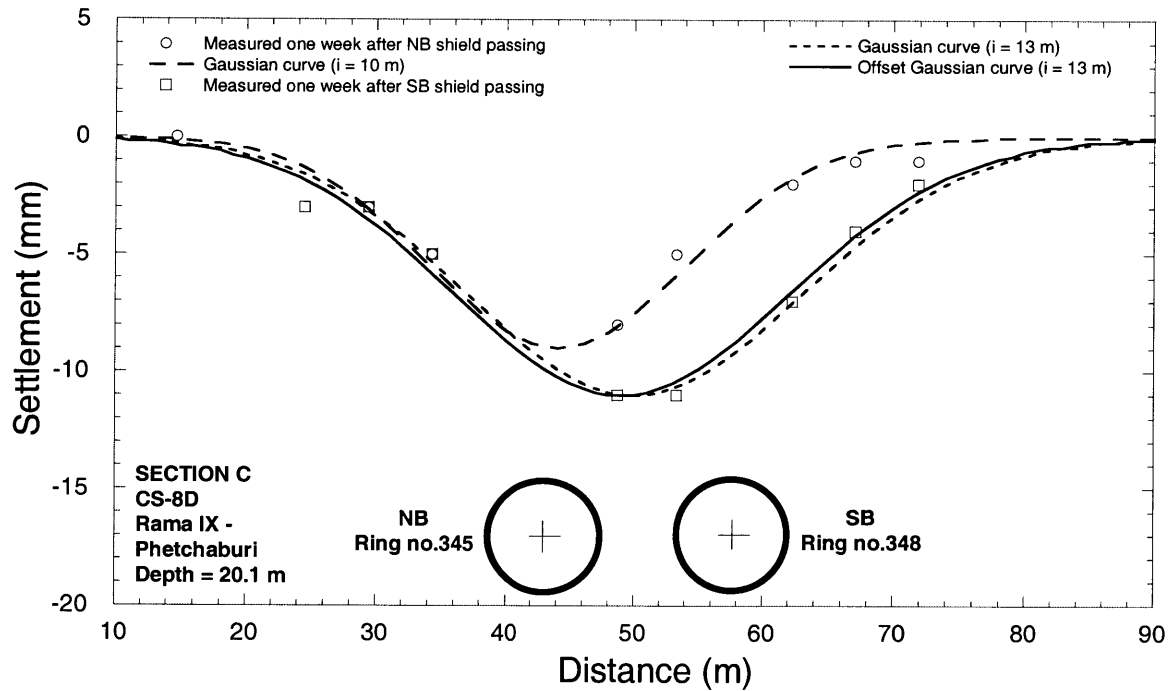


Figure 8.23 Surface settlements measured in CS-8D and settlement troughs described by Gaussian curves

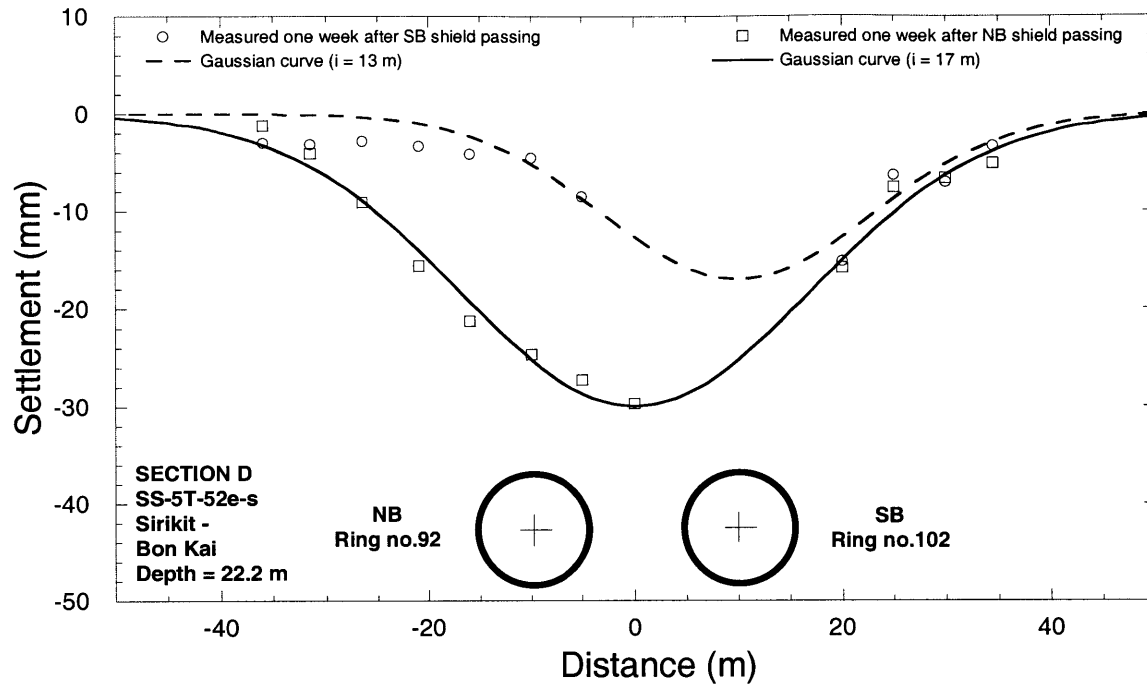


Figure 8.24 Surface settlements measured in SS-5T-52e-s and settlement troughs described by Gaussian curves

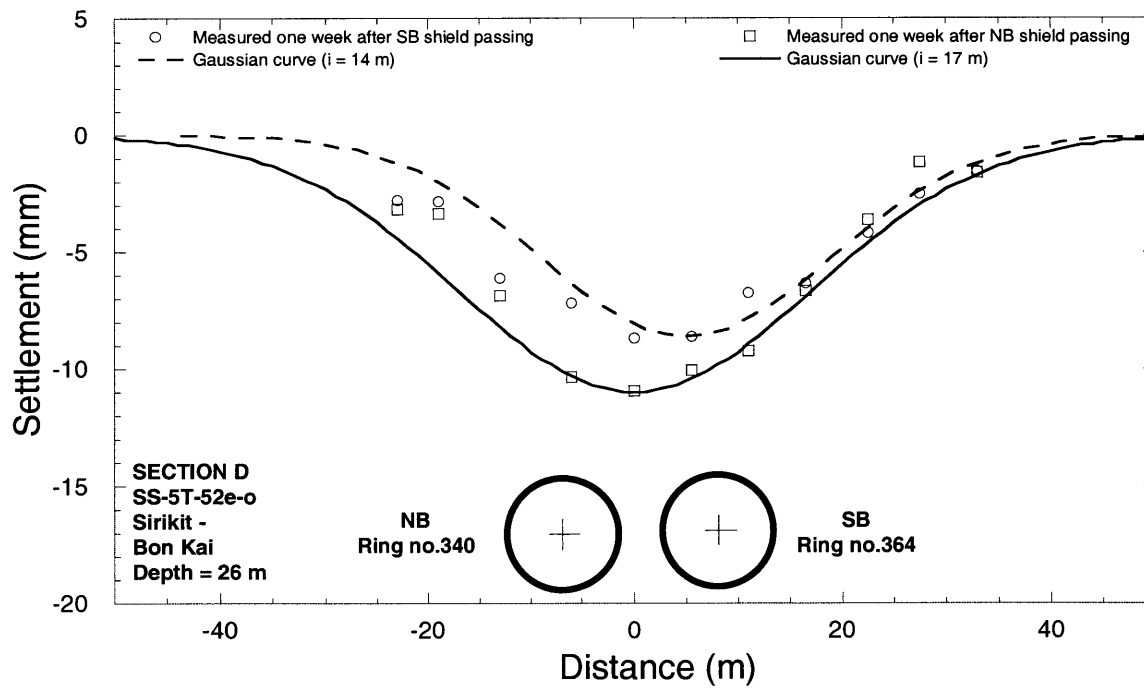


Figure 8.25 Surface settlements measured in SS-5T-22e-o and settlement troughs described by Gaussian curves

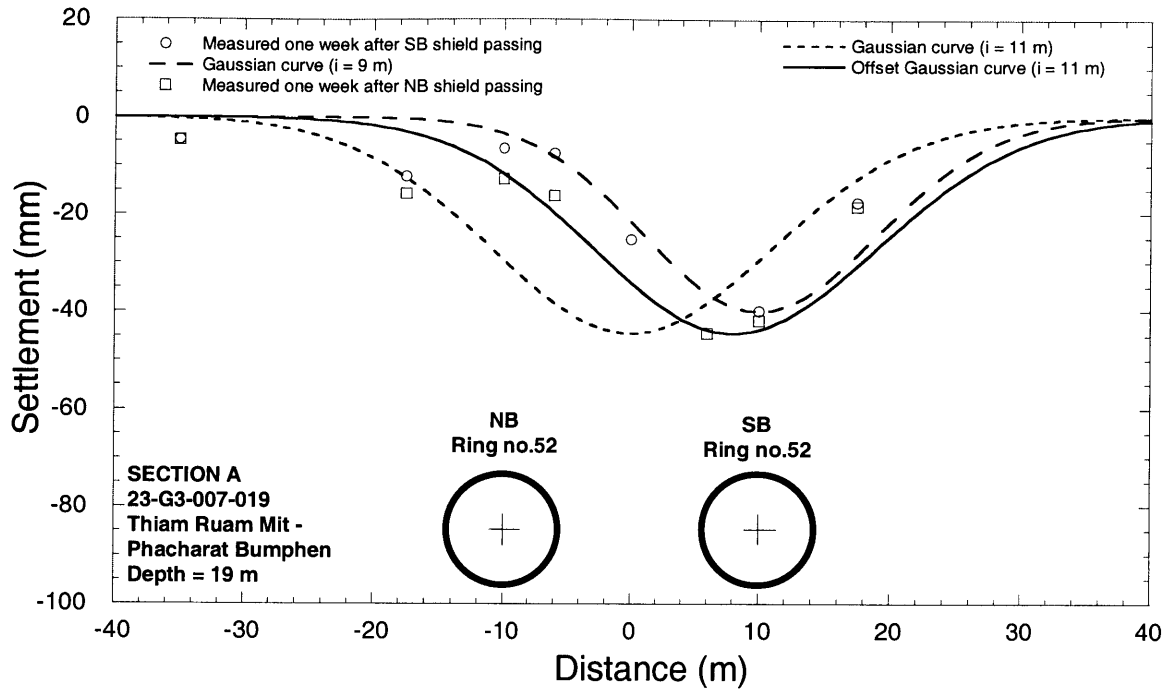


Figure 8.26 Surface settlements measured in 23-G3-007-019 and settlement troughs described by Gaussian curves

8.3.2 Superposition Curve

In the last section, the Gaussian curve with the offset parameter was found to be able to provide a fairly good fit for surface settlement data observed over twin tunnels as the maximum settlement tends to shift toward the first tunnel. In other words, this approach implies that the settlement curve is perfectly symmetric (i.e. left side and right side are identical). However, as mentioned earlier, laboratory experiments and results from several field observations demonstrated that ground loss into the second tunnel was different from ground loss into the first tunnel. As a result, total surface settlement troughs measured after the excavation of the second tunnel are likely to be asymmetric.

To investigate the ground response induced by the second tunnel, one needs to determine the additional surface settlements developing after the first shield passing. As shown in Figure 8.27, additional settlements can be obtained by subtracting settlements measured after the first shield passing from settlements measured after the second shield passing. The results can be plotted to represent surface settlements induced by the second shield only (Figure 8.27). This normalization technique is applied to the same sections used in Section 8.3.1. Results are then plotted in Figure 8.28 through Figure 8.34. As can be seen, the results demonstrate that in most cases, additional settlements induced by the second shield are smaller than the settlements induced by the first shield. Although, only a small number data points were recorded along the transverse sections, there are enough to see a trend of settlement troughs. Thus, if one takes a detailed look at the “additional settlement” troughs, it was found that they are relatively symmetric with respect to the second tunnel centerline.

As described earlier in Chapter 7, the Gaussian curve or normal probability function was found to be an appropriate technique for describing surface settlement troughs induced by “a single tunnel.” The technique may be applicable to additional settlements (i.e. normalized settlements over the second tunnel) as well since this represents surface settlements induced by the second tunnel only. Hence, the Gaussian curve is used to describe the additional settlement data as shown in Figure 8.28 through Figure 8.34. As

can be seen, by adjusting trough width parameters (i), the Gaussian curve can fit settlement troughs well.

The trough width parameters of “additional settlement” curves are shown together with the $i = Kz$ lines recommended by O’Reilly and New (1982) in Figure 8.35. Most of the data points fall within the envelope bounded by $i = 0.4z$ and $i = 0.6z$. This is similar to the case of settlement troughs measured over a single tunnel and in agreement with the conclusion of O’Reilly and New (1982) that for most cases, $i = 0.5z$ irrespective of whether the tunnel is in soft or stiff clays as discussed earlier in Section 7.2.2. One distinct point is located between $i = 0.4z$ and $i = 0.3z$ lines. The data for this point was obtained where the twin tunnels were excavated within a sand layer

It appears that one can construct a settlement curve induced by the first shield and a settlement curve caused by the second shield using the Gaussian function. Therefore, a superposition technique can be used to obtain a total settlement trough as a result of the twin tunnels. The settlement troughs are plotted in Figure 8.28 through Figure 8.34 to compare them with settlement data recorded after the second shield passed. Note that surface settlements measured with section CS-8G (Figure 8.18) are not considered in this section since significant ground heave, which cannot be described with the Gaussian function, was observed.

As can be seen in Figure 8.28 through Figure 8.34, the superposition curves appear to fit the data points very well except for section 23-G3-007-019 (Figure 8.34). Based on observations, unlike other settlement array sections, it was found that face pressures applied when the first shield passed section 23-G3-007-019 were much higher than face pressures applied during the second shield passing (see also Figure 8.16) so that this may affect the additional settlement trough caused by the second shield and the Gaussian curve may be not applicable to describe the trough.

In all cases, if one takes a detailed look at the superposition curves, it was found that the settlement curves after second shield passing are asymmetric and their shapes depend on

the magnitude and the shape of the settlement curves over the first and the second tunnels. As a consequence, most (but not all) of the total settlement curves seem to lean towards the first tunnel whose settlement curves are larger than caused by the second tunnel.

Based upon this finding, the following procedures can be suggested. (1) Measure the maximum surface settlement with a settlement marker installed over the centerline of the first tunnel (i.e. point A in Figure 8.27) and describe the entire settlement trough induced by the first shield using the Gaussian function. (2) Observe settlements over the second tunnel centerline (i.e. point B in Figure 8.27) after second shield passing. (3) Calculate the additional or normalized settlement over the second tunnel (i.e. point C in Figure 8.27). (4) Construct an additional settlement trough induced by the second shield using the Gaussian curve and superimpose it on the settlement trough induced by the first shield to obtain the total settlement curve caused by the twin tunnels. This new approach appears to be more suitable than applying the Gaussian function with the offset parameter to describe the total settlement since it does not require trial and error and produces a better fit than the offset approach.

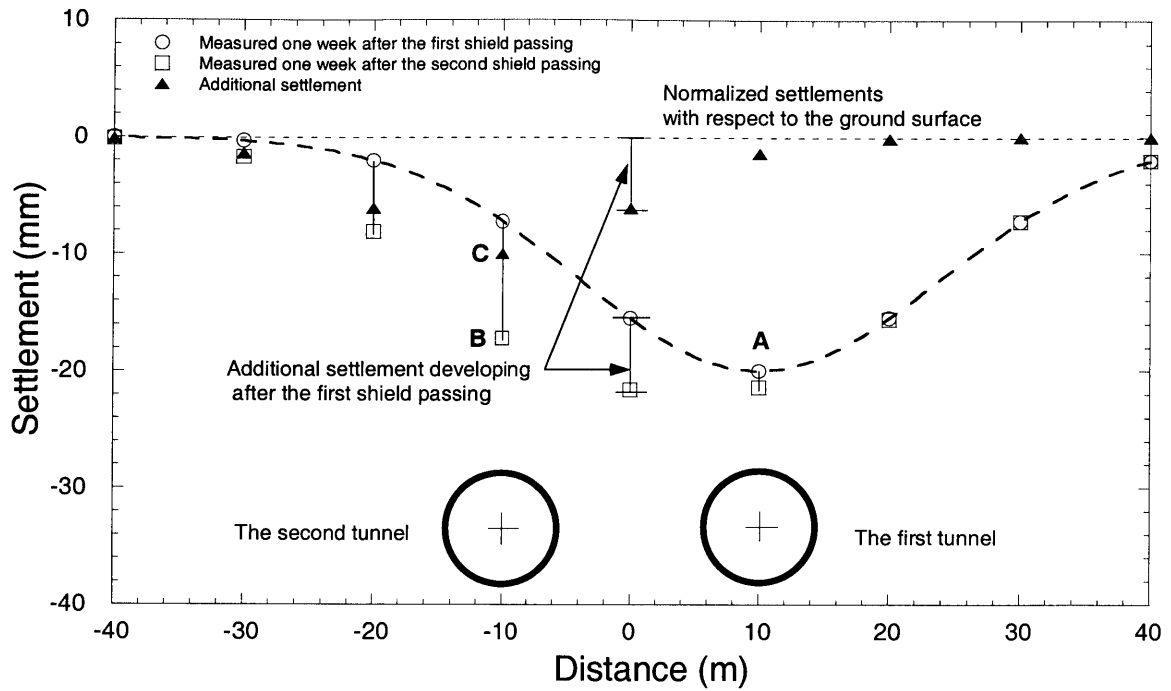


Figure 8.27 Additional settlement developing after the first shield passing

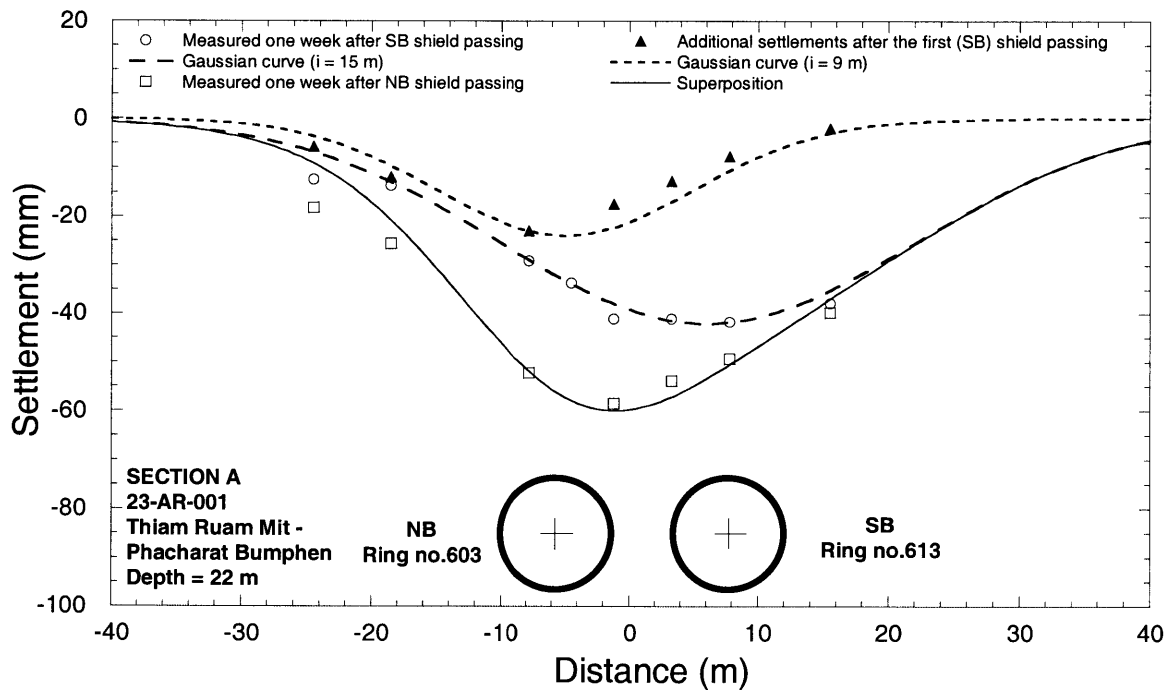


Figure 8.28 Surface settlements measured in 23-AR-001, settlement troughs described by Gaussian curves and superposition curve

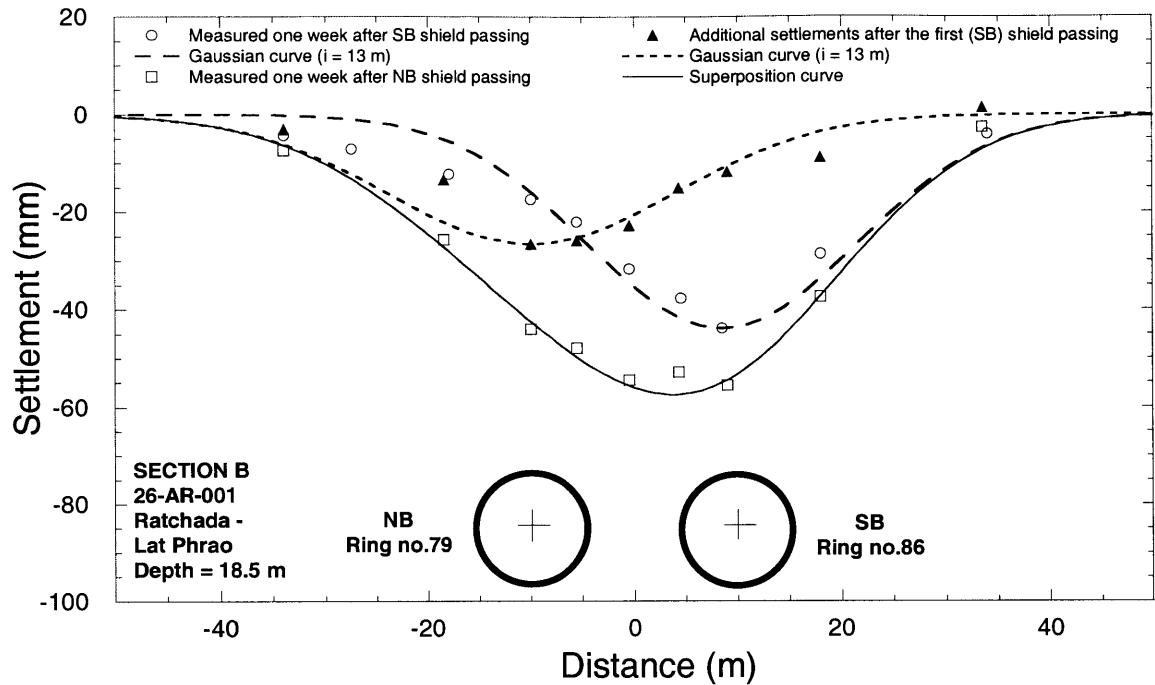


Figure 8.29 Surface settlements measured in 26-AR-001, settlement troughs described by Gaussian curves and superposition curve

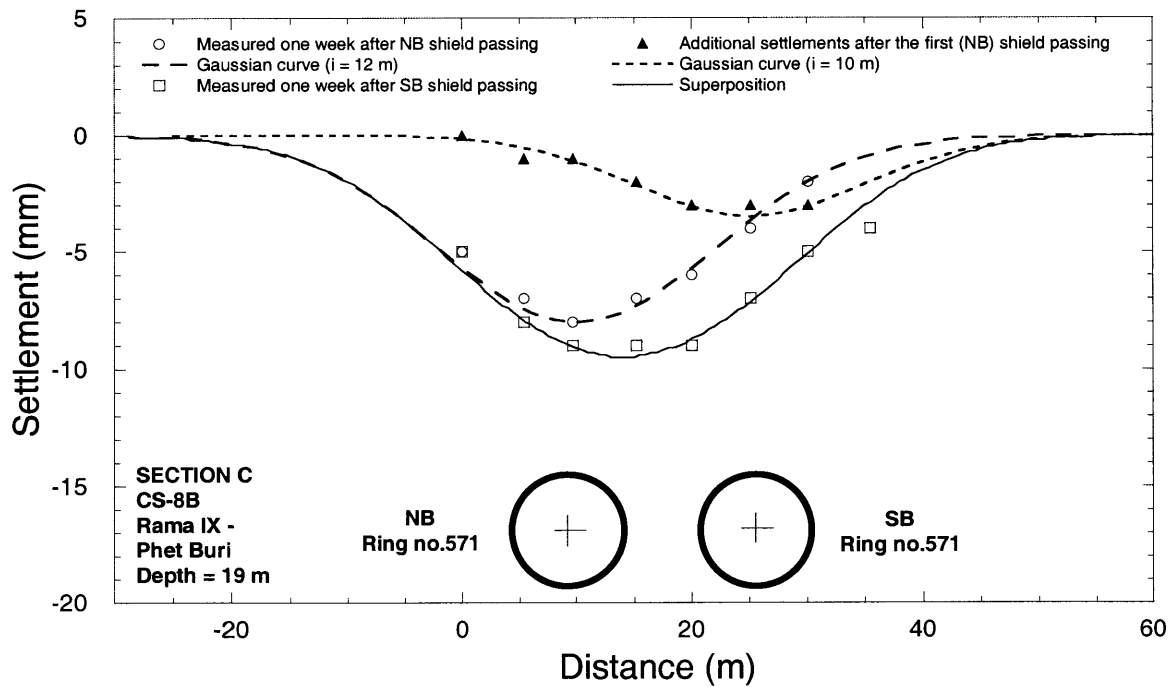


Figure 8.30 Surface settlements measured in CS-8B, settlement troughs described by Gaussian curves and superposition curve

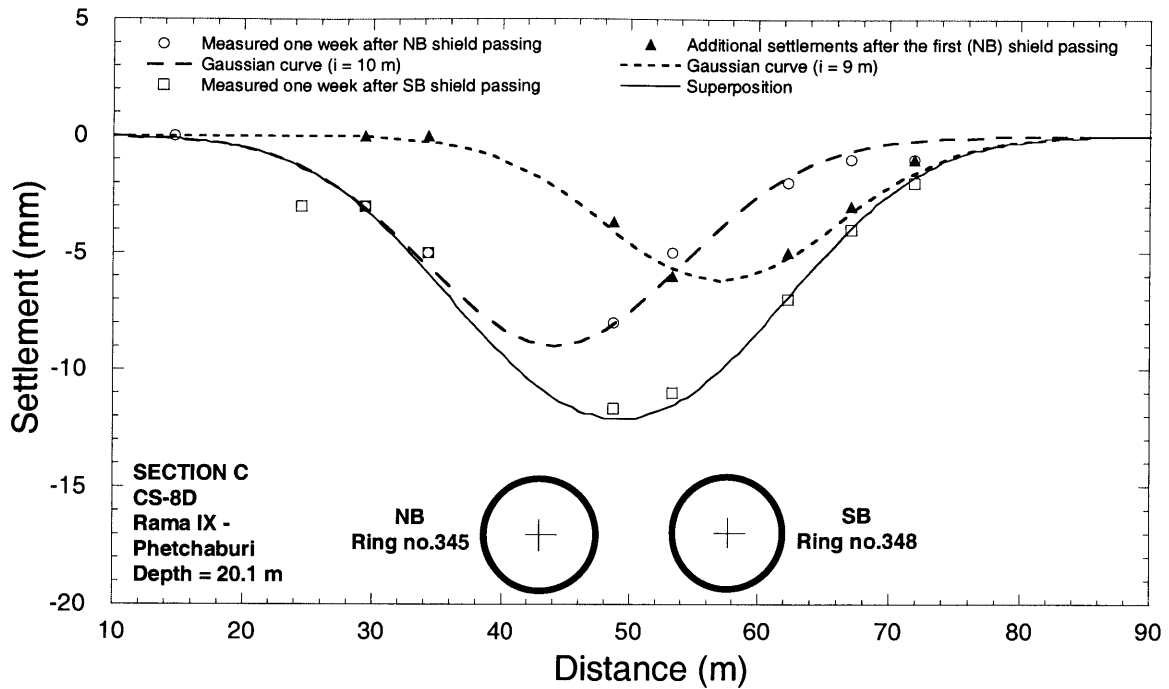


Figure 8.31 Surface settlements measured in CS-8D, settlement troughs described by Gaussian curves and superposition curve

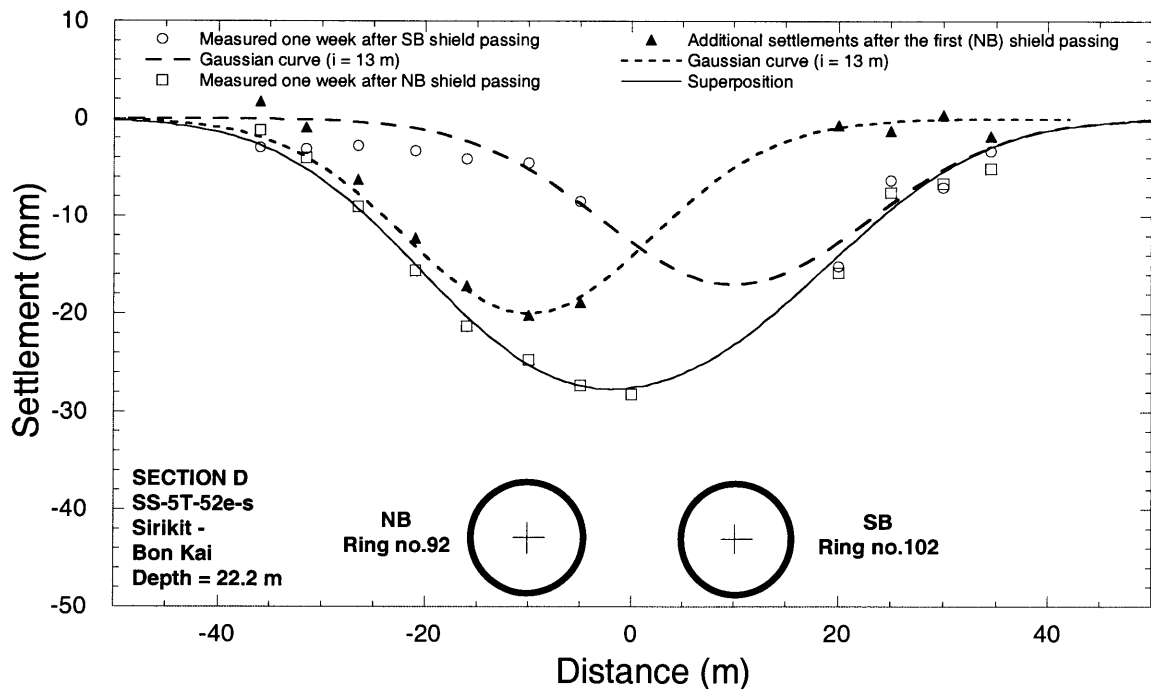


Figure 8.32 Surface settlements measured in SS-5T-52e-s, settlement troughs described by Gaussian curves and superposition curve

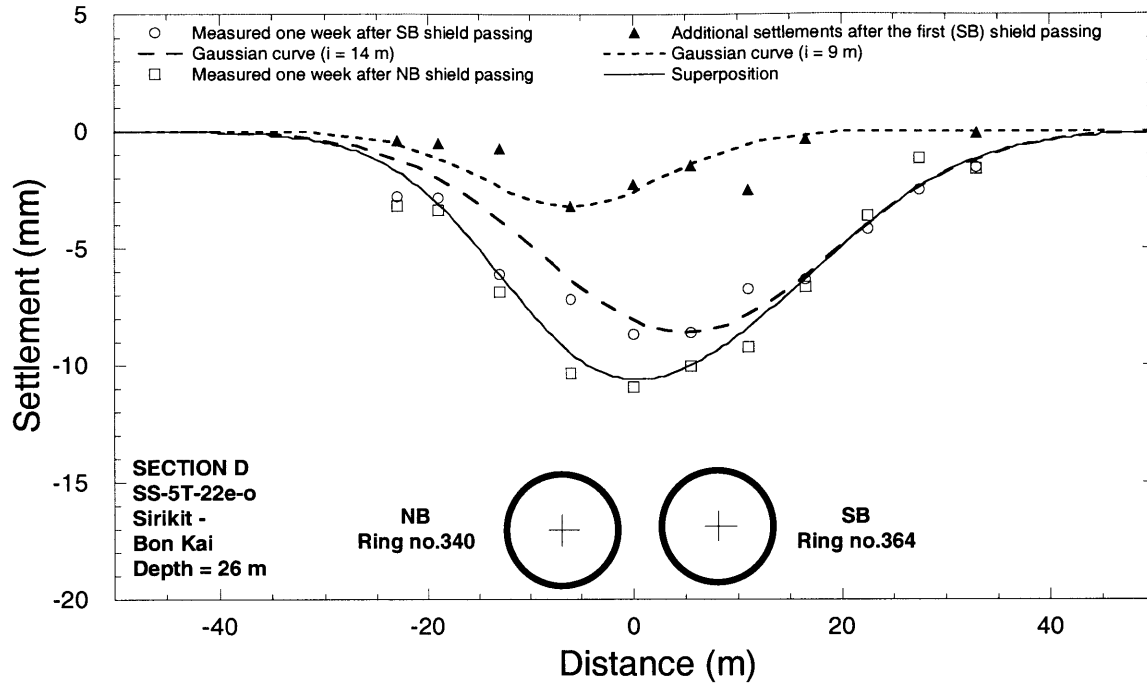


Figure 8.33 Surface settlements measured in SS-5T-22e-o, settlement troughs described by Gaussian curves and superposition curve

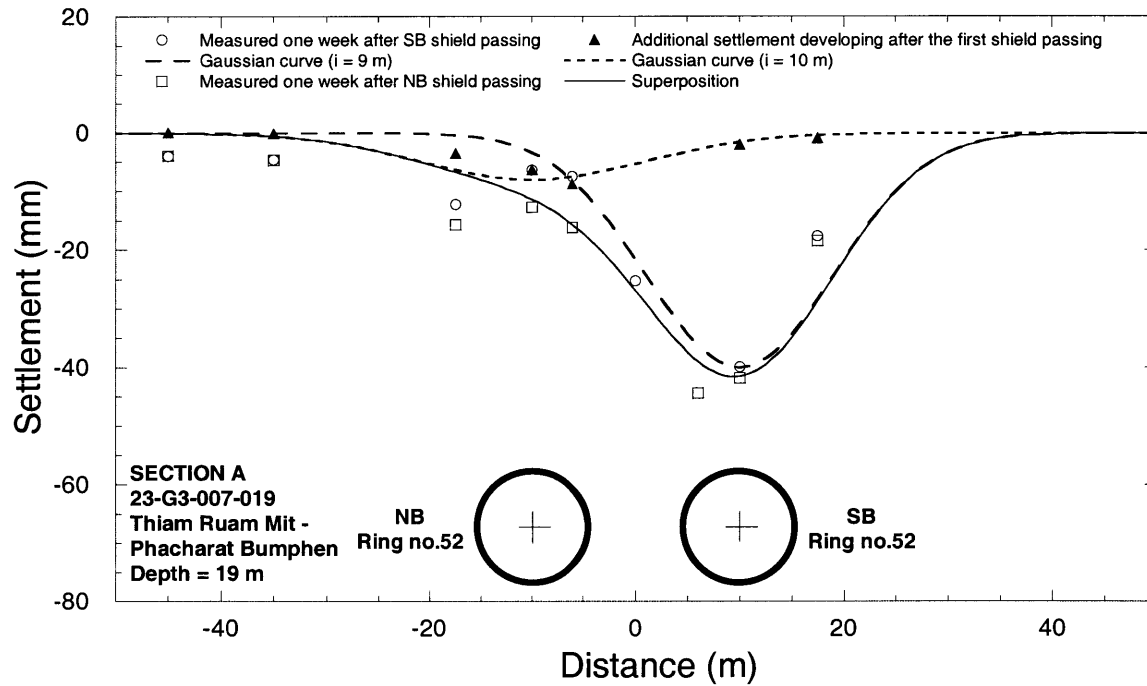


Figure 8.34 Surface settlements measured in 23-G3-007-019, settlement troughs described by Gaussian curves and superposition curve

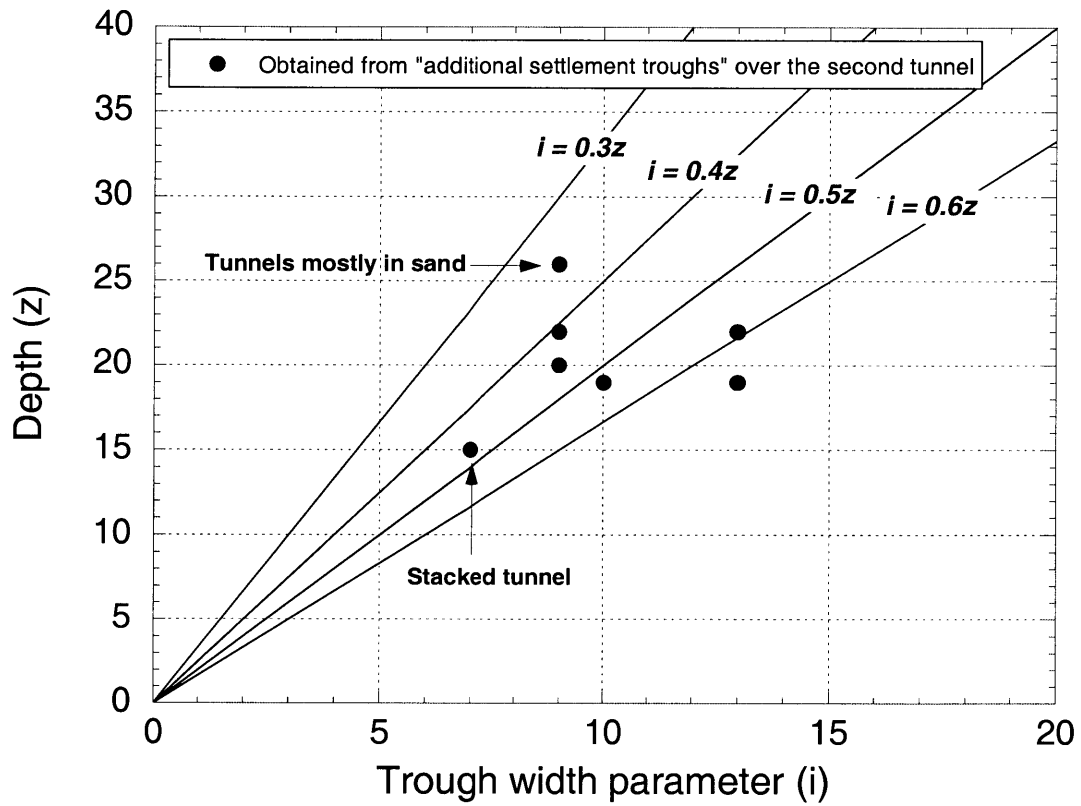


Figure 8.35 Settlement trough parameters obtained from additional (normalized) settlement curves over the second tunnel compared with the parameter recommended by O'Reilly and New (1982)

8.3.3 Interaction between Twin Tunnels

Several authors observed the interaction occurring between closely spaced tunnels. For instance, as reported by Terzaghi (1942) and Ward and Thomas (1965), a set of field instrumentation records on tunnels excavated in Chicago Clay and London Clay indicated that significant lining deformations occurred in the first tunnel as the second tunnel was being excavated. Physical tests were also conducted to investigate the response of the first tunnel's lining on the approaching of the second shield. Kim et al. (1996, and 1998) performed laboratory tests using a miniature shield to simulate the effect of tunneling on an existing tunnel. The results of their model tests showed that the interaction effects are greatest in the springline and crown of the existing tunnel. However, the interactions between tunnels are unlikely to be significant unless the spacing between the tunnel centerlines is less than about two tunnel diameters (Kim et al., 1996). Additionally, numerical analyses of this interaction problem were carried out by Leca (1989), Addenbrooke and Potts (1996), Yamaguchi et al. (1998). Their results were similar in that the influence of driving of a second tunnel on the previously installed lining of the first tunnel depends upon relative tunnel position and on the spacing between two tunnels.

It is clear that the problem of interaction between adjacent tunnels is complex, and the interaction depends on the geometry of the tunnels, the shield operation, lining properties, soil characteristics, and relative stiffness of soil and lining. Operational parameters such as face pressure and grouting pressure are among the most significant factors. Nevertheless, although many studies on the interaction between two tunnels excavated side by side were carried out, very few were based upon field instrumentation and operational parameter records.

In the MRTA project, some parts of the tunnels were designed to run close to each other due to the limitation of underground space in Bangkok. To investigate the lining response when an EPB shield was driven very close to another tunnel, convergence bolts were installed to measure changes in the tunnel shape as shown in Figure 8.36. Results of the monitoring are shown in Figure 8.37 through Figure 8.46. Note that the convergence

bolts were observed relative to the advance of the second shield and the data were all plotted in the polar graphs (i.e. in some cases, it is difficult to see the development so that it is recommended to look at the plots also in Figure 8.38 through Figure 8.46 of lining deflection versus distance from the second shield face). It was found that the first tunnel lining was deformed during the passing of the second shield. It is evident that the second tunnel can induce stresses acting on the first tunnel. The stresses can cause inward deflections in the tunnel lining particularly at the location between springline and invert as clearly shown in Figure 8.37 and Figure 8.45. However, the pattern of the lining deflection observed in the MRTA project is not a typical result. Theoretically, the most significant inward deflection was expected to occur at the springline. As the second shield approaches the measurement section, it should induce inward movement at the springline and outward movement at the crown and the invert of the existing tunnel.

If one takes a detailed look at the plots of lining deflection versus distance from the second shield face, it was found that the lining begins to deform about 4-6 m ahead of the shield. As the second shield face approached the ring equipped with the convergence bolts, the lining deflected. However, the deflection decreases or the lining moves toward its initial shape shortly after the shield face passes the section as is clearly shown in Figure 8.37b. Therefore, based on this observation, it was suggested that the first tunnel lining was affected by the approaching second shield.

As can be seen in Figure 8.37 through Figure 8.46, the deflection magnitude of the first tunnel appears to be proportional to the face pressure level of the 2nd shield applied during passing. For example, in Figure 8.38, during the northbound shield (i.e. the second shield) arrival at SB ring 449 where the first series of convergence bolts were installed (see also Figure 8.36), the shield was operated at high face pressure up to 200 kPa. As a result, the first tunnel lining deflects significantly (i.e. 11 mm at the 298 degree location: see also Figure 8.37). Thus, shield operators had to reduce face pressure to 150 kPa and maintain this pressure level until the end of the tunneling drive in order to ensure that no significant deflection takes place at the lining of the southbound or the first tunnel. Accordingly, as the northbound shield continued to excavate to the end of the tunneling

drive, other series of convergence bolts (i.e. Rings 471, 483, 491, and 499) installed in the first tunnel measured much smaller deflection compared to that installed in ring 449 as can be seen in Figure 8.39 through Figure 8.46.

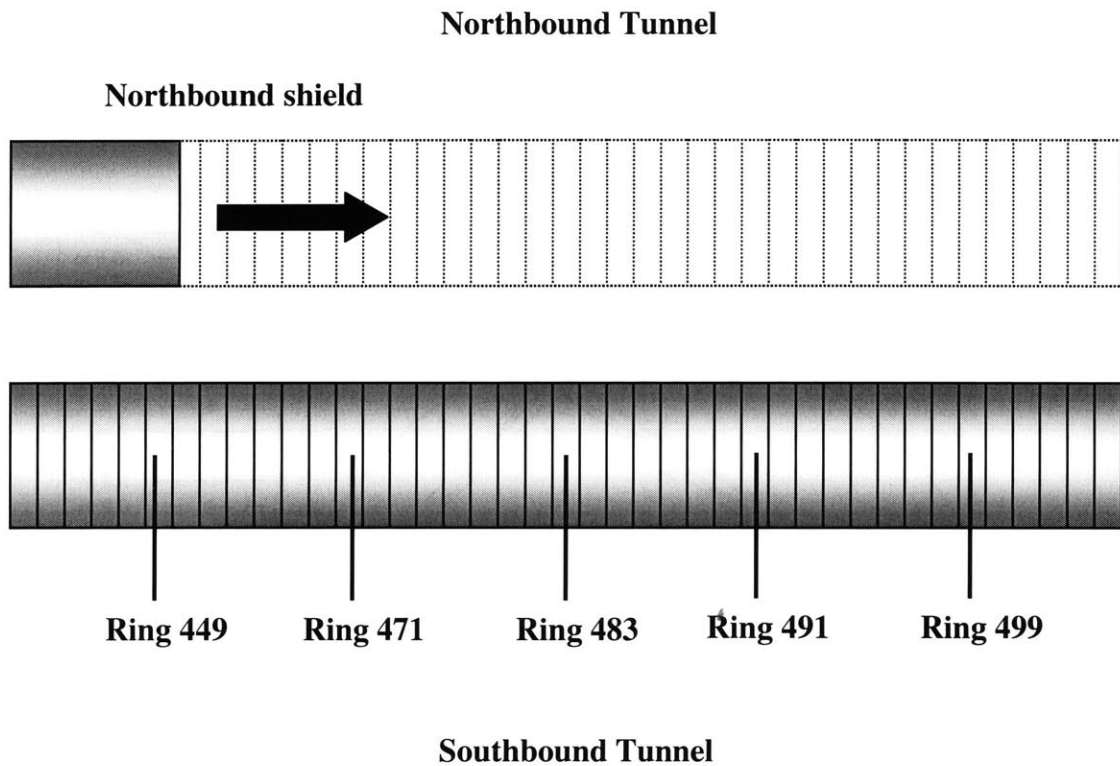
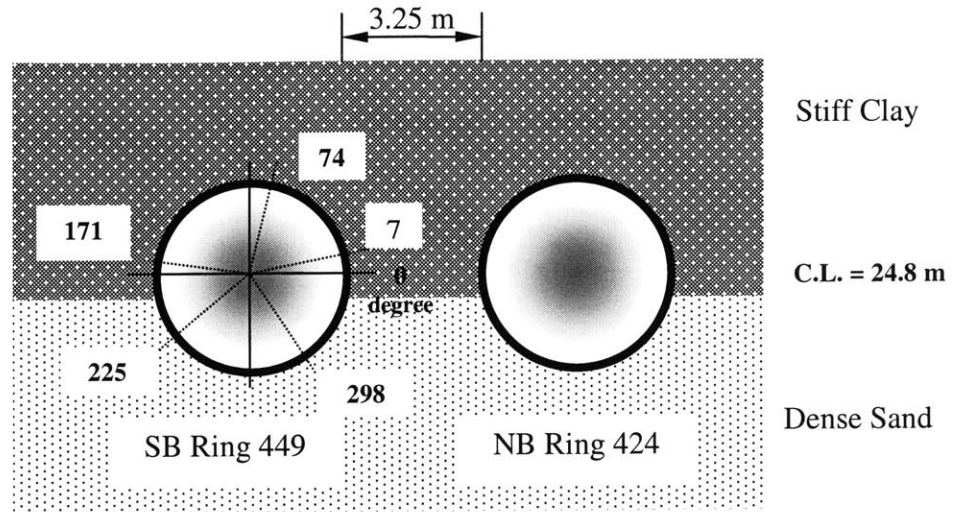
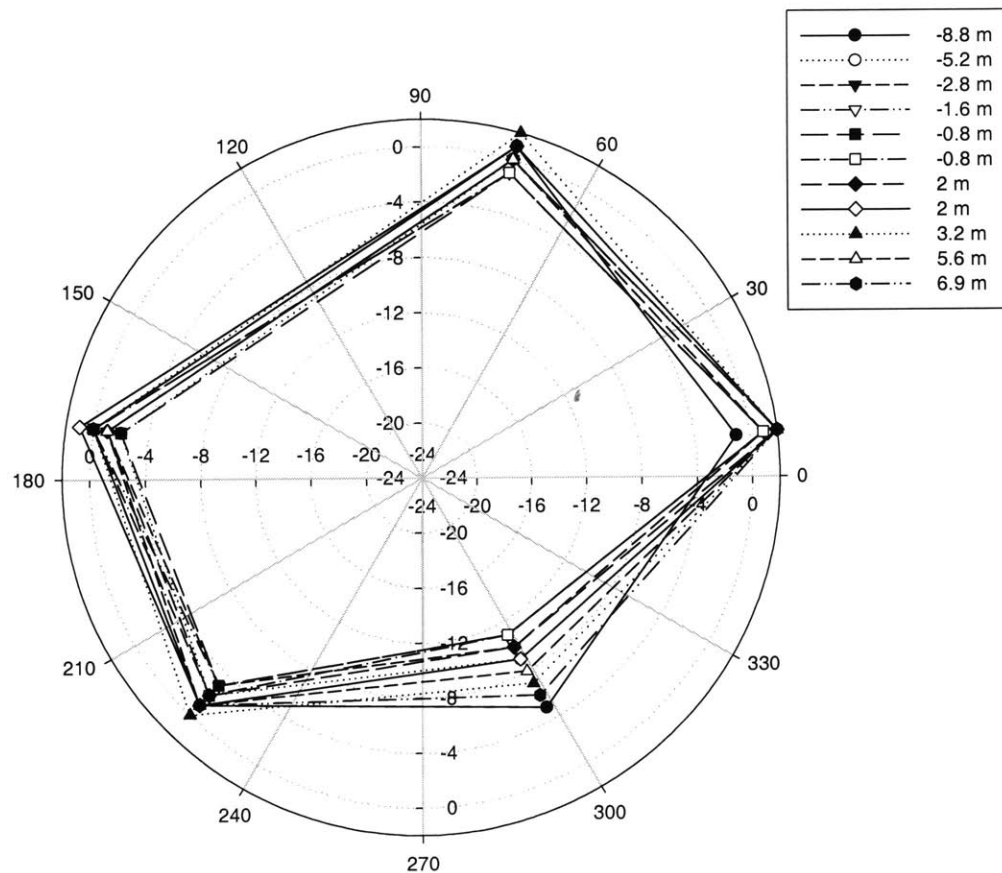


Figure 8.36 Schematic diagram of the twin tunnels and installed locations of convergence bolts in Tunneling Section D (Sirikit – Bon Kai)

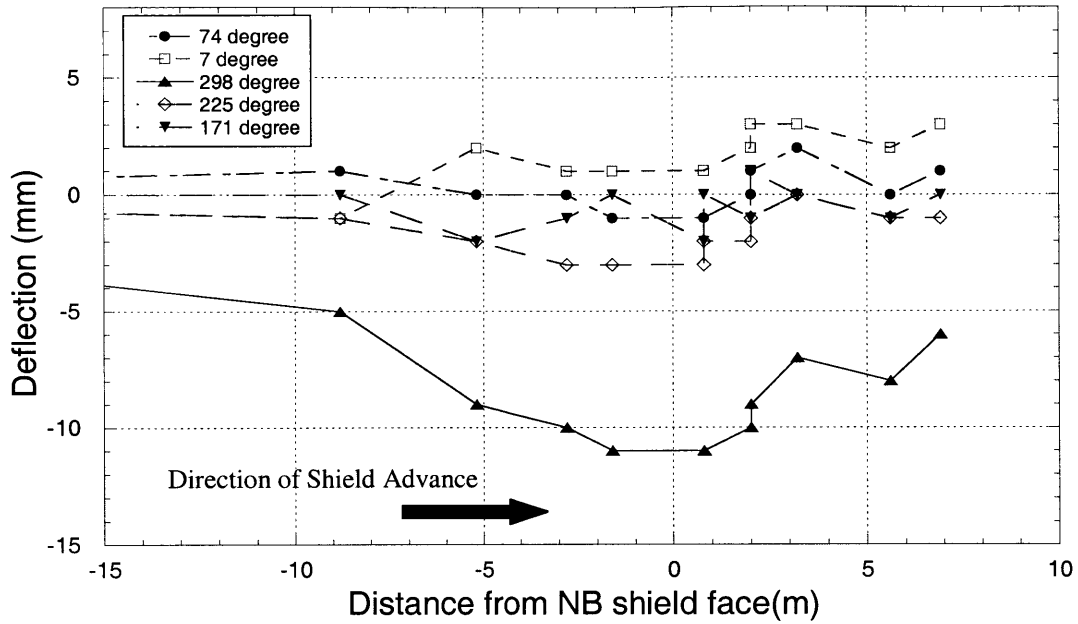


(a) Tunnel section

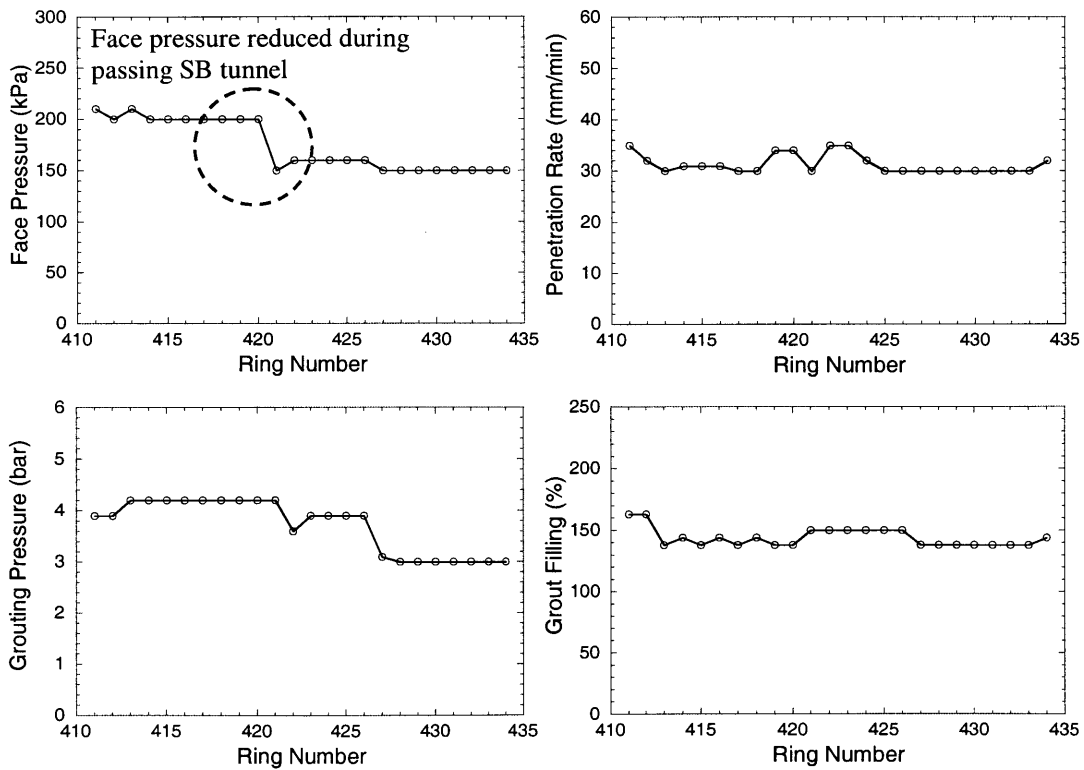


(b) Polar graph showing the lining deflection

Figure 8.37 Measurement points (convergence bolts) on SB tunnel lining Ring 449 and the lining response affected by the passing of the northbound shield

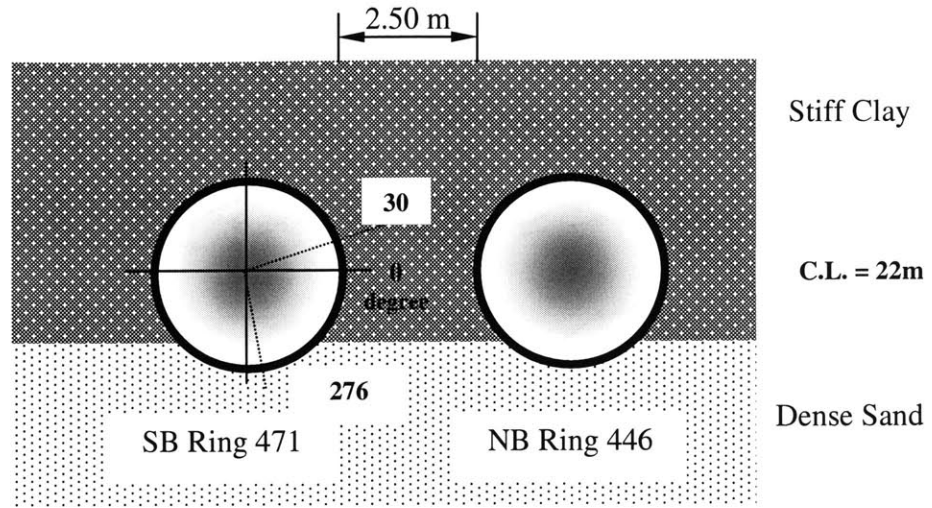


(a) Lining deflection in SB tunnel versus distance from the second (NB) shield face

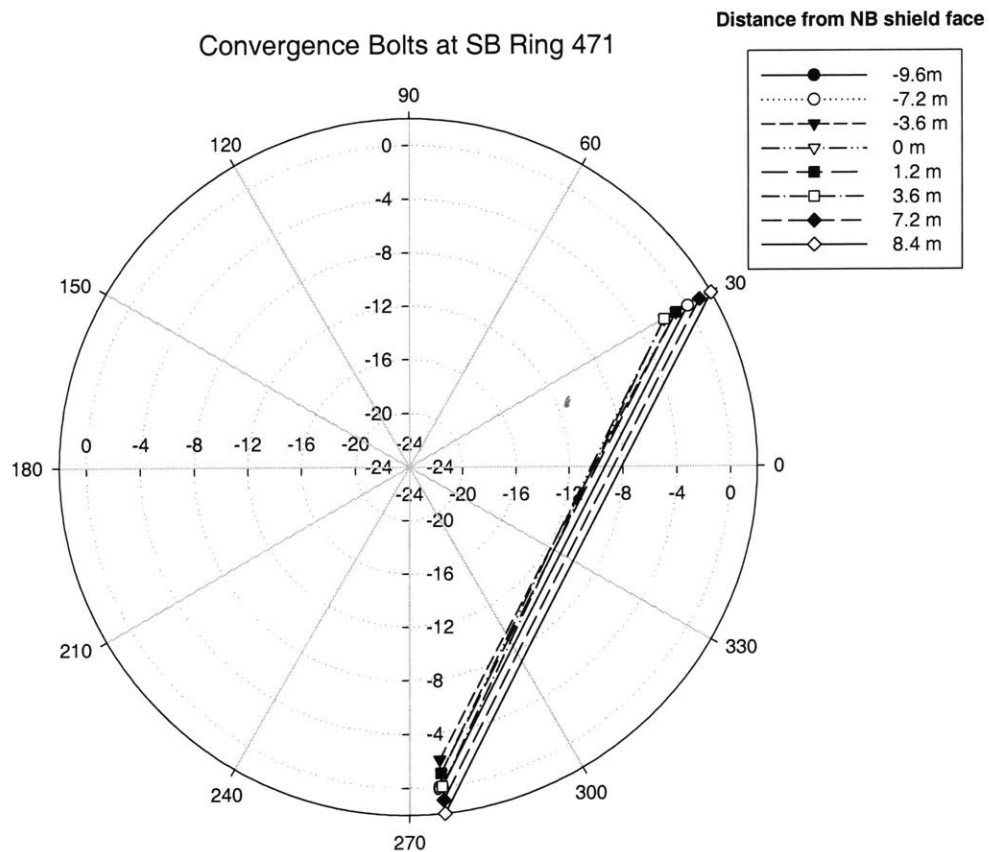


(b) Operational parameters recorded in the second (NB) shield

Figure 8.38 Deflection of SB tunnel Ring 449 during the passing of NB shield and operational parameters recorded in NB shield corresponding to the NB Ring 424

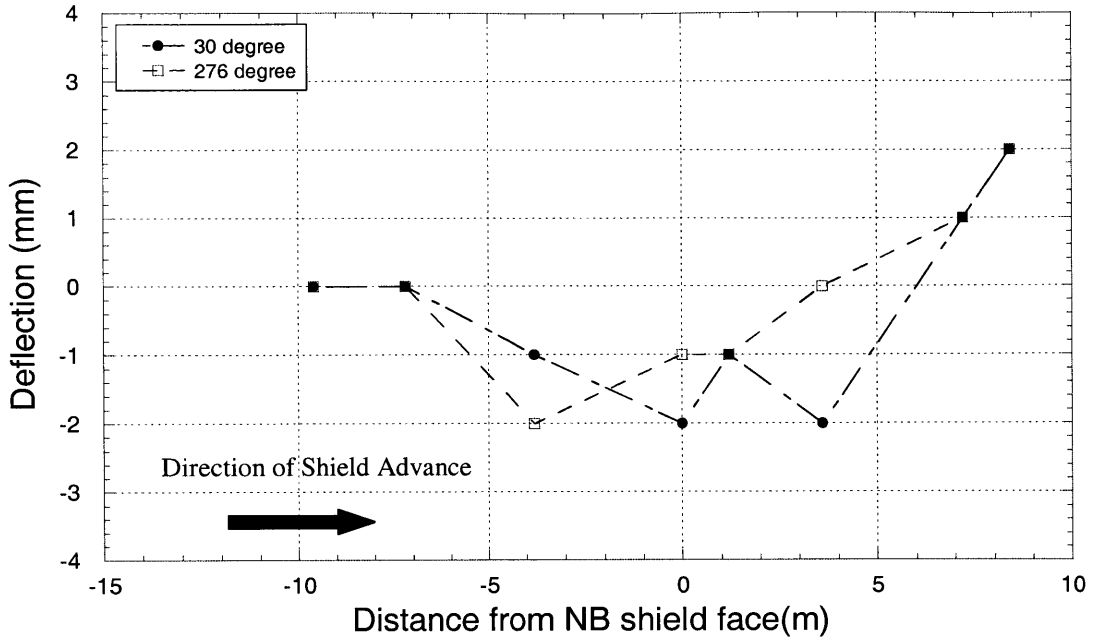


(a) Tunnel section

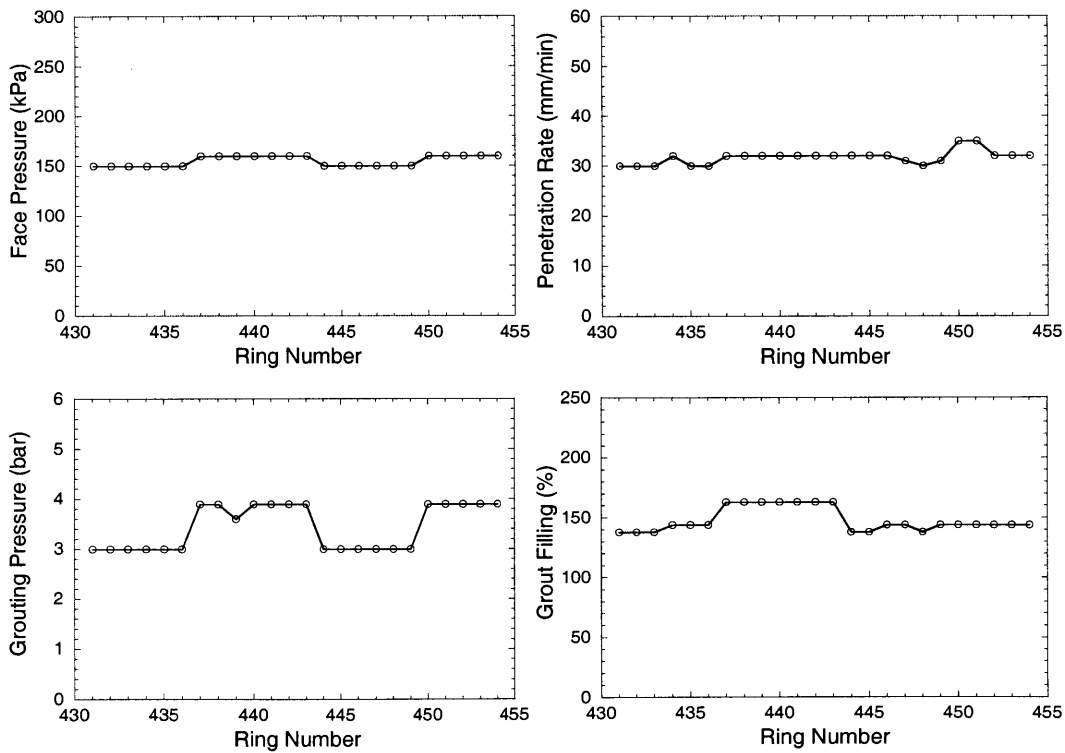


(b) Polar graph showing the lining deflection

Figure 8.39 Measurement points (convergence bolts) on SB tunnel lining Ring 471 and the lining response affected by the passing of the northbound shield

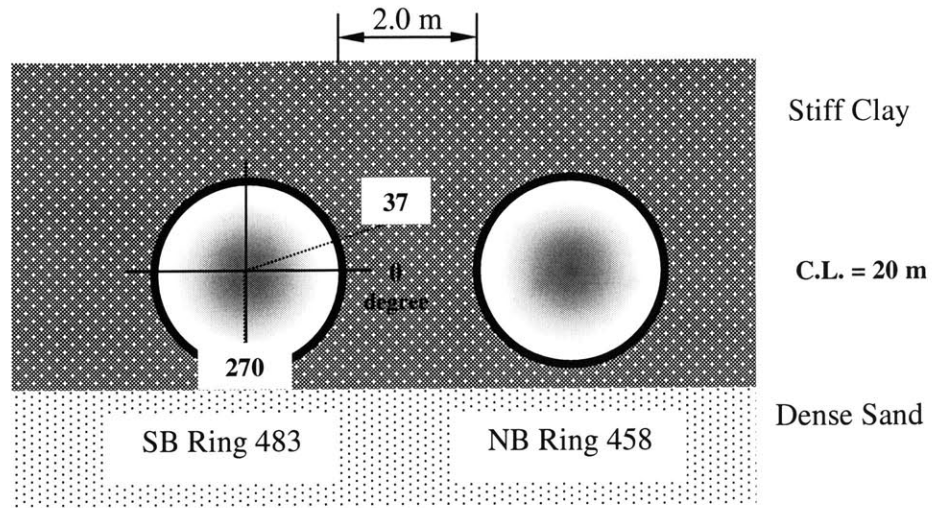


(a) Lining deflection in SB tunnel versus distance from the second (NB) shield face

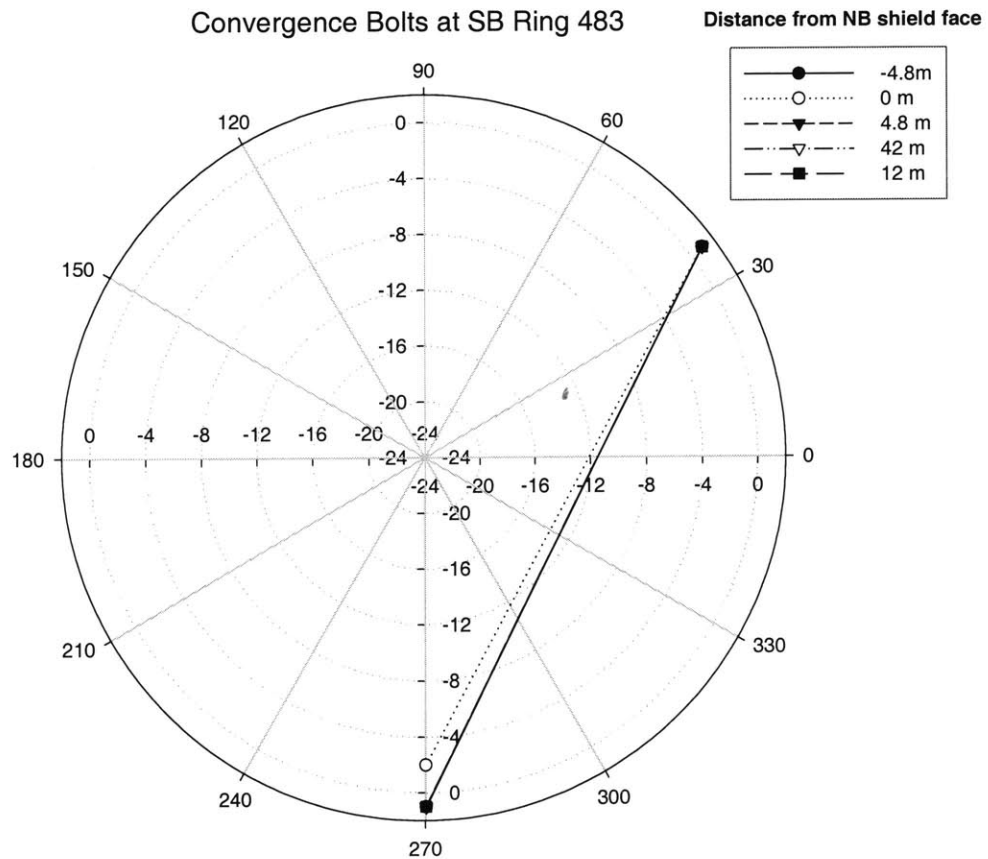


(b) Operational parameters recorded in the second (NB) shield

Figure 8.40 Deflection of SB tunnel Ring 471 during the passing of NB shield and operational parameters recorded in NB shield corresponding to the NB Ring 446

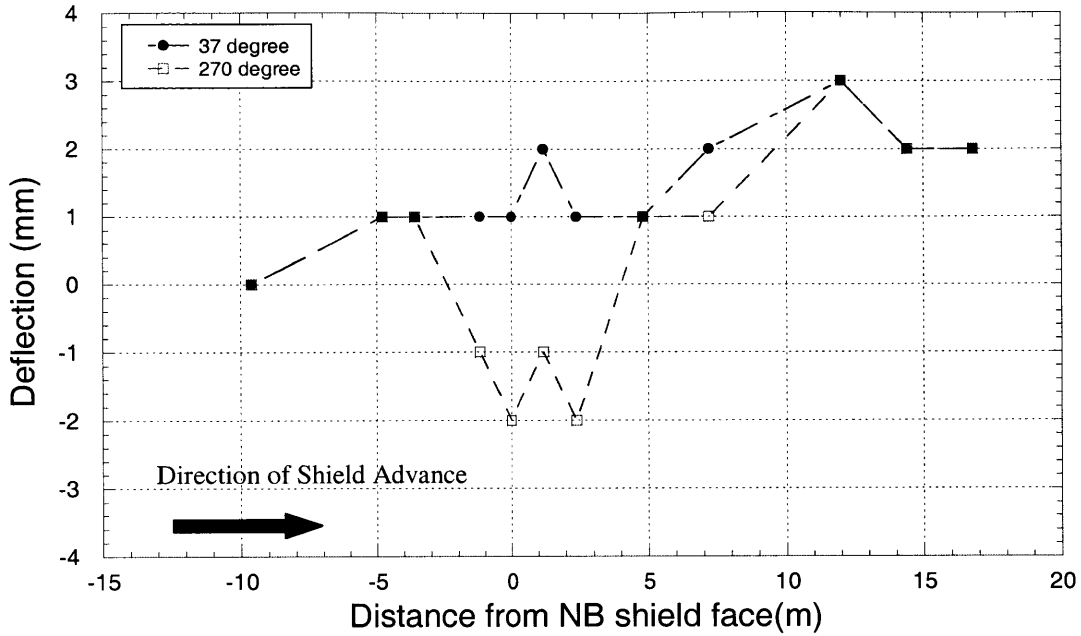


(a) Tunnel section

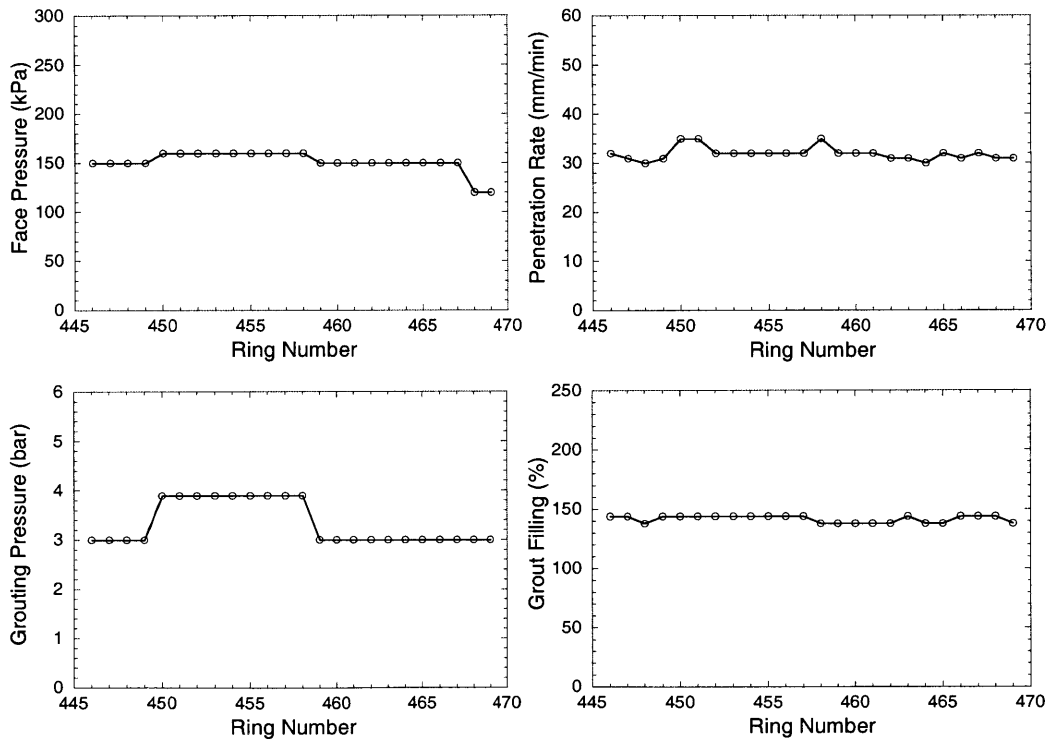


(b) Polar graph showing the lining deflection

Figure 8.41 Measurement points (convergence bolts) on SB tunnel lining Ring 483 and the lining response affected by the passing of the northbound shield

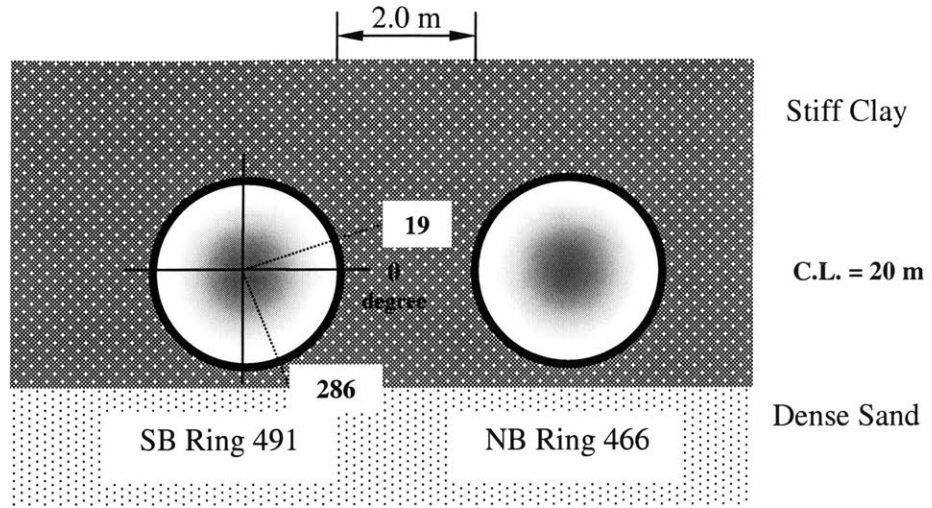


(a) Lining deflection versus distance from the second shield face

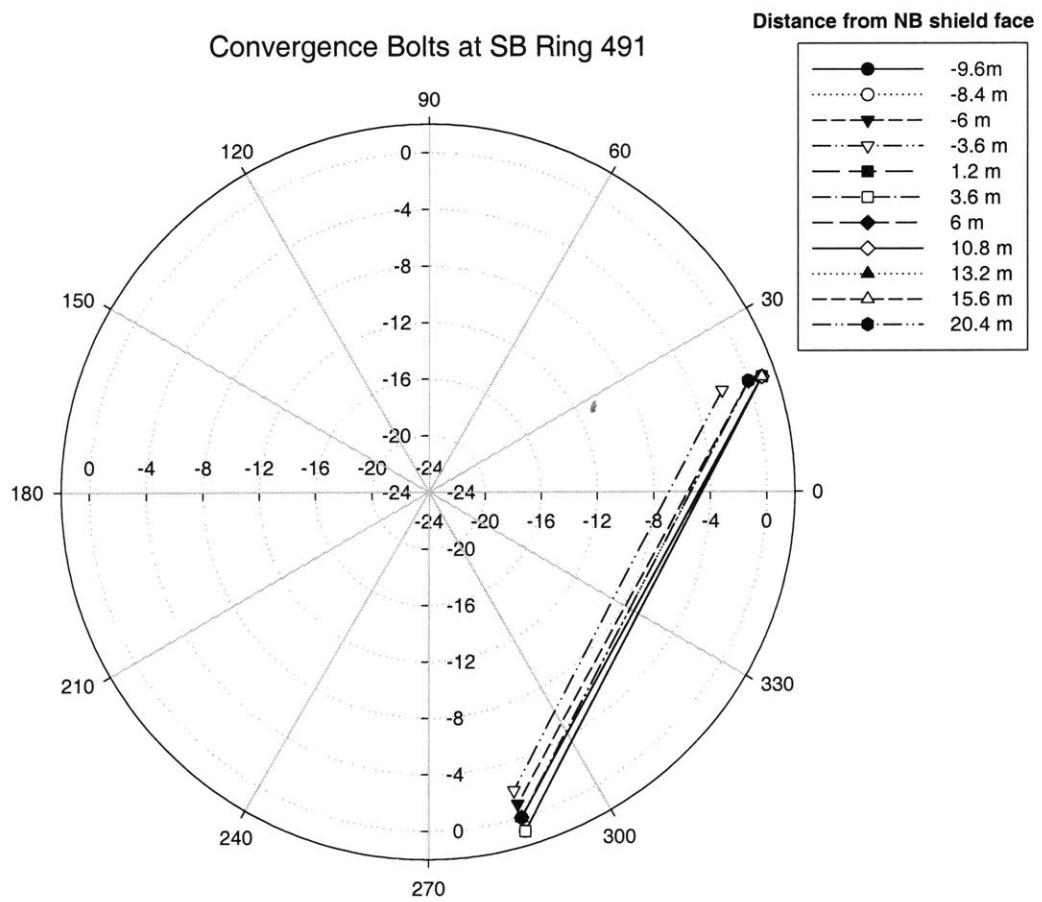


(b) Operational parameters recorded in the second (NB) shield

Figure 8.42 Deflection of SB tunnel Ring 483 during the passing of NB shield and operational parameters recorded in NB shield corresponding to the NB Ring 458

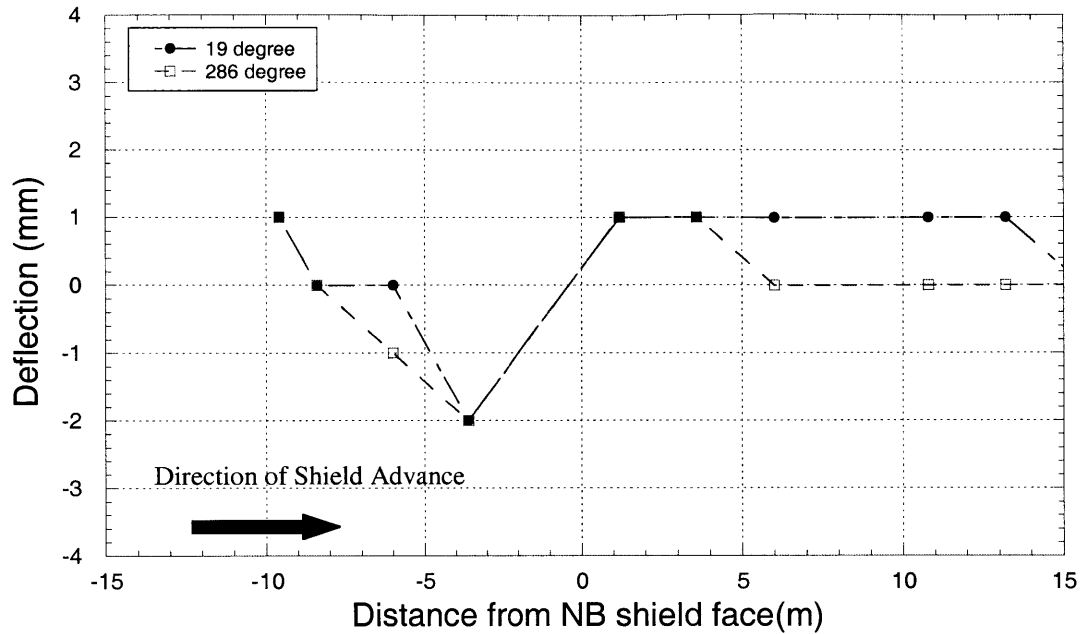


(a) Tunnel Section

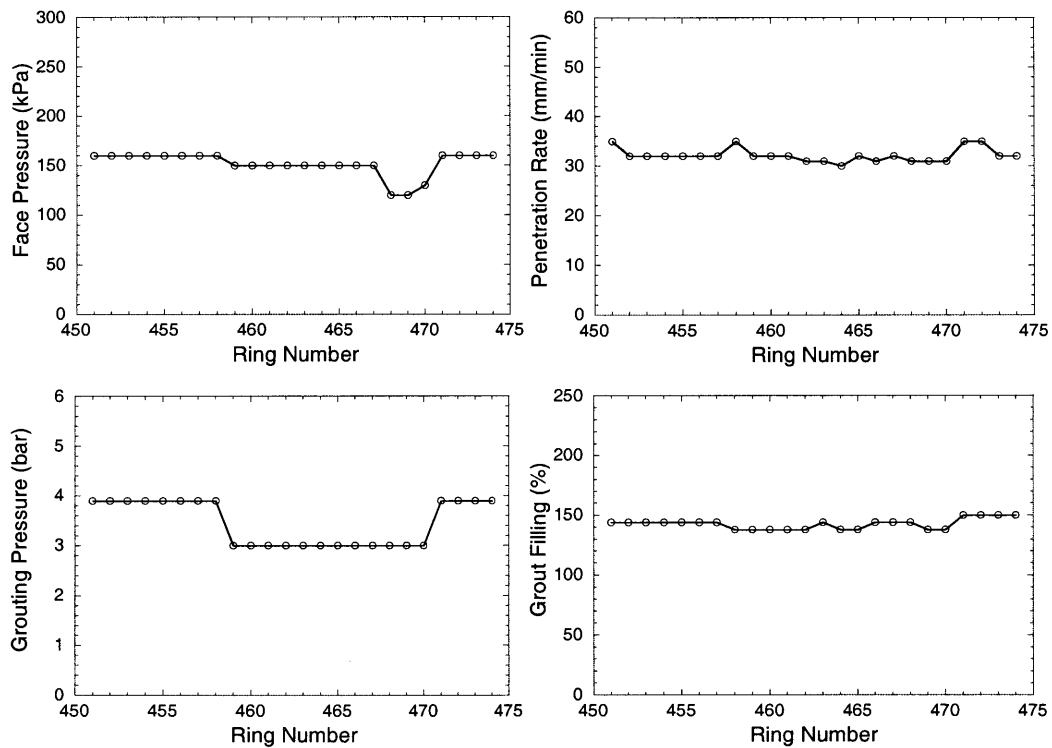


(b) Polar graph showing the lining deflection

Figure 8.43 Measurement points (convergence bolts) on SB tunnel lining Ring 491 and the lining response affected by the passing of the northbound shield

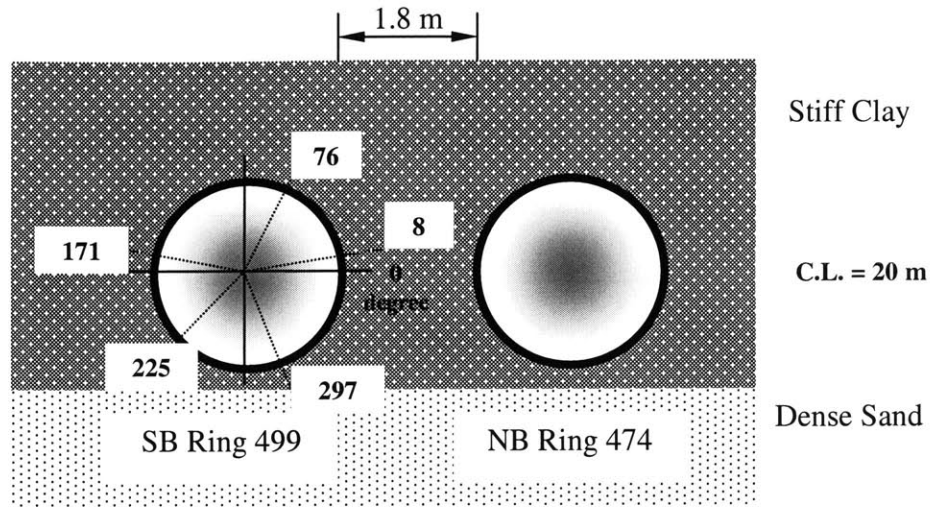


(a) Lining deflection in SB tunnel versus distance from the second (NB) shield face

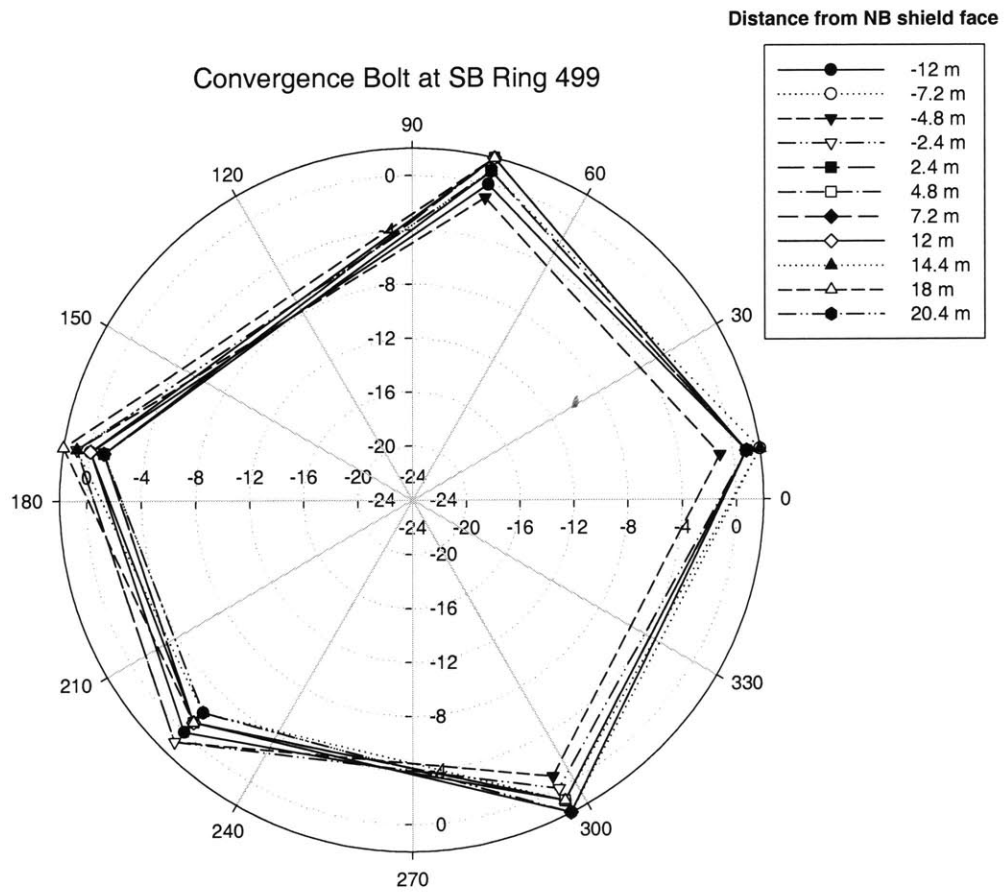


(b) Operational parameters recorded in the second (NB) shield

Figure 8.44 Deflection of SB tunnel Ring 491 during the passing of NB shield and operational parameters recorded in NB shield corresponding to the NB Ring 466

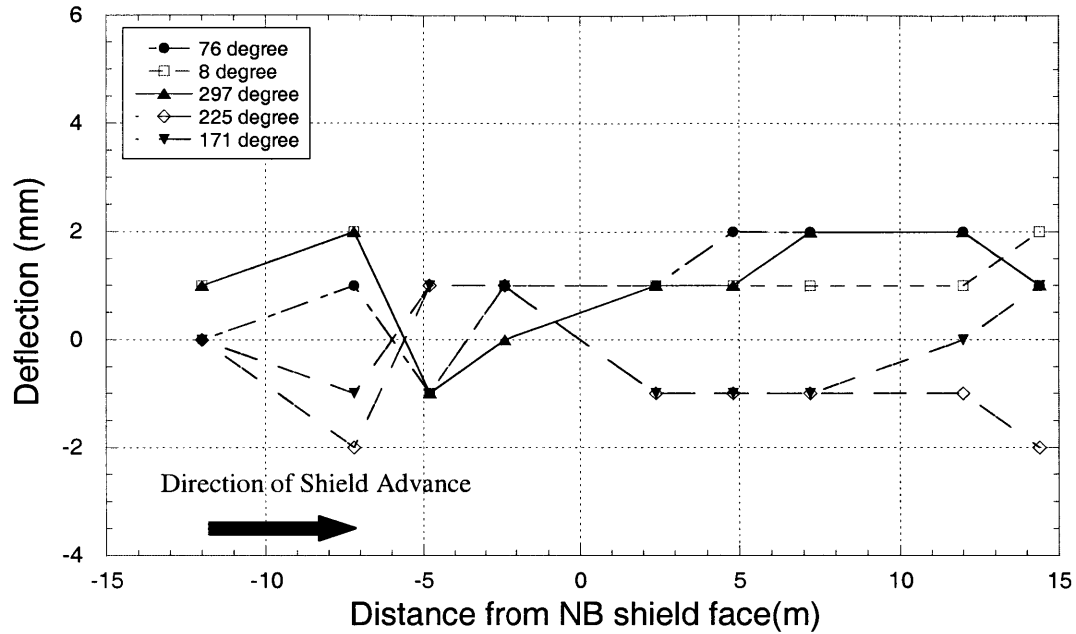


(a) Tunnel section

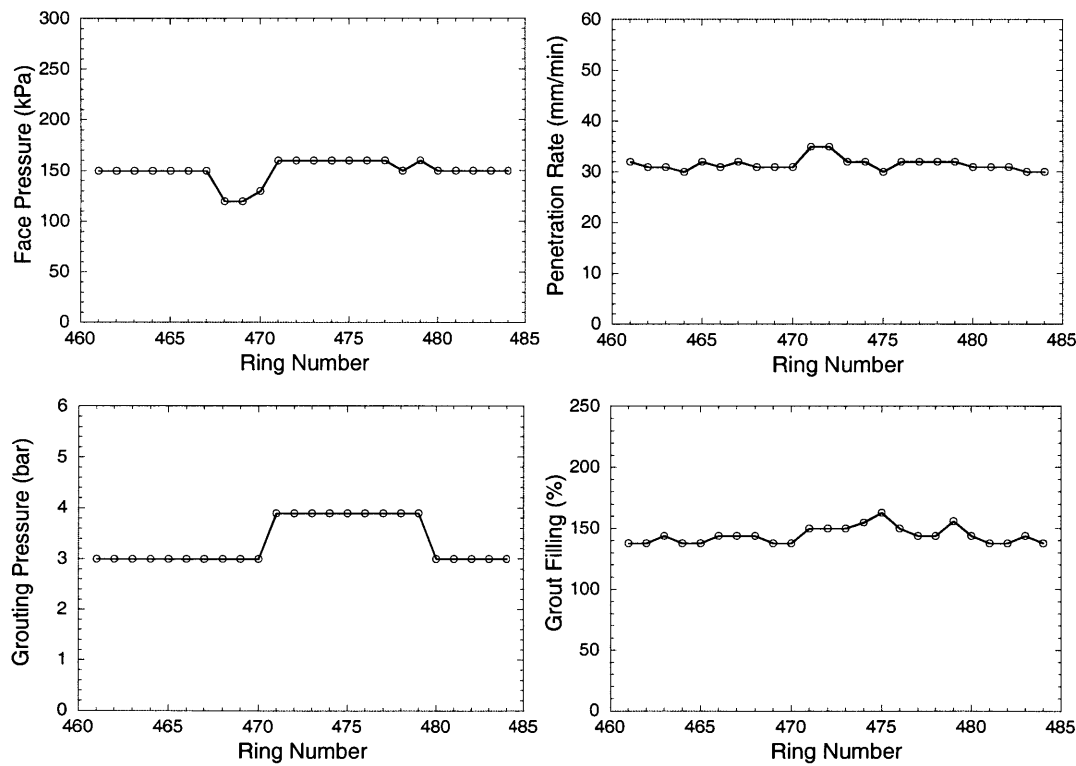


(b) Polar graph showing the lining deflection

Figure 8.45 Measurement points of (convergence bolts) on SB tunnel lining Ring 499 and the lining response affected by the passing of the northbound shield



(a) Lining deflection in SB tunnel versus distance from the second (NB) shield face



(b) Operational parameters recorded in the second (NB) shield

Figure 8.46 Deflection of SB tunnel Ring 499 during the passing of NB shield and operational parameters recorded in NB shield corresponding to the NB Ring 474

8.4 Settlements above Stacked Tunnels

In most of tunneling drives in Section D, the northbound tunnel was stacked over the southbound tunnel in order to avoid pile foundations of existing fly-over bridges along Rama IV road. The SB shield excavated the lower southbound tunnel first and the following NB shield then excavated the upper northbound tunnel. Details of the tunneling in Section were provided in Chapter 5. The northbound tunnel was located in the Stiff Clay layer, but in some sections where the tunnel was very shallow, the tunnel crown was located within the Soft Clay layer. The southbound tunnel was mostly located within the Sand layer.

Arrays of surface settlement markers were installed over the tunnel alignments to measure surface settlement troughs caused by the first- and the second shields. Figure 8.47 shows surface settlement troughs measured in CS-4C and the instrumentation layout. Based on the observation, the ground surface began to deform as the first (SB) shield approached the measurement section. The deformation continued to develop until about 3 days after the shield passed. As can be seen in the figure, one week after the SB shield passed, the surface settlement trough indicates very narrow trough width where large settlements are concentrated at the centerline of the tunnel. As the second (NB) shield approached the section, the surface settlement developed further until the shield passed the section for approximately 3 days. The trough caused by second shield passing shows that “additional settlement” develops over the tunnel centerline and mostly just as the shield passes, whereas only very small changes occur in the tail portion of the settlement trough. Additionally, settlement troughs appear to be symmetric with respect to the centerline of the stacked tunnels as expected.

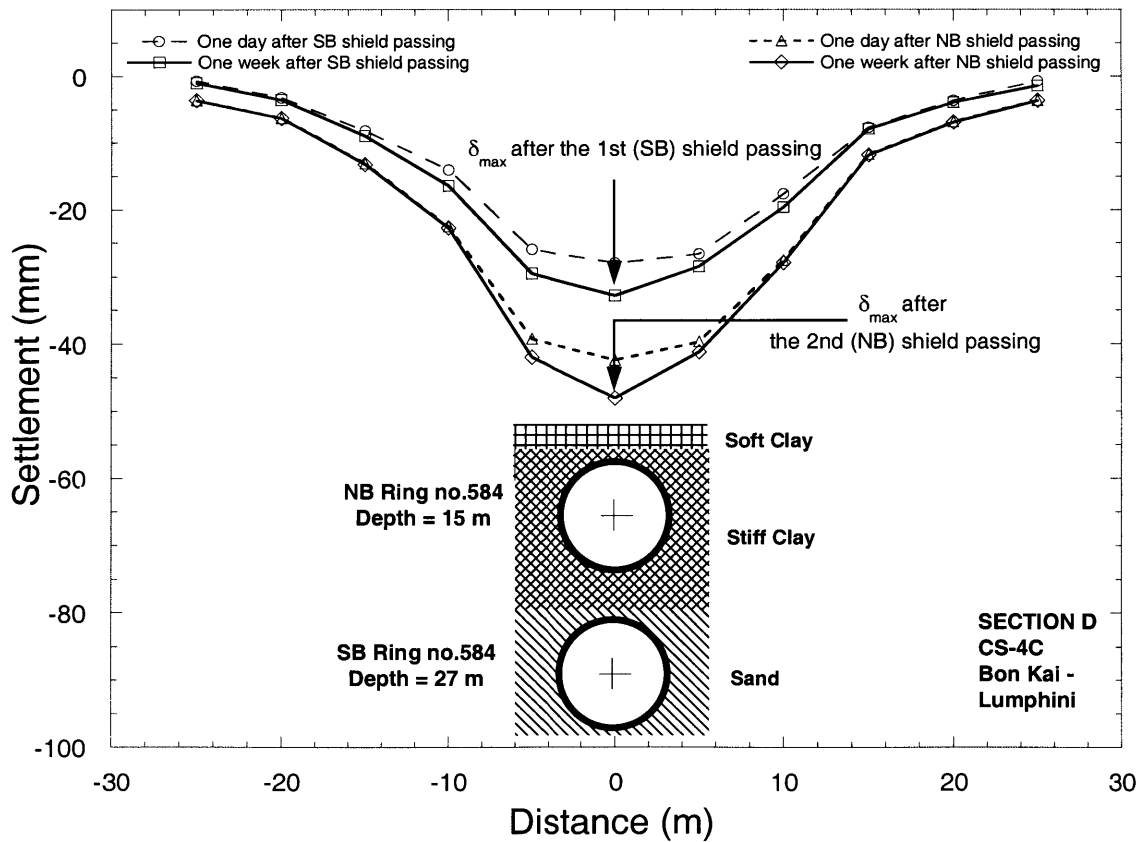
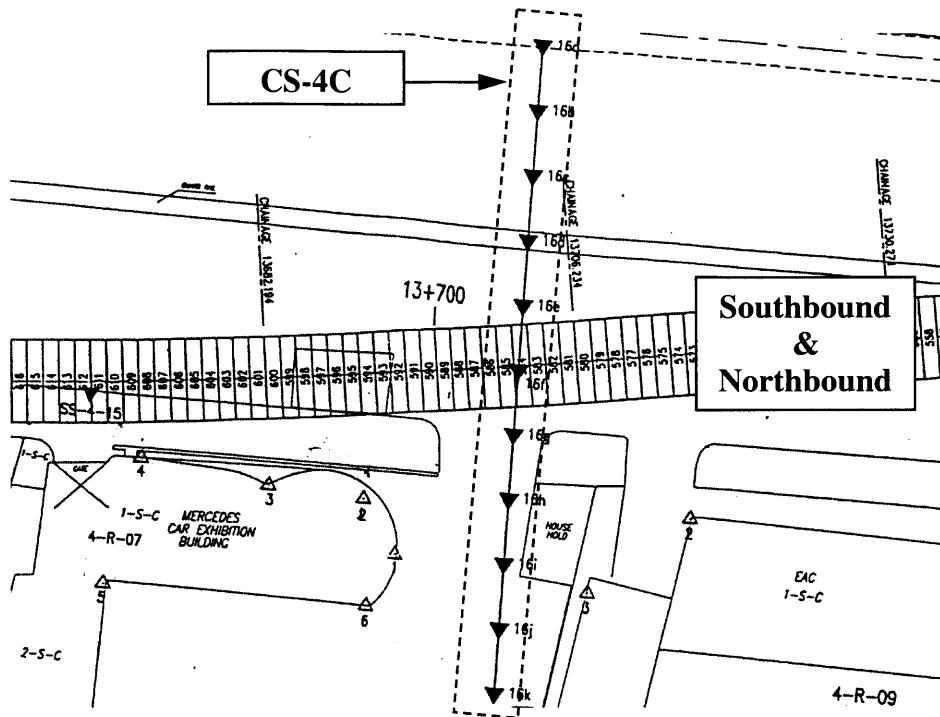


Figure 8.47 Surface settlement troughs measured in CS-4C and the instrumentation layout

Stacking tunnels vertically above each other are exceptional and so far no method has been proposed to describe the settlement troughs caused by the stacked tunnels. Since (as expected) a symmetric shape is observed, an attempt is made to use the Gaussian curve to describe the settlement trough. Clearly the settlement above the first tunnel should correspond to what has been stated in the literature and reported earlier. Indeed, it was found that the Gaussian curve does fit the settlement trough of the first tunnel very well as shown in Figure 8.48. However, the settlement curve appears to be much narrower compared to the troughs where the tunnel was excavated in the Stiff Clay layer. This phenomenon was also observed in other instrumentation sections where the tunnel was excavated within the Sand layer as discussed earlier in Section 7.2.2. The trough width parameter (i) obtained from the settlement curve is 9 m. Therefore, this is in agreement with O'Reilly and New (1982) that $i = 0.3z$, where z is the tunnel depth (27 m), when the tunnel is located within the Sand layer.

The Gaussian curve is also applied to the settlement trough caused by a combination of effects of the stacked tunnels. As can be seen in Figure 8.48, the Gaussian curve fits the settlement trough very well and the trough width parameter ($i = 9$ m) is equal to that of the settlement curve caused by the first tunnel. However, to investigate the ground response induced by the second (upper) tunnel, one needs to determine “additional surface settlements” developing after the first (SB) shield passing by using the normalization technique previously introduced in Section 8.3.2. As shown in Figure 8.48, the additional settlement trough induced by the second (NB) shield is much smaller than the settlement trough caused by the first (SB) shield. This was unexpected as the upper (NB) tunnel is much shallower than the lower (SB) and one would expect the surface settlements induced by the upper tunnel to be larger than those of the lower tunnel. This assumption may be true in cases of open-faced tunneling as the ground response is mainly affected by tunnel geometry and geological conditions. On the other hand, if the tunnel is excavated using the EPB tunneling method, one should consider operational parameters as well.

Operational parameters recorded in the first- and the second shields as the shields passed the instrumentation section (i.e. Ring 584) are plotted in Figure 8.49. As clearly shown in the plot, low face pressures were measured as the first (SB) shield passed the instrumentation section. As a result, large surface settlements were found after shield passing (see Figure 8.48). In contrast, high face pressures (up to 220 kPa) were applied in the second (NB) shield. Note that this level of face pressure is very high relative to the tunnel depth (i.e. only 15 m) which explains that small additional surface settlements were observed as shown in Figure 8.48.

Using the Gaussian function to describe the “additional surface settlement” trough also indicates a good fit (see Figure 8.48). The trough width parameter (i) is 7 m and it is plotted in Figure 8.35. It was found that the trough width parameter falls within the bound of $i = 4z$ and $i = 5z$ which is similar to most cases of tunneling in clay layers (see also Section 7.22). Since the settlement curves of the second shield and the settlement curves for the combined effect of both tunnels appear to depend on geological and operational conditions, one has to be careful when applying this approach.

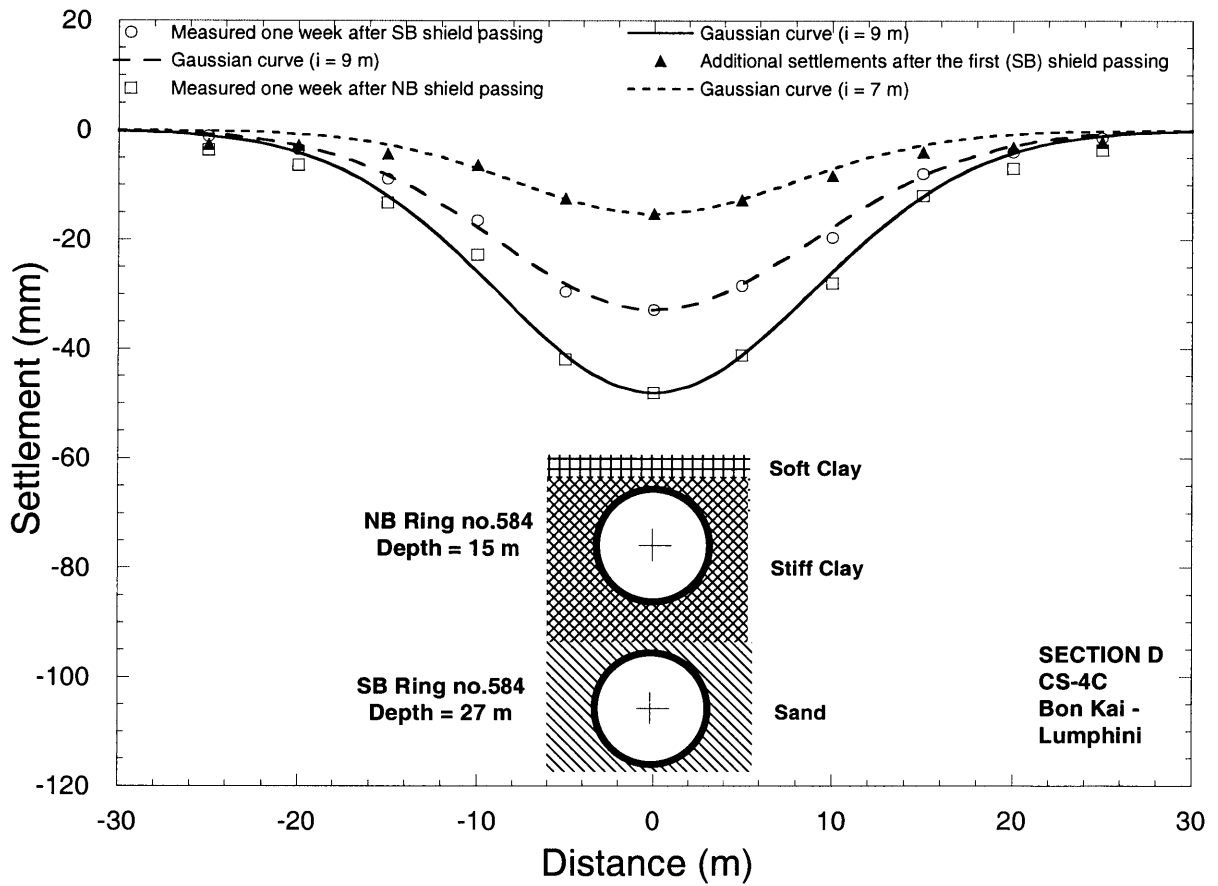


Figure 8.48 Surface settlements measured in CS-4C, settlement troughs described by Gaussian curves

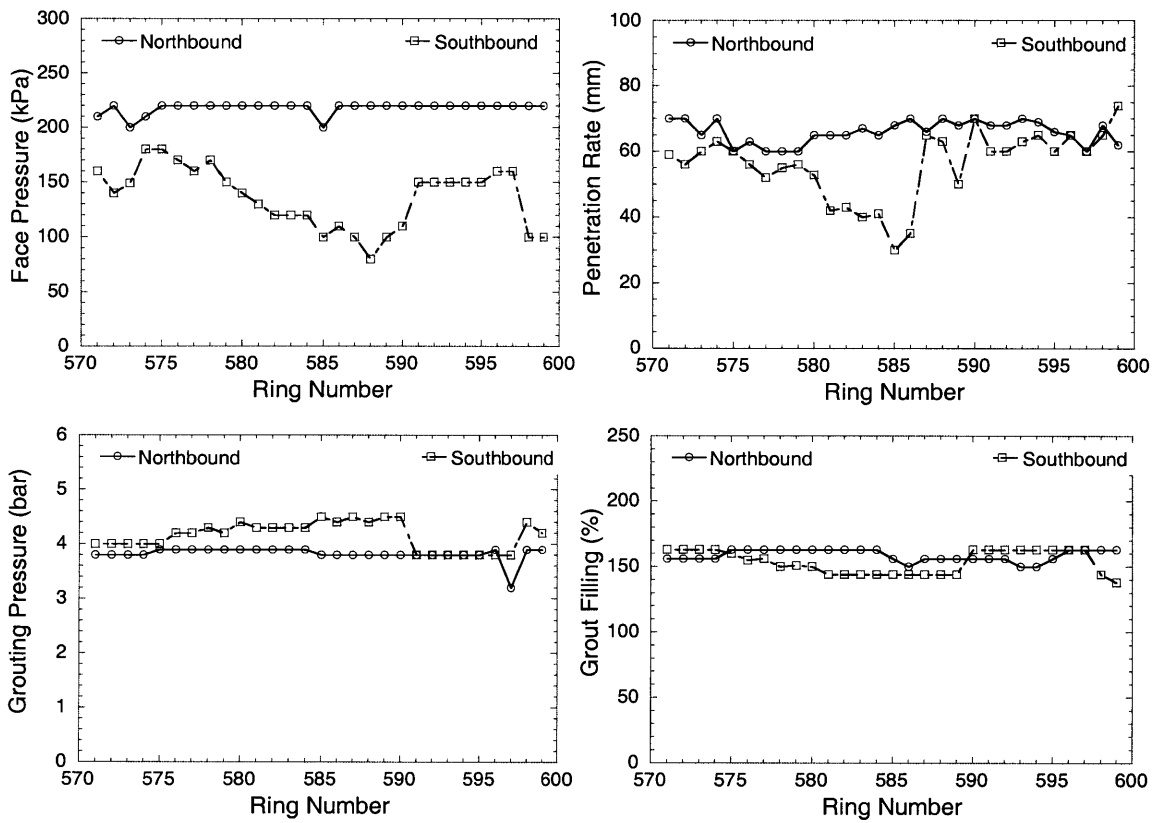


Figure 8.49 operational parameters recorded from NB and SB shields as they pass the measurement section over lining Ring no. 584

8.5 Summary

1. Observed surface settlement troughs measured after the first shield passing are symmetric with the maximum settlement (δ_{max}) over the centerline of the first tunnel. Therefore, by selecting an appropriate trough width parameter, one can use the Gaussian curve or normal probability function to estimate the complete settlement trough. However, for twin tunnels, surface settlement troughs observed after the second shield passing showed a variety of shapes. Nevertheless, as recommended by Peck (1969), the Gaussian curve was applied to the settlement troughs and it was found that by introducing an offset parameter to the normal probability function, one can obtain a fairly good fit also for twin tunnels.

2. A normalization and superposition technique was also introduced to describe settlement troughs caused by twin tunnels. It was found that the “additional settlement” trough induced by the second tunnel can be obtained and described by the Gaussian curve. Hence, the total settlement can be constructed by superimposing the additional curve on the settlement trough observed after the first shield passing. As a result, in most cases, a superposition curve can fit the total settlement trough very well. The total settlement curves can be either symmetric or asymmetric depending on the shapes of settlement curves induced by the first- and the second shields. Note that the degree of asymmetry depends on the differences of the magnitude of settlements between two curves (i.e. over the first tunnel and over the second tunnel). This superposition method demonstrated that it can provide a better fit than using a Gaussian curve with an offset parameter.

3. If surface settlements over the centerline of the first tunnel measured after the first shield passing and surface settlements over the centerline of the second tunnel measured after the second shield passing are known, one can construct total settlement troughs over twin tunnels. In Chapter 10, the Artificial Neural Networks (ANN) method will be introduced. With this method, surface settlements over the first tunnel and the second tunnel can be predicted. A combination of the normalization-superposition technique and the ANN will allow one to describe both settlement troughs induced by the first tunnel

and total settlement troughs induced by the twin tunnels. This finding is very useful in practice since engineers can estimate settlement troughs and influence zones by installing only two settlement markers over the first and the second tunnel instead of an entire settlement marker array. As a result, instrument cost may be reduced.

4. It was evident that the second shield can induce deflection at the first tunnel liner particularly between springline and invert. Moreover, the deflection magnitude of the first tunnel appeared to be proportional to the face pressure level of the second shield.

5. Surface settlements developing over the stacked tunnels were investigated. The Gaussian curve can be used to fit the settlement troughs very well. It was found that the magnitude of settlements depends on operational parameters such as face pressure in particular. The troughs indicated very narrow trough widths. This phenomenon may be due to excavating the first lower tunnel in the Sand layer.

References

Addenbrooke, T. I. and Potts, D. M. (1996). "Twin tunnel construction – Ground Movements and Lining Behaviour". *Proc. International Symposium on Geotechnical Aspects of Underground Construction in Soft Ground*, London, pp. 441-446.

Cooper, M. L., Chapman, D. N., and Rogers C. D. F. (2002). "Prediction of Settlement in an Existing Tunnel caused by the Second of Twin Tunnels". *Paper submitted for the 81st TRB Annual Meeting*, January 13-17, 2002.

Cording, E. J., and Hansmire, W. H. (1975). "Displacements around Soft Ground Tunnels". *General Report 5th Pan American Conference on Soil Mechanics and Foundation Engineering*, Buenos Aires, Session IV, pp. 571-632.

Kim, S. H., Burd, H. J. and Milligan, G. W. E. (1996). "Interaction between Closely Spaced Tunnel in Clay". *Proc. International Symposium on Geotechnical Aspects of Underground Construction in Soft Ground*, London, pp. 543-548.

- Kim, S. H., Burd, H. J. and Milligan, G. W. E. (1998). "Model Testing of Closely Spaced Tunnels in Clay". *Geotechnique*, Vol. 48, No. 3, pp. 375-388.
- Leca, E. (1989). "Analysis of NATM and Shield Tunneling in Soft Ground". Ph.D. Thesis, Virginia Institute and State University, Blacksburg, Va.
- Mair, R. J. and Taylor, R. N. (1997). "Bore Tunneling in the Urban Environment". Theme Lecture, Plenary Session 4, *Proc. 14th Int. Conf. of Soil Mechanics and Foundation Engineering*, Hamburg, Vol. 4, pp. 2353-2385.
- New, B. M. and Bowers, K. H. (1993). "Ground Movement Model Validation at the Heathrow Express Trial Tunnel". *Tunnelling 94*, IMM, London, pp. 301-329.
- O'Reilly, M. P. and New, B. M. (1982). "Settlement above Tunnels in the United Kingdom – Their Magnitude and Prediction". *Tunneling 88*, London, pp. 231-241.
- Peck, R. B. (1969). "Deep Excavations and Tunneling in Soft Ground". *Proc. 7th Int. Conf. on Soil Mechanics and Foundation Engineering*, Mexico City, State of the Art Volume, pp. 225-290.
- O'Reilly, M. P. and New, B. M. (1982). "Settlement above Tunnels in the United Kingdom – Their Magnitude and Prediction". *Tunneling 88*, London, pp. 231-241.
- Shirlaw, J. N., Doran, S. and Benjamin, B. (1988). "A Case Study of Two Tunnels Driven in the Singapore 'Boulder Bed' and in Grout Coral Sands". *Engineering Geology and Underground Movements*, Geological Society Engineering Geology Special Publication, No. 5, pp. 93-103.
- Terzaghi, H. (1942). "Liner-Plate Tunnels on the Chicago Subway". *Proc. ASCE*, Vol. 68, No. 6, pp. 862-899.
- Ward, W. H. and Thomas, H. S. H. (1965). "The Development of Earth Loading and Deformation in Tunnel Linings in London Clay". *Proc. 6th Int. Conf. of Soil Mechanics and Foundation Engineering*, Toronto, Vol. 2, pp. 432-436.
- Yamaguchi, I., Yamazaki, I. and Kiritani, Y. (1998). "Study of Ground-Tunnel Interactions of Four Shield Tunnels Driven in Close Proximity, in Relation to Design and Construction of Parallel Shield Tunnels". *Tunnelling and Underground Space Technology*, Vol. 3, No. 3, pp. 289-304.

CHAPTER 9

Analyses of Parameters Influencing Surface Settlements

9.1 Introduction

The behavior of ground movements associated with EPB shield tunneling in the MRTA project was investigated In Chapter 7. It was found that there are many factors affecting the ground movement including operational factors, tunnel geometry, and geological conditions. This observation is also in agreement with several case histories summarized in Chapter 4. However, up to now not much information exists about those influencing factors.

In the MRTA project, since large amounts of data were recorded through the computerized database (see Chapter 6), all information on essential parameters is now available. Therefore, the effect of those parameters on surface settlements can be investigated. By plotting each parameter versus the magnitude of settlements, one can determine the relationship between the parameter and surface settlement or a trend of the effect if it exists.

9.2 Face Pressure

As earlier described in Chapter 2, an Earth Pressure Balance shield is operated by controlling the amount of excavated soil extraction that is transported from the shield face by a balanced screw conveyor. As a result, the shield face can be supported by the excavated soil held in the front chamber at a controlled pressure. In practice, the face pressure is usually used as a primary control parameter during excavation. Hence, the face pressure in the chamber plays a crucial role in maintaining stability of the excavation and minimizing settlements. The face pressure can be monitored using pressure cells installed inside the earth chamber.

Based on this fundamental aspect of EPB shield tunneling, face pressure is one of the most significant factors that have a direct effect on the magnitude of surface settlements. As shown in case histories and observations in the MRTA project (Chapter 4 and Chapter 7), one would expect that applying low face pressures would cause large settlements. On the other hand, if high face pressures are applied, smaller surface settlements would be observed. In cases of very high face pressure, surface heaves occurred. In contrast, if the shield was operated at very low face pressure (i.e. less than 60 kPa or face pressure ratios less than 4 as shown in Figure 9.1 and Figure 9.2, respectively), its consequences are difficult to predict since the data are strongly dispersed. This is probably due to the complex behavior of ground-shield interaction in that there is a combination of many factors affecting the surface settlement at the same time. In Figure 9.3, the plot of face pressure versus maximum settlements is classified by geological conditions. It was found that in most geological conditions, the greater the face pressure, the smaller the settlement. However, no trend was found between face pressure and surface settlements when the tunnel was excavated entirely in sand.

Nevertheless, it is still unclear how exactly the face pressure affects the magnitude of surface settlements. Note that the face pressure referred in this section is the average face pressure recorded during shield passing (i.e. from 10 m. before shield arrival to 10 m after shield arrival) as shown in Figure 9.4.

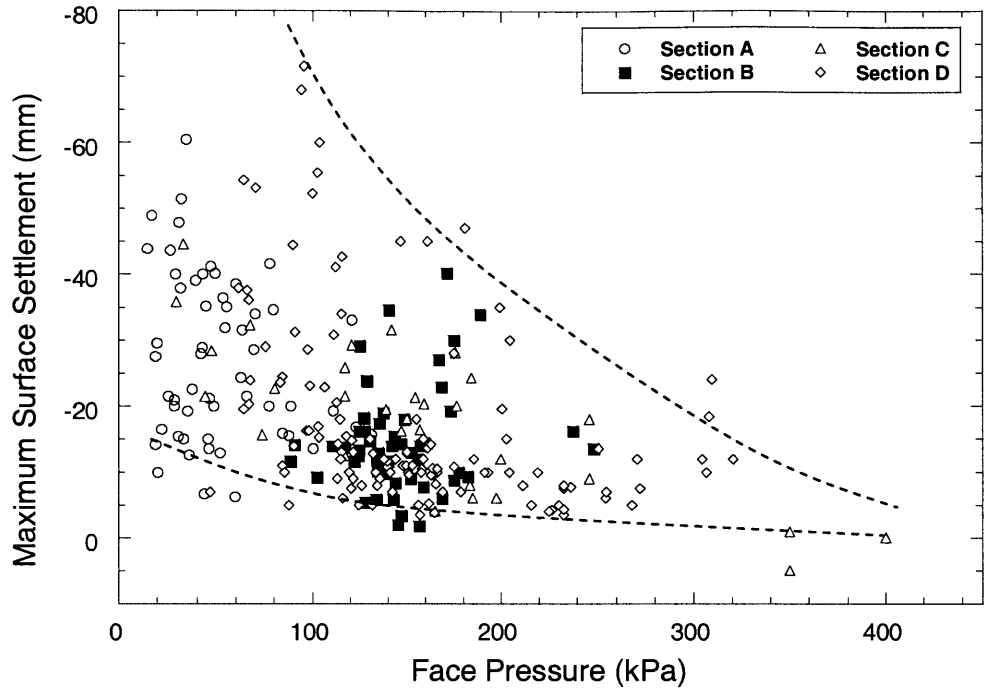


Figure 9.1 Face pressure versus the maximum surface settlement after shield passing

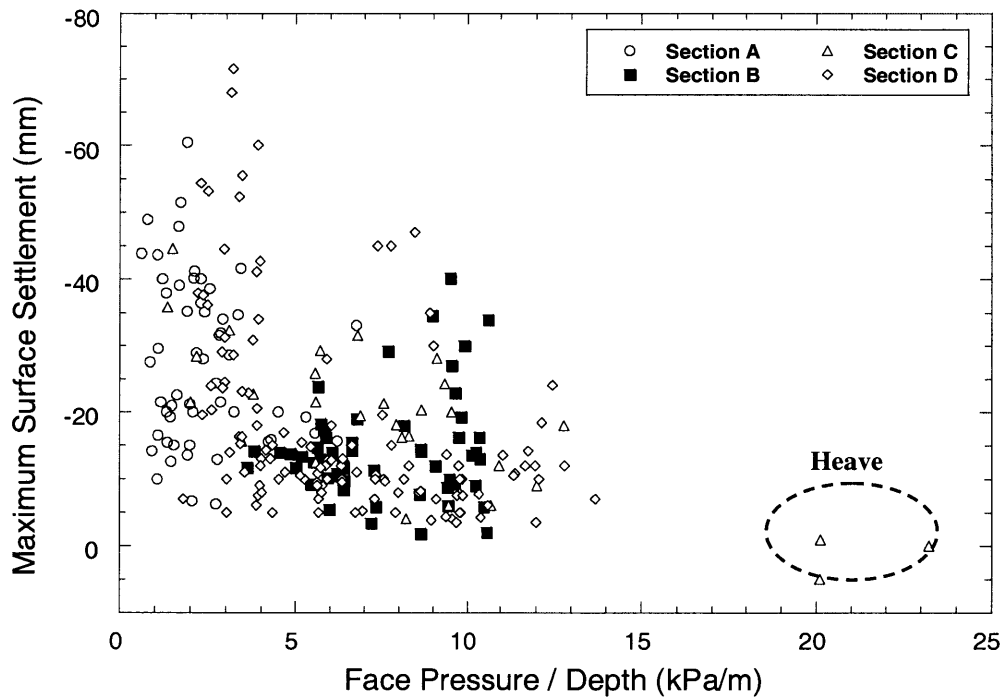


Figure 9.2 Face pressure ratio versus the maximum surface settlement after shield passing

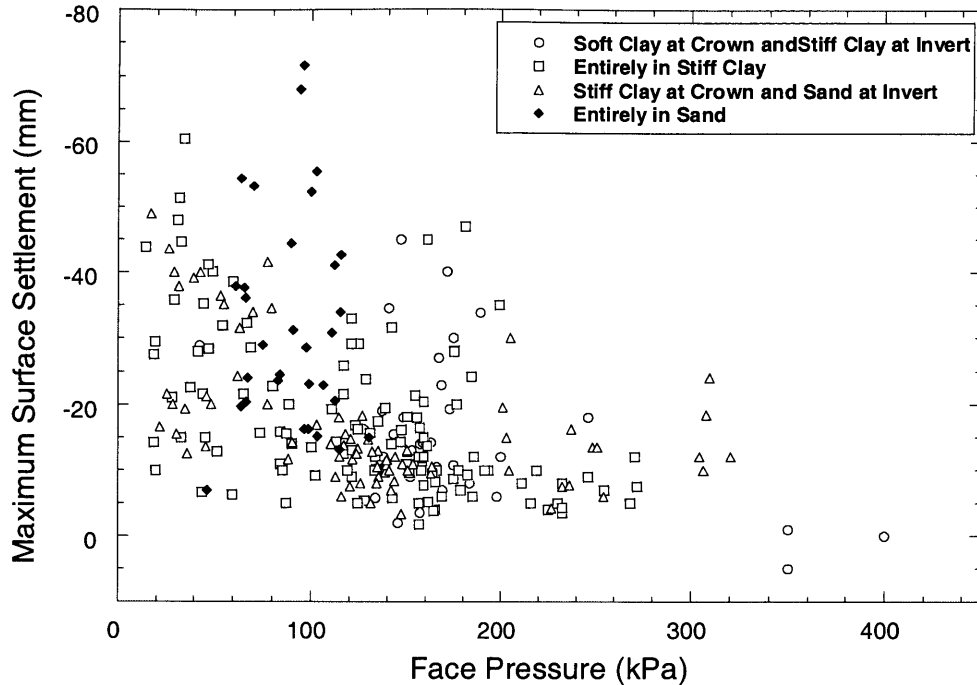


Figure 9.3 Face Pressure classified by geological conditions versus the maximum surface settlement after shield passing

Moreover, if one takes a detailed look at each tunneling section (Figure 9.1 and Figure 9.2), it was found that the data obtained in most sections generally follow the trend (i.e. higher face pressure, smaller settlement) except the data recorded in Section B in which large surface settlements were observed even though high face pressures were applied. A possible explanation is that unlike other tunnel sections, the contractor of Section B used a pipe transportation method instead of muck locomotive so that the shields have to be operated at low penetration rate as mentioned earlier in Chapter 7. Hence, penetration rate may be also an important factor influencing the surface settlement as well as face pressure.

Based on the observations discussed in Chapter 7, surface settlements induced by EPB tunneling can be divided into three zones namely, (1) Zone 1, (2) Zone 2, and (3) Zone 3 as shown in Figure 9.5. The first zone originates approximately 30 m ahead of the shield, where the ground surface begins to deform. The surface settlement then continues to develop as the shield advances close to the measurement section. About 10 m in front of

the shield, the surface settlement develops significantly and accelerates over the shield body. This stage of the surface settlement creates a clear inflection point separating “Zone 1” and “Zone 2”. It was found that the magnitude of surface settlements occurring in Zone 1 appeared to be associated with the face pressure level applied. To investigate the effect of face pressures on the settlement developing in Zone 1, face pressures are plotted against surface settlements measured at the end of Zone 1 (i.e. at the inflection point between Zone 1 and Zone 2) as shown in Figure 9.6. Although, a clear relationship cannot be established, it can be suggested that surface settlements occurring in Zone 1 are related to face pressures. At high face pressures, surface settlements developing in Zone 1 are small. On the other hand, if the applied face pressure level is low, large settlements are observed. A similar trend is also found in Figure 9.7 where face pressures are normalized by tunnel depths.

The surface settlement in Zone 2 was found to be the largest portion of overall settlements induced by EPB shields. Based on the centrifuge test results performed by Kimura and Mair (1981) and Nomoto et al (1999) as shown in Figures 3.43 and 3.49, respectively, the face loss zone can extend over the shield body (see also Section 7.2.1). Therefore, the supporting pressure applied at the shield face may have an influence on the magnitude of surface settlements developing over the shield (Zone 2). To verify this assumption, face pressure and face pressure ratio are plotted against surface settlements occurring over the shield in Zone 2 as shown in Figure 9.8 and Figure 9.9, respectively. As can be seen from those figures, face pressure appears to have an effect on the surface settlement developing within Zone 2 as lower face pressures were found to be associated with large settlements and vice versa. Note that most data followed this trend except the data obtained from Tunneling Section B (see Section 7.2.1.2 for further comments).

After the shield tail passes the measurement section (i.e. about 15 m from the shield face), the settlement development begins to slow down; this is the beginning of Zone 3. The surface settlement in this final zone typically stops about 30 m after shield passing. Face pressure has no influence on this final settlement zone as shown in Figure 9.10 and Figure 9.11. As can be seen in those figures, settlements within Zone 3 fall between the

bound of 1 mm to 7 mm independent of the level of face pressure applied during passing the instrument section.

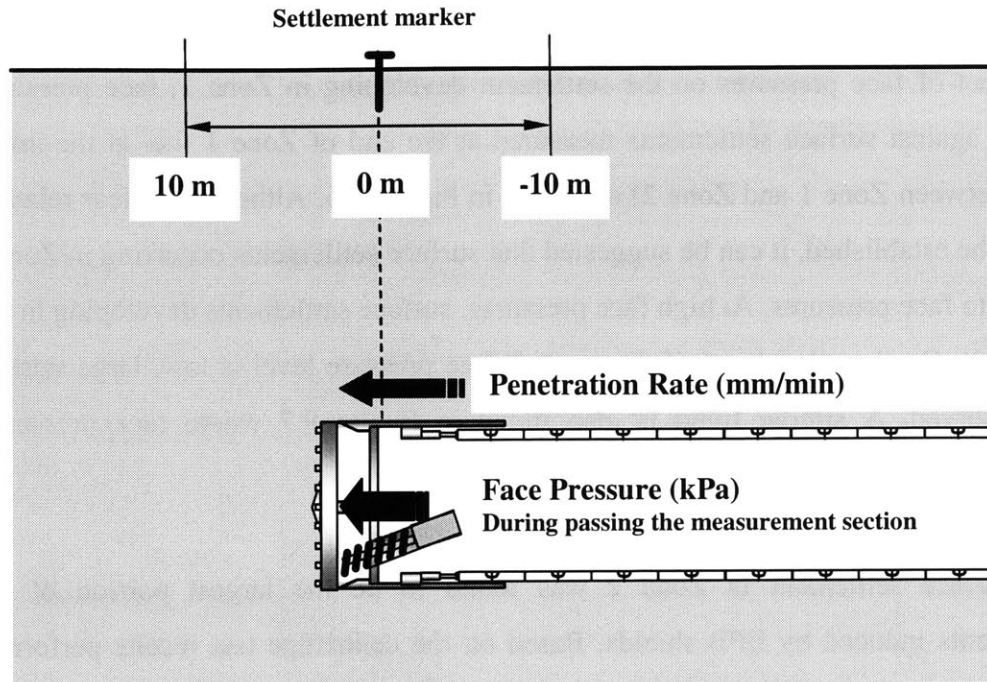


Figure 9.4 Average face pressure and average penetration rate

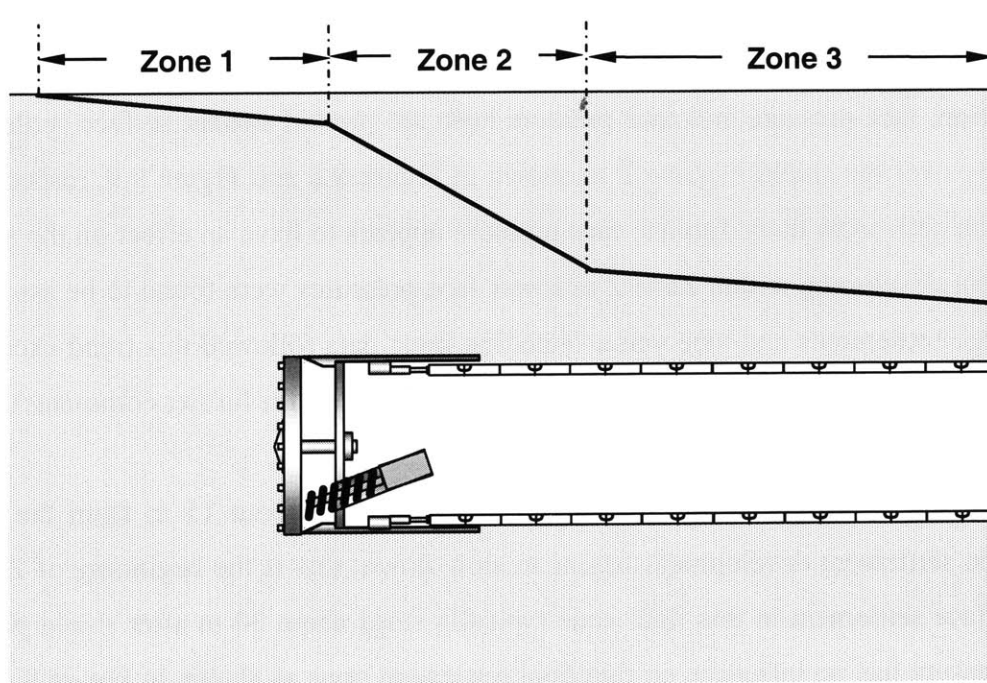


Figure 9.5 Schematic diagram of a typical longitudinal surface settlement profile

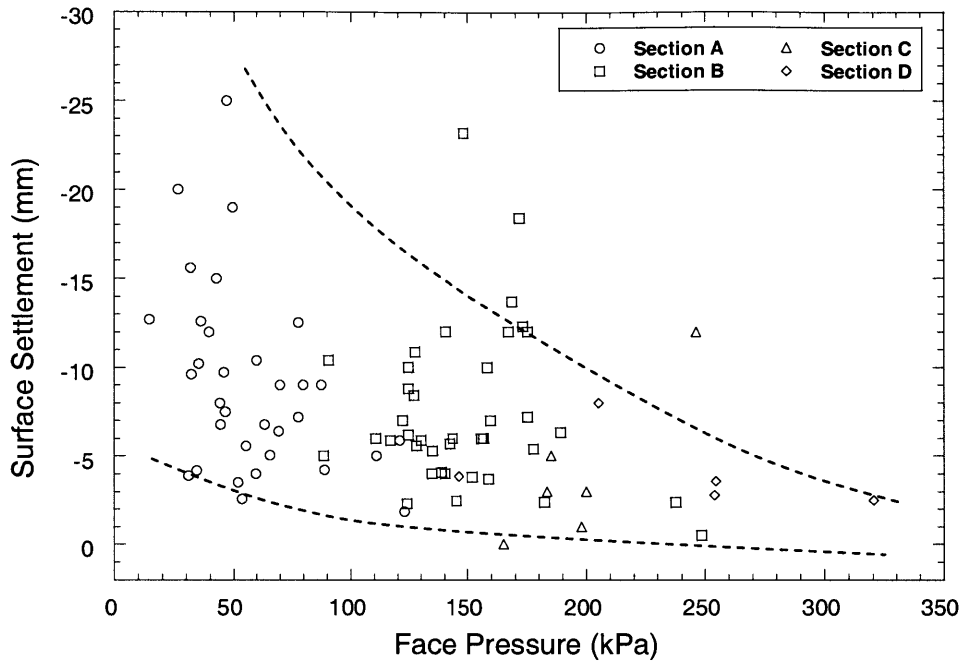


Figure 9.6 Face pressure versus surface settlement measured at the end of Zone 1

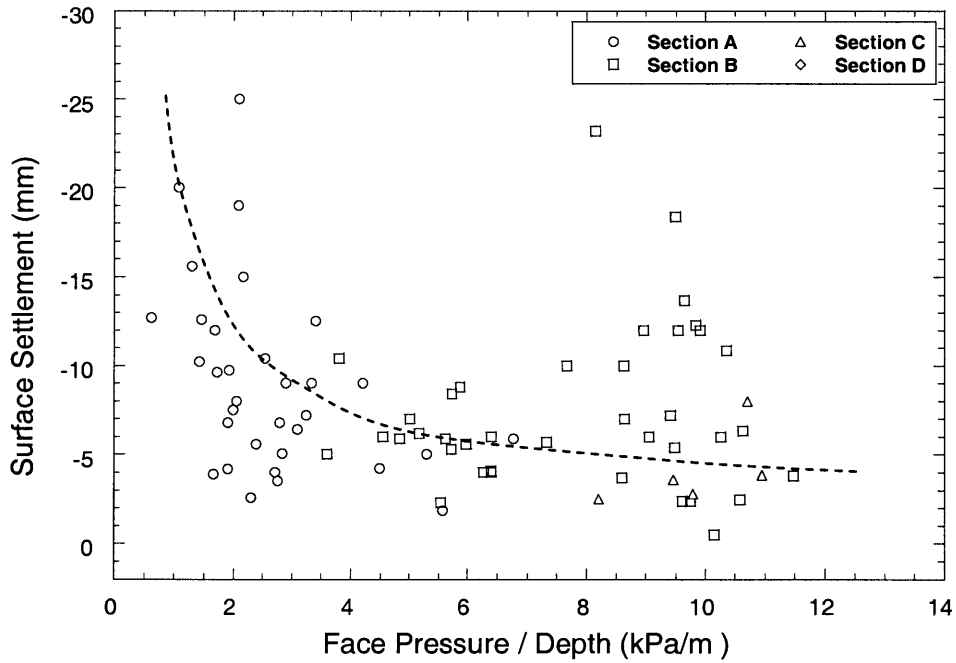


Figure 9.7 Face pressure ratio versus surface settlement measured at the end of Zone 1

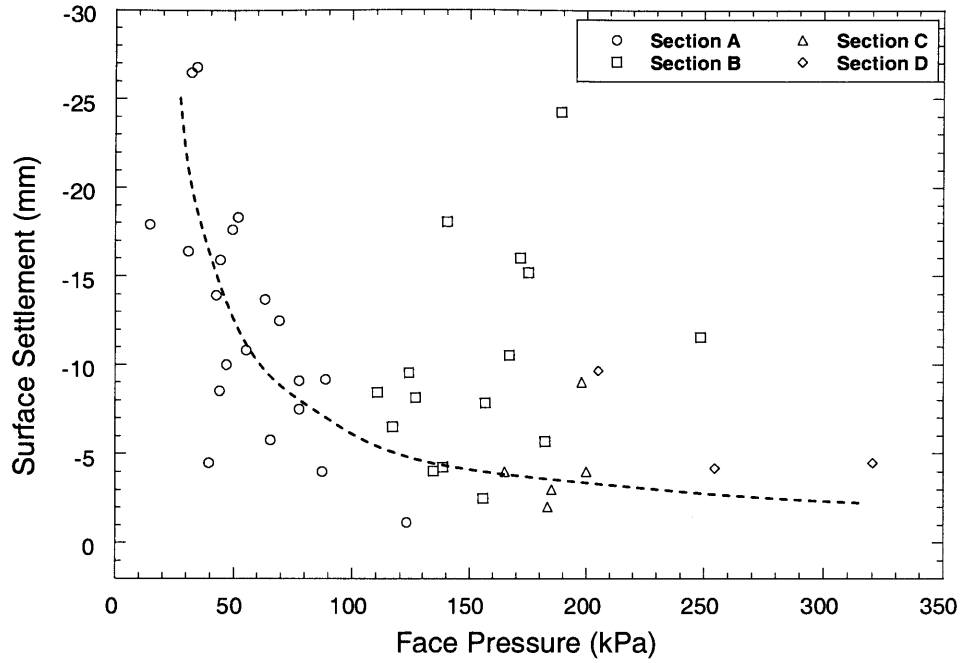


Figure 9.8 Face pressure vs. surface settlement developing in Zone 2

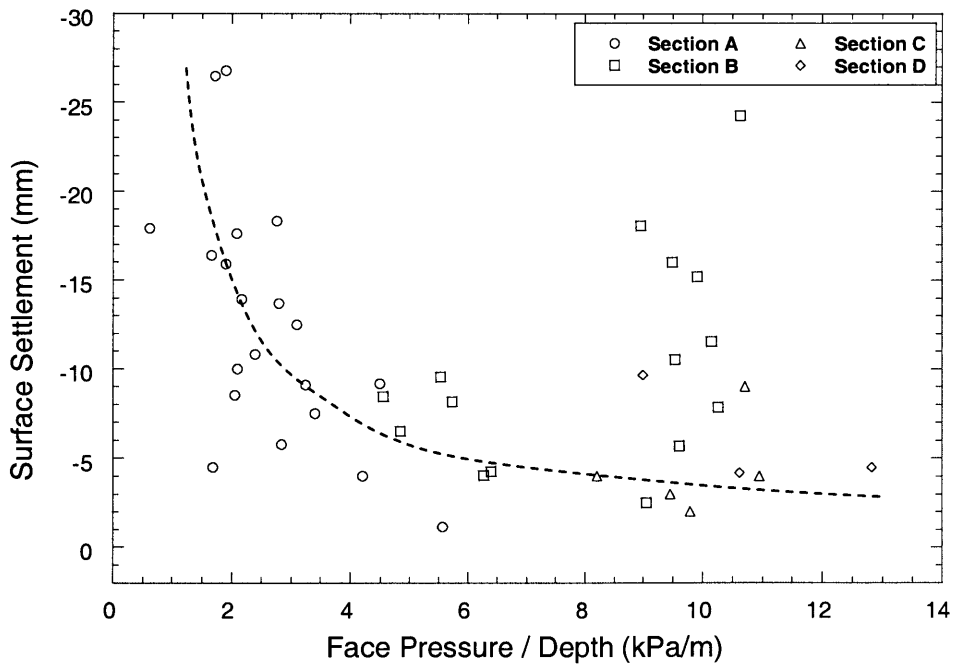


Figure 9.9 Face pressure ratio vs. surface settlement developing in Zone 2

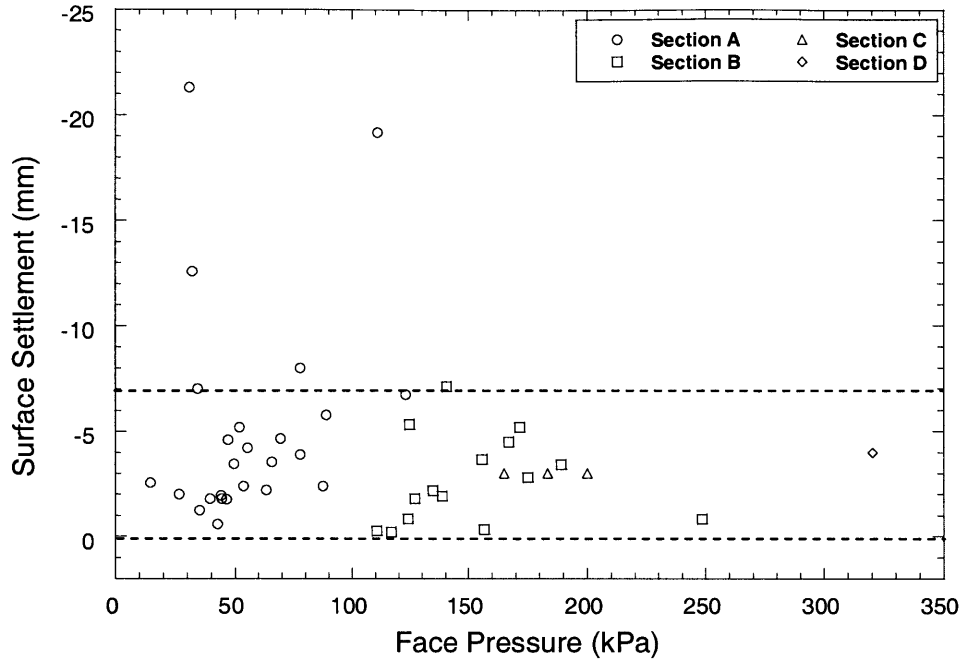


Figure 9.10 Face pressure vs. surface settlement developing in Zone 3

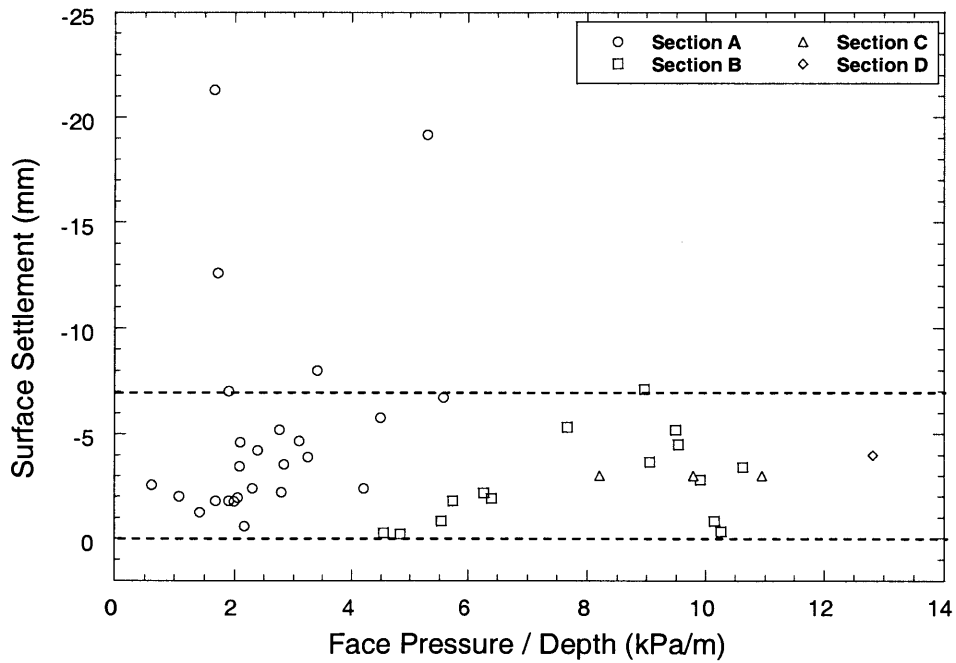


Figure 9.11 Face pressure ratio vs. surface settlement developing in Zone 3

9.3 Penetration Rate

As mentioned in the previous section, penetration rate appears to influence surface settlements. The penetration rate measures how fast the shield can move forward (mm/min), and it is typically measured in every excavation cycle. In practice, to achieve an earth pressure balance mode, shield operators have to control the rate of spoil extraction to correspond to the penetration rate. If the extraction rate is too high compared to the penetration rate, it means that the shield excavates too much volume of soil relative to the volume replaced by the shield. As a result, the excavated volume of the soil becomes unbalanced with the volume of soil that is occupied by the shield advance so that large ground loss would be expected. On the other hand, if the extraction rate is too low compared to the penetration rate, it means that the volume of excavation is less than the volume replaced by the shield advance. As a result, the shield may generate too high a face pressure.

The most important factor affecting the penetration rate is the capacity or speed of the soil removal system. For instance, if the rate of shoving the shield increases, the muck removal rate has to also increase to maintain a desired face pressure. Based on the operation records of six EPB shields in the MRTA project, a typical penetration rate is approximately between 40 and 70 mm/min (Figure 9.12). Only the two Kawasaki shields used in Section B operated at very low penetration rates (i.e. 10-30 mm/min) since the contractor of Section B adopted the pumping pipe transportation technique to remove muck from the earth chamber instead of a combination of screw conveyor and belt transport. Although pipe transport has some advantages over other methods, it can cause some problems that were described in Chapter 2. One of the problems is that pipe transport typically removes muck much more slowly than the combination of screw conveyor and belt transport. Accordingly, the shields have to operate at very low penetration rates to accommodate the low muck-pumping rate in order to maintain the desired face pressure. Based on observations in the MRTA project, it was found that low penetration rates cause difficulties in minimizing the surface settlement even though the

EPB shield is operated at high face pressure. Detailed discussions regarding the effect of the penetration rate were also provided in Chapter 7.

Evidently, such a low penetration rate was found to be associated with large surface settlements measured over the shield, particularly in Section B. However, as can be seen in Figure 9.12 particularly in other sections, it is still difficult to establish a clear relationship between the penetration rate and the surface settlement. Furthermore, no clear relationship was found between penetration rate and surface settlements developing in Zone 1 and Zone 2 as shown in Figure 9.13 and Figure 9.14, respectively.

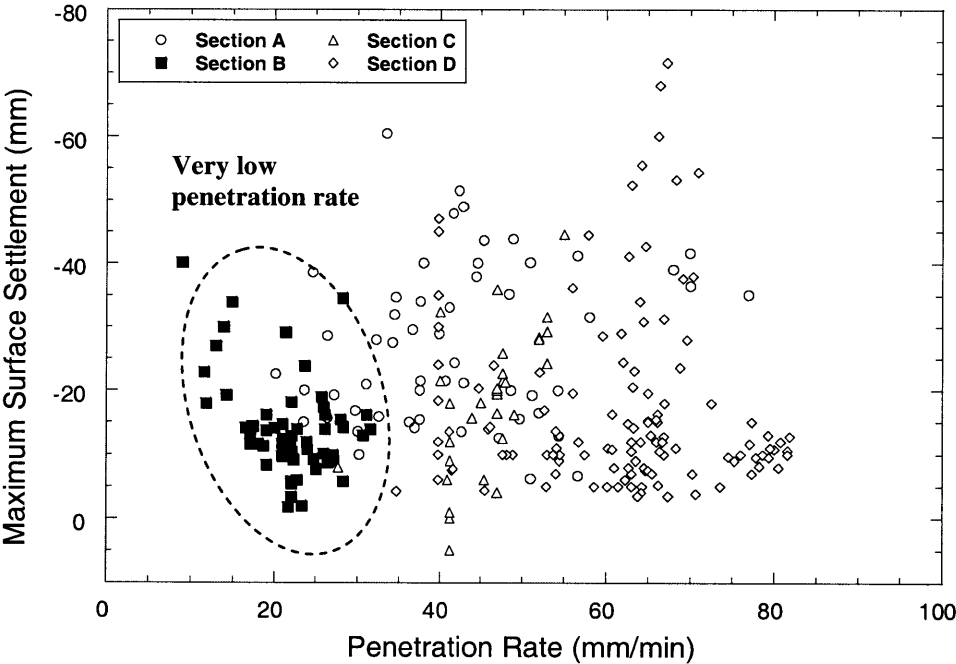


Figure 9.12 Penetration rate versus surface settlement

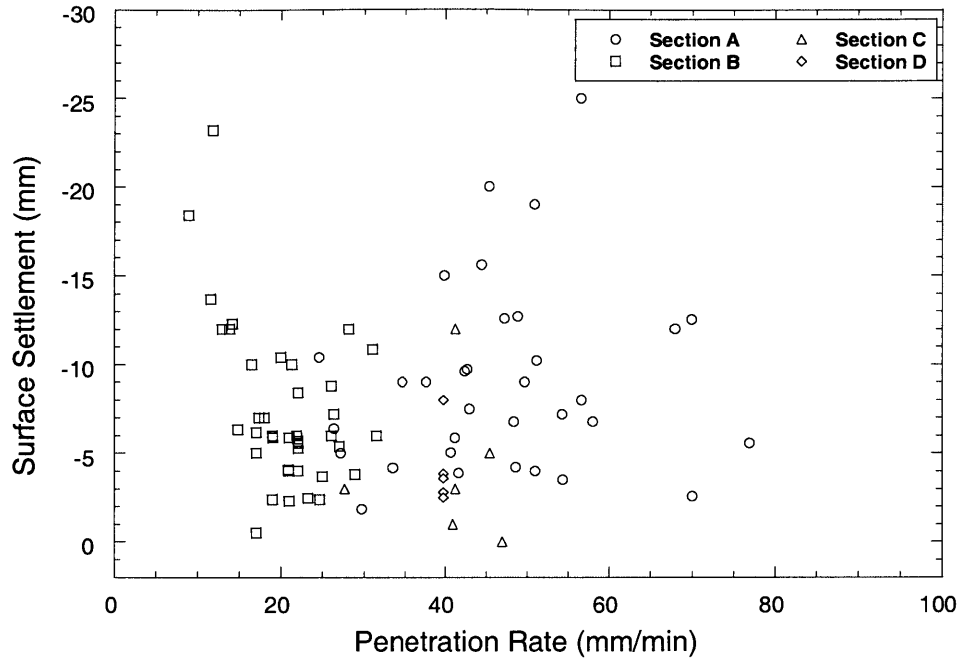


Figure 9.13 Penetration rate versus surface settlement measured at the end of Zone 1

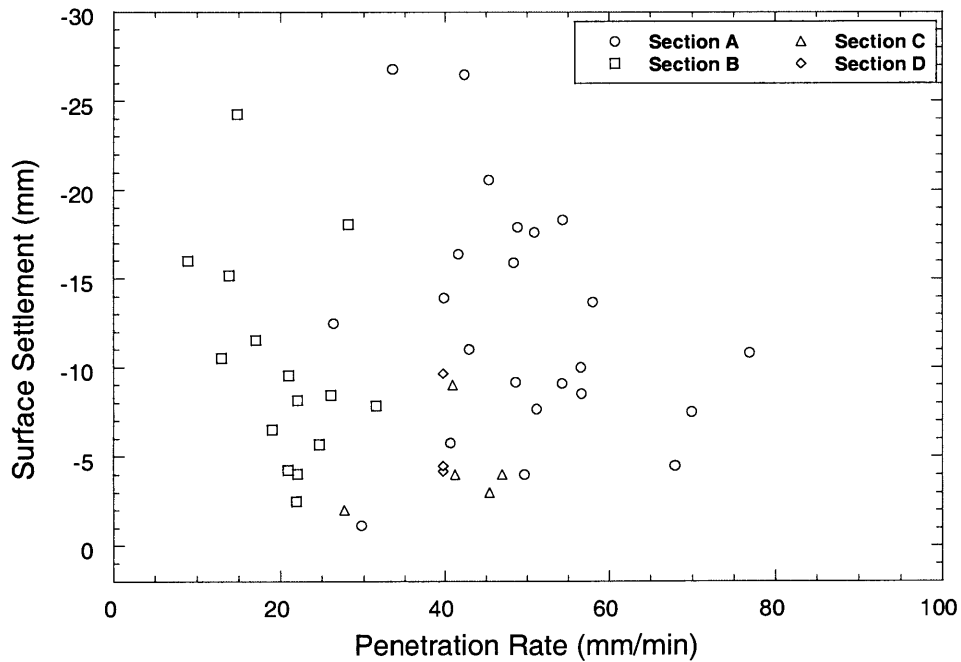


Figure 9.14 Penetration rate versus surface settlement developing within Zone 2

9.4 Pitching Angle

The shield position is represented by the pitching angle, which indicates the actual position of the shield during excavation. Theoretically, shield operators have to keep the shield as much as possible within the designed alignment both vertically and horizontally. However, in practice, it is impossible to maintain the accurate position all the time. When the shield pitches, it induces either ground settlement or ground heave as observed in the Fukuoka City Subway project (see Section 4.5). Especially, at high pitching angles, a large void/gap may be created. This causes the surrounding ground to move towards the shield as depicted in Figure 9.15.

In the MRTA project, the pitching angle was recorded at every excavation cycle. As shown in Figure 9.16, the average pitching angle as the shield passes the settlement markers was plotted against surface settlements measured with the instruments. However, no clear relationship was found, although the pitching angle theoretically influences surface settlements.

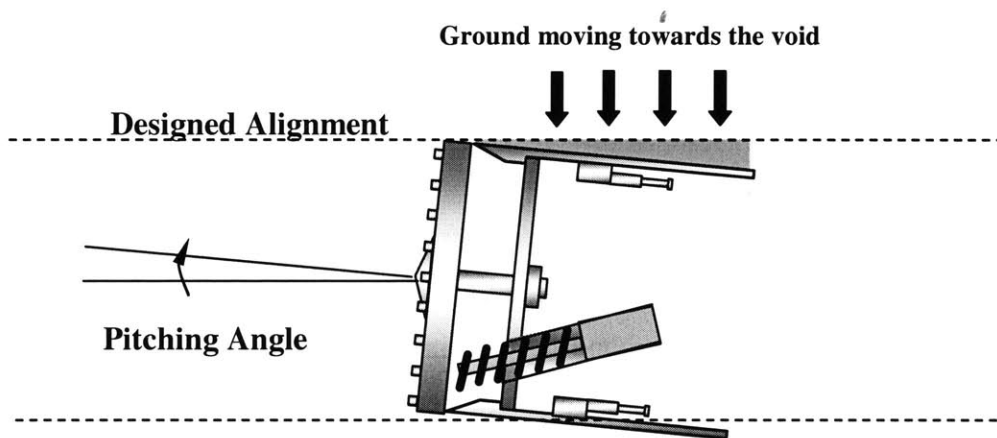


Figure 9.15 Ground movement caused by pitching angle

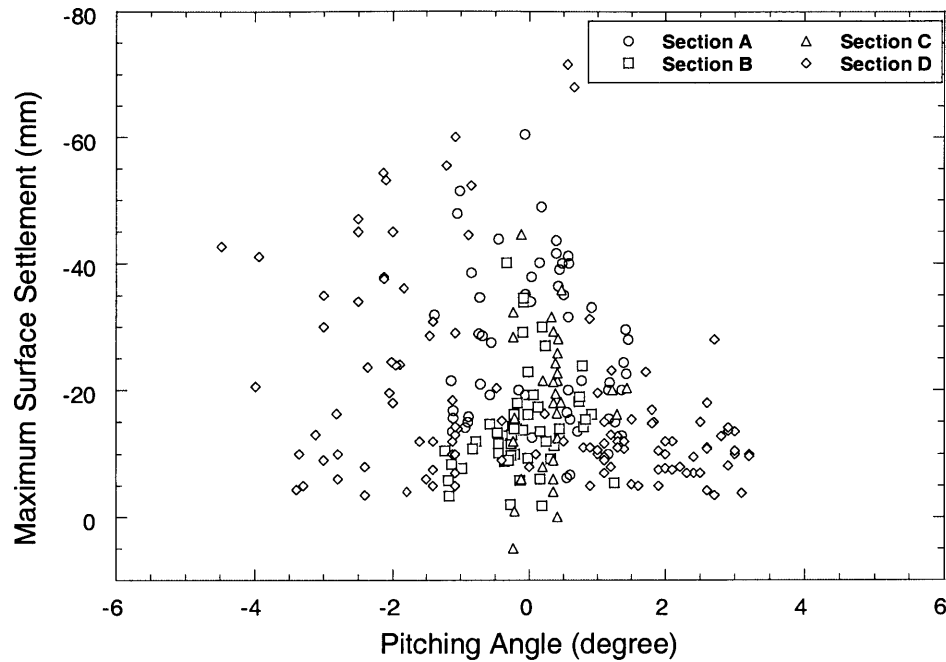


Figure 9.16 Pitching angle versus the maximum surface settlement

9.5 Grouting Quality

Grouting quality also contributes to the extent of the ground settlement. As the shield is jacked forward, a tail void around the outside of the lining is created as shown in Figure 9.17. Tail void grouting is necessary in order to prevent ground moving towards the void. In general practice, *grouting pressure* should be high enough to guarantee the flow of grout material and to resist the ground moving into the void as shown in Figure 9.18. Another criterion to check the grouting performance is *percent grout filling* that has to be maintained at a level higher than the theoretical void as also shown in Figure 9.18. Tunneling operations with high grouting pressure and high percent of grout filling can considerably reduce settlements developed after the shield passing (examples: the WMTA project; Leca, 1989; and the MRTA project).

Most sections adopted an automatic grouting control in which grouting pressure and percent grout filling can be set to be constant during excavation. As can be seen in Figure 9.19, although the grouting pressure is constant, surface settlements were found to vary significantly. Hence, a clear relationship cannot be established from the plot. This may be caused by the fact that surface settlements can be also affected by other parameters. Likewise, even though percent grout filling is constant particularly in Section B (see Figure 9.20); surface settlements were found to be very different.

However, comparing the overall surface settlement to grouting quality may be not suitable since the grouting quality only affects the settlement developing after the shield tail. Hence, to make the comparison more meaningful, surface settlements measured in Zone 3 are plotted against grouting pressure and grout filling as shown in Figure 9.21 and Figure 9.22, respectively. As can be seen in those figures, most settlements recorded in Zone 3 are smaller than 7 mm in all sections. This observation is not only found in the MRTA project but also found in cases of the WMATA project and the Fukuoka City subway project (see Chapter 4) where the settlements attributed to tail void closure were significantly reduced by grouting. On the other hand, no clear relation between grouting pressure or grout filling and settlements in Zone 3 was found.

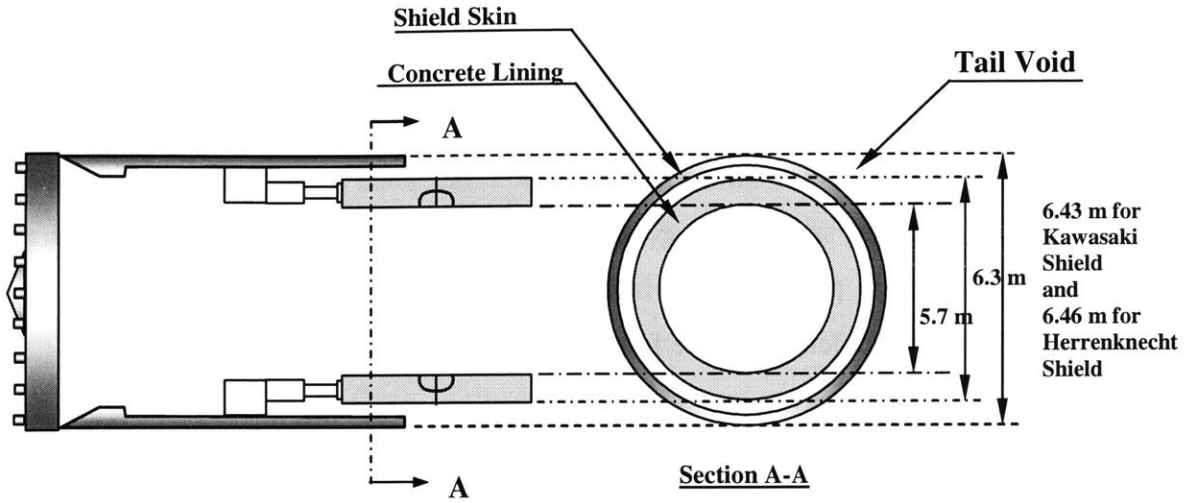


Figure 9.17 Schematic diagram showing a tail void between tunnel lining and the liner

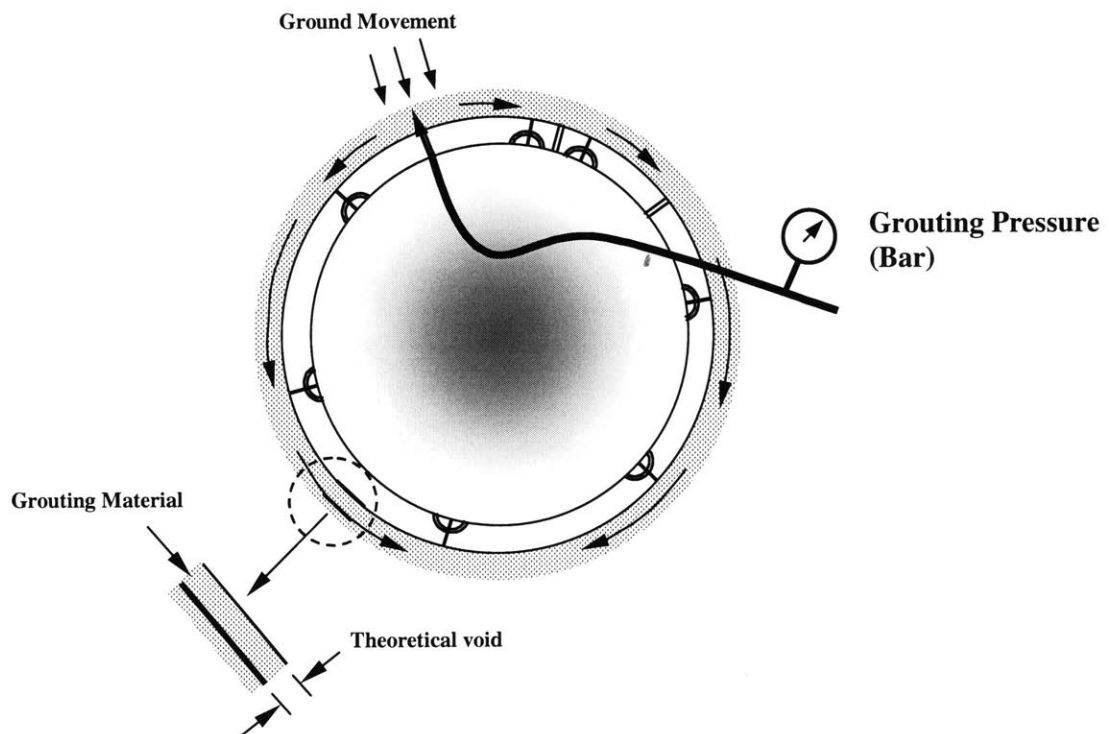


Figure 9.18 Grouting pressure and grout filling

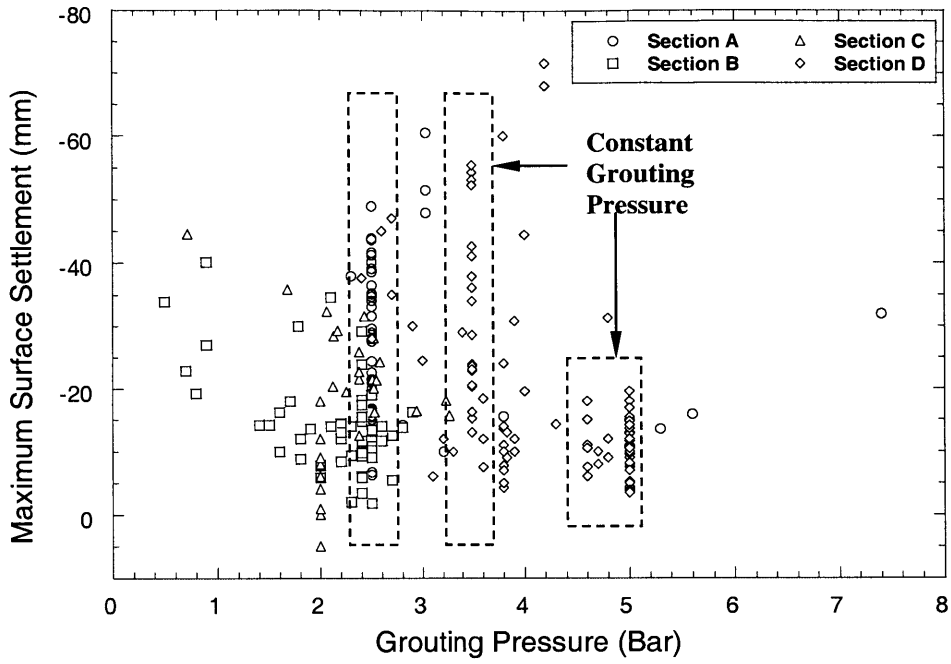


Figure 9.19 Grouting pressure versus the maximum surface settlement after shield passing

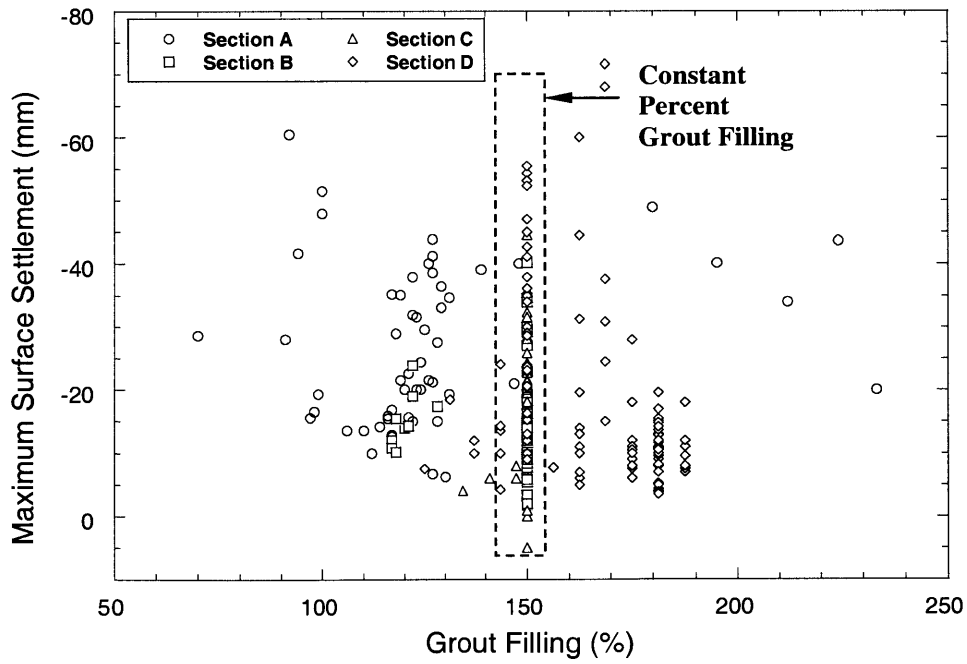


Figure 9.20 Grout filling (%) versus the maximum surface settlement after shield passing

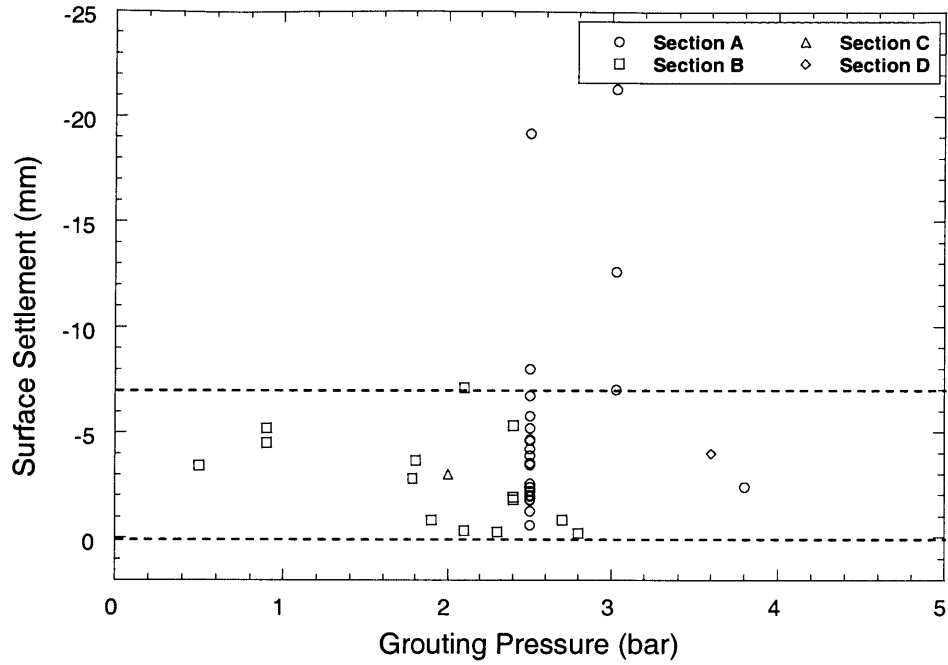


Figure 9.21 Grouting pressure versus surface settlement developing in Zone 3

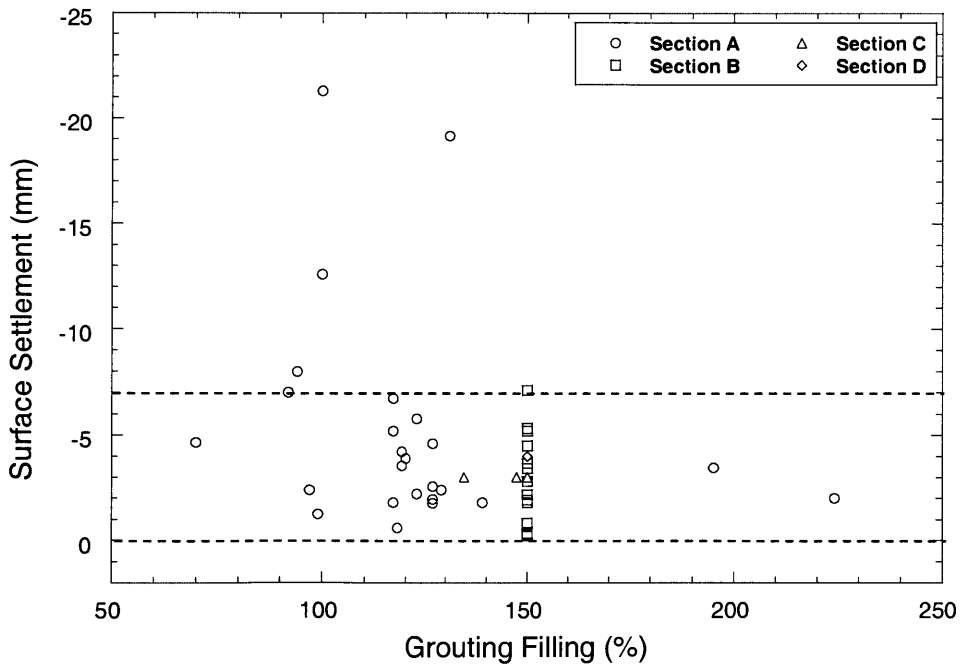


Figure 9.22 Grout filling (%) versus surface settlement developing in Zone 3

9.6 Distance from Launching Station

The distance from the shield launching station (Figure 9.23) has a significant effect on the magnitude of surface settlements. It quantitatively represents a combination of several effects including the learning skill of tunneling crews and shield performance. In this part of the initial drive, shield operators often determine by trial and error an optimum pressure balance mode that causes the smallest settlement by varying face pressure, penetration rate, and other operational parameters. In addition, construction workers might not be able to perform tasks (i.e. surveying, lining installation, and other logistic processes) effectively due to a lack of experience at the beginning. All of this often causes either large settlements or surface heave (see also Chapter 7).

After the shield operators have achieved the desired operational mode (i.e. after driving the shield for a distance from the launching station), and workers have improved their performance, less surface settlement is normally observed. The familiarization of tunnel crews with shield operation and with the logistic system is generally referred to as the learning curve. To be able to investigate the effect of the learning curve on the surface settlement, distances from launching station are plotted against surface settlements in Figure 9.24. As can be seen in the figure, large or more variable (oscillating) settlements were measured in the early part of the EPB shield tunnel. Large surface settlements tend to occur in the initial drive. Furthermore, major collapses were often found at the beginning of excavation (examples: the Taipei Subway Tunnel and the MRTA project). All this has also been observed in many other shield tunneling projects as discussed in Chapter 4. Therefore, the surface settlement is more unpredictable in the early drive than after the shield has completed a number of excavation lengths.

Launching
Station

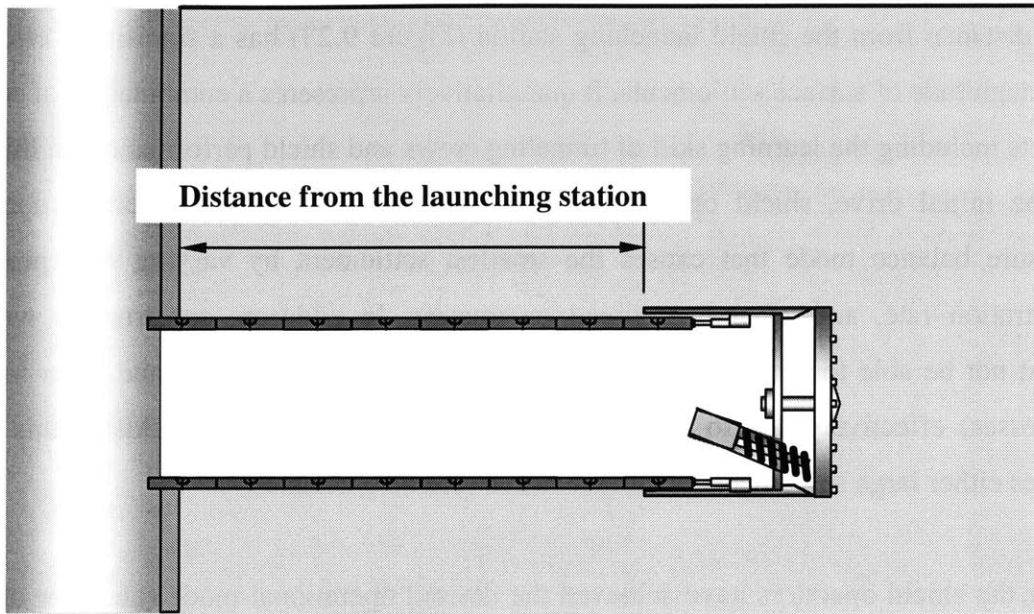


Figure 9.23 Geometry parameter: distance from launching station

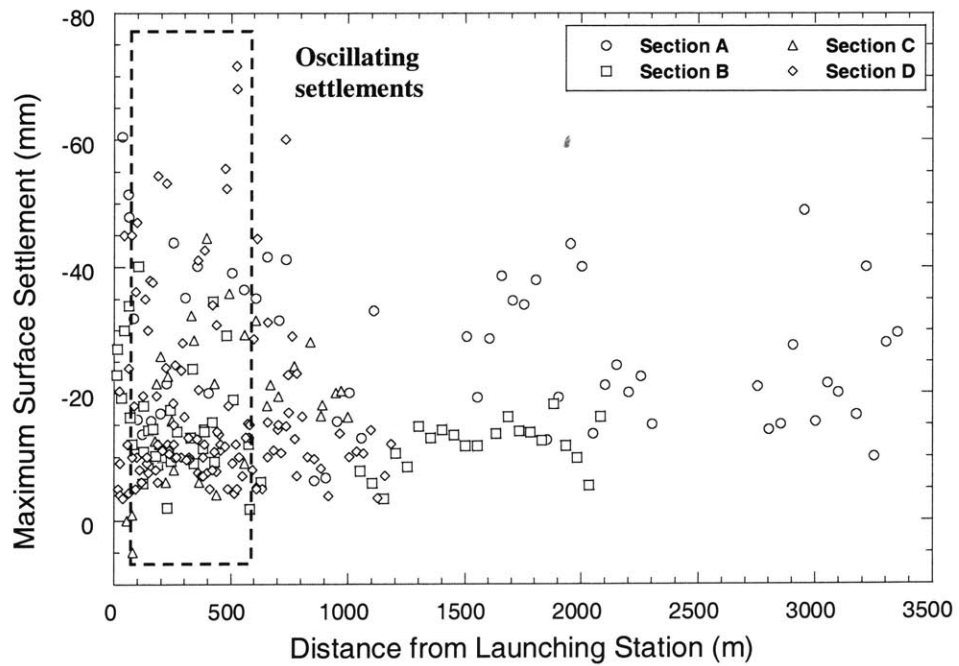


Figure 9.24 Distance from launching station versus the maximum surface settlement after shield passing

9.7 Tunnel Depth

Tunnel depth is also an important geometry factor. Figure 9.25 shows the plot of tunnel depth versus surface settlement. Note that, in this study, tunnel depth means “depth to the tunnel axis.” Theoretically, at a constant diameter, a deep tunnel appears to induce less surface settlements than a shallow tunnel. However, as can be seen in the figure, the expected relationship between tunnel depth and settlement does not exist. For instance, even though the tunnel was excavated at a great depth, large surface settlements were observed particularly in Section C, where several parts of the tunnel were located in a sand layer. On the other hand, at shallow depths, surface settlements were relatively small. This small surface settlement occurring in the shallow tunnel may be due to operating the EPB shield at earth pressure balance mode so that the settlement can be controlled. The results also suggest that although tunnel depth is an important factor influencing the surface settlement, there are other factors such as operational parameters and geological conditions making the relationship between tunnel depth and surface settlement unclear.

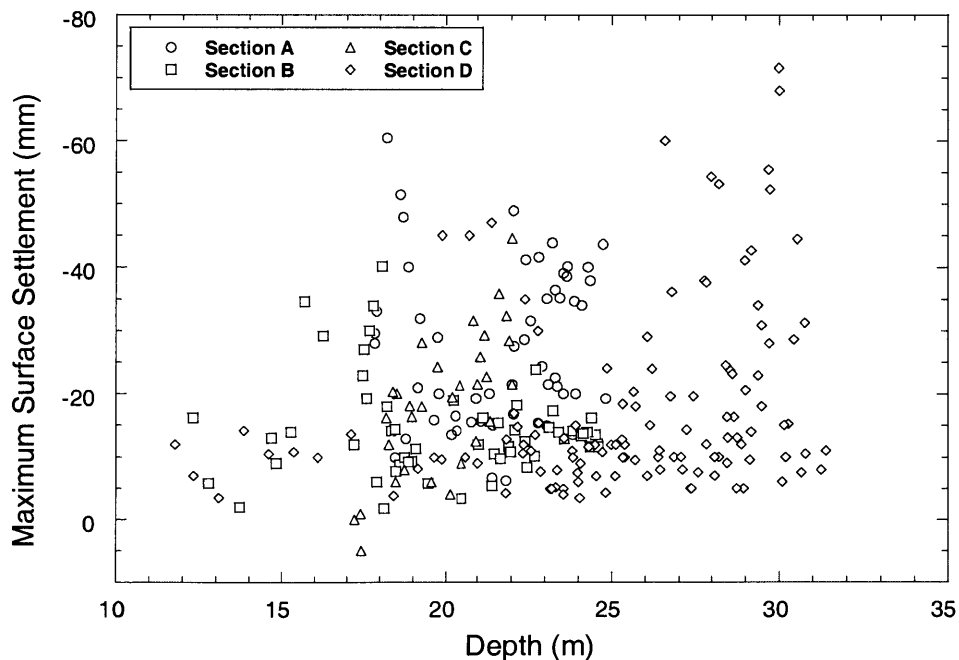


Figure 9.25 Tunnel depth versus the maximum surface settlement after shield passing

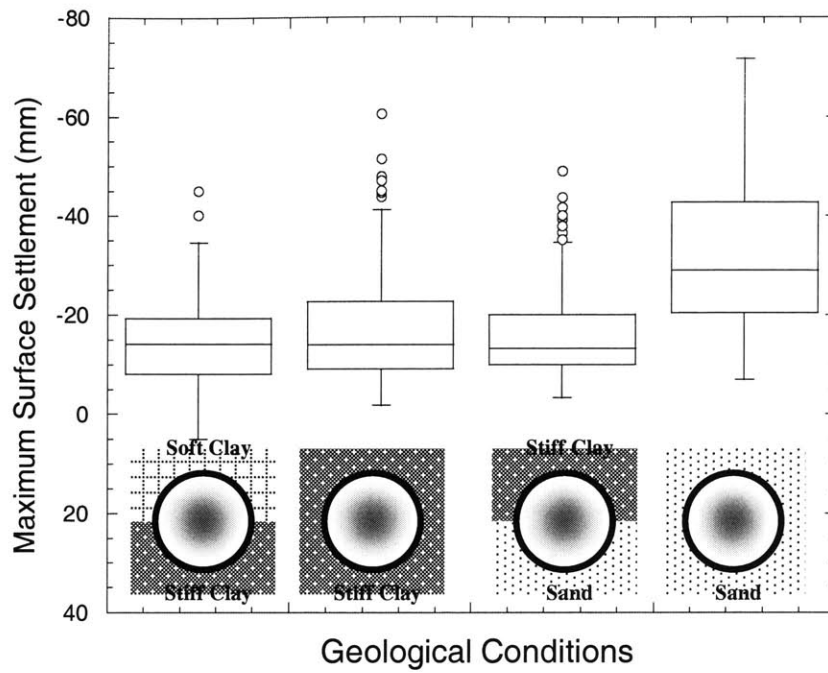


Figure 9.26 Geological conditions versus the maximum surface settlement after shield passing

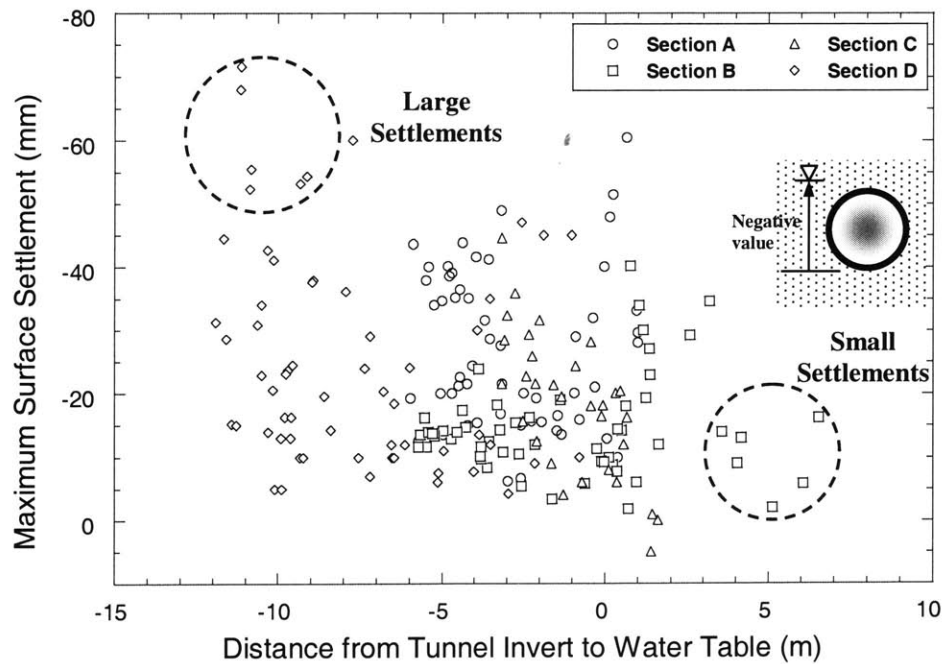


Figure 9.27 Distance from tunnel invert to water table versus the maximum surface settlement after shield passing

9.8 Geological Conditions

Geological conditions are very important factors in every tunneling method. *The type of soil*, which is excavated by the EPB shield, is clearly related to how effective the shield can perform the excavation and how large a settlement would be expected. In general, stiff clay appears to be the most favorable ground condition for EPB tunneling based on several case histories and the field observations in the MRTA project as shown in Figure 9.26. With high shear strength (S_u), the stiff clay layer provides face stability during excavation. Muck removing processes via screw conveyor and belt transport can be performed smoothly with clayey materials. Moreover, since one of the most important properties of stiff clays is low hydraulic conductivity, this prevents water seepage towards the tunnel that might cause difficulties in maintaining a desired face pressure in the earth chamber during excavation, which in turn causes the larger ground loss towards the tunnel face and leads to larger surface settlement. As discussed in Chapters 4 and 7, tunneling within a sand layer can cause serious problems in shield operation control and excavation stability resulting in large surface settlements or collapse. It was found that the face pressure applied in the front of a shield dropped significantly if the shield face encountered a sand layer. Specifically, large settlements occurred in the case where a sand layer was found at the tunnel crown and a clay layer existed in the lower part of the tunnel face (example: WMATA project; Clough and Leca, 1993).

The ground water level can also affect the settlement. The water table has always been a critical concern in all methods of deep excavation. It can be suggested that the higher the water level over the tunnel invert, the greater the possibility that water can flow towards the tunnel face causing difficulties in face pressure control and muck removal. This is often followed by large surface settlements or collapse. In addition, flow of this groundwater also leads to the consolidation settlements above the tunnel. Figure 9.27 shows a plot of distance from the tunnel invert to the water table versus surface settlements. When the water table is high and above the tunnel invert (i.e. high negative value), particularly in Section D where the tunnels were stacked, large surface settlements were observed in some instrumented sections. On the other hand, when the water table is

much lower than the tunnel invert (i.e. highly positive value), much smaller settlements were observed (see Figure 9.27). However, a clear trend still cannot be established.

9.9 Summary

All information on essential factors including operational factors, tunnel geometry, and geological conditions was recorded in the MARTA project. Each factor was plotted versus surface settlements in order to provide an analysis on the effect of the factor on surface settlements. The surprisingly consistent conclusion one can draw is that there are no strong trends in the relationship between each parameter and the surface settlement. Only in the plots of face pressure versus surface settlements, small trends were observed. This indicates that more than one parameter influences the magnitude of surface settlements. In practice, it is impossible to hold other parameters constant while varying a parameter for investigating the effect of the parameter on surface settlements. Furthermore, even though large amounts of data were recorded, sensitivity analyses can provide only limited results due to the complex behavior of EPB shield tunneling. In the next chapter, a new approach, Artificial Neural Networks (ANN) will be introduced with the intent to relate several parameters to surface settlements. The method allows one to integrate the theoretical background, observation, and learning such that a relationship between the influencing factors and surface settlements can be formulated.

References

- Clough, G. W., Sweeney, B. P., and Finno, R. J. (1982). "Measured Soil Response to EPB Shield Tunneling". *Journal of Geotechnical Engineering*, Vol. 109, No. 2, pp. 131-149.
- Clough, G. W. and Leca, E. (1993). "EPB Shield Tunneling in Mixed Face Conditions". *Journal of Geotechnical Engineering*, Vol. 119, No. 10, pp. 1640-1656.
- Chiorboli, M. A. and Marcheselli, P. P. (1996). "Analysis and Control of Subsidence due to Earth Pressure Shield Tunneling in Passante Ferroviario of Milano". *Proc. of Int. Conf. on North American Tunneling '96*, Balkema, Rotterdam, pp. 97-106.
- Finno, R. J. (1983). "Response of Cohesive Soil to Advanced Shield Tunneling". Ph.D. Thesis, Stanford University, Ca.
- Hwang, R. N. and Moh, Z-C. (1996). "Pore Pressures induced in Soft Ground due to Tunneling". *Proc. of Int. Symp. On Geotechnical Aspects of Underground Construction in Soft Ground*, Balkema, Rotterdam, pp. 695-700.
- Ju, D., Moh, Z-C., and Hwang, R. N. (1999). "Soft Ground Tunneling for Taipei Rapid Transit Systems". *Proc. of the 3rd Conf. on Geo-Engineering for Underground Facilities*, ASCE, pp.610-621.
- Kuesel, T. R. (1972). "Soft Ground Tunnels for the BART Project". *Proc. of 1st Rapid Excavation Tunneling Conference*, Chicago, Vol. 1, pp. 287-313.
- Leca, E. (1989). "Analysis of NATM and Shield Tunneling in Soft Ground". Ph.D. Thesis, Virginia Institute and State University, Blacksburg, Va.
- Maconochie, D. and Suwansawat, S. (1999) "Bangkok MRTA: Chaloem Rachamongkhon Line". *Tunnel & Tunneling International*, November 1999, pp.19-22.
- Matsushita, Y., Hashimoto, T., Iwasaki, Y., and Imanishi, H. (1995). "Behavior of Subway Tunnel driven by Large Slurry Shield". *Proc. of Int. Conf. on Underground Construction in Soft Ground*, Balkema, Rotterdam, pp. 253-256.
- Moh, Z-C., Hwang, R. N., and Ju, D. H. (1996). "Ground Movements around Tunnels in Soft Ground". *Proc. of Int. Symp. On Geotechnical Aspects of Underground Construction in Soft Ground*, Balkema, Rotterdam, pp. 725-730.

CHAPTER 10

Artificial Neural Networks

10.1 Introduction

Many tasks involving intelligence or pattern recognition are extremely difficult to automate, but can be performed very easily by humans and animals. For instance, we recognize various objects and make sense out of the large amount of visual information in our surroundings based on our experience. It stands to reason that computing systems that attempt similar tasks will profit enormously from understanding how humans perform these tasks, and simulating these processes to the extent allowed by physical limitations. This necessitates the study and simulation of Neural Networks.

The biological neural network is a part of the nervous system, containing a large number of interconnected neurons (nerve cells). “Neural” is an adjective for neuron, and “network” denotes a graph-like structure. Artificial neural networks (ANN) refer to computing systems whose central theme is borrowed from the analogy of the biological neural networks. In other words, a (artificial) neural network is an interconnected assembly of simple processing elements, units or nodes, whose functionality is loosely based on the animal neuron. The processing ability of the network is stored in the inter-unit connection strengths, or weights, obtained by a process of adaptation to, or learning from, a set of training patterns. The neural networks are also referred to as “neural nets,” “artificial neural systems,” “parallel distributed processing systems,” and “connectionist

systems.” Note that this chapter is based on a review of a fundamental ANN from literature:

1. Flood, I. and Kartam, N. (1994). “Neural Networks in Civil Engineering. I: Principles and Understanding”. *Journal of Computing in Civil Engineering*, ASCE, Vol. 8, No. 2.
2. Haykin, S. (1999). *Neural Networks: A Comprehensive Foundation (2nd edition)*.
3. Hertz, J., Krogh, A., and Palmer, R. G. (1991). *Introduction to the Theory of Neural Computation*.
4. Mehrotra, K., Mohen, C. K., and Ranka, S. (1997). *Artificial Neural Networks*.
5. Pham, D. T., and Liu, X. (1995). *Neural Networks for Identification, Prediction and Control*.
6. Philippe, D. W., (1997). *Neural Network Models*.

10.1.1 Biological Neurons

A typical biological neuron is composed of a cell “body,” a tubular “axon”, and a multitude of hair-like “dendrites” shown in Figure 10.1. The dendrites form a very fine filamentary brush surrounding the body of the neuron. The axon is essentially a long, thin tube that splits into branches terminating in little end bulbs that almost touch the dendrites of other cells. The small gap between an end bulb and a dendrite is called a “synapse,” across which information is propagated. The axon of a single neuron forms synaptic connections with many other neurons; the “presynaptic” side of the synapse refers to the neuron that sends a signal, while the “postsynaptic” side refers to the neuron that receives the signal. However, the real picture of neuron is a little more complicated as shown in Figure 10.2. The figure illustrates a single interneuron in the retina of a rabbit. The cell has been injected with a fluorescent dye to reveal all its branches. Each of the small knobs at the tips of the branches makes a synapse with another cell in the retina.

The number of synapses received by each neuron range from 100 to 100,000. Morphologically, most synaptic contacts are of two types (i.e. more details of the neuron system are provided by Hodgkin and Huxley, 1952).

Type 1: Excitatory synapses with asymmetrical membrane specializations; membrane thickening is greater on the postsynaptic side. The presynaptic side contains round bogs

(synaptic vesicles) believed to contain packets of a neurotransmitter (a chemical such as glutamate or aspartate) as shown in Figure 10.3.

Type 2: Inhibitory synapses with symmetrical membrane specializations; with smaller ellipsoidal or flattened vesicles. Gamma-amino butyric acid is an example of an inhibitory neurotransmitter.

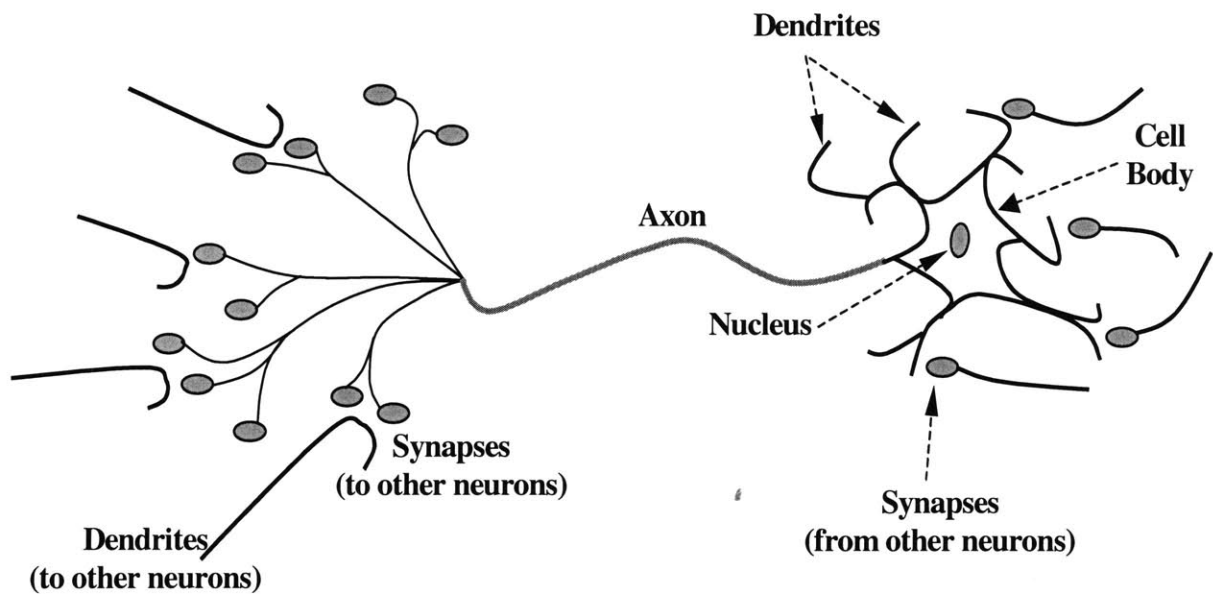


Figure 10.1 Biological neural networks

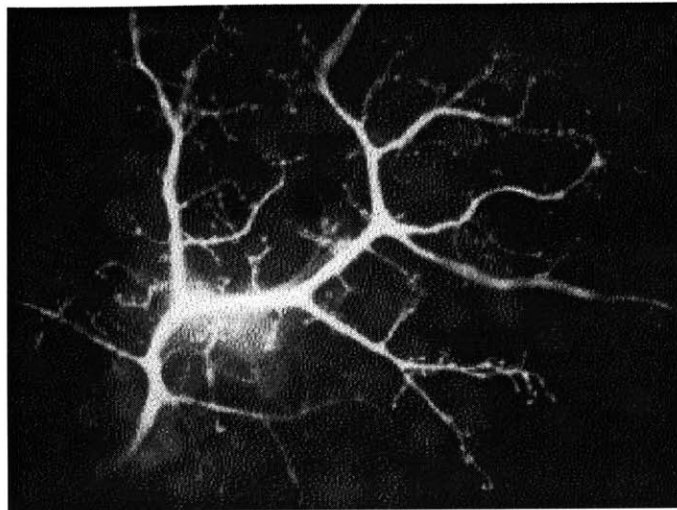


Figure 10.2 A single inter-neuron in the retina of a rabbit

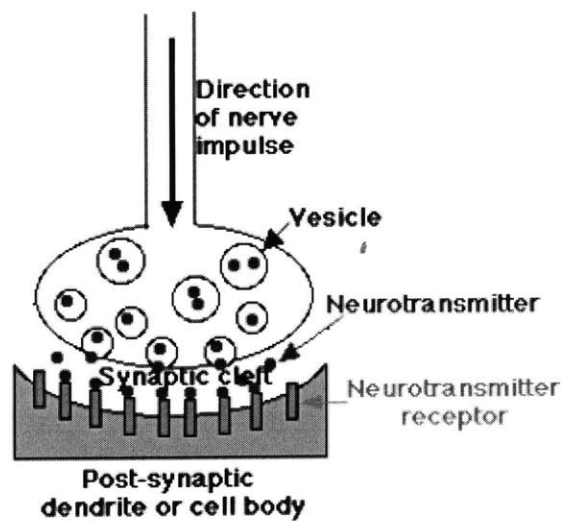


Figure 10.3 Synaptic connection and neurotransmitter

The following is paraphrased from Mehrotra et al. (1997). An electrostatic potential difference is maintained across the cell membrane, with the inside of the membrane being negatively charged. Ions diffuse through the membrane to maintain this potential

difference. Inhibitory or excitory signals from other neurons are transmitted to a neuron at its dendrites' synapses. The magintude of the signal received by a neuron (from another) depends on the efficiency of the synaptic transmission, and can be thought of as the strength of the connection between the neurons. The cell membrane becomes electrically active when sufficiently excited by the neurons making synapses onto this neuron. A neuron will fire (i.e. send an output impulse of about 100mV down its axon), if sufficient signals from other neurons fall upon its dendrites in a short period of time, called the period of latent summation. The neuron fires if its net excitation exceeds its inhibition by a critical amount, the threshold of the neuron. Firing is followed by a brief refractory period during which the neuron is inactive. If the input to the neuron remains strong, the neuron continues to deliver impulses at frequencies up to a few hundred impulses per second. It is this frequency which is often refered to as the output of the neuron. Impulses propagate down the axon of a neuron and reach up to the synapses, sending signal of various strengths down the dendrites of other neurons.

10.1.2 Artificial Neuron Networks (ANN)

To make it easy, the dicussion of artificial neural network should begin by introducing terminology that establishes the correspondence between biological and artificial neurons as shown in Table 10-1.

Table 10-1 Terminology between biological neural networks and artificial neural networks

Biological Terminology	Artificial Neural Network Terminology
Neuron	Node/Neuron/Unit/Cell
Synapse	Connection/Edge/Link
Synaptic Efficiency	Connection Strength/Weight
Firing Frequency	Node Output

Figure 10.4 describes a general model of artificial neural network, where x = input; w = weight; and Σ = summation; f = activation or transformation function. The neuron (node/unit/cell) is a processing element that takes a number of inputs, weights them, sums them up, and uses the result as the argument for a singular valued function, the activation or transformation function.

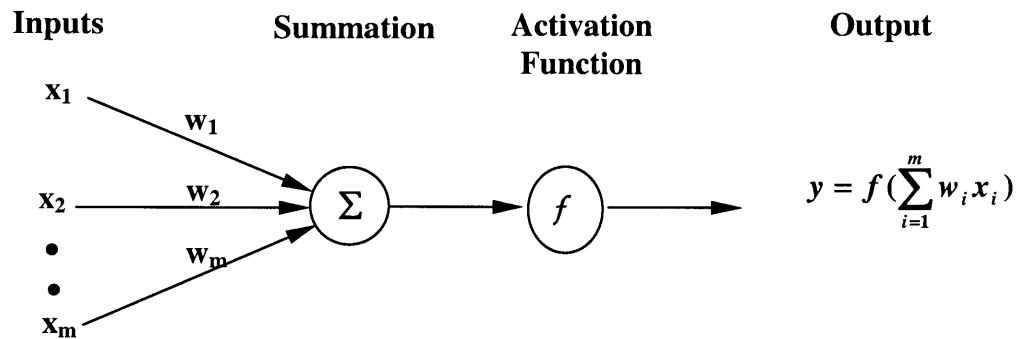


Figure 10.4 General details of a neuron

10.2 Type of Neural Networks

In terms of their structures or architectures, neural networks can be divided into two types: feedforward networks and recurrent networks.

10.2.1 Feedforward Networks

In a feedforward network, the neurons are generally grouped into layers. Signals flow from the input layer through to the output layer via connections, the neurons being connected from one layer to the next, but not within the same layer. Examples of feedforward networks include the multi-layer perceptron (MLP), the learning vector quantization (LVQ) network, the cerebellar model articulation control (CMAC) network, and the group method of data handling (GMDH) network. A feedforward network can be viewed as a graphical representation of a parametric function which takes a set of input

values and maps them to a corresponding set of output values. Figure 10.5 shows an example of a multi-layer perceptron, a feedforward network of a kind that is widely used in practical applications. Details of the multi-layer perceptron will be described in the next section.

Figure 10.6 shows a learning vector quantization (LVQ) network, which comprises three layers of neurons: an input buffer layer, a hidden layer and an output layer. The network is fully connected between the input and hidden layer and partially connected between the hidden and output layers, with each output neuron linked to a different cluster of hidden neurons. The weights of the connections between the hidden layer and output are fixed to 1. The weights of the input-hidden neuron connections form the components of the *reference vector* (i.e. one reference vector is assigned to each hidden neuron). They are modified during the training of the network. Both the hidden neurons and the output neuron have binary output.

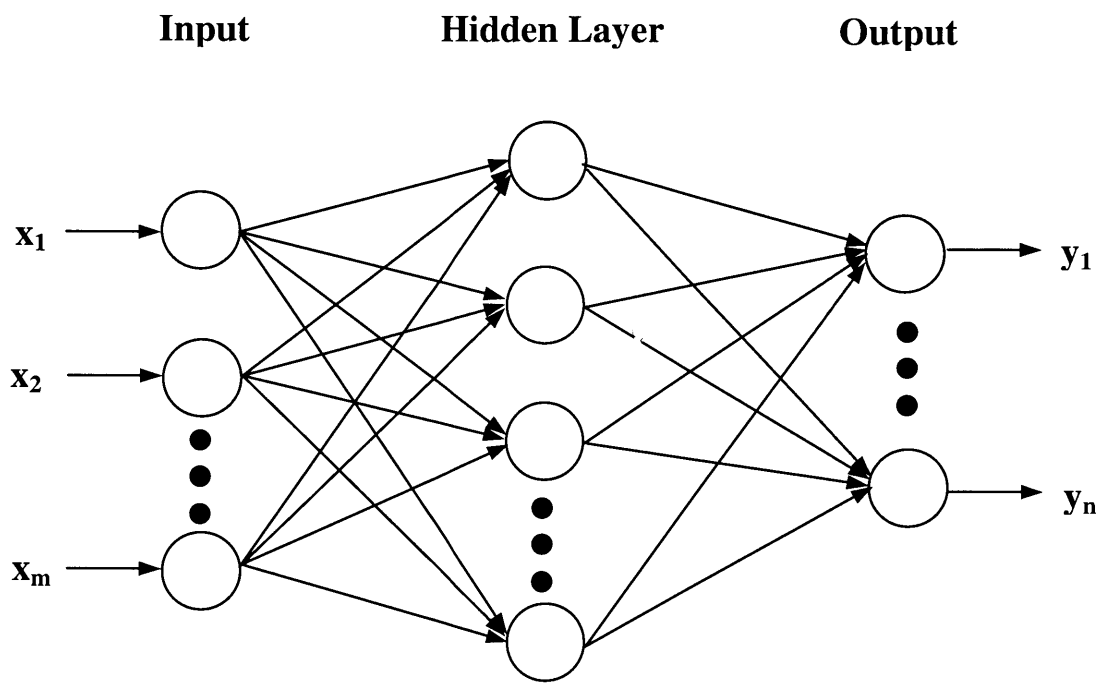


Figure 10.5 A feedforward network (multi-layer perceptron)

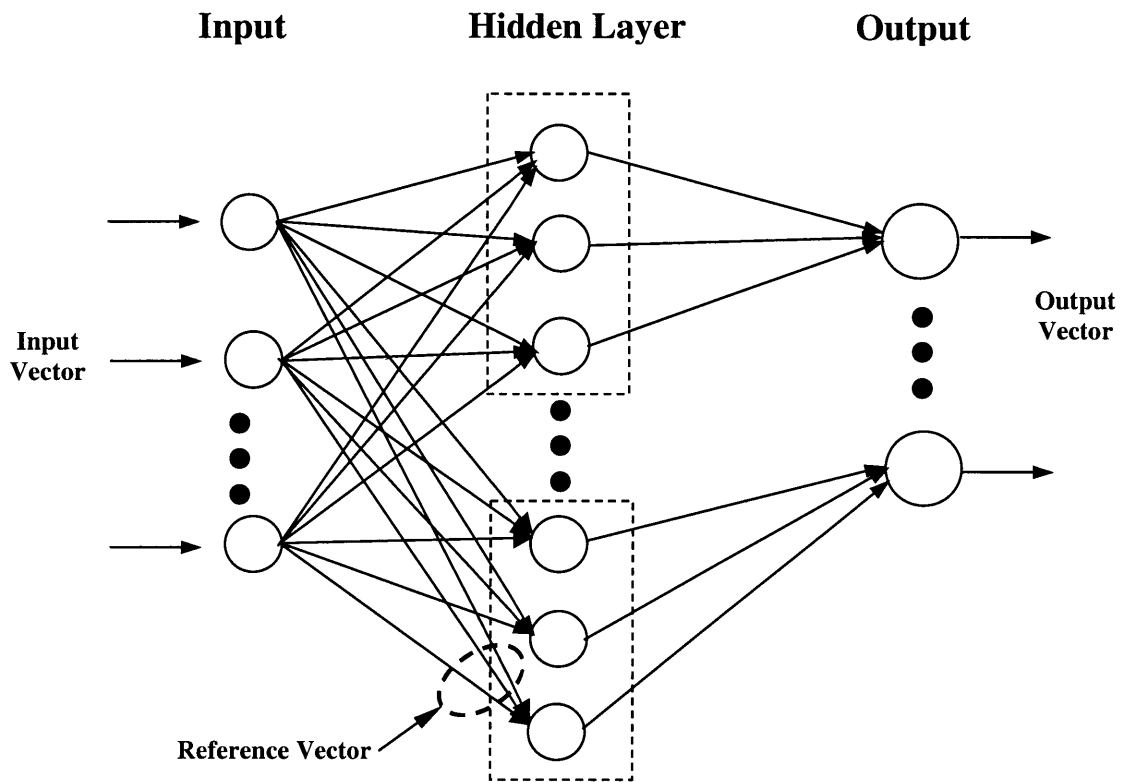


Figure 10.6 Learning vector quantization network

The cerebellar model articulation control (CMAC) can be considered a supervised feedforward neural network that models the structure and function of the part of brain known as cerebellum. CMAC is a kind of memory, or table look-up mechanism that is capable of learning. A basic CMAC module is shown in Figure 10.7.

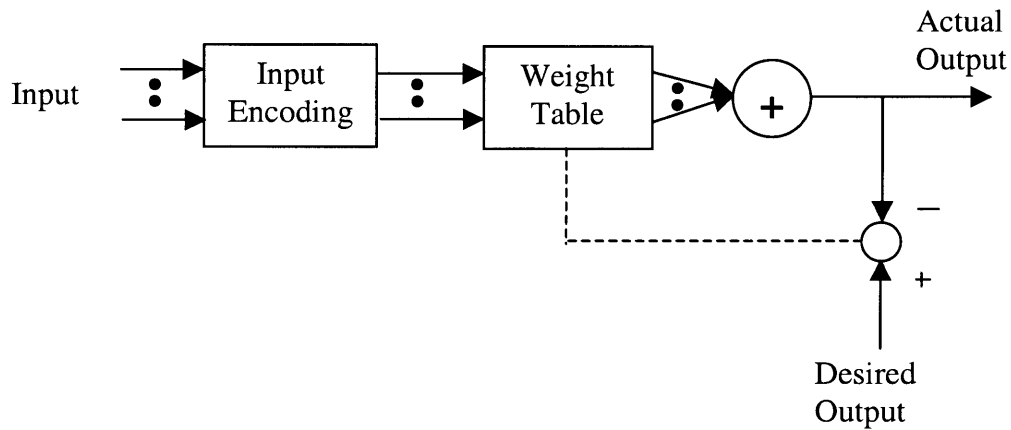


Figure 10.7 A basic CMAC module

As illustrated in Figure 10.8, unlike the feedforward neural networks previously described, which have a fixed structure, a GMDH has a structure in which the layer number in the network increases during training. Each neuron in a GMDH network usually has two input x_1 and x_2 and produces an output y that is a quadratic combination of these inputs.

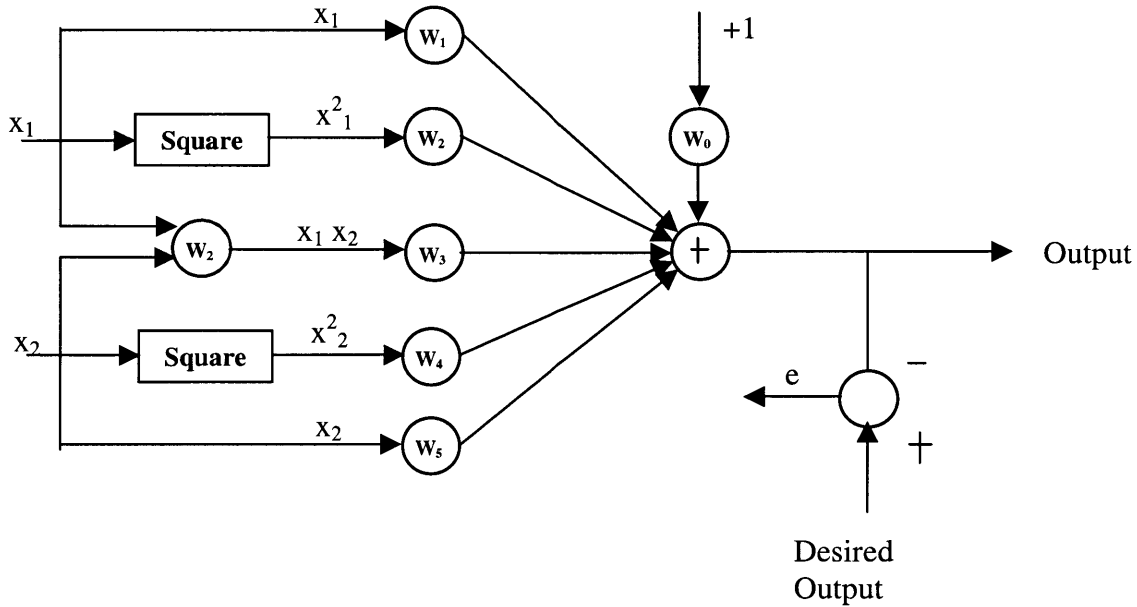


Figure 10.8 Detail of a GMDH network

10.2.2 Recurrent Networks

In a recurrent network, the outputs of some neurons are fed back to the same neurons or to neurons in preceding layers. Thus, signals can flow in both forward and backward directions. Examples of recurrent networks include the Hopfield network, the Elman network and the Jordan network. Recurrent networks have a dynamic memory: their outputs at a given instant reflect the current input as well as previous inputs and outputs. Figure 10.9 shows a version of Hopfield network. It has a single layer of neurons (i.e. no hidden layer), each connected to all the others, giving it a “recurrent” structure.

Figure 10.10 and Figure 10.11 show an Elman net and a Jordan net, respectively. These networks have a multi-layered structure similar to the structure of the multi-layer perceptron. In both nets, in addition to an ordinary hidden layer, there is another special hidden layer sometimes called the context or state layer. This layer receives feedback

signals from the ordinary hidden layer (i.e. in the case of of an Elman net) or from the output layer (i.e. in the case of a Jordan net). The Jordan net also has connections from each neuron in the context layer back to itself. With both nets, the outputs of neurons in the context are fed forward to the hidden layer.

The multi-layer feedforward neural network is the most popular model among other types of artificial neural network models since the network is not very complicated to implement compared to other types of networks described above. Moreover, multi-layer feedforward neural networks have been applied successfully in various areas of engineering problems.

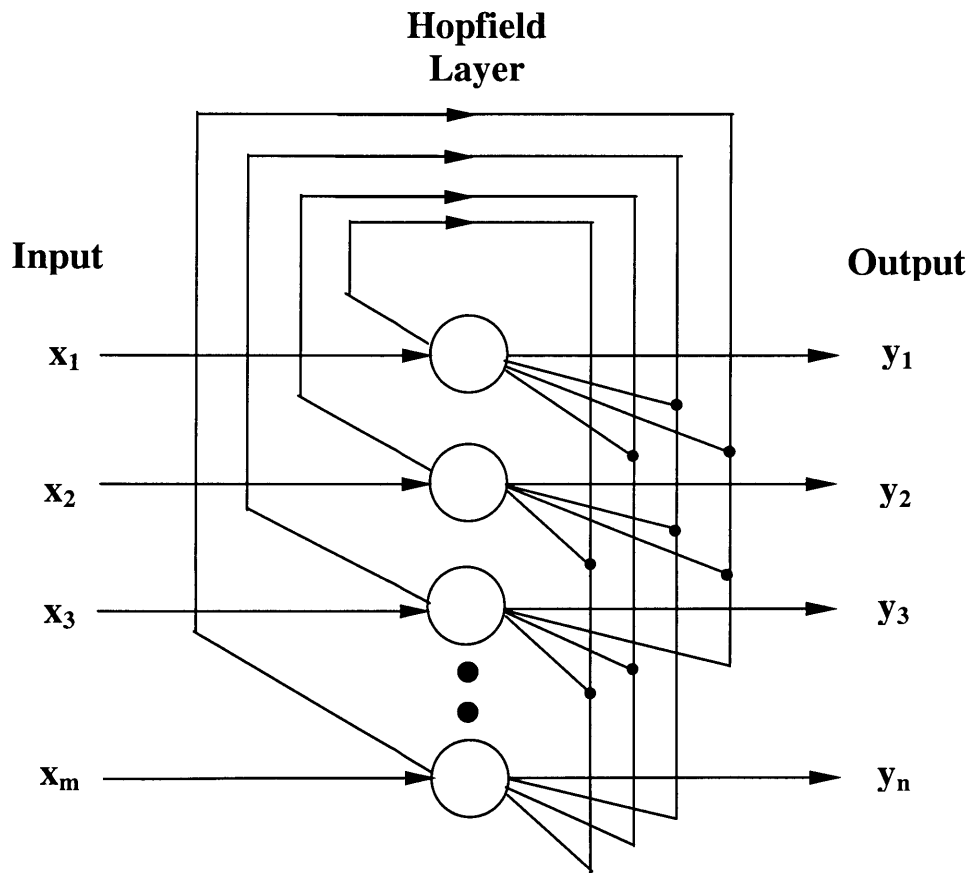


Figure 10.9 A Hopfield network

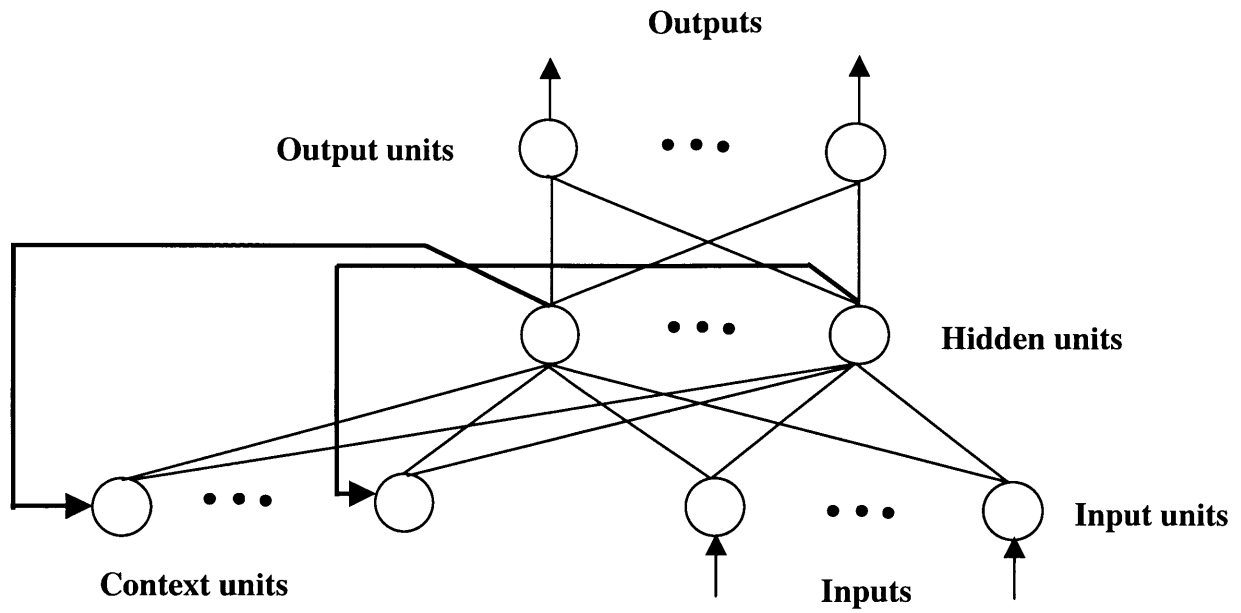


Figure 10.10 An Elman network

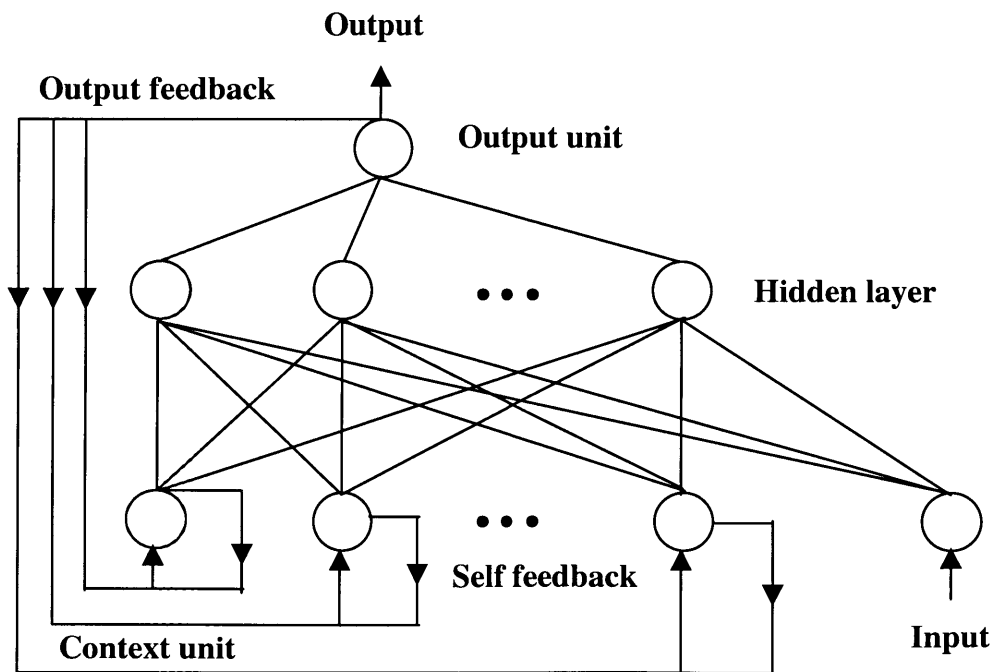


Figure 10.11 A Jordan network

10.3 Neural Network Modeling

Many neural network models have been introduced as described earlier. It is found that the multi-layer (feed forward) neural network is the most popular neural network used recently. It has been applied successfully to solve many difficult and diverse problems by training them with a highly popular learning algorithm known as *back-propagation algorithm* introduced by Rumelhart et al. (1986). This section introduces basic aspects of the feedforward mechanism of the multi-layer neural network. Details of the back-propagation will be explained in the next section.

As can be seen in Figure 10.5, the general architecture of a multi-layer feedforward neural network consists of an input layer, one or multiple hidden layers and an output layer. The units in the hidden layer play a key role in the internal representation of the input patterns. Figure 10.12 illustrates a neural network in a layered feed-forward circuit. A problem is presented to the network as an array of input values (x_i). The input neurons transmit these values across the links to the second layer of neurons. Each link has a weight ($w_{j,i}$) used to multiply transmitted values. The weighted values converging at a neuron in the hidden layer are summed along with a bias (b_j) associated with that neuron. The result is then put through a transformation function to generate a signal result for the neuron. The results of the hidden neurons are then transmitted across their outgoing links to the neurons in the output layer. As before, these values are weighted ($w_{k,j}$) and biased (b_k) during transmission across the links, then summed at the output neuron and put through a transformation function. The function signal generated at the output neuron(s) is the network's solution or output (y_k) to the problem presented at the inputs. All neurons within a layer in this type of network operate synchronously in the sense that, at any point in time, they will be at the same stage in processing.

Typically, there will be many neurons in each layer in such a network, including the output layer, and often there will be more than one hidden layer. The following equations provide a generalized description of the mode of operation of the feedforward network, independent of the number of neurons in each layer:

$$y_j = f\left(\sum_{i=1}^m (w_{j,i} \cdot x_i) + b_j\right) \tag{10-1}$$

$$y_k = f\left(\sum_{j=1}^n (w_{k,j} \cdot y_j) + b_k\right) \tag{10-2}$$

where x_i = input value; y_j = signal result from hidden node j ; y_k = signal or output value generated at neuron k ; $w_{j,i}$ and $w_{k,j}$ = weight on the connection between the input node i and the hidden node j , and weight on the connection between the hidden node j and the output node k , respectively; b_j and b_k = biases; and $f(\)$ = transformation or activation function used to transform the incoming values and transfer them to the next layer.

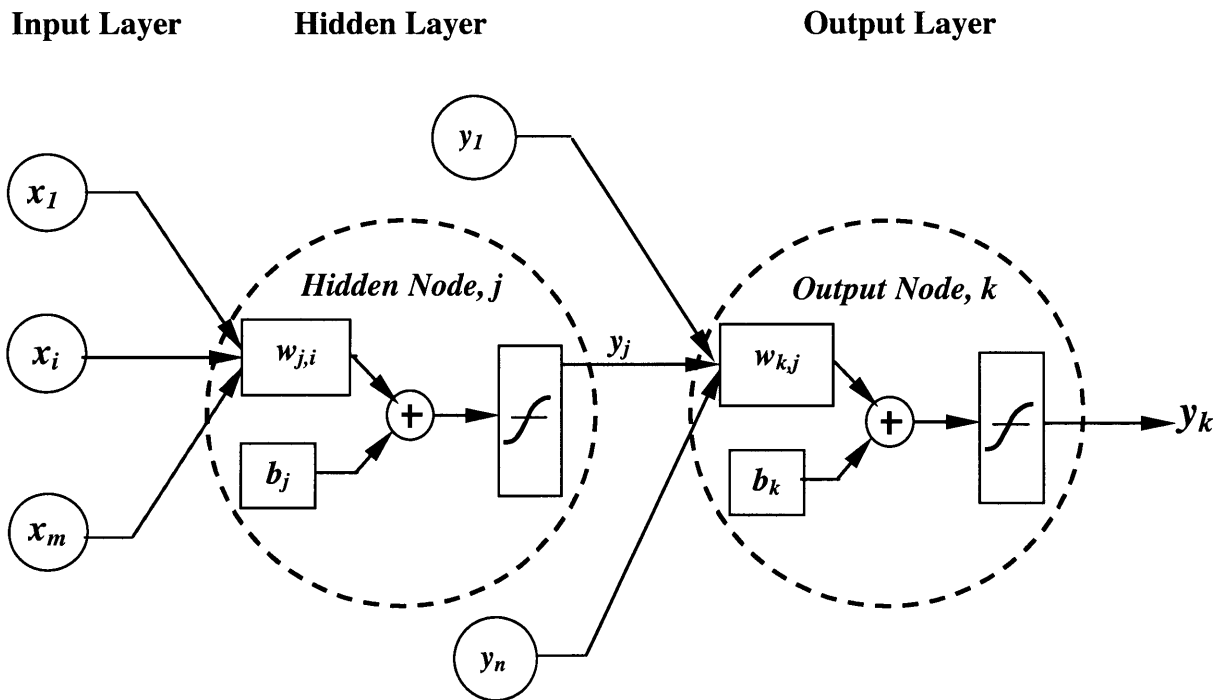


Figure 10.12 Schematic diagram of neurons and transmission processes

There are three basic types of activation or transformation function:

1. *Threshold or Step Function*: for this type of activation function as shown in Figure 10.13, it can be expressed as:

$$f(u) = \begin{cases} 1 & \text{if } u \geq 0 \\ 0 & \text{if } u < 0 \end{cases}$$

(10-3)

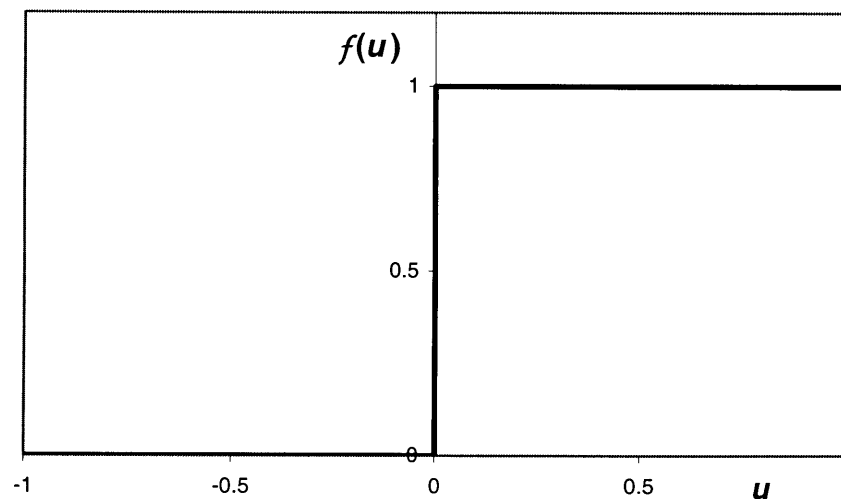


Figure 10.13 Threshold or step function

2. *Linear Function*: the function as depicted in Figure 10.14 can be described as:

$$f(u) = w \cdot u + b$$

(10-4)

where w = slope of the straight line and b = the $f(u)$ -intercept.

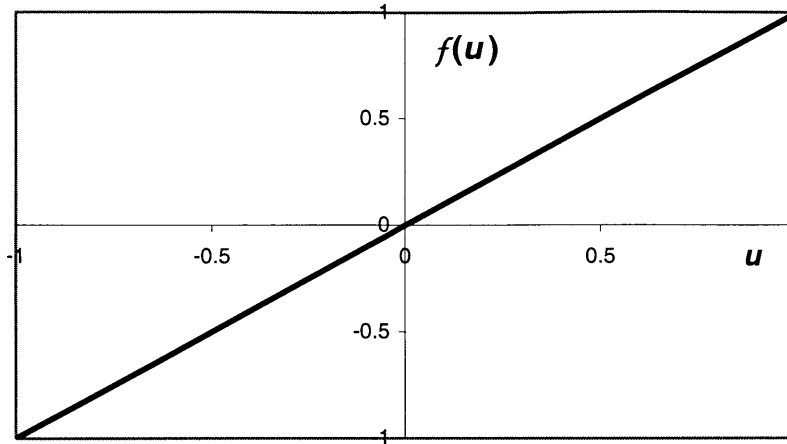


Figure 10.14 Linear Function

3. *Sigmoid Function*: the function is the most common transformation function used in the construction of artificial neural network. The function is composed of the sigmoid function and the tangent sigmoid function. The graph of a sigmoid function has the shape of a flattened “S,” hence the name “sigmoid.” The sigmoid function is expressed as:

$$f(u) = \frac{1}{1 + e^{-wu}}$$

(10-5)

where w is the slope parameter. The function has lower bound value of 0 and upper bound value of 1 as shown in Figure 10.15.

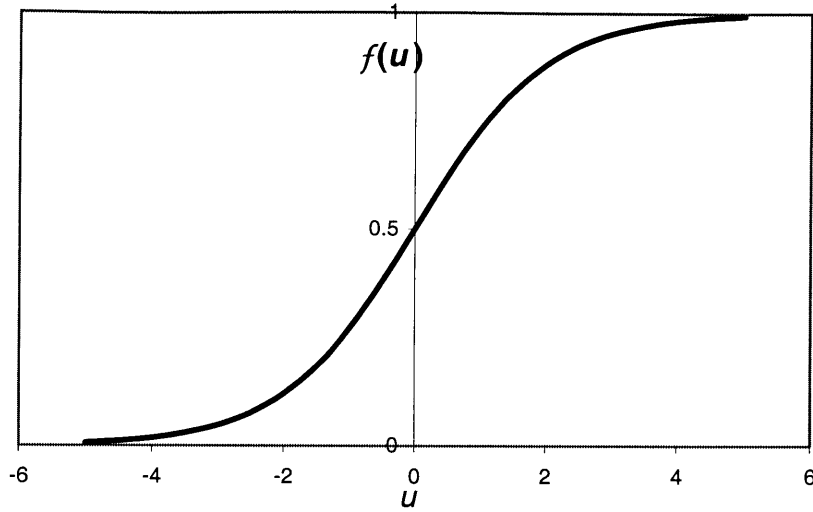


Figure 10.15 Sigmoid function

Another sigmoid function known as the tangent sigmoid function giving output values between -1 and 1 (Figure 10.16) is expressed as:

$$f(u) = \frac{e^{wu} - e^{-wu}}{e^{wu} + e^{-wu}}$$

(10-6)

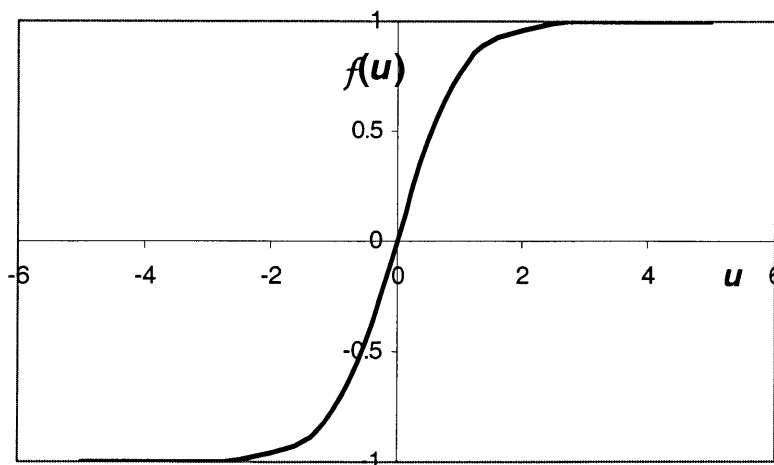


Figure 10.16 Tangent sigmoid function

The advantage of these sigmoid functions are that they are continuous and smooth, without gaps or corners so that they can be differentiable everywhere. Furthermore, by varying the parameter w : see Figure 10.17, one can obtain sigmoid functions with different slopes that enable one to fit various data patterns. All these sigmoid functions serve equally well, and they are interchangeable. The differences in their bounds may lead to a preference for one or the others, depending on the range of normalized values desired (0 to 1 or -1 to 1), because the network output must fall between these bounds. The bounds do not, however, determine the range of possible inputs to the network, which may take any values, regardless of which sigmoid function is chosen.

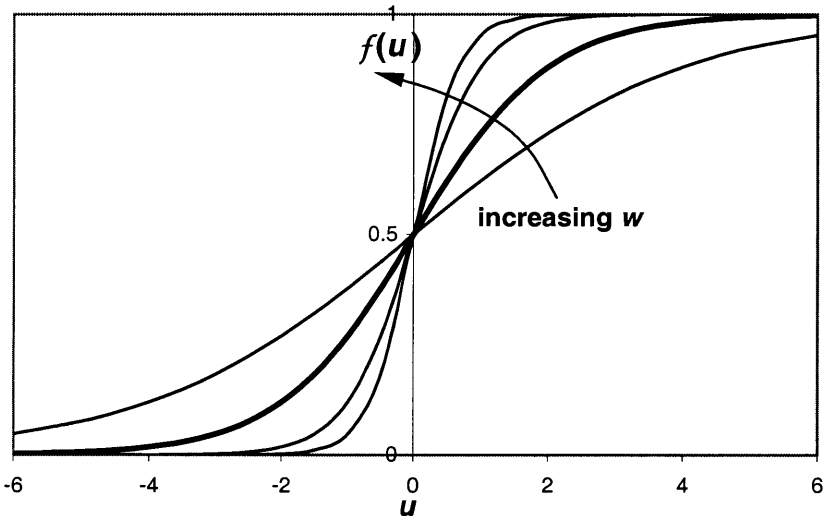


Figure 10.17 Sigmoid function with different slope parameters, w

10.4 Learning Processes Using Back-Propagation Algorithm

The property that is of primary significance for a neural network is the ability of the network to learn from samples and to improve its performance through learning. A neural network learns about relationships between input and output data through an interactive process of adjustment applied to its weights and bias levels. Ideally, the network becomes more knowledgeable about the relationships after each iteration of the learning process.

Basically, back-propagation learning consists of two passes through the different layers of the network: a forward pass and a backward pass. In the forward pass as described in Section 10.3, input pattern is applied to the nodes of the network, and its effect propagates through the network layer-by-layer. Finally, an output is produced as the actual response of the network. If the response is different from the desired value, error corrections will be required to adjust weights and bias levels in the network accordance with the error value. Hence, the back-propagation or error back propagation algorithm is used for this purpose.

As shown in Figure 10.5, the network architecture of a multi-layer perceptron is fully connected. This means that a neuron in any layer of the network is connected to all nodes/neurons in the previous layer. Signal flow through the network progresses in a forward direction, from left to right and on a layer-by-layer basis. Figure 10.18 depicts a portion of the multi-layer perceptron. In the back propagation network, two kind of signals are identified in this network:

- (1) **Function Signal:** a function signal is an input signal (stimulus) that comes in at the input end of the network, propagates forward (neuron by neuron) through the network, and emerges at the output end of the network as an output signal.
- (2) **Error Signal:** an error signal originates at an output neuron of the network, and propagates backward (layer by layer) through the network.

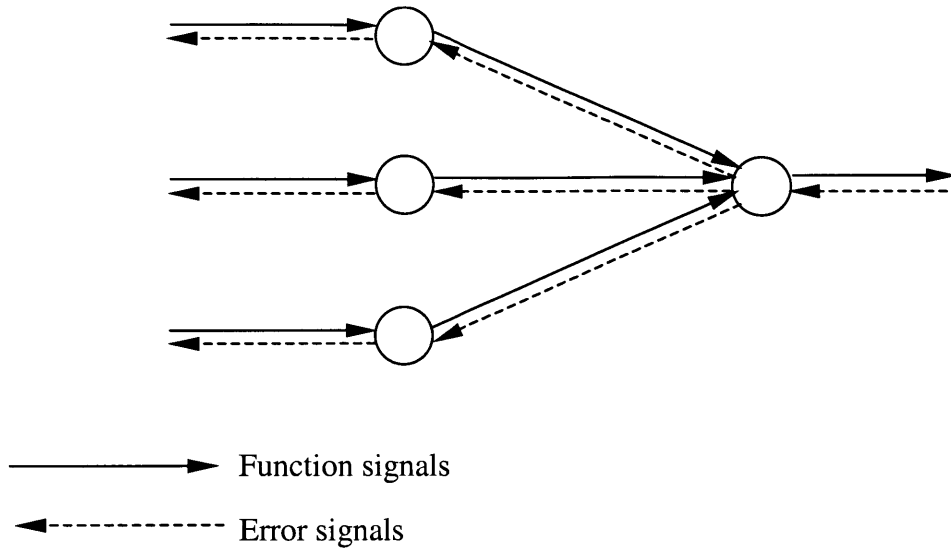


Figure 10.18 Directions of two basic signal flows in a multi-layer perceptron: forward propagation of function signals and back-propagation of error signals

To illustrate the back-propagation algorithm, consider a simple case of a neuron j constituting the only computational node in the output layer of a feedforward neural network, as depicted in Figure 10.19. The argument n denotes the time step of an iterative process also known as epoch involved in adjusting the weights of neuron j . Neuron j is driven by function signals produced by one or more previous layers. The output signal of neuron j is denoted by $y_j(n)$. This output signal is compared to a desired response or target output, denoted by $d_j(n)$. Consequently, an error signal, denoted by $e_j(n)$, is produced:

$$e_j(n) = d_j - y_j(n)$$

(10-7)

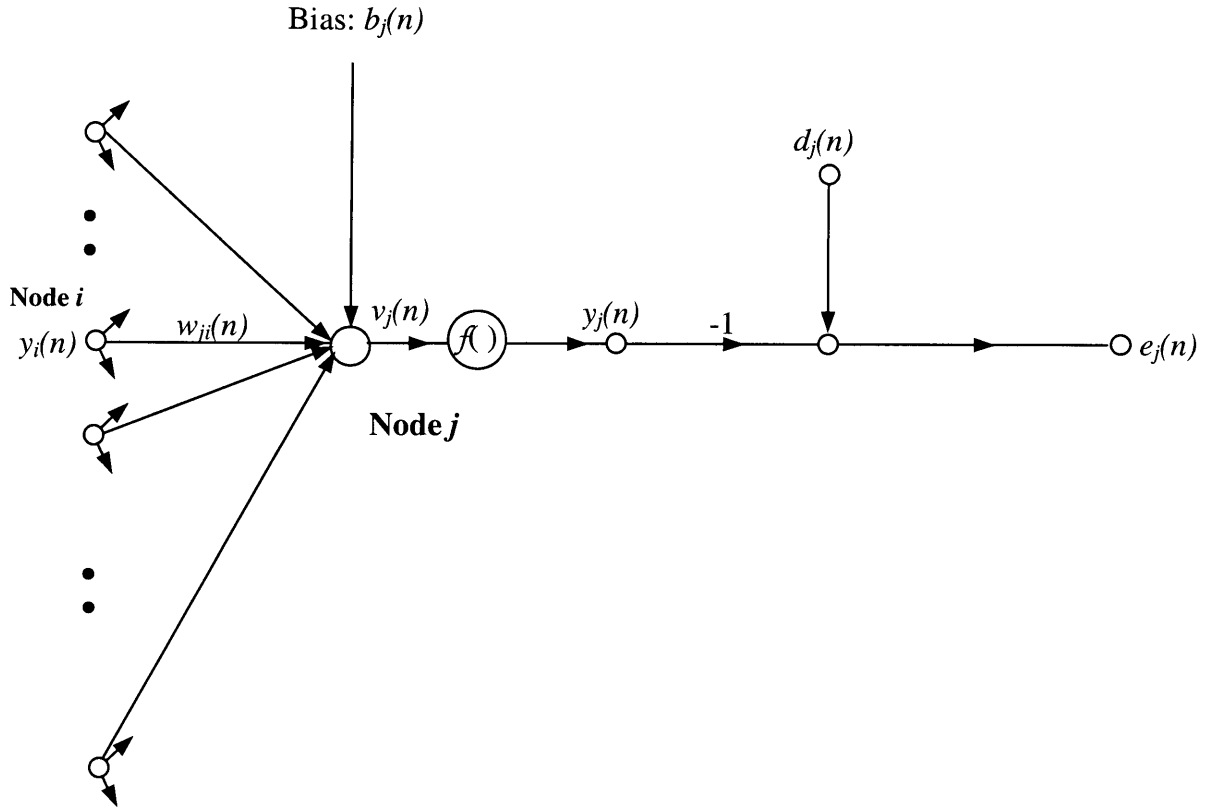


Figure 10.19 Signal-flow schematic diagram showing the detail of output neuron j

The error signal $e_j(n)$ actuates a control mechanism, the purpose of which is to apply a sequence of corrective adjustments to the weights of neuron j . The corrective adjustments are designed to make the output signal $y_j(n)$ come closer to the desired response $d_j(n)$ in a step-by-step manner. This objective is achieved by minimizing a cost function or index of performance, $E_0(n)$, defined in term of the error signal as:

$$E_0(n) = \frac{1}{2} e_j^2(n) \tag{10-8}$$

Correspondingly, the value of the total error energy is obtained by summing (10-8) over all neurons in the output layer where can be expressed as:

$$E(n) = \frac{1}{2} \sum_{j \in C} e_j^2(n) \quad (10-9)$$

where the set C includes all the neurons in the output layer of the network. The average squared error energy shown below is obtained by summing $E(n)$ over all n and then normalizing with respect to the size N that represents the total number of patterns or samples, which are presented to the neural network as the training set.

$$E_{av} = \frac{1}{N} \sum_{n=1}^N E(n) \quad (10-10)$$

The error energy $E(n)$, and therefore the average error energy $E_{av}(n)$, is a function of all free parameters (i.e. weights and bias levels) of the network. For a given training set, $E_{av}(n)$ represents the cost function as a measure of learning performance. The objective of the learning process is to adjust the weights and biases in the network to minimize $E_{av}(n)$.

Consider Figure 10.19, which depicts neuron j being fed by a set of function signals produced by a layer of neurons to its left. The induced local field $v_j(n)$ produced at the input of the activation function associated with neuron j is therefore,

$$v_j(n) = \sum_{i=0}^m w_{ji}(n) y_i(n) + b_j(n) \quad (10-11)$$

where m is the total number of inputs and $b_j(n)$ is the bias value applied to neuron j : see Figure 10.19. Hence, the function signal $y_j(n)$ appearing at the output of neuron j at iteration n is

$$y_j(n) = f_j(v_j(n)) \quad (10-12)$$

The back-propagation algorithm applies a correction $\Delta w_{ji}(n)$ to the weight $w_{ji}(n)$, which is proportional to the partial derivative $\partial E(n)/\partial w_{ji}(n)$ as shown below. According to the chain rule of calculus, we may express this gradient as:

$$\frac{\partial E(n)}{\partial w_{ji}(n)} = \frac{\partial E(n)}{\partial e_j(n)} \cdot \frac{\partial e_j(n)}{\partial y_j(n)} \cdot \frac{\partial y_j(n)}{\partial v_j(n)} \cdot \frac{\partial v_j(n)}{\partial w_{ji}(n)}$$

(10-13)

The partial derivative $\partial E(n)/\partial w_{ji}(n)$ represents a sensitivity factor, determining the direction of search in weight space for the weight $w_{ji}(n)$.

Differentiating both sides of (10-9) with respect to $e_j(n)$, we get

$$\frac{\partial E(n)}{\partial e_j(n)} = e_j(n)$$

(10-14)

Differentiating both sides of (10-7) with respect to $y_j(n)$, we get

$$\frac{\partial e_j(n)}{\partial y_j(n)} = -1$$

(10-15)

Next, differentiating (10-12) with respect to $v_j(n)$, we get

$$\frac{\partial y_j(n)}{\partial v_j(n)} = f'_j(v_j(n))$$

(10-16)

where the use of prime signifies differentiation with respect to the argument. Finally, differentiating (10-11) with respect to $w_{ji}(n)$ yields

$$\frac{\partial v_j(n)}{\partial w_{ji}(n)} = y_i(n) \tag{10-17}$$

The use of (10-12) and (10-17) in (10-13) yields

$$\frac{\partial E(n)}{\partial w_{ji}(n)} = -e_j(n) \cdot f'_j(v_j(n)) \cdot y_i(n) \tag{10-18}$$

The correction $\Delta w_{ji}(n)$ applied to $w_{ji}(n)$ is defined by the *delta rule*:

$$\Delta w_{ji}(n) = -\eta \frac{\partial E(n)}{\partial w_{ji}(n)} \tag{10-19}$$

where η is the learning-rate parameter of the back-propagation algorithm. Note that this rule is based on the idea of continuously modifying the strengths of the input connections to reduce the difference (the delta) between the desired output value and the actual output of a neuron. This rule changes the connection weights in the way that minimizes the mean squared error, $E(n)$, of the network. The error is back propagated into previous layers one layer at a time. The process of back-propagating the network errors continues until the first layer is reached.

The use of the minus sign in (10-19) accounts for *gradient descent* in weight space (i.e. seeking a direction for weights change that reduces the value of $E(n)$). A simple illustration of the gradient decent is shown in Figure 10.20.

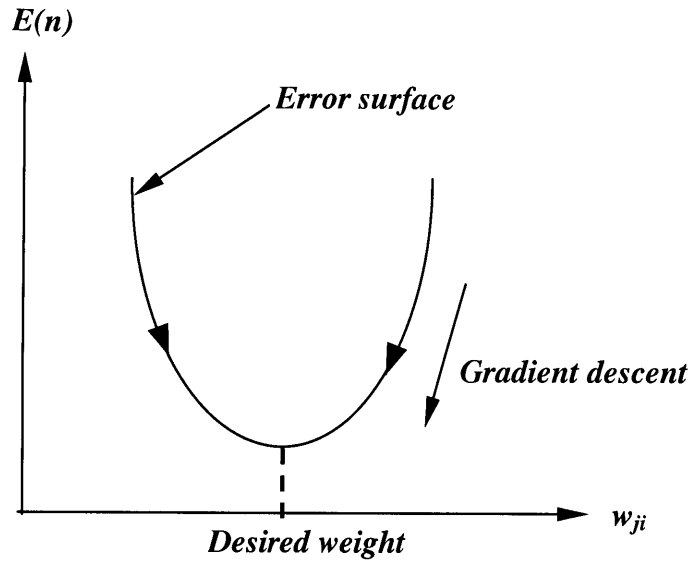


Figure 10.20 Gradient descent in weight space

Accordingly, the use of (10-18) and (10-19) yields

$$\Delta w_{ji} = \eta \cdot \delta_j(n) \cdot y_i(n) \tag{10-20}$$

where the local gradient $\delta_j(n)$ is defined by

$$\delta_j(n) = -\frac{\partial E(n)}{\partial v_j(n)} = -\frac{\partial E(n)}{\partial e_j(n)} \cdot \frac{\partial e_j(n)}{\partial y_j(n)} \cdot \frac{\partial y_j(n)}{\partial v_j(n)} = -e_j(n) \cdot f'_j(v_j(n)) \tag{10-21}$$

The local gradient points to required changes in weights. According to (10-21), the local gradient $\delta_j(n)$ for output neuron j is equal to the product of the corresponding error signal $e_j(n)$ for that neuron and the derivative $f'_j(v_j(n))$ of the associated activation function.

From (10-20) and (10-21), note that a key factor involved in the calculation of the weight adjustment $\Delta w_{ji}(n)$ is the error signal $e_j(n)$ at the output of neuron j . In this context, we

may identify two distinct cases, depending on where in the network neuron j is located. In case 1, neuron j is an output node. This case is simple to handle because each output node of the network is supplied with a desired response of its own, making it a straightforward matter to calculate the associated error signal. In case 2, neuron j is a hidden node. Even though hidden neurons are not directly accessible, they share responsibility for any error made at the output of the network.

Case 1 Neuron j is an Output Node

When neuron j is located in the output layer of the network, it is supplied with a desired response of its own. We may use (10-7) to compute the error signal $e_j(n)$ associated with this neuron; see also Figure 10.19. Having determined $e_j(n)$, it is a straightforward matter to compute the local gradient $\delta_j(n)$ using (10-21).

Case 2 Neuron j is a Hidden Node

When neuron j is located in a hidden of the network, there is no desired response for that neuron. Hence, the error signal for a hidden node would have to be determined recursively in terms of the error signals of all the neurons to which that hidden node is directly connected; this is where the development of the back-propagation algorithm gets complicated. Consider the situation shown in Figure 10.21, which depicts neuron j as a hidden node of the network.

As described earlier, the local gradient points to required changes in weights. According to (10-21), the local gradient $\delta_j(n)$ can be redefined for hidden neuron j is equal to the product of the corresponding error signal $e_j(n)$ for that neuron and the derivative $f'_j(v_j(n))$ of the associated activation function.

$$\delta_j(n) = -\frac{\partial E(n)}{\partial v_j(n)} = -\frac{\partial E(n)}{\partial y_j(n)} \cdot \frac{\partial y_j(n)}{\partial v_j(n)} = -\frac{\partial E(n)}{\partial y_j(n)} \cdot f'_j(v_j(n)) \tag{10-22}$$

where neuron j is a hidden node. From Figure 10.21, we see that

$$E(n) = \frac{1}{2} \sum_{k \in C} e_k^2(n) \tag{10-23}$$

where neuron k is an output node (i.e. index k used in place of index j in order to avoid confusion in Case 2). Differentiating (10-23) with respect to the function signal $y_j(n)$, we get

$$\frac{\partial E(n)}{\partial y_j(n)} = \sum_k e_k \frac{\partial e_k(n)}{\partial y_j(n)} \tag{10-24}$$

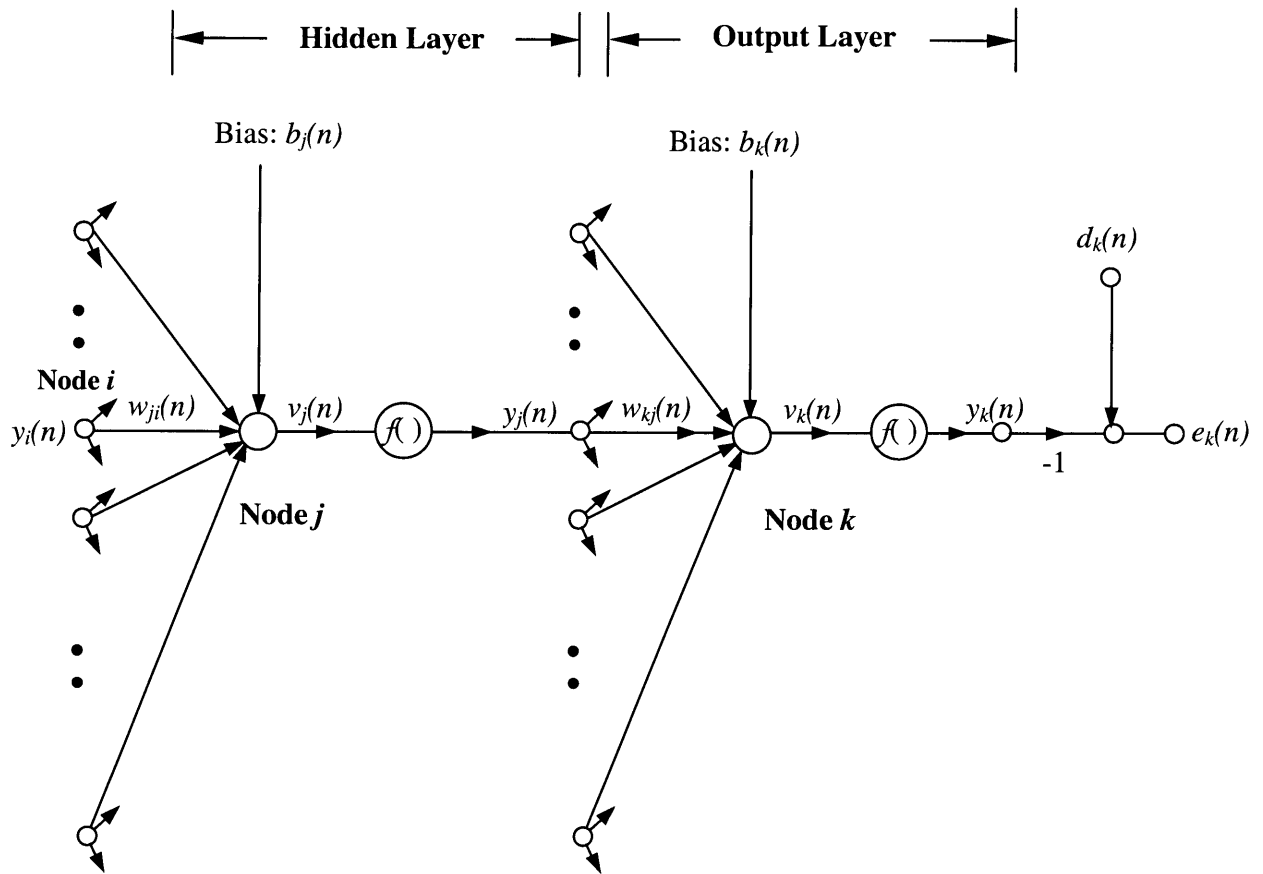


Figure 10.21 Signal-flow schematic diagram showing the detail of output neuron k connected to hidden neuron j

Applying the chain rule to (10-24):

$$\frac{\partial E(n)}{\partial y_j(n)} = \sum_k e_k(n) \frac{\partial e_k(n)}{\partial v_k(n)} \frac{\partial v_k(n)}{\partial y_j(n)} \quad (10-25)$$

However, from Figure 10.21, note that the output error signal is

$$e_k(n) = d_k(n) - y_k(n) = d_k(n) - f_k(v_k(n)) \quad (10-26)$$

where k is an output node. Differentiating both sides of (10-26) with respect to $v_k(n)$. Hence,

$$\frac{\partial e_k(n)}{\partial v_k(n)} = -f'_k(v_k(n)) \quad (10-27)$$

From Figure 10.21, for neuron k , the induced local field is

$$v_k(n) = \sum_{j=0}^m w_{kj}(n) \cdot y_j(n) + b_k \quad (10-28)$$

where m is the total number of inputs and b_k is the bias value applied to neuron k .

Differentiating (10-28) with respect to $y_i(n)$ yields

$$\frac{\partial v_k(n)}{\partial y_j(n)} = w_{kj}(n) \quad (10-29)$$

By using (10-27) and (10-29) in (10-25):

$$\frac{\partial E(n)}{\partial y_j(n)} = -\sum_k e_k(n) \cdot f'_k(v_k(n)) \cdot w_{kj}(n) = -\sum_k \delta_k(n) \cdot w_{kj}(n) \quad (10-30)$$

Note that the definition of the local gradient δ_k was given in (10-22) with the index k substituted for j . Finally, using (10-30) in (10-22), we get the back-propagation formula for the local gradient $\delta_j(n)$ as described:

$$\delta_j(n) = f'_j(v_j(n)) \cdot \sum_k \delta_k(n) \cdot w_{kj}(n) \quad (10-31)$$

Note that neuron j is a hidden node. Figure 10.22 shows the signal flow representing (10-31).

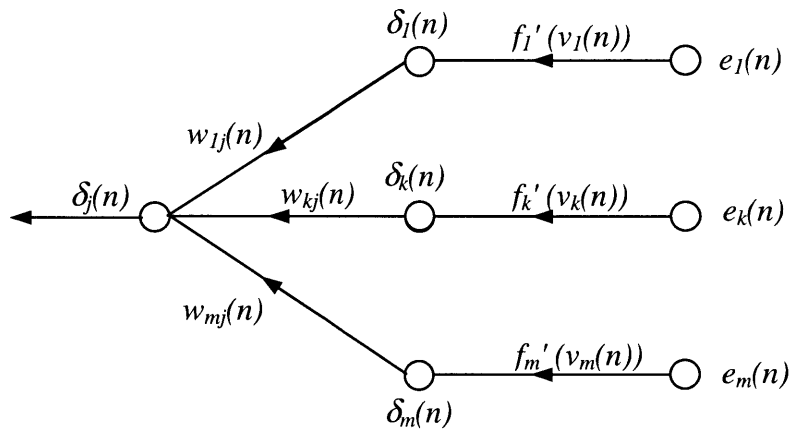


Figure 10.22 Signal flow of a part of the adjoint system pertaining to back-propagation of error signal

The factor $f'_j(v_j(n))$ involved in the computation of the local gradient $\delta_j(n)$ in (10-31) depends solely on the activation function associated with hidden neuron j . The remaining factor involved in this computation, namely the summation over k , depends on two sets of terms. The first set of terms, the $\delta_k(n)$, requires knowledge of the error signal $e_k(n)$, for all neurons that lie in the layer to the immediate right of hidden neuron j , and that are directly connected to neuron j : see Figure 10.21. The second set of terms, the $w_{kj}(n)$, consists of the weights associated with these connections.

The back-propagation algorithm can be summarized as follows: first, the correction $\Delta w_{ji}(n)$ applied to the weight connecting neuron i to neuron j is defined by the delta rule:

$$\begin{pmatrix} \text{Weight} \\ \text{correction} \\ \Delta w_{ji}(n) \end{pmatrix} = \begin{pmatrix} \text{Learning rate} \\ \text{parameter} \\ \eta \end{pmatrix} \cdot \begin{pmatrix} \text{Local} \\ \text{gradient} \\ \delta_j(n) \end{pmatrix} \cdot \begin{pmatrix} \text{Input signal} \\ \text{of neuron } j \\ y_i(n) \end{pmatrix} \quad (10-32)$$

Second, the local gradient $\delta_j(n)$ depends on whether neuron j is an output node or a hidden node:

1. If neuron j is an output node, $\delta_j(n)$ equals the product of the derivative $f'_j(v_j(\mathbf{n}))$ and the error signal $e_j(n)$, both of which are associated with neuron j : see (10-21).
2. If neuron j is a hidden layer, $\delta_j(n)$ equals the product of the associated derivative $f'_j(v_j(\mathbf{n}))$ and the weighted sum of the local gradient computed for the neurons in the next hidden or output layer that are connected to neuron j : see (10-31).

10.5 Number of Hidden Neurons in Neural Networks

Generally, there is no direction and precise method for determining the most appropriate number of neurons to include in each hidden layer. This problem becomes more complicated as the number of hidden layers in the network increases. From the concept of the neural network, it appears that increasing the number of hidden neurons provides a greater potential for developing a solution that maps or fits closely the training patterns since they increase the complexity of function calculation within the network. However, a large number of hidden neurons can lead to a solution that, while mapping the training

points closely, deviates dramatically from the optimum trend as will be discussed in the next section. Furthermore, a large number of hidden neurons slow down operation of the network, both during training and in use.

To obtain the optimum number of hidden nodes for a given problem requires a pilot experiment. The experiment should begin with an intermediate number of samples. Figure 10.23 illustrates an example of the data processing, in which the pilot experiment set is a subset of all data sets. In the pilot experiment data set, the samples are divided into a training set and a validation set. Networks with different numbers of hidden nodes will be trained all the way to the convergence on the training samples, measuring their performance on the validation set, and choosing the network that yields the best performance of the validation set. Finally, this selected network model will be used for the whole data set. Details of this experiment and its training will be presented in the next chapter.

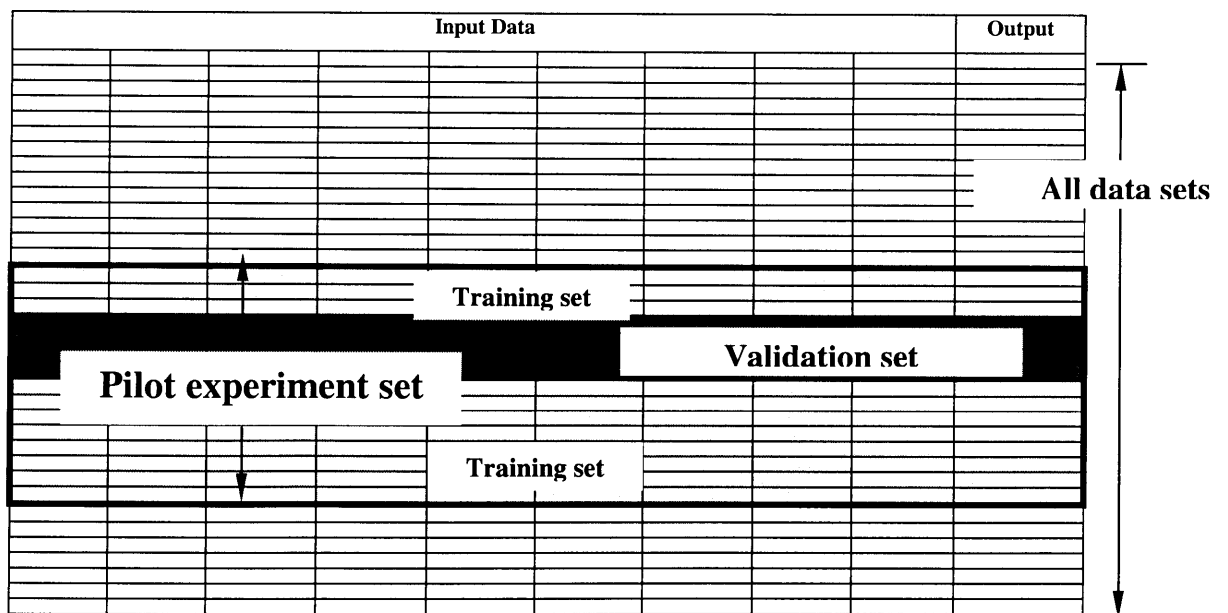


Figure 10.23 An example of data processing for the neural network modeling

10.6 Number of Samples in Training Set

An important factor that can significantly influence a network's ability to learn and generalize is the number of samples/patterns in the training set. Since to ensure that the network can properly map input training data to the target/desired output, it is essential that the samples in the training set presented to the network is selected to cover the upper bound and lower bound of the problem that one want to solve as shown in Figure 10.24.

In general, increasing the number of samples provides more information for the network to learn more about the relationship between input data and target outputs and can compensate for the noise or the error in the data. Accordingly, it leads to increase the potential level of accuracy that can be achieved by the network.

At the beginning, a pilot experiment as described above should be performed to determine the appropriate network architecture (i.e. number of layers, number of hidden nodes, and number of training epoch). The first experiment may use a relatively small to intermediate number of training samples instead of a large number of data (Figure 10.23). In other words, this experiment is used as a parametric study to verify the efficiency of the neural network model in mapping the problem before applied to a larger problem.

The distribution of the training samples within the problem domain, which is the region in the input space embracing all problems that could be input to the network, can have a significant effect on the learning and generalization performance of a network. Since artificial neural networks are not usually able to extrapolate, the training samples should go at least to the edges of the testing domain in all dimensions. In other words, the problem domain should be equal to, or a subset of, the training domain, it is also advisable to have the training samples evenly distributed within this region. If this is not the case, training tends to focus on those regions where training samples are densely clustered and neglect those that are sparsely populated.

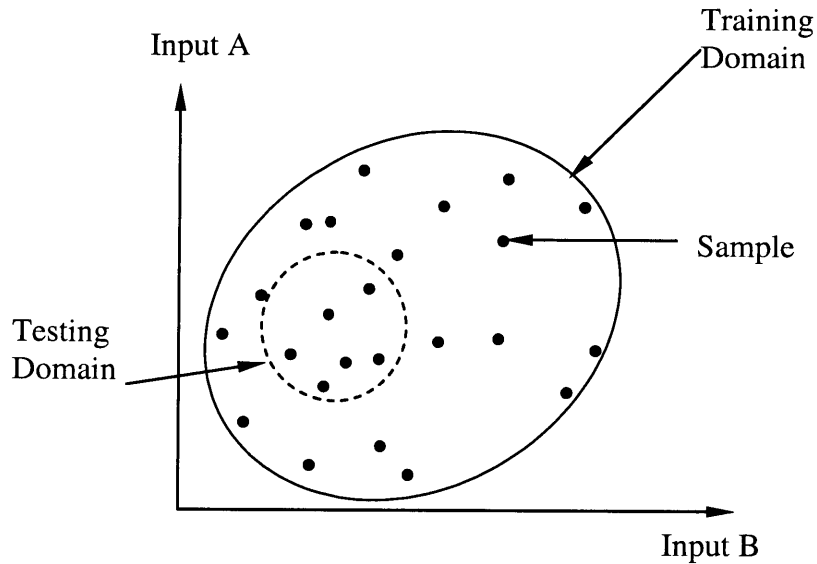
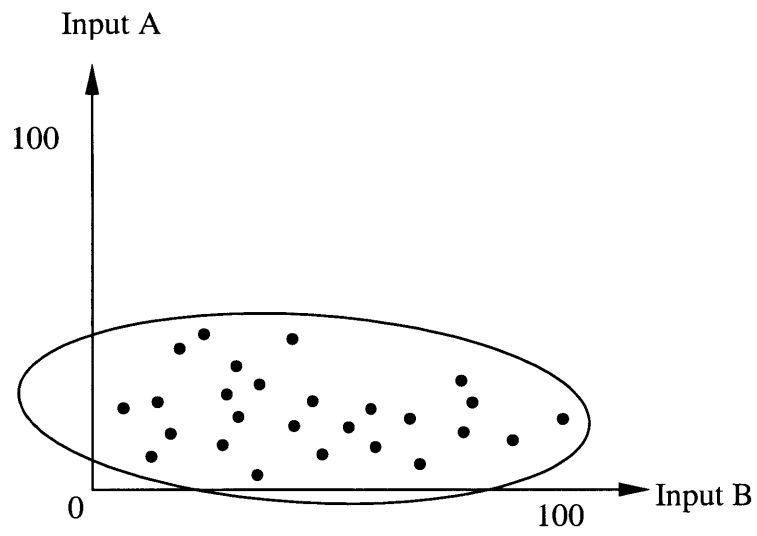
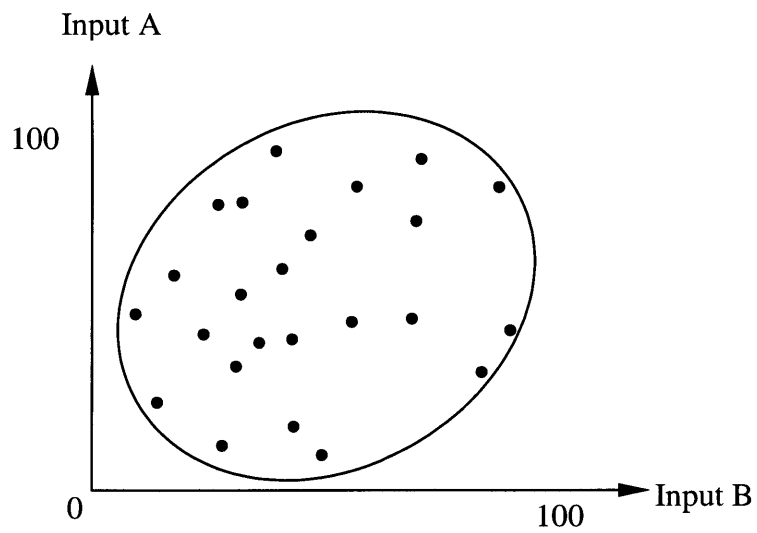


Figure 10.24 Example of training and testing domain

Flood and Kartam (1994) suggested that the progress of training can be impaired if the training samples mark a region that is relatively narrow in some dimensions and elongated in others such as in Figure 10.25(a). This problem can be alleviated by normalizing the training samples across each input, thereby improving the proportions of the problem domain, as in Figure 10.1(b). The normalization is consistent with the transformation function used in the network, typically a sigmoid function. Hence, input and output will be normalized into a range of 0 to 1 or -1 to 1 for the sigmoid function and the tangent sigmoid function, respectively. It is recommended to normalize the input and output data before presenting them to the network. In addition, the normalization can also improve the learning speed of the network (Rafiq M. et. al., 2001)



(a) Training domain before normalization



(b) Training domain after normalization

Figure 10.25 Effect of normalizing input of training data

10.7 Overfitting

Since the objective of using the neural network is to predict what will happen in the future, thus, we want the network to learn something about the past by learning from the training set that can *generalize* to the future. Although neural networks are very powerful tools for mapping a complex problem to find a best solution, its strength is also its weakness. The network output can fit data too closely. It models noises in addition to the underlying function we want to find. The problem is called “overfitting” that is the major problem of using neural network. There are three main approaches to prevent overfitting: first, increasing the size of training samples; second, limiting number of hidden nodes; and third, limiting the number of training epochs.

Increasing Size of Training Samples

As mentioned earlier, increasing the number of training samples provides more information for the network to learn more about the correlation between input data and target outputs and can compensate for the noise or the error in the data.

Limiting the Number of Hidden Nodes

Each weight in the network is a parameter that adds to the capacity of the network since it allows a transformation function (i.e. a sigmoid function as shown in Figure 10.17) to develop a more complicated function to fit the data. In other words, a number of weights determine the degrees of freedom with which the network can map the input to the output data. To limit the capacity of the network, the number of weight needs to be limited. The number of weight in the network is a function of the number of nodes it has as described earlier. Since the number of output nodes is generally determined by the nature of the problem or it is fixed based on the end product we expect (i.e. we only expect the surface settlement (δ_{\max}) as an output for example, so that there is only one output node). Hence, we can control the number of weights by controlling the number of input nodes and hidden nodes.

The number of input nodes is also important. Using several input nodes to represent one variable gives the network more degrees of freedom or more capacity to accurately model complex functions and on the other hand, more capacity to overfit. The number of the input nodes depends on how much one understands about the nature of a particular problem. If one puts a large number of input nodes into the network without investigating the correlation between each input and the output (face pressure and the surface settlement, for example), it would create redundant input parameters. The input should be reduced before they are presented to the network. Thus, the better the understanding of the parameters, the better the design of the number of input nodes.

Limiting the Number of Training Epochs

During the training process, the mapping function grows more complex, it passes at some point through one configuration that gives the best generalization; after that point, whatever the network learns will lead to overfitting. If we can determine when the network reaches that point, we can stop the training before overfitting occurs and use the network configuration that generalizes best. The overfitting can be spotted by evaluating the error in a validation sample as discussed in the next chapter.

References

- Elman, J. L. (1990). "Finding Structure in Time". *Cognitive Science*, Vol. 14.
- Flood, I. and Kartam, N. (1994). "Neural Networks in Civil Engineering. I: Principles and Understanding". *Journal of Computing in Civil Engineering*, ASCE, Vol. 8, No. 2.
- Haykin, S. (1999). *Neural Networks: A Comprehensive Foundation (2nd edition)*. Prentice Hall, New Jersey.
- Hertz, J., Krogh, A., and Palmer, R. G. (1991). *Introduction to the Theory of Neural Computation*. Addison-Wesley, CA.
- Hodgkin, A. L. and Huxley, A. F. (1952). "A Quantitative Description of Membrane Current and Its Application to Conduction and Excitation in Nerves". *Journal of Physiology*, Vol. 117.
- Hopfield, J. (1982). "Neural Networks and Physical Systems with Emergent Collective Computational Properties". *Proc. National Academy of Science*, Vol. 79.
- Mehrotra, K., Mohen, C. K., and Ranka, S. (1997). *Artificial Neural Networks*. MIT Press, Cambridge, MA.
- Pham, D. T., and Liu, X. (1995). *Neural Networks for Identification, Prediction and Control*. Springer-Verlag, London.
- Philippe, D. W., (1997). *Neural Network Models*. Springer-Verlag, London.
- Rumelhart, D. E., Hinton, G. E., and McClelland, J. L. (1986). "A General Framework for Parallel Distribution Processing". *Parallel Distribution Processing*. Vol. 1, MIT Press, Cambridge, MA.
- Smith, M. (1993). *Neural Networks for Statistical Modeling*. Van Nostrand Reinhold, NY.

CHAPTER 11

Pilot Experiment and Network Validation

11.1 Introduction

In attempts to design and control the behavior of systems, both man-made and natural, engineers find that they must be able to predict the complex behavior of these systems, knowing the configuration of the system and the loads and boundary conditions to which it is exposed. Engineers model system behavior to be able to make predictions. However, this behavior (1) is often governed by nonlinear multi-variable (and sometimes unknown) interrelationships, (2) occurs within “noisy” uncontrollable physical environments. Especially in the geotechnical field, in which complex behavior of geological and construction systems is common, prediction is very difficult.

As discussed in previous chapters, studying the interaction between the surrounding ground and the EPB shield is very complicated since many factors are involved. Predicting settlements induced by this tunneling method is even more difficult. Many earlier empirical solutions such as Peck’s (1969), and Attewell’s and Woodman’s (1982), which were proposed to describe the surface settlement trough all require the knowledge of the maximum settlement (δ_{\max}). There are also several analytical and numerical methods available such as closed form solutions (examples: Verruijt and Booker; 1996, and Pinto; 1999), or any 2-D and 3-D finite element approaches for predicting ground

surface settlement; however, these methods cannot replicate all aspects of EPB shield tunneling behavior, which are very complex. Furthermore, since changing operational parameters during the excavation can cause a change in the surrounding ground behavior, the ground response to the EPB shield may vary from section to section.

Since the advantage of the artificial neural networks is the ability of mapping input to output patterns, ANN may enable one to map all influencing parameters to surface settlements. Furthermore, combined with the extensive computerized database (Chapter 6) that provides all parameters needed for the network inputs and outputs such as construction activities, tunneling operational factors, subsurface conditions, and instrumentation readings, the artificial neural networks can become a very powerful approach for predicting the maximum settlement.

The objectives of this chapter are (1) to investigate the potential of artificial neural networks (ANN) for predicting the maximum surface settlement (δ_{\max}) caused by EPB shield tunneling, and (2) to develop an optimal neural network model for this purpose. To achieve these objectives, artificial neural network models with various numbers of hidden layers and various numbers of hidden nodes are trained for various numbers of training epochs. A number of samples selected from the computerized database are used for network training and testing/validation. All the models are then evaluated quantitatively to determine the optimal model that will be applied for further predictions of surface settlements in the MRTA project.

11.2 Factors Affecting Surface Settlements

Based upon the case history review (Chapter 4) and extensive observations in the MRTA project (Chapters 7, 8 and 9), the factors causing settlements can be grouped into three major categories (Figure 11.1): (1) tunnel geometry; (2) geological conditions; and (3) operational factors. These parameters will be used as input data to design neural networks for predicting the maximum surface settlement. The relationship between these parameters and surface settlements was discussed earlier in Chapter 9 and is summarized in Table 11-1.

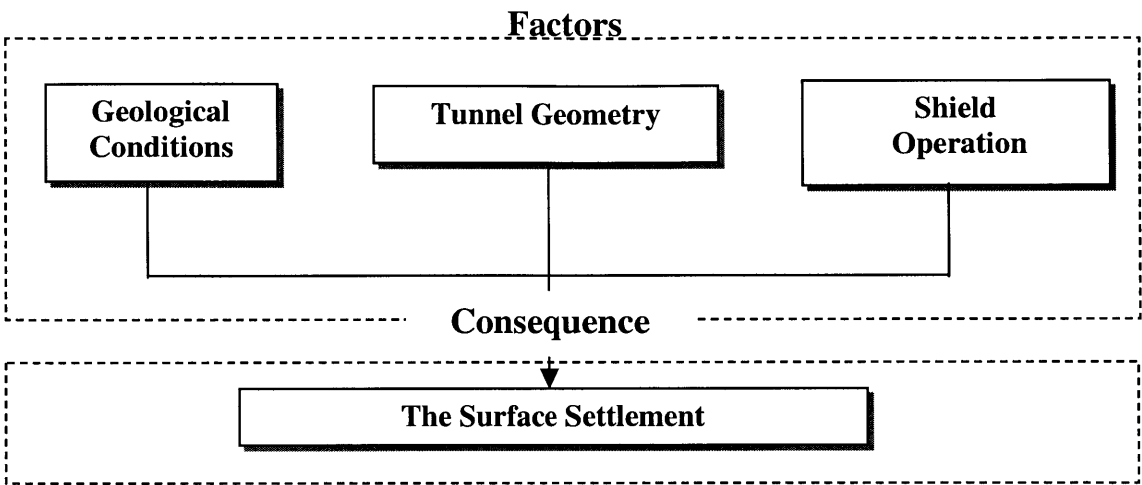


Figure 11.1 Main factors causing the surface settlement

Table 11-1 Summary of factors affecting the surface settlement

Category	Factors
Tunnel Geometry	Tunnel depth (m)
	Distance from launching station (m)
Geological Conditions	Geology at tunnel crown
	Geology at tunnel invert
	Ground water level from tunnel invert (m)
Shield Operation Factors	Average face pressure (kPa)
	Average penetration rate (mm/min)
	Average pitching angle (degree)
	Grouting pressure (bar)
	Percent grout filling

Note that the soil types in the tunnel used for neural network input are divided into two categories: (1) geology or soil type at the tunnel crown, and (2) geology at the tunnel invert, as illustrated in Figure 11.2.

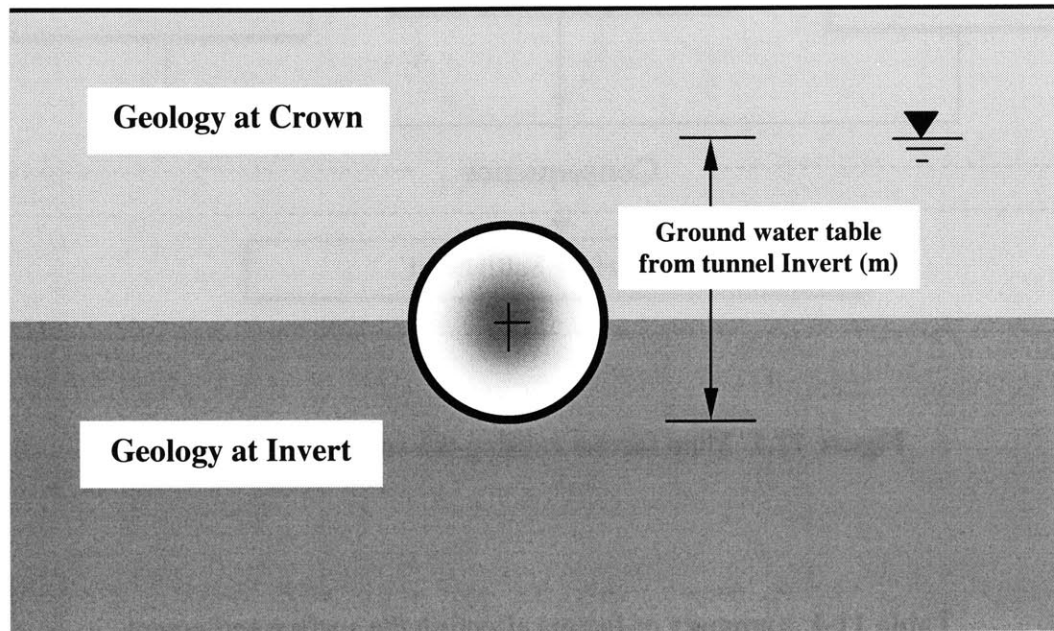


Figure 11.2 Geological parameters: geology at crown, geology at invert, and ground water table

Additionally, it is also important to note that another tunnel geometry factor obviously affecting the surface settlement is *tunnel diameter*. Tunnel diameter affects the magnitude of surface settlements, as a large tunnel tends to cause greater surface settlements than smaller tunnels. With a larger diameter, the cross sectional area is greater so that in the case of constant ground loss (%), one would expect a greater volume of ground moving towards the larger diameter tunnel. However, since the entire length of the MRTA tunnel project has a constant diameter of 6.30 m, the effect of tunnel diameter is negligible in the present settlement prediction model. Therefore, only two geometry factors are considered in the neural network modeling namely, *the distance from the launching station* and *the tunnel depth*. Details of how the tunnel geometry affects the settlements were provided in Chapter 9.

11.3 Development of the Neural Network Model

In this section, the application of the modeling framework to the prediction of surface settlements caused by EPB tunneling is presented. Before a neural network can be applied, it needs to be developed as shown in Figure 11.3. The first step (*Step 1*) is the fundamental process with the aim of understanding the mechanism of EPB tunneling and ground movement. This step requires not only theoretical background and case history review, but also field observations and data analysis. Since constructing a predictive model is not a straightforward procedure, proper understanding and formulation of the problem at hand are necessary. All of this was already discussed in the previous chapters in that the theoretical background of the ground movement induced by tunneling was provided in Chapter 3, case histories were reviewed in Chapter 4, and the tunneling in MRTA was discussed in Chapters 7 and 8.

In *Step 2*, on the basis of intensive case studies and field observation in the MRTA project, the most relevant parameters that affect settlement are determined as described earlier. *Step 3* to *Step 6* represent the network development processes. The objectives of these processes are (1) to investigate if the neural network method is applicable to the EPB tunneling problem, and (2) to establish an optimal network that can be used for predicting the surface settlement. To fulfill these objectives, a pilot experiment is used by first selecting samples as a training set and a testing/validation set (*Step 3*). Various architectures of neural network models are designed (*Step 4*). All of these models are trained and validated with the validation set (*Step 5*). The results from the validation set are used for comparison, which can be viewed in plots and tables (*Step 6*), this will lead to the optimal network model. Finally, *Step 7* is the application after the optimal network has been established in Step 6. The selected neural network model is then ready to be applied to other predictions of surface settlements in the MRTA project.

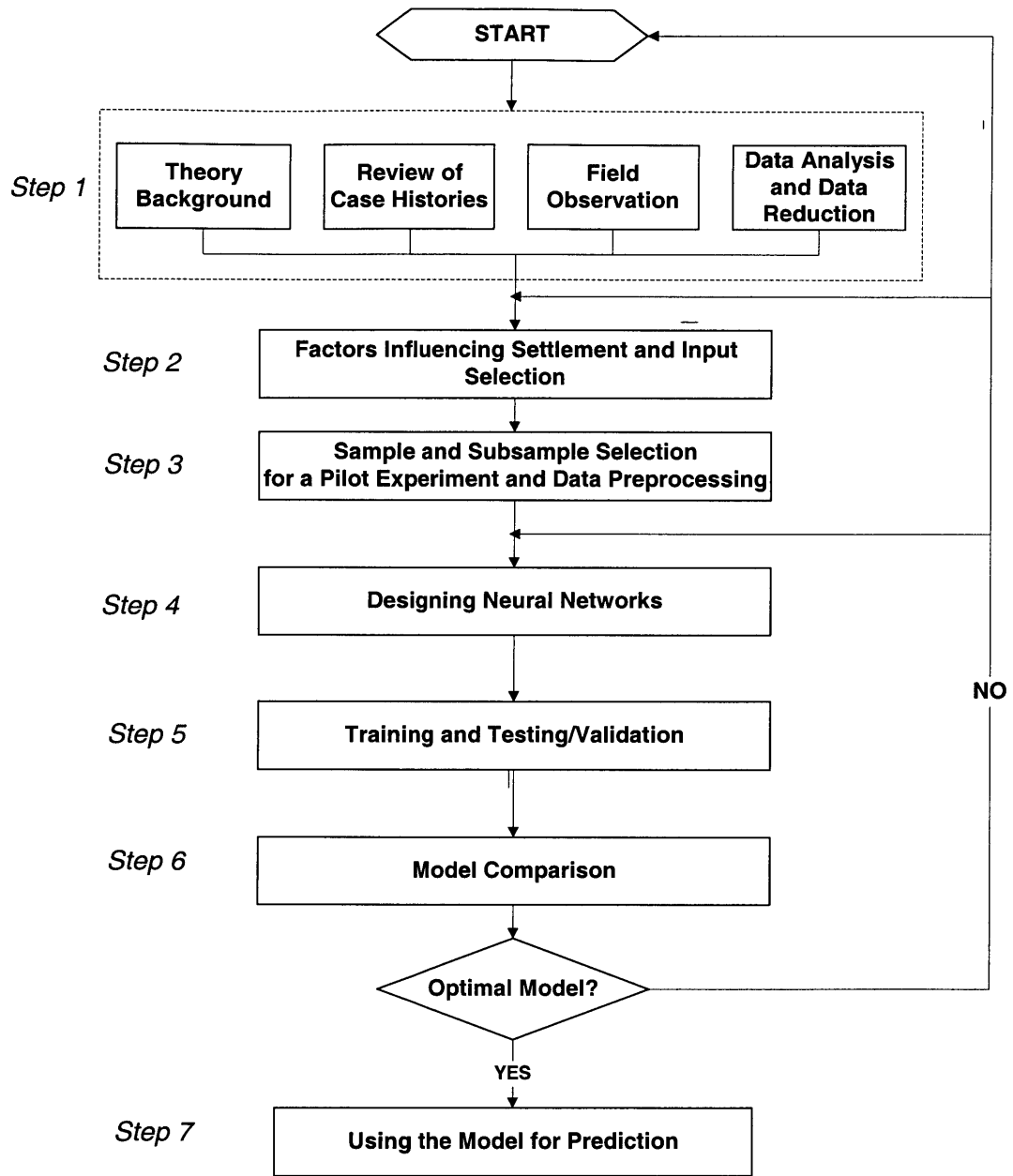


Figure 11.3 Diagram of the ANN modeling development for settlement prediction

11.3.1 Sample and Subsample Selection

Before a neural network model can be used with any degree of confidence, there is a need to establish the validity of the results it generates. A network could provide almost perfect answers to the set of problems with which it was trained, but fail to produce meaningful answer to other problems. Usually, validation involves evaluating the network performance on a set of test problems that were not used for training, but for which solutions are available for comparison. The correct solutions (measured values) and those produced by the network (predicted values) may be compared in a qualitative manner such as a visual comparison of plotted points, or in a quantitative manner using statistical tests.

First, the data obtained from the *southbound tunnel in Section A* which is composed of Zones 23, 24, and 25 are selected: see Figure 11.4. In this section, 6.30 m outer diameter twin tunnels were excavated underneath Ratchada Road, an eight-lane road located in the Northern region of Bangkok (Figure 11.5 to 11.7). In this study, only the data from the southbound tunnel, which is the first tunnel excavated, were used. The tunnel, which is 3,636 m long, was entirely excavated by a Kawasaki machine operated by Nishimatsu. The tunnel started in Zone 23 (i.e. at Thiam Ruam Mit station) and was excavated northward to the end of the Zone 25. Details about this tunnel were provided in Chapter 5.

As mentioned earlier, the factors causing settlement can be grouped into three main categories: (1) tunnel geometry; (2) ground condition; and (3) operational factors. All of these are used as neural network inputs as summarized in Table 11-2. Thirteen input nodes are used to represent these categories. The first two nodes are used to define the tunnel geometry in terms of *the tunnel depth* and *the distance from launching station*, respectively. Input neurons No. 3 to 8 represent the geological condition category. Qualitative, discrete indicators are used in this category. For example, the geology at the tunnel crown can be either soft clay, stiff clay, or sand. Binary numbers 0 and 1 represent “No” and “Yes,” respectively. The same indicators are also used for the geology at the tunnel invert nodes.

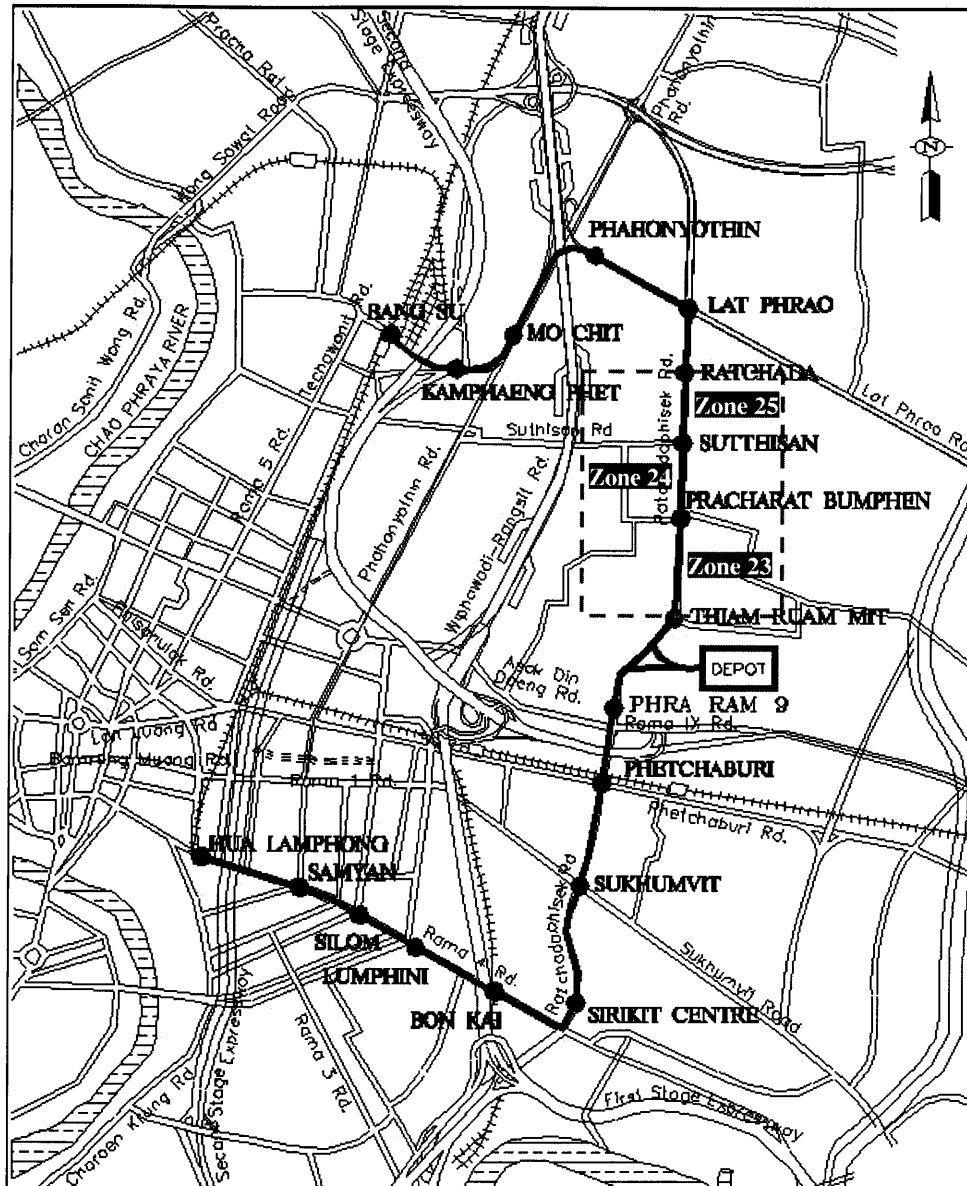


Figure 11.4 Locations of the tunneling drive used as experimental training data

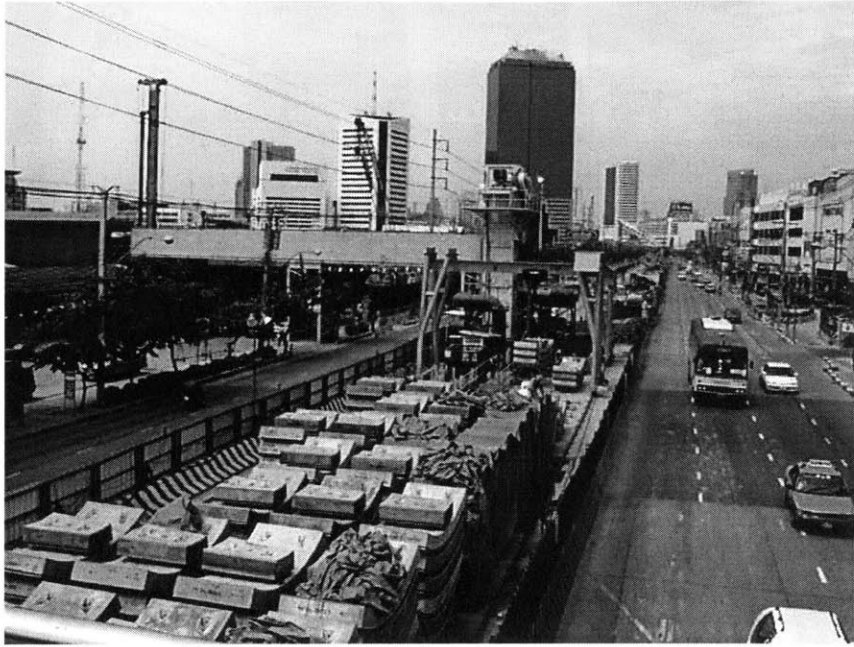


Figure 11.5 Location of the tunnel in Zone 23 (Thiam Ruam Mit - Pracharat Bumphen)



Figure 11.6 Location of the tunnel in Zone 24 (Pracharat Bumphen – Sutthisan)



Figure 11.7 Location of the tunnel in Zone 25 (Sutthisan - Ratchada)

Table 11-2 Input parameters used for the NN model

Category	Parameter	Detailed Items	Input Node No.
Tunnel Geometry	(1) Tunnel depth (m)		1
	(2) Distance from launching station (m)		2
Geological Conditions	(3) Geology at tunnel crown	Soft Clay (No = 0, or Yes =1)	3
		Stiff Clay (No = 0, or Yes = 1)	4
		Sand (No = 0, or Yes = 1)	5
Geological Conditions	(4) Geology at tunnel invert	Stiff Clay (No = 0, or Yes =1)	6
		Sand (No = 0, or Yes = 1)	7
Geological Conditions	(5) Ground water level from tunnel invert (m)		8
Shield Operation Factors	(6) Average face pressure (kPa)		9
	(7) Average penetration rate (mm/min)		10
	(8) Average pitching angle (degree)		11
	(9) Grouting pressure (bar)		12
	(10) Percent grout filling		13

Operational factors are represented by input nodes No. 9 to 13. Face pressure (node No. 9) is the average supporting pressure applied during passing of the measurement section. Penetration rate and pitching angle are also average recorded data. Grouting pressure and percent grout filling inputs are recorded at a tunnel segmental ring that is located underneath the measurement section. These factors are illustrated in Figure 11.8.

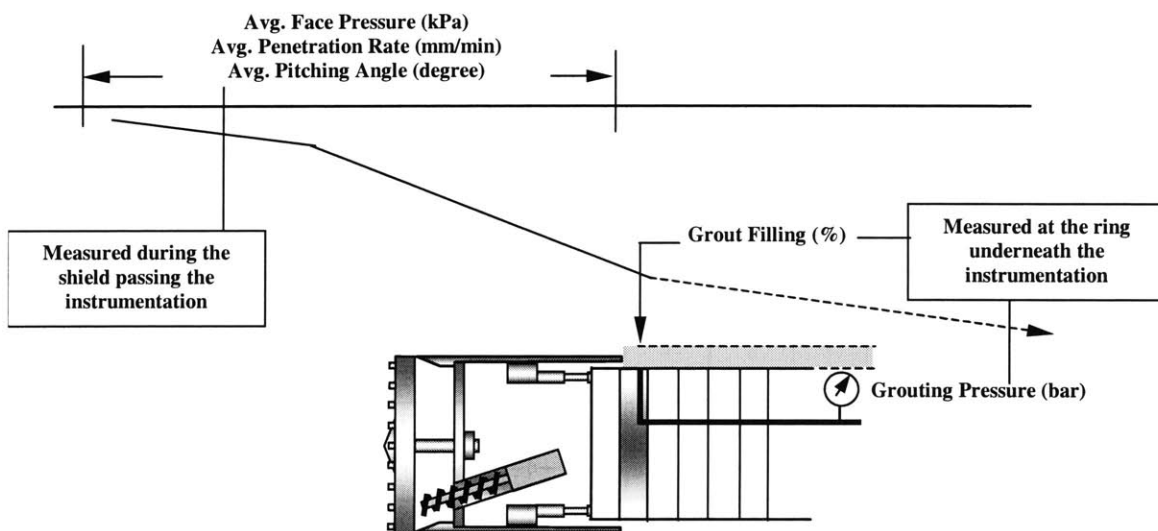


Figure 11.8 Measured operational parameters used for ANN inputs

Table 11-3 shows the data obtained from tunnel section A. The data are divided into a *training set* and a *validation or testing set*. There are 39 data patterns and 10 data patterns in the training set and validation set, respectively. Various networks are trained with this training set and are validated with the testing or validation set. Performance of the validation set of each network is then used for comparison analyses to determine an optimal network.

Table 11-3 Samples used for training and validation testing

Section	Max Sett. (mm)	Depth (m)	Distance from shaft (m)	Geology at Crown			at Invert		Invert to WT (m)	Avg. Face Pres. (kPa)	Avg. Penetrate (mm/min)	Pitching (degree)	Grouting Pres.(bar)	% Grout Filling
				Soft Clay	Stiff Clay	Sand	Stiff Clay	Sand						
Zone 23 SB	-60.50	18.20	33.6	0	1	0	1	0	0.65	34.50	33.5	-0.07	3.03	92
	-51.40	18.61	58.8	0	1	0	1	0	0.24	32.00	42.4	-1.01	3.03	100
	-47.90	18.70	62.4	0	1	0	1	0	0.15	31.00	41.65	-1.05	3.03	100
	-31.90	19.21	82.8	0	1	0	1	0	-0.36	54.50	34.45	-1.38	7.40	122
	-15.90	19.63	99.6	0	1	0	1	0	-0.78	84.50	32.55	-0.88	5.60	116
	-13.50	20.17	121.2	0	1	0	1	0	-1.32	100.50	30	-1.12	5.30	110
	-15.70	21.10	158.4	0	1	0	1	0	-2.25	131.00	26.4	-1.11	2.50	121
	-16.80	22.06	196.8	0	1	0	1	0	-3.21	123.00	29.75	-1.11	2.50	117
	-21.50	23.09	223.2	0	1	0	1	0	-4.24	65.50	40.65	-1.14	2.50	119
	-43.80	23.22	252	0	1	0	1	0	-4.37	14.50	48.9	-0.45	2.50	127
	-35.20	23.45	304.8	0	1	0	1	0	-4.60	44.50	48.4	-0.06	2.50	117
	-48.80	23.68	355.2	0	1	0	1	0	-4.83	49.50	50.95	0.15	2.50	195
	-29.16	23.91	404.4	0	1	0	0	1	-5.06	77.50	54.25	-0.16	2.50	120
	-39.10	23.56	504	0	1	0	0	1	-4.71	39.50	67.9	0.45	2.50	139
	-36.40	23.31	555.6	0	1	0	0	1	-4.46	53.50	70	0.42	2.50	129
	-35.10	23.05	607.2	0	1	0	0	1	-4.20	55.25	76.85	0.5	2.50	119
	-41.60	22.81	656.4	0	1	0	0	1	-3.96	77.75	69.9	0.4	2.50	94
	-31.50	22.56	708	0	1	0	0	1	-3.71	63.25	58	0.57	2.50	123
	-41.20	22.43	735.6	0	1	0	1	0	-3.58	47.00	56.6	0.57	2.50	127
	-6.25	21.84	855.6	0	1	0	1	0	-2.99	59.50	51	0.55	2.50	130
-6.67	21.42	904.8	0	1	0	1	0	-2.57	44.00	56.65	0.6	2.50	127	
-15.56	20.80	954	0	1	0	1	0	-1.95	87.50	49.7	1.17	3.80	97	
-20.00	19.78	1005.6	0	1	0	1	0	-0.93	88.75	48.6	1.36	2.50	123	
-12.86	18.78	1056	0	1	0	1	0	0.07	51.75	54.35	1.36	2.50	117	
-33.00	17.89	1107.6	0	1	0	1	0	0.96	121.00	41.2	0.92	2.50	129	
Zone 24 SB	-28.91	19.74	1508.4	1	0	0	1	0	-0.89	42.75	39.85	-0.74	2.50	118
	-19.28	20.95	1552.8	0	1	0	1	0	-2.10	111.00	27.2	-0.58	2.50	131
	-28.57	22.39	1605.6	0	1	0	1	0	-3.54	69.25	26.35	-0.69	2.50	70
	-38.57	23.64	1654.8	0	1	0	1	0	-4.79	60.00	24.55	-0.84	2.50	127
	-34.57	23.87	1704	0	1	0	0	1	-5.02	79.50	34.65	-0.72	2.50	131
	-41.08	24.11	1753.2	0	1	0	0	1	-5.26	70.00	37.7	0.02	2.50	212
	-37.86	24.35	1804.8	0	1	0	0	1	-5.50	31.75	44.45	0.03	2.50	122
	-12.57	24.58	1852.8	0	1	0	0	1	-5.73	36.00	47.2	0.04	2.50	117
	-19.28	24.82	1902	0	1	0	0	1	-5.97	35.25	51.15	-0.06	2.50	99
	-43.57	24.74	1953.6	0	1	0	0	1	-5.89	26.50	45.4	0.4	2.50	224
	-40.00	24.28	2004	0	1	0	0	1	-5.43	29.25	44.65	0.48	2.50	148
	-13.57	23.83	2053.2	0	1	0	0	1	-4.98	46.00	42.7	0.71	2.50	106
	-21.14	23.36	2104.8	0	1	0	0	1	-4.51	46.50	43	1.18	2.50	127
	-24.30	22.92	2152.8	0	1	0	0	1	-4.07	62.50	41.8	1.39	2.50	124
	-20.00	23.55	2203.2	0	1	0	0	1	-4.70	48.75	23.55	1.16	2.50	124
-22.50	23.30	2253.6	0	1	0	1	0	-4.45	37.75	20.1	1.43	2.50	121	
-15.00	23.06	2304	0	1	0	1	0	-4.21	45.75	23.5	1.26	2.50	122	
Zone 25 SB	-21.01	19.15	2752.8	0	1	0	1	0	-0.30	28.33	31	-0.71	2.50	147
	-14.22	20.33	2802	0	1	0	1	0	-1.48	18.75	36.9	-0.93	2.50	114
	-15.00	21.43	2852.4	0	1	0	1	0	-2.58	33.06	36.25	-0.89	2.50	128
	-27.50	22.07	2904	0	1	0	1	0	-3.22	18.75	34.25	-0.56	2.50	128
	-48.89	22.05	2953.2	0	1	0	0	1	-3.20	17.00	42.9	0.18	2.50	180
	-15.50	22.78	3002.4	0	1	0	0	1	-3.93	30.75	37.55	0.6	2.50	116
	-21.50	22.01	3055.2	0	1	0	0	1	-3.16	25.50	37.65	0.77	2.50	126

Note: Shaded numbers are the patterns used for the neural network model validation

Before the data in Table 11-3 are used as input and output values, they are normalized to be in a range corresponding to the transformation function in the network. In this study, since tangent sigmoid functions are used, all values of input attributes and the associated outputs were transformed to values varying from -1 to 1 by the equation as:

$$P_n = 2 \frac{(P - P_{min})}{(P_{max} - P_{min})} - 1 \quad (11-1)$$

where P_n = normalized value; P = original value; P_{max} = maximum value of the input or the output; and P_{min} = minimum value of the input and the output. For instance, assume that an average face pressure is 220 kPa, while the maximum face pressure and the minimum face pressure recorded in the selected data are 300 kPa and 50 kPa, respectively. Using (11-1), a normalized input for face pressure node is 0.36, which is in the bounds -1 and 1 .

11.3.2 Neural Network Design

The feedforward neural network with back-propagation algorithm provided in MATHLAB-ANN Toolbox is used for the settlement prediction as illustrated in Figure 11.9. The input layer consists of 13 input nodes that represent all influencing factors. Note that each input node uses normalized values preprocessed by (11-1). In order to obtain a good performance of the neural network that can make prediction based on “new” data, it is necessary to have an optimal network model. However, there is no method or “rule of thumb” capable of determining an optimal network, except for the trial and error process. The process attempts to establish the optimal neural network model and an appropriate number of training epochs for the problem. The variables used for trial and error are: (1) the architecture of the neural networks, which is composed of a number of hidden layers and a number of hidden nodes in each hidden layer; and (2) the number of training epochs.

Eighteen neural network models were designed for this pilot experiment as shown in Table 11-4. These various models represent different variables including:

- (1) Number of hidden layers: 1,2
- (2) Number of hidden nodes in each hidden layer: 10, 15, 20
- (3) Number of training epochs: 1000, 2000, 3000

Each model is trained with the training set until it reaches the specified training epoch shown in Table 11-4. After training, the model is tested with the validation set. Input parameters of this validation set are fed to the model via the input nodes and weighted layer-by-layer from the hidden layer(s) to the output layer. Outputs, which are “predicted settlement values” from the network, are then used to compare with the desired outputs (measured settlement values). If the network outputs are in agreement with the measured data as indicated by small differences between output and desired/target data, the network is useable for the application. The network that yields the best agreement with the validation set will be selected as the optimal neural network.

Although, this trial and error process for training and validation is a time consuming procedure, it is indispensable to verify if the neural network method is applicable to the problem and to ensure that the designed model can converge and produces a generally valid solution.

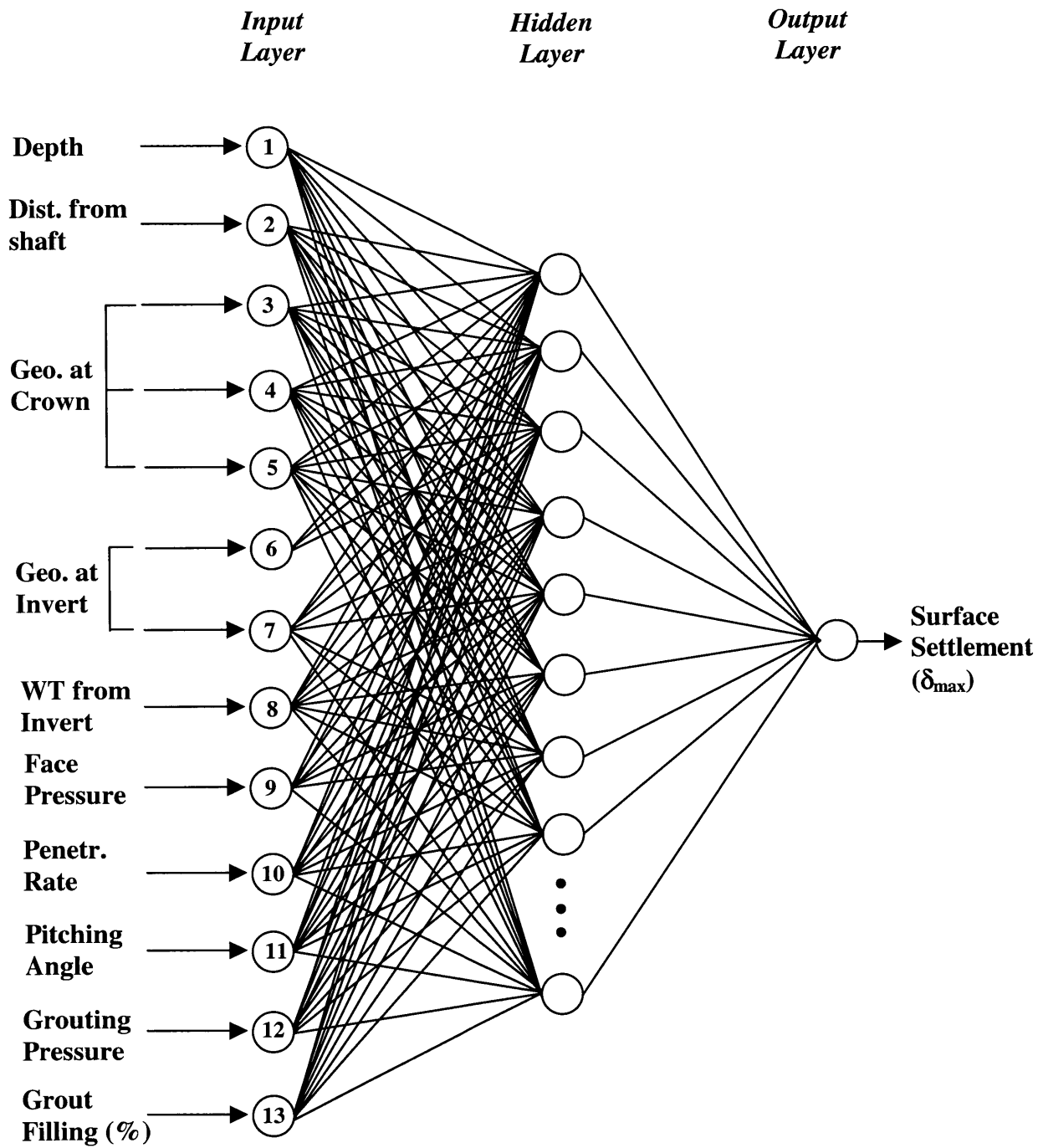


Figure 11.9 Structure of two-layer neural network model for predicting the surface settlement

Table 11-4 Neural network models used in the pilot experiment

Model	Number of Hidden Layers	Number of Hidden Nodes in Each Layer	Number of Training Epochs
1	1	10	1,000
2	1	15	1,000
3	1	20	1,000
4	1	10	2,000
5	1	15	2,000
6	1	20	2,000
7	1	10	3,000
8	1	15	3,000
9	1	20	3,000
10	2	10	1,000
11	2	15	1,000
12	2	20	1,000
13	2	10	2,000
14	2	15	2,000
15	2	20	2,000
16	2	10	3,000
17	2	15	3,000
18	2	20	3,000

11.4 Model Validation

All of the 18 models summarized in Table 11-4 are trained with samples and tested with the validation set. Figure 11.10 through Figure 11.15 depict the results of the models using the training sample and validation testing samples. To evaluate the performance of the models, the root mean square error (RMSE) was used for comparison purposes as summarized in Table 11-5. The definition of root mean square error is given as follows:

$$RMSE = \sqrt{\frac{\sum_{i=1}^N (o_i - t_i)^2}{N}}$$

(11-2)

where, N is the number of patterns in the validation set, o is the output produced by the network, and t is the target (desired) output. RMSE is a popular method used for performance comparison between networks. In this study, o is a settlement value predicted by the neural networks and t is an actual settlement measured in the field.

Table 11-5 Performance of the neural network models

Model	Network Architecture	Training Epochs	Training Samples (RMSE)	Validation Samples (RMSE)
1	1 hidden layer, 10 hidden nodes	1,000	5.97	10.49
2	1 hidden layer, 15 hidden nodes	1,000	5.41	8.01
3	1 hidden layer, 20 hidden nodes	1,000	5.13	8.22
4	1 hidden layer, 10 hidden nodes	2,000	4.79	9.26
5	1 hidden layer, 15 hidden nodes	2,000	4.97	9.39
6	1 hidden layer, 20 hidden nodes	2,000	5.08	7.33
7	1 hidden layer, 10 hidden nodes	3,000	4.59	9.30
8	1 hidden layer, 15 hidden nodes	3,000	3.74	9.18
9	1 hidden layer, 20 hidden nodes	3,000	3.53	10.37
10	2 hidden layers, each 10 hidden nodes	1,000	5.27	11.26
11	2 hidden layers, each 15 hidden nodes	1,000	4.07	12.26
12	2 hidden layers, each 20 hidden nodes	1,000	4.90	13.21
13	2 hidden layers, each 10 hidden nodes	2,000	2.96	12.72
14	2 hidden layers, each 15 hidden nodes	2,000	3.47	8.46
15	2 hidden layers, each 20 hidden nodes	2,000	2.23	10.45
16	2 hidden layers, each 10 hidden nodes	3,000	2.47	15.37
17	2 hidden layers, each 15 hidden nodes	3,000	2.19	9.81
18	2 hidden layers, each 20 hidden nodes	3,000	1.48	12.61

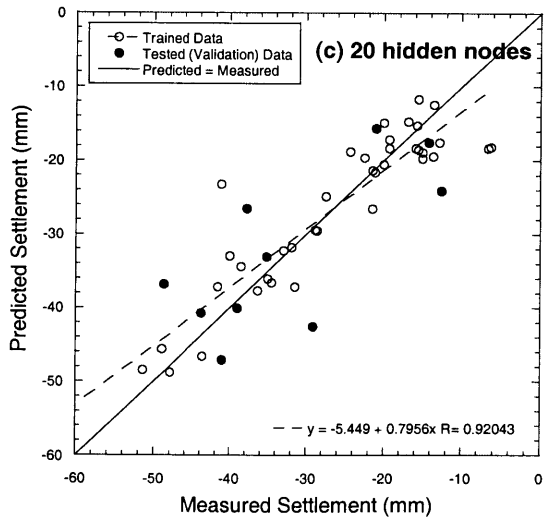
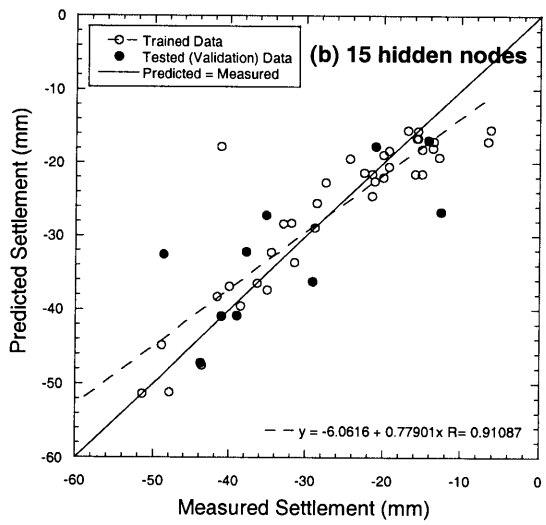
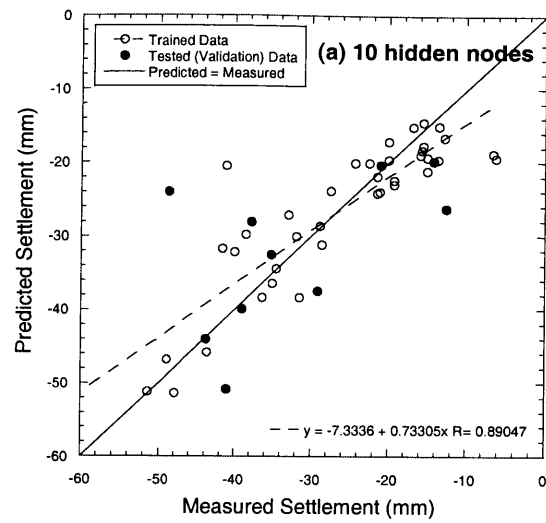


Figure 11.10 Performances of ANN with 1 hidden layer at 1,000 epochs: (a) Model 1 (10 hidden nodes), (b) Model 2 (15 hidden nodes), and (c) Model 3 (20 hidden nodes)

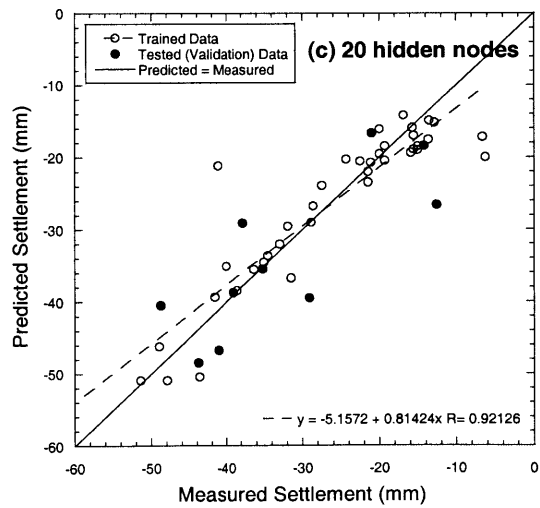
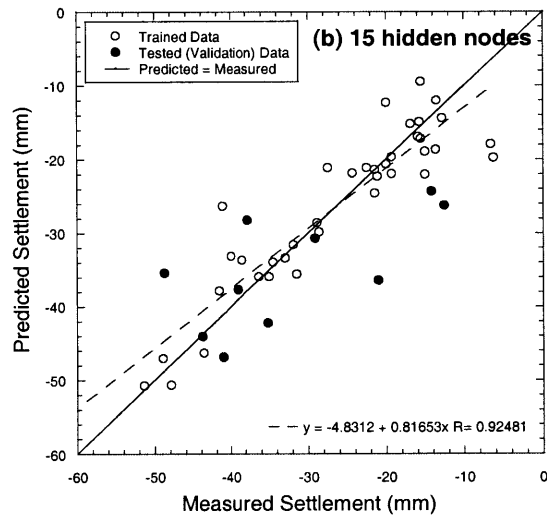
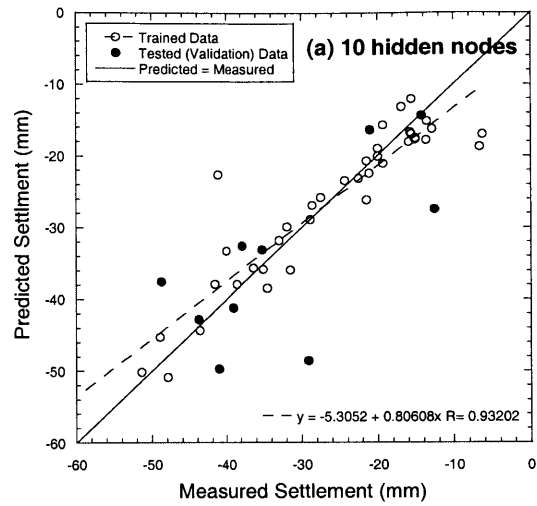


Figure 11.11 Performances of ANN with 1 hidden layer at 2,000 epochs: (a) Model 4 (10 hidden nodes), (b) Model 5 (15 hidden nodes), and (c) Model 6 (20 hidden nodes)

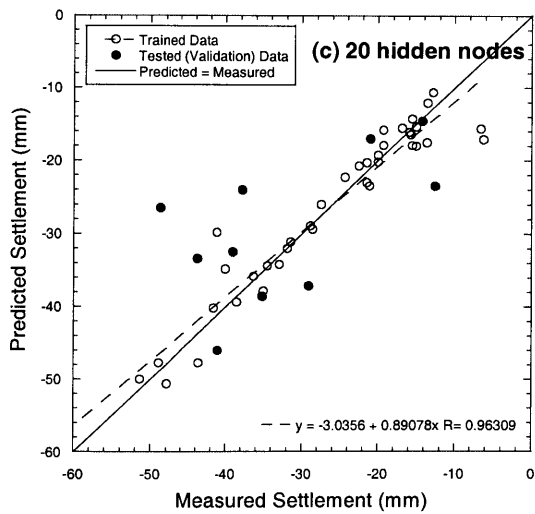
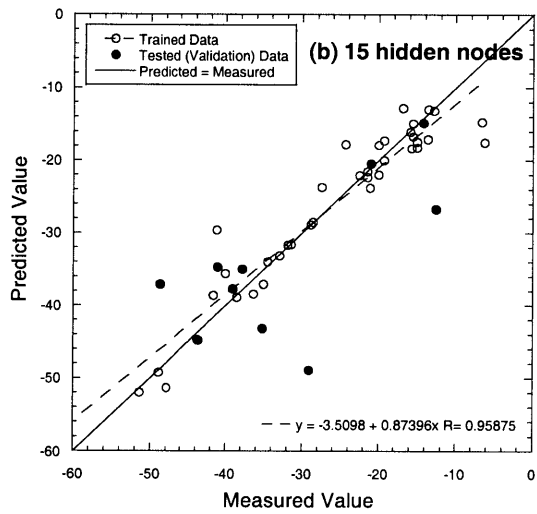
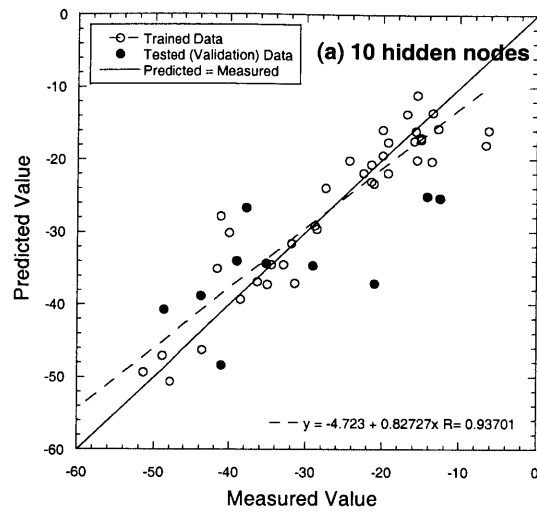


Figure 11.12 Performances of ANN with 1 hidden layer at 3,000 epochs: (a) Model 7 (10 hidden nodes), (b) Model 8 (15 hidden nodes), and (c) Model 9 (20 hidden nodes)

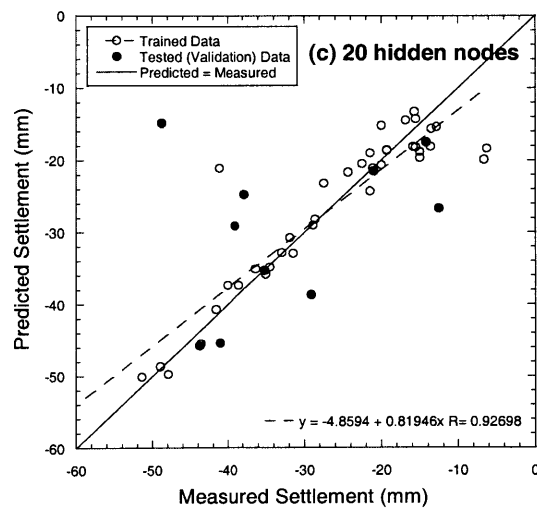
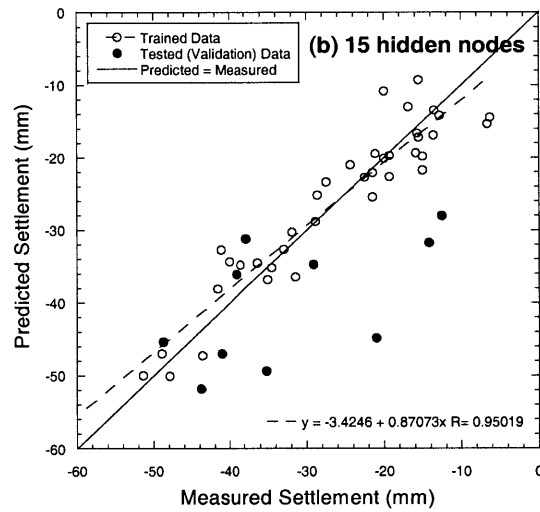
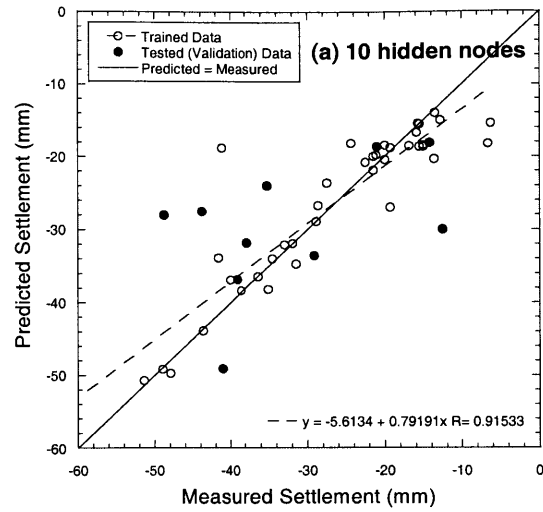


Figure 11.13 Performances of ANN with 2 hidden layers at 1,000 epochs: (a) Model 10 (10 hidden nodes), (b) Model 11 (15 hidden nodes), and (c) Model 12 (20 hidden nodes)

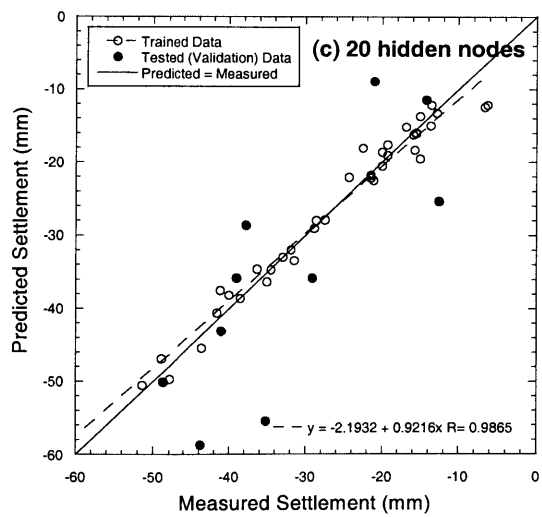
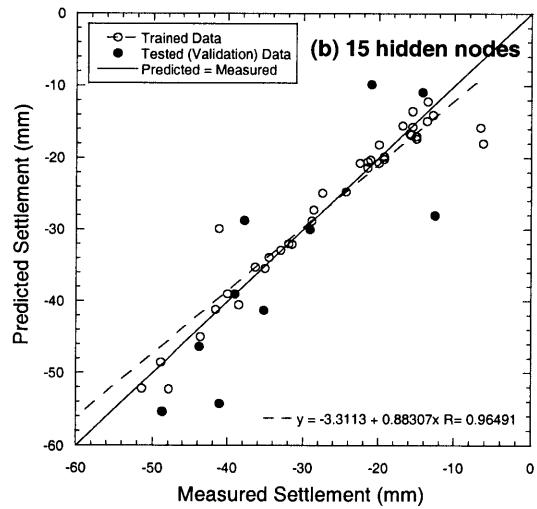
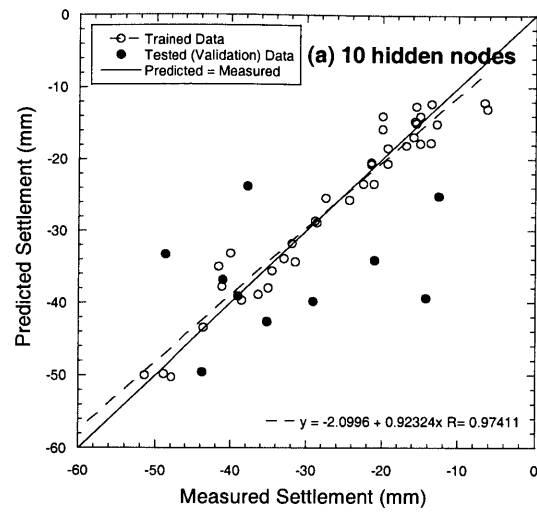


Figure 11.14 Performances of ANN with 2 hidden layers at 2,000 epochs: (a) Model 13 (10 hidden nodes), (b) Model 14 (15 hidden nodes), and (c) Model 15 (20 hidden nodes)

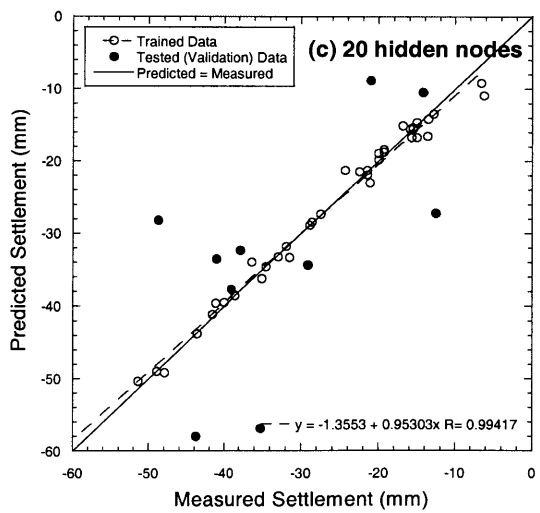
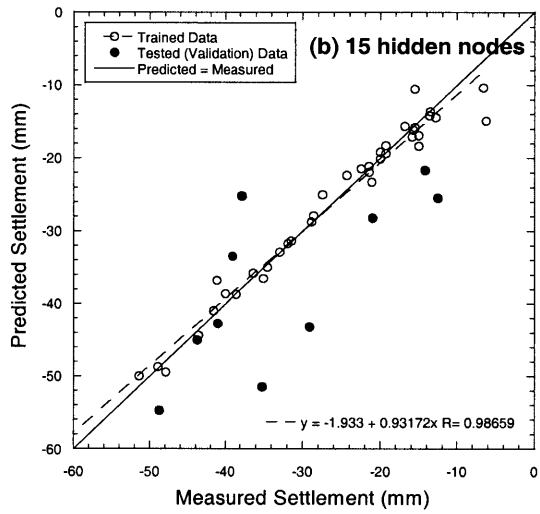
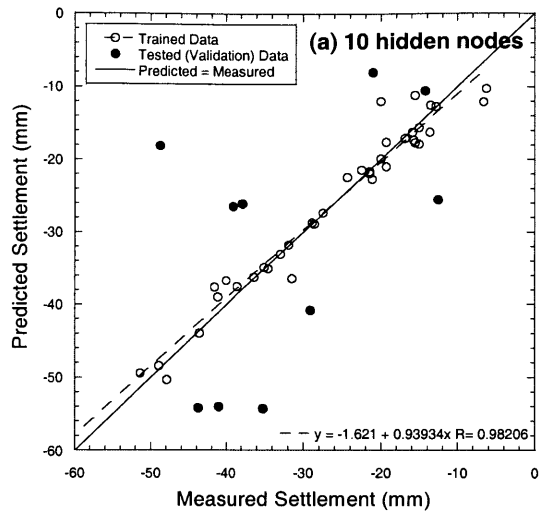


Figure 11.15 Performances of ANN with 2 hidden layers at 3,000 epochs: (a) Model 16 (10 hidden nodes), (b) Model 17 (15 hidden nodes), and (c) Model 18 (20 hidden nodes)

11.4.1 Training and Testing Results

In (Figure 11.10), training the networks with 1 hidden layer for 1,000 epochs shows that the neural networks are likely to map the input data to the output data; in fact, although only 10 hidden nodes were used in Model 1 (Figure 11.10a), we can see that the network is still able to map the data to some extent. Increasing the number of hidden nodes from 10 nodes to 15 nodes and then 20 nodes as shown in Figure 11.10b and c, respectively, illustrates improvements in the mapping ability. These plots clearly indicate that using the back-propagation algorithm allows the networks to successfully learn from the training samples and to be able to map many influencing factors (inputs) to surface settlements (outputs). Needless to say, these results also imply that the neural network approach has a potential for predicting the settlement.

When the networks described above are tested with validation samples, they are more or less in agreement with the validation samples. Based on this result, we need to further investigate how the networks will improve their performance or learning if we increase the number of training epochs from 1,000 to 2,000 epochs. As expected, the errors in training samples are reduced compared to those of models with 1,000 epochs as shown in Table 11-5. Furthermore, as can be seen in Figure 11.11, when the networks are tested with validation samples, the predicted settlements are also improved in that they are closer to the measured settlements, especially in Model 6 (Figure 11.11c).

Hence, it appears that if we keep increasing the training epochs, the results would become to be more and more accurate. Thus, we increased the training epochs to 3,000 epochs. As shown in Figure 11.12, the networks show improvements in the training samples compared to the above models with lower number of epochs. However, when they are validated with the validation samples, they show no improvement; in fact, they yield even greater errors than the networks with 2,000 epochs: see also Table 11-5.

Another way to improve a network performance is to increase the number of hidden layers, since we increase complex mapping functions within the network. Thus, Models 10 to 18

designed with 2 hidden layers are used for this purpose. Starting with 1,000 epochs, the networks show small improvements as shown in Figure 11.13 compared with the networks with 1 hidden layer trained for the same epochs (i.e. Models 1 to 3). However, when tested with the validation samples, their results are in every poor agreement with the measured data.

We again increase the number of training epochs to 2,000. As also expected, since we increase the number of learning epoch in the networks, substantial improvements are found as illustrated in Figure 11.14. However, tested with validation samples, their performance is still very poor.

Finally, we trained the networks with 2 hidden layers for 3,000 epochs (Models 16, 17, and 18). As a result, the training set fit the data almost perfectly as shown in Figure 11.15. Yet, when they are compared with the validation samples, their predictions are extremely poor and unacceptable (i.e. RMSE = 15.37 in Model 16).

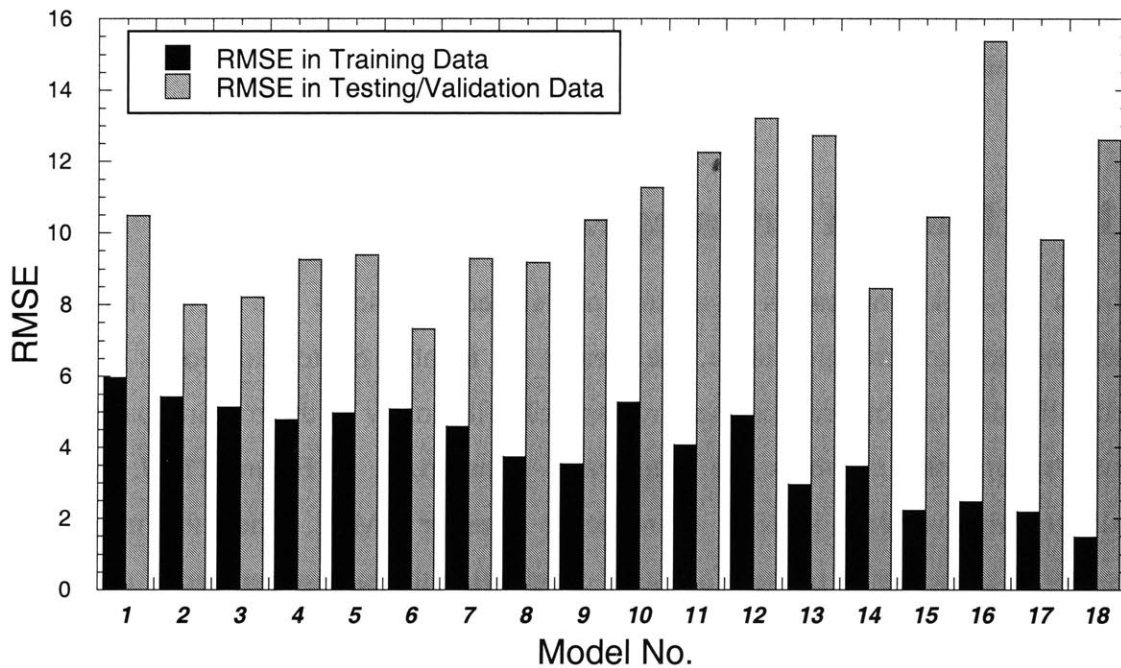


Figure 11.16 Comparison of errors in training data and validation data

Results from training various network models indicate that increasing either the numbers of hidden nodes or hidden layers or training epochs can lead to improved mapping ability between inputs and outputs of the training set. As can be seen in Figure 11.15, for 2 hidden layers and trained for 3,000 epochs, the networks provide predicted outputs almost the same as the targeted outputs in the training set. Obviously, with a greater number of hidden nodes, a network can converge to very small differences between predicted outputs and targeted outputs in the training samples. However, trying to reduce the error too much may lead to overfitting or poor generalization. For example, errors in training samples of the networks with 2 hidden layers are very small. Nevertheless, when they are tested with the validation samples, their predicted settlements are very different from the measured settlements as illustrated in Figure 11.16. These significant differences are not acceptable if we want to apply the network to the real problems. In other words, it means that the network is not reliable for the application.

This clearly shows that although a network can converge to zero error in a training set, it may fail when applied to “new” data. Hence, to evaluate the performance of a network model regarding the training error alone is not appropriate. For this purpose, the error in the validation set is more important.

11.4.2 Effect of Training Epoch

Within the back-propagation algorithm, neural networks learn and correct errors in every iteration they go through. Hence, the greater the number of iteration loops or epochs, the better the network can reduce the error and can fit closely to the training patterns. Results from training the networks are graphically summarized in Figure 11.17. All networks indicate improvements in term of reducing error or RMSE, when the training epochs increase. The networks trained for 3,000 epochs (i.e. the largest number of epochs used in this study) show excellent agreements with the training patterns that almost fit the data perfectly: see also Figure 11.15.

However, when the networks trained for 3,000 epochs are tested with the validation set, they show very poor agreements with the validation samples. Their RMSE are very high as plotted in Figure 11.18. As can be seen in the figures, Model 18 gives the best result in term of the least error in training samples (i.e. $RMSE = 1.48$) but as it attempts to predict the settlements in validation samples, the RMSE increases to 12.61, which is very high. Needless to say, it cannot be used for further application.

In contrast, training the networks for only 1,000 epochs also cannot provide a general solution since the networks still need to learn more. As shown in Figure 11.10 and Figure 11.13, both networks with one or two hidden layers trained for 1,000 epochs are unlikely to map the training samples very well. Moreover, tested with the validation samples, the results are also poor.

As a network is trained (the number of training epochs increases), it passes from relatively simple to relatively complex mapping functions. During the training process, the network learns more and more. At low training epochs, the network still cannot adjust its function to find a general solution for the given problem. This results in large errors in both the training samples and validation samples. On the other hand, if the network has learned or trained for a long time (i.e. large number of epochs); the network would be able to adjust its function to fit the training data very closely. However, during the training process, the networks have passed through intermediate stages that give the best general solution for the problem. To determine the suitable number of epochs used for training, networks must be trained for different epochs and then validated with the validation set.

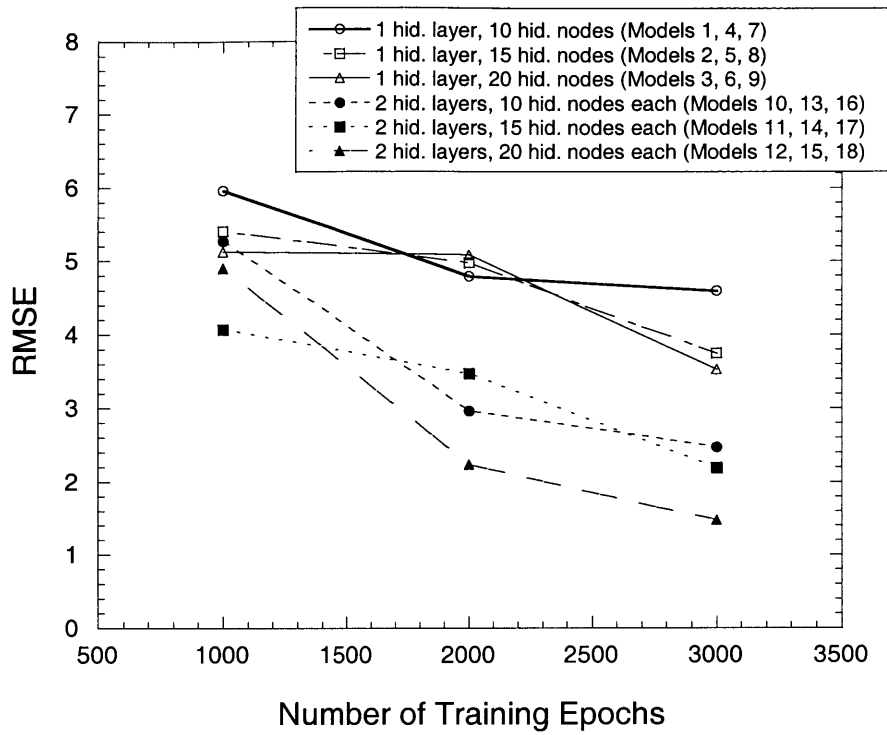


Figure 11.17 Number of training epochs versus RMSE as results from *training samples*

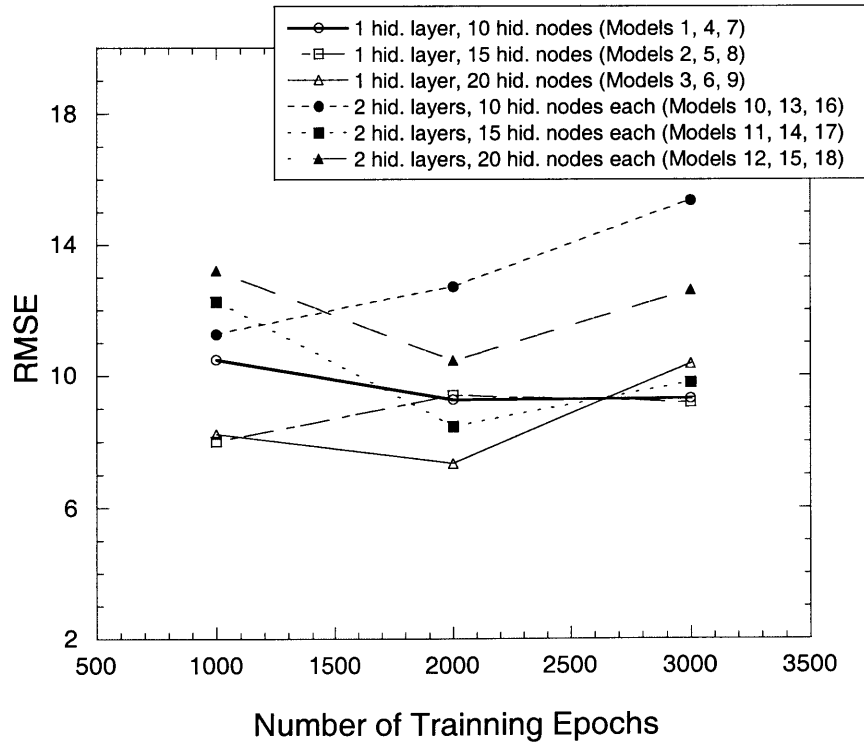


Figure 11.18 Number of training epochs versus RMSE as results from *validation samples*

11.4.3 Effect of Hidden Layers and Hidden Nodes

Generally, increasing the number of hidden layers or increasing number of hidden nodes can affect the network performance. Theoretically, they both lead to an increase in mapping accuracy between input and output data. However, as can be seen in Figure 11.19, not all networks indicated significant improvement in terms of decreases in RMSE, when the number of hidden nodes increases, because increasing hidden nodes from 10 nodes to 20 does not drastically affect the mapping accuracy of the networks. On the other hand, if we change the number of hidden nodes from 5 nodes to 20 nodes, a significant decrease of RMSE would be expected as shown in Figure 11.20.

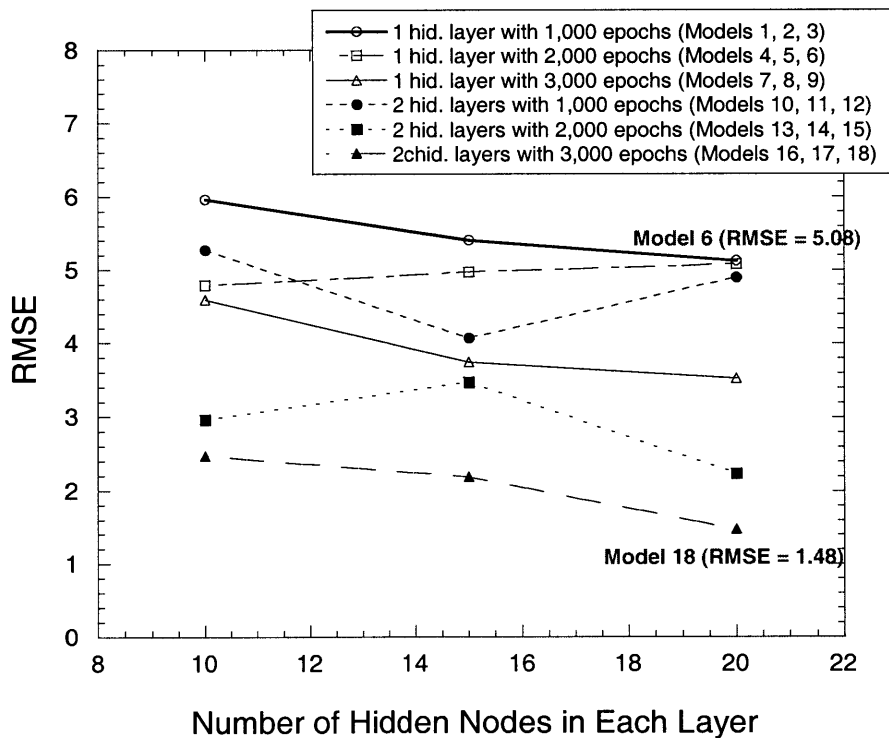


Figure 11.19 Number of hidden nodes versus RMSE as results from *training samples*

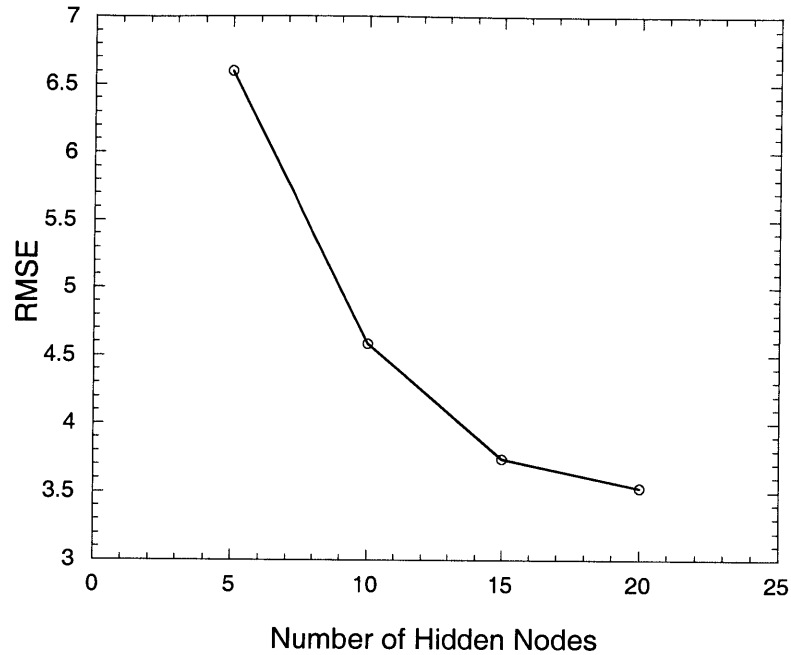


Figure 11.20 RMSE as the number of hidden nodes changes from 5 to 20

Therefore, based on the results of network training, one has learned that increasing the number of hidden nodes or increasing the number of the hidden layer increases accuracy for developing a solution that maps or fits closely the training samples since it increases the complexity of the function in the neural networks.

However, a neural network model with a higher number of the hidden nodes and hidden layers does not mean that it is a better model compared with a network with the lower number. Although, the network could provide almost perfect answers to the set of problems (i.e. $RMSE = 0$) with which it was trained, it may fail to produce meaningful answer to other “new” problems. This is a result of “overfitting.” For example, the network with 2 hidden layers and 20 hidden nodes in each layer trained for 3,000 epochs (Model 18 in Figure 11.15c) shows an excellent agreement with training samples (i.e. $RMSE = 1.48$). However, when it is applied to the test/validation samples, the agreement becomes very poor (i.e. $RMSE = 12.61$). This shows a significant difference between errors in training samples and error in validation samples as a good example for overfitting: see also Figure 11.16.

In contrast, the network with only one hidden layer and 20 hidden nodes trained for 2,000 epochs (Model 6 in Figure 11.11c) yields the lowest RMSE = 7.33, when it is tested with validation samples. The network provides the best settlement prediction as its outputs are in good agreement with measured settlement data. Although the network does not perform very well in the training set (i.e. RMSE = 5.08) compared to other more complex models such as Model 18, it can predict the new data in the validation set much better than all other models as shown in Figure 11.21.

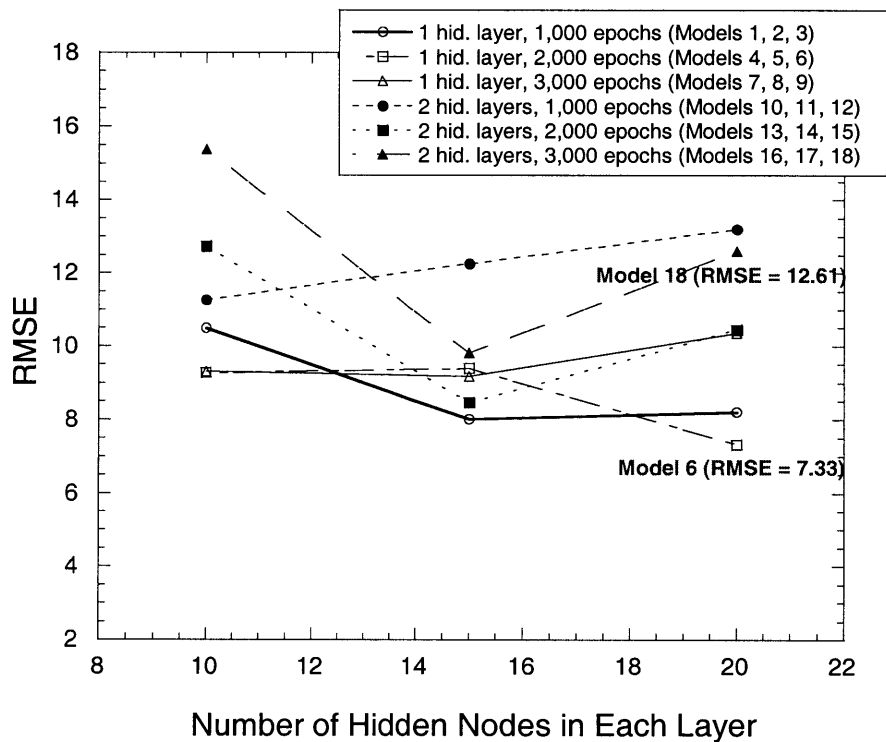


Figure 11.21 Number of hidden nodes versus RMSE as results from *validation samples*

11.5 Summary

This study investigates the potential of artificial neural networks (ANN) for predicting surface settlements. It was found that the feedforward back-propagation neural network models successfully learn from training samples such that their outputs converged to values very close to the desired outputs.

Using a trial and error process, various networks were trained and tested with the validation set. As a result, one can learn that the number of hidden layers and the number of hidden nodes are important variables. The higher the number of the hidden layers and hidden nodes, the better the network fit the training data. However, this may lead to “overfitting.” As can be seen in results of testing various network models, the extreme model with large number of hidden layers and hidden nodes failed to predict surface settlements in the validation set.

To evaluate a network only on its error in training set is not appropriate. Instead, the error in training set is more significant. Hence, to obtain an optimal network that can learn and generalize from examples to produce meaningful solutions, the trial and error is required for this purpose. In this study, based on all performances of the designed network models in the validation set, the optimal network is:

The Optimal Neural Networks for Predicting Ground Surface Settlement	
Network Type	Feedforward-Backpropagation
Transformation Function	Tangent Sigmoid
Number of Input Nodes	13
Hidden Layer	One Layer
Number of Hidden Nodes	20 Nodes
Number of Training Epochs	2,000

In the next chapter, this network then will be applied to predict surface settlements in other tunneling sections.

References

- Attewell, P. B. and Woodman J. P. (1982). "Predicting the Dynamics of Ground Settlement and its Derivatives caused by Tunneling in Soil". *Ground Engineering*, Vol. 15, No. 8, pp. 13-22 and 36.
- Bhokha, S., and Ogunlana, S. O. (1999). "Application of Artificial Neural Network to Forecast Construction Duration of Building at the Pre-design Stage". *Journal of Engineering Construction and Architecture Management*, Vol. 6, No. 2, 1999, .
- Goh, T. C., Wong, K. S., and Broms, B. B. (1995). "Estimation of Lateral Wall Movements in Braced Excavations Using Neural Networks". *Canadian Geotechnical Journal*, Vol. 32, 1995, pp. 1059-64.
- Lee, C., and Sterling, R. (1992). "Identifying Probable Failure Mode for Underground Openings Using a Neural Network". *International Journal of Rock Mechanics and Mining Sciences*, Vol. 29, No. 1, 1992, pp. 49-67.
- Lee, I. M., and Lee, J. H. (1996). "Prediction of Pile Bearing Capacity Using Artificial Neural Networks". *Computers and Geotechnics*, Vol. 13, No. 3, 1996, pp. 189-200.
- Peck, R. B. (1969). "Deep Excavations and Tunneling in Soft Ground". *Proc. 7th Int. Conf. on Soil Mechanics and Foundation Engineering*, Mexico City, State of the Art Volume, pp. 225-290.
- Rafiq, M. Y., Bugmann, G., and Easterbrook, D. J. (2001). "Neural Network Design for Engineering Applications". *Computers and Structures*, Vol. 79, 2001, pp. 1541-52.
- Shi, J., Ortigao, A. R., and Bai, J. (1998). "Modular Neural Networks for Predicting Settlements during Tunneling". *Journal of Geotechnical and Geoenvironmental Engineering*, Vol. 124, No. 5, 1998, pp. 566-472.
- Sirat, M., and Tabbot, C., J., (2001). "Application of Artificial Neural Networks to fracture analysis at the Aspö HRL, Sweden: Fracture Set Classification". *International Journal of Rock Mechanics & Mining Sciences*, Vol. 38, 2001, pp.621-639.
- Teh, C. I., Wong, K. S., Goh, T. C., and Jaritngam, S. (1997). "Prediction of Pile Capacity Using Neural Networks". *Journal of Computing in Civil Engineering*, Vol. 11, No. 2, 1997, pp. 129-38.
- Yang, Y., and Zhang, Q. A. (1997). "Hierarchical Analysis for Rock Engineering Using Artificial Neural Networks". *Rock Mechanics and Rock Engineering*, Vol. 30, No. 4, 1997, 207-22.

Zhang, Q., Song, J., and Nie, X. (1991). "Application of Neural Network Models to Rock Mechanics and Rock Engineering". *International Journal of Rock Mechanics and Mining Sciences*, Vol. 28, No. 6, 1991, pp. 535-40.

CHAPTER 12

Applications of Artificial Neural Networks (ANN) on the MRTA Project

12.1 Introduction

As discussed in Chapter 11, the Nishimatsu drive (Tunnel Section A) was used as a pilot experiment to develop an optimal neural network model. It has been found that the neural network model, with one hidden layer and 20 hidden nodes trained for 2,000 epochs, can predict surface settlements well as shown when comparing observations with validation samples. This proves that the neural network approach may be used for predicting surface settlements caused by a single tunnel.

In this chapter, the use of neural networks for predicting surface settlements caused by EPB tunneling is demonstrated. The objectives of this chapter are: (1) to investigate the applicability of neural networks for predicting surface settlements, (2) to examine the limitations of using the ANN models for predicting settlements in practice. To achieve these objectives, the network models will be applied to various scenarios using the data from the MRTA project. These applications include:

- (1) The prediction of maximum settlements caused by a single tunnel and by twin tunnels.
- (2) The prediction of settlements occurring in Zones 1 and 2.
- (3) The prediction of maximum settlements induced by tunneling in clays.

- (4) The prediction of maximum settlements using data only from the beginning of the tunnel drive to train the network and then apply the trained network to predict surface settlements occurring in the rest of the tunnel drive.

12.2 Prediction of Maximum Surface Settlements induced by a Single Tunnel

In this section, the performance of the neural network model used for predicting surface settlements caused by the first tunnel is investigated. Various application scenarios are considered as summarized in Table 12-1.

12.2.1 Scenario 1: Trained with samples recorded from Section A for predicting settlements in other tunnel sections

In Chapter 11, the network was trained with samples from Section A. The result of the training shows that the network can closely fit the measured data. Tested with the validation samples also selected from Section A, the optimal network yielded low error (i.e. RMSE = 7.33). Both the training and testing results of the network are plotted in Figure 12.1. The objective of Scenario 1 is to verify whether this network trained with data from Section A can also be used for predicting surface settlements in other tunnel sections (i.e. Sections B, C, and D) with the same degree of confidence.

Table 12-1 Summary of the scenarios used for settlement predictions

Scenario	Objective	Trained Samples	Tested Sample/Predicting
1	Max. settlement of the first tunnel	<i>Note: From Chapter 11</i>	
1.1		Section A	Section B
1.2		Section A	Section C
1.3		Section A	Section D
2	Max. settlement of the first tunnel		
2.1		Section B	Section B
2.2		Section C	Section C
2.3		Section D	Section D
3	Max. settlement of the first tunnel	Sections A and B	Sections A and B
4	Max. settlement of the first tunnel	Section A, B, and C <i>Note: All used Kawasaki machines</i>	Section A, B, and C
5	Max. settlement of the first tunnel	All sections (A, B, C, and D)	All sections (A, B, C, and D)
6	Max. settlement of the first tunnel	All sections (A, B, C, and D) <i>Note: adding shield model node</i>	All sections (A, B, C, and D)
7	Reduction of input parameters		
7.1	No penetration rate input node	Section A; Sections A and B; and Sections A, B, and C	Section A; Sections A and B; and Sections A, B, and C
7.2	No grouting quality input nodes	Section A; Sections A and B; and Sections A, B, and C	Section A; Sections A and B; and Sections A, B, and C
7.3	No face pressure input node	Section A; Sections A and B; and Sections A, B, and C	Section A; Sections A and B; and Sections A, B, and C
8	Using small amounts of data	Each section	Each section
9	Settlement in Zone 2 (the first tunnel)	All sections (A, B, C, and D)	All sections (A, B, C, and D)
10	Settlement in Zone 1 (the first tunnel)	All sections (A, B, C, and D)	All sections (A, B, C, and D)

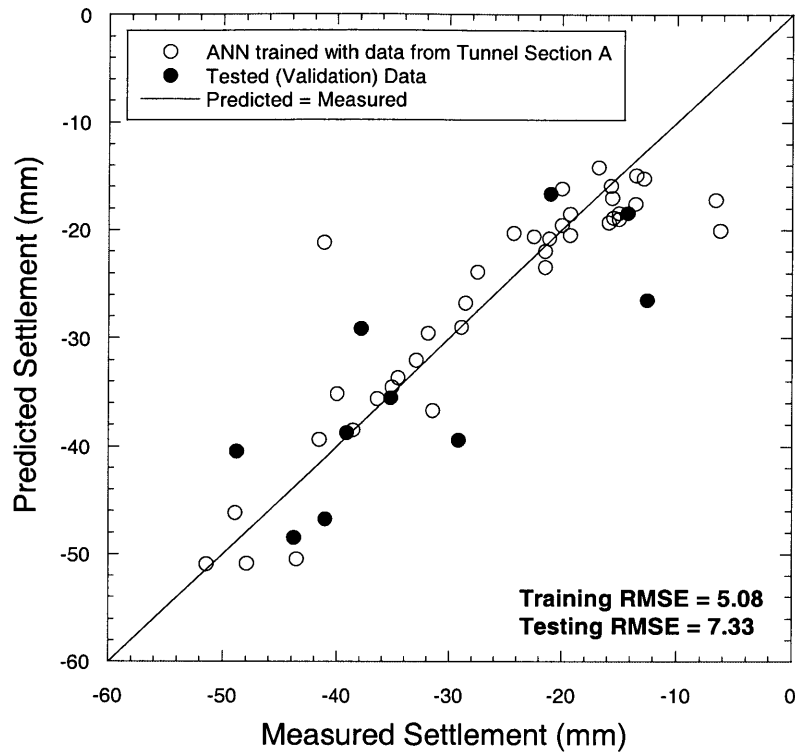


Figure 12.1 Training and testing results from Section A given by the optimal neural network model

12.2.1.1 Settlement Prediction in Section B

Tunnel Section B is a part of the North tunneling section (from Thiam Ruam Mit station to Bang Sue station: see Figure 12.2). The North section was excavated by two contractors: Nishimatsu and Obayashi. From Rama IX station to Ratchada station, classified as Tunnel Section A in this study, the tunnel was excavated by Nishimatsu. The rest of the tunnel, built by Obayashi, was excavated from Ratchada station to Bang Sue station. This section is known as Tunnel Section B. Details on the tunnel sections are provided in Chapter 5.

The soil profile in the entire North tunneling section is quite uniform with soft clay underlain by stiff clay along the tunnel alignment (Figure 12.3). The tunnel was

excavated mostly within the stiff clay layer (i.e. about 15-25 m below ground surface). In general, Obayashi operated the shield in the EPB mode by keeping the face pressure approximately between 150 to 200 kPa during excavation.

To examine whether the network can predict surface settlements occurring in this section, testing samples were selected from the computerized database. The samples contained all 10 influencing parameters (i.e. represented by 13 nodes: see Chapter 11), which were used as inputs to the network. The results are shown in Figure 12.4. Apparently, the predicted settlements calculated by the neural networks show poor to very poor agreement with the measured data in this section.

The most significant factor leading to the failure of the network is that the parameters used as the testing inputs are outside the training boundary (i.e. trained with data from Section A). Although both Sections A and B of the tunnel used similar EPB shield models, manufactured by Kawasaki, the shield operating parameters used in each section were very different. For example, as shown in Figure 12.5, the penetration rate represented by node 10 in the network was between 26.4 and 76.85 mm/min; these were the rates used from Section A to train the network. However, Obayashi (Section B) operated their shields at lower penetration rate due to limitations of their pipe transport. Specifically the penetration rate recorded in Section B was as low as 8 mm/min, which is far from the range in which the network was trained (Figure 12.5). In addition the face pressure (input node 9) applied to Tunnel Section B is in the higher range (up to 250 kPa), which is also out of the range used for network training as shown in Figure 12.6.

As indicated, it is essential that the training samples presented to the network be selected to cover the upper bound and lower bound of the problem that one wants to solve (illustrated in Figure 12.7). Otherwise as shown above, the input parameters (shown in Figure 12.8) can result in the failure of the network in predicting surface settlements.

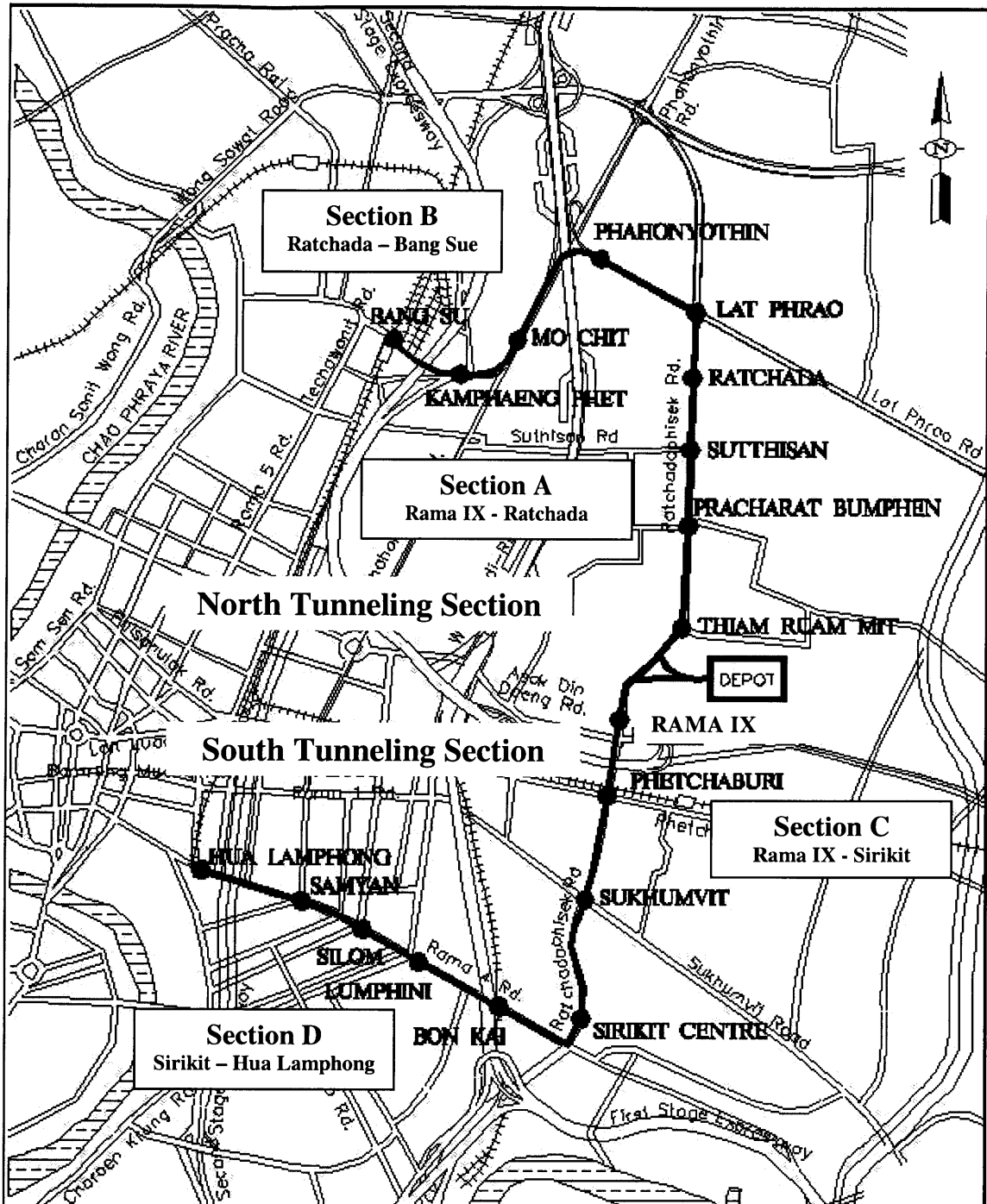


Figure 12.2 Locations of tunnel sections in the MRTA project

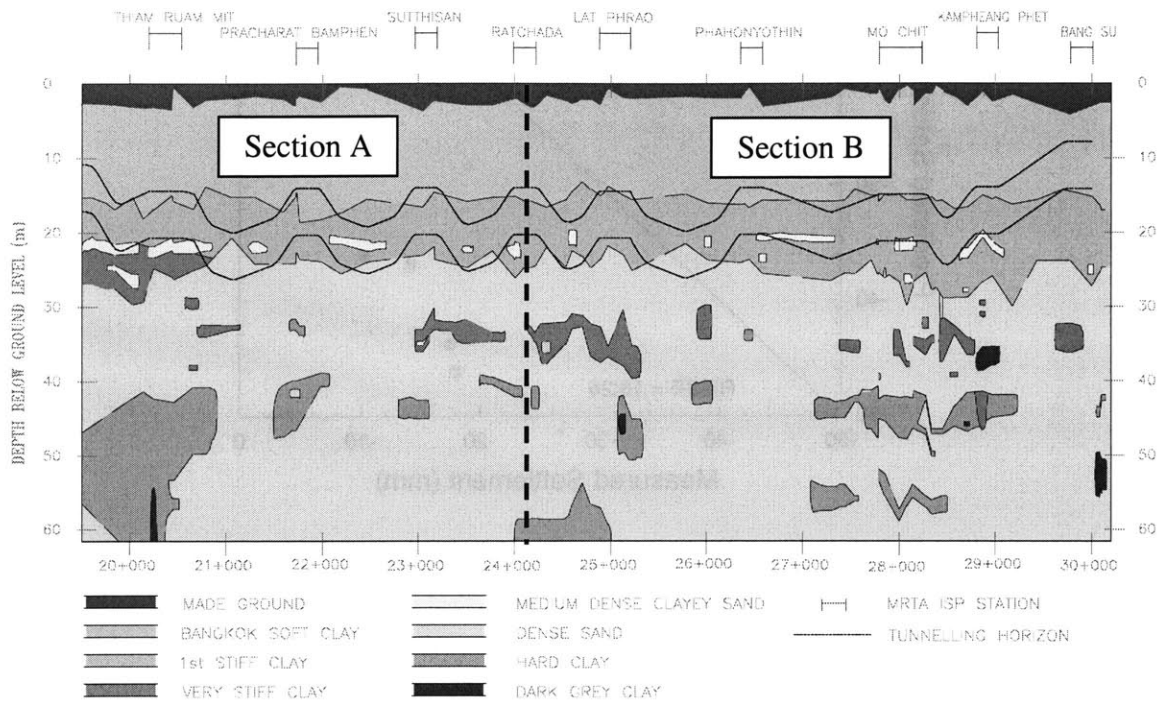


Figure 12.3 Geological profile of North Tunnel Section representing Sections A and B

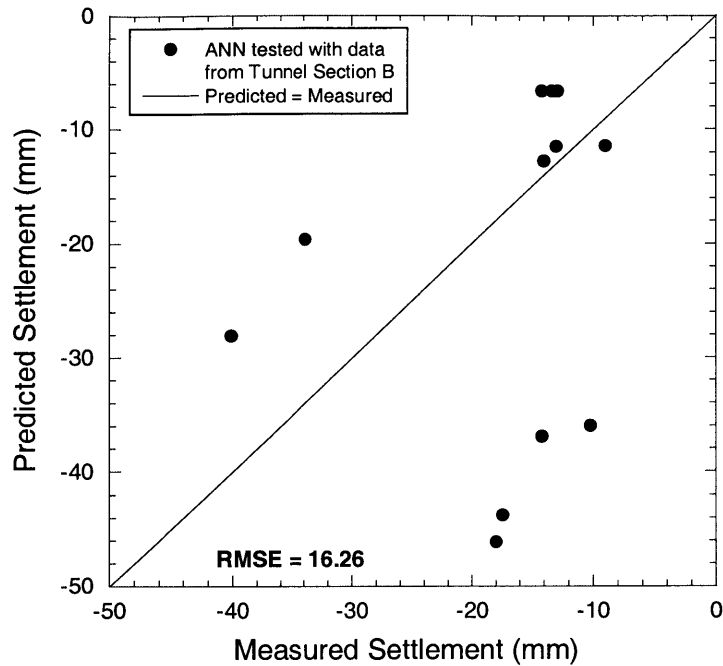


Figure 12.4 Results of using the neural network for predicting settlements in Section B

12.2.1.2 Settlement Prediction in Section C

Kumagai Kumi excavated section C, a part of the South tunnel section. The rest of the South tunnel section underneath Rama IV road is known as Section D and was excavated by Bilfinger and Berger: see Figure 12.2. The soil profile in the South section is different from that of the North section in that the ground condition is not uniform throughout the alignment. Additionally in Section C, the dense sand layer is located 50 m. below the ground surface, which is much deeper than in the North tunnel section: see Figure 12.3 and Figure 12.9.

The soil profile of Section C is quite consistent along its route. This tunnel drive commenced mostly in stiff clay. In general the shield was operated in the EPB mode thus maintaining face pressures of typically 200 kPa or higher. Only at the beginning did the

applied face pressure reach 400 kPa as a result of tests to determine an optimal EPB mode.

In this scenario, samples are selected from Section C for testing the prediction accuracy of the network trained with data from Section A. It was found that predicted settlements are in very poor agreement with measured settlements as shown in Figure 12.10. One crucial factor that might cause the failure of prediction is due again to the limitation of the training boundary. As can be seen in Figure 12.6, face pressures recorded in the Kumagai Kumi drive are very high compared to the much lower pressure applied in the Nishimatsu drive (i.e. typical face pressure is 50 kPa in Section A).

12.2.1.3 Settlement Prediction in Section D

In section D, the tunnel was excavated from Sirikit station to Hua Lumphong station using a Herrenknecht machine operated by Bilfinger and Berger. Operational principles of the shield are very similar to those employed by the Kawasaki shields in all other sections. Only its specifications are slightly different as summarized in Table 5-8.

Section D is a unique tunnel drive because tunnels were stacked so that the lower southbound tunnel, from which data was taken for ANN use, was excavated within a deep sand layer to avoid the existing foundations of a fly-over bridge. As result the tunnel depth was much greater than in the other sections.

Results from using the network to predict surface settlements are shown in Figure 12.11. As can be seen, the overall predicted settlements are in poor agreement with the measured settlements. Again the problem is caused by the training boundary not covering the testing domain sufficiently. In general, the face pressure applied in Section D is greater than that of Section A (see Figure 12.6). Additionally, the tunnel depth (input node 1) is great (i.e. up to 33 m when tunnels are stacked) as shown in Figure 12.12, and grouting pressure (input node 12) is also as high as 5 bars: see Figure 12.13. Both parameters are far outside the training boundary that was used to train the network.

Besides the boundary problem, the specifications of the Herrenknecht machine used in Section D are somewhat different from Kawasaki machines used in all the other sections. Its length is 6.19 m which is shorter than the Kawasaki machine (8.33 m). Its outer diameter of 6.46 m is larger than the 6.43 m diameter of the Kawasaki (see also Section 5.4). Hence the Herrenknecht machine appears to create a larger gap between the shield and outer lining diameter than the Kawasaki machines. Therefore the network, trained with data recorded in Section A established relationships is not applicable to the data obtained from Section D.

Table 12-2 summarizes the testing results when using the network trained with data from Section A to predict settlements in other tunnel sections. Obviously the network only performs well with the testing data from Section A (i.e. the same section) but fails to predict surface settlements in other sections because it has been trained on data that does not cover the range of the given problem.

Table 12-2 Summary of testing results in Scenario 1

Tunnel Section	A (Chapter 11)	B	C	D
Testing RMSE	7.33	16.26	19.69	21.96

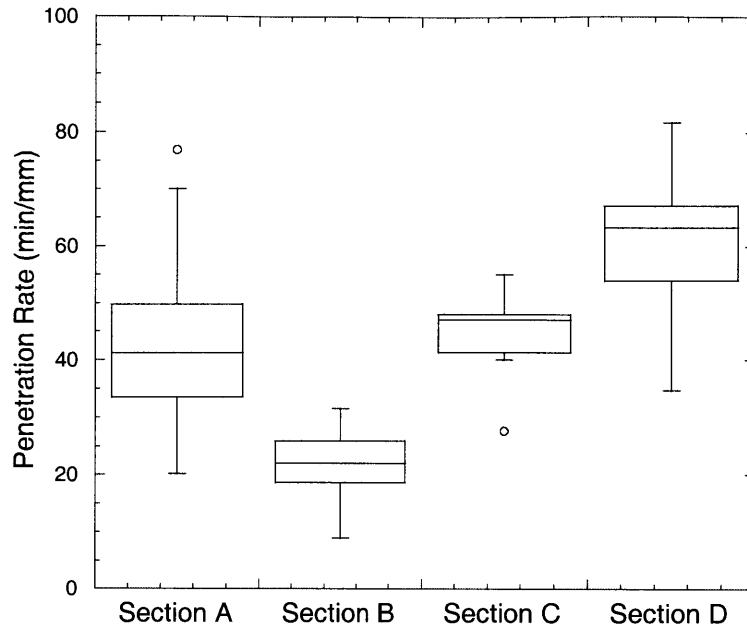


Figure 12.5 Ranges of penetration rate recorded in the MRTA project

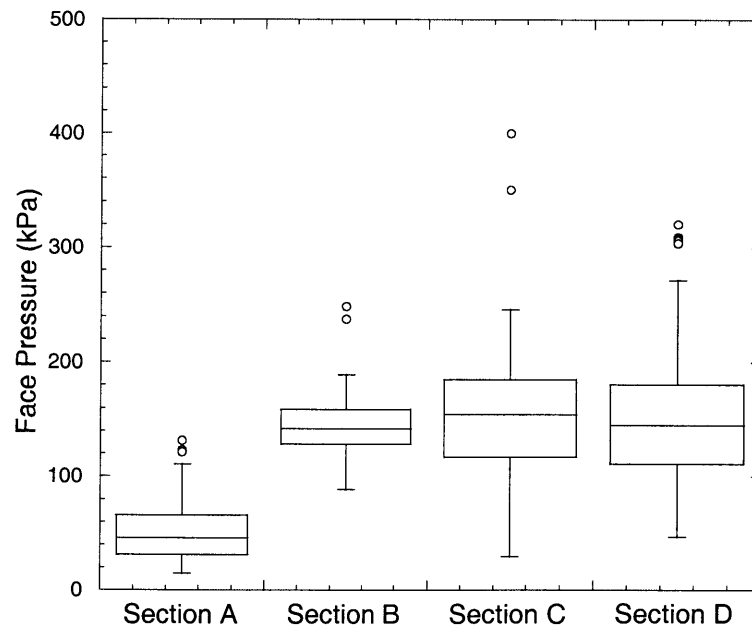


Figure 12.6 Ranges of face pressure recorded in the MRTA project

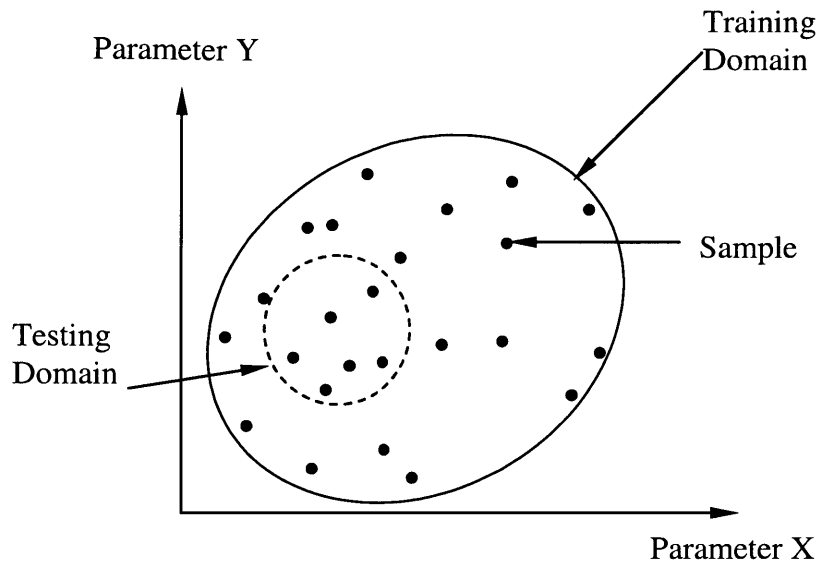


Figure 12.7 Example of training sample and testing sample domains needed for neural network application (see also Section 10.6)

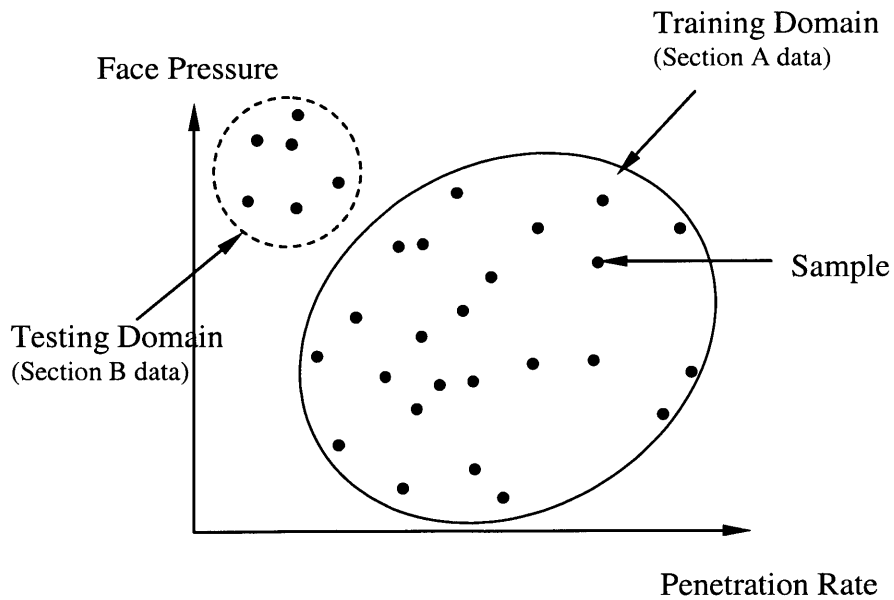


Figure 12.8 Example of training sample and testing sample domains actually applied in Scenario 1.1

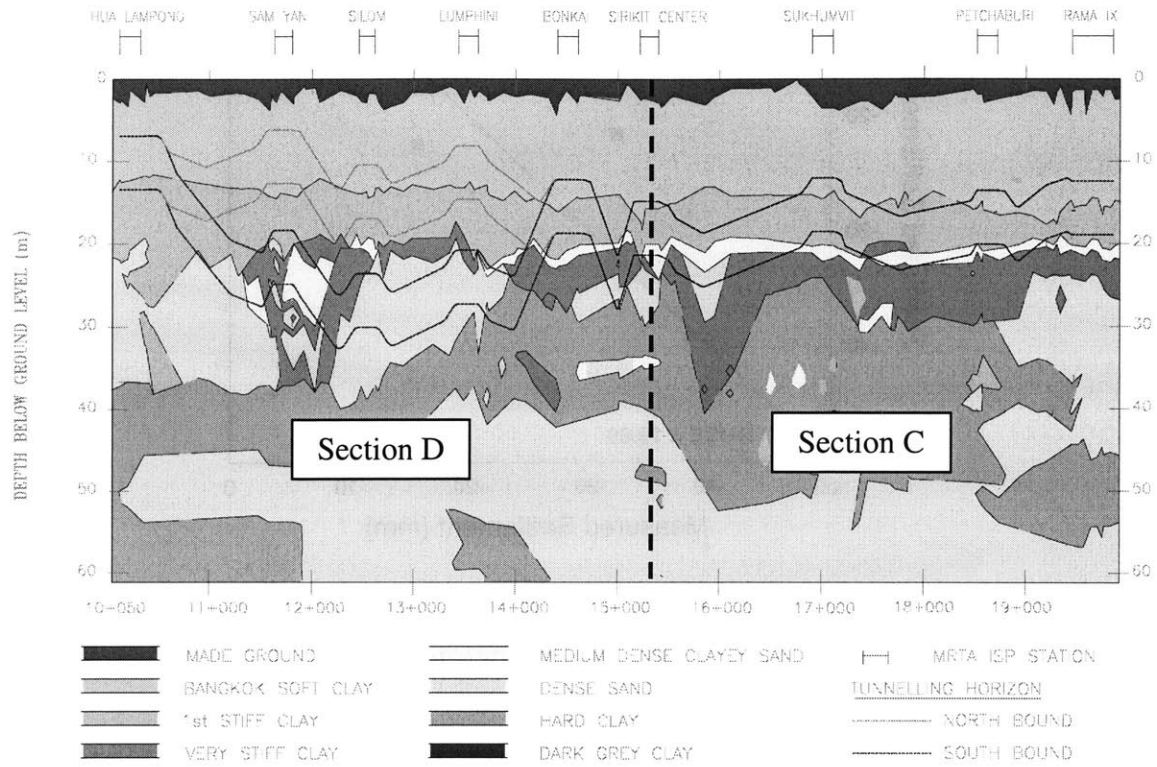


Figure 12.9 Geological profile of South Tunnel Section representing Sections C and D

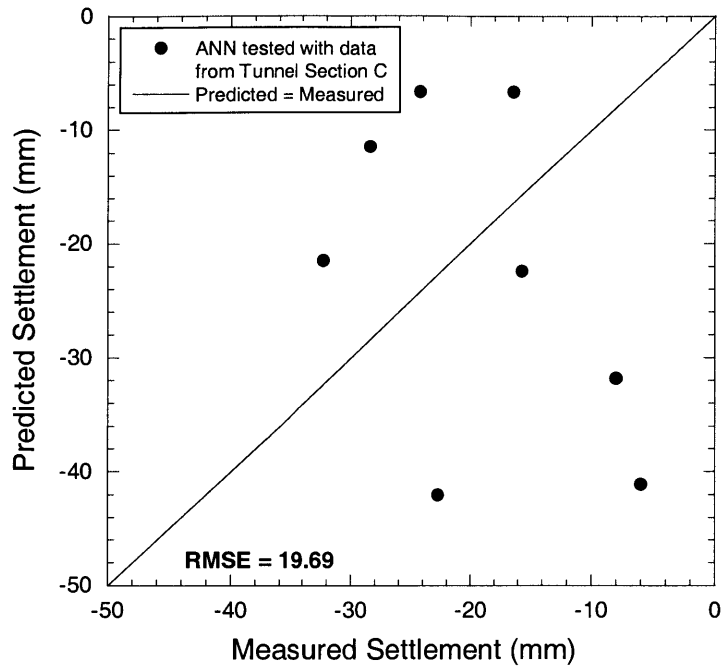


Figure 12.10 Results of using the network for predicting settlements in Section C

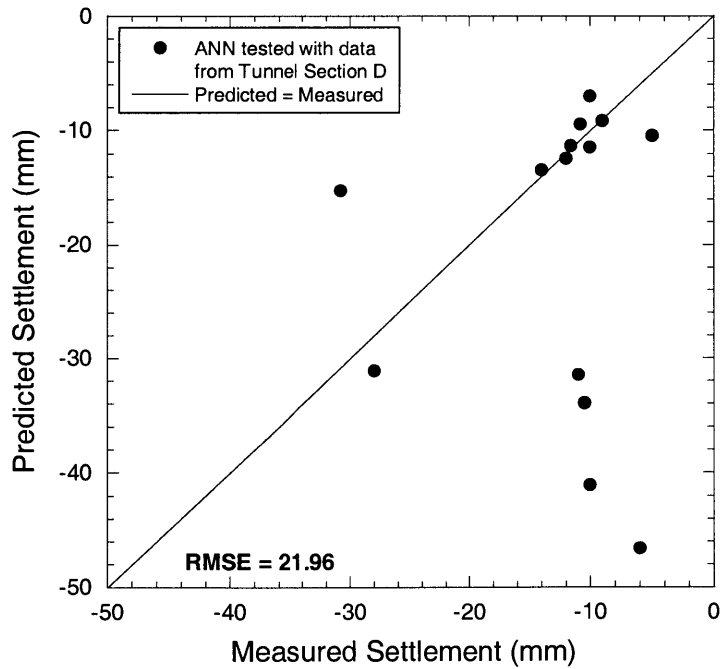


Figure 12.11 Results of using the network for predicting settlements in Section D

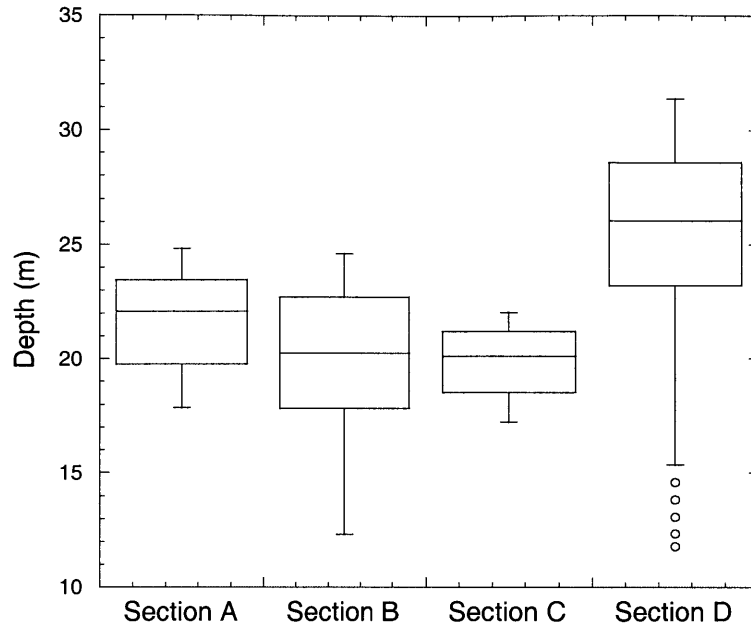


Figure 12.12 Ranges of tunnel depth in the MRTA project

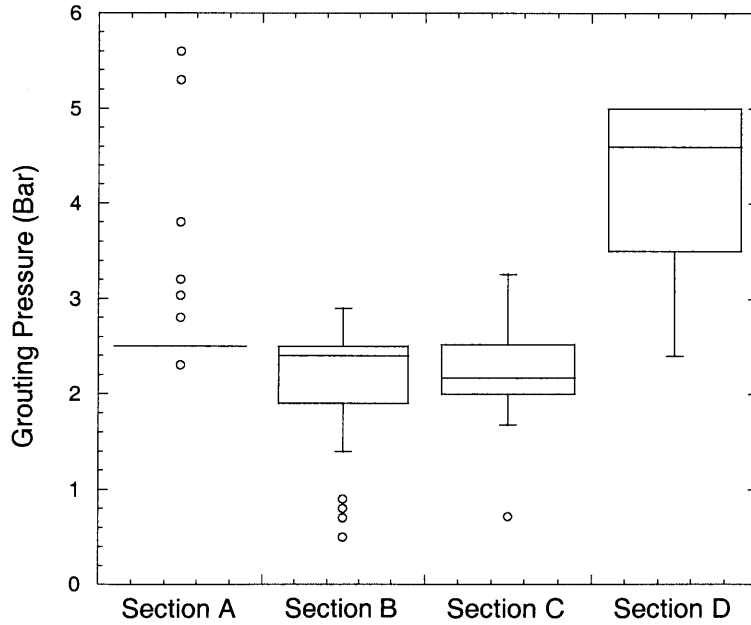


Figure 12.13 Ranges of grouting pressure recorded in the MRTA project

12.2.2 Scenario 2: Trained and tested with samples recorded from the same tunnel section

Based on results from Scenario 1, one can observe that using a network model only trained with samples from Section A to predict settlements in other sections shows very poor agreement with measured data since the testing domains are outside the training boundary. However, if its training domain covers all possible testing domains as shown in Figure 12.7, it should be able to predict the settlement more accurately. Hence we need to investigate this further by training the same network model with samples from each section and likewise test it with samples selected from the same tunnel section: see Table 12-1.

12.2.2.1 Settlement Prediction in Section B

The ANN model used in this section has one hidden layer with 20 hidden nodes and the number of training epochs is set to be 2,000 as before. After the network has been trained, it is tested with new samples also selected from Tunnel Section B. The results from training and testing are plotted together in Figure 12.14. As can be seen, the ANN predictions fit the data in the training samples with a low RMSE of 2.55. Moreover, tested with new data, the network predicts surface settlements very close to the measured settlement with relatively small error (i.e. RMSE = 6.22) except one point (see Figure 12.14). This might be caused by a lack of training data in that range, resulting in the network being ill trained to formulate a generalized solution for that region.

12.2.2.2 Settlement Prediction in Section C

Figure 12.15 shows results from training and testing the network with data from Section C. The training results almost fit the data perfectly and yield very low error (i.e. RMSE = 2.31). Using the trained network to predict settlements also shows excellent agreement with measured settlements (i.e. RMSE = 5.90).

12.2.2.3 Settlement Prediction in Section D

Results from training and testing the network with data from Section D are illustrated in Figure 12.16. Overall training results are in agreement with the measured data, especially for low settlements where there are many the data points. Using the trained network for predicting surface settlements in that section also shows very good agreement with measured data in the range between -5 and -25 mm. However, for large settlements, the prediction accuracy is quite low.

Table 12-3 summarizes the training and testing results of Scenario 2. When comparing these test results with those of Scenario 1 (Table 12-2), one can see that the prediction accuracy of the network trained and tested with data from the same section is much higher than the results given by the network trained with data from Section A and used to predict settlement in other sections (Table 12-2).

Table 12-3 Summary of training and testing results from Scenario 2

Tunnel Section	A (Chapter 11)	B	C	D
Training RMSE	5.08	2.55	2.31	5.98
Testing RMSE	7.33	6.22	5.90	7.56

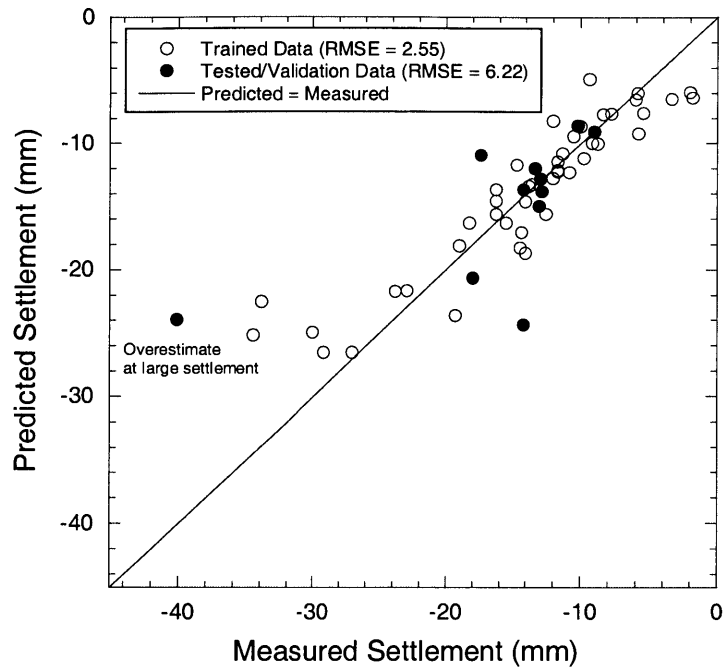


Figure 12.14 Performances of neural networks on trained and tested data in Section B

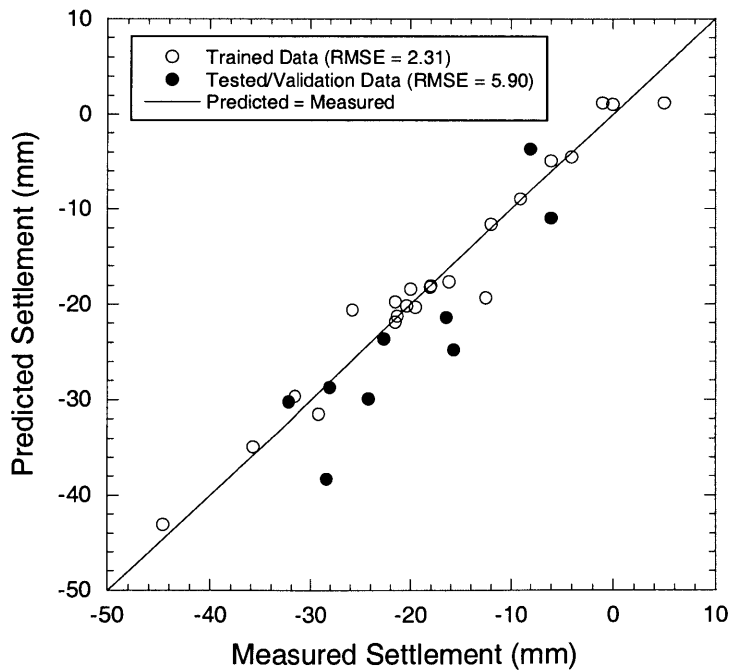


Figure 12.15 Performance of neural networks on trained and tested data in Section C

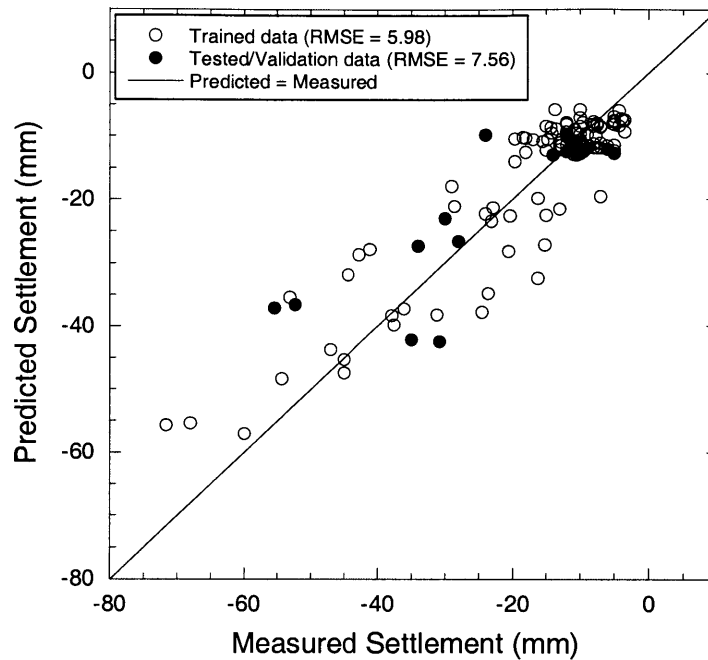


Figure 12.16 Performance of neural networks on trained and tested data in Section D

12.2.3 Scenario 3: Trained and tested with samples recorded from Sections A and B (North Section)

In this scenario, the performance of the neural network model is investigated when the model is trained with data from Sections A and B and then used for predicting surface settlements in these sections. Both sections are parts of the North tunneling section, which was excavated within a very uniform soil profile as illustrated in Figure 12.3. Their tunnel alignments and geometries are also very similar. In addition, the same type of EPB shields were used in Sections A and B. The only major difference between the two sections is that operational parameters recorded from each section are quite different (see Figure 12.5 and Figure 12.6).

Based on the training results, it was found that the training error given by the network is low (i.e. RMSE = 5.96). When the network is used for prediction, it also gives good

results as its predicted settlements are very close to the measured data. Results from training and testing are plotted in Figure 12.17.

12.2.4 Scenario 4: Trained and tested with samples recorded from Sections A, B, and C

The results of Scenario 3 shows that the network trained with data from Sections A and B performs well for settlement predictions in those sections. This trend leads to the assumption that if the network is trained with a combination of data from different tunnel sections, where tunnels were excavated using similar machines; a generalized solution can be obtained to predict the surface settlement with high accuracy. To verify this assumption, the data from Section C in the South tunnel (which employed Kawasaki machines, similar to the machines used in the North section) is used to train the network together with data from Sections A and B. The trained network is then used for the prediction. In other words, Scenario 4 is designed to represent the condition that all data is recorded from tunnel sections excavated with Kawasaki machines (i.e. Sections A, B, and C) and then using this network to predict surface settlements occurring in Sections A, B, and C.

Results from training and testing/prediction are shown in Figure 12.18. The network performs very well with training samples; results converge to a small error (i.e. RMSE = 5.87). Using the network for predicting surface settlements also indicates excellent agreements with the measured data. Compared to Scenario 3, including the data from Section C into the training set gives similar training and testing results. This suggests that the network model trained with data from different tunneling sections where shields were operated differently can also predict surface settlements accurately.

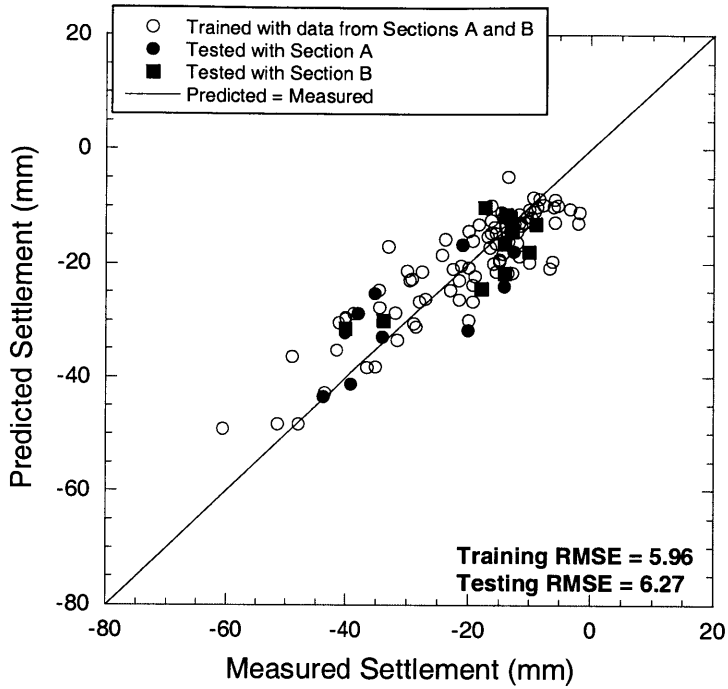


Figure 12.17 Training and testing results from neural networks trained with data from Sections A and B (Scenario 3)

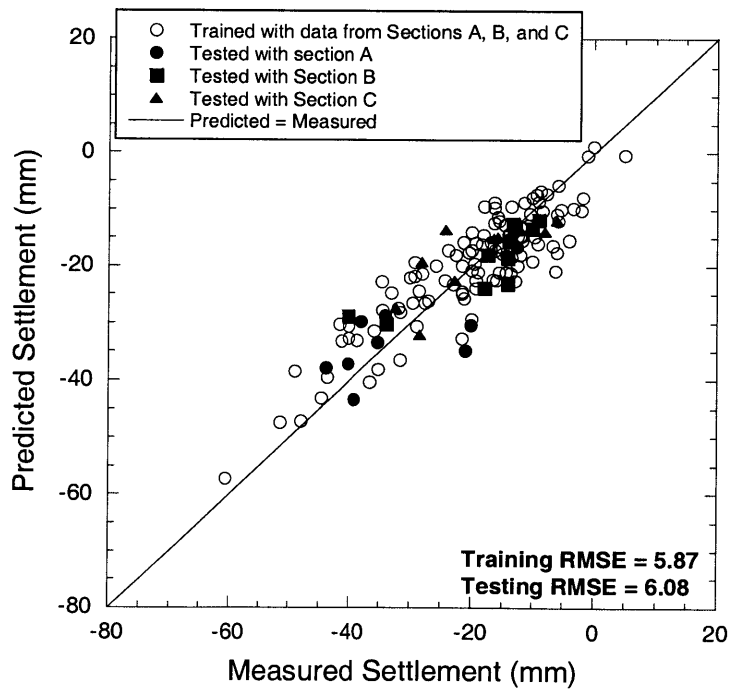


Figure 12.18 Training and testing results from neural networks trained with data from Sections A, B, and C (Scenario 4)

12.2.5 Scenario 5: Trained and tested with samples recorded from all Sections

In Scenario 5, the network is trained using all the data recorded from all sections. Results from training and testing are shown in Figure 12.19. As can be seen, the network maps all data in the training set quite well. However for settlement prediction, its overall error is still statistically high (RMSE = 8.39) compared with previous cases. This may be affected by the fact that there are some differences between Kawasaki and Herrenknecht machines as mentioned earlier.

12.2.6 Scenario 6: Trained and tested with samples recorded from all Sections (adding shield model node)

The results of Scenario 5 raise questions regarding the effect of machine type on the network model. The network model may need more input parameters or needs to be modified in order to accommodate the difference between Kawasaki and Herrenknecht types and increase the predictive accuracy.

Originally, the network model has 13 input nodes representing 10 influencing parameters. To capture the difference between two EPB machines, an input node no. 14 is added to represent the machine model. If the machine is manufactured by Kawasaki, the input will be “1.” In contrast, if the Herrenknecht machine is used, the input will be “0.” The modified model is shown in Figure 12.21.

The modified neural network model is then trained and tested with the same samples used in Scenario 5. As shown in Figure 12.20, the network indicates some improvements in both training and testing samples, i.e. it yields lower error than Scenario 5.

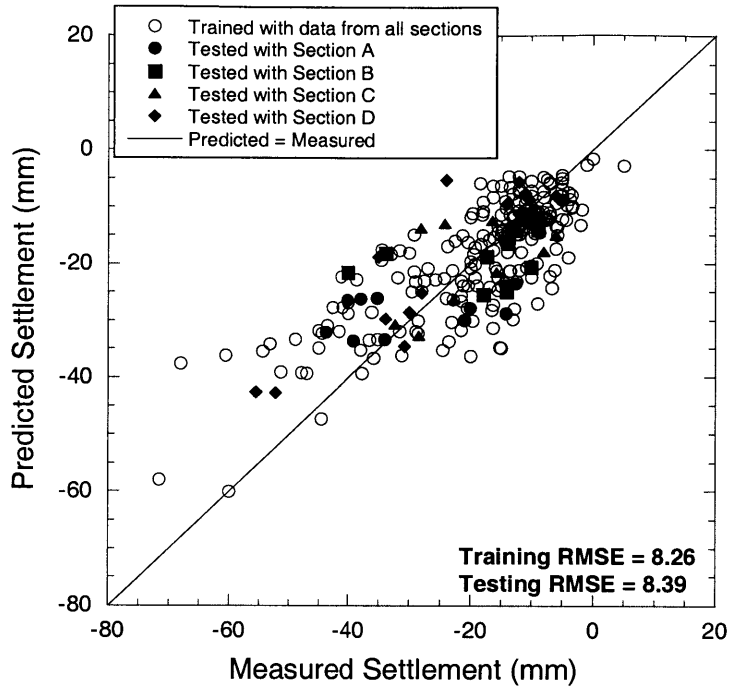


Figure 12.19 Training and testing results from neural networks trained with all data from all sections (Scenario 5)

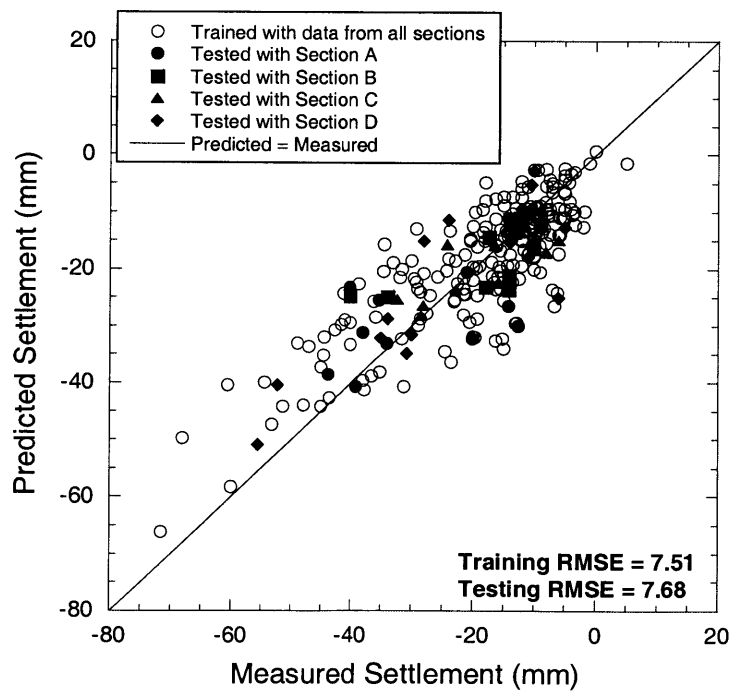


Figure 12.20 Training and testing results from neural networks (adding machine model input node) trained with all data from all sections (Scenario 6)

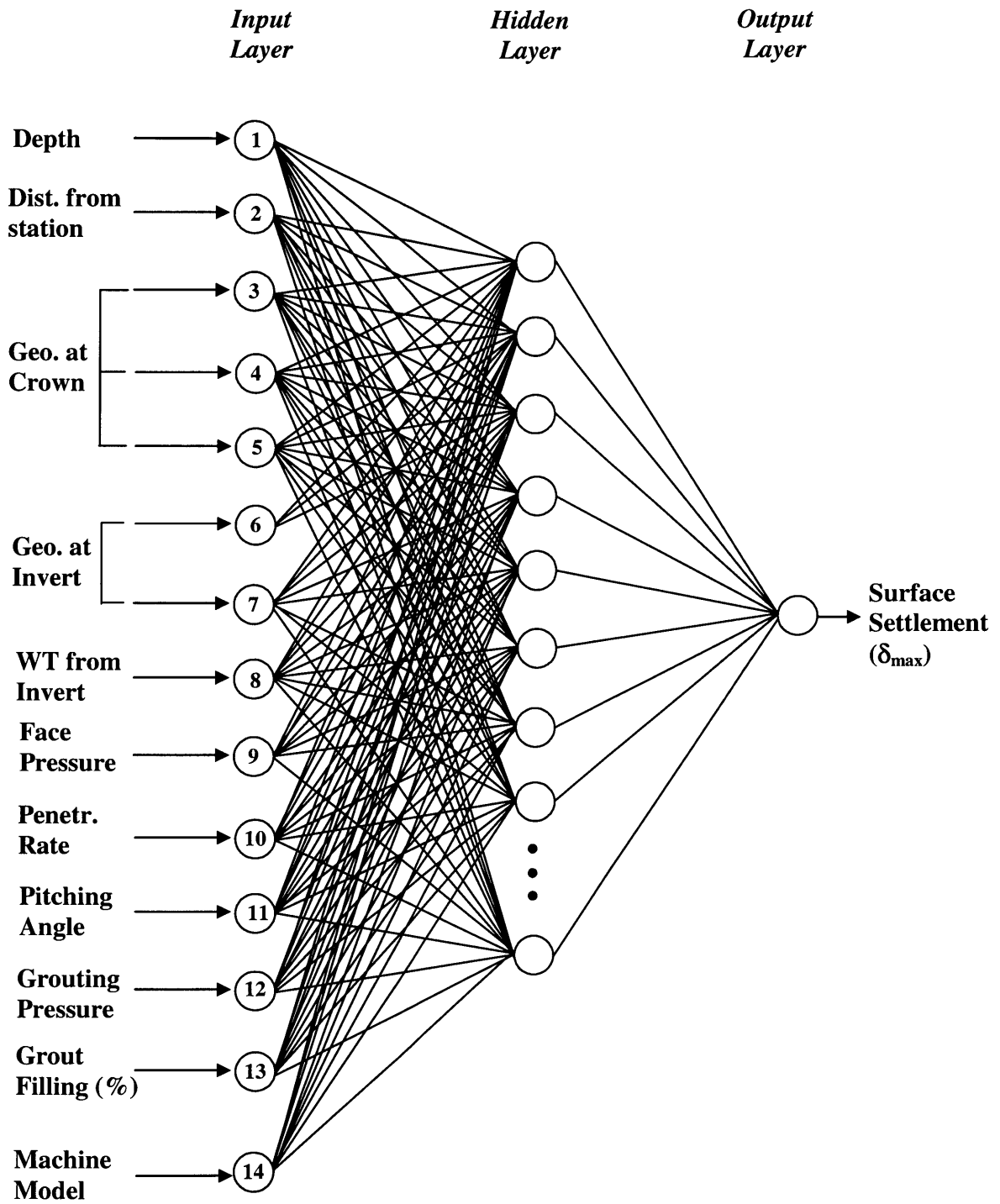


Figure 12.21 Structure of the modified neural network model for predicting surface settlements in the entire MRTA project

12.2.7 Scenario 7: Reduction of input parameter nodes

In a feedforward network, the nodes are generally grouped into layers. Signals flow from the input layer through to the output layer via connections, the nodes being connected from one layer to the next. Each link between nodes has a weight (w) so that in the network, there are a large number of weights used for transferring values between input and output. Therefore, it is very difficult and not practical for one to determine all weights linking an input parameter to an output parameter.

An alternative way to determine if an input is important to the network is to exclude the particular parameter and examine the network performance. This is done here for three parameters (i.e. four input nodes): (1) ANN model without the penetration rate input node and (2) ANN model without the grouting quality input nodes (i.e. no grouting pressure and grout filling nodes) and (3) ANN model without the face pressure input node.

12.2.7.1 Neural network model without the penetration rate input node

The input nodes of the neural network model used in previous sections are reduced by excluding the penetration rate node. First, the new network without the penetration rate inputs is trained with samples from Section A and tested with validation samples from the same section. Results of training and testing are shown in Figure 12.22. As can be seen, the training error given by the network is quite low (RMSE = 4.87). However, when the network is used for prediction, it produces poor results (RMSE = 10.05) since the predicted settlements are very different from the measured data.

The new network is investigated further by training it with samples from Sections A and B and likewise test it with samples selected from the same tunnel sections. As shown in Figure 12.23, it was found that both training and testing errors given by the network are relatively high. The final case is to train and test the network with data from Sections A, B, and C. Results from training and testing are shown in Figure 12.24. As can be seen, the network gives high errors in both sets. When comparing training and testing errors

(RMSE) of the network with those of the network including the penetration rate node (Figure 12.25 and Figure 12.26, respectively), one can see that the prediction accuracy of the network without the penetration rate input node is lower than the results given by the networks that include the penetration rate input node. Hence, it can be concluded that the penetration rate is an essential input factor which has to be represented by the network if one wants to predict surface settlements with high accuracy.

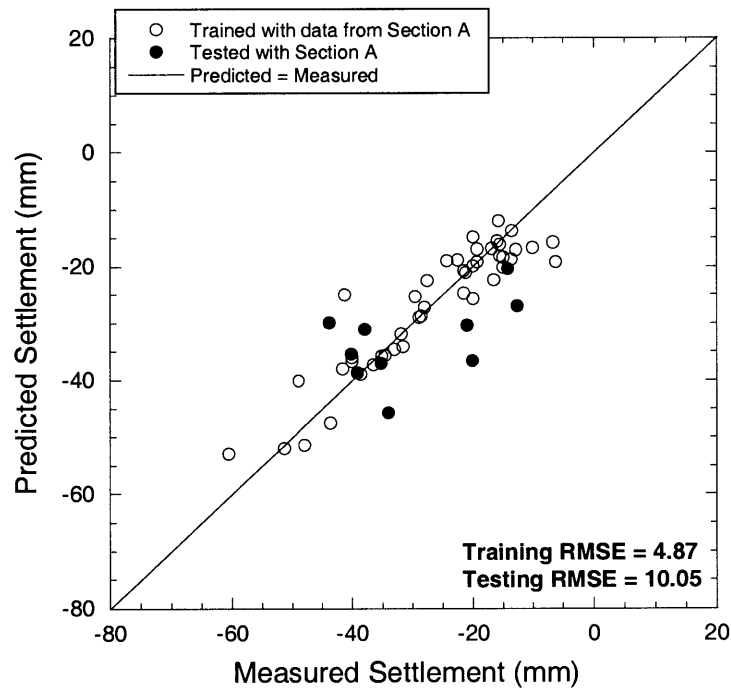


Figure 12.22 Results from neural networks without penetration rate input node trained and tested with data from Section A

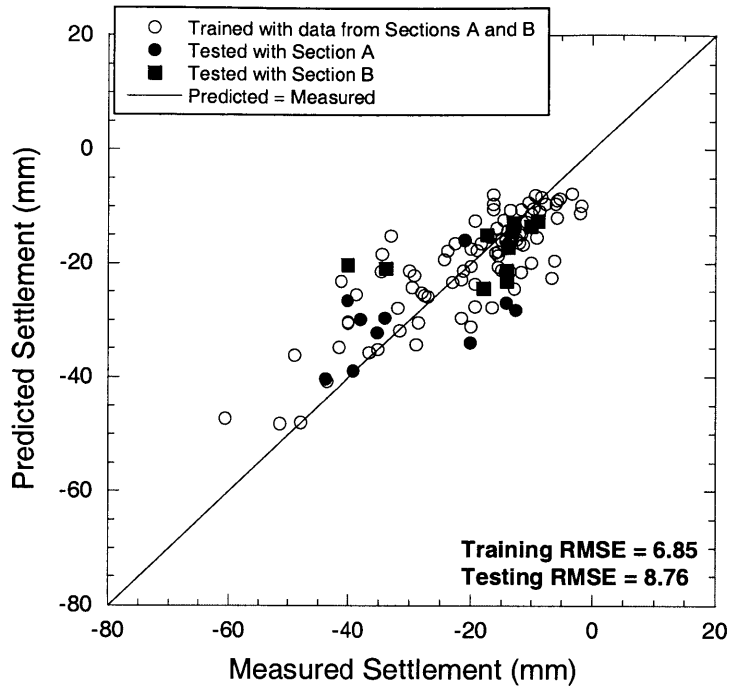


Figure 12.23 Results from neural networks without penetration rate input node trained and tested with data from Sections A and B

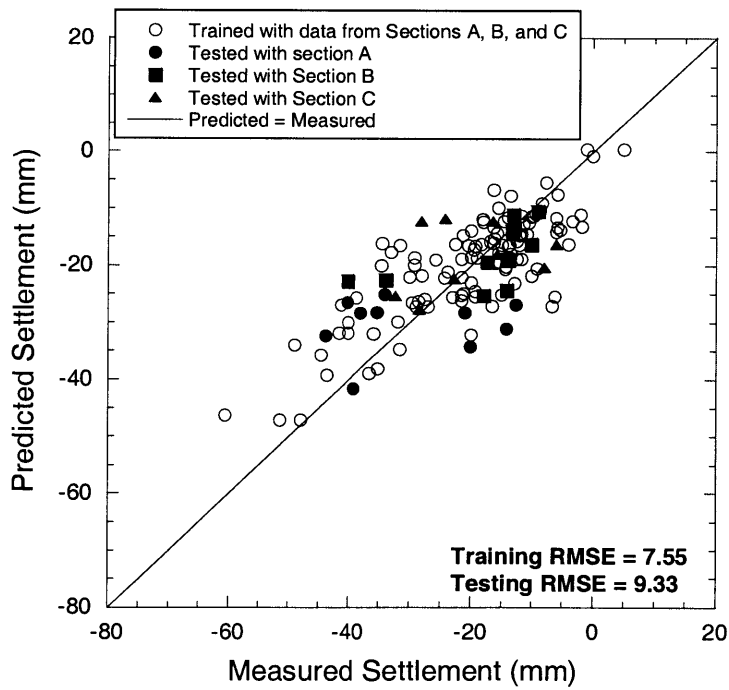


Figure 12.24 Results from neural networks without penetration rate input node trained and tested with data from Sections A, B, and C

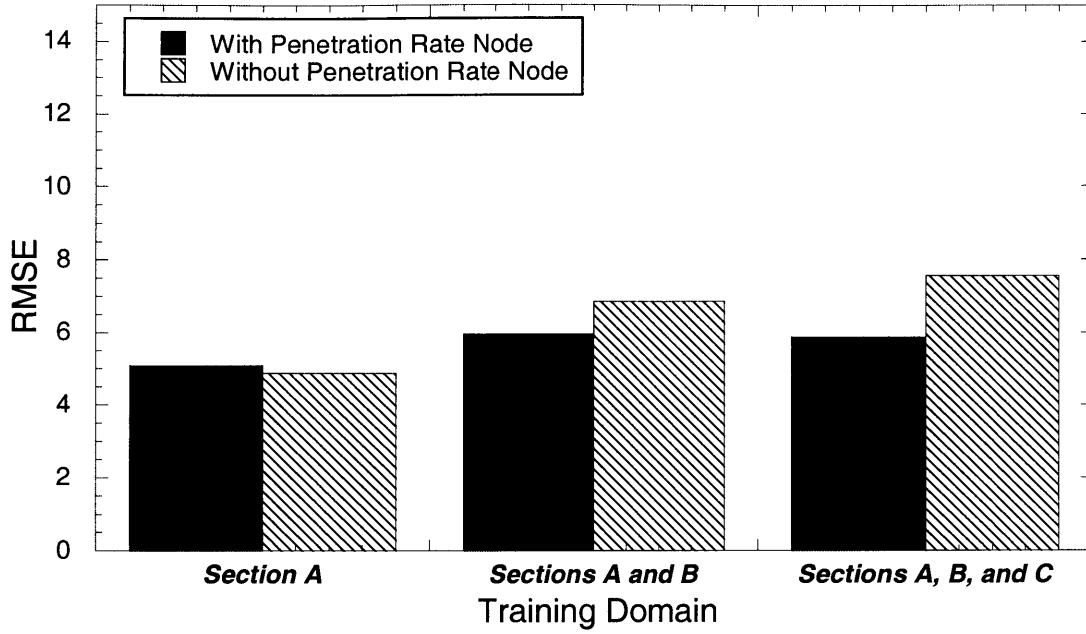


Figure 12.25 Summary of training RMSE of neural network models with and without the penetration rate input node

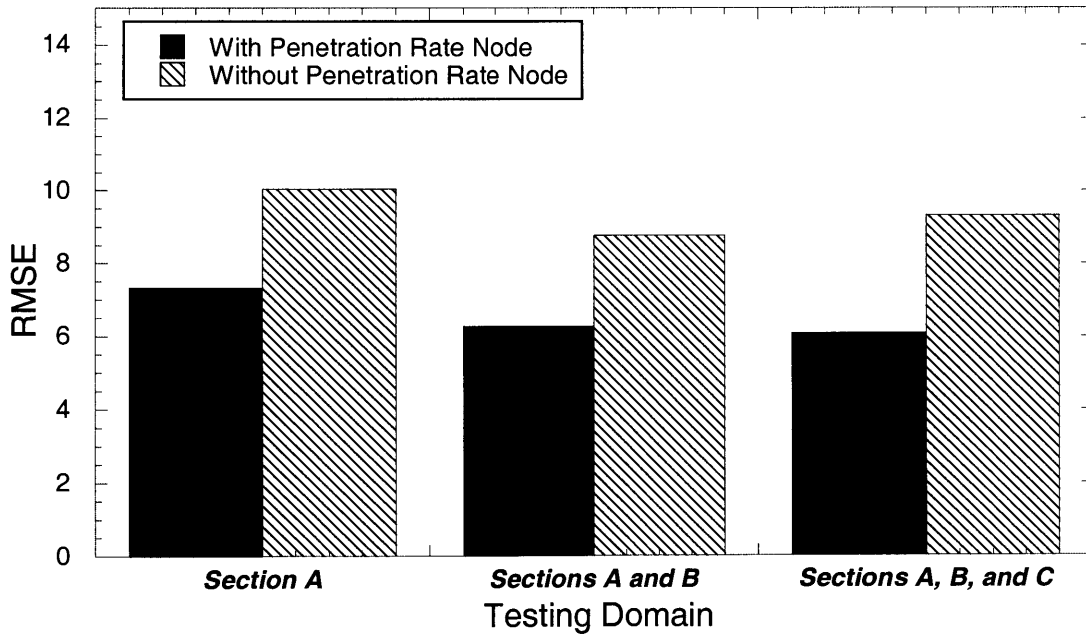


Figure 12.26 Summary of testing RMSE of neural network models with and without the penetration rate input node

12.2.7.2 Neural network model without the grouting quality input nodes

In this section, two input nodes are eliminated, namely the grouting pressure node and the grout filling node. The objective of this section is to investigate whether the grouting quality nodes affect performances of the neural network model. Like the previous section, the network without grouting quality nodes is trained and tested with three different cases. First, data from Section A are used as training and testing sets. As can be seen in Figure 12.27, the network has a low RMSE in the training set but a high RMSE in the testing set. When the network is trained and tested with samples from Sections A and B (Figure 12.28), similar results are observed as RMSE in the testing set is quite high. The network is also applied to the data from Sections A, B, and C. Results from training and testing are shown in Figure 12.29. It was found that training and testing errors are high compared to those of the network with grouting quality nodes. To make this clear, Figure 12.30 and Figure 12.31 show comparisons of training and testing results between the networks with and without grouting quality input nodes. As can be seen, even though both networks perform well in the training set, the network with grouting quality inputs predicts surface settlements more accurately than the network without grouting quality input nodes. Therefore, one can conclude that grouting pressure and grout filling are necessary to be inputs of the neural network model for predicting surface settlements.

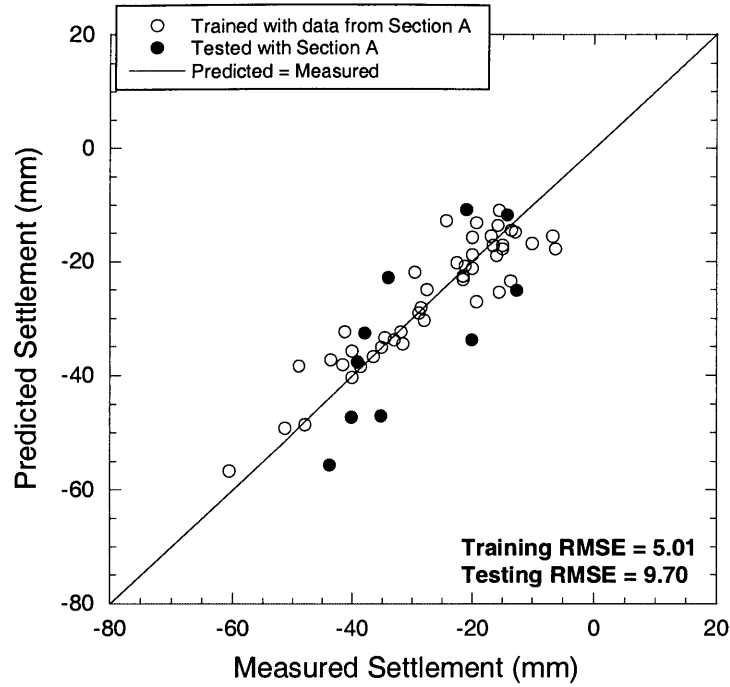


Figure 12.27 Results from neural networks without grouting quality input nodes trained and tested with data from Section A

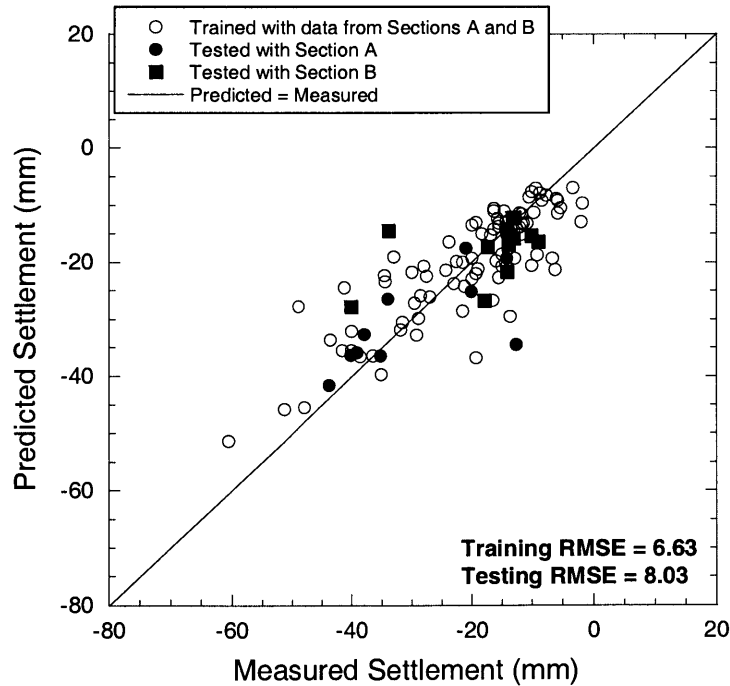


Figure 12.28 Results from neural networks without grouting quality input nodes trained and tested with data from Sections A and B

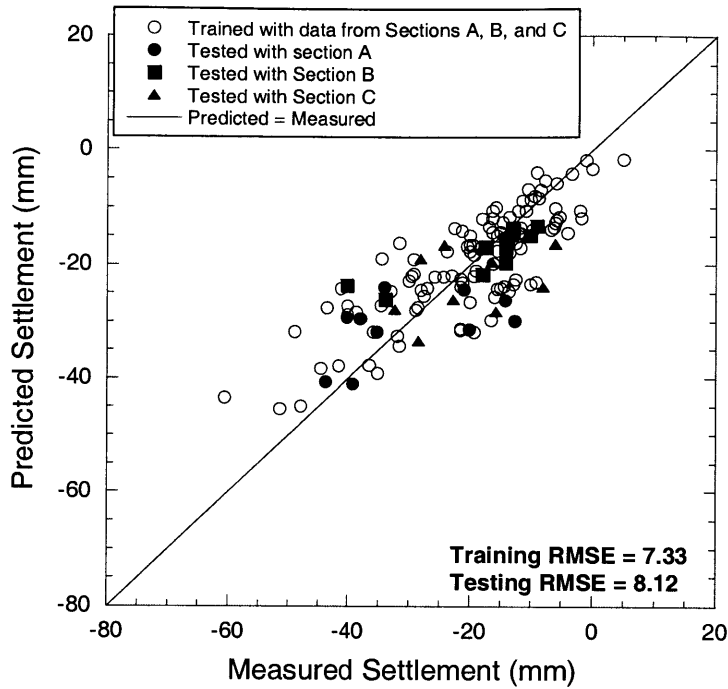


Figure 12.29 Results from neural networks without grouting quality input nodes trained and tested with data from Sections A, B, and C

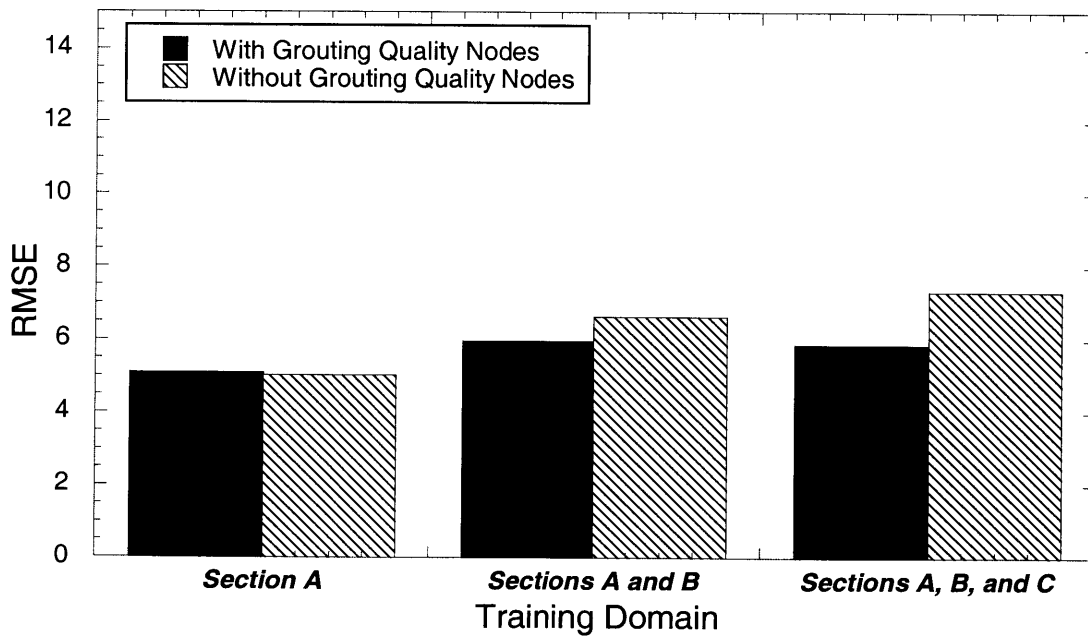


Figure 12.30 Summary of training RMSE of neural network models with and without the grouting quality input nodes

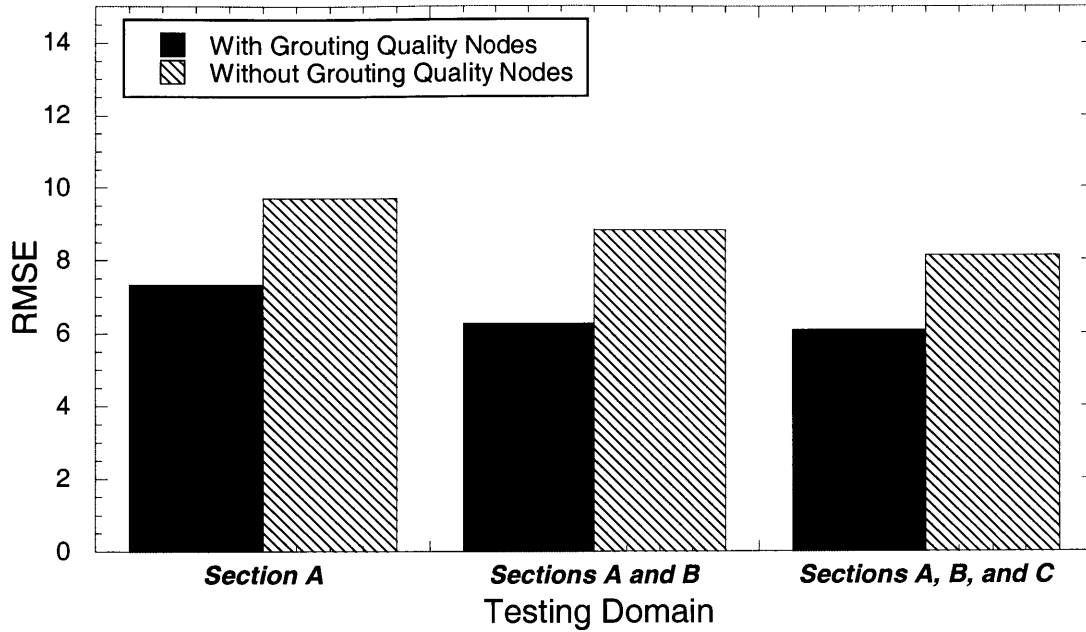


Figure 12.31 Summary of testing RMSE of neural network models with and without the grouting quality input nodes

12.2.7.3 Neural network model without the face pressure input node

In this section, the face pressure node is excluded from the neural network model in order to examine whether the face pressure parameter is important to the performance of the network model. As in the preceding sections, the network without the face pressure node is trained and tested with three different cases. In the first case as the network is trained and tested with data from Section A only, the network has low errors in the training set but high errors (RMSE = 13.39) in the testing set as can be seen in Figure 12.32. In the second case, as the network is trained and tested with samples from Sections A and B (Figure 12.33), similar results are observed as the RMSE in the testing set is high. The network is also applied to the data from Sections A, B, and C. Results from training and testing are shown in Figure 12.34. Training and testing errors are both very high.

When comparing training and testing errors (RMSE) of the complete network with those of the network including the face pressure node (Figure 12.35 and Figure 12.36, respectively), one can see that the prediction accuracy of the network without the face pressure input node is much lower than the results given by the networks that include the face pressure input node. One can conclude that face pressure is an important parameter needed to be represented by the network if one wants to predict surface settlements with accuracy. Moreover, the error in the testing set provided by the network without the face pressure input node is higher than the errors without the penetration rate node and without grouting quality nodes.

Based on these results, one can conclude that face pressure has more significant effect on surface settlements than the other factors. As can be seen when compares in Figure 12.26, Figure 12.30, and Figure 12.36, not considering face pressure leads to 50% increase of the RMSE, while this increase is roughly 20-25% for not considering grouting quality and penetration rate.

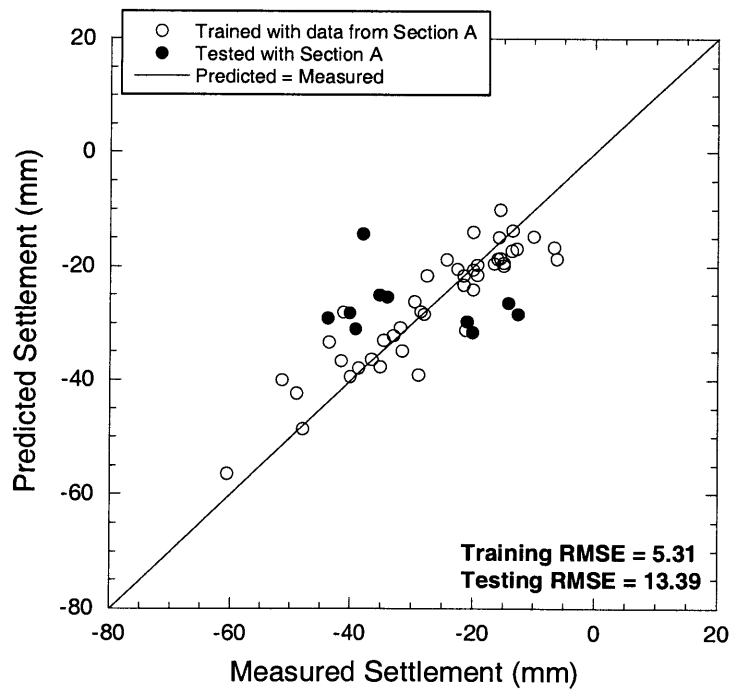


Figure 12.32 Results from neural networks without the face pressure input node trained and tested with data from Section A

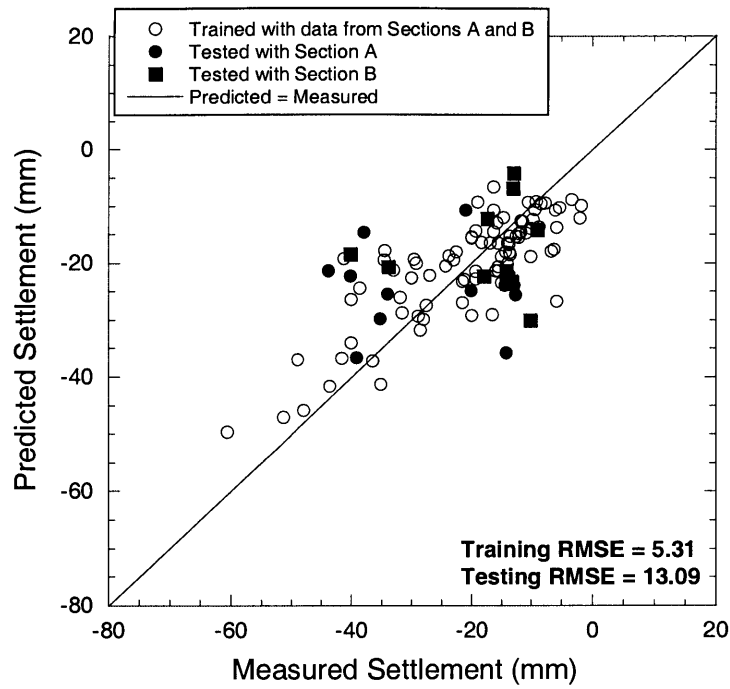


Figure 12.33 Results from neural networks without the face pressure input node trained and tested with data from Sections A and B

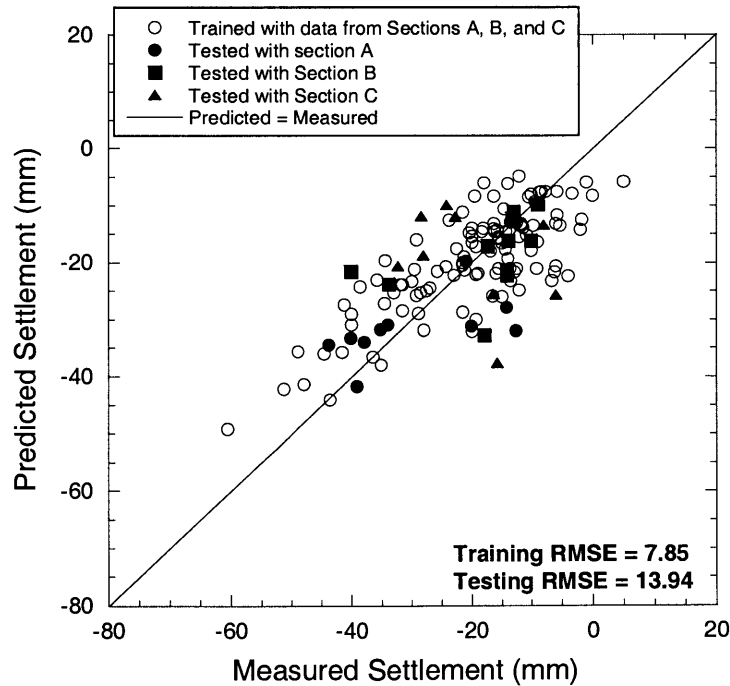


Figure 12.34 Results from neural networks without the face pressure input node trained and tested with data from Sections A, B, and C

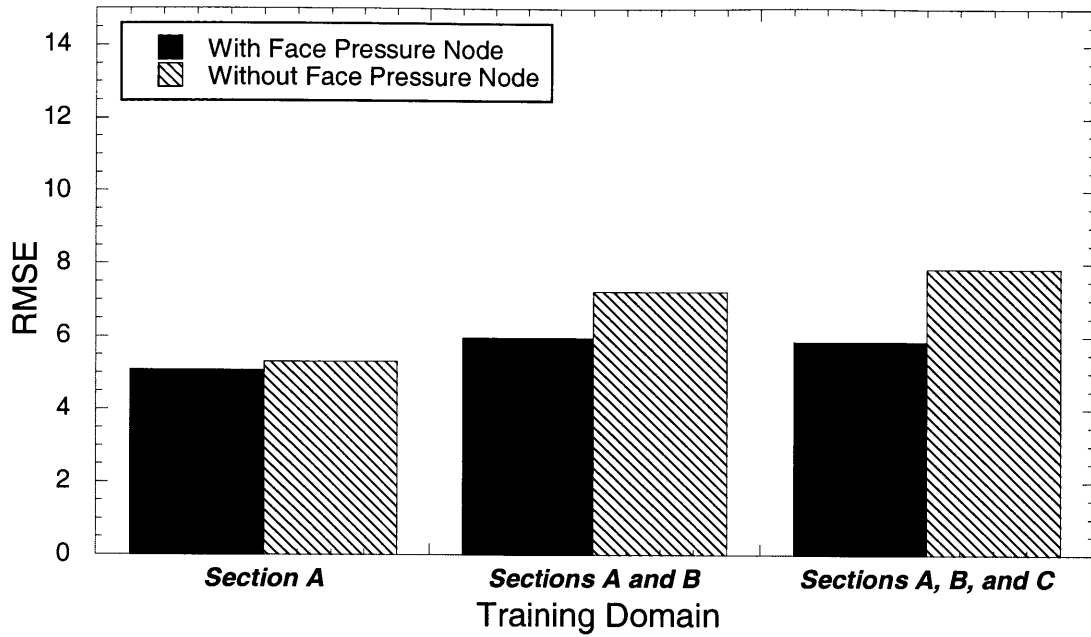


Figure 12.35 Summary of training RMSE of neural network models with and without the face pressure input node

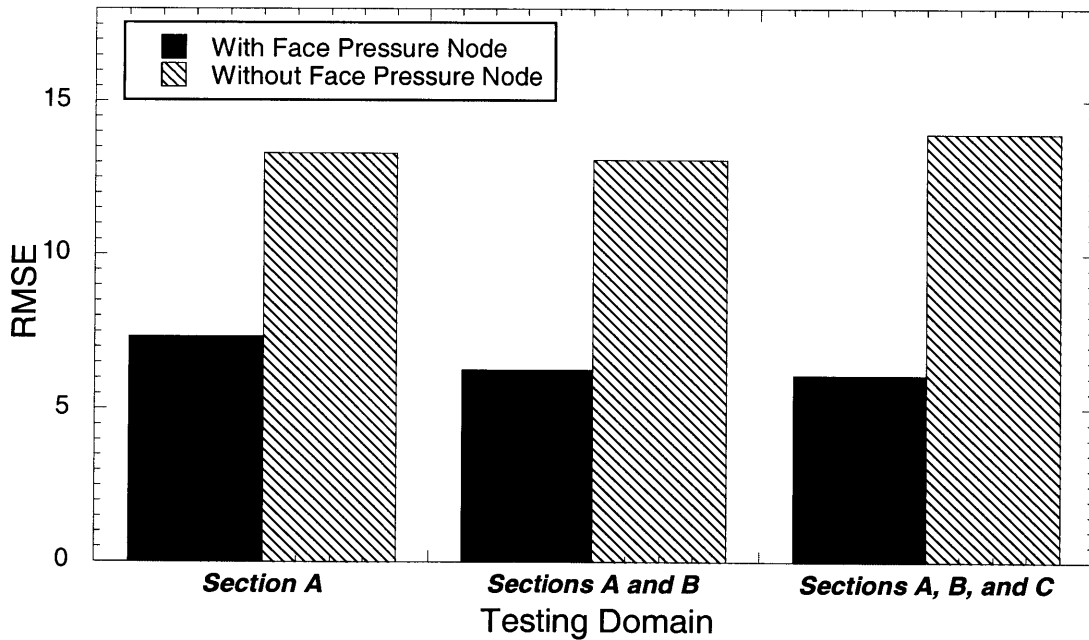


Figure 12.36 Summary of testing RMSE of neural network models with and without the face pressure input node

12.2.8 Scenario 8: Settlement Prediction by Training Data Recorded at the Beginning of the Tunnel Drive

In the previous sections, the applicability of the neural network model for predicting surface settlements in the MRTA was investigated. The data were input into the model and tested with selected validation data. The predictive model performed well in most scenarios except for the models without the penetration rate, grouting quality, and face pressure inputs. This confirmed that artificial neural networks can be successfully used for predicting surface settlements in the MRTA project. However the question is how those who operate EPB shields can use the predictive model in practice. Specifically, one would like to record data at the beginning of the tunnel drive and make ANN predictions for settlements of the remainder. This section investigates to what extent this can be done.

The first scenario is that the neural network model is trained with data recorded from the first half of each tunneling section. Then, after the network is trained, it is used to predict surface settlements that occur in the second half of each tunneling section. Training and testing results are plotted in Figure 12.37 through Figure 12.40. Throughout all sections the network model can predict settlements well, particularly in Section D, where a large number of data was recorded. Even though only the data of the first half were used in network training, the predictive model produced good predictions (see also Figure 12.53 through Figure 12.55).

This implies that contractors can train the neural network model with the first half of the data and use this as a predictive tool for surface settlements occurring in the latter half of the tunneling drive. As described in Chapter 7, settlement markers were normally installed at 50 m intervals along the tunnel alignment. Within the first half of each tunneling drive, the EPB shield had usually excavated the tunnel for a long distance. The shield has usually gone through a wide range of operating conditions and different subsurface conditions. In other words, the shield has experienced all or most of the operations that one would expect in the entire tunneling drive. Using the data from the first half, the neural network model is therefore able to learn and map the relationship

between affecting parameters and surface settlements and it can be used for predicting surface settlements in the future (i.e. the rest of the tunneling drive) with a high degree of confidence.

From the economic point of view, fewer instruments installed over the tunnel alignment is favorable to the tunnel contractors. Based upon normal practices, instrumentation was installed to guarantee the safety of the excavation. However if one could predict surface settlements with high accuracy using the predictive method, the number of instruments could be reduced particularly in the second half of tunneling drives and the construction costs would be reduced (see Figure 12.53 through Figure 12.55 for comparison).

In the second scenario, the data used for network training was reduced to 40% of the entire tunneling drive. The trained network model was used for predicting surface settlements occurring in the rest of each tunneling drive as shown in Figure 12.41 to Figure 12.44. As can be seen from the figures, although the trained model yields higher prediction errors than the networks trained with 50% of the data, in Sections B, C, and D, the errors are still acceptable. Only in Section A, are the predicted settlements considerably different from measured settlements.

The third scenario is to reduce the training data further to 30% of the entire tunneling drive. As shown in Figure 12.45 to Figure 12.48, large errors occurred in Sections A, and C, while smaller errors were found in Sections B, and D. In Section A, the neural network model significantly overestimated surface settlements (Figure 12.45) because it was trained using the first 30% of the data where the shield excavated the tunnel for only a short distance. Although large settlements were observed in the initial drive due to several factors including the learning curve effect of tunnel crews as described earlier, after the shield had excavated the tunnel for a distance, the face pressure and penetration rate increased causing a decrease in surface settlements: see also Chapter 7. Accidentally after ring No. 177 was completed, one of the four cutter drive motors broke causing a problem in the cutter face such that it could not rotate at the desired pressure, thus leading the face pressure level to drop dramatically. As a result, the shield was operated at very

low face pressures (i.e. 40-45 kPa on average) or at the open mode till the end of the tunneling drive. The networks were trained only with data in which the shield was operated in the earth pressure balance mode (i.e. first 30%). Its predictive or mapping ability is based upon the training data, which was taken when the face pressure was high. As the face pressure became substantially lower, the network cannot predict well since the testing/predicting domain is outside the training boundary as discussed earlier in Section 12.2.1.

In Section C, very small amounts of data were used in training the model. As a result the network model could not establish an accurate relationship between input parameters and outputs. Additionally at the beginning of the tunneling drive, shield operators determined by trial and error an optimum face pressure that caused high surface heave, and therefore the networks never “learned” the range where larger settlement occurred. The neural networks thus underestimated the settlement as shown in Figure 12.47.

Based on instrumentation records in Sections B and D, EPB shields were operated more consistently than in Sections A and C. In other words, the first 30% of the data were not very different from the rest of the data. Hence even though only small amounts of data were trained (i.e. first 30%), the neural networks could establish the relationship between affecting parameters and surface settlements to some extent. This results in smaller errors than in Sections A and C (Figure 12.55) where the operation of the shields was very inconsistent.

The fourth scenario is to reduce the training data to only 20% of the whole record. This means that very small amounts of data were used in the cases of Sections A, B, and C. In particular, only 6 samples were used for network training in Section C. As shown in Figure 12.49 to Figure 12.52, very high errors were found at all sections but Section D, where relatively large amounts of data were trained. This trend suggests that the neural networks approach cannot perform well if a very small number of data are used for training.

Results from using the neural network model to predict surface settlements in the given scenarios are shown statistically in Figure 12.53 to Figure 12.55. Based on the results, one can observe that there are two main factors influencing the performance of the neural networks. First is the amount of data used for training. The greater the number of samples, the better the networks can establish the relationship between input parameters and surface settlements. For instance as can be seen in the case of Section D, there were large amounts of instrumentation data that were recorded in the first 30%. Hence the neural network model provided good prediction in agreement with measured settlements and its overall performance was much better than any of the other sections. Second, given the same amount of data, the way the shield was operated also affected the network performance. For example, although the amount of data used for training was the same in Sections A and B (Figure 12.53), the neural networks trained with data from Section B appeared to predict surface settlement better: see Figure 12.55. This is due to effects from the operation of the EPB shields; in Section A the shield was operated differently after a cutting motor was broken, whereas the shield in Section B was operated consistently along the tunnel drive. Even though the same small amount of data was used for training, the data from Section B represented the overall behavior of the shield and ground better than the data from Section A (see also Figure 12.53 through Figure 12.55).

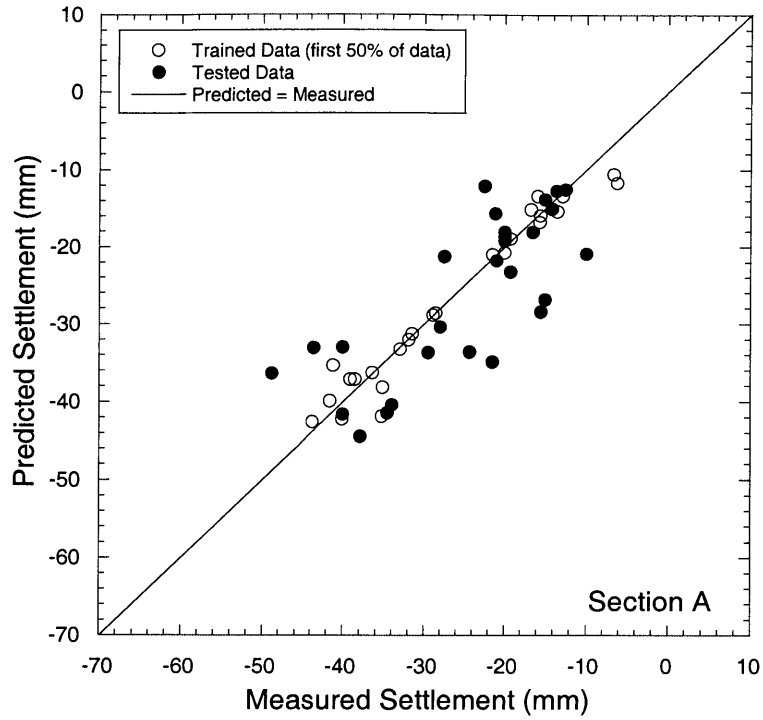


Figure 12.37 Results of using the model trained with the first 50% of data to predict surface settlements in the remaining 50% of Section A

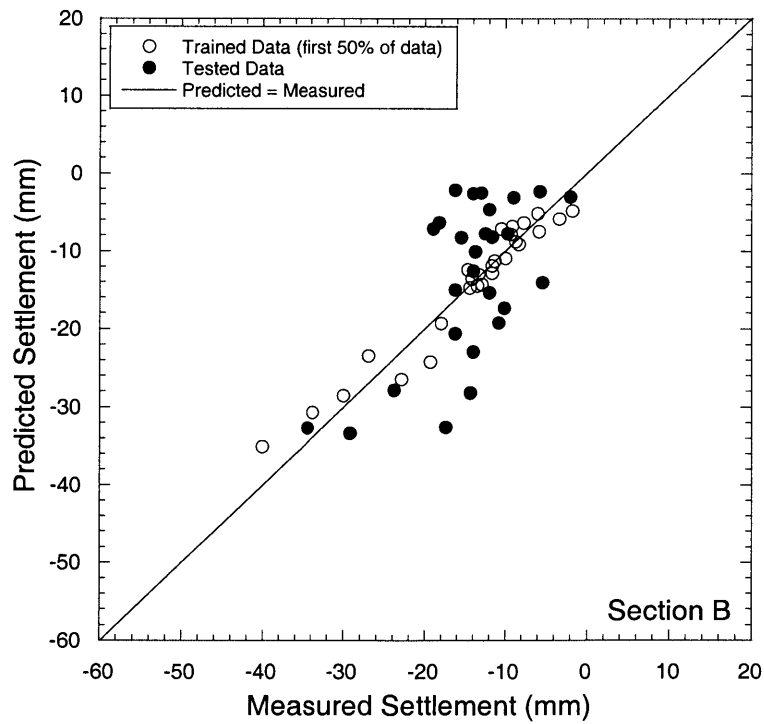


Figure 12.38 Results of using the model trained with the first 50% of data to predict surface settlements in the remaining 50% of Section B

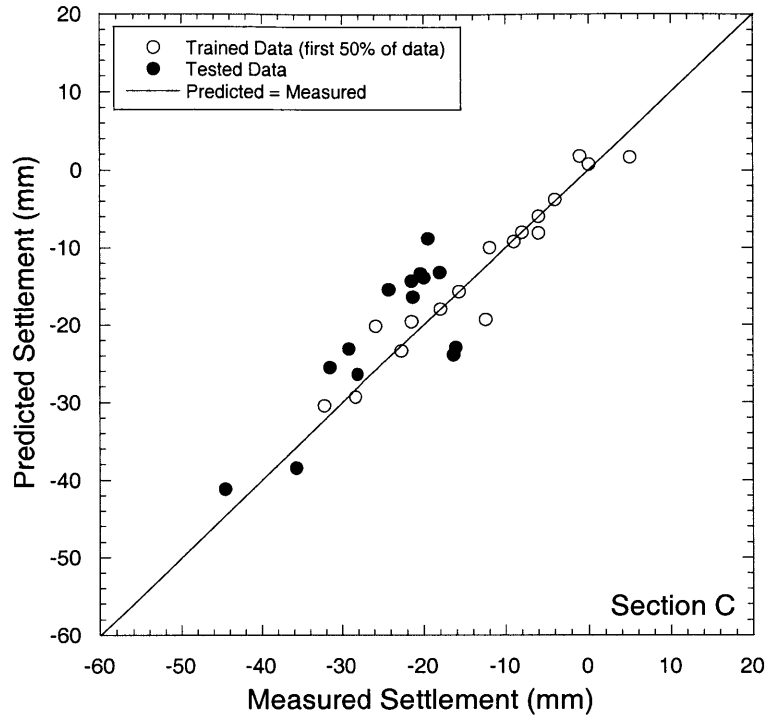


Figure 12.39 Results of using the model trained with the first 50% of data to predict surface settlements in the remaining 50% of Section C

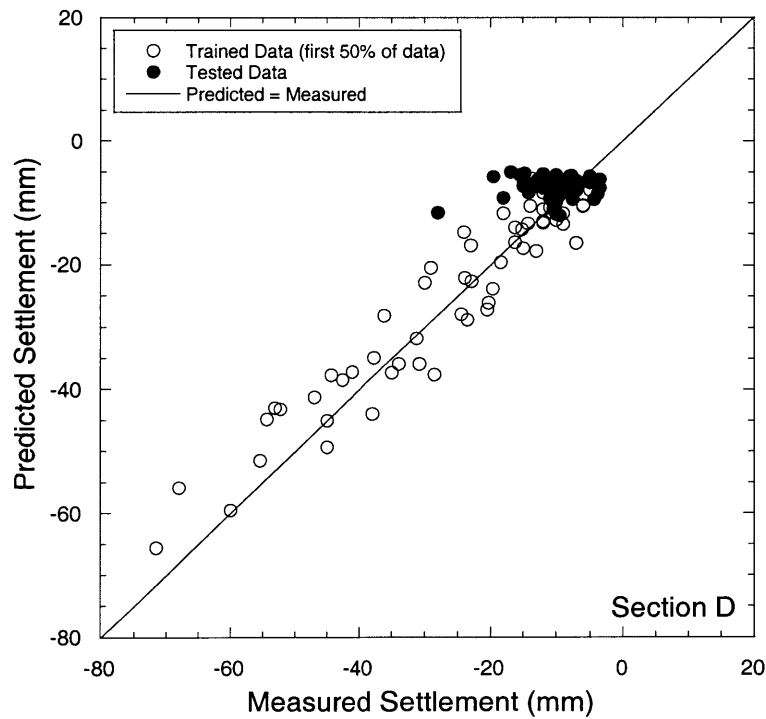


Figure 12.40 Results of using the model trained with the first 50% of data to predict surface settlements in the remaining 50% of Section D

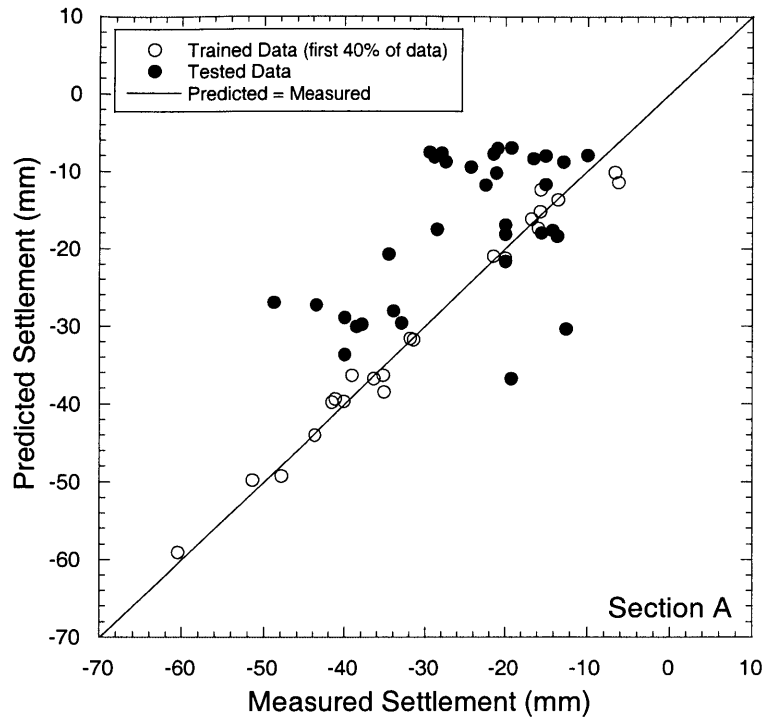


Figure 12.41 Results of using the model trained with the first 40% of data to predict surface settlements in the remaining 60% of Section A

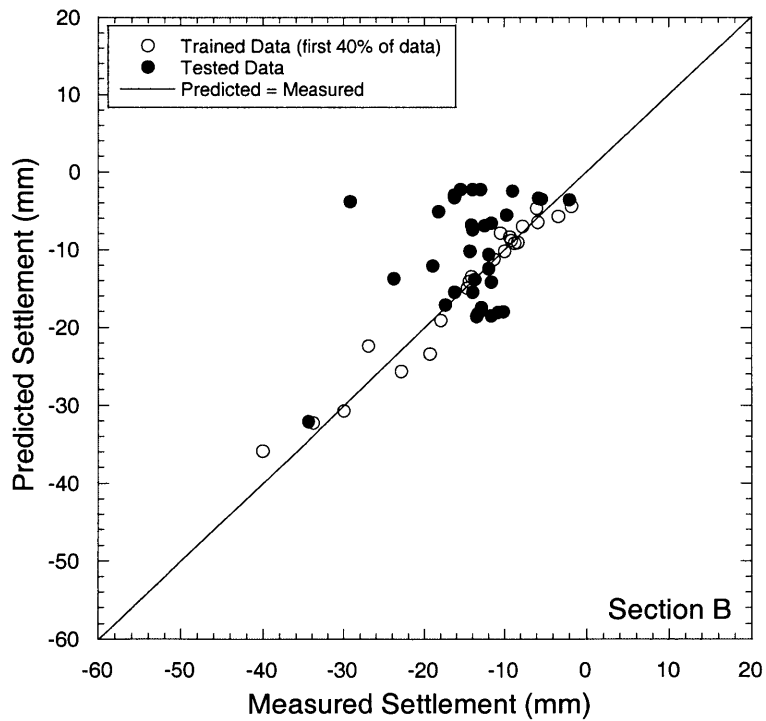


Figure 12.42 Results of using the model trained with the first 40% of data to predict surface settlements in the remaining 60% of Section B

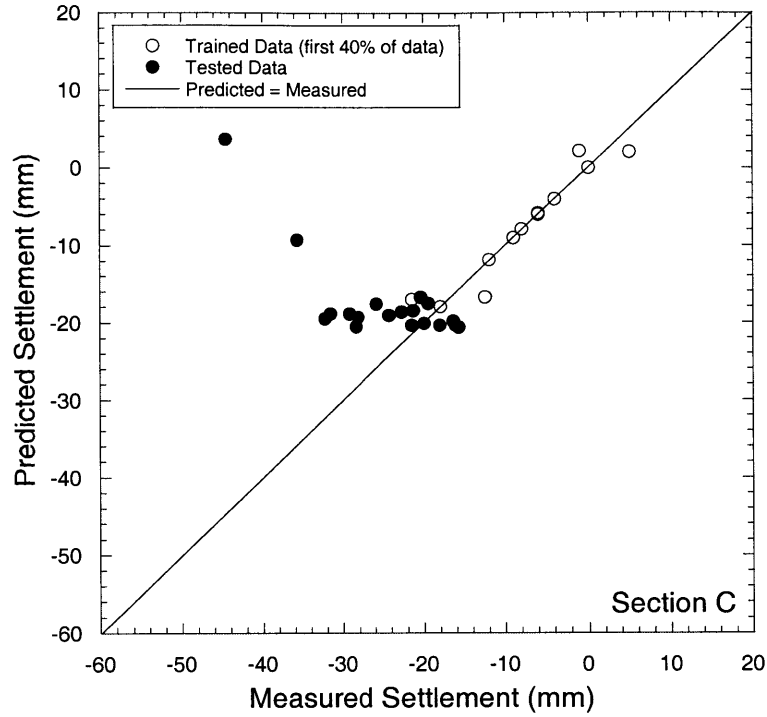


Figure 12.43 Results of using the model trained with the first 40% of data to predict surface settlements in the remaining 60% of Section C

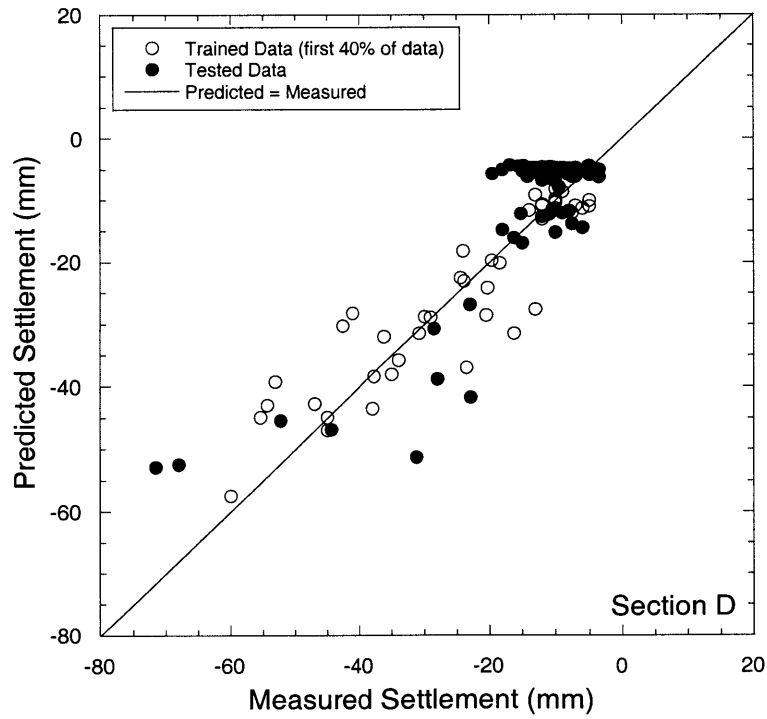


Figure 12.44 Results of using the model trained with the first 40% of data to predict surface settlements in the remaining 60% of Section D

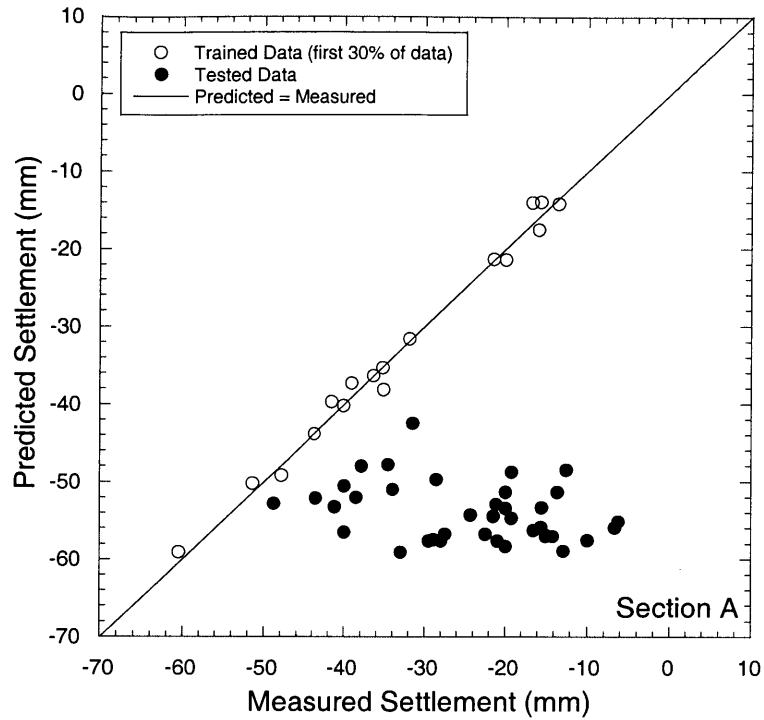


Figure 12.45 Results of using the model trained with the first 30% of data to predict surface settlements in the remaining 70% of Section A

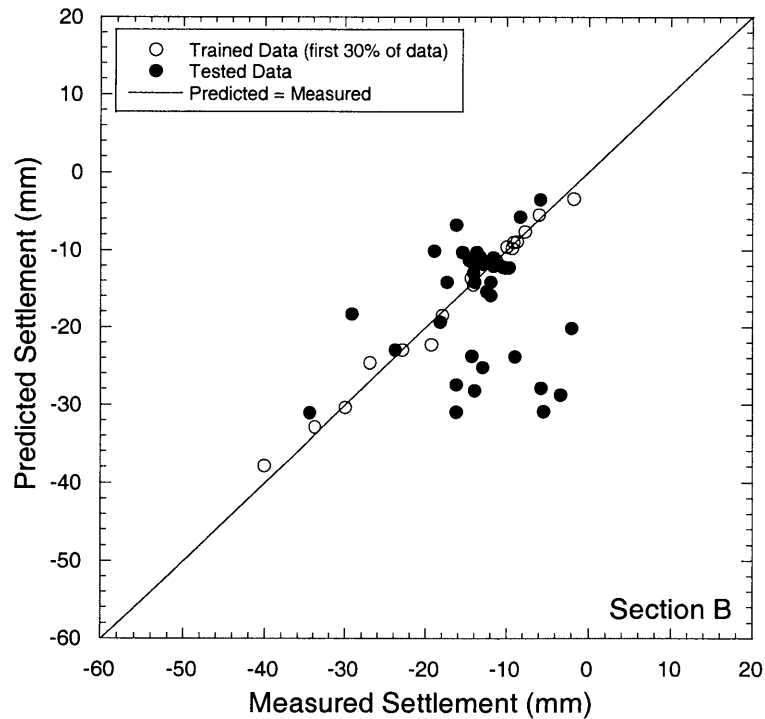


Figure 12.46 Results of using the model trained with the first 30% of data to predict surface settlements in the remaining 70% of Section B

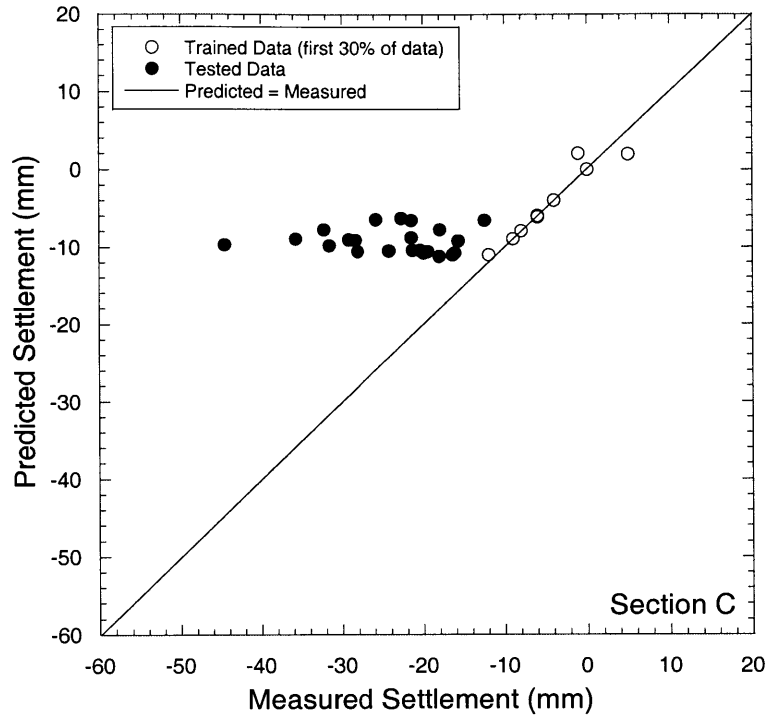


Figure 12.47 Results of using the model trained with the first 30% of data to predict surface settlements in the remaining 70% of Section C

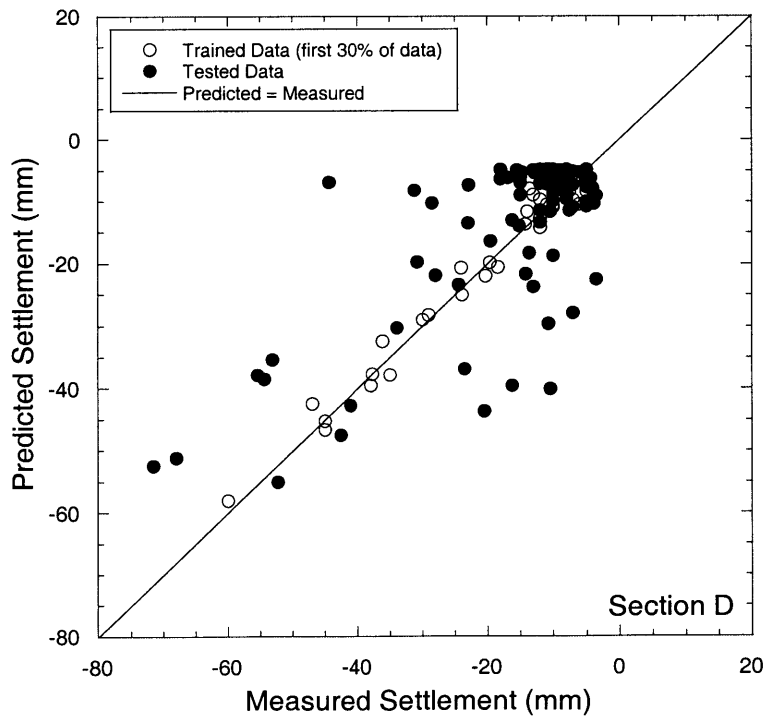


Figure 12.48 Results of using the model trained with the first 30% of data to predict surface settlements in the remaining 70% of Section D

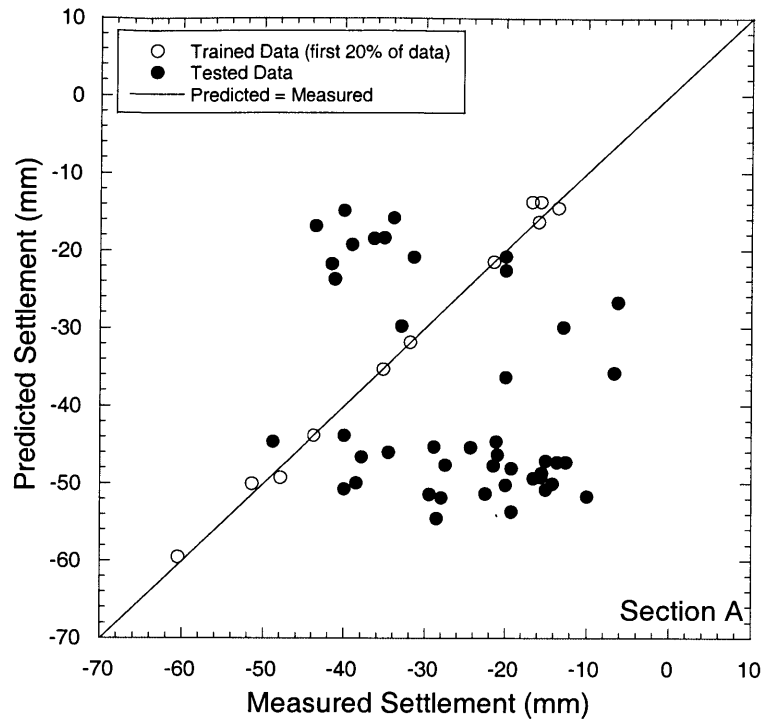


Figure 12.49 Results of using the model trained with the first 20% of data to predict surface settlements in the remaining 80% of Section A

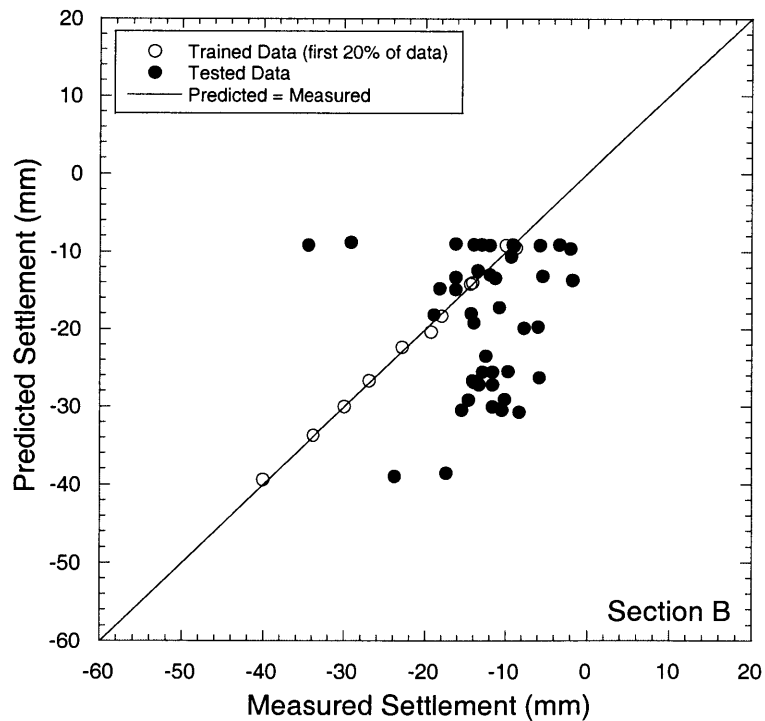


Figure 12.50 Results of using the model trained with the first 20% of data to predict surface settlements in the remaining 80% of Section B

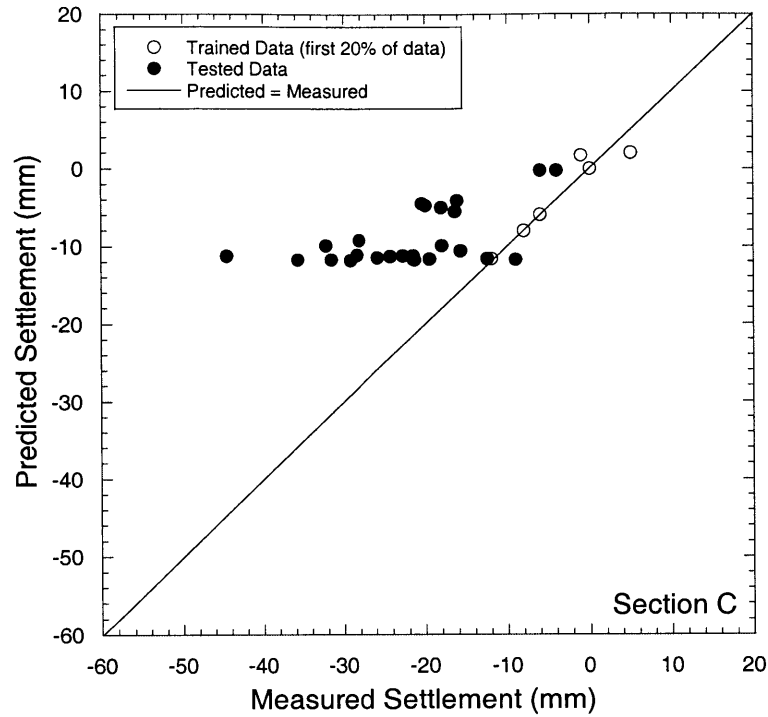


Figure 12.51 Results of using the model trained with the first 20% of data to predict surface settlements in the remaining 80% of Section C

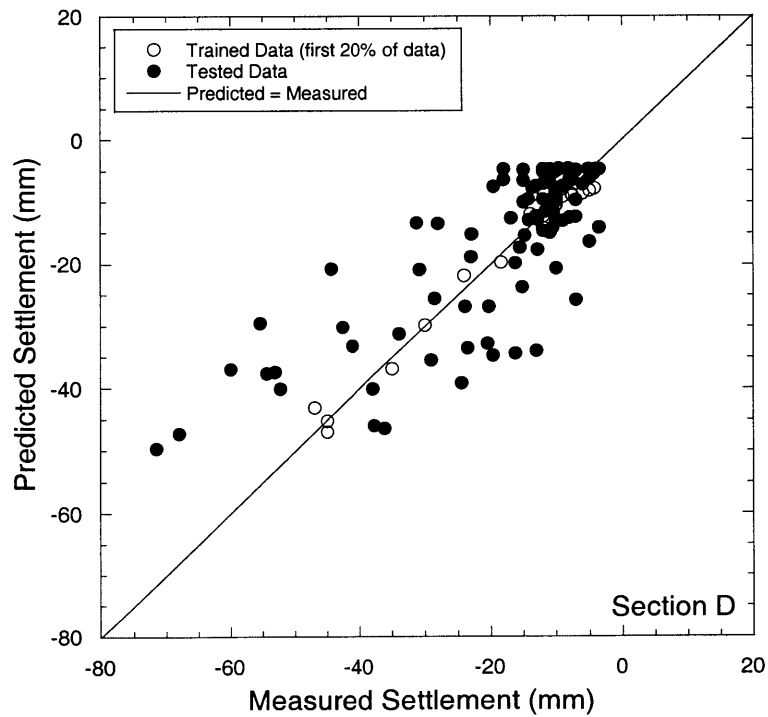


Figure 12.52 Results of using the model trained with the first 20% of data to predict surface settlements in the remaining 80% of Section D

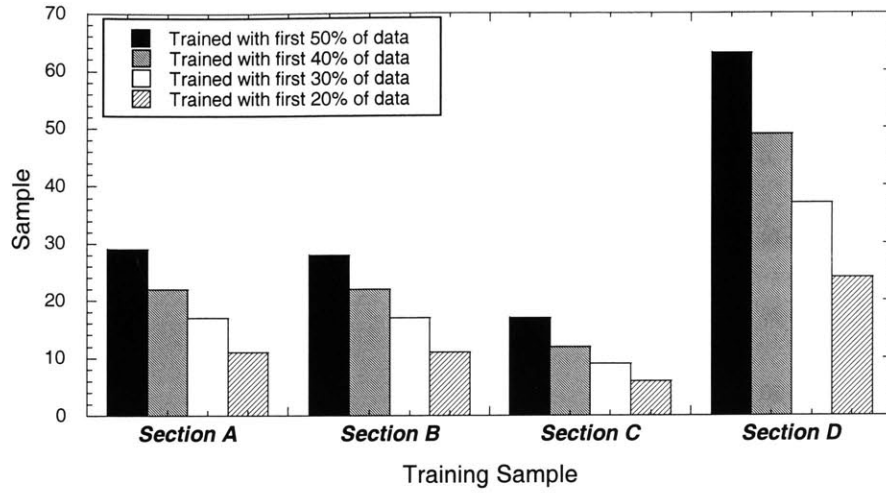


Figure 12.53 Comparison of samples used for network training

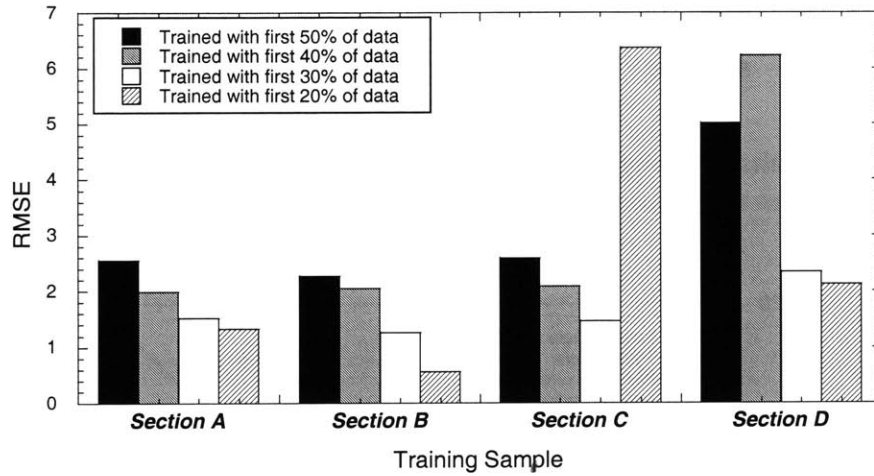


Figure 12.54 Comparison of errors in training samples

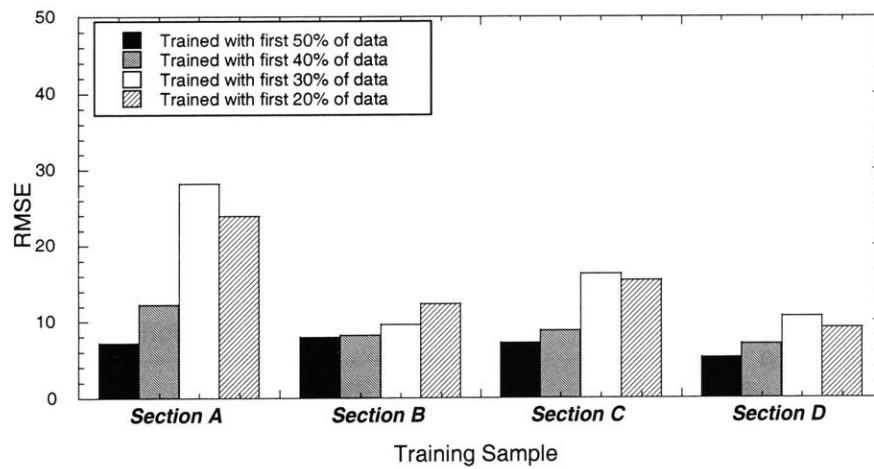


Figure 12.55 Comparison of errors in prediction

12.2.9 Scenario 9: Predicting surface settlements in Zone 2

Based on the observations discussed in Chapter 7, surface settlements induced by EPB tunneling can be divided into three zones namely, (1) Zone 1, (2) Zone 2, and (3) Zone 3 as shown in Figure 12.56. In the previous sections, the neural network model was successfully used for predicting the maximum surface settlement after shield passing or at the end of Zone 3 (Point A in Figure 12.56). In this section, an attempt is made to apply the neural network model for predicting surface settlements at the end of Zone 2 (Point B in Figure 12.56).

The network used in this scenario is the same neural network model used in the preceding sections and has the same structure as shown in Figure 12.21. Data obtained from all sections (A, B, C, and D) were input into the model and tested with selected validation data. Results from training and testing are shown in Figure 12.57. It was found that the predictive model performed well in both training and testing sets. This verified that artificial neural networks could be also successfully used for predicting surface settlements occurring in Zone 2.

12.2.10 Scenario 10: Predicting surface settlements in Zone 1

The neural network model performed well in the preceding scenario where it was applied to predict surface settlements at the end of Zone 2. The objective of this section is to examine the applicability of the network for predicting surface settlements at the end of Zone 1 (point C in Figure 12.56). Based on the observations from several case histories (Chapter 4), and from the MRTA project (Chapters 7 and 9), grouting quality and pitching angle probably affect surface settlements during and after shield passing. In other words, these parameters only influence surface settlements within Zones 2 and 3 not Zone 1. Accordingly, the grouting quality and pitching angle input nodes should be eliminated if one wants to predict surface settlements occurring in Zone 1.

In this scenario, only 11 input nodes are presented to the network. Like Section 12.2.8, the network is trained with the data obtained from all sections (A, B, C, and D) and tested with validation data. Results from training and testing are shown in Figure 12.58. As can be seen, the network performed very well in both training and testing sets (i.e. low RMSE in both sections). Hence, one can conclude that artificial neural networks can be applied for predicting surface settlements in Zone 1 with a high degree of confidence.

Table 12-4 Input parameters used for predicting surface settlements at the end of Zone 1

Category	Parameter	Detailed Items	Input Node No.
Tunnel Geometry	(1) Tunnel depth (m)		1
	(2) Distance from launching station (m)		2
Geological Conditions	(3) Geology at tunnel crown	Soft Clay (No = 0, or Yes =1)	3
		Stiff Clay (No = 0, or Yes = 1)	4
		Sand (No = 0, or Yes = 1)	5
(4) Geology at tunnel invert	Stiff Clay (No = 0, or Yes =1)	6	
	Sand (No = 0, or Yes = 1)	7	
(5) Ground water level from tunnel invert (m)		8	
Shield Operation Factors	(6) Average face pressure (kPa)		9
	(7) Average penetration rate (mm/min)		10
Machine Model	(8) Machine model	Kawasaki =1 Herrenknecht = 0	11

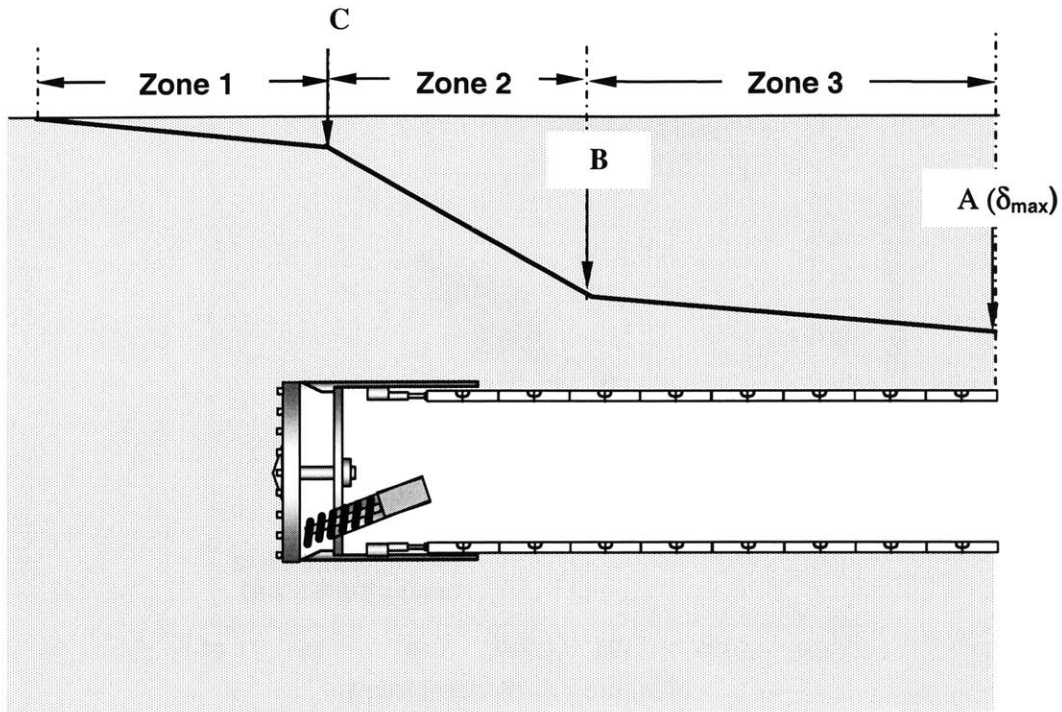


Figure 12.56 Schematic diagram of a typical longitudinal surface settlement profile

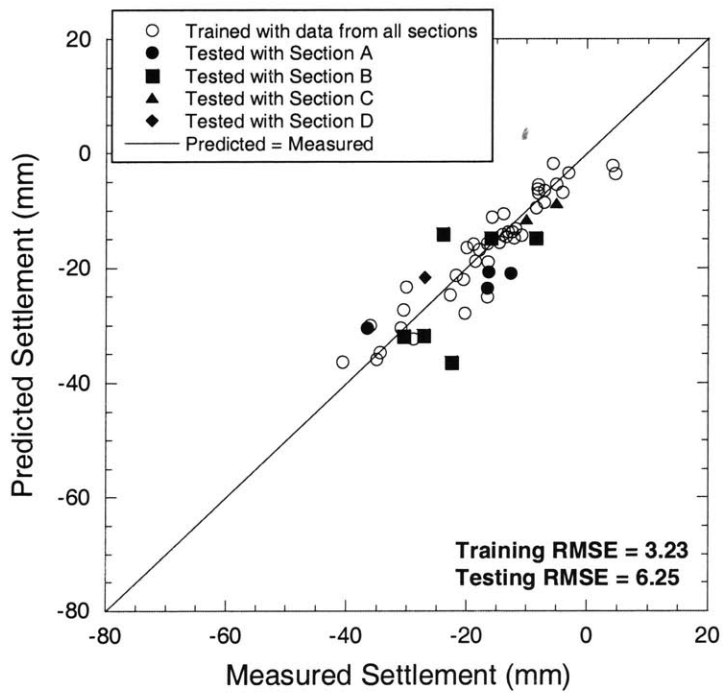


Figure 12.57 Performances of neural networks used for predicting surface settlements in Zone 2

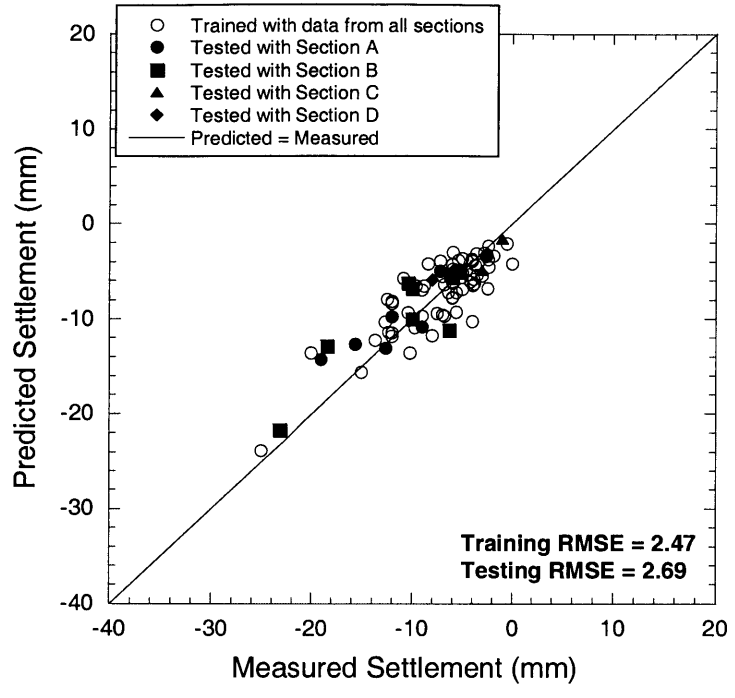


Figure 12.58 Performances of neural networks used for predicting surface settlements in Zone 1

12.2.11 Result Summary of Scenarios 1 to 10

Scenario descriptions and prediction accuracies obtained by applying the neural network model to predict the maximum surface settlement over a single tunnel (i.e. Scenarios 1-6) are summarized in Table 12-5. In order to clearly demonstrate the performance of the network in training and testing samples, all RMSE values from Scenarios 1-6 are also plotted in Figure 12.59.

Table 12-5 Summary of prediction accuracies when using the neural network model in Scenarios 1-6

Scenario	Trained Samples	Tested Samples/Predicting	Prediction RMSE
1			
1.1	Section A	Section B	16.26
1.2	Section A	Section C	19.69
1.3	Section A	Section D	21.96
2			
2.1	Section B	Section B	6.22
2.2	Section C	Section C	5.90
2.3	Section D	Section D	7.56
3	Sections A and B	Sections A and B	6.27
4	Section A, B, and C <i>Note: All used Kawasaki machines</i>	Section A, B, and C	6.08
5	All sections (A, B, C, and D)	All sections (A, B, C, and D)	8.39
6	All sections (A, B, C, and D) <i>Note: Modified ANN input</i>	All sections (A, B, C, and D)	7.68

As can be seen from the figure, one can conclude that:

- (1) Applying the neural network model trained only with data from Section A to different tunneling sections (see Scenario 1.1 – 1.3 in Figure 12.59), produced results show that the network failed to predict surface settlements accurately.

- (2) Training and testing the network with data selected from the same tunnel section (Sections A, B, C, and D) yielded excellent results as the network successfully predicted settlements with very high accuracy compared with the measured data.
- (3) In Scenario 3, applying the network trained with data from Sections A and B (i.e. an entire North tunneling section) to predict surface settlements in these sections also yielded good results.

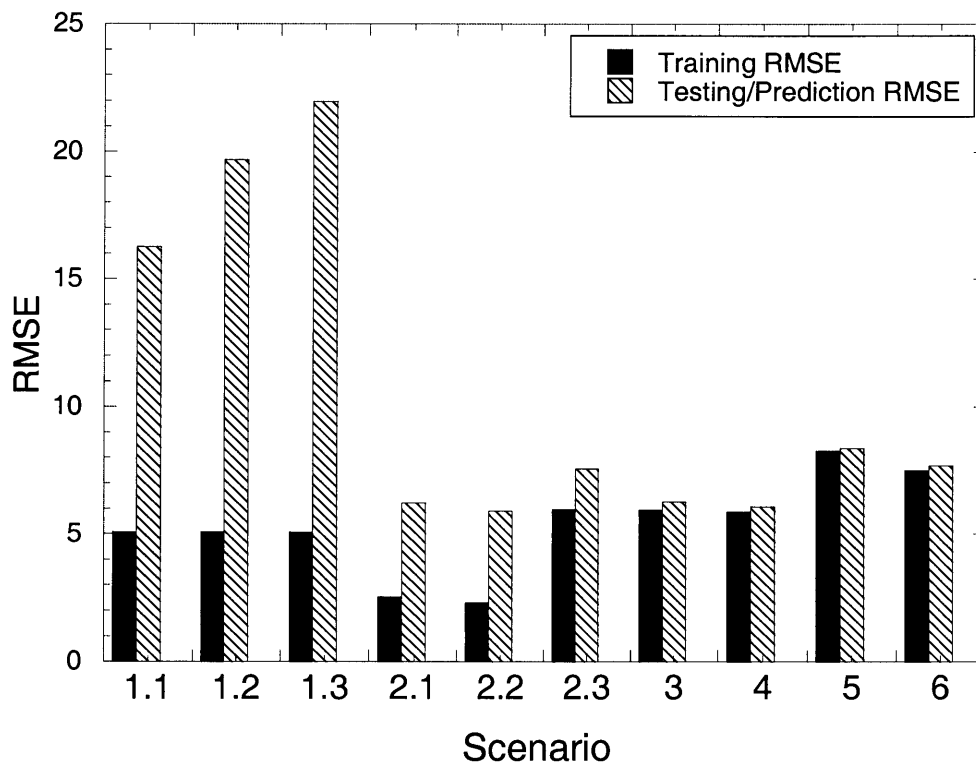


Figure 12.59 Summary of training and testing RMSE

- (4) The network trained with data from Sections A, B, and C is used for predicting settlements in these sections (Scenario 4). All sections employed a similar model of EPB machines but were operated differently. The prediction accuracy given by the network is also excellent. These results suggest that the neural network model

can be used for predicting surface settlements with confidence when the machines are similar, even if the shields are operated differently.

- (5) Scenario 5 represents the condition that all the data recorded from all sections was used for training the network. When the network was used to predict surface settlements, it also gave good results with acceptable error although the error was statistically higher than that of Scenarios 2 and 3.
- (6) The difference between EPB machines may play a significant role on the network performance in Scenario 5. The network model was modified by adding an input node to represent the “machine model.” As a result, the prediction accuracy somewhat improved.

In Scenario 7, results from testing the ANN model without the penetration rate, the grouting quality, and the face pressure suggested that the prediction accuracy of the network without these parameters is lower than the results produced by the networks that include the parameters. In particular, the network without the face pressure node produces very high errors when it was used for predictions. Hence, one can conclude that these parameters are important input parameters which have to be represented by the network to predict surface settlements with high accuracy.

In Scenario 8, data recorded at the beginning of tunnel drives are used for training the network. For instance, using the data from the first half, the neural network model learns and maps the relationship between affecting parameters and surface settlements, and then uses the relationship for predicting surface settlements in the second half. This can be done with a high degree of confidence. However, with smaller amounts of training data (i.e. less than 40% of all data), the network cannot perform well except in Section D where there were data more than the other sections. Scenarios 9 and 10 show that artificial neural networks can be also successfully used for predicting surface settlements occurring in Zones 1 and 2.

12.3 Prediction of Surface Settlements induced by EPB Tunneling in Clay

Since most of the tunnel alignment in the MRTA project was located in clay layers, an attempt is made to modify the network model to predict surface settlements caused by tunneling in clay. In this section, the stability number (N) is therefore introduced to be a new input parameter:

$$\text{Stability Number } N = \frac{\gamma H}{S_u} \quad (12-1)$$

where,

γ = Soil unit weight (kN/m³)

H = Depth to tunnel axis (m)

S_u = Undrained shear strength (kN/m²)

Three stability numbers obtained from different locations namely, N at tunnel crown, N at tunnel springline and N at tunnel invert (Figure 12.60) are represented in the new network. However, in order to compare the stability of excavation to surface settlements, the face pressure has to be included which leads to a more meaningful parameter, the overload factor (N') which can be defined as:

$$\text{Overload Factor } N' = \frac{(\gamma H - \text{Face Pressure})}{S_u} \quad (12-2)$$

Stability number (N) and overload factor (N') versus the maximum surface settlement are shown in Figure 12.61 and Figure 12.62, respectively. As can be seen, no relationship was found between these parameters and surface settlements again due to the complex ground-shield behavior with many other factors involved.

The new ANN structure uses stability number (N) instead of overload factor (N') since the face pressure parameter node is already presented in the network. All input parameters are summarized in Table 12-6. As can be seen in the table, tunnel depth node and soil type nodes were excluded since they are already represented by the stability number. The structure of neural network model for predicting surface settlements induced by tunneling in clay is shown in Figure 12.63.

The objective of this section is to determine if the new neural network structure can predict surface settlements caused by tunneling in clays. As described earlier in Chapter 11, before the network can be applied with any degree of confidence, one first needs to determine an optimum neural network. Table 12-7 shows network models used for determining the optimum network. The network that yields the best agreement with the validation set will be selected as the optimal neural network. Data recorded from only tunneling in clays (i.e. not all tunnels were excavated in clays) were divided into a training set and a validation set. All network models are trained with the training data and then tested with the validation (testing) data. All RMSE values from all models are summarized in Figure 12.64. Results from the training and testing are plotted together in Figure 12.65 through Figure 12.80.

Based on all performances of the network models in the validation set, the optimal network for predicting surface settlements induced by tunneling in clays is the network with 1 hidden layer and 15 hidden nodes trained for 3,000 epochs. As shown in Figure 12.69, it was found that the network predicts surface settlements well with small errors. The new neural network structure may be used for predicting surface settlements induced by tunneling in clays. However, it should be noted that the tunnels in the MRTA project were not only excavated in clay layers but in the sand layer as well. Hence, the ANN model used in the preceding section is recommended for predicting surface settlements in the MRTA project.

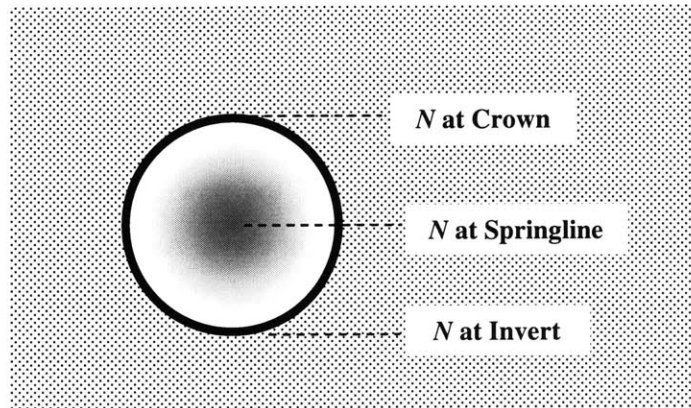


Figure 12.60 Stability numbers (N) used as inputs for the network

Table 12-6 Input parameters used for the NN model for clay

Category	Parameter	Input Node No.
Tunnel Geometry	(1) Distance from launching station (m)	1
	(2) N at Tunnel Crown	2
Stability Number and Geological Condition	(3) N at Tunnel Springline	3
	(4) N at Tunnel Invert	4
	(5) Ground water level from tunnel invert (m)	5
Shield Operation Factors	(6) Average face pressure (kPa)	6
	(7) Average penetration rate (mm/min)	7
	(8) Average pitching angle (degree)	8
	(9) Grouting pressure (bar)	9
	(10) Percent grout filling	10
	(11) Machine Model	11

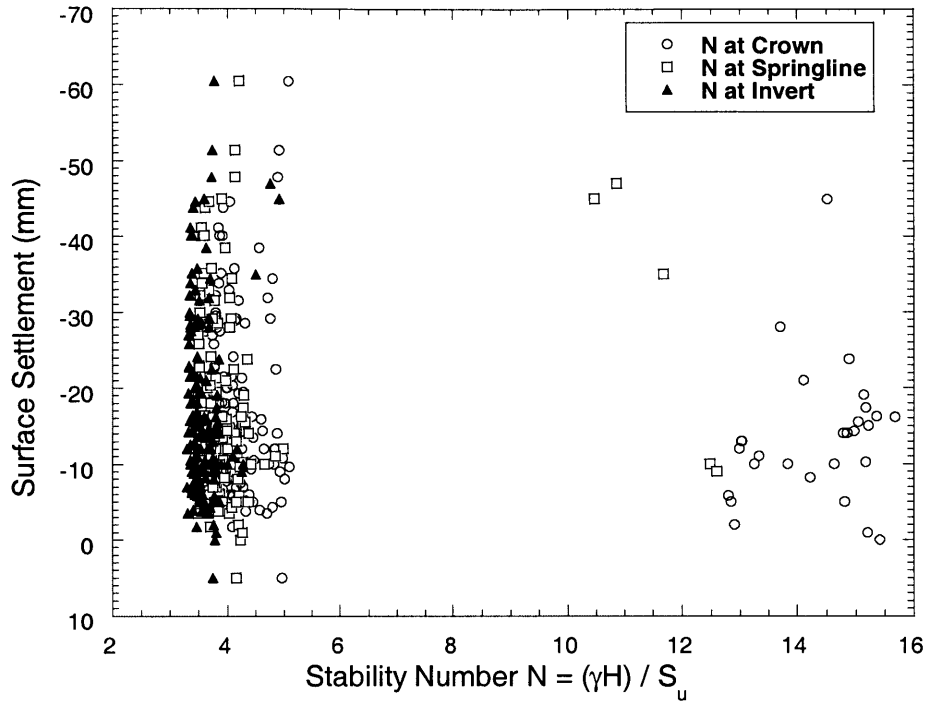


Figure 12.61 Stability number (N) versus surface settlements

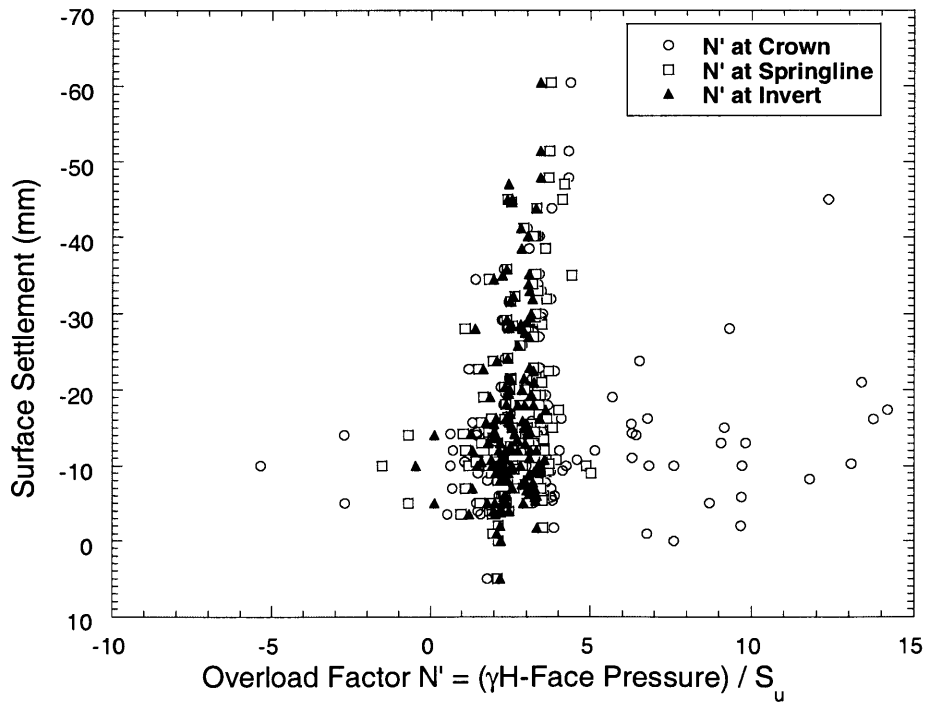


Figure 12.62 Overload factor (N') versus surface settlements

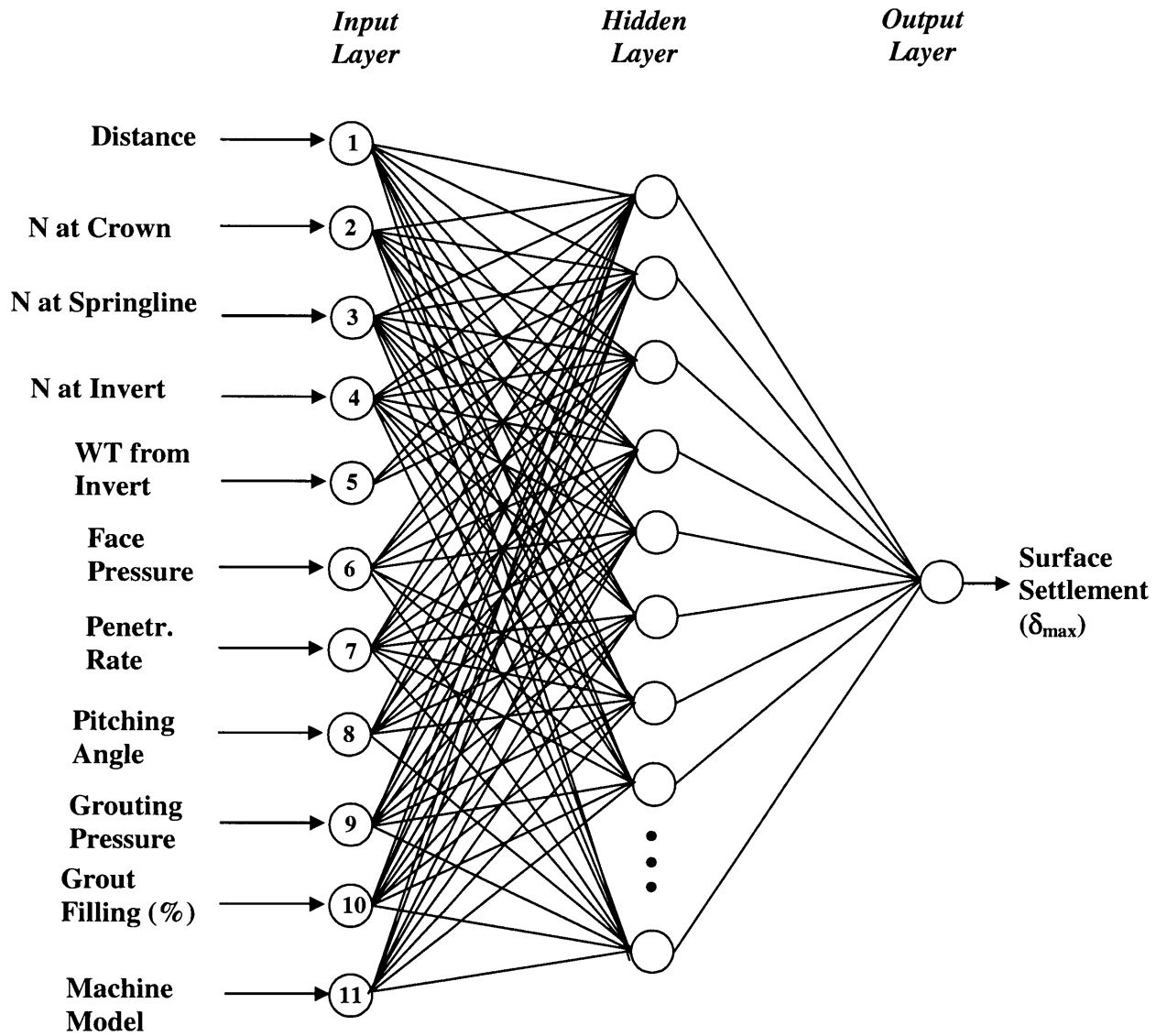


Figure 12.63 Structure of neural network model for predicting surface settlements induced by tunneling in clay

Table 12-7 Neural network models used in the prediction of surface settlements induced by tunneling in clay and their training and testing results

Model	Network Architecture	Training Epochs	Training Samples (RMSE)	Testing/Prediction Samples (RMSE)
1	1 hidden layer, 15 hidden nodes	1,000	7.45	9.22
2	1 hidden layer, 20 hidden nodes	1,000	7.57	9.19
3	1 hidden layer, 15 hidden nodes	2,000	6.65	7.85
4	1 hidden layer, 20 hidden nodes	2,000	6.25	8.09
5	1 hidden layer, 15 hidden nodes	3,000	6.05	6.70
6	1 hidden layer, 20 hidden nodes	3,000	6.16	7.99
7	1 hidden layer, 15 hidden nodes	4,000	5.53	9.42
8	1 hidden layer, 20 hidden nodes	4,000	5.60	9.18
9	2 hidden layers, each 15 hidden nodes	1,000	6.69	9.38
10	2 hidden layers, each 20 hidden nodes	1,000	5.92	9.72
11	2 hidden layers, each 15 hidden nodes	2,000	5.54	7.80
12	2 hidden layers, each 20 hidden nodes	2,000	5.70	8.90
13	2 hidden layers, each 15 hidden nodes	3,000	5.23	8.18
14	2 hidden layers, each 20 hidden nodes	3,000	4.90	7.26
15	2 hidden layers, each 15 hidden nodes	4,000	5.36	7.81
16	2 hidden layers, each 20 hidden nodes	4,000	4.40	8.12

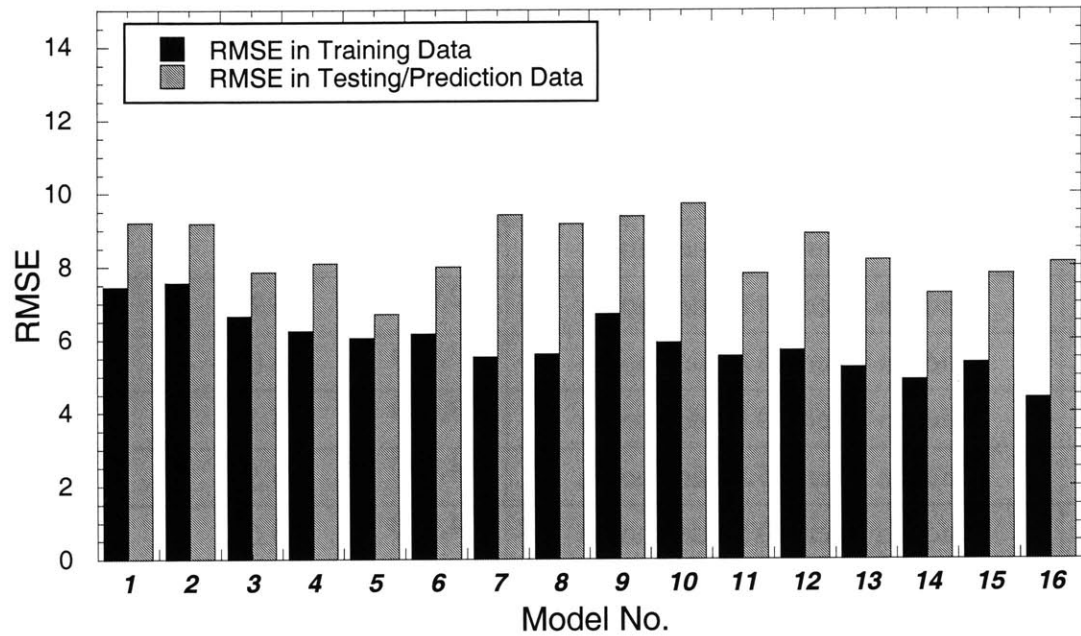


Figure 12.64 Summary of training and testing RMSE of neural network models used in the prediction of surface settlements induced by tunneling in clay

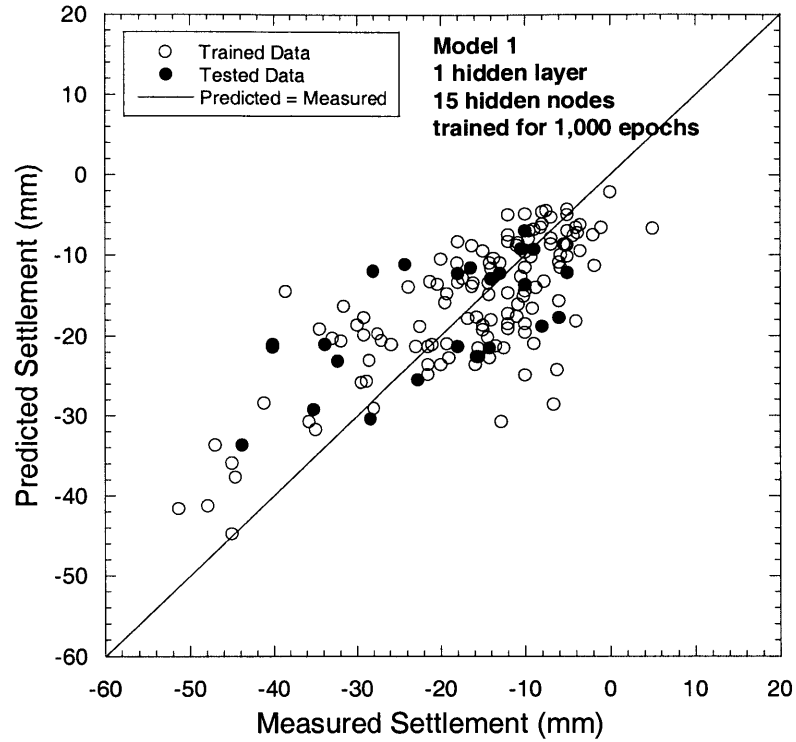


Figure 12.65 Performance of ANN with 1 hidden layer and 15 hidden nodes trained for 1,000 epochs for predicting settlements induced by tunneling in clays

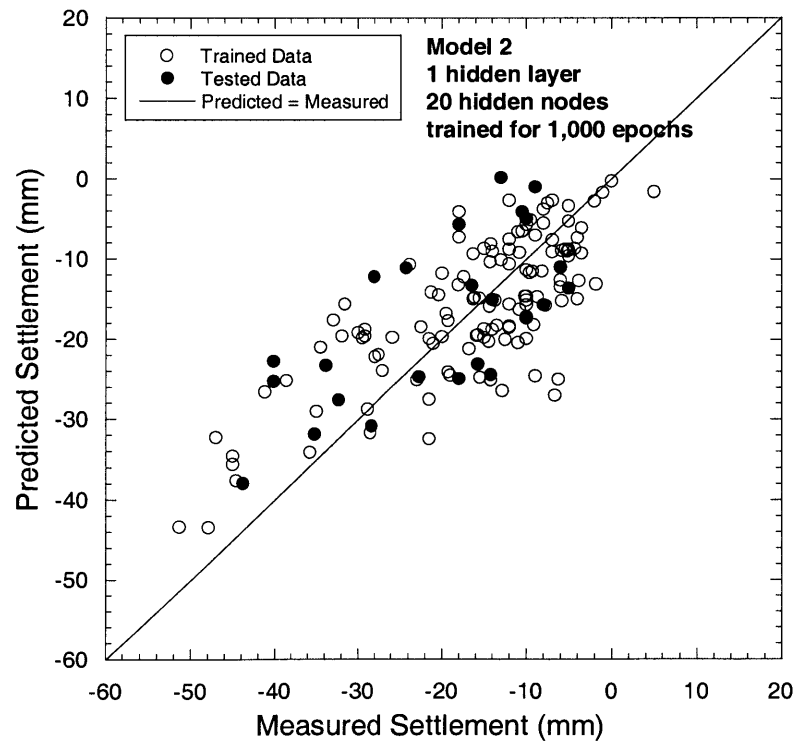


Figure 12.66 Performance of ANN with 1 hidden layer and 20 hidden nodes trained for 1,000 epochs for predicting settlements induced by tunneling in clays

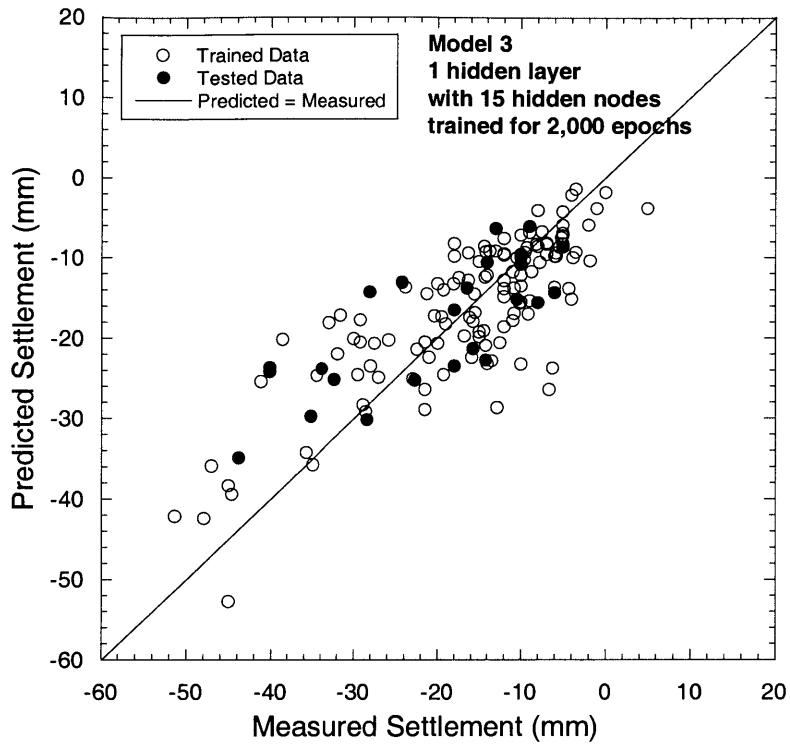


Figure 12.67 Performance of ANN with 1 hidden layer and 15 hidden nodes trained for 2,000 epochs for predicting settlements induced by tunneling in clays

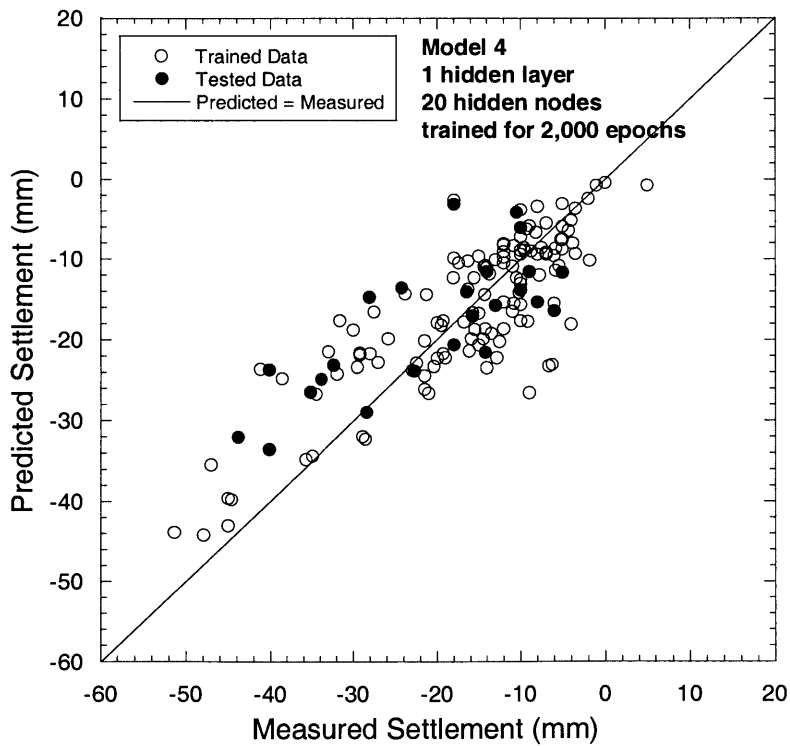


Figure 12.68 Performance of ANN with 1 hidden layer and 20 hidden nodes trained for 2,000 epochs for predicting settlements induced by tunneling in clays

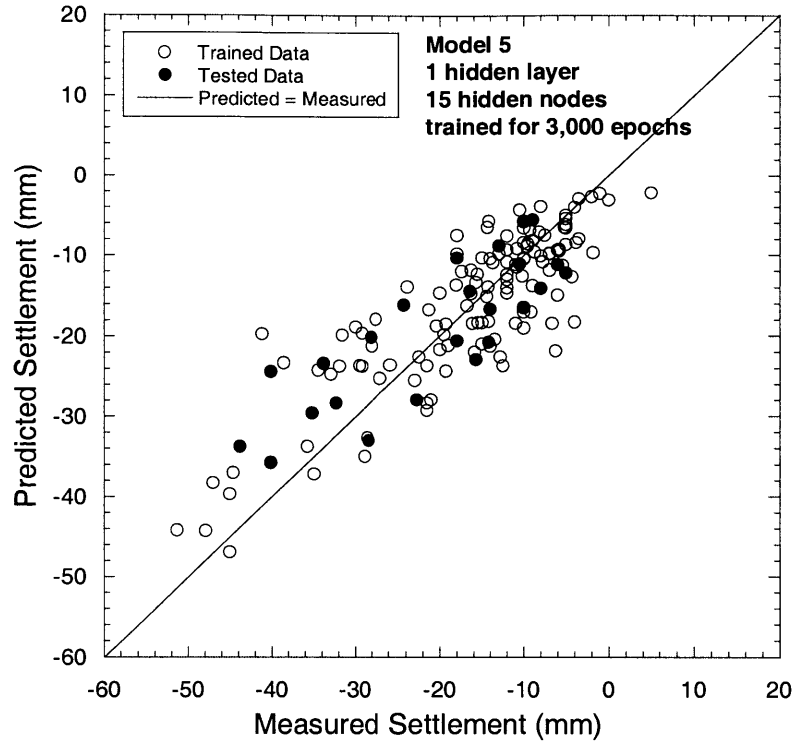


Figure 12.69 Performance of ANN with 1 hidden layer and 15 hidden nodes trained for 3,000 epochs for predicting settlements induced by tunneling in clays

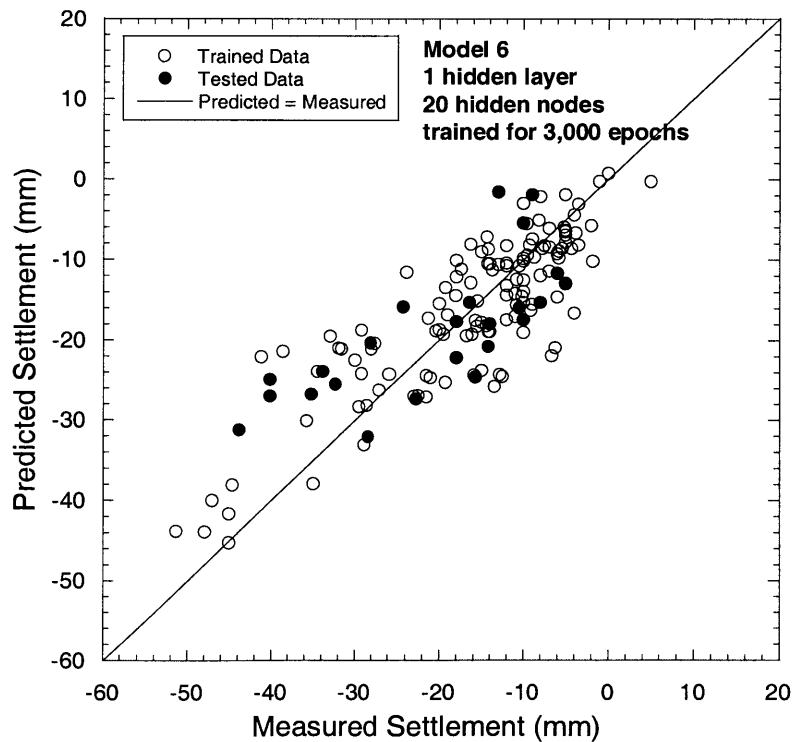


Figure 12.70 Performance of ANN with 1 hidden layer and 20 hidden nodes trained for 3,000 epochs for predicting settlements induced by tunneling in clays

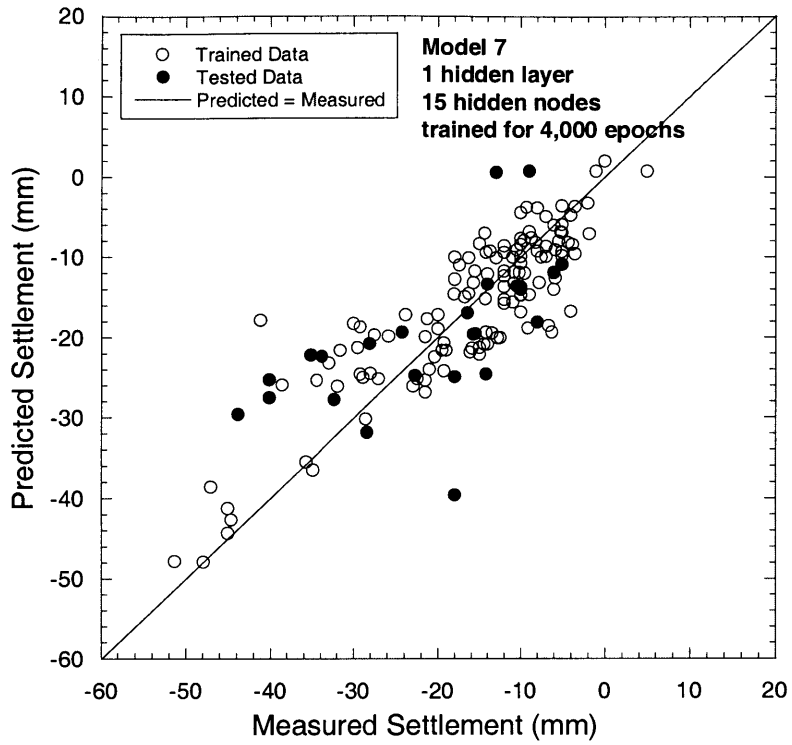


Figure 12.71 Performance of ANN with 1 hidden layer and 15 hidden nodes trained for 4,000 epochs for predicting settlements induced by tunneling in clays

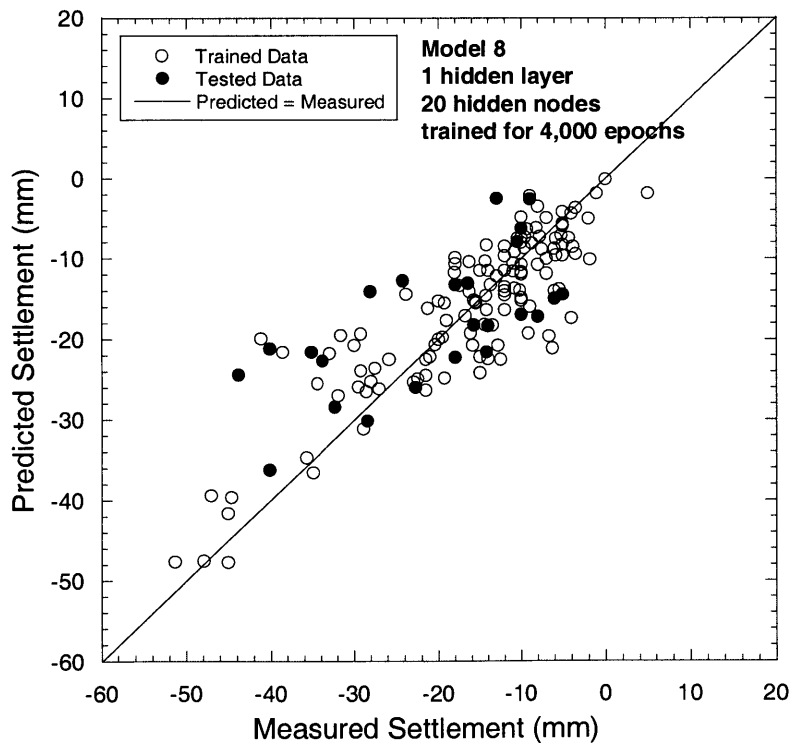


Figure 12.72 Performance of ANN with 1 hidden layer and 20 hidden nodes trained for 4,000 epochs for predicting settlements induced by tunneling in clays

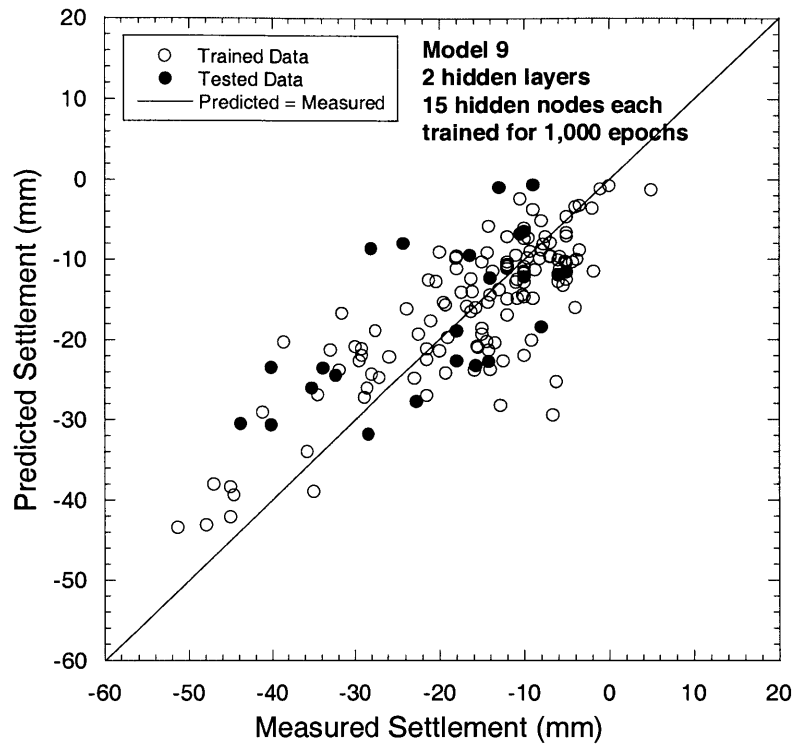


Figure 12.73 Performance of ANN with 2 hidden layers and 15 hidden nodes each trained for 1,000 epochs for predicting settlements induced by tunneling in clays

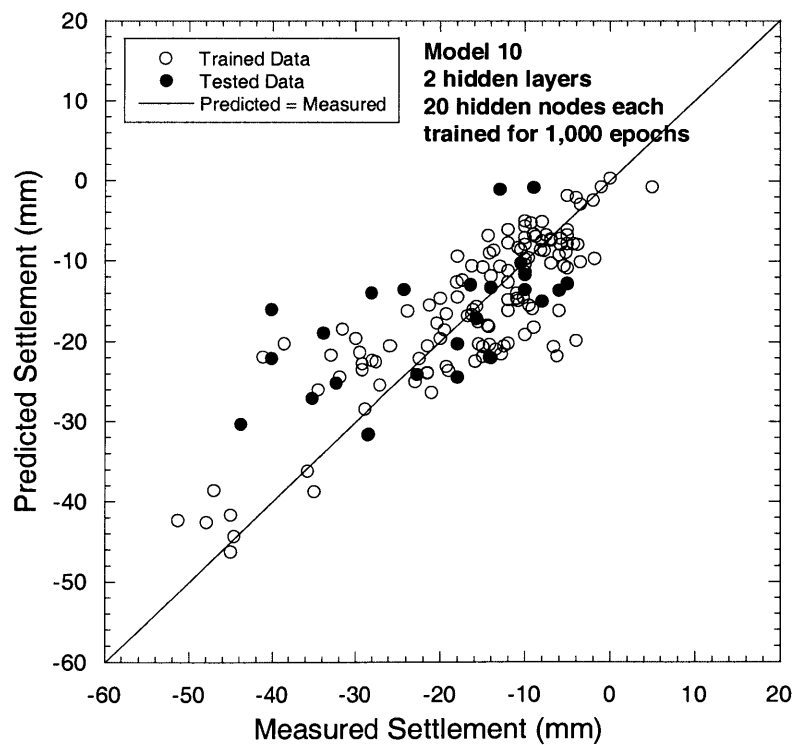


Figure 12.74 Performance of ANN with 2 hidden layers and 20 hidden nodes each trained for 1,000 epochs for predicting settlements induced by tunneling in clays

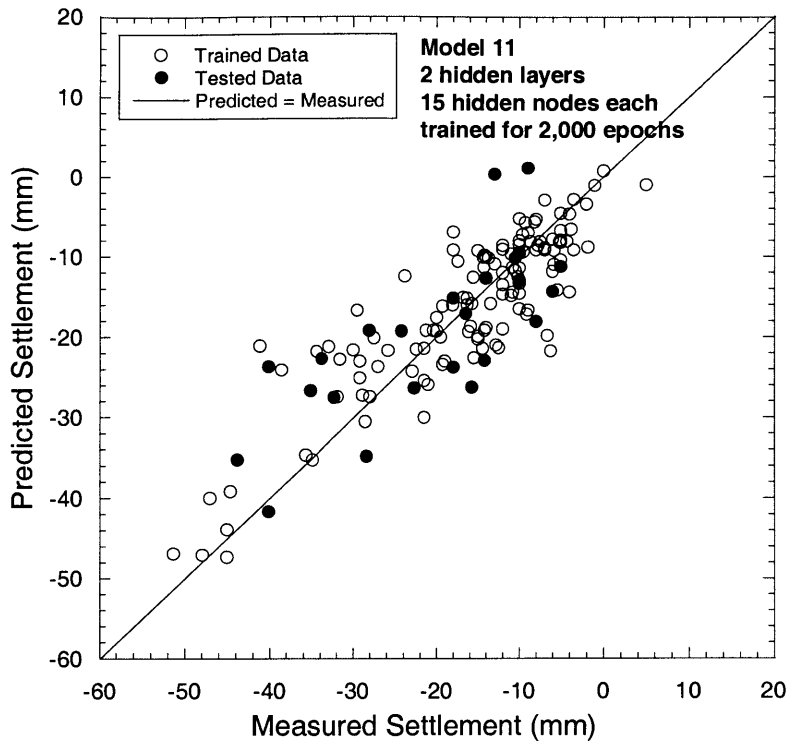


Figure 12.75 Performance of ANN with 2 hidden layers and 15 hidden nodes each trained for 2,000 epochs for predicting settlements induced by tunneling in clays

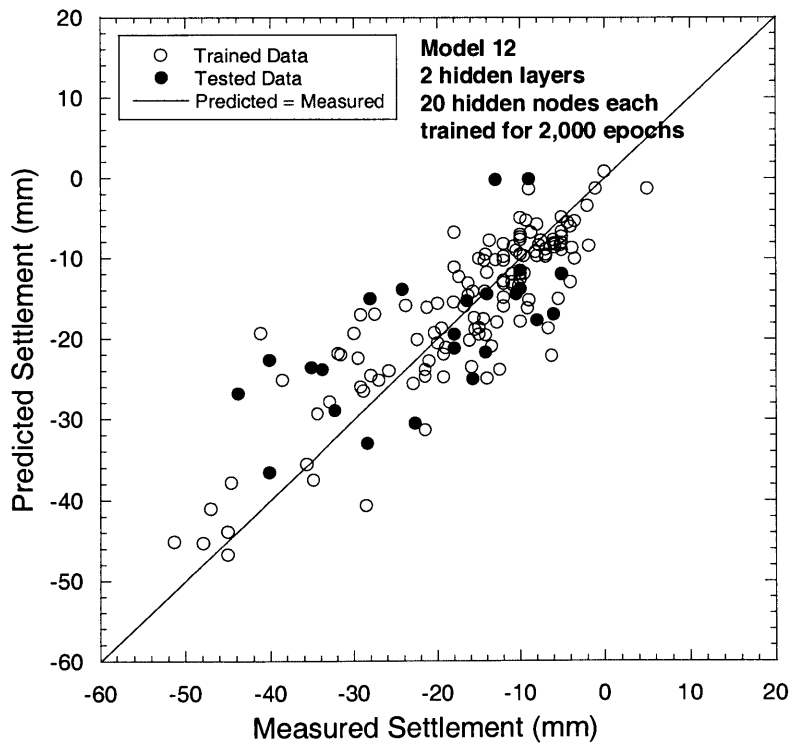


Figure 12.76 Performance of ANN with 2 hidden layers and 20 hidden nodes each trained for 2,000 epochs for predicting settlements induced by tunneling in clays

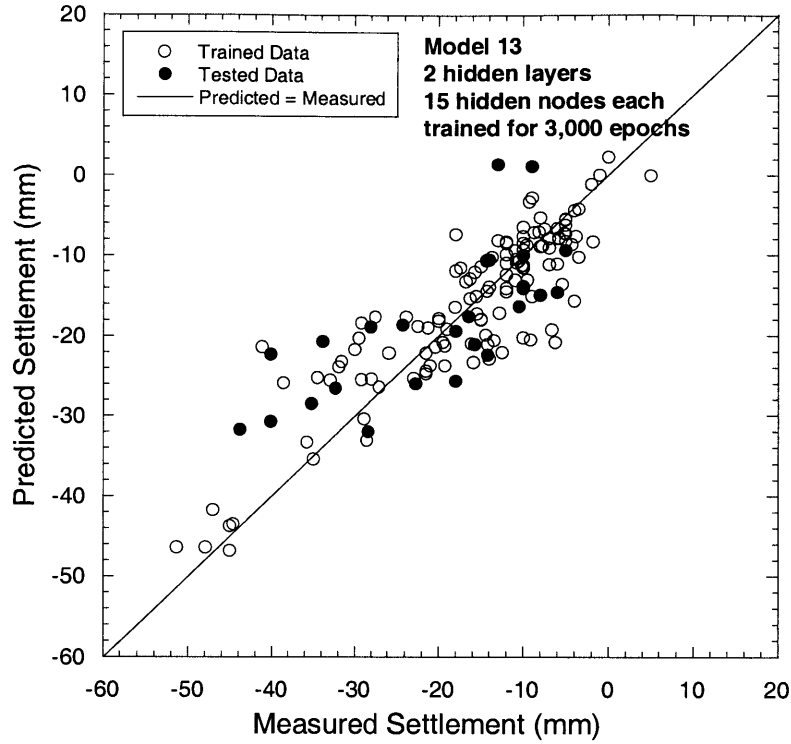


Figure 12.77 Performance of ANN with 2 hidden layers and 15 hidden nodes each trained for 3,000 epochs for predicting settlements induced by tunneling in clays

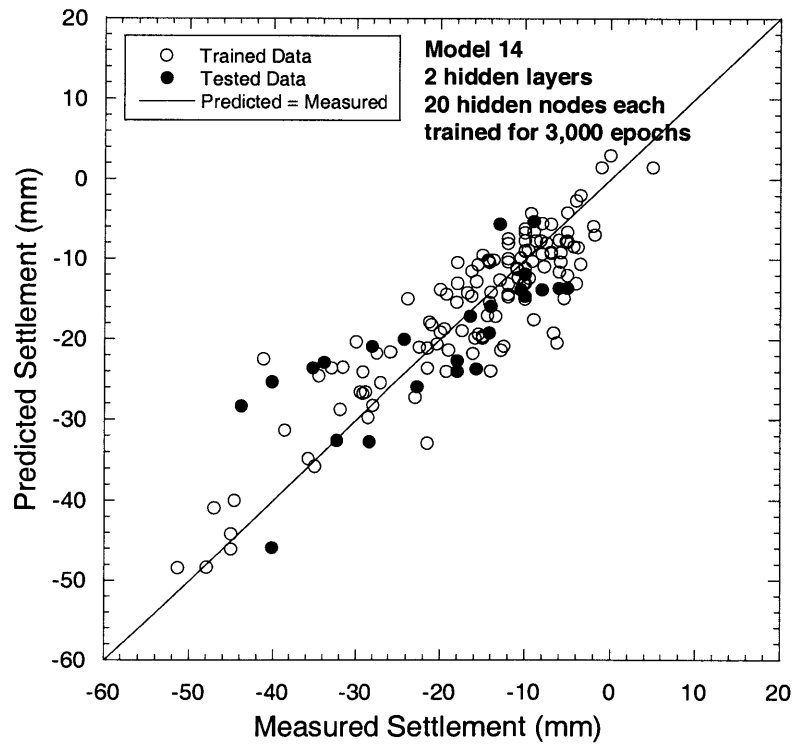


Figure 12.78 Performance of ANN with 2 hidden layers and 20 hidden nodes each trained for 3,000 epochs for predicting settlements induced by tunneling in clays

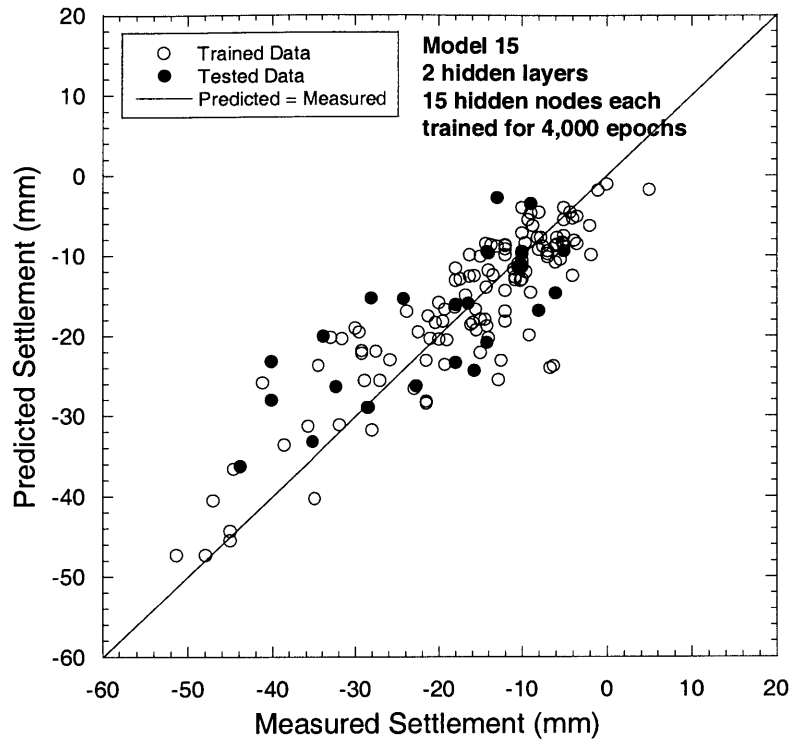


Figure 12.79 Performance of ANN with 2 hidden layers and 15 hidden nodes each trained for 4,000 epochs for predicting settlements induced by tunneling in clays

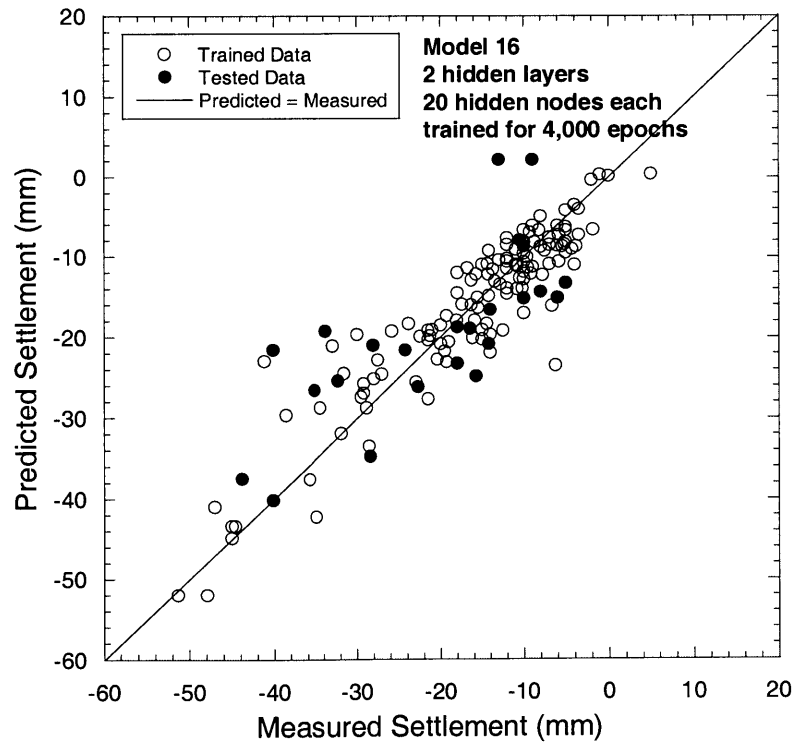


Figure 12.80 Performance of ANN with 2 hidden layers and 20 hidden nodes each trained for 4,000 epochs for predicting settlements induced by tunneling in clays

12.4 Prediction of Surface Settlements induced by Twin Tunnels

Based on the results presented so far, it appears that one can apply artificial neural networks (ANN) to predict the maximum surface settlement induced by the first shield. As discussed in Chapter 7, the Gaussian curve or normal probability function was found to be a good approximation of the surface settlement trough above a single tunnel. Hence, if the maximum surface settlement (δ_{max}) over the tunnel centerline is known (point A in Figure 12.81), one can describe the whole settlement trough using the Gaussian function (see Section 7.2.2).

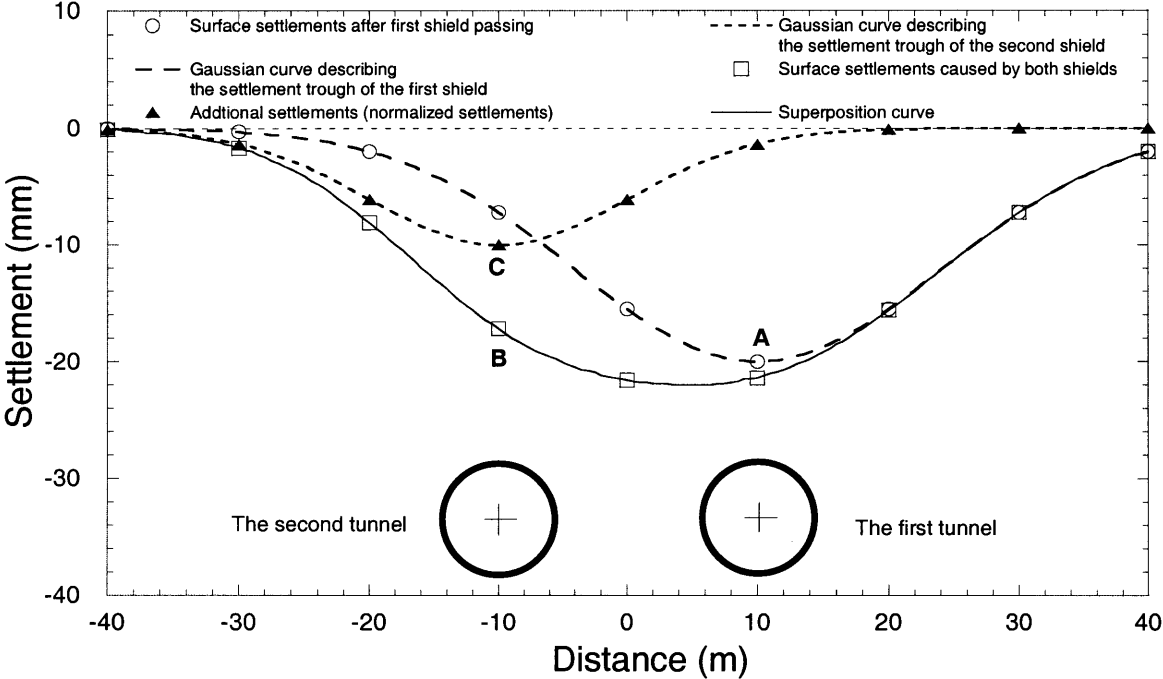


Figure 12.81 Surface settlements caused by twin-tunnels

In the MRTA project, twin tunnels were excavated (i.e. the northbound and southbound tunnels). In Chapter 8, effects of the second tunnel on surface settlements were investigated. Based on observations, the magnitude of surface settlements caused by the second shield (i.e. additional settlements after first shield passing) appears to be different

from that of the first shield. A normalization and superposition technique was introduced to describe settlement troughs caused by twin tunnels. It was found that the “additional settlement” trough (Figure 12.81) induced by the second shield can be also described by the Gaussian curve. The total settlement can then be constructed by superimposing the additional settlement curve on the settlement trough observed after the first shield passing. Hence, if one can estimate the surface settlement over the second tunnel after the second shield passes the section (point B in Figure 12.81), point C can be calculated and the additional settlement trough can be described. Using the superposition technique, the final settlement trough can be constructed as shown in Figure 12.81.

In this section, an attempt is made to apply artificial neural networks (ANN) for predicting surface settlements over the second tunnel after second shield passing (point B in Figure 12.81). Since the magnitude of additional settlements caused by the second tunnel is very different from that of the first tunnel, there should be other factors involved besides the influencing parameters used in previous network models. As indicated in the literature (i.e. Cording and Hansmire, 1975 and Cooper et al., 2002), the distance between the twin tunnels is one of the factors affecting the total settlement trough. Another important factor is the interval time between the first shield and the second shield arrivals. Additionally, operational parameters of the second shield obviously affect the additional settlement as discussed in Chapter 8. The influencing factors causing settlements after second shield passing are summarized in Table 12-8. 21 input nodes are used to represent these parameters as shown in Figure 12.82.

To determine an optimum network model for this problem, ten neural network models were used for training and testing as shown in Table 12-9. RMSE values obtained from training and testing the models are summarized in Figure 12.83. Performances of the network models are graphically shown in Figure 12.84 through Figure 12.93. As can be seen, the results indicate that increasing either the numbers of hidden nodes or hidden layers or training epochs can lead to improved mapping ability between inputs and outputs of the training set. For instance, as can be seen in Figure 12.92, for 2 hidden layers and 20 hidden nodes each trained for 7,000 epochs (Model 9), the network

provides predicted outputs almost the same as the targeted outputs in the training set (i.e. RMSE of the training set = 1.11). Obviously, the network can converge to very small differences between predicted outputs and targeted outputs in the training samples. However, trying to reduce the error too much may lead to overfitting or poor generalization when the network is tested with the validation samples; the predicted settlements are very different from the measured settlements as illustrated in Figure 12.92 and RMSE of the validation set is very high (RMSE = 10.82 as shown in Table 12-9). These significant differences are not acceptable since this means that the network is not reliable in application. In contrast, the network with only one hidden layer and 20 hidden nodes trained for 2,000 epochs (Model 2) yields the lowest RMSE = 7.40, when it is tested with validation samples. The network provides the best settlement prediction as its outputs are in good agreement with measured settlement data as shown in Figure 12.85. Therefore, one can conclude that ANN method can predict surface settlements over the second tunnel with a network with one hidden layer and 20 hidden nodes trained for 2,000 epochs.

As shown in previous sections, the maximum surface settlement over the first tunnel can be predicted by the ANN model. Using the Gaussian curve, one can describe surface settlement troughs over the first tunnel (see Section 7.2.2). Based on the result in this present section, surface settlements over the second tunnel (i.e. measured after the second shield passing) can be also predicted using the ANN method. One can then fit a Gaussian curve to the incremental surface settlement over the second tunnel and superimpose this curve to the curve over the first tunnel to obtain a total settlement trough over both tunnels (see also Figure 12.81).

This approach is checked with settlement data obtained from Tunnel Sections A, B, C, and D as shown in Figure 12.94 through Figure 12.97. First, the ANN-single tunnel model (Section 12.2) is applied to predict the maximum surface settlement over the first tunnel after the first shield passed the instrumentation section. The Gaussian curve is then used to describe the settlement trough by assuming the trough width parameter $i = 0.5z$, (i.e. based on the empirical relation found in the project as shown in Figure 7.58) where z

is the tunnel depth. The ANN-twin tunnel model developed in this section is then used to predict surface settlements over the second tunnel (point B in Figure 12.81) as the second shield passes the instrumentation sections. From this predicted settlement, one then measures the settlement at the first settlement trough over the second tunnel to obtain the incremental surface settlement over the second tunnel (point C in Figure 12.81). The Gaussian curve is again used to describe the additional settlement trough with $i = 0.5z$. Finally, the second curve is superimposed to the first curve to obtain the total settlement trough as a result of the twin tunnels. Note that all these settlements we predicted compared to the observed settlements. Note that all these settlements we predicted are here compared to the observed settlements.

As can be seen in Figure 12.94 (for Section A), the predicted settlement trough does not fit the observed data as the ANN-twin-tunnel model underestimates the settlement over the second tunnel. The reason for the deviation between predictions and observations in Section A appears to be due to the fact that the measured settlements in Section A (Figure 12.94) are larger than 50 mm which is outside this training boundary. On the other hand, the predicted surface settlement troughs are in agreement with observed data in Sections B, C, and D (Figure 12.95 through Figure 12.97). Additionally, as shown in Figure 12.95 through Figure 12.97, total settlement troughs in Sections B, C, and D predicted by using the combined superposition/ANN approach as described above are also in agreement with observed settlement data. In Section A (Figure 12.94), there is again a discrepancy as the predicted total settlement does not fit the observed data due to the error in the ANN prediction.

Table 12-8 Input parameters used for the ANN model using for predicting surface settlements over the second tunnel

Category	Parameter	Detailed Items	Input Node No.
Tunnel Geometry	(1) Tunnel depth (m)		1
	(2) Distance from launching station (m)		2
	(3) Distance between tunnels		3
Geological Conditions	(4) Geology at tunnel crown	Soft Clay (No = 0, or Yes =1) Stiff Clay (No = 0, or Yes = 1) Sand (No = 0, or Yes = 1)	4 5 6
	(5) Geology at tunnel invert	Stiff Clay (No = 0, or Yes =1) Sand (No = 0, or Yes = 1)	7 8
	(6) Ground water level from tunnel invert (m)		9
Operational Factors of The First Shield	(7) Average face pressure (kPa)		10
	(8) Average penetration rate (mm/min)		11
	(9) Average pitching angle (degree)		12
	(10) Grouting pressure (bar)		13
	(11) Percent grout filling		14
Operational Factors of The Second Shield	(12) Average face pressure (kPa)		15
	(13) Average penetration rate (mm/min)		16
	(14) Average pitching angle (degree)		17
	(15) Grouting pressure (bar)		18
	(16) Percent grout filling		19
Machine	(17) Machine Model	Kawasaki =1 Herrenknecht = 0	20
Time Interval	(18) Time Interval (day)		21

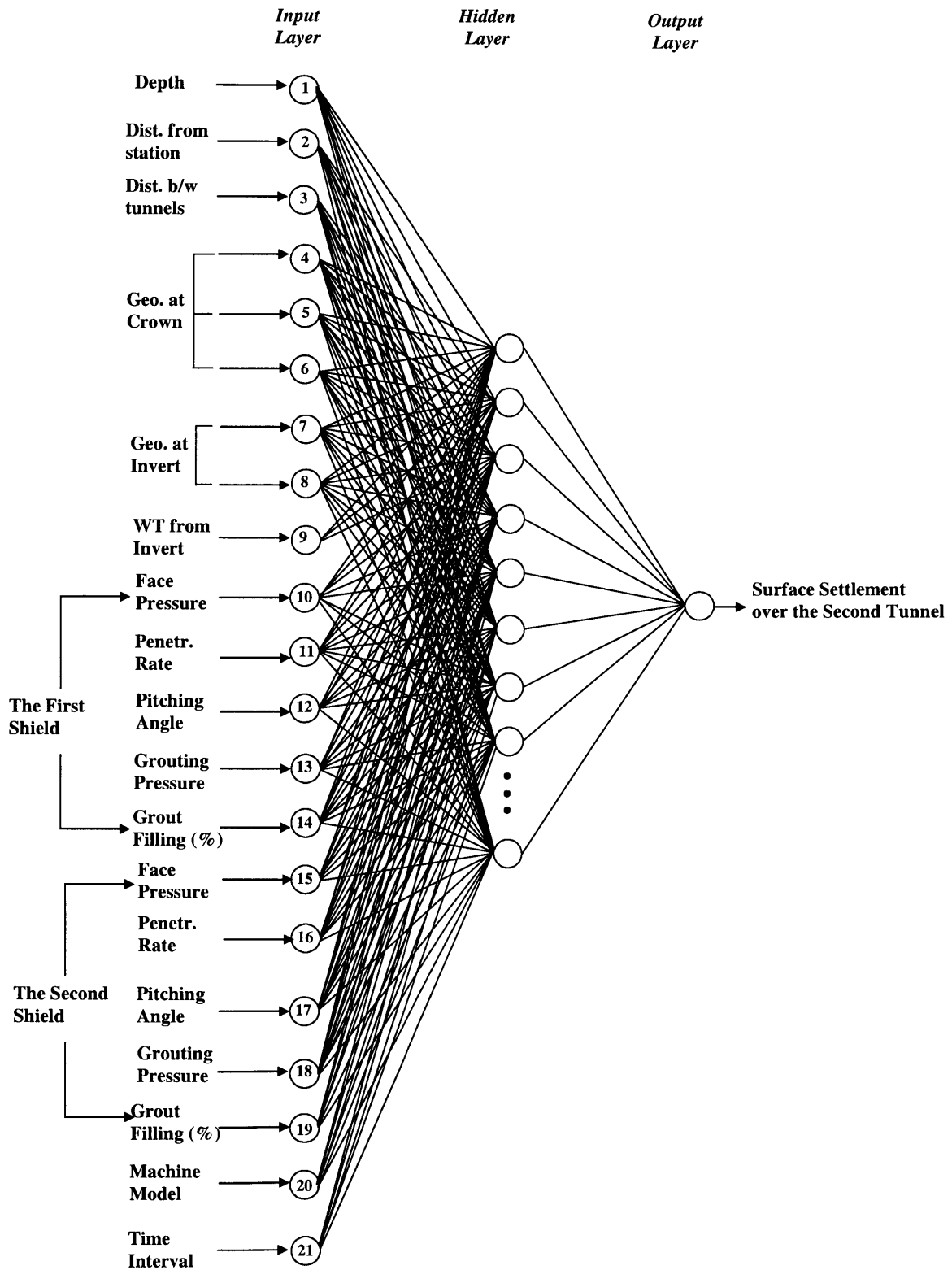


Figure 12.82 Structure of neural network model for predicting surface settlements over the second tunnel

Table 12-9 Neural network models used in the prediction of surface settlements induced by the twin tunnels and their training and testing results

Model	Network Architecture	Training Epochs	Training Samples (RMSE)	Testing/Prediction Samples (RMSE)
1	1 hidden layer, 20 hidden nodes	1,000	5.79	9.06
2	1 hidden layer, 20 hidden nodes	2,000	4.86	7.40
3	1 hidden layer, 20 hidden nodes	3,000	4.28	9.15
4	1 hidden layer, 20 hidden nodes	4,000	3.68	10.08
5	2 hidden layer, 20 hidden nodes	3,000	3.44	9.89
6	2 hidden layer, 20 hidden nodes	4,000	2.60	9.61
7	2 hidden layer, 20 hidden nodes	5,000	1.77	8.17
8	2 hidden layer, 20 hidden nodes	6,000	2.16	9.15
9	2 hidden layer, 20 hidden nodes	7,000	1.11	10.82
10	2 hidden layer, 20 hidden nodes	8,000	1.79	10.41

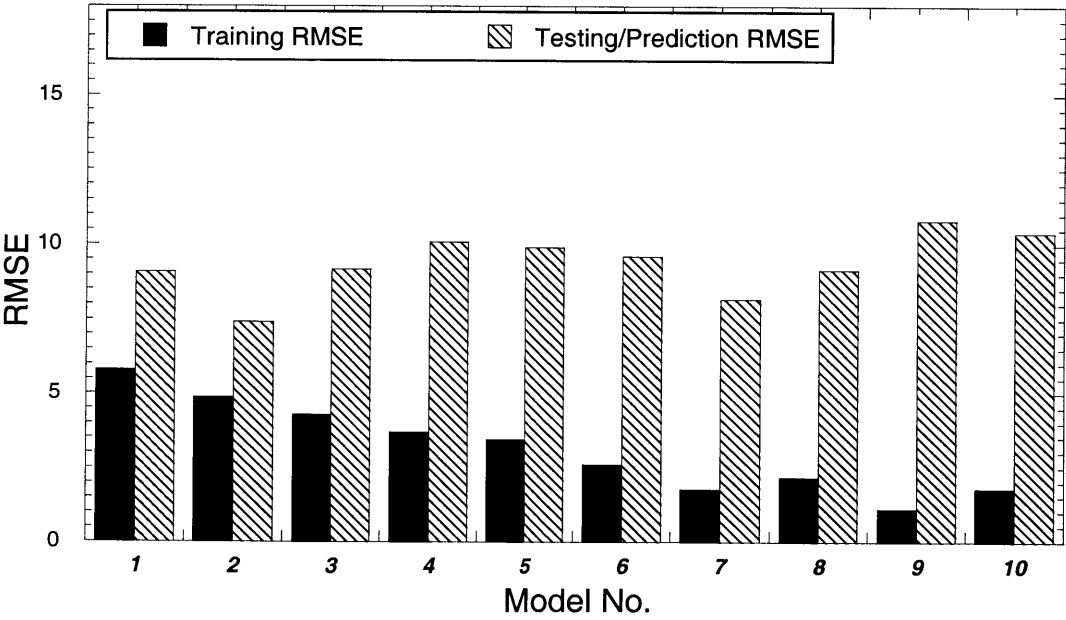


Figure 12.83 Summary of training and testing RMSE of neural network models used in the prediction of surface settlements over the second tunnel

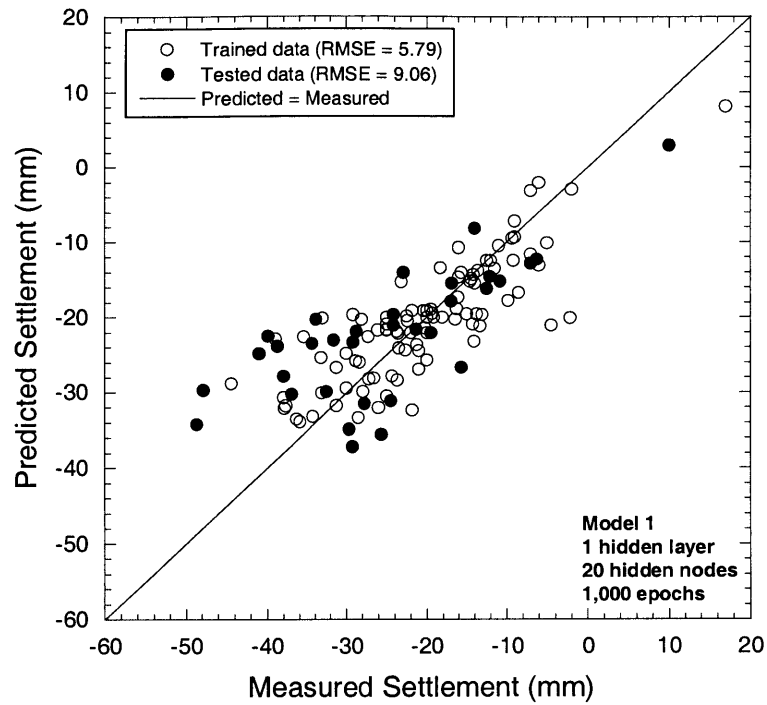


Figure 12.84 Performance of ANN (twin-tunnel model) with 1 hidden layer and 20 hidden nodes trained for 1,000 epochs

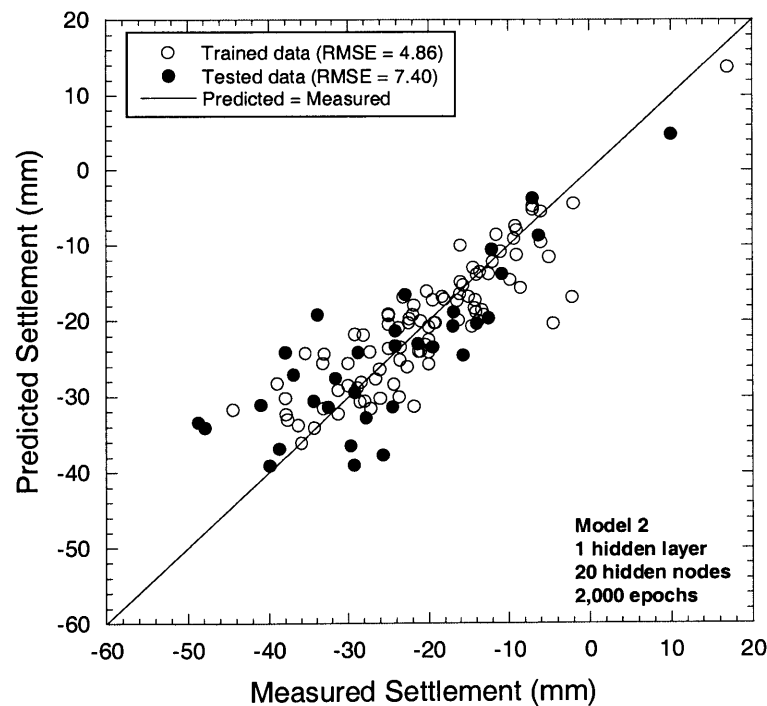


Figure 12.85 Performance of ANN (twin-tunnel model) with 1 hidden layer and 20 hidden nodes trained for 2,000 epochs

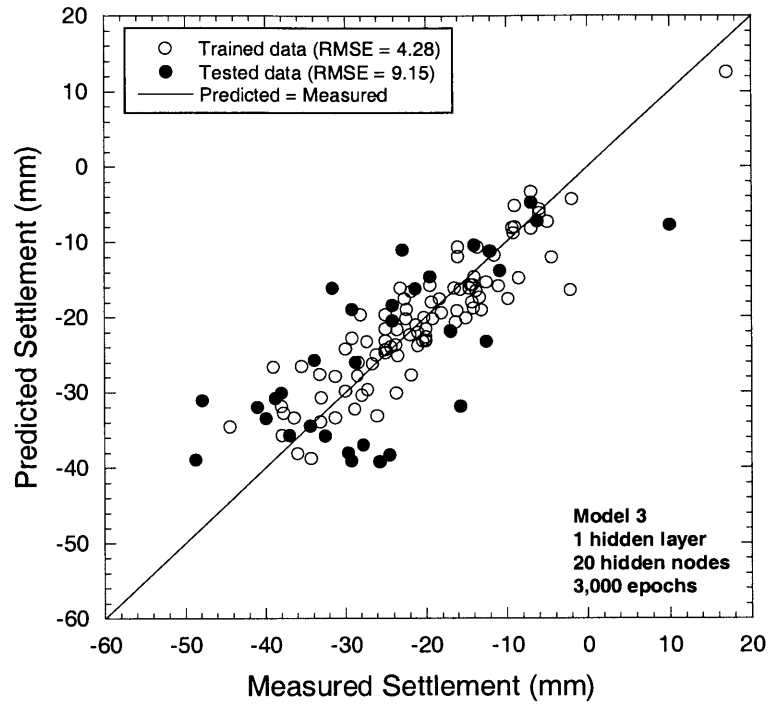


Figure 12.86 Performance of ANN (twin-tunnel model) with 1 hidden layer and 20 hidden nodes trained for 3,000 epochs

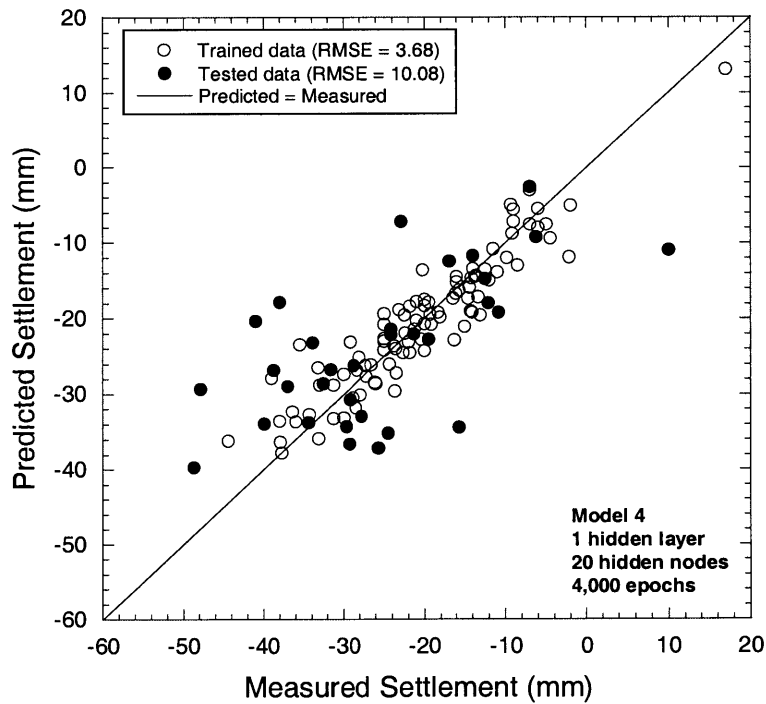


Figure 12.87 Performance of ANN (twin-tunnel model) with 1 hidden layer and 20 hidden nodes trained for 4,000 epochs

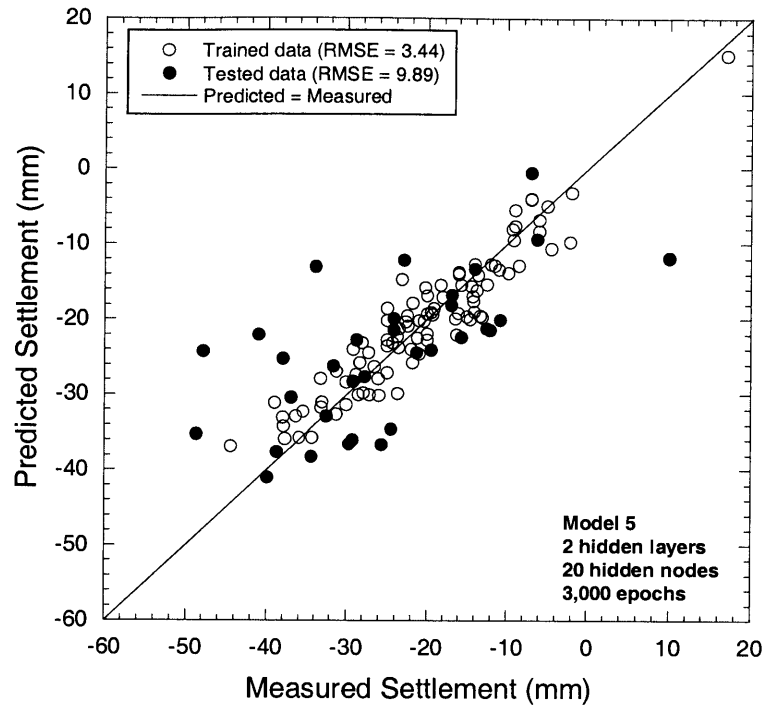


Figure 12.88 Performance of ANN (twin-tunnel model) with 2 hidden layers and 20 hidden nodes each trained for 3,000 epochs

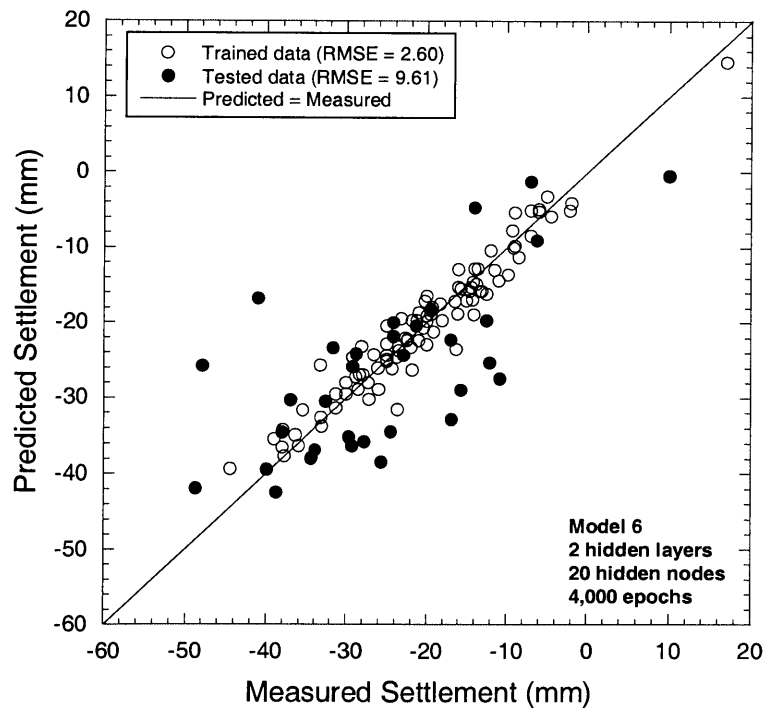


Figure 12.89 Performance of ANN (twin-tunnel model) with 2 hidden layers and 20 hidden nodes each trained for 4,000 epochs

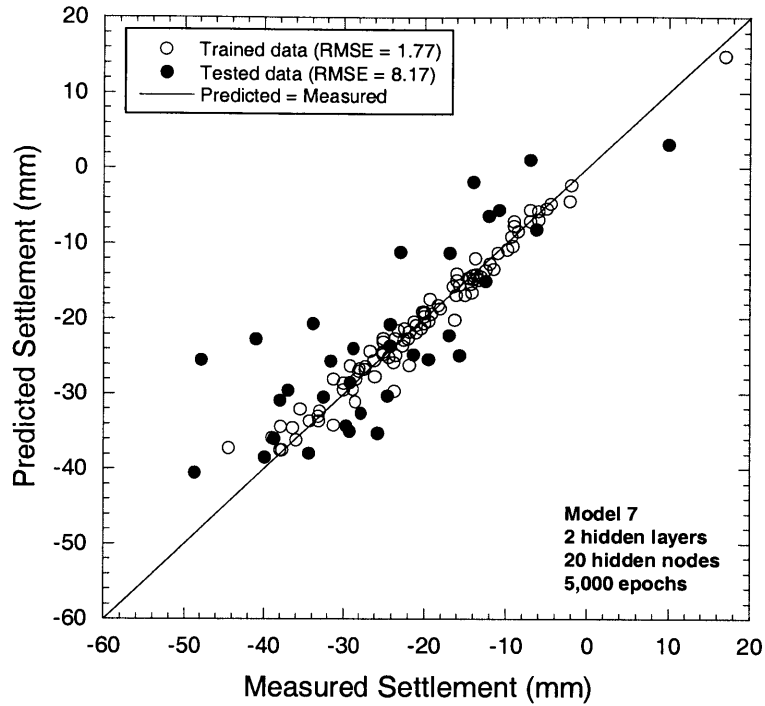


Figure 12.90 Performance of ANN (twin-tunnel model) with 2 hidden layers and 20 hidden nodes each trained for 5,000 epochs

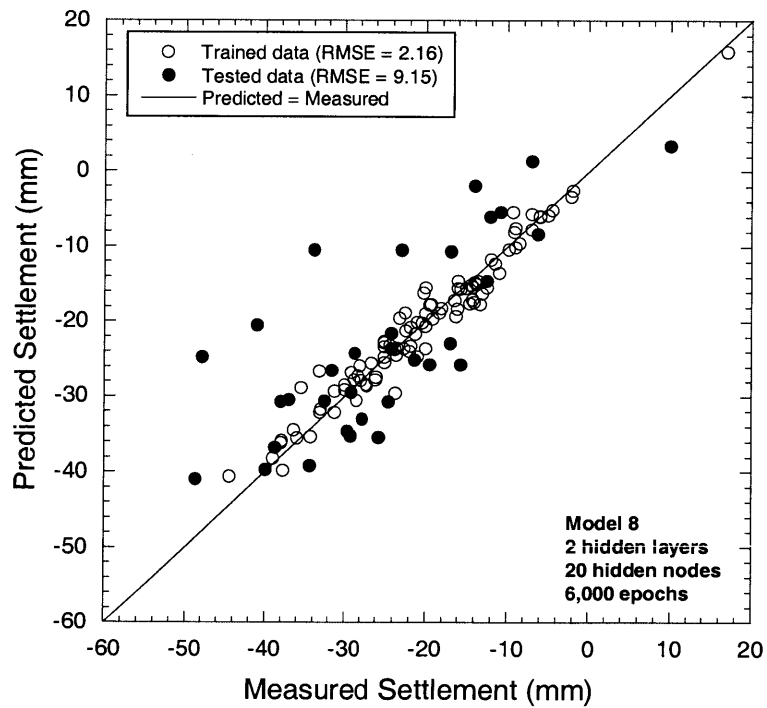


Figure 12.91 Performance of ANN (twin-tunnel model) with 2 hidden layers and 20 hidden nodes each trained for 6,000 epochs

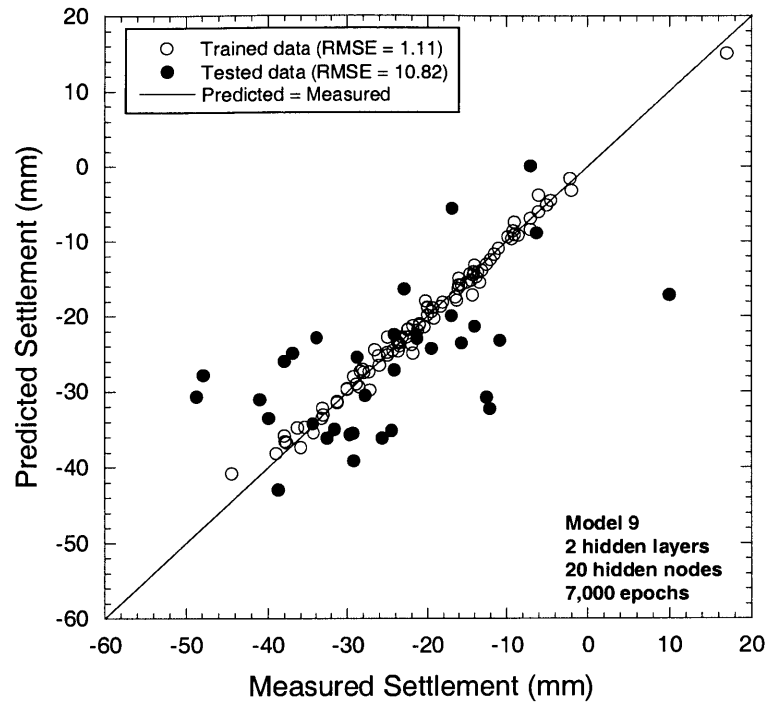


Figure 12.92 Performance of ANN (twin-tunnel model) with 2 hidden layers and 20 hidden nodes each trained for 7,000 epochs

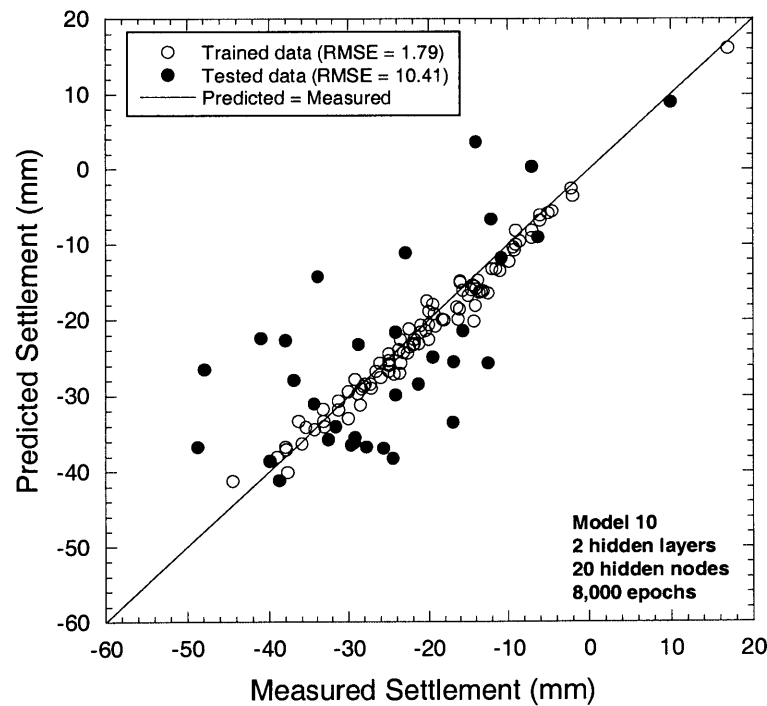


Figure 12.93 Performance of ANN (twin-tunnel model) with 2 hidden layers and 20 hidden nodes each trained for 8,000 epochs

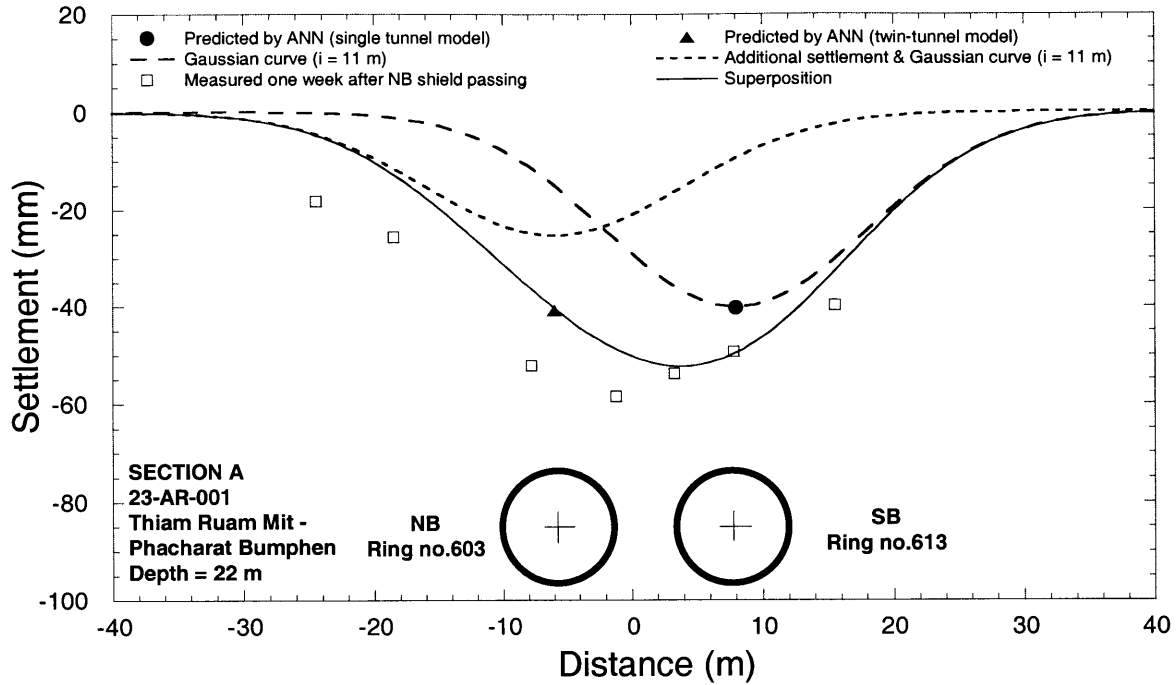


Figure 12.94 Predicted surface settlements using the combination of ANN and the normalization technique compared to measured surface settlements caused by twin tunnels in Section A

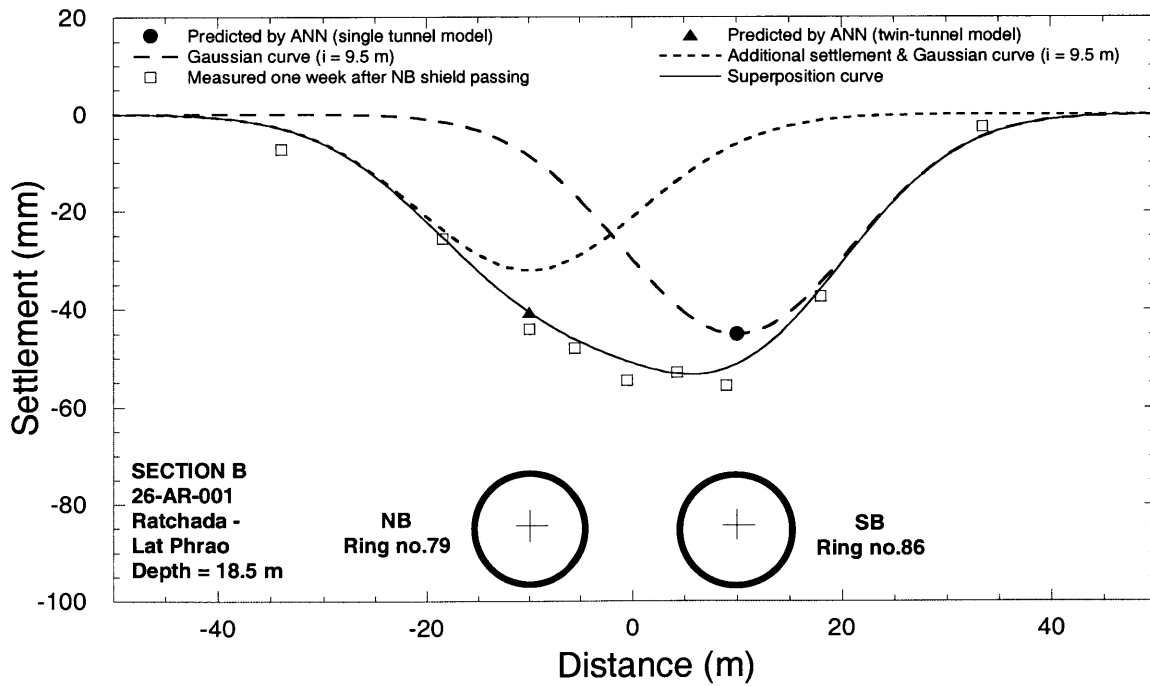


Figure 12.95 Predicted surface settlements using the combination of ANN and the normalization technique compared to measured surface settlements caused by twin tunnels in Section B

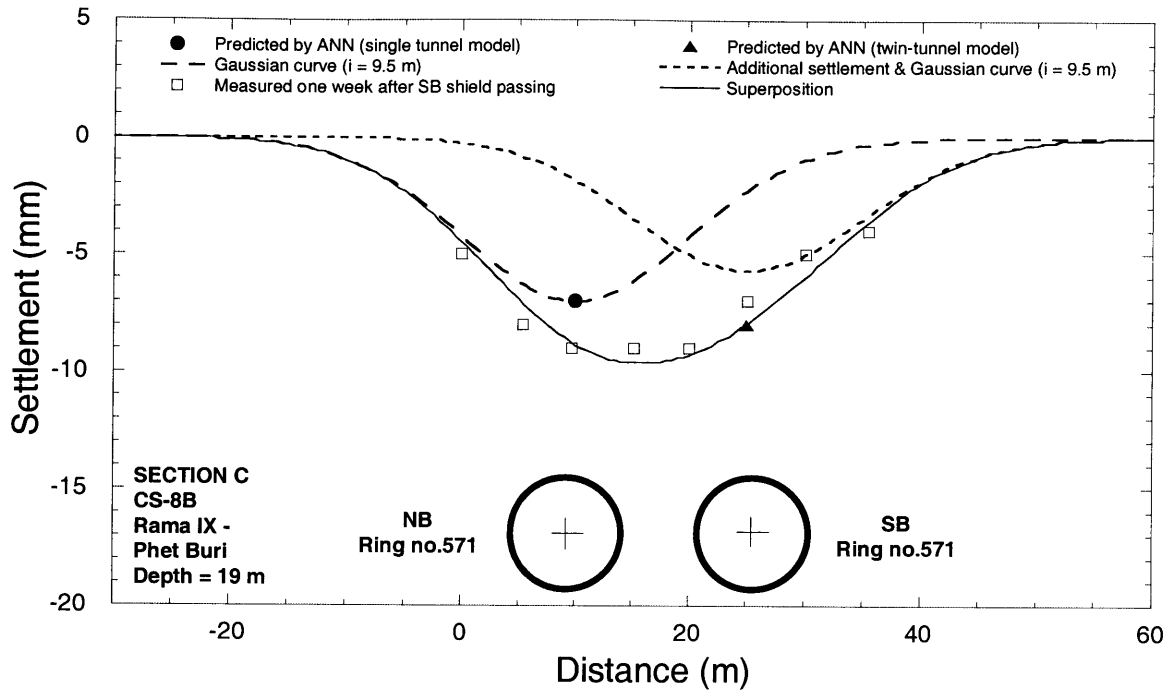


Figure 12.96 Predicted surface settlements using the combination of ANN and the normalization technique compared to measured surface settlements caused by twin tunnels in Section C

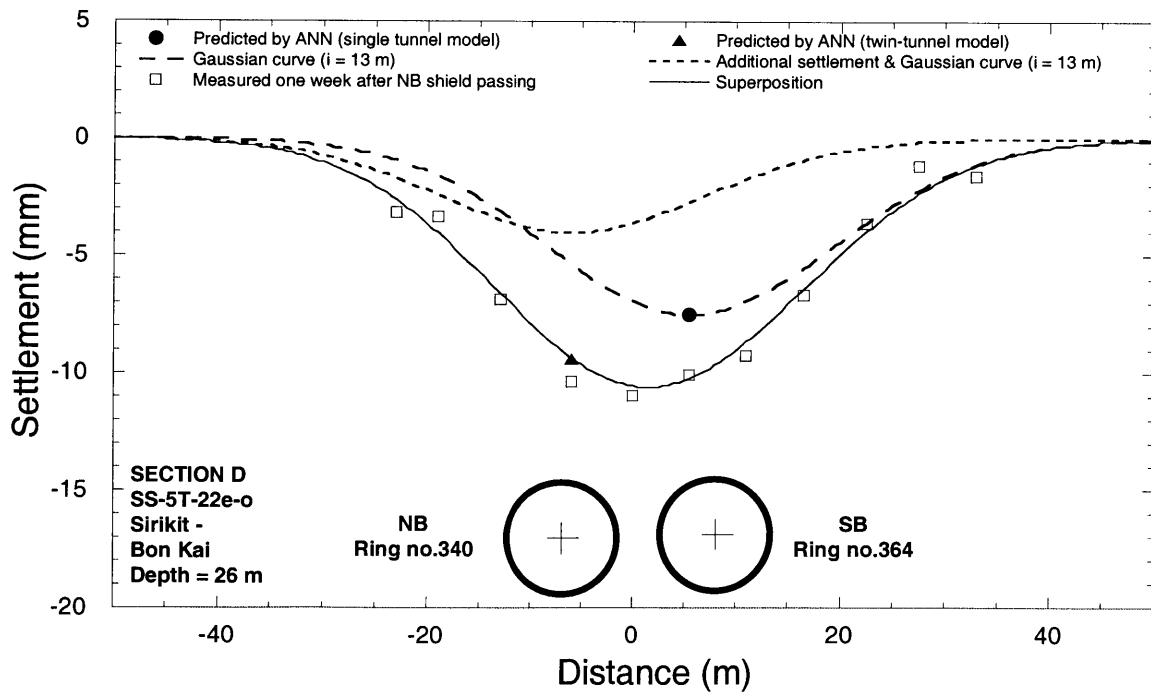


Figure 12.97 Predicted surface settlements using the combination of ANN and the normalization technique compared to measured surface settlements caused by twin tunnels in Section D

CHAPTER 13

Summary, Conclusions and Recommendations

13.1 Summary

A major problem in studying the EPB shield tunneling method and its effects on surface settlements is that extensive field instrumentation data and continuous observation of operational factors have not often been available, i.e. information on some essential factors is missing. In order to understand the governing mechanisms, comprehensive information including geological conditions, reliable settlement measurements, and operational records of EPB shields are needed. Therefore, the data from the Bangkok MRTA project provided an excellent opportunity to evaluate the performance of EPB shield tunneling in soft ground.

In this thesis, a comprehensive EPB tunneling database was developed. This database contains monitoring results that include all shield operational records and field instrumentation readings, specifically:

1. Records of operational parameters along the tunnel alignment such as face pressure, penetration rate, and grouting pressure.
2. Instrumentation readings from surface settlement markers, surface settlement marker arrays, inclinometers, extensometers, and piezometers.
3. Tunnel alignment coordinates

4. Instrumentation layouts
5. Geological conditions

Using the information from the computerized database, the following can be addressed:

1. Establish in detail what ground deformations occur under which conditions. This allows one to evaluate to what extent current predictive methods can be used.
2. Show that ground behavior related to EPB shield tunneling depends on the complex interrelation of many parameters, with no single parameter having an overriding effect on ground deformation, notably on surface settlements.
3. Given the fact that the development of a mechanically based model is very difficult, show that Artificial Neural Networks (ANN) can be used to improve on the present predictive approaches. This leads to ANN-based settlement predictions and combined ANN/empirical methods for predicting surface settlement troughs.

Before working with the Bangkok MRTA data, a comprehensive literature review was conducted to evaluate if available methods can be used to predict surface settlements induced by EPB shield tunneling. Several case histories of shield tunneling projects around the world were also reviewed.

Next, the effects of EPB shield operational parameters on ground movements in the MRTA project were investigated to evaluate the behavior of ground movements associated with EPB shield tunneling and to investigate effects of EPB shield operational parameters on ground movements. This was done by plotting each influencing parameter versus surface settlements in order to analyze the effect of these factors on surface settlements. The surprisingly consistent conclusion one can draw is that there are no strong trends in the relationship between any one of the parameters and the surface settlement. This indicates that more than one parameter influences the magnitude of surface settlements.

Therefore, Artificial Neural Networks (ANN) were introduced with the intent to relate several parameters to surface settlements. As described in Chapters 10 and 11, using MATHLAB-ANN Toolbox, ANN are first trained with observed data and then the ANN

predictions are compared to these training data (i.e. in the training set). Second, the ANN are applied to new observed data in a testing set and the ANN predictions are compared to observations. This is called “validation.” It was found that the coincidence of prediction by the ANN and observed data depends on the network structure, specifically on the number of hidden layers, the number of hidden nodes, and the number of training epochs. The training of the ANN (see Chapter 11) involved:

1. Number of hidden layers: 1,2
2. Number of hidden nodes in each hidden layer: 10, 15, 20
3. Number of training epochs: 1000, 2000, 3000

It was found that the extreme model with a large number of hidden nodes trained for a large number of epochs produced a near perfect fit with the training data but failed to predict surface settlements in the testing (validation) set. This so called “overfitting” can be avoided through a trial and error process, which leads to an optimum model with regard to validation. All this individual that available prediction methods are limited used only.

After development of ANN models for predicting surface settlements, they were applied to various scenarios using the data from the MRTA project. These scenarios include the prediction of maximum settlements caused by a single tunnel and by twin tunnels, the prediction of settlements occurring in Zones 1 and 2 (Figure 7.17, page 285), the prediction of maximum settlements induced by tunneling in clays, and the prediction of maximum settlements by only training with data recorded at the beginning of a tunnel drive.

13.2 Conclusions

Based on the case histories and observations in the Bangkok MRTA project, the longitudinal surface settlement along the tunnel axis induced by EPB tunneling can be divided into three major zones (see also Figure 7.17, page 285):

1. The settlement in front of the shield (Zone 1)
2. The settlement over the shield body (Zone 2)
3. The settlement after shield passing (Zone 3)

Large settlements (up to 25 mm) found in Zone 1 are associated with low face pressures (50-150 kPa) and low penetration rates (5-15 mm/min). In contrast, if applied face pressures and penetration rates are very high (i.e. the face pressure is 200-400 kPa and the penetration rate is greater than 50 mm/min), less surface settlements (less than 10 mm) or even ground heave (up to 17 mm) occurred in Zone 1. Face pressure and penetration rate also affect settlements in Zone 2 during shield passing. However, settlements occurring in Zone 3 are mainly influenced by tail void grouting. Clearly, the maximum settlement as resulting from the settlements in Zone 1, 2, and 3 involves all these influencing factors. Very important is the conclusion that no single parameter has an overriding effect on surface settlements.

Based on observations and data analyses of the MRTA project, one can conclude that the normal probability or Gaussian curve remains appropriate for fitting transverse settlement profiles or surface settlement troughs over a single tunnel. Observed surface settlement troughs measured after the first shield passing are symmetric with the maximum settlement (δ_{max}) over the centerline of the first tunnel. Therefore, by selecting an appropriate trough width parameter, one can use the Gaussian curve to estimate the complete settlement trough. Based on observations from the MRTA project, the trough width parameter is $i = 0.4z$ and $0.6z$ for tunnels in clay (average $i = 0.5$), and $i = 0.35z$ for tunnels in sand. This is consistent with recent data reported elsewhere (e.g. Mair and Taylor, 1997)

The limitation of this empirical method is that it requires knowledge of the maximum settlement (δ_{\max}) to describe settlement troughs. This maximum settlement can be obtained from instrumentation readings only after shield passing or it can be estimated from an empirical ground loss (G.L.%) parameter. However, since the ground loss induced by EPB tunneling does depend on many factors including geological conditions, operational parameters, and tunnel geometry, estimating the precise ground loss parameter is extremely difficult. Therefore, this thesis proposes another way to determine the maximum settlement through the use of ANN.

Surface settlement troughs over twin tunnels observed after second shield passing showed a variety of shapes which were again dependent on many factors such as geological conditions, operational parameters and tunnel geometry. A normalization and superposition technique was introduced to describe settlement troughs caused by twin tunnels. It was found that the “additional settlement” trough induced by the second tunnel can be obtained and described by the Gaussian curve. Consequently, the total settlement trough can be constructed by superimposing the additional curve on the settlement trough observed after the first shield passing. This superposition curve fits the total settlement trough well except in cases showing ground heave.

Additionally, it was found that the Gaussian curve can be used to fit the settlement troughs over the stacked tunnels very well. The troughs showed very narrow trough widths probably caused by the fact that the lower tunnel was excavated in the Sand layer.

It was also shown that the second shield could induce deflections in the first tunnel liner particularly between the springline and invert. The deflection magnitude of the first tunnel, which was up to 10 mm, appeared to be proportional to the face pressure level of the approaching second shield.

Lateral ground deformation caused by EPB tunneling was measured with inclinometers in the MRTA project. Two distinct portions of lateral deformation curves were observed. The first portion was the deformation above the tunnel crown, where the ground tended

to deform towards the tunnel. The largest inward deformation (up to 10 mm) occurred during shield passing (similar to the behavior of Zone 2 of the longitudinal surface settlement). In contrast, at the level below the crown, the ground deformed outward (up to 6mm) during shield passing. It was found that this mechanism was affected by tail void grouting and the magnitude of outward deformation appeared to correspond to the magnitude of the applied grouting pressure.

The ANN applications showed that the ANN can be used for predicting surface settlements with confidence when:

1. Training the network with data from the same tunnel section for which one wants to predict surface settlements. For example, training the network with data from Section A and using it for predicting settlements occurring in Section A.
2. Using the data recorded from several different tunneling sections or from all tunneling sections for training the network and then applying the network to predict surface settlements in any of those sections.
3. Using the data from the first half of a tunnel drive for training the network and then using the network to predict surface settlements in the second half.

However, it was also found that ANN cannot predict surface settlement well when:

1. Training the network with data from a particular tunneling section but using it for predicting surface settlement in other sections.
2. Using less than the first 50% of data of a tunnel drive for training the network and applying the trained network to predict surface settlements in the remainder of the drive.

Additionally, the significance of some input parameters of the ANN in predicting surface settlements was investigated. Three parameters (i.e. penetration rate, grouting quality, and face pressure) were considered. It was found that face pressure has a more significant effect on surface settlements than the other factors but that all input parameters play a role.

13.3 Recommendations

Having introduced and used ANN in the context of EPB tunneling in Bangkok one can draw a number of practical conclusions. Regarding practice, one is interested to what extent ANN can be used in other tunnel projects in Bangkok and elsewhere:

Other Tunnels in Bangkok

If the tunnel sizes and depths are comparable to what has been done so far and given the fact that all relevant geological conditions were encountered, one can:

- Use the specific ANN (the single tunnel model: Figure 12.21 or the twin-tunnel model: Figure 12.82) with the same input nodes and the same structure, which are developed in this thesis with data contained in the computerized database to predict surface settlements in other tunnel projects in Bangkok.
- Use the specific ANN developed in this thesis with data obtained from the first 50% of a new tunnel section for training the ANN and then applying the trained ANN to predict surface settlements in the remainder of the tunnel section.

Tunnel Projects Elsewhere

(These comments also apply when building tunnels in Bangkok, which are substantially different from what was considered in this thesis.)

With the work in this thesis, one can:

- Realize what parameters are important and should be considered for predicting surface settlements induced by EPB tunneling.
- Apply the same network models developed in this thesis to other EPB tunneling projects elsewhere by beginning with the same input nodes, hidden layers, hidden nodes, and epochs. However, one then needs to apply judgment if the models accommodate all influencing parameters involved in the project, which may be different from the MRTA project, particularly regarding geological conditions.

References

Mair, R. J. and Taylor, R. N. (1997). "Bore Tunneling in the Urban Environment". Theme Lecture, Plenary Session 4, *Proc. 14th Int. Conf. of Soil Mechanics and Foundation Engineering*, Hamburg, Vol. 4, pp. 2353-2385.

VITA

Suchatvee (Vince) Suwansawat was born in Chonburi, an eastern province in Thailand, on April 20, 1972. He spent the first part of his life in Rayong where he graduated first in high school and went on to be enrolled to the “White Elephant” program at the Engineering School of King Mongkut Institute of Technology Ladkrabang, one of the most prestigious technical universities in Thailand. During his undergrad years, he actively engaged himself in many extracurricular activities and went on to become president of the class of 1994.

After graduating with honors in civil engineering in 1995, he came to the US to pursue his graduate degree at the University of Wisconsin-Madison where he worked with Prof. Craig H. Benson in the arena of Geotechnical and Geoenvironmental Engineering. After earning his master’s degree, he came to MIT in 1997. Prof. Herbert H. Einstein became his close advisor and supervised his doctoral research in tunneling. To add invaluable insight into his doctoral research, Suchatvee returned to Thailand from 1999 to 2000 to work as a Geotechnical Engineering specialist in the Bangkok MRTA project. In that time he founded the Young Member Committee of Engineering Institute of Thailand (YMEIT), where he served as its first chairperson. He also became a member of the Geotechnical Engineering Committee of the Engineering Institute of Thailand in 1999.

At MIT he took an interest in a number of fields outside Civil Engineering, including Technology and Policy in which he also earned a Masters Degree. He was also affiliated with the World Bank in the Asia Economy project and was supervised by Prof. Suzanne Berger. He also obtained minors in business management and political economy during his time at MIT. In his free time he loves to read books in history and political science and also enjoys boxing and cooking.

Suchatvee (Vince) Suwansawat
May 2002